Estimation of the Lightning Performance of Transmission Lines with Focus on Mitigation of Flashovers

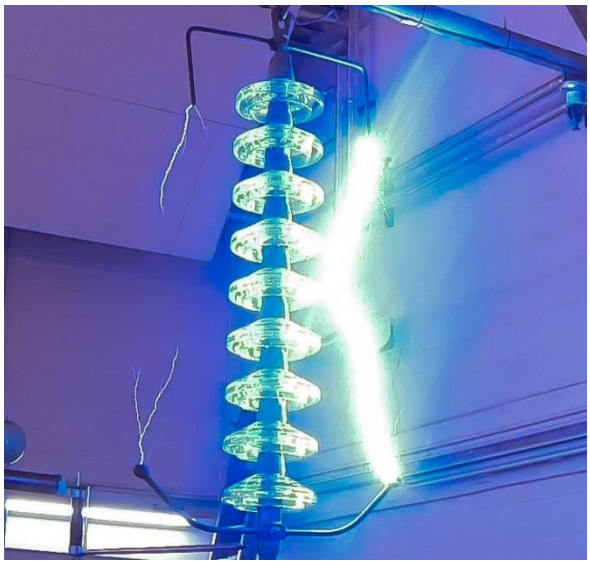

Volume 1 of 2

Fabian Matthias Koehler

Submitted for the degree of Doctor of Philosophy

Heriot-Watt University

School of Engineering & Physical Sciences

Institute of Mechanical, Process and Energy Engineering

August 2018

ABSTRACT

The growth of transmission networks into remote areas due to renewable generation features new challenges with regard to the lightning protection of transmission systems. Up to now, standard transmission line designs kept outages resulting from lightning strokes to reasonable limits with minor impacts on the power grid stability. However, due to emerging problematic earthing conditions at towers, topographically exposed transmission towers and varying lightning activity, such as encountered at the 400 kV Beauly-Denny transmission line in Scotland, the assessment of the lightning performance of transmission lines in operation and in planning emerges as an important aspect in system planning and operations.

Therefore, a fresh approach is taken to the assessment of the lightning performance of transmission lines in planning and construction, as well as possible lightning performance improvements in more detail, based on the current UK/Scottish and Southern Energy 400 kV tower design and overhead line arrangements. The approach employs electro-magnetic transient simulations where a novel mathematical description for positive, negative and negative subsequent lightning strokes, which are all scalable with stroke current, is applied. Furtermore, a novel tower foot earthing system model which combines soil ionisation and soil frequency-dependent effect is used. Novel lightning stroke distribution data for Scotland as well as novel cap-and-pin insulators with arcing horn flashover data derived from laboratory experiments are applied. For overhead lines, transmission towers, and flashover mitigation methods describing their physical behaviour in lightning stroke conditions state-of-the-art models are utilised. The investigation features a variety of tower and overhead line arrangements, soil conditions and earthing designs, as well as the evaluation of various measures to improve the performance. Results show that the lightning performance of a transmission line is less dependent on the tower earthing conditions, but more dependent on the degree of lightning activity and stroke amplitude distribution. The assessment of flashover mitigation methods shows that cost-effective and maintenance free solutions, such as underbuilt wires can effectively replace a costly improvement of the tower earthing system. However, in locations where challenging earthing conditions prevail, tower line arresters or counterpoise are the only options to maintain an effective lightning protection.

ACKNOWLEDGEMENTS

Thanks go to Scottish and Southern Electricity Networks, Perth, Scotland (SSEN) under the OFGEM Network Innovation Allowance (NIA_SHET_0011) for the funding of the PhD and my supervisor Jonathan Swingler for the support during my PhD.

Special thanks go to the High Voltage Laboratory of the University of Manchester for the support of the experiments.

ACADEMIC REGISTRY
Research Thesis Submission

Name*:*	Fabian Matthias Koehler		
School:	School of Engineering and Physical Science		
Version: *(i.e. First, Resubmission, Final)*	First	Degree Sought:	PhD in Electrical Engineering

Declaration

In accordance with the appropriate regulations I hereby submit my thesis and I declare that:

1) the thesis embodies the results of my own work and has been composed by myself
2) where appropriate, I have made acknowledgement of the work of others and have made reference to work carried out in collaboration with other persons
3) the thesis is the correct version of the thesis for submission and is the same version as any electronic versions submitted*.
4) my thesis for the award referred to, deposited in the Heriot-Watt University Library, should be made available for loan or photocopying and be available via the Institutional Repository, subject to such conditions as the Librarian may require
5) I understand that as a student of the University I am required to abide by the Regulations of the University and to conform to its discipline.
6) I confirm that the thesis has been verified against plagiarism via an approved plagiarism detection application e.g. Turnitin.

* *Please note that it is the responsibility of the candidate to ensure that the correct version of the thesis is submitted.*

Signature of Candidate*:*		Date:	

Submission

Submitted By *(name in capitals):*	
Signature of Individual Submitting:	
Date Submitted:	

For Completion in the Student Service Centre (SSC)

Received in the SSC by *(name in capitals):*			
CHAPTER 1 Method of Submission *(Handed in to SSC; posted through internal/external mail):*			
CHAPTER 2 E-thesis Submitted ***(mandatory for final theses)***			
Signature:		Date:	

TABLE OF CONTENTS

VOLUME 1

VOLUME 2

ABBREVIATIONS

AC	Alternating Current
BFOR	Back-Flashover Rate
BS	British Standard
CCSC	Custom Current Source and Conductance Interface
CIGRE	Conseil International des Grands Réseaux Électriques
DC	Direct Current
DSO	Distribution System Operator
EAT	EATechnology
EGM	Electro-Geometric Model
EMF	Electromagnetic Field
EMT	Electro-Magnetic Transient
FEM	Finite Element Method
FOR	Flashover Rate
FTDT	Finite Difference Time Domain
GEQ	Equivalent Conductance Electric Interface
GMR	Geometric Mean Radius
HV	High Voltage
HWU	Heriot-Watt University
IEC	International Electrotechnical Commission
IEEE	Institute of Electrical and Electronics Engineers
LCP	Line Constant Program
LFOR	Line Flashover Rate
LPM	Leader Progression Model
LV	Low Voltage
MCOV	Maximum Continuous Operating Voltage
Mom	Method of Moments
SFFOR	Shielding Failure Flashover Rate
SSE	Scottish and Southern Energy
TEM	Transversal Electromagnetic Mode
TL	Transmission Line
TLA	Tower Line Arrester
TSO	Transmission System Operator

UK	United Kingdom
UoM	University of Manchester

LIST OF PUBLICATIONS

Peer-Reviewed Journals:

F. Koehler and J. Swingler, "Simplified Analytical Representation of Lightning Strike Waveshapes," in *IEEE Transactions on Electromagnetic Compatibility*, vol. 58, no. 1, 2016.

F. Koehler, J. Swingler, and V. Peesapati, "Breakdown Process Experiments of Cap-and-Pin Insulators and their EMT Leader-Progression Model Implementation," in *IET Generation, Transmission & Distribution*, 2017.

F. Koehler, J. Swingler, "Practical Model for Tower Earthing Systems in Lightning Simulations," in *Electric Power Systems Research*, 2018.

Conference Proceedings:

F. Koehler and J. Swingler, "An Evaluation Procedure for Lightning Strike Distributions on Transmission Lines," in *International Conference on Lightning Protection*, 2016.

F. Koehler and J. Swingler, "Unconventional Flashover Mitigation Measures to Improve the Lightning Performance of Transmission Lines," in *International Conference on Resilience of Transmission and Distribution Networks*, 2017.

F. Koehler, J. Swingler, "Analysis of Flashover Mitigation Measures to Improve the Lightning Performance of Transmission Lines," in *International Universities Power Engineering Conference*, 2018.

CHAPTER 1: INTRODUCTION

1.1: MOTIVATION

In general the lightning performance of transmission lines played a secondary role for TSOs and DSOs in day-to-day network operation and transmission line planning in the last decades, although lightning strokes to overhead transmission lines are a major cause for overhead transmission line outages. International statistics show that the unexpected switch-off of transmission lines caused by lightning attributes to approximately 65% of total outages [1]–[3]. However, standard transmission line designs kept outages resulting from lightning strikes to reasonable limits with minor impacts on the power grid stability, but this is subject to change now and in the coming decades. The three main reasons for that are, first, the expected increase in lightning activity as a result of global warming and prospective increase in lightning strokes to transmission lines [4], [5]. Second, the reduction of power grid stability due to the decrease of conventional power generation and transmission in favour of converter-based renewable generation and transmission and resulting increase in sensitivity of the power grid to lightning strokes. Third, the growth of transmission networks into remote areas due to renewable generation, which feature challenging earthing conditions, topographically exposed transmission towers and varying lightning activity. As a result the importance of the lightning performance of transmission lines in operation and in planning is underestimated. Therefore a re-evaluation of existing transmission lines and possible lightning performance improvements and a more-detailed evaluation of the lightning performance of transmission lines in planning and construction with up-to-date methods and tools is necessary.

1.2: OBJECTIVES

The overall objective of this thesis is to investigate the current UK/SSE 400 kV tower design and practice of overhead line arrangements with regard to the lightning performance of a whole transmission line taking into consideration varying lightning activity and low to high soil resistivity. Furthermore, various measures to improve the line performance are evaluated, for both measures compatible with lines in operation as well as future lines to provide guidance to design engineers.

To achieve this goal, the lightning performance of a whole transmission line is assessed with the so-called line flashover rate (LFOR), consisting of back-flashover rate (BFOR) and shielding failure flashover rate (SFFOR). The process of the occurrence of a back-flashover is described with the attachment of a lightning stroke to the uppermost wire on a transmission line tower, called shield wire. This wire is connected to ground via the tower structure and tower earthing system. The primary purpose of this wire is to provide the least resistance path to earth for lightning strokes to an overhead line, thus attracting the lightning and shielding the phase conductors. This maintains an undisturbed operation of the AC system, namely the phase conductors insulated from the tower steel structure through insulator strings. When a tower cannot be sufficiently earthed and the footing resistance is high, e.g. where a tower is built into rock and the soil resistivity is high, the voltage across the insulators may exceed the insulators threshold voltage due to ground potential rise at the tower and voltage wave reflection at the tower foot during lightning stroke conditions. As a result a conducting path between the tower structure (earth) and phase conductors is established, which is called back-flashover. This can result in a short-circuit of the AC system, potentially causing damage to the conductors and insulators in case of high earth fault currents, with the risk of conductor or insulator failure and power outages depending on the time duration of the back-flashover [1], [6], [7]. A shielding failure flashover is the lightning stroke attachment to a phase wire and following flashover of the insulator to the earthed tower structure.

To determine the flashover rate for BFOR and SSFOR with reasonable accuracy related to the real process, computer simulations are utilized. To perform simulations, a simulation model of a transmission line in an electromagnetic transient (EMT) program has to be built, which necessitates a review and development of models of lightning strokes, lines, towers, tower earthing networks, insulators, and arresters, based on state-of-the-art literature and obtained data from field measurements and laboratory experiments.

To perform an evaluation of the various methods to reduce the flashover rate (FOR), simulations have to be conducted for a variety of tower arrangements, soil conditions and earthing designs. Finally a comparison of the different FOR reduction methods with regard to cost-effectiveness, practicality and soil characteristics has to be made to help overhead line design engineers with decision-making in the planning process.

1.3: SOFTWARE

Computer-based lightning stroke simulations to transmission lines are normally performed with an electromagnetic transient program. In this piece of work the EMT program PSCAD/EMTDC is used, which is a renowned power systems computer aided design program, used throughout the power systems industry for lightning overvoltage calculations. The program offers a wide range of models, but also enables programming of custom models. For further information on this program it is referred to [8], [9].

1.4: SAMPLE DATA

Throughout this piece of work, data from a 400 kV transmission line with high tower footing resistance and cap-and-pin glass insulators built through the Scottish Low- and Highlands is taken as an example to fulfill the mentioned objectives and demonstrate the applicability of this work in an industrial context.

1.5: STRUCTURE

The structure of this thesis is informed by the different models needed for the simulation of lightning strokes to transmission lines and evaluation of flashover of insulator strings, which is as follows:

CHAPTER 1: Introduction

specifies the boundaries of this thesis and gives a brief introduction to the issues at hand

CHAPTER 2: The Lightning Flash

deals with the formation of lightning, the engineering approach to describe lightning strokes, obtain suitable local data of lightning distributions, where novel data for Scotland is presented, and the modelling of negative and positive lightning return strokes, where a novel mathematical description of these is described

CHAPTER 3: The Transmission Line

discusses the behaviour of a transmission line under lightning stroke conditions and investigates the different transmission line models used to simulate the effects encountered at high frequencies

CHAPTER 4: The Transmission Line Insulator

explains the flashover process over the arcing horns of an insulator, different models to simulate this process and shows how models can be validated and improved through measurements, which is demonstrated with novel data of cap-and-pin insulators with arcing horns and the derivation of parameter sets for the EMT simulation

CHAPTER 5: The Transmission Tower

investigates various ways of describing the impulse response of transmission towers and compares tower models for the simulation of lightning strokes

CHAPTER 6: Tower Earthing Systems

describes the general behaviour of earthing systems of transmission line towers and the application range of earthing models available in the literature followed by modelling of selected tower earthing systems, which includes a novel model of tower footing with ionization and frequency-dependent effects of soil

CHAPTER 7: Lightning Performance Improvement Measures

investigates several mitigation methods to reduce the number of flash-overs of insulators, including modelling of arresters and earthing improvements

CHAPTER 8: Simulation Methodology of Lightning Strokes to Transmission Lines

presents the simulation methodology and addresses issues not discussed in the previous chapters needed for the full simulation model and deals with the deployment of individual models for the simulations followed by the proposed scenarios

CHAPTER 9: Simulation Results and Evaluation

summarizes novel results and evaluations of the simulations of various 400 kV tower configurations and lightning stroke distributions for Scotland for two methods to determine the line flashover rates

CHAPTER 10: Discussion

presents the contribution and novelty in the field and main findings of this work as well as recommendations for a general procedure to evaluate the lightning performance of a transmission line and specifically for the deployment of the investigated mitigation methods

CHAPTER 11: Conclusion

summarizes the work and highlights the most important findings

CHAPTER 2: THE LIGHTNING FLASH

In the process of developing software models of a lightning stroke, first the formation of lightning is explained in this chapter, followed by the engineering approach to lightning, derived models for simulation of lightning and their mathematical description.

2.1: THE PHYSICS OF LIGHTNING

Up to now there is no conclusive full understanding of how the charge distribution leading to lightning inside thunderclouds is generated [7]. One hypothesis, derived from cloud electric field measurements, suggests that the charge transfer process may involve hydrometeors, more specifically the collision between falling or stationary soft hail particles and upward moving small crystals of ice in the cloud at a temperature range of -10°C to -20°C [10], [11]. An idealized prevalent charge structure in a thundercloud is illustrated in figure 2-1.

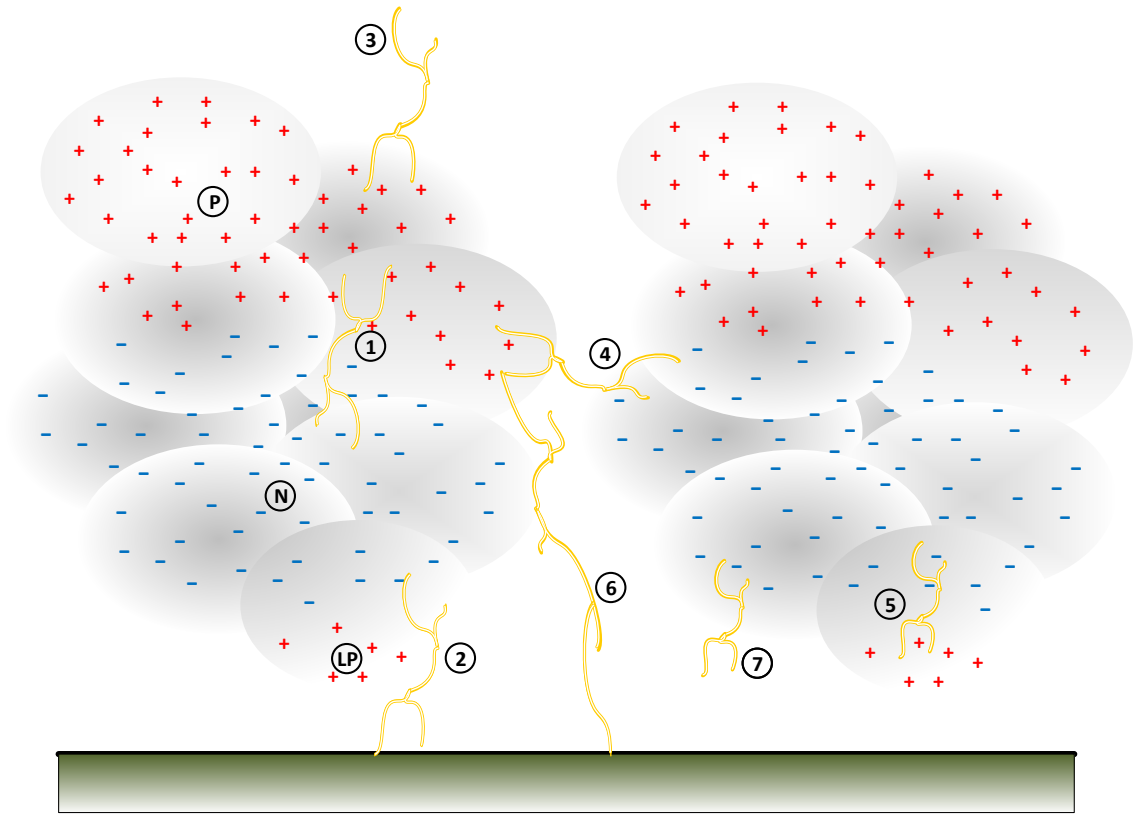

Figure 2-1: Charge structure of two isolated simplified thunderclouds, adapted from [4]

A mature thundercloud comprises a mainly positive charge region (P) in its upper levels, a mainly negative charge region (N) in its lower levels and a lower positive charge region

(LP) at the clouds underside. It has to be noticed that the charge structure of a thundercloud is actually more complex and can also be very different from the illustrated tripole model as it varies from storm to storm, for instance the negative charge region may be at the upper level and positive charge region at lower level. [10]

In some small regions, where the potential between the main charge regions, or the so-called electric field strength, is high enough, a fraction of the drifting electrons will have enough energy and velocity for collision ionization of air particles, starting with a "seed" electron. The "seed" electron may be supplied by high-energy cosmic ray particles, ultra-violet light or simply by collision between the rapidly rising air molecules and the slower ice crystals. This ionization process leads to the generation of additional electrons, which may also ionize air, hence continuing the process alongside with the increase of the ionization rate. However, the process has to compete with the loss of electrons due to attachment. If the ionization rate increases rapidly enough to surpass the attachment rate at the conventional breakdown field, an avalanche of electrons is formed. If the number of electrons at the tip exceeds a value of $N_e \approx 10^6 \ldots 10^8$ the electric field at the front of the avalanche is locally enhanced in comparison to the surrounding base electric field E_0 as a result of the separation of slower positive and faster negative charge carriers. This electric field leads to an increased ionization and photoionization, which generates "seed" electrons for leading and lagging secondary avalanches, as illustrated in figure 2-2 [12].

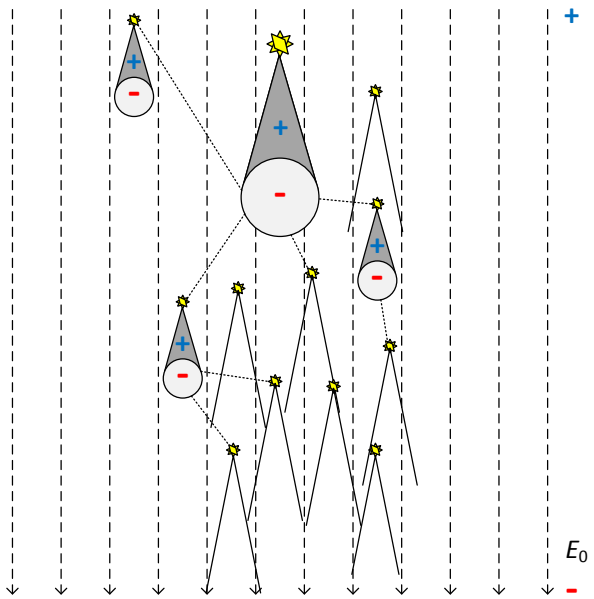

Figure 2-2: Illustrative description of streamer mechanism

This multitude of avalanches then forms a conducting path, which is called a "streamer". Through the leading secondary avalanches in front of the negative streamer and the enhanced electric field, the streamer is able to propagate into lower electric field ambient. When a streamer propagates through a strong base electrical field, the charge at the tip may become large enough to lead to multiple streamers forming a network of streamer branches. The current flow in these branches may be high enough to heat the surrounding air and subsequently increase the current flow in a continually repeating process constricting the current along a narrow hot channel, which is called "leader". These highly conductive leaders themselves produce large electric fields at their tips, which further results in the propagation of streamers in front of them and allow the delivery of current and heat to the leader [10], [13]. Observations show that the propagation of negative leaders is performed in a stepwise fashion. To enable the leader to move forward, a newly formed "space leader" in front of the old leader has to connect to the old leader channel out of the preceding corona streamer. In the initial moment the leaders connect, a potential equalisation occurs, triggering the propagation of a burst of streamers in front of the space leader tip and repeat the described cycle. When the leader connects to a charge region of opposite polarity a lightning is initiated as a result potential equalization of the two charge regions. A number of possible lightning discharge locations is marked in figure 2-1, which are (1) intra-cloud positive, (2) cloud-to-ground negative, (3) cloud-to-air positive, (4) inter-cloud, (5) intra-cloud negative, (6) cloud-to-ground positive, (7) cloud-to-air negative.

The attachment process of the most typical negative cloud-to-ground lightning leader may be described as follows (see also figure 2-3, (a) to (d)) although this process is not comprehensively understood up to now [14]. In the literature the common understanding is that the attachment process of the downward leader to ground starts with the initiation of an upward leader of opposite polarity from ground in response to the downward leader. In the break-through phase, the up- and downward streamer zones ahead of the leaders form a common streamer zone, where the leaders or plasma channels connect. The channel's connection causes high currents to flow into the ground and produces a luminous light of the channel at the ground. The channel current and luminosity propagate continuously up the channel, which is called "first return stroke". However the movement of electrons is always down the channel, representing the main component of current, injected into the ground or ground connected objects [4].

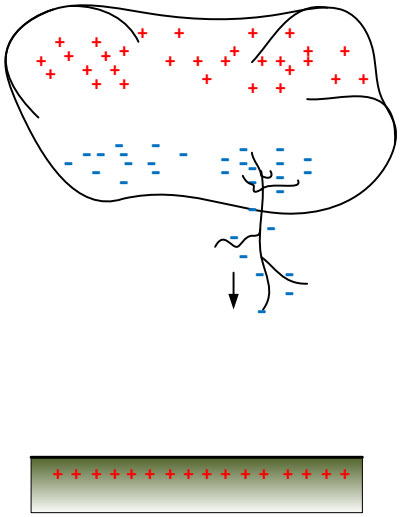

a) Downward stepped leader propagation

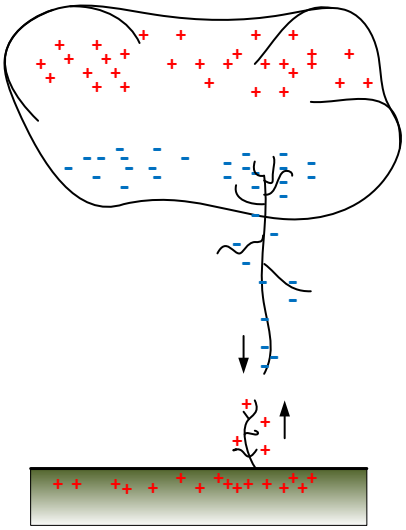

b) Upward leader propagation

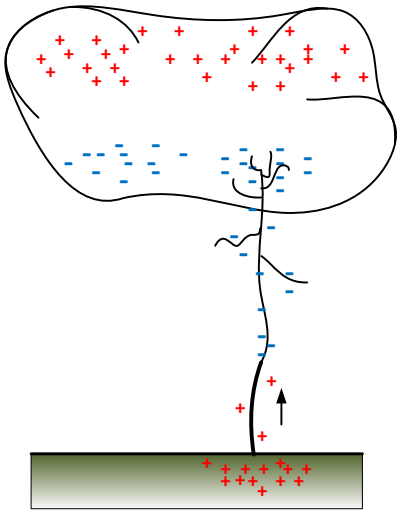

c) First return-stroke initialization

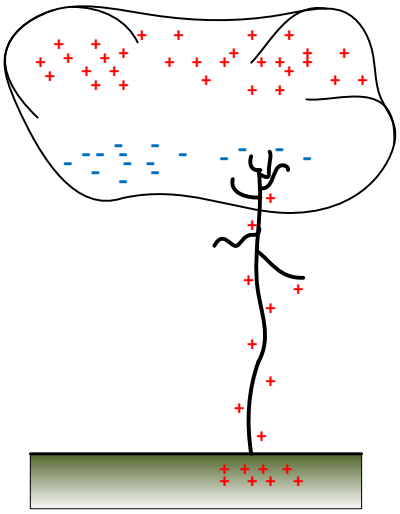

d) First return-stroke

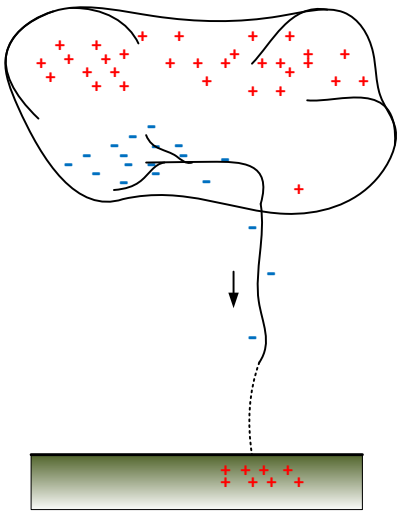

e) Dart leader initialization

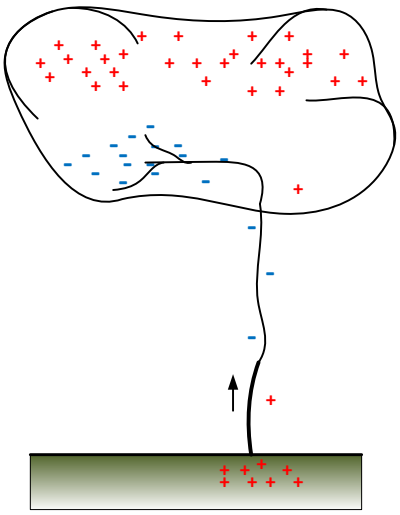

f) Second (subsequent) return-stroke

Figure 2-3: Development of a negative cloud-to-ground flash, adapted from [10]

If the lightning flash ends after the first stroke, then it is called a single lightning flash. However in most of the cases a flash contains more than one stroke, so-called "subsequent strokes". If another negative charge region in the cloud connects via the described streamer-leader process to the previous stroke channel as depicted in figure 2-3 (e) a subsequent stroke is initiated. This conducting path of the previous stroke channel, basically consisting of ionized air, only remains for a short time interval of about 100 ms after cessation of the current of the previous stroke [10]. In contrast to the first stroke, the leader propagates continuously along the defunct previous return-stroke channel, called dart leader, followed by the return-stroke (see figure 2-3 (f)).

The lightning charge brought to ground can be divided into three modes of charge transfer [15]–[17], illustrated in figure 2-4. First, the return stroke (figure 2-4 (a)), second the continuing current (figure 2-4 (b)) and third the M-component (figure 2-4 (c)) [17]. Continuing currents may be seen as a quasi-stationary arc between the cloud charge region and the ground and amount to hundreds of amperes with duration of up to hundreds of milliseconds. M-components can be viewed as surges in the continuing current, and may be originated from the superposition of propagating waves in the lightning channel. [18]

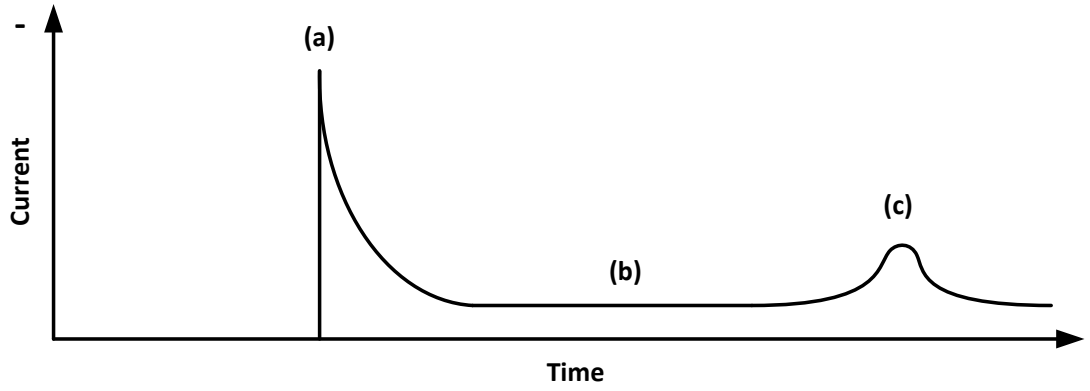

Figure 2-4: Modes of charge transfer of a negative cloud-to-ground lightning stroke

The above explained negative cloud-to-ground lightning flash is not the only type, since four types of flashes can be distinguished as shown in figure 2-5 [19].

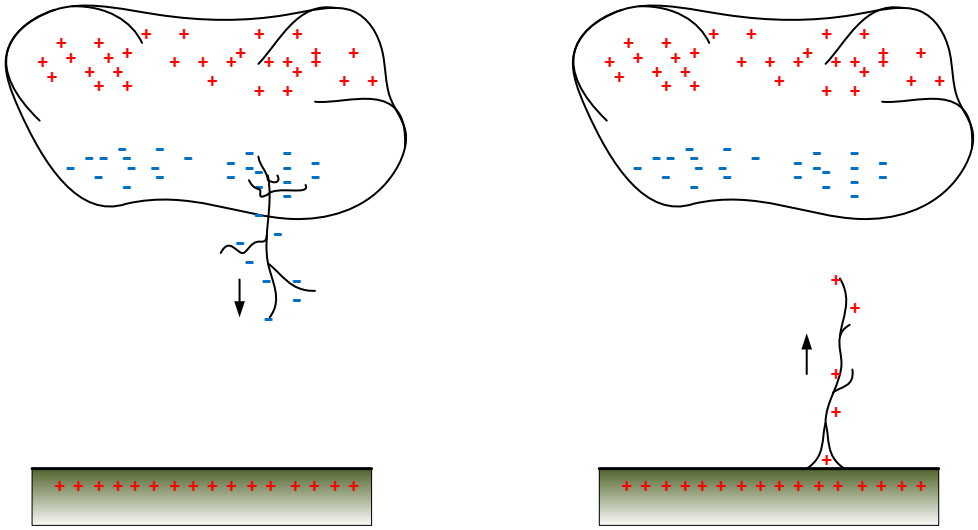

a) Downward lightning negatively-charged leader **b) Upward lightning positively-charged leader**

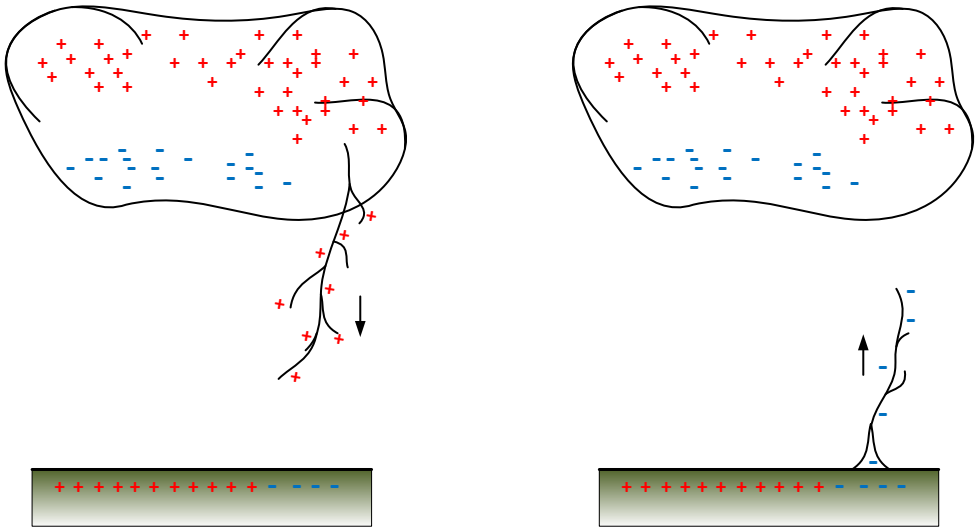

c) Downward lightning positively-charged leader **d) Upward lightning negatively-charged leader**

Figure 2-5: Types of cloud-to-ground lightning flashes, adapted from [19]

As already mentioned the most common is the downward lightning negatively-charged leader (figure 2-5 (a)), which accounts for approximately 90% and more of the global lightning flashes and less than 10% are downward lightning positively-charged leaders (figure 2-5 (c)). It is assumed that upward lightning only occurs from tall objects or objects on mountain tops [19]. As cloud-to-ground lightning strokes pose the greatest thread to transmission lines and apparatus due to high current crests, wavefront steepness and charge transfer, investigations on lightning strokes are concentrated on these stroke types [20]. Since this thesis aims to evaluate the flashover behaviour of the overhead line insulators during a lightning stroke, the previous mentioned continuing currents and M-components are not considered further.

2.2: THE ENGINEERING APPROACH TO LIGHTNING

After giving a short description of the lightning stroke mechanism, the engineering approach to lightning in the context of electric power systems is presented in this section. The main goal of the engineering approach is to examine the important characteristics of a lightning cloud-to-ground return-stroke at its point of connection to an object and find a suitable mathematical description of the lightning flash to study the impact of lightning on electrical equipment, in this case transmission lines [7].

The major groundwork for the lightning current impulse characteristics was conducted by Berger, who performed measurements at a pylon at the top of Mt. San Salvatore (Switzerland). From the manually evaluated 1296 recorded flashes of first and subsequent strokes Berger et. al. produced a first summary of impulse parameters, statistical distribution and correlations amongst various parameters [21]. Anderson and Eriksson re-examined the later digitalized flash data to find a better representation of front wave shapes of lightning flashes alongside with additional correlations and parameter distributions [22], [23]. Berger's, Anderson and Eriksson's as well as work from others was discussed in the CIGRE Working Group 33.01 for Lightning and consolidated in a "Guide to Procedures for estimating the Lightning Performance of Transmission Lines"[24]. Up to now, this guide remains a fundamental reference for parameters for lightning investigations, where Berger's data is the main source. More recently, an update on the subject was released by CIGRE Working Group C4.407, "Lightning Parameters for Engineering Applications", which evaluates recent direct current measurements from towers and rocket-triggered lightning, as well as the old data, to give recommendations on their applicability on engineering applications [18], [25]–[31]. All over the world, direct current measurements as well as electric field measurements of lightning flashes are still ongoing, as the overall consensus of researchers is that more data is needed to improve the understanding and modelling parameters of lightning.

The most important parameters to assess the severity of lightning strokes to power lines and apparatus are the lightning return-stroke current and the charge delivered by the lightning flash. The return-stroke current is described by its peak and waveshape, in which the waveshape is specified by the front time, defined as the time from zero to peak, and the subsequent tail time, specified as the decay from crest to half value. [32]

2.2.1: NEGATIVE DOWNWARD FLASH WAVESHAPES

As most lightning strokes are negative downward flashes, and thus there is a significant number of direct current measurement data available, the analysis of these features the most reliable waveshapes and parameters. A typical current waveshape of a negative downward first stroke is shown in figure 2-6.

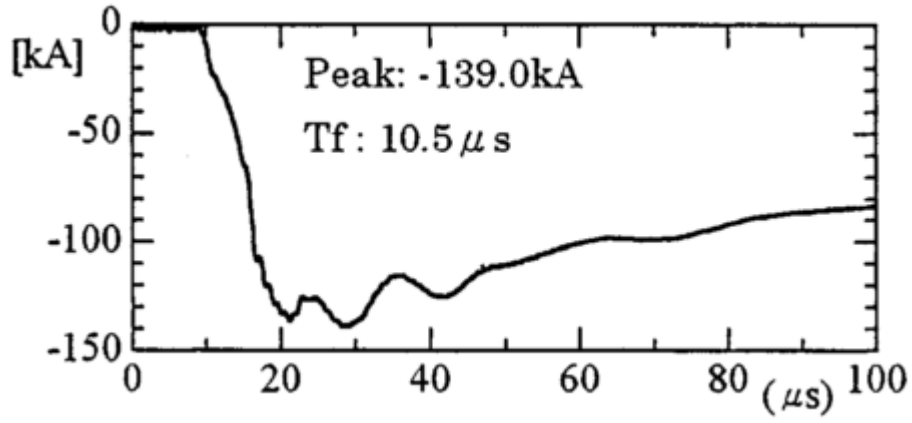

Figure 2-6: **Typical current oscillogram of a negative downward stroke, crest current 139 kA** [26]

Negative downward first strokes are characterized by a slow concave rise, followed by a steep rise to its crest value. An idealized wave form of a negative impulse, describing the defined parameters by Anderson [23] is depicted in figure 2-7.

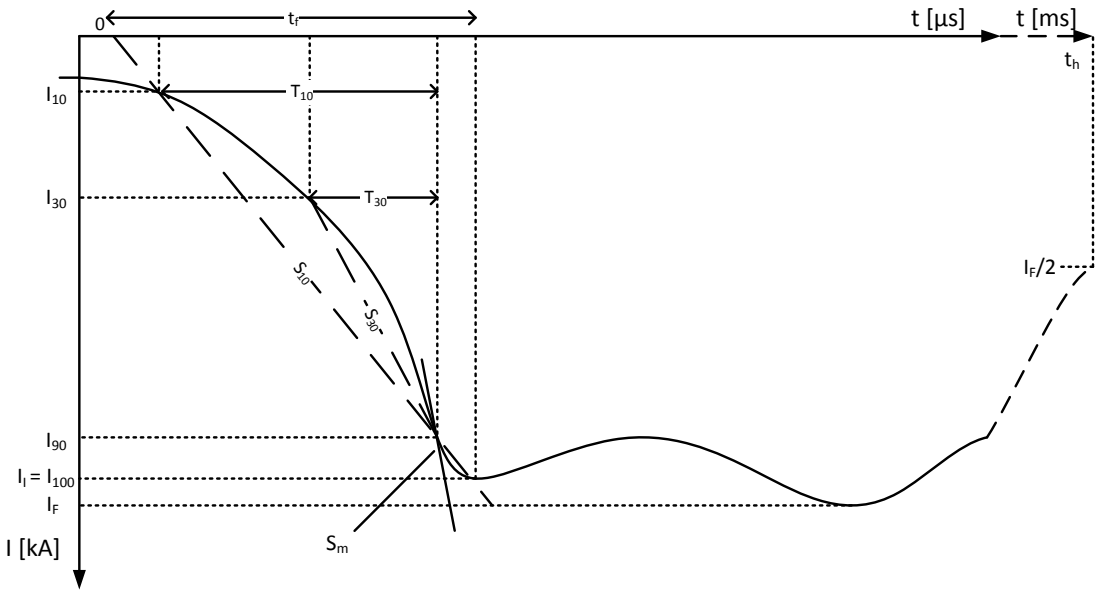

Figure 2-7: **Definition of impulse-front parameters for a negative downward stroke, adapted from** [23]

Here the 90% (I_{90}) amplitude on the wavefront is used to define most of the parameters, which are:

t_f: the wavefront duration, expressed as the interval between the virtual 0 to the intersection of the straight line connecting 10% (I_{10}) and 90% (I_{90}) amplitude intercept on the wavefront

T_{10}: the wavefront duration, expressed as the interval between the 10% (I_{10}) and 90% (I_{90}) amplitude intercept on the wavefront

T_{30}: the wavefront duration, expressed as the interval between the 30% (I_{10}) and 90% (I_{90}) amplitude intercept on the wavefront

S_{10}: the average current steepness or rate of rise of current between the 10% (I_{10}) and 90% (I_{90}) amplitude intercepts

S_{30}: the average current steepness or rate of rise of current between the 30% (I_{30}) and 90% (I_{90}) amplitude intercepts

S_{m}: the maximum rate of rise of current on the wavefront

I_I: initial/first peak of current

I_F: crest (second) peak of current

Additionally the following parameters are of importance for later use:

t_h: time interval from 2 kA on wave front to 50% of crest value (I_F) on the wavetail

$t_{\mathrm{m}} = \frac{I_{\mathrm{F}}}{S_{\mathrm{m}}}$: minimum equivalent front or time-to-crest

t_d: equivalent front time, either $t_{\mathrm{d10}} = \frac{T_{10}}{0.8}$ or $t_{\mathrm{d30}} = \frac{T_{30}}{0.6}$

In contrast to negative first downward strokes, negative downward subsequent strokes are characterized by a steep rise to the crest value and do not feature the slow concave rise, as depicted in figure 8-18. This is attributed to the already existing conducting path to earth formed by the first stroke.

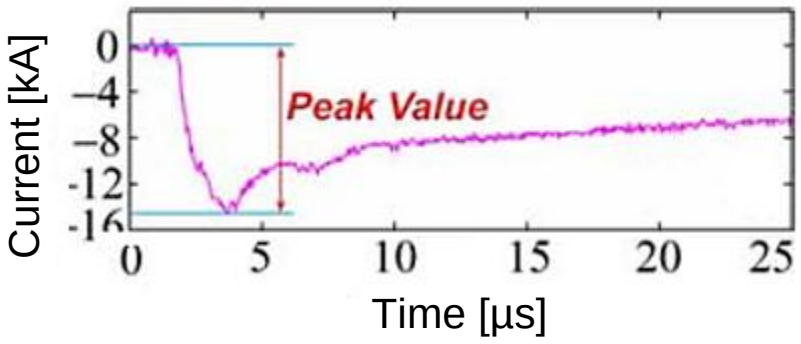

Figure 2-8: **Typical triggered lightning return-stroke current waveform, similar to subsequent stroke** [33]

An idealized waveshape of a subsequent negative downward stroke is illustrated in figure 2-9, following the recommendation in [24] to neglect S_{30} or t_{d30}.

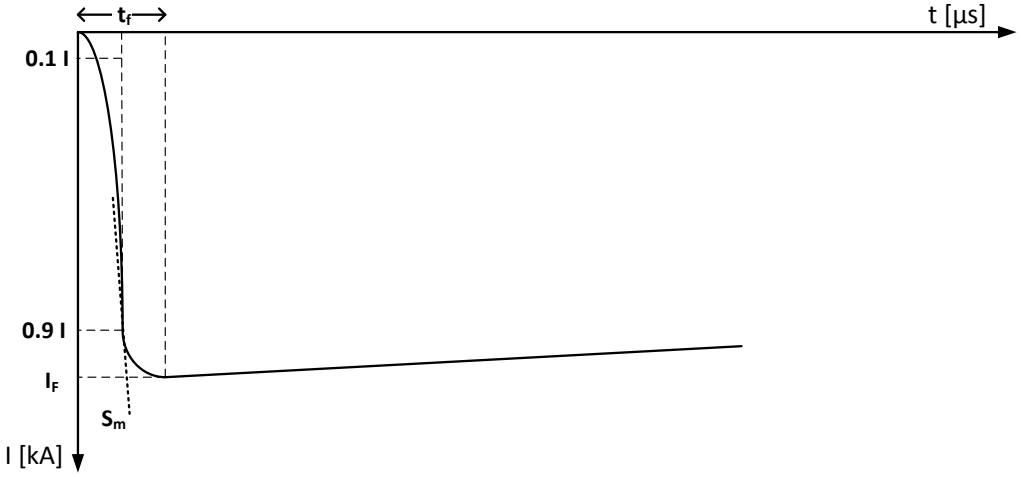

Figure 2-9: **Definition of impulse-front parameters for a subsequent negative downward stroke**

2.2.2: NEGATIVE DOWNWARD FLASH PEAK CURRENTS

As lightning is random in its nature, flash parameters must be expressed in probabilistic terms extracted from data measured in the field. Therefore parameters of a flash are described with a log normal distribution with the probability density function,

$$f(x) = \frac{1}{\sqrt{2\pi}\beta x}\, e^{-\frac{1}{2}\left(\frac{ln\left(\frac{x}{M}\right)}{\beta}\right)^2}. \qquad (2.1)$$

Where M is the median and β is the log standard deviation, where median means that 50% of the observations are above a certain value x. The median value can be calculated from the geometric mean of n values in formula (2.2) and the log standard deviation from the geometric standard deviation in formula (2.3).

$$M = e^{\frac{1}{n}\sum_{i=1}^{n} ln(x_i)} = e^{\mu} = GM \tag{2.2}$$

$$\beta = \sqrt{\frac{\sum_{i=1}^{n}(\ln(x_i)-\mu)^2}{(n-1)}} \tag{2.3}$$

In [18], a summary of return-stroke peak currents for first strokes is provided, which shows that distributions from all over the world can differ very much. Furthermore, it is mentioned that local distributions of return-stroke peak currents can be significantly different from regional or global distributions. In table 2-1 recommended parameters from [24] for the log normal distribution of the final crest current and division into shielding failure (stroke to phase wire) and backflash over (stroke to ground wire) domain for first negative downward strokes are listed. It has to be noted, that the authors from [18] argue that these parameters inherit some less accurate indirect measurements of "questionable quality", but […]"since these "global" distributions have been widely used in lightning protection studies and are not much different (within 20% for currents up to 40 kA and within 40% for currents up to 90 kA for the CIGRE distribution) from that based on direct measurements only"[…][18] (Berger et al.'s distribution [21]), they still recommend their use. For subsequent strokes, parameters from [21] are recommend by [18], which are based on direct current measurements only.

Table 2-1: Current parameters of log-normal distribution for negative downward strokes, adapted from [21], [24]

Parameter	First Stroke		Subsequent Stroke	
	M	β	M	β
I_F, final crest in kA [24]	31.1	0.484	12.3	0.530
Shielding Failure $I_F < 20$ kA [24]	61	1.33	-	-
Backflash $I_F > 20$ kA [24]	33.3	0.605	-	-
I_F, final crest in kA [21]	30	0.6102	12	0.6102

From equation (2.4) and (2.5) the probability of a peak current exceeding a certain value can be calculated with the parameters from table 2-1. $\phi(z)$ is the cumulative distribution function of the standard normal distribution.

$$P(X < x) = \int_x^{\infty} \frac{1}{\sqrt{2\pi}\beta x}\, e^{-\frac{1}{2}\left(\frac{ln\left(\frac{x}{M}\right)}{\beta}\right)^2} dx. \tag{2.4}$$

$$P(X > x) = 1 - \phi(z) \text{ with } z = \frac{ln\left(\frac{x}{M}\right)}{\beta} \tag{2.5}$$

A summary of probability limits is presented in table 2-2. The corresponding cumulative statistical distribution of negative downward flash peak currents of first and subsequent strokes with parameters from table 2-2 is plotted in figure 2-10 for percent of cases exceeding abscissa values. Relationship of first and subsequent strokes are derived from stroke counts in different locations around the world, which show an average of 3 to 5 negative cloud-to-ground strokes per flash [29], [34], [35], whereas the geometric mean interstroke interval, which is usually measured between the peaks of current, is approximately 60 ms [15], [36]. Typically subsequent strokes are 2 to 3 times smaller than first strokes. However it is reported in literature, that one third of subsequent strokes contains a stroke with a 200% increase in crest value in comparison to first strokes [18].

Table 2-2: Selected probabilities of log-normal distributions for negative downward strokes, adapted from [21], [24]

Distribution	P(I > 50 kA) in %	P(I > 100 kA) in %	P(I > 200 kA) in %
Berger, first stroke ($M = 30$ kA, $\beta = 0.61$)	20.1	2.4	0.09
CIGRE, first stroke ($M = 31.1$ kA, $\beta = 0.484$)	16.3	0.8	0.0006
CIGRE, first stroke, domains ($M = 61$ kA, $\beta = 1.33$ for $I < 20$ kA and $M = 33.3$ kA, $\beta = 0.605$ for $I > 20$ kA)	25.1	3.4	0.15
Berger, subsequent stroke ($M = 12$ kA, $\beta = 0.61$)	0.1	-	-
CIGRE, subsequent stroke ($M = 12.3$ kA, $\beta = 0.53$)	0.4	-	-

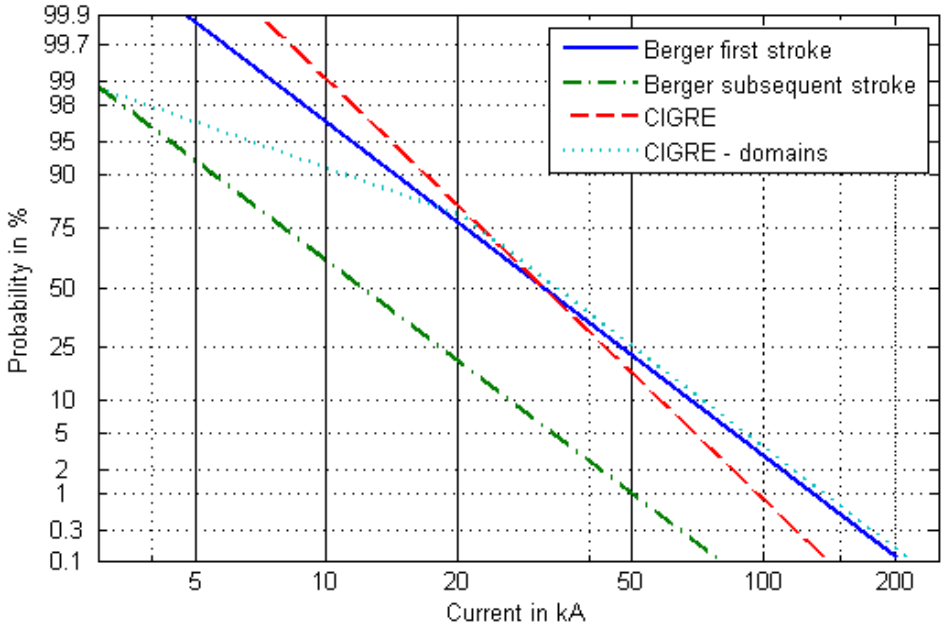

Figure 2-10: **Cumulative statistical distribution of peak currents for first and subsequent negative downward strokes exceeding abscissa values for log normal distributions in table 2-2**

From table 2-2 it can be concluded that the two-part CIGRE distribution is the most conservative for lightning over-voltage calculations with regard to the probability of maximum stroke currents.

2.2.3: NEGATIVE DOWNWARD FLASH PEAK CURRENT CORRELATED PARAMETERS

To obtain correlations amongst various parameters from measurement data, a regression analysis can be performed assuming linear regression of the form

$$y_{mc} = a \cdot x^b \text{ or } \ln y_{mc} = a + b \cdot \ln x \tag{2.6}$$

with the peak current amplitudes as the independent variables. From the correlation parameter ρ_C, the cumulative distribution median M (denoted with index m) and the log standard deviation in the form $\sigma_{ln} = \frac{\beta}{\ln 10}$, conditional distributions of parameters in the form $y|x$ can be calculated with equation (2.7) to (2.9).

$$\ln a = \ln y_m - \rho_C \frac{\sigma_{\ln y}}{\sigma_{\ln x}} \ln x_m \tag{2.7}$$

$$b = \rho_C \frac{\sigma_{\ln y}}{\sigma_{\ln x}} \tag{2.8}$$

$$\sigma_{\ln y|x} = \sigma_{\ln y}\sqrt{1 - {\rho_C}^2} \tag{2.9}$$

Various regression analysis of direct current measurements of natural and rocket-triggered lightning has indicated, that there exists

- no correlation between first and subsequent stroke peak current amplitudes [23],
- a significant correlation between S_m, S_{30} and peak current amplitude I_F [23], [25], [26], [28], [37],
- a weak correlation between first and subsequent stroke peak current amplitudes I_F [18], [21],
- no correlation between peak current amplitude and rise-time (rocket-triggered lightning) [25], [26], [30], [37], [38]
- a significant correlation between charge transfer up to 100 µs for first strokes, 50 µs for subsequent strokes and their respective current peak amplitude [39].

However, obtained correlations through regression analysis differ in their value, which may be related to different measurement methods and settings and regional and seasonal variations of lightning discharges [18]. In [18] concerns are brought forward, that Berger's data, which is the main source for lightning parameters in [24], underestimates the maximum current steepness due to the measurement method. This is supported by measurements on 500 kV transmission line towers in Japan [25]. In table 6-3, a summary of derived distribution parameters for the maximum steepness S_{m}, S_{30} and S_{10} is provided. Although the index "F" is denoted to the overall current crest value, the distribution of first peak values I_{100} is used to calculate the derived distributions.
Generally, the rate of rise as well as correlation derived from tower measurements in [25] is higher than those from Anderson and CIGRE, mostly derived from Berger's measurements.

Table 2-3: Summarized derived distribution parameters of rate of rise of first negative downward strokes, (1) 3 kA ≤ I ≤ 20 kA, (2) I > 20 kA

	$S_m \mid I_F$ in $\frac{\text{kA}}{\mu\text{s}}$	ρ_C	$S_{30} \mid I_F$ in $\frac{kA}{\mu s}$	ρ_C	$S_{10} \mid I_F$ in $\frac{kA}{\mu s}$	ρ_C
Anderson [23]	$3.9 \cdot I_F^{0.55}$	0.423	$3.2 \cdot I_F^{0.25}$	0.185	$1.24 \cdot I_F^{0.42}$	0.3
CIGRE [24]	$12 \cdot I_F^{0.171}$ (1) $6.5 \cdot I_F^{0.376}$ (2)	0.43	$0.565 \cdot I_F^{0.812}$ (1) $1.1 \cdot I_F^{0.589}$ (2)	0.19	$1.24 \cdot I_F^{0.42}$	0.3
Takami [25]	$1.27 \cdot I_F^{0.81}$	0.846	$0.72 \cdot I_F^{0.75}$	0.787	$0.372 \cdot I_F^{0.827}$	0.83

In comparison to the above, the degree of correlation of rise time and peak value is vice versa for the derived distribution parameters t_{30} and t_{10}, listed in table 2-4. As a result of the higher steepness value of S_{30} in [25], the rise time t_{30} is lower than in [23] and [24]. However, when t_{10}-values are compared, the rise time in [25] is longer than in [23] and [24].

Table 2-4: Summarized derived distribution parameters of rise time of first negative downward strokes, (1) 3 kA ≤ I ≤ 20 kA, (2) I > 20 kA

	$t_{30} \mid I_F$ in μs	ρ_C	$t_{10} \mid I_F$ in μs	ρ_C
Anderson [23]	$0.526 \cdot I_F^{0.444}$	0.47	$0.855 \cdot I_F^{0.5}$	0.4
CIGRE [24]	$1.77 \cdot I_F^{0.188}$ (1) $0.906 \cdot I_F^{0.411}$ (2)	0.45	$2.209 \cdot I_F^{0.173}$	0.4
Takami [25]	$1.98 \cdot I_F^{0.143}$	0.223	$2.39 \cdot I_F^{0.209}$	0.345

The global variation of parameters can also be seen in the half-time value in table 2-5, where data from Berger (Switzerland) [21], CIGRE (mostly Switzerland and Africa) [24] and Visacro (Brazil) [30] are compared.

Table 2-5: Summarized half-time t_h (trigger value to half –peak on wavetail) of first negative downward strokes

	Percent of cases exceeding tabulated values in µs		
	95%	50%	5%
Berger [21]	30	75	200
CIGRE [24]	30	77.5	200
Visacro [30]	19.7	53.5	145.2

Another important parameter is the charge brought to ground through the return-stroke. For first strokes information about charge transfer is limited to the measurement data from Berger, summarized in table 2-6. There, it is distinguished between the flash charge, which is the total charge transferred by a flash, the impulse charge, which is the charge transported by the rapidly changing part of the stroke (normally up to 2 ms excluding continuing currents) and the stroke charge, which is the total charge of a stroke (impulse charge together with any charge transported by continuing currents) [21].

Table 2-6: Summarized derived distribution parameters of charge of first negative downward strokes

	$Q\|I_F$ in C	β	ρ_C
Impulse Charge first 100 µs [39]	$0.061 \cdot I_F$	-	0.94
Impulse Charge [21]	$0.918 \cdot I_F^{1.14}$	0.578	0.77
Stroke Charge [21]	$0.22 \cdot I_F^{0.929}$	0.737	0.61
Flash Charge [21]	$0.35 \cdot I_F^{0.9}$	0.856	0.54

From the correlation parameter ρ_C in table 2-6, it can be concluded that the correlation is weakened with increasing time span, since $Q = \int I(t)\, dt$. This may be explained with the variation in wavetail time and continuing current along with the likelihood of subsequent strokes.

The regression analysis results for subsequent strokes are shown in the following. A summary of steepness parameters is given in table 2-7.

Table 2-7: Summarized derived distribution parameters of rate of rise of subsequent negative downward strokes

	$S_m\|I_F$ in $\frac{\text{kA}}{\mu\text{s}}$	ρ_C	$S_{30}\|I_F$ in $\frac{kA}{\mu s}$	ρ_C	$S_{10}\|I_F$ in $\frac{kA}{\mu s}$	ρ_C
Anderson [23]	$3.8 \cdot I_F^{0.93}$	0.56	$6.9 \cdot I_F^{0.42}$	0.23	$3.85 \cdot I_F^{0.55}$	0.31
CIGRE [24]	$4.17 \cdot I_F^{0.93}$	0.56	$7.1 \cdot I_F^{0.42}$	0.23	$3.85 \cdot I_F^{0.55}$	0.31
Visacro [30]	$7.57 \cdot I_F^{0.49}$	0.383	$7.88 \cdot I_F^{0.41}$	0.309	$7.19 \cdot I_F^{0.35}$	0.239

The correlation between steepness and current peak of negative subsequent strokes features partly the same properties. For steepness parameters S_{10} and S_{30} the results are

very similar, but differ much for steepness parameter S_m, where the maximum steepness from Visacro [30] is only half the steepness from CIGRE [24] and Anderson [23].

As already mentioned, there exists no remarkable correlation between rise time and current crest value [23], [24].

The half-time values in table 2-8 of subsequent strokes are smaller than of first strokes due to the faster rise to the current crest value. The same variability, with regard to different measurement methods and settings, and regional and seasonal variations, as for first strokes can also be encountered in subsequent strokes.

Table 2-8: Summarized half-time t_h (trigger value to half –peak on wavetail) of subsequent negative downward strokes

	Percent of cases exceeding tabulated values t_h in µs		
	95%	50%	5%
Berger [21]	6.5	32	140
CIGRE [24]	6.5	30.2	140
Visacro [30]	2.2	16.4	122.3

Negative downward lightning charge measurements are not limited to direct current measurements only, but can also be obtained by triggered-lightning [33], [38]. Therefore a great number of measurement data is available to supplement the data from Berger [21]. A summary of derived parameters is listed in table 2-9.

Table 2-9: Summarized derived distribution parameters of charge of subsequent negative downward strokes

	$Q\|I_F$ in C	β	ρ_C
Impulse Charge first 50 µs [39]	$0.028 \cdot I_F$	-	-
Impulse Charge first 50 µs [40]	$0.027 \cdot I_F$	-	0.92
Impulse Charge [21]	$0.081 \cdot I_F^{.988}$	0.632	0.69
Stroke Charge [21]	$0.156 \cdot I_F^{0.883}$	1.131	0.43
Variable Charge up to 1 ms [40]	$0.0068 \cdot t^{0.39} \cdot I_F$	-	0.99 – 0.7

As already discussed for first strokes, the correlation between charge and crest current amplitude is weakened with increasing time span of current integration. Therefore a

prediction of total charge within the time span of 60 ms until a subsequent stroke occurs may inherit greater uncertainty. Also the associated continuing current of a stroke may amount an eligible charge, depending on the time span, as depicted in figure 2-11. There, the dependency of the duration of continuing current on peak current is plotted for 248 negative and 9 positive strokes. From the plot, it can be derived that peak currents greater 20 kA feature a continuing current duration less than 40 ms and peak currents smaller 20 kA a continuing current duration up to 350 ms.

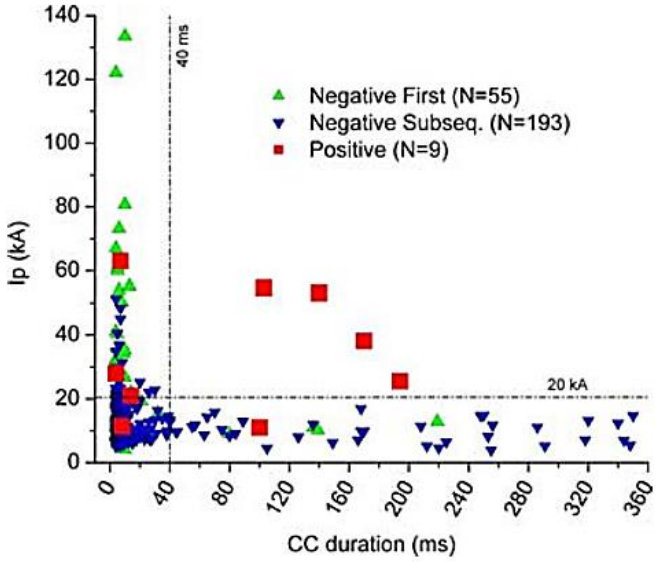

Figure 2-11: Peak current versus continuing current duration [41]

With regard to the number of negative subsequent strokes following a first negative stroke, [18], [35] give summaries of counts of strokes per flash and percentage of single strokes in various locations of the world. The percentage of single strokes ranges from 13% to 21%, in which the value of 39% from Berger [21] is excluded due to the note in [18], that Berger's value is highly overestimated. Furthermore, the average number of strokes per flash is in the range of 3 to 6.

2.2.4: POSITIVE DOWNWARD FLASH WAVESHAPES

Positive lightning strokes to ground globally attribute less than 10% to the total number of lightning flashes [24]. Up to now the main source for positive flashes are Berger's 26 direct current measurements, where separation of up- and downward flashes is not clear [19]. Due to the limited number of direct current measurements, derived parameters have to be dealt with caution [18]. Therefore nowadays, data from electric field measurement stations is used to improve the knowledge about positive lightning strokes [42], [43].

A typical current waveshape of a positive first stroke is shown in figure 2-12.

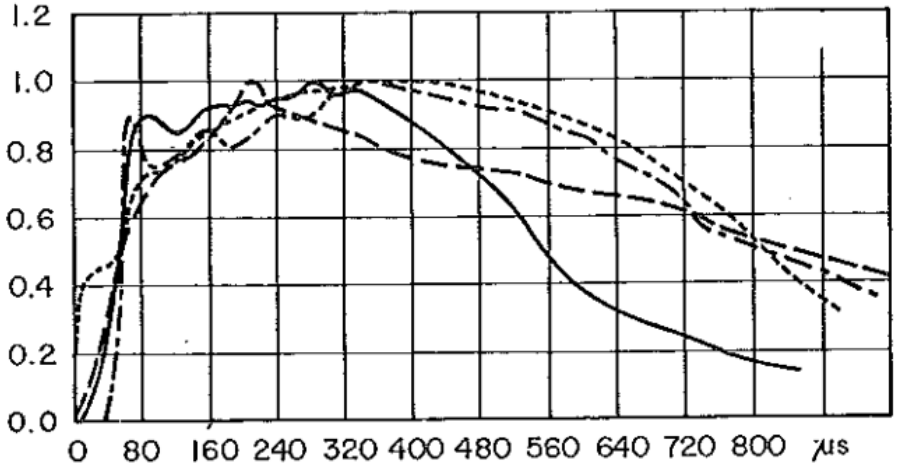

Figure 2-12: Typical current oscillogram of four positive downward strokes, normalized crest current [21]

Positive strokes do not feature an acceptable mean common waveshape, as depicted in the four examples in figure 2-12 [21]. Therefore waveforms and stroke parameters have either to be assumed or adapted from direct current or electric field measurements.

2.2.5: POSITIVE DOWNWARD FLASH PEAK CURRENTS

From Berger's data, the log-normal distribution for positive strokes is listed in table 2-10, alongside with the probability curve in figure 2-13 and selected calculated probabilities for peak currents in table 2-11.

Table 2-10: Current parameters of log-normal distribution for positive strokes, adapted from [21]

Parameter	First Stroke	
	M	β
I_F, final crest in kA [21]	35	1.195

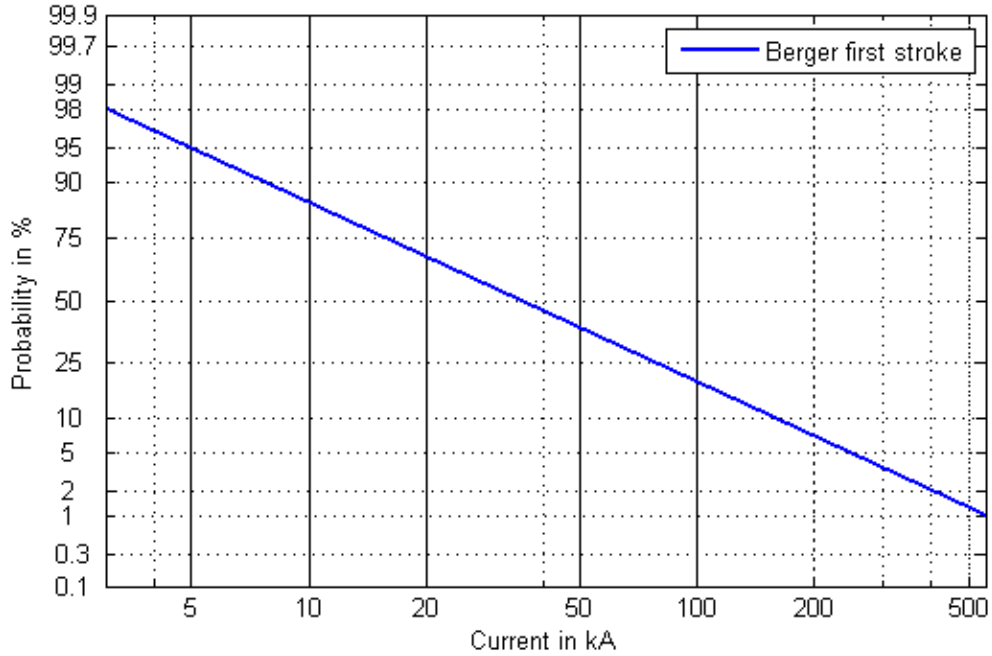

Figure 2-13: Cumulative statistical distribution of peak currents for positive strokes exceeding abscissa values for log normal distributions in table 2-10

Table 2-11: Selected probabilities of log-normal distributions for positive strokes, adapted from [21]

Distribution	P(I > 50 kA) in %	P(I > 100 kA) in %	P(I > 200 kA) in %	P(I > 550 kA) in %
Berger, first stroke ($M = 35$ kA, $\beta = 1.195$)	38.2	18.9	7.2	1.0

As can be derived from the probability of log-normal distributions for positive strokes, positive strokes feature the highest lightning currents. In [44], positive strokes to measurement towers in Japan are reported with peak current amplitudes up to 340 kA, alongside with the highest charge transfer to ground (up to 400 Coulomb). Also positive strokes are mostly of single stroke nature for a stroke objects, because positive strokes generally feature separate channels to ground for subsequent strokes. Additionally, positive strokes tend to be followed by continuing currents, lasting from tens to hundreds of milliseconds with currents up to tens of kilo-amperes (Japanese winter season) [42], [45].

2.2.6: POSITIVE DOWNWARD FLASH PEAK CURRENT CORRELATED PARAMETERS

Although there does not exist an acceptable mean common waveshape for positive strokes, correlations between peak current and other parameters can still be investigated. The regression analysis indicates that there exists

- a strong correlation between peak currents and impulse charge and action integral [18],
- no correlation between peak current and front time [18],
- a weak correlation between peak current and maximum rate of rise [18].

Using the correlation parameters, median and standard deviation parameter distributions for steepness, charge and half-time can be calculated, as shown in table 2-12.

Table 2-12: Summarized derived distribution parameters correlated to peak current of positive strokes, adapted from [21], [31]

$S_m \mid I_F$ in $\frac{kA}{\mu s}$	ρ_C	Q_{Stroke} in C	ρ_C	$Q_{Impulse}$ in C	ρ_C	$t_h \mid I_F$ in μs	ρ_C
$0.242 \cdot I_F^{0.645}$	0.49	$15.3 \cdot I_F^{0.465}$	0.62	$0.709 \cdot I_F^{0.876}$	0.77	$85.97 \cdot I_F^{0.277}$	0.68

As already derived for negative strokes, the correlation of charge and peak current is also weakened for positive strokes with increasing time span.

Further parameters of positive lightning are listed in table 2-13, obtained from other direct current measurements.

Table 2-13: Summarized parameters of log-normal distribution for positive strokes derived from other direct current measurements [46]

First Stroke	M	β
$S_{average}$ in μs	0.2	2.378
T_{front} in μs	178	2.06
T_{tail} in μs	596	1.89

From the amount of available data and the distribution of positive stroke continuing currents in figure 2-11, it can be seen that there are not enough parameters to describe a

standard waveform for positive lightning strokes. Furthermore, front time parameters and stroke current distributions vary regionally and seasonally [46]. Therefore the description of positive stroke waveforms remains difficult. In [47] a proposal for a median (50%-values) and severe (1%-values) positive lightning stroke is given composed from various measurement sources. Although these parameters may be applied to model a positive lightning stroke, the composition of data from various sources - keeping in mind the seasonal and regional variation of parameters – may lead to an overestimation of worst-case condition. Furthermore a set of data ranging from 3 kA to 250 kA is normally needed for evaluation of the lightning performance of a transmission line to calculate the back-flashover rate, rather than medium and worst-case parameters.

2.2.7: REGIONAL LIGHTNING DATA

The acquired data demonstrates that lightning stroke parameters vary regionally, but also topographically. CIGRE recommends that local data is used, if it is available, to adjust lightning stroke parameters [18] and thus increase the accuracy of the overall evaluation of overvoltages and back-flashover risk of transmission lines. For the United Kingdom, EA Technology (EAT) [48] maintains a lightning location sensor network with 8 stations in the UK. Their database of measured electromagnetic fields originated from lightning strokes contains recorded events since 1995, which can be utilized to derive the local lightning stroke current distribution, lightning stroke density and the stroke polarity distribution.

As a transmission line may be of hundreds of kilometers length and thus the terrain features various topographical and regional variations with regard to lightning attraction and lightning activity, a great number of data sets of lightning distribution along a transmission line are needed. However the electric field-to-current (*E*-*I*) conversion needs to be considered, which may contain some inaccuracy. To account for this inaccuracy of the *E*-*I*-unit conversion, a safety factor may be multiplied to the resulting current probability density function, e.g. the U.S. National Lightning Detection network features an absolute error of 10-20% for negative strokes [49].

The EA Technology database is only provided in 10 kA steps, meaning if a stroke is in the range of 10 kA to 20 kA, a value of 20 kA is stored. To account for these inaccuracies and add a safety margin, the database value is taken into account at its highest value in the category, e.g. the stroke is in the 10 kA to 20 kA range, a 20 kA value is assumed. The location accuracy can be in a radius from 0 m up to 99900 m. Furthermore, the data

is restricted to the highest current in a flash and does not record the first stroke current value, or any subsequent stroke value apart from the stroke multiplicity. Nevertheless these data can be used for the determination of the stroke current range applied in the simulations, the final estimation of the flashover risk of the line, distribution of stroke polarity and stroke multiplicity.

To be able to compare results from the last section to the sample line route of the 400 kV line through the Scottish Highlands and Scotland as a whole, first the average distributions for central Scotland are investigated. With a developed sorting algorithm, the database (1995 to 2016) is scanned for strokes within the area of 55.9° to 57.7° latitude and -6° to -2.3° longitude, which is an area of 45070 km^2. Only values with a location error of 99900 m are excluded. The processed results are summarized in table 2-14 and table 2-15.

Table 2-14: Summarized results of EAT LLS database (1995-2016) query for flashes in central Scotland, probability distributions

	M/μ	σ
Negative Current (log-normal distribution)	13.47	0.456
Positive Current (log-normal distribution)	25.23	0.9848
Unknown Polarity Current (log-normal distribution)	13.06	0.5051
Negative Stroke Multiplicity (normal distribution)	1.241	1.127
Positive Stroke Multiplicity (normal distribution)	1.0671	1.0399
Unknown Stroke Multiplicity (normal distribution)	1.2633	1.1333

Table 2-15: Summarized results of EAT LLS database (1995-2016) query for flashes in central Scotland, flash counts

	No.	Flash Density in flashes/km^2/year
Negative Flashes	20533	0.0414
Positive Flashes	8178	0.0165
Unknown Polarity Flashes	10018	0.0202
Negative Strokes, Multiplicity Count	25477	-
Positive Stroke, Multiplicity Count	8727	-
Unknown Stroke, Multiplicity Count	12656	-

The results already show that the recommendation to use local lightning data is justified. In comparison to data provided in the previous section, the negative and positive current distribution is much lower than the CIGRE distribution, although a safety margin is considered. Also the stroke multiplicity is lower than in other areas of the world. In comparison to the stroke multiplicity for negative strokes mentioned in literature, which is 3 to 5 subsequent strokes, in most of the cases only a single stroke occurs, but at certain locations, one subsequent stroke is very likely. The multiplicity of positive strokes is in accordance with the literature, as the occurrence of a subsequent stroke is unlikely. The neglect of strokes of positive polarity does not hold for the stroke count in central Scotland, where 53% are negative, 21% are positive and 26% are unknown polarity strokes. Since the EAT LLS tends to count intra-cloud strokes or bipolar strokes as unknown, unknown polarity is excluded. This results in a share of 71.6% for negative and 28.4% for positive downward strokes.

To evaluate the lightning stroke current distribution along a line route, the collection area to be inputted into the developed sorting algorithm needs to be defined. In figure 2-14, the definition of the collection area alongside the principle of how to decide if a stroke location is within the collection area are illustrated. The distance d from the straight line through two adjacent tower centres marks one outer boundary, the perpendicular line through the tower centre the other boundary. The maximum distance d can either be calculated with the electro-geometric model, discussed in section 8.1.2, which is dependent on the tower geometry or with a simplified approach based on the maximum stroke current. This approach is based on equation (2.5) and the attachment distance of the shield wire $d = 8 \cdot \mathrm{I}^{0.65}$, which is dependent on the stroke current, where the likelihood of a maximum current is evaluated. First, with the likelihood that 95% of strokes are below a value I with $P(x < X)$ and the maximum median stroke current in table 2-14, the maximum current results in 131 kA. The associated distance from the line span then is 190 m. In comparison to this approximate calculation, the EGM calculation in section 8.1.2 results in a maximum attachment distance for the maximum tower height of 146 m.

With the known distance d and a, and the coordinates of each stroke location in the EAT database, a criterion for the stroke collection area is readily calculated with triangle geometry, as written in (2.10).

$$\left(b_{max} = \sqrt{d^2 + a^2} \ \wedge \ c_{max} = d\right) \vee \left(b_{max} = d \ \wedge \ c_{max} = \sqrt{d^2 + a^2}\right) \qquad (2.10)$$

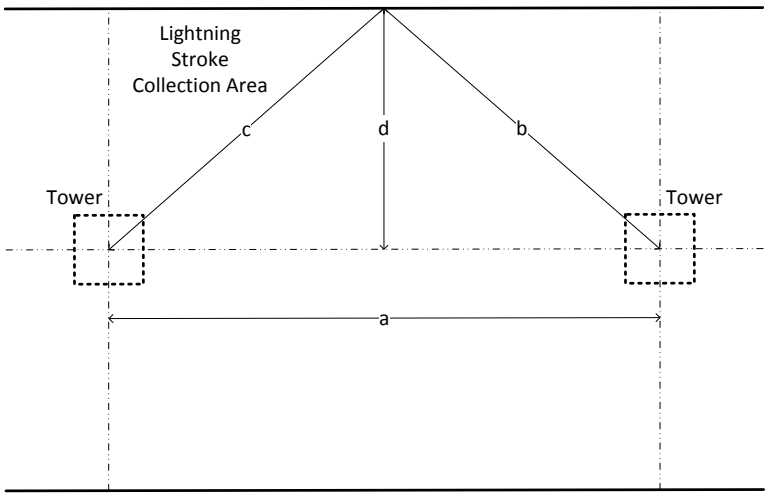

Figure 2-14: Calculation of lightning stroke collection area

An initial screening of the 400 kV Scottish transmission line data revealed that no strokes with $d = 146$ m or $d = 190$ m search could be found with the described algorithm. Therefore it is decided to use a standard 1 km band in this thesis and query the EAT database on lightning strokes with a custom-written Matlab program. Thereby, the data from 1995 to 2016 is used to increase the number of available measurements and only exclude strokes with an estimated error radius of 99900 m. In figure 2-15 to figure 2-18 an excerpt of the results in appendix A.2 of the evaluation are presented.

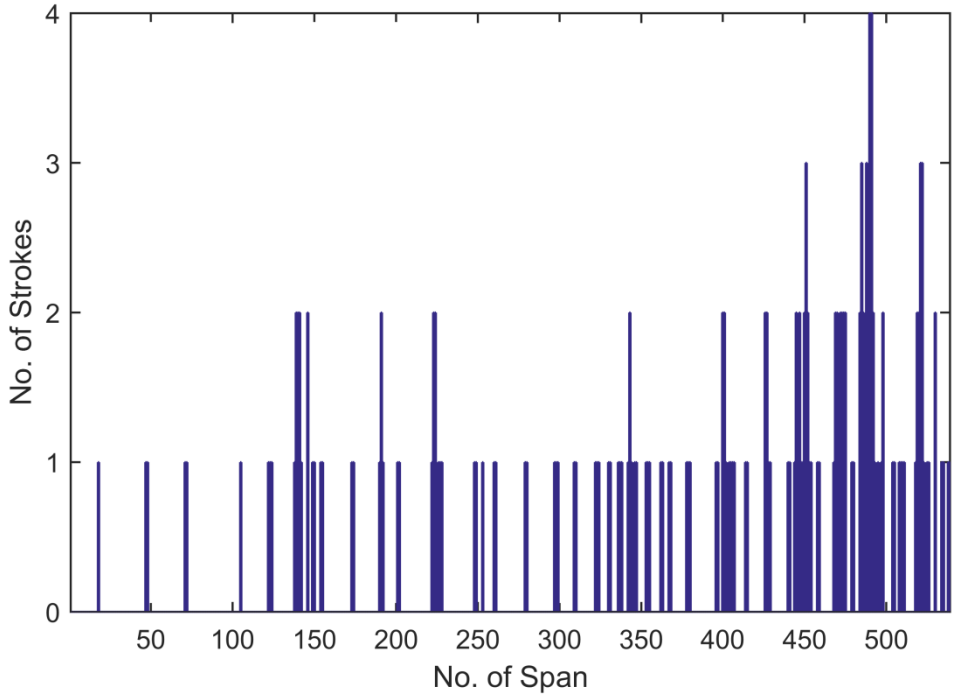

Figure 2-15: Evaluation of lightning location system query for 400 kV line route through the Scottish Highlands, number of negative strokes

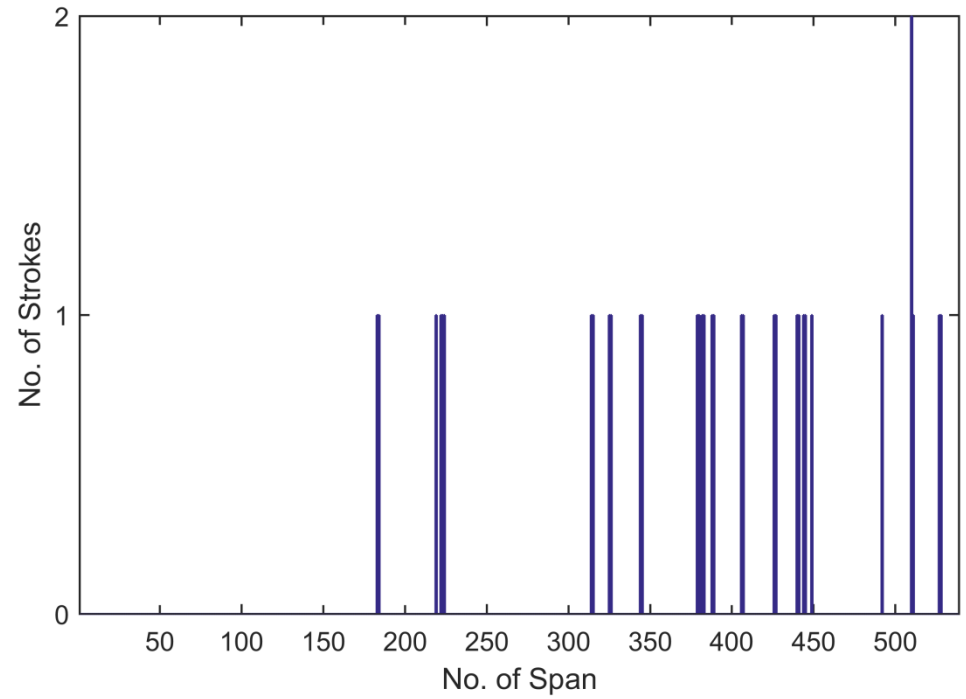

Figure 2-16: Evaluation of lightning location system query for 400 kV line route through the Scottish Highlands, number of positive strokes

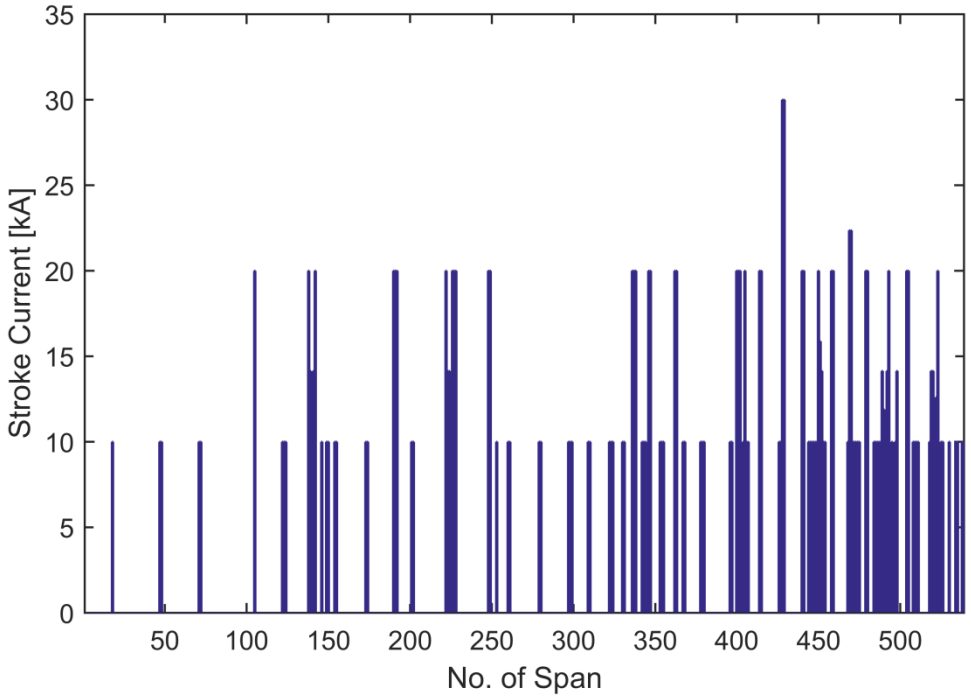

Figure 2-17: Evaluation of lightning location system query for 400 kV line route through the Scottish Highlands, negative stroke current

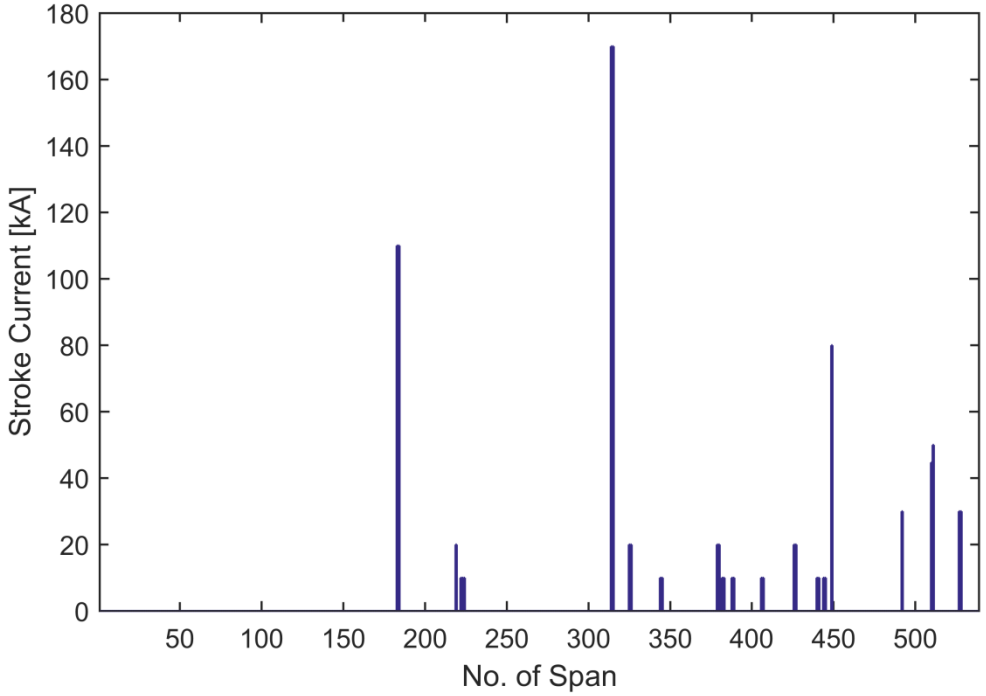

Figure 2-18: Evaluation of lightning location system query for 400 kV line route through the Scottish Highlands, positive stroke current

This evaluation of a 400 kV line route through the Scottish Highlands reveals that generally the lightning stroke density is very low, as parts of the line route feature no or just a single recorded stroke. Due to the small number of samples, the calculation of the median stroke current amplitude of negative and positive strokes reflects the value of single strokes rather than a median. With regard to the stroke multiplicity, the evaluation results match with those from the evaluation of central Scotland. The flash density, although not directly calculated, is much higher than the average for central Scotland where strokes are recorded. Due to the low number of samples, the flash density derived from the line route has to be considered with care when employed in the evaluation of strokes transmission line. In general standards recommend a number of 400 samples for a reliable estimation [50].

2.3: MODELLING OF LIGHTNING STROKES

Engineering software models of lightning strokes, which can be implemented as equivalent circuits into electromagnetic transient programs (EMT software), can be divided into lightning-induced effect models and direct-stroke effect models [51]. Lightning-induced models feature the distribution of current along the lightning channel to compute electric and magnetic fields, which induce voltage into conductors, such as

overhead lines. As this piece of work deals solely with the effects of direct strokes to transmission lines, lightning-induced effect models are not considered further. To implement a direct stroke lightning source model, first the equivalent circuit of such a model needs to be determined, followed by the mathematical description of the various waveforms described in the last sections. Then, with selected lightning stroke parameters from section 2.2.3 and 2.2.6, various mathematical models can be developed to describe the standardized waveshape of the first negative strokes and the waveshape of subsequent negative and positive strokes. This includes the CIGRE mathematical model for negative first strokes for the determination of lightning performance of transmission lines and new improved mathematical models developed for negative first and subsequent and positive strokes. Furthermore, a universal mathematical model, found in the literature is investigated.

2.3.1: EQUIVALENT CIRCUIT FOR LIGHTNING STROKE SOURCES

The purpose of direct-stroke models is to inject a specified current over time into a network node, whereas electromagnetic coupling effects are neglected. Therefore a Thevenin- or Norton-equivalent circuit-approach can be applied [18], [51]. However, due to the easier application in simulation software Norton-equivalents are preferred, as illustrated in figure 2-19.

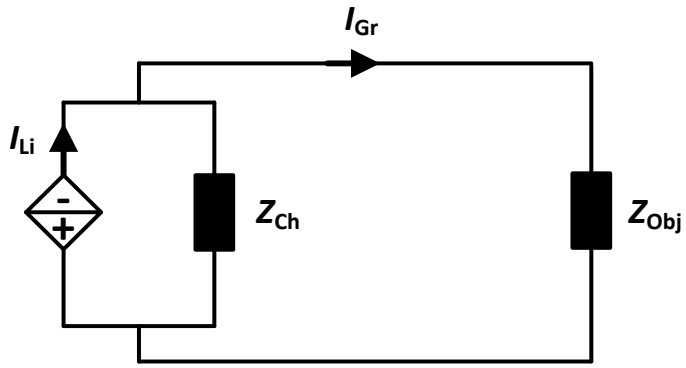

Figure 2-19: Equivalent circuit of an engineering model of a lightning stroke

A Norton-equivalent circuit features an ideal current source, in figure 2-19 I_{Li} in parallel to an impedance Z_{Ch}, which represents the wave impedance of the lightning channel. The resulting current, injected into the stroke object, represented by the lumped impedance Z_{Obj}, is I_{Gr}, calculated with formula (2.11).

$$I_{Gr} = I_{SC} \frac{Z_{Ch}}{Z_{Ch}+Z_{Obj}} \tag{2.11}$$

Theoretical considerations and practical measurements show that the lightning channel surge impedance is in the range of 900 Ω to 3000 Ω and assumed substantially larger than the surge impedance of the stroke object [18], [24], [52], [53]. Therefore the lightning-channel impedance in the Norton-equivalent circuit approach may be neglected. This also ensures to maintain a conservative approach for calculation of overvoltages, which is illustrated in the following example and figure 2-20.

The stroke object's impedance network, in this case an overhead line or overhead line tower in figure 2-20(a), can be represented as a simplified equivalent circuit in figure 2-20(b) neglecting additional towers. At the stroke point, for instance the overhead line earth wire as illustrated in figure 2-20(a), the injected current I_{Gr} is divided equally between the earth wire ends connected to the towers. Therefore the impedance Z_{Obj} seen from the lightning stroke is a parallel circuit of earth wires $Z_{EarthWire}$ and tower impedances Z_{Tower}. Assuming that the lightning channel impedance is 3000 Ω and the earth wire impedance and tower impedance are 400 Ω, the equivalent impedance seen by the lightning stroke calculates to 400 Ω resulting in the injection of approximately 88% of the stroke current at the stroke point. When additional towers and lines are added to the simplified equivalent circuit, the equivalent impedance will further decrease resulting in a further increase of the injected stroke current.

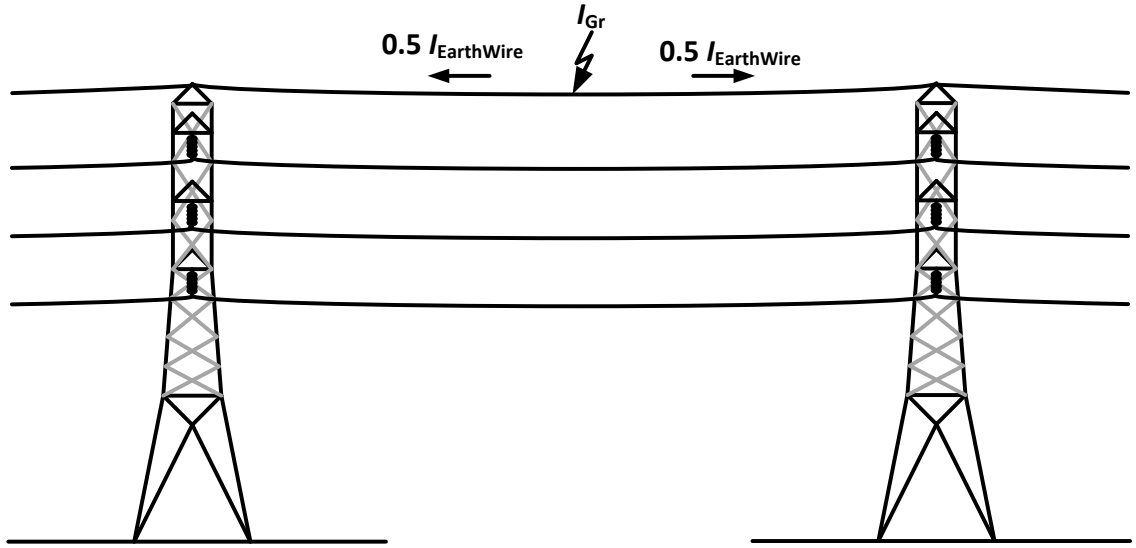

a) Simplified illustration of an overhead line tower with conductors

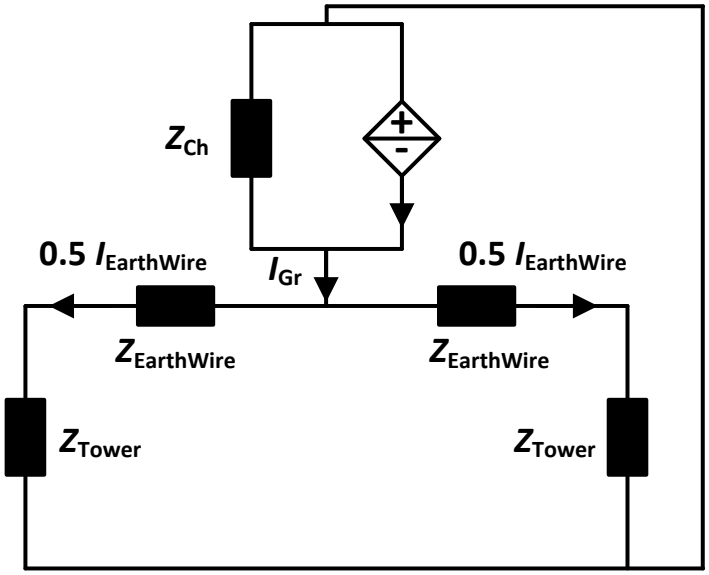

b) Simplified single-phase equivalent circuit of stroke object

Figure 2-20: Simplified equivalent network of a stroke object

The resulting simplified Norton-equivalent circuit with infinite channel impedance can be applied to simulate a lightning stroke to a shielding or phase wire of a transmission line.

To generate waveshapes of lightning strokes, which are injected by the discussed Norton-equivalent circuit, mathematical models of the waveform generation are needed, discussed on the next sub-section.

2.3.2: HEIDLER-FUNCTION MODEL

The Heidler function was originally introduced to overcome mathematical problems when calculating lightning-induced voltages using a channel-base lightning current model with a lightning electromagnetic pulse (LEMP). Existing analytical functions, such as double-exponential functions, had problems with the elimination of the discontinuity of the current derivatives at the time $t = 0$ [54]. Therefore Heidler introduced a channel-base current function in equation (2.12), which overcame these drawbacks [55] and which also provided more flexibility in waveshape creation than the double-exponential function.

$$i(t) = \frac{\mathrm{I_0}}{\eta} \cdot \mathrm{x(t)} \cdot \mathrm{y(t)} = \frac{\mathrm{I_0}}{\eta} \left[\frac{\left(\frac{t}{\tau_1}\right)^n}{\left(1+\left(\frac{t}{\tau_1}\right)^n\right)} \right] e^{-\frac{t}{\tau_2}} \qquad (2.12)$$

The power function in equation (2.12) controls the rise and the exponential function the decay, where I_0 is the peak current, η the correction factor of the current peak, n a current steepness factor and τ_1 and τ_2 the current rise and decay time constants. An example of a lightning impulse waveshape with parameters from [54] is depicted in figure 2-21.

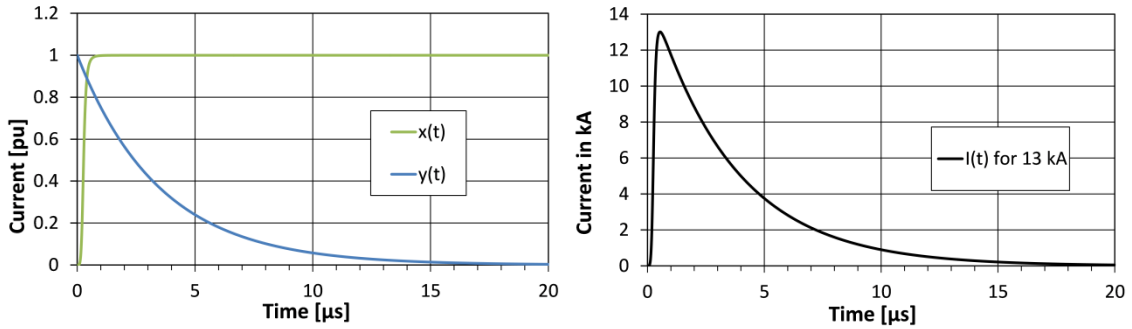

a) Rise and decay function curve progression **b) Resulting waveshape of 13 kA lightning impulse**

Figure 2-21: Example of Heidler-function waveform for 13 kA with η = 0.84, n = 5, τ_1 = 0.27 µs and τ_2 = 3.5 µs

The $x(t)$- and $y(t)$-functions can be decoupled by the application of a relatively high exponent n, illustrated in figure 2-21 (a) [20]. However this results in a very fast transition from wavefront to wavetail (see figure 2-21 (b)). Therefore a lower exponent n may provide a smoother change [20]. The exponent n also controls the current level where the maximum steepness occurs, which can be varied between the 0 %- and 50%-current levels ($n \to \infty$). In the example waveshape in figure 2-21 (b) the maximum steepness occurs nearly at the current half-peak value with $n = 5$.

Due to these limitations, the sum of two Heidler-functions was applied in [56] to better represent the lightning current waveshape of a negative subsequent stroke. In [57], this approach was developed further using six and seven Heidler-functions to synthesize typical single- and more-realistic double-peak lightning current waveforms (equation (2.13) and (2.14)).

$$i(t) = \sum_{k=1}^{m} \frac{I_{0k}}{\eta_k} \left[\frac{\left(\frac{t}{\tau_{1k}}\right)^{n_k}}{\left(1+\left(\frac{t}{\tau_{1k}}\right)^{n_k}\right)} \right] e^{-\frac{t}{\tau_{2k}}} \tag{2.13}$$

$$\eta_k = e^{-\left[\left(\frac{\tau_{1k}}{\tau_{2k}}\right)\cdot\left(\frac{n\cdot\tau_{2k}}{\tau_{1k}}\right)^{\frac{1}{n_k}}\right]} \left| \left(\frac{t_{Imax,k}}{\tau_{1k}}\right)^{n_k} \gg 1 \right. \tag{2.14}$$

Despite the flexibility to produce various waveshapes, the main drawback of summing m Heidler functions is the determination of $4 \cdot m$ parameters, I_0, n, τ_1 and τ_2.

Examples of resulting waveshapes created from m Heidler functions are shown in figure 2-22 with parameters in table 2-16 to

table 2-20. Parameters were derived through visual inspection of the waveform with an educated guess of starting parameters [32].

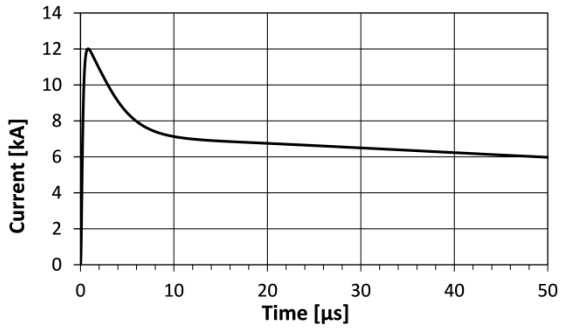

a) Resulting waveshape of a negative continuing current (one Heidler function)

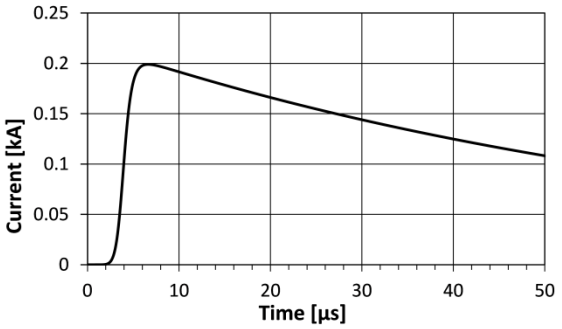

b) Resulting waveshape of a negative subsequent stroke current (two Heidler functions)

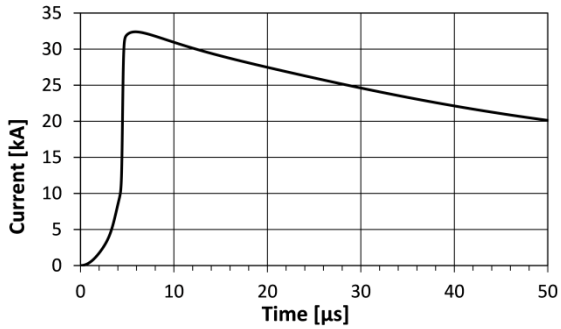

c) Resulting waveshape of a negative first stroke current (six Heidler functions)

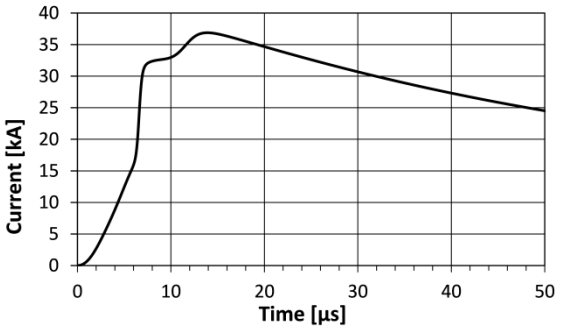

d) Resulting waveshape of a negative double-peak first stroke current (seven Heidler functions)

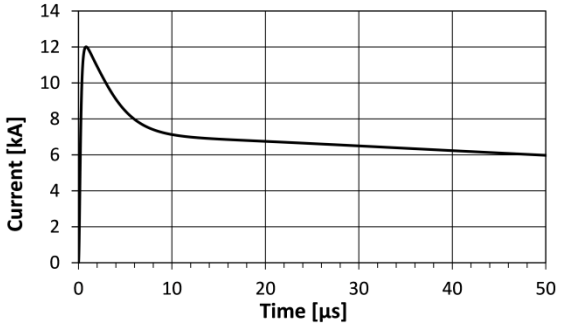

e) Resulting waveshape of a positive first stroke current (four Heidler functions)

Figure 2-22: Examples of *m* Heidler function waveforms, parameters from [47], [57]

Table 2-16: Calculated values of Heidler function parameters for a medium negative continuing current [47]

k	I_{0k} in kA	n_k	τ_{1k} in µs	τ_{2k} in µs
1	0.20	9	4	70

Table 2-17: Calculated values of Heidler function parameters for a medium negative subsequent stroke current [57]

k	I_{0k} in kA	n_k	τ_{1k} in µs	τ_{2k} in µs
1	10.7	2	0.25	2.5
2	6.5	2	2.1	230

Table 2-18: Calculated values of Heidler function parameters for a medium negative first stroke current [47]

k	I_{0k} in kA	n_k	τ_{1k} in µs	τ_{2k} in µs
1	3	2	4	20
2	3	3	4	20
3	3	9	4	20
4	3	11	4	20
5	20	85	4.5	23
6	15	2	20	240

Table 2-19: Calculated values of Heidler function parameters for a medium double-peak negative first stroke current [57]

k	I_{0k} in kA	n_k	τ_{1k} in µs	τ_{2k} in µs
1	3	2	3	76
2	4.5	3	3.5	25
3	3	5	5.2	20
4	3.8	7	6	60
5	13.6	44	6.6	60
6	11	2	10	600
7	5.7	15	11.7	48.5

Table 2-20: Calculated values of Heidler function parameters for a medium positive first stroke current [47]

k	I_{0k} in kA	n_k	τ_{1k} in µs	τ_{2k} in µs
1	20	116	6	50
2	5	3	9	20
3	6	2.5	8	30
4	7	4	6	30

Up to now, the determination of parameters is a manual iterative process, as described in [57] and recorded lightning current waveshapes are necessary for parameter determination. However, the patterns of increasing steepness parameter n_k and τ_{1k} for the first negative strokes alongside with the requirements of first and second time derivation of the Heidler functions may serve as a starting point for an automated iterative determination of parameters as described in [58]. Furthermore, as pointed out in [20] a simplified Heidler-function, in equation (2.11) can be employed, which is capable to represent a subsequent stroke with one parameter set.

$$I(t) = \frac{I_F}{\eta} \frac{a\left(\frac{t}{T}\right)^k + \left(\frac{t}{T}\right)^n}{\left(1+\left(\frac{t}{T}\right)^n\right)} \cdot e^{-\frac{t}{\tau}} \tag{2.15}$$

As discussed before, the maximum steepness S_m is placed at $0.9I_F$, which can be achieved with a fixed parameter $n = 60$ according to [20]. Since the peak correction factor η and a are close to 1, they are set to a fixed value of 1. However, a more simplified iterative process is still required to determine the parameters.

2.3.3: CIGRE-MODEL

The mathematical model of the lightning stroke waveshape to calculate the lightning performance of equipment proposed by CIGRE [24] is based on a piece-wise formula for the front (0 to 0.9 I_F) and the wavetail (0.9 I_F ongoing). CIGRE does not take into account subsequent negative and positive strokes and hence only a model for the first negative strokes is proposed. Thereby the following requirements should be fulfilled by the model:

- Reach the specified current amplitude
- Feature the highest steepness S_m at 0.9 I_F
- Feature the correct average steepness S_{30} for first strokes

- Feature a steady transition from wavefront to wavetail formula
- Describe the current wavetail

The resulting wave shape for a first stroke as a combination of both parts is depicted in figure 2-23.

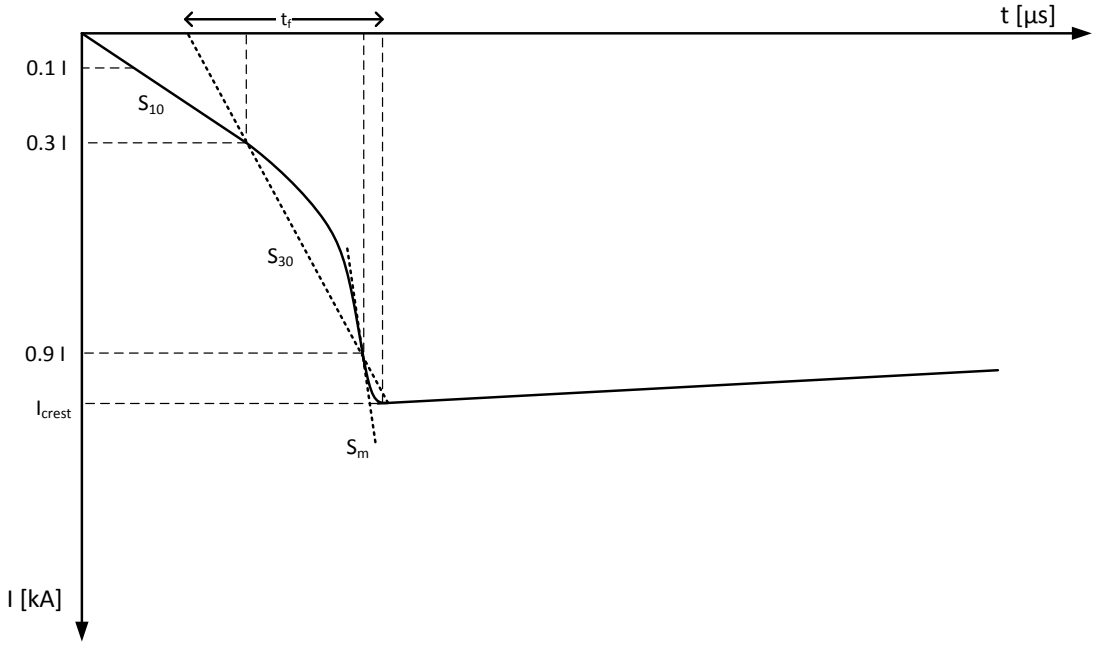

Figure 2-23: CIGRE lightning current impulse wave shape for a first stroke [24]

The front is described with a linear and potential functions in equation (2.1) (see figure 2-24) with input parameters in equation (2.16) to (2.21). In this model it is assumed that the maximum steepness is reached at $0.9\ I_F$ at a time t_n dependent on the exponent n.

$$I(t) = A \cdot t + B \cdot t^n \tag{2.16}$$

$$S_N = S_m \cdot \frac{t_f}{I_F} \tag{2.17}$$

$$t_n = 0.6 \cdot t_f \left[\frac{3\,{S_N}^2}{1+{S_N}^2}\right] \tag{2.18}$$

$$n = 1 + 2(S_N - 1)\left(2 + \frac{1}{S_N}\right) \tag{2.19}$$

$$A = \frac{1}{n-1}\left(0.9\ \frac{I_F}{t_n} \cdot n - S_m|_{I_F}\right) \tag{2.20}$$

$$B = \frac{1}{{t_n}^n (n-1)}\left(S_m|_{I_F} \cdot t_n - 0.9\ I_F\right) \tag{2.21}$$

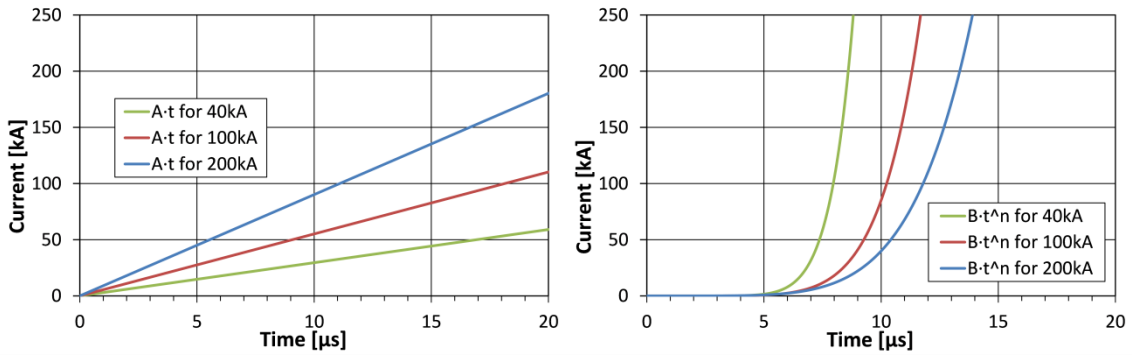

a) Linear part of front equation **b) Power function part of front equation**

Figure 2-24: Curve progression of front equation summands, CIGRE (1991) model

The wavetail is described with a double exponential function in equation (2.22) (see figure 2-25) with input parameters in equation (2.23) to (2.26). The first exponential function describes the decay, the second exponential function ensures the smooth transition from the wavefront to the wavetail and to reach the current peak amplitude.

$$I(t) = C \cdot e^{-\frac{t-t_n}{t_1}} - D \cdot e^{-\frac{t-t_n}{t_2}} \tag{2.22}$$

$$t_1 = \frac{(t_h - t_n)}{\ln 2} \tag{2.23}$$

$$t_2 = \frac{0.1\, I_F}{S_m} \tag{2.24}$$

$$C = \frac{t_1 t_2}{t_1 - t_2}\left(S_m + 0.9\frac{I_F}{t_2}\right) \tag{2.25}$$

$$D = \frac{t_1 t_2}{t_1 - t_2}\left(S_m + 0.9\frac{I_F}{t_1}\right) \tag{2.26}$$

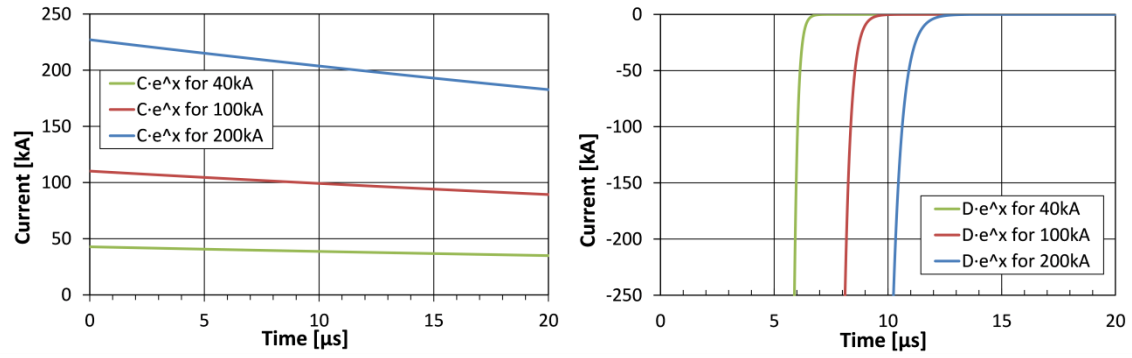

a) Peak part of wavetail equation **b) Decay part of wavetail equation**

Figure 2-25: Curve progression of wavetail equation summands, CIGRE (1991) model

A complete waveform for three different peak current amplitudes is depicted in figure 2-26. According to recommendations in [24], the probability distribution for current amplitude and median values for maximum steepness $S_m|I_F$, $t_{d30}|I_F$ (recalculated to S_{30}) and half-time medium value $t_h = 75\,\mu s$ are used as input parameters for curve generation, taken from table 2-1, table 2-3 and table 2-4.

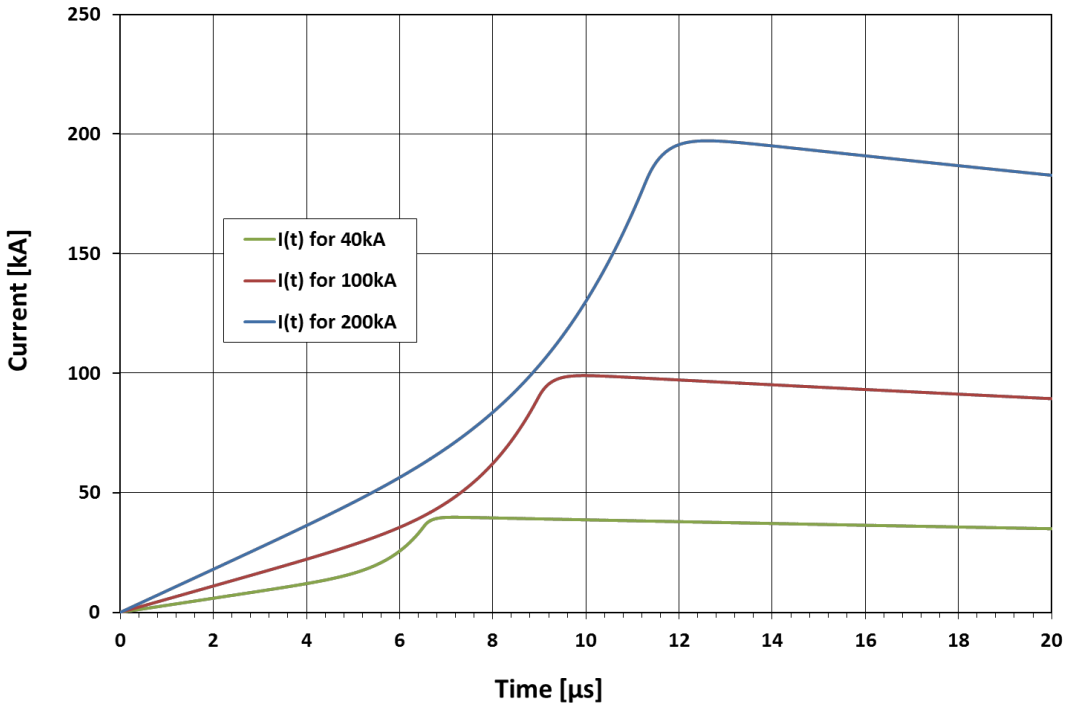

Figure 2-26: Curve progression of combined wavefront and wavetail, CIGRE (1991) model

From the 200 kA current waveform in figure 2-26 it can be seen that the maximum current amplitude of 200 kA is not reached. Therefore an analysis of the wavetail equation is performed to investigate the deviation from the specified crest value. The maximum value is determined with a goal-seek function and the deviation is expressed by

$$dev = 1 - \frac{I_{max}(t)}{I_F}. \tag{2.27}$$

The results of the analysis (see figure 2-27) using shielding and backflash domain parameters from table 2-1 show an exponential increase of deviation. The deviation originates from the assumption in equation (2.24), that the current crest amplitude is reached after one time constant.

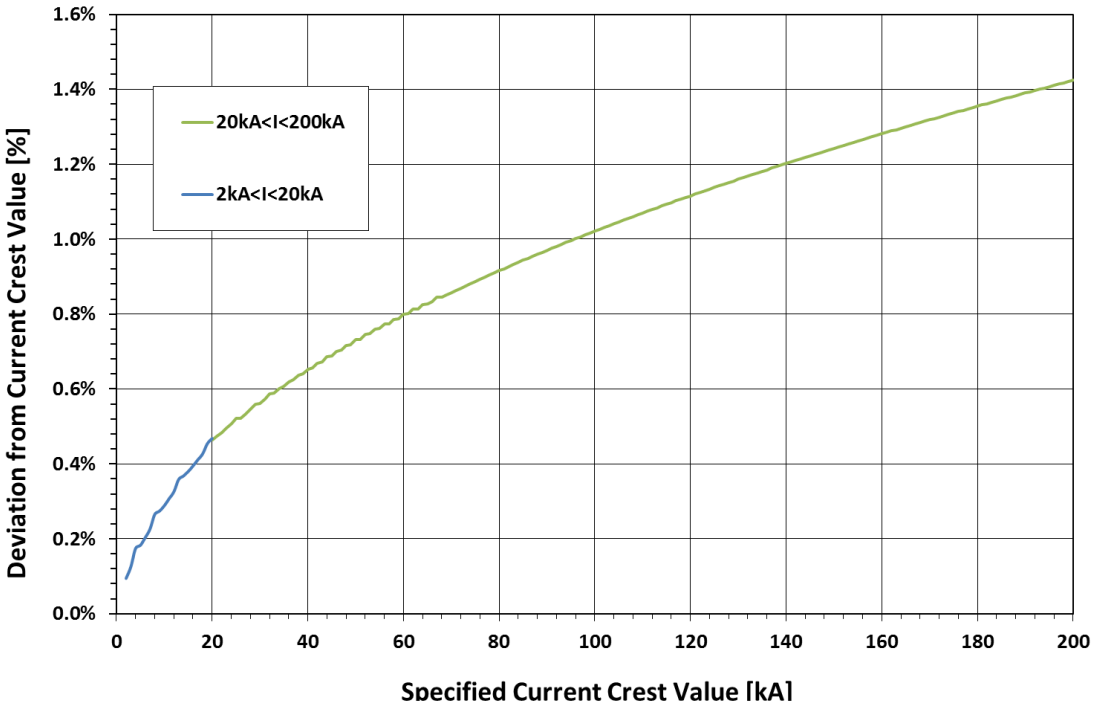

Figure 2-27: Wavetail formula deviation from specified crest value, CIGRE (1991) model

For the later simulations the deviation from the specified crest may have an influence on occurring overvoltages through the injecting of less current, resulting in an underestimation of overvoltages and probability of insulator back-flashover risk. Therefore an improved model is developed in the next section to minimize the deviation.

2.3.4: IMPROVED DOUBLE-EXPONENTIAL-FUNCTION MODEL FOR NEGATIVE FIRST STROKE WAVESHAPES

As shown in the previous section, the CIGRE model is based on a fixed half-time value t_h and features an increasing deviation from the specified crest value with increasing current amplitude. As outlined in the objectives in chapter 1.2, the application of tower line arresters is investigated in the later simulation, thus the charge brought to ground or energy stored in the arrester is important. To include the charge as an input parameter in the mathematical description rather than using t_h and to improve the performance with respect to the current crest amplitude, a new approach is taken in this thesis, but still following the basic assumptions and requirements from [24]. To enable an evaluation of the loss of accuracy due to simplifications in the different analytical models of lightning stroke waveshapes, the exact numerical solution of variables is calculated as a reference.

For negative first stroke waveshapes, the wavefront, can be described with a linear and an exponential function in equation (2.28) with the exponential function depending on the parameter *n*.

$$I(t) = A \cdot t + B \cdot e^{n \cdot t} - B \tag{2.28}$$

To obtain the unknown parameters *A*, *B* and *n* analytically, conditions for steepness and current values are applied and simplified, summarized in equation (2.29) to (2.32).

$$0.9\, I_F - A \cdot t_{90} - B \cdot e^{n \cdot t_{90}} + B = 0 \tag{2.29}$$

$$S_m - A - n \cdot B \cdot e^{n \cdot t_{90}} = 0 \tag{2.30}$$

$$S_{30} = \frac{0.9 I_F - 0.3 I_F}{t_{90} - t_{30}} \xrightarrow{yields} t_{90} - t_{30} - \frac{0.6 I_F}{S_{30}} = 0 \tag{2.31}$$

$$0.3\, I_F - A \cdot t_{30} - B \cdot e^{n \cdot t_{30}} + B = 0 \tag{2.32}$$

With the assumption that *A* has a linear correlation to the average steepness S_{30},

$$A = p \cdot S_{30}, \tag{2.33}$$

the parameters for the wavefront can be derived, listed in equations (2.34) to (2.36).

$$n = \frac{S_N - p}{1 - p} \cdot \frac{S_{30}}{0.6 I_F} \tag{2.34}$$

$$t_{90} = \frac{0.9 I_F}{A} - \frac{1}{n}\left(\frac{S_m}{A} - 1\right) \tag{2.35}$$

$$B = (1 - p) \cdot 0.6 I_F \cdot e^{-n \cdot t_{90}} \tag{2.36}$$

To determine a value for the parameter *p*, equation (2.29) is subtracted from equation (2.32) and equation (2.31) is applied to obtain

$$\underbrace{n \cdot \frac{0.6\, I_F}{S_{30}}}_{x} \cdot \underbrace{\frac{1 - p}{S_N - p}}_{y} = 1 - e^{-n \cdot \frac{0.6\, I_F}{S_{30}}} \xrightarrow{yields} e^{-x} + x \cdot y - 1 = 0\,. \tag{2.37}$$

From equation (2.37), it can be assumed that for small values of x, y is approximately $1/x$. To investigate if equation (2.37) meets this condition, a sensitivity analysis is performed for the p and y value, calculated either from $y = \frac{1-p}{S_N - p}$ or $y = \frac{1 - e^{-x}}{x}$ to

determine the deviation. Using CIGRE parameters, the results of this analysis are displayed in figure 2-28 and show that the deviation decreases with increasing p. Hence the assumption that A has a linear correlation to the average steepness S_{30} for values of $p > 0.5$ features a minor error (below 8%) for crest current amplitudes smaller 200 kA. In comparison to this, the CIGRE (1991) model features a variable p, which is in the range of $0.29 \leq p \leq 0.36$.

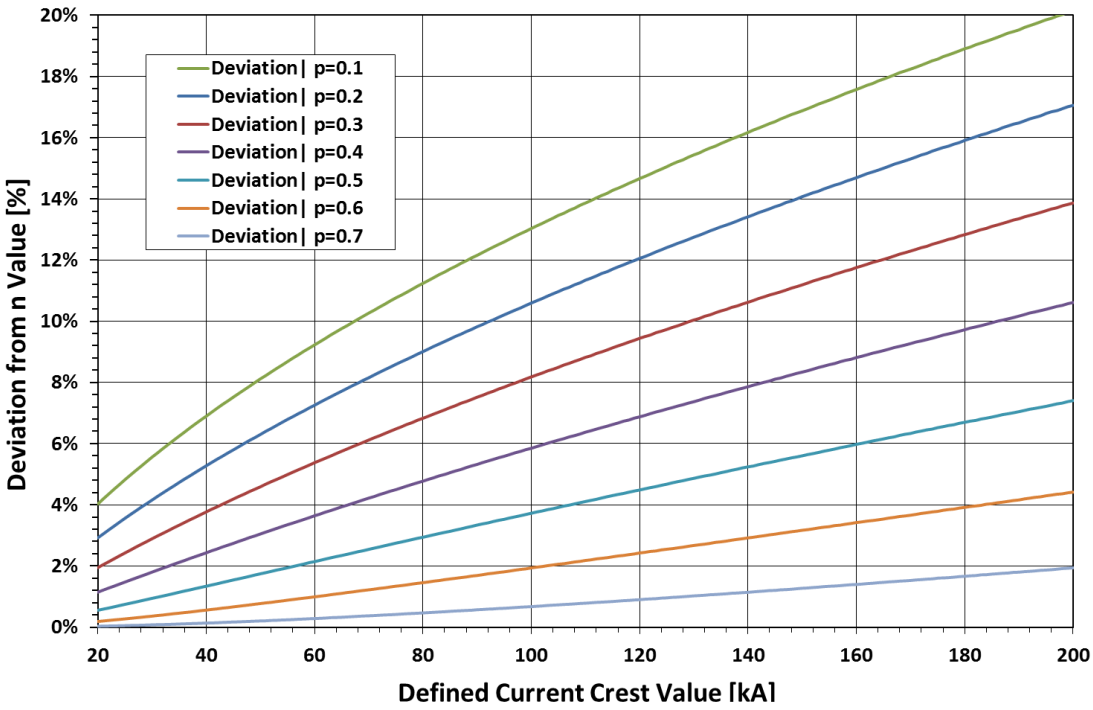

Figure 2-28: Results of sensitivity analysis for *p*-value of linear part of wavefront formula, improved double exponential model

In contrast to the CIGRE parameters of negative first strokes, the correlation between the maximum crest value I_F and the average steepness S_{10} for measured parameters in [25] (see table 6-3) is strong. Therefore the assumption in equation (2.33) that the first part of the wavefront equation is solely dependent on S_{30} is not needed to calculate the unknown variables in the wavefront equation (2.28). With equation (2.38) and (2.39) a fourth equation can be formulated.

$$S_{10} = \frac{0.9I_F - 0.1I_F}{t_{90} - t_{100}} \xrightarrow{yields} t_{90} - t_{10} - \frac{0.8I_F}{S_{10}} = 0 \tag{2.38}$$

$$0.1\, I_F - A \cdot t_{10} - B \cdot e^{n \cdot t_{10}} + B = 0 \tag{2.39}$$

With some simplification of these nonlinear equations, the variables can be determined with formula (2.40) to (2.43).

$$A = \left(\frac{1}{\frac{4}{S_{10}} - \frac{3}{S_{30}}} \right) \tag{2.40}$$

$$B = (0.9\, I_F - A \cdot t_{90}) \cdot e^{-n \cdot t_{90}} \tag{2.41}$$

$$t_{90} = \left(\frac{1.2}{S_{10}} - \frac{0.3}{S_{30}} \right) I_F \tag{2.42}$$

$$n = \frac{S_m - A}{0.9\, I_F - A \cdot t_{90}} \tag{2.43}$$

To evaluate the accuracy of the simplified analytical formulas for the front variables, an analysis of the deviation from the numerical calculation of variables is performed. For the CIGRE and Japan input parameters, the evaluation results for each variable in dependency of the stroke current for different values of parameter *p* are depicted in appendix A.1. Furthermore, a comparison of the deviation with Japan parameters using the additional steepness S_{10} to determine the variable A is included.
These results show that the deviation using CIGRE parameter is increased with increasing crest current, but decreased for Japan parameters. Although the overall deviations of analytically calculated variables from the numerical ones for the wavefront are remarkable, the impact of their combined deviation on the whole waveform needs to be determined first together with the wavetail formulation.

The wavetail formula in equation (2.44) is the same as in the CIGRE (1991) model, but it is rewritten for ease of derivation.

$$I(t) = C \cdot e^{-\frac{t - t_{90}}{\tau_1}} - D \cdot e^{-\frac{t - t_{90}}{\tau_2}} \tag{2.44}$$

To obtain equations for the unknown parameters C, D, τ_1 and τ_2, boundary conditions in equation (2.45) to (2.49) are applied.

$$0.9\, I_F - C + D = 0 \tag{2.45}$$

$$S_m + \frac{1}{\tau_1} C - \frac{1}{\tau_2} D = 0 \tag{2.46}$$

$$I_F - C \cdot e^{-\frac{t_{100} - t_{90}}{\tau_1}} + D \cdot e^{-\frac{t_{100} - t_{90}}{\tau_2}} = 0 \tag{2.47}$$

$$-\frac{1}{\tau_1} C \cdot e^{-\frac{t_{100} - t_{90}}{\tau_1}} + \frac{1}{\tau_2} D \cdot e^{-\frac{t_{100} - t_{90}}{\tau_2}} = 0 \tag{2.48}$$

$$Q = \frac{1}{2}A{t_{90}}^2 + \frac{B}{n}(e^{nt_{90}} - t_{90}) + \tau_1 C\left(1 - e^{-\frac{t_{end}-t_{90}}{\tau_1}}\right) - \tau_2 D\left(1 - e^{-\frac{t_{end}-t_{90}}{\tau_2}}\right) \quad (2.49)$$

With some simplifications and an assumption for τ_2, the variables C, τ_1, and D can be determined analytically in formula (2.50) to (2.53).

$$\tau_2 = \frac{0.1\, I_F}{S_m} \quad (2.50)$$

$$\mathrm{C} = 0.5\ \mathrm{Q} \cdot \left(\frac{1}{\tau_2} - \sqrt{\left(\frac{1}{\tau_2}\right)^2 - 40\frac{S_m}{Q}}\right) \quad (2.51)$$

$$\tau_1 \approx \frac{Q}{C} \quad (2.52)$$

$$D = C - 0.9\, I_F \quad (2.53)$$

As already performed for the wavefront variables, an analysis of the deviation from the numerical solution is conducted. The results of this evaluation are depicted in appendix A.1 for both CIGRE and Japan input parameters. In comparison to the remarkable deviation of the wavefront variables, the wavetail variables feature a very small deviation from their numerical counterparts.

The resulting waveshape using the improved double exponential formula with both CIGRE and Japan parameters for a crest current of 200 kA is plotted in figure 2-29 and in figure 2-30. The matching numerically calculated waveshapes are plotted in black.

The deviation between numerically and analytically calculated waveshapes decreases with increasing p for both input parameter sets. In comparison with the CIGRE formulation of the waveshape in section 2.3.3, the deviation from the specified crest value decreases to -0.8% at 200 kA for the CIGRE parameters, for Japan parameters with steepness parameter S_{10} this deviation decreases further to -0.5%. The waveshape with $p = 0.5$ for the variable solution of A approximates the waveshape using steepness parameter S_{10} with increasing crest current. In summary, the combination of analytically calculated variables for wavefront and wavetail produces a waveshape, which is very close to one with numerically calculated variables.

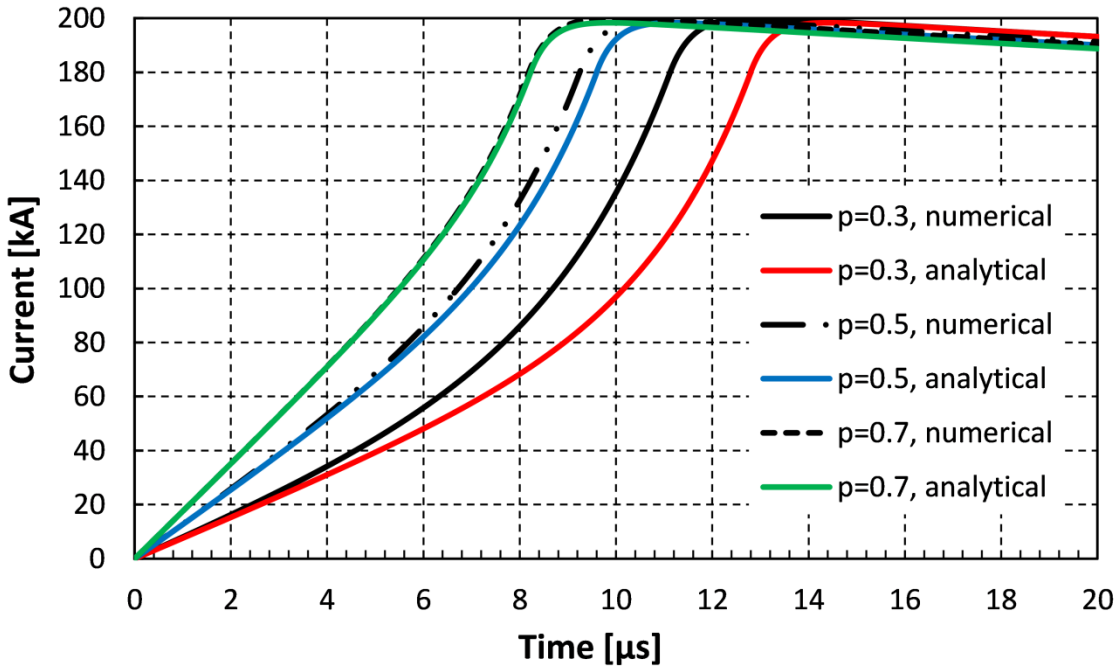

Figure 2-29: **200 kA current waveshapes of negative first strokes in dependency of parameter *p*, CIGRE parameters for negative first strokes**

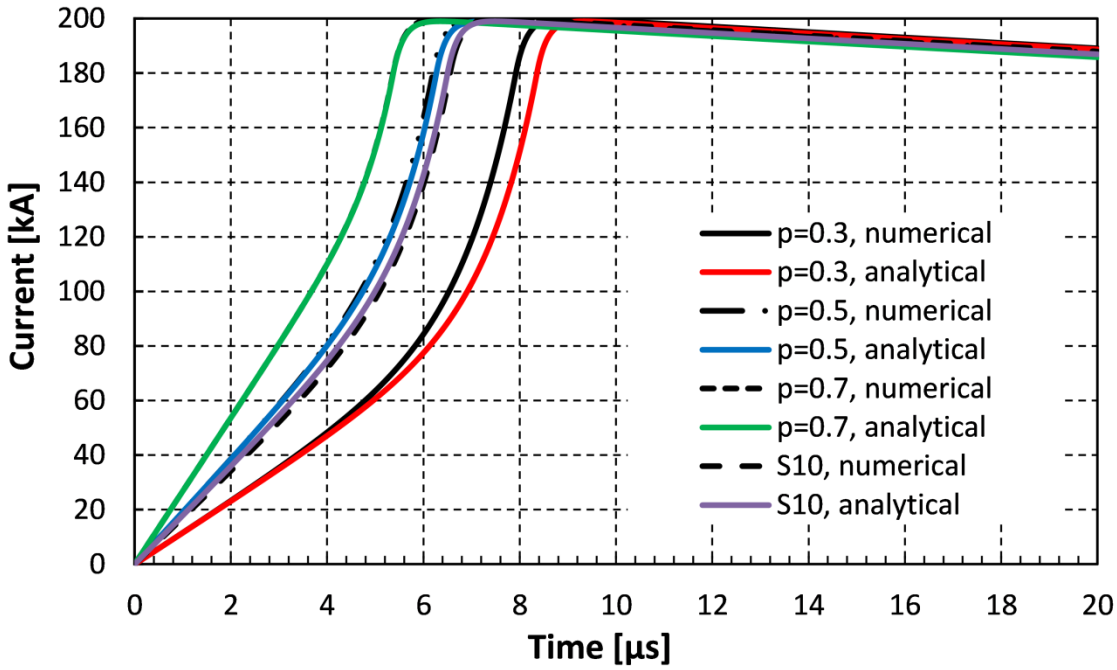

Figure 2-30: **200 kA current waveshapes of negative first strokes in dependency of parameter *p*, Japan parameters for negative first strokes**

2.3.5: IMPROVED DOUBLE-EXPONENTIAL-FUNCTION MODEL FOR NEGATIVE SUBSEQUENT STROKE WAVESHAPES

With the improved double-exponential function for the peak and wavetail, a mathematical description for negative subsequent strokes can be formulated, following the guidelines from [24]. Unlike first negative strokes, subsequent strokes feature only a fast rise to the peak value as illustrated in figure 2-9.

Therefore a new mathematical function for the wavefront with a fast rise from zero to $0.9\,I_F$ has to be applied. An adapted wavefront, shown in equation (2.54), from the negative first stroke front is used for this purpose, additionally to the improved double-exponential function for peak and wavetail.

$$I(t) = B \cdot e^{n \cdot t} - B \tag{2.54}$$

As there exists only a weak correlation between the peak current and the rise-time S_{30}, the average steepness S_{10} alongside with the correlation between peak current and maximum steepness S_m are applied as input parameter. With the requirements of current and steepness value at $0.9\,I_F$ and $0.1\,I_F$, the wavefront equation parameters can be determined in equation (2.55) to (2.58).

$$0.9\,I_F - B\,(e^{n \cdot t_{90}} - 1) = 0 \tag{2.55}$$

$$S_m - B\,(e^{n \cdot t_{90}} - 1) = 0 \tag{2.56}$$

$$0.1\,I_F - B\,(e^{n \cdot t_{10}} - 1) = 0 \tag{2.57}$$

$$S_{10} - \frac{0.8\,I_F}{t_{90} - t_{10}} = 0 \tag{2.58}$$

The equations can be simplified to obtain an analytical solution, as written in formula (2.59) and (2.60).

$$n = \frac{S_m}{0.9\,I_F} \tag{2.59}$$

$$B = 0.9\,I_F e^{-\frac{S_m}{S_{10} \cdot 0.9}} \tag{2.60}$$

As already performed for negative first strokes, an evaluation of the deviation from numerical results is performed for the wavefront variables. The results are presented in figure 2-31, which show a decreasing deviation with increasing crest current.

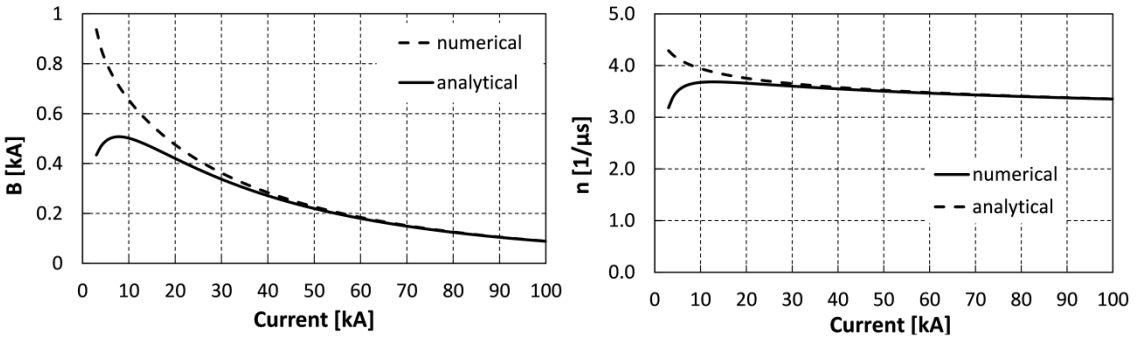

a) Variable B **b) Variable n**

Figure 2-31: Deviation of analytical wavefront variable calculation from numerical solution in dependency of parameter *p*, CIGRE parameters for negative subsequent strokes

Together with the analytical wavetail formulation for negative first strokes, the complete waveform for negative subsequent can be described. The resulting waveshape for two different values of I_F is shown in figure 2-32, which shows a minor deviation for small crest currents only. In comparison to negative first strokes, the total charge brought to ground is small. Therefore an integration time of 100 µs to obtain the charge value is sufficient, which results in a deviation of 0.1% for 100 kA crest current in comparison to the numerically obtained result.

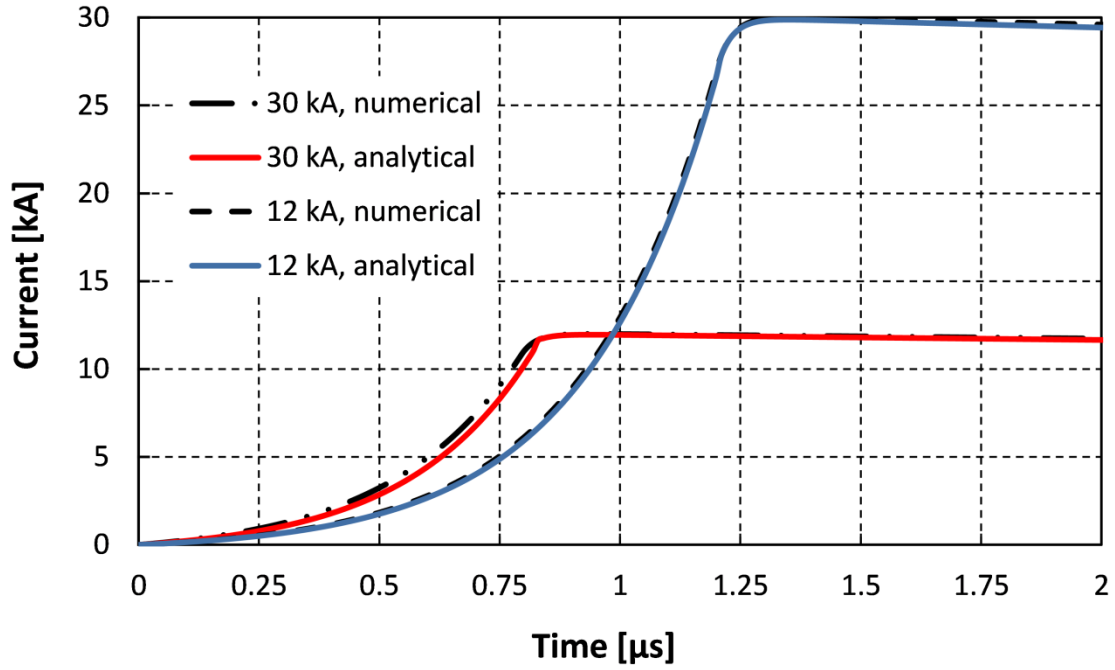

Figure 2-32: 12 kA and 30 kA current waveshapes of negative subsequent strokes, CIGRE parameters for negative subsequent strokes

2.3.6: IMPROVED DOUBLE-EXPONENTIAL-FUNCTION MODEL FOR POSITIVE STROKE WAVESHAPES

As already explained in section 2.2.4, there currently exists no standardized waveshape for positive lightning strokes and thus modelling of waveforms is based on recorded waveshapes and available data. As only the maximum steepness parameter is available for calculation of the rise time, a similar approach as for calculation of the front of negative subsequent strokes is applied as shown in figure 2-33. Recorded waveshapes feature the maximum steepness in the range of 30% to 70% of [21], [27], [31], [43], [46], therefore a value of 0.6 I_F for the maximum steepness S_m is chosen.

The wavefront can be described with a single power function in equation (2.61).

$$I(t) = B \cdot t^n \tag{2.61}$$

However an assumption for the time t_{60}, which specifies the transition point to the wavetail, has to be made, as illustrated in figure 2-33 and written in equation (2.62) in dependency of the parameter r.

$$t_{60} = \frac{I_F}{S_m}\left(\frac{0.1+0.5 \cdot r}{r}\right) \tag{2.62}$$

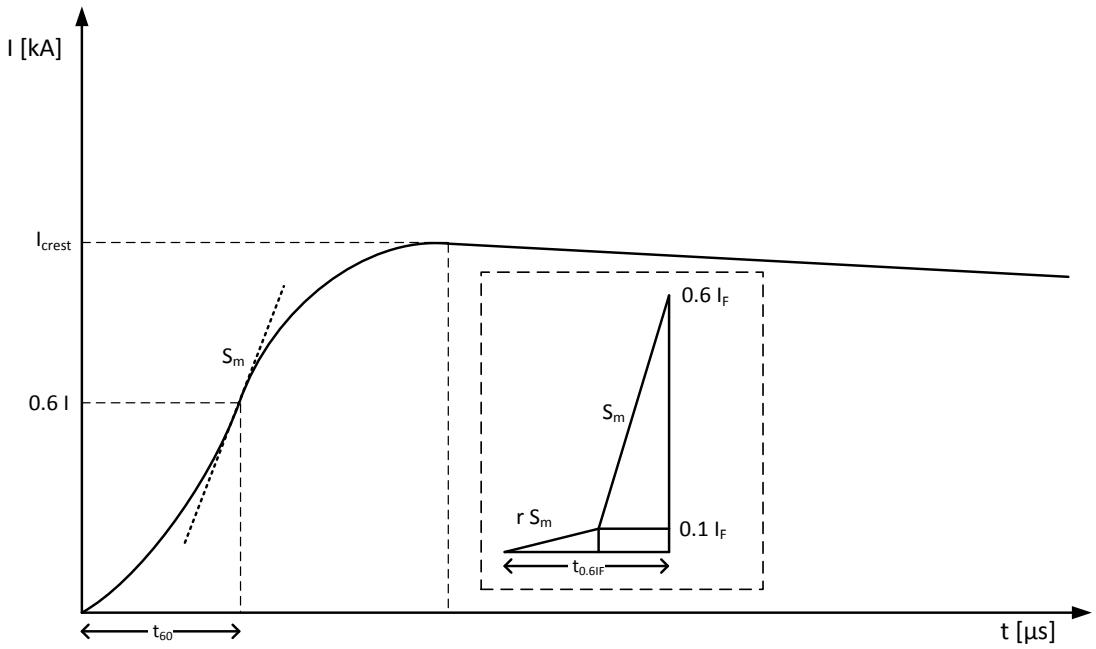

Figure 2-33: Illustration of a positive stroke waveshape and assumed rise-time

As a result the wavefront parameters can be calculated without using a numerical solution, as performed in equation (2.63) to (2.66).

$$0.6\, I_F - B \cdot {t_{60}}^n = 0 \tag{2.63}$$

$$S_m - n \cdot B \cdot t^{n-1} = 0 \tag{2.64}$$

$$n = \frac{S_m \cdot t_{60}}{0.6\, I_F} \tag{2.65}$$

$$B = \frac{0.6\, I_F}{{t_{60}}^n} \tag{2.66}$$

The parameter r can be chosen in a range of 0.1 to 0.5 to achieve a waveform similar to measurements. In the following $r = 0.25$ is chosen to achieve a sufficient rise time to $0.6\, I_F$.

The wavetail may be described with the double exponential function applied for negative strokes using the stroke charge as input. However, due to the missing specification of integration time for charge calculation, rather the half-time t_h, also featuring a better correlation, is applied to calculate the variables.

From the following conditions in equation (2.67) to (2.71) the parameters C, D, τ_1 and τ_2 can be calculated.

$$0.6\, I_F - C + D = 0 \tag{2.67}$$

$$S_m + \frac{1}{\tau_1} C - \frac{1}{\tau_2} D = 0 \tag{2.68}$$

$$1.0\, I_F - C \cdot e^{-\frac{t_{100}-t_{60}}{\tau_1}} + D \cdot e^{-\frac{t_{100}-t_{60}}{\tau_2}} = 0 \tag{2.69}$$

$$S_m + \frac{1}{\tau_1} C \cdot e^{-\frac{t_{100}-t_{60}}{\tau_1}} - \frac{1}{\tau_2} D \cdot e^{-\frac{t_{100}-t_{60}}{\tau_1}} = 0 \tag{2.70}$$

$$0.5\, I_F - C \cdot e^{-\frac{t_h-t_{60}}{\tau_1}} + D \cdot e^{-\frac{t_h-t_{60}}{\tau_2}} = 0 \tag{2.71}$$

With some simplifications, the variables can be calculated analytically, as shown in formula (2.72) to (2.75).

$$\tau_2 \approx \frac{0.465\, I_F}{S_m} \tag{2.72}$$

$$\tau_1 = -\frac{t_h - t_{60} - 5\,\tau_2}{ln(0.5) - ln(1 - 0.6\, e^{-3})} \tag{2.73}$$

$$C = 0.5\, I_F\, e^{\frac{t_h - t_{60}}{\tau_1}} \tag{2.74}$$

$$D = C - 0.6\, I_F \tag{2.75}$$

The resulting waveshapes for three different values of I_F are shown figure 2-34. The numerically calculated waveshapes are in black, but overlay with the analytically calculated waveshapes.

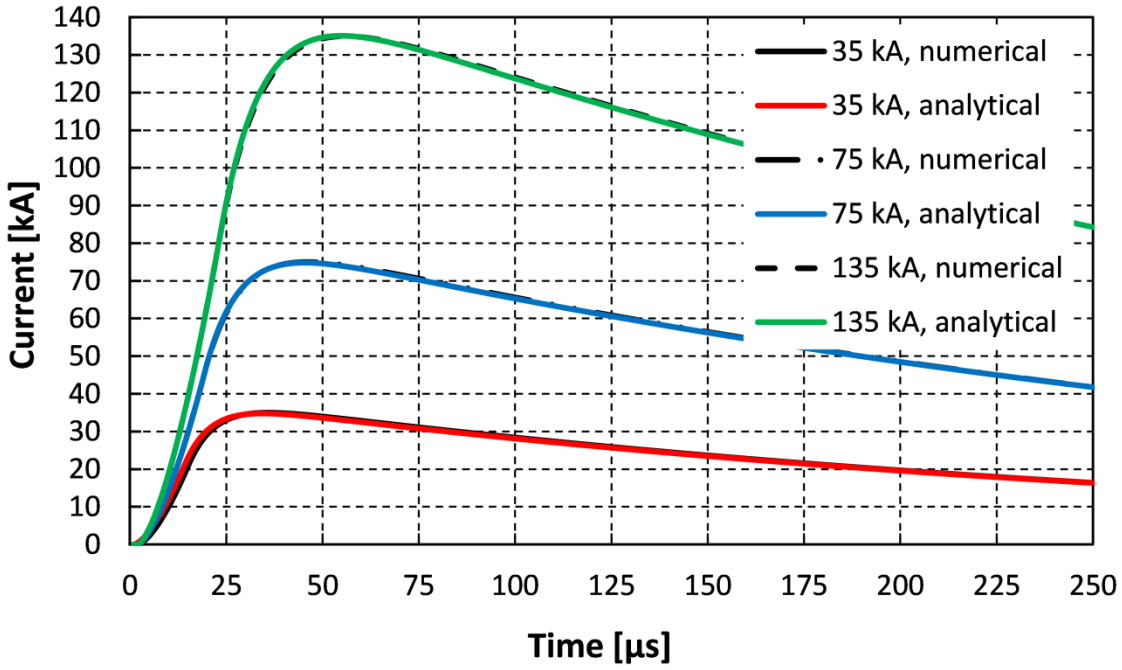

Figure 2-34: 35 kA, 75 kA and 135 kA current waveshapes of positive strokes, Berger parameters for positive strokes

2.4: SUMMARY AND CONCLUSION ON LIGHTNING

In this chapter, first the physical formation of lightning and the development of cloud-to-ground lightning channels are explained, where the important return-stroke types for the assessment of the lightning performance of a transmission line are downward negative first and subsequent stroke and downward positive stroke. Since the major portion of charge is transferred to ground within the first hundreds of microseconds, continuing currents and M-components are neglected.

Second, the engineering approach to lightning flashes is examined. This approach includes the measurement and evaluation of negative and positive cloud-to-ground direct lightning strokes to find the dominant characteristics of a lightning cloud-to-ground return-stroke at its point of connection to an object and derive suitable mathematical

descriptions for engineering applications. Since lightning is random in its nature, a probabilistic approach to extract lightning parameters and common properties of waveshapes is taken.

Most recorded direct lightning stroke measurements are of negative cloud-to-ground nature and thus a standardized waveshape as well as an extensive evaluation of data is found in the literature. In this evaluation, correlations between various lightning stroke parameters are investigated and it is concluded that the fixed parameter, on which all other parameters, like steepness or charge transfer, are dependent on is the crest current. Unlike for negative strokes, there exist only limited direct current measurements on positive lightning strokes, which impede the extraction of standardized waveshapes and profound evaluation of parameter correlations. In the process of gathering parameters of lightning return-stroke waveforms in the literature, it is found that historical data of negative first strokes underestimate the maximum steepness of the wavefront and more up-to-date data has to be used as substitution. To account for the variation of negative lightning stroke parameters and their different correlation to crest current value in the literature, only parameters with good correlation or suggested parameters from standards are applied. For positive strokes the limited available data from the literature is used, alongside with recorded waveshapes, even though it is known that these data inherit some uncertainties.

Third, the determination of polarity and current distribution of return-strokes is investigated. The common approach in the literature to the evaluation of lightning protection of overhead transmission lines and substations suggests the neglect of positive flashes, because their global contribution to all cloud-to-ground strokes is less than 10%. However, it is suggested that local data is used as far as possible, because measured data found in literature shows variations, which may be attributed to the measurement devices used or to topographical, regional and seasonal variations. Nowadays lightning stroke data is either obtained from direct current or electric field measurement systems. Although direct current measurements feature a higher accuracy than electric field measurements, due to the electric field to current conversion, direct current measurement data is limited to specific locations and measurement equipment often located in exposed positions to attract lightning.

Following the suggestion to use local lightning data, available local data from two different lightning location systems, is sourced for an evaluation. To obtain return-stroke polarity and current amplitude distributions, a calculation and evaluation software is developed in Matlab, which accesses the database and searches for recorded strokes

within a specified area. The selected local available data from electric field measurements (EAT system) is evaluated with regard to stroke amplitude, polarity distribution and multiplicity of strokes for the whole of Scottish Mainland. The evaluation revealed that the median current amplitude is much lower than the global CIGRE distribution, 13.5 kA in comparison to 31 kA for negative strokes, and 25 kA in comparison to 35 kA for positive strokes. The percentage of positive strokes is approximately 30%, which shows that positive strokes cannot be disregarded. With regard to multiplicity, since only the number of strokes within a flash are recorded, the average number of strokes per flash is 1.24 for negative strokes and 1.06 for positive strokes. From this number it can be concluded that only a minor number of positive strokes are accompanied by a subsequent stroke and can therefore be neglected.

To produce more accurate stroke distributions, the programmed Matlab algorithm is used to search for strokes in a band along the line route of the 400 kV transmission line through the Scottish Highlands. The evaluation revealed that due to the low number of samples along the line route, either the search band for strokes along the transmission line route needs to be extended or average data from the evaluation in table 2-14 and
table 2-15 utilized. However, as mentioned in [59], lightning hot spot locations at mountain tops have a greater influence on an extended search band than on the average of a bigger area. Furthermore, the variation along the line route and small sample size leads to a possible overestimation of the flash density, when compared to the average data. Therefore the average data in table 2-14 and
table 2-15 should be used for the evaluation of a transmission line.

Finally, modelling of a lightning stroke for simulations is discussed. Generally a lightning stroke model consists of its equivalent circuit and the lightning stroke waveshape generation. In a simple example, it is shown that the lightning channel surge impedance can be neglected and thus the equivalent circuit is reduced to a current source only. For the generation of a specific lightning stroke waveform, a mathematical description is necessary. A review of mathematical descriptions of lightning stroke in the literature reveals, that in general two mathematical functions are utilized to represent the lightning stroke waveform, the so-called Heidler and double-exponential function.

A review of these functions and their application for the description of negative and positive strokes is performed with respect to the utilization of available waveshape parameters, which are solely dependent on the current amplitude. From the review it is concluded, that a sum of Heidler functions can be used to describe various waveshapes,

which makes it a very flexible function in contrast to the waveshape description with double-exponential functions. However, the determination of variables remains difficult, because for each Heidler function four variables have to be determined. E.g., for a first negative stroke six Heidler functions are needed and thus 24 equations are required to determine the 24 variables, in comparison to only four equations for the double-exponential function. Therefore, the application of the Heidler function found in the literature is limited to the description of recorded waveshapes, unless many assumptions for missing equations are made to determine the unknown variables. For the later lightning stroke simulations and estimation of the back-flashover risk of insulators a variation of the lightning stroke crest current dependent on the local lightning stroke current probability function is necessary. As there is no data available to manually produce waveshapes for a broad range of crest currents with the Heidler model, it is concluded that this function is not suitable for the task at hand.

The review of double-exponential functions shows that only recommendations for first negative strokes by CIGRE are available, but determination of parameters is a straightforward procedure. However the first negative stroke model proposed by CIGRE features an increasing deviation from the specified lightning stroke crest value and does not take the energy or charge brought to ground into account. Furthermore the initial steepness of the lightning stroke is not taken into account. Therefore a more accurate double-exponential function for first and subsequent negative and positive return-strokes is developed. In this respect the standardized waveform for negative first and subsequent strokes is taken as a reference. For positive strokes, the mathematical description is oriented towards recorded waveforms. Depending on the assumptions for the peak and wavetail formula of the improved double-exponential function for first negative strokes, the deviation from the specified crest value can be reduced to less than 0.8% for lightning stroke peak currents up to 200 kA in contrast to 1.4% of the CIGRE model without taking the initial steepness parameter into account. In case the initial steepness of the waveform is considered, the deviation decreases to -0.5% at 200 kA.

Furthermore a mathematical description for negative subsequent strokes as well as positive strokes is developed, using a combination of either a single exponential or single power function for the wavefront, and the improved double-exponential function for peak and wavetail. For all developed analytical formulations of waveshapes, an analysis of the deviation from their numerically generated counterpart is performed, which shows that the deviation is depending on the assumptions and simplifications in the analytical formulation. However, in general, there is a good agreement between both analytically

and numerically generated waveshapes, even being identical for certain parameters. At last it has to be mentioned, that the developed mathematical functions are solely dependent on the input of the lightning stroke current amplitude, and therefore enable a direct variation of the lightning stroke crest current and waveform generation dependent on the local lightning stroke current probability function.

CHAPTER 3: THE TRANSMISSION LINE

To estimate the impact of a lightning stroke to an overhead transmission line, the appropriate representation is an essential requirement, because its line characteristics and occurring phenomena determine the resulting surge voltage on the transmission line [24]. Generally, two types of time-domain models for the representation of a transmission line exist, first, the lumped parameter model, e.g. the π-circuit model, and second the distributed parameter model, e.g. the travelling wave model. Depending on the time span of interest and the line length, a suitable line model has to be selected to describe the transmission line behaviour [60]. As lightning strokes are in the range of hundreds of kilohertz, and therefore are categorized as fast front transients, they can be sufficiently described with a distributed parameter or travelling wave model [24], [60], [61].

Within this chapter a brief overview of the different transmission line models and the theory behind them associated with the occurring phenomena during lightning stroke conditions is presented. Furthermore, the implementation into the used software PSCAD is discussed and a comparison of models applying the lightning stroke models from chapter 2.3 is performed.

3.1: TRANSMISSION LINE THEORY

3.1.1: TRAVELLING WAVES

The charge transfer during the lightning stroke initiates an electromagnetic surge in the struck conductor, which propagates along the line [62]. This behaviour can be described with the telegrapher's equation in the frequency domain derived from the Maxwell equations to determine the voltage and current magnitude along the transmission line. The equivalent circuit of a differential section of a single-phase transmission is illustrated in figure 3-1 alongside with the telegrapher's equation in equation (3.1) and (3.2). Further examples of different equivalent circuits are found in [7], [63].

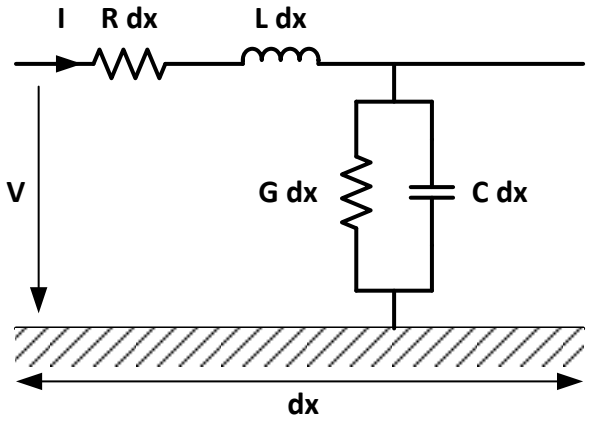

Figure 3-1: Equivalent circuit of a differential section of a single-conductor transmission line

$$\frac{d^2V(\omega)}{dx^2} - \big(R(\omega) + j\omega L(\omega)\big)\big(G(\omega) + j\omega C(\omega)\big) \cdot V(\omega) = 0 \tag{3.1}$$

$$\frac{d^2I(\omega)}{dx^2} - \big(R(\omega) + j\omega L(\omega)\big)\big(G(\omega) + j\omega C(\omega)\big) \cdot I(\omega) = 0 \tag{3.2}$$

In transmission line theory, a possible solution for these equations is found in the form of

$$V = V_R \cosh \gamma x - I_R Z_w(\omega) \sinh \gamma x \tag{3.3}$$

$$I = I_R \cosh \gamma x - V_R Y_w(\omega) \sinh \gamma x \tag{3.4}$$

with $V = V_R$, $I = I_R$ at $x = 0$, $V = V_S$, $I = I_s$ at $x = x_1$.

Thereby $Z_w(\omega) = \frac{1}{Y_w(\omega)} = \sqrt{\frac{R(\omega)+j\omega L(\omega)}{G(\omega)+j\omega C(\omega)}}$ is called the wave impedance of the transmission line and $v(\omega) = \frac{1}{\gamma(\omega)} = \sqrt{\big(R(\omega) + j\omega L(\omega)\big)(G(\omega) + j\omega C)(\omega)}$ the propagation speed.

At points of discontinuity, such as a junction of different conductor types, one part of the wave is reflected and the other part is transmitted onwards [63]. This is illustrated in figure 3-2, where a surge is reflected at $t = t_2$. The reflected and transmitted wave can be expressed with the reflection factor Γ and transmission factor T in formula (3.5) and (3.6).

$$\Gamma = \frac{Z_{w2} - Z_{w1}}{Z_{w2} + Z_{w1}} \tag{3.5}$$

$$\mathrm{T} = \frac{2Z_{w2}}{Z_{w2} + Z_{w1}} \tag{3.6}$$

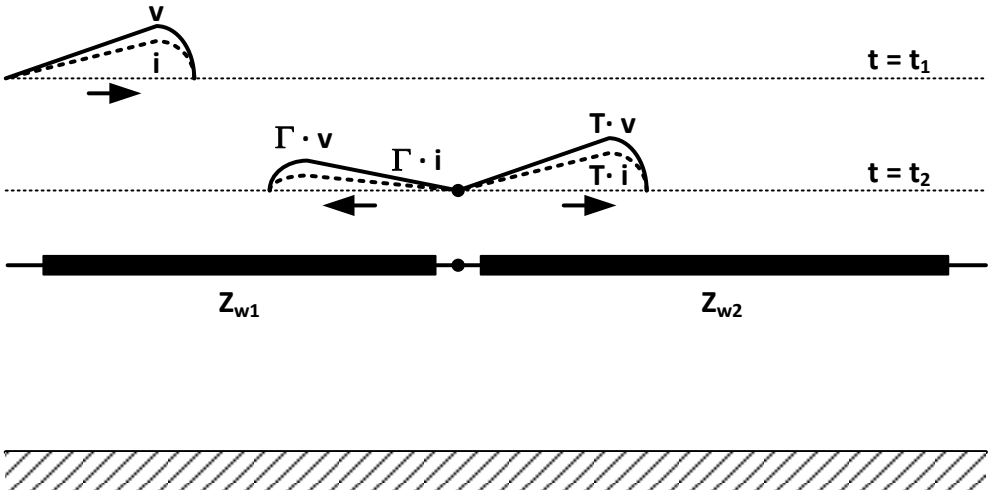

Figure 3-2: Example of wave propagation for an equivalent circuit of wave impedances with discontinuity

From this example it can be concluded that the reflection of waves leads to either a decrease or increase of amplitude due to superposition at various junction points.

3.1.2: SKIN-EFFECT

The skin effect describes the increase of a conductor's resistance as a result of the increase in frequency of the alternating current. Its origin can be explained with the distribution of current inside of a conductor as illustrated in figure 3-3.

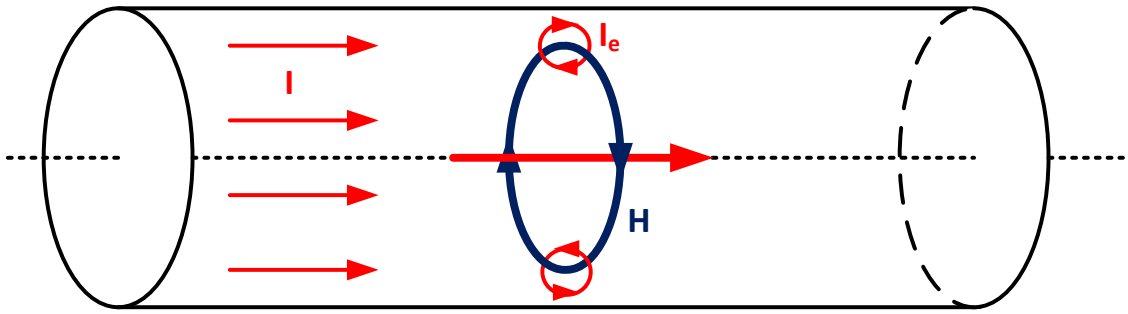

Figure 3-3: Illustration of eddy currents in a conductor

As a result of the flow of an alternating current (denoted *I* in figure 3-3) in a conductor, an alternating magnetic field (denoted *H*) inside and outside of the conductor is produced. Further, the change of the magnetic field creates an opposing electric field, also called the "back emf", which leads to eddy currents inside the conductor (denoted I_e). As more magnetic flux lines enclose the centre of the conductor, the eddy current density in the centre is higher than near the surface of the conductor. This leads to a displacement of current in the centre of the conductor and intensifies the current density near the conductor

surface. As a result the conductor's resistance is effectively increased, but its inductance is slightly decreased [64].

The transmission line metal conductor has a very high conductivity (see equation (3.7)) and the absolute penetration depth of the conductor can be simplified, according to equation (3.8) [62], [65].

$$\sigma \gg \omega\left|\underline{\varepsilon}\right| \tag{3.7}$$

$$\delta = \sqrt{\frac{2}{\omega\mu\sigma}} \tag{3.8}$$

For calculation of the transmission lines conductors internal resistance and reactance, the skin effect can be included in the geometric mean radius (GMR) of a hollow conductor [66]–[68]. In conjunction with this, the GMR calculation of stranded conductors is normally included to derive an equivalent for the GMR of a hollow conductor [69]. Together with the description of the earth-return in the next section, the frequency-dependent self- and mutual impedance of a transmission line multi-conductor system can be calculated.

3.1.3: INFLUENCE OF CURRENT EARTH-RETURN

The behaviour of multiconductor systems, such as 3-phase transmission lines, can be described with a complex symmetrical matrix system in the form of equation (3.9) and (3.10) [70], [71] as an extension of the equations in section 3.1.1.

$$\frac{d^2[V(\omega)]}{dx^2} = [Z_w(\omega)][Y_w(\omega)] \cdot [V(\omega)] \tag{3.9}$$

$$\frac{d^2[I(\omega)]}{dx^2} = [Y_w(\omega)][Z_w(\omega)] \cdot [I(\omega)] = 0 \tag{3.10}$$

Calculation of series impedances can be performed using either the well-established Carson-formulas [72], which contain infinite integrals with complex arguments or the Deri-Semlyen-formulas [73], where the concept of the "complex ground return plane" is applied. This concept introduces a superconducting current return plane (plane ideal ground) at the complex depth *D'*, which is equal to the complex penetration depth for plane waves, as illustrated in figure 3-4. The complex plane represents the mirroring surface for conductor images i' and j' at height -h_i and -h_j over real ground to derive formula for self and mutual impedances with ground return.

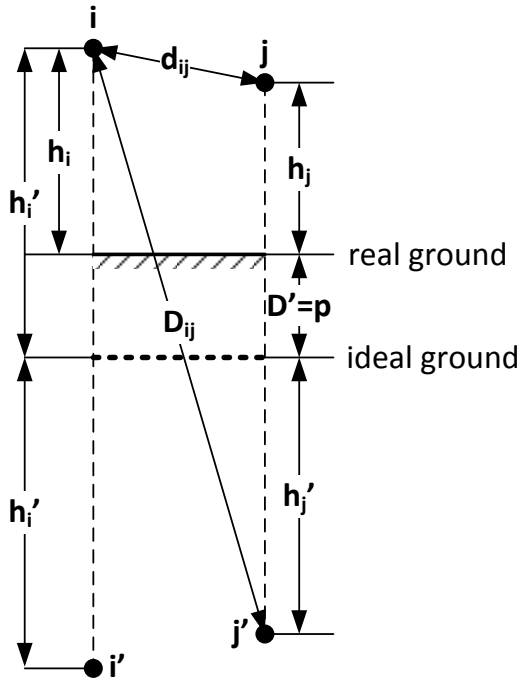

Figure 3-4: Example for the complex ground plane model, adapted from [74]

The complex depth D' in formula (3.11) is derived from the Maxwell equations and simplified with the assumption that the displacement current can be neglected, which is also applied in the Carson formulas.

$$\mathrm{D}' = \frac{1}{\sqrt{j\omega\mu_0(\sigma+j\omega\varepsilon)}} \cong \frac{1}{\sqrt{j\omega\mu_0\sigma}} \tag{3.11}$$

The series impedance matrix is comprised of

$$Z_{w,ij}(\omega) = R_{ij}(\omega) + j\omega L_{ij}(\omega) = Z_{w,i=j}(\omega) + Z_{w,i\neq j}(\omega)\,, \tag{3.12}$$

where the diagonal element ($i = j$) is the series self-impedance formed by the loop of the conductor i and the ground return, and where the off-diagonal element ($i \neq j$) is the series mutual impedance between conductors i and j [67].

The series self-impedance for a hollow conductor, taking the skin-effect penetration depth into account, is written in equation (3.13), where r_0 and r_1 are the inner and outer radius of the conductor and $I_k(x)$ and $K_k(x)$ are the modified Bessel functions of first and second kind.

$$Z_{w,i=j}(\omega) = j\omega\,\frac{\mu_0\mu}{2\pi\, r_1\, m}\cdot\frac{I_0(mr_1)\cdot K_1(mr_0)+I_1(mr_0)\cdot K_0(mr_1)}{I_1(mr_1)\cdot K_1(mr_0)-I_1(mr_0)\cdot K_1(mr_1)}\;,\; m = \sqrt{j\omega\mu_0\mu\sigma} \tag{3.13}$$

The mutual impedance between conductors (and conductor images) in equation (3.14) includes the complex penetration depth D' due to $h_i' = h_i + D'$.

$$Z_{w,i\neq j}(\omega) = j\omega\frac{\mu_0}{2\pi}\ln\frac{D_{ij}}{d_{ij}} \tag{3.14}$$

For aerial conductors, the admittance is normally calculated under the assumption, that the conductance is neglectable due to air being a lossless medium. The capacitance to ground $(i = j)$ and mutual capacitance between conductors $(i \neq j)$ in equation (3.15) then can be calculated from geometrical dimensions [67].

$$Y_{w,ij}(\omega)^{-1} = \frac{1}{j\omega C_{ij}(\omega)} = \frac{1}{j\omega 2\pi\varepsilon_0}\ln\frac{D_{ij}}{d_{ij}} \tag{3.15}$$

For both of the mentioned earth-return formulas, a constant electric ground conductivity and permittivity is assumed. However, in reality electric conductivity as well as permittivity are highly frequency-dependent [75], [76]. For frequencies in the range of kHz to MHz, which are considered in lightning studies, a significant difference between the simplified and the original complex depth D' (see formula (3.11)) exists [77]–[79]. The inclusion of a frequency-dependent electric ground conductivity and permittivity alters the waveshape of lightning strokes mainly as a result of a lower transmission line resistance at higher frequencies in comparison to the Carson or Deri-Semlyen approach [80]–[82]. It is recommended to include the frequency-dependency of the ground return path to improve the modelling of transmission lines during lightning stroke conditions, especially for high resistive soils [83]–[85].

There exist several methods of including the frequency-dependency of ground return in transmission line models summarized in a comparison of models in [80], [86]. All these methods propose formulas for the determination of the term in equation (3.16) as part of the penetration depth D'.

$$\sigma + \omega\varepsilon'' + j\omega\varepsilon' = \sigma + j\omega\varepsilon \tag{3.16}$$

In the following, it is focused on the three most recent and relevant approaches by Visacro/Alipio [87], Alipio [88] and Portela [78], [81], which all are based on measurements, although using different measurement approaches. However they all feature the separation of equation (3.16) into a low-frequency part at 100 Hz and an additional real and imaginary part for higher frequencies as generally formulated in equation (3.17) and (3.18) [89].

$$\sigma + j\omega\varepsilon = \sigma_0 + K_\sigma \omega^\alpha + jK_\varepsilon \omega^\alpha \tag{3.17}$$

$$K_\varepsilon = \frac{K_\sigma}{2\pi} \tan\left(\frac{\pi}{2}\alpha\right) \tag{3.18}$$

$$\sigma + j\omega\varepsilon = K_\sigma \left[1 + j \tan\left(\frac{\pi}{2}\alpha\right)\right] \omega^\alpha \tag{3.19}$$

Visacro's measurements are focused on the lightning response of grounding electrodes and field measurements performed in the frequency interval of 100 Hz to 4 MHz to obtain a formula for the frequency-dependency of soil.

In Alipio's approach, using Visacro's measurement data, this is developed further to take the dispersion of real soil into account. This originates from the fact that measurement of different types of soil can lead to the same low-frequency resistivity σ_0 due to the combination of factors, such as soil moisture, compactness and grain size of material.

Portela performed lab measurements on various soil blocks in the frequency interval of 100 Hz to 2 MHz. As real soil samples of the same site showed a dispersion of measurement results, the soil main electrical parameters are obtained through a statistical distribution.[78]

In table 3-1 these different formulations of the average frequency-dependency of soil are summarized. Visacro recommends using the low-frequency value of soil conductivity and permittivity up to a frequency of 10 kHz, as values do not change very much up to this frequency. However, this recommendation can be disregarded for lightning stroke applications, because the frequency range of concern is much higher.

Table 3-1: Summary of frequency-dependent soil formulations

Visacro [77]
$$\sigma = \sigma_0 + 1.5 \cdot 10^{-2.19}\ {\sigma_0}^{0.27} \left(\frac{f - 100\text{Hz}}{10^6}\right)^{0.65} \quad (3.20)$$ $$\omega\varepsilon = \omega\varepsilon_0(7.6 \cdot 10^3 \cdot f^{-0.4} + 1.3) \quad (3.21)$$
Alipio [88]
$$\sigma = \sigma_0 + {\sigma_0}^{0.27} \cdot 1.26 \cdot 10^{-2.19} \cdot \left(\frac{f}{1\ \text{MHz}}\right)^{0.54} \quad (3.22)$$ $$\omega\varepsilon = 12\ \omega\varepsilon_0 + \tan\left(\frac{\pi}{2}0.54\right) \cdot {\sigma_0}^{0.27} \cdot 1.26 \cdot 10^{-2.19} \cdot \left(\frac{f}{1\ \text{MHz}}\right)^{0.54} \quad (3.23)$$
Portela [78]
$$\sigma = \sigma_0 + 9.33444 \cdot 10^{-8}\omega^{0.705519} \quad (3.24)$$ $$\sigma + j\omega\varepsilon = 9.33444 \cdot 10^{-8}\omega^{0.705519} \tan\left(\frac{\pi}{2}0.705519\right) \quad (3.25)$$

In appendix B.1 a comparison of the different formulas for average values in table 3-1 and selected soil measurement results from [77], [78], [81]–[83], [87]–[90] is performed to investigate the consistency of these formulas.

From the plots comparison in appendix B.1 the following can be derived:

- the frequency-dependency of soil is significant above frequencies of 10 kHz, especially the change from resistive to inductive behaviour, seen in the phase angle
- phase angle values from different formulation of frequency-dependency of soil tend to the same value in the MHz range
- for low-conductive soils the change in the phase angle is much higher than for high-conductive soils
- the frequency-dependency of soil using Portela's average formulation is higher than Visacro's and Alipio's formulation
- Portela's average formulation differs more from specific measurement results than Visacro's and Alipio's

- Alipio's formulation tends to have a slower linear rise in the phase angle change, in comparison to the faster rise in Visacro's and Portela's formulation

Overall the trend of increasing conductivity and change to inductive behaviour of soil with increasing frequency is present in all formulations. The difference in the formulations can be attributed to the different measurement methods used to obtain parameters, different soil samples, soil moisture content [91], evaluation techniques and approximations made. As already suggested by Alipio [88], by taking the dispersion of measurement results into account, different parameters for optimistic, average and conservative frequency-dependent soil behaviour are used. This approach can be generalized to utilize Portela's formula for optimistic and Visacro's or Alipio's formula for average frequency-dependent soil behaviour.

The simulation software PSCADs earth-return model features only the Portela formulation of frequency-dependent ground return as an input parameter. Therefore the Visacro and Alipio formulations have to be recalculated to be inputted in a variation of Portela's formula (3.26) in case these are applied.

$$\sigma + j\omega\varepsilon = K_\varepsilon \left[\cot\left(\frac{\pi}{2}\alpha\right) + j\right]\left(\frac{\omega}{2\pi\cdot 10^6}\right)^\alpha \tag{3.26}$$

In appendix B.2 the results of a comparison of the performed curve-fitting to the Portela formulation in equation (3.19) and original curve progression for different soil conductivities is presented. The resulting parameters are summarized in table 3-2.

Table 3-2: Summary of average frequency-dependent soil parameters in Portela formulation

Model	K_ε	α
Portela	0.0117094	0.705519
Visacro	$(1.3 \cdot 10^{-2.19}\ {\sigma_0}^{0.05})/tan\left(\frac{\pi}{2}\alpha\right)$	0.65
Alipio	$(1.3 \cdot 10^{-2.19}\ {\sigma_0}^{0.13})/tan\left(\frac{\pi}{2}\alpha\right)$	0.65

3.1.4: CORONA-EFFECT

In non-uniform electric fields, emitted from stranded transmission line conductors, an increase in voltage causes the ionization of the surrounding air, which leads to a discharge in air at points with the highest electric field density [92]. This discharge is called corona discharge, or just corona with regard to transmission lines. Corona on transmission lines

features two effects. First, the ionized air surrounding the conductor causes an increase of the effective size of the conductor at a certain corona inception voltage, which also increases the capacitance of the conductor. And secondly, corona produces a considerable resistive loss due to its discharge process [93].
Derived from these effects, corona leads to significant attenuation of a lightning surge travelling on a transmission line and distortion and delay of the wavefront of the surge, respectively [92], [94]–[97]. Both effects are dependent on the properties of the conductor bundle, the wavefront steepness and polarity, as shown in field tests [92], [94]–[96], [98]–[103].

With respect to the surge voltages generated by a lightning stroke to a transmission line and the possible flashover of insulators, the corona effect leads to a decrease of overvoltages and flashover number [100], [102], [104]–[114].

The losses are dependent on the voltage surge applied to the conductor [94] and therefore loss formulas for half- or full cycle measurements as proposed in [100], [115] are not considered. However the losses can be described with the quadratic law of corona loss by Peek [116]. For the frequency range of a lightning surge, the corona attenuation loss can be simplified described with equation (3.27) as performed in [107], [113].

$$i(t) = \mathrm{k}_R \cdot \frac{(v(t)-v_c)^2}{v(t)} \tag{3.27}$$

Where, k_R is a constant, depending on the conductor radius r, height above ground h and the corona loss constant σ_G in formula (3.28). For a single conductor $\sigma_G = 1 \cdot 10^7$ according to [117].

$$\mathrm{k}_R = \sigma_G \cdot \sqrt{\frac{r}{2h}} \cdot 10^{-11}\,\frac{S}{m} \tag{3.28}$$

The corona behaviour with regard to the line capacitance can generally be described with the charge-voltage (q-v)-response of a conductor exemplarily illustrated in figure 3-5. Up to the corona inception voltage V_i, the conductors capacitance is equal to its geometric capacitance C. Although V_i can readily be calculated through Peek's Law [96] for various conductor sizes and bundle configurations for slow front surges, the corona inception voltage is dependent on the wavefront steepness, especially in the range of lightning [94], [98], [99], [118]. The main cause for this is a time delay until the corona starts, which

originates from the generation of free electrons to start the ionization process of air around the conductor. Therefore, to improve the calculation of the corona inception voltage, which is dependent on the rise-time and corona polarity, a $\frac{dq}{dt}$- or $\frac{dv}{dt}$-component or time delay τ can be added to V_i to increase the inception voltage to V_c [98], [99], [118]–[120]. Above V_c the voltage-dependent dynamic corona capacitance $\frac{dq}{du}$ is added. At the voltage decay of the wavefront, which normally features a small steepness, the conductor's capacitance can again be represented by its geometric capacitance.

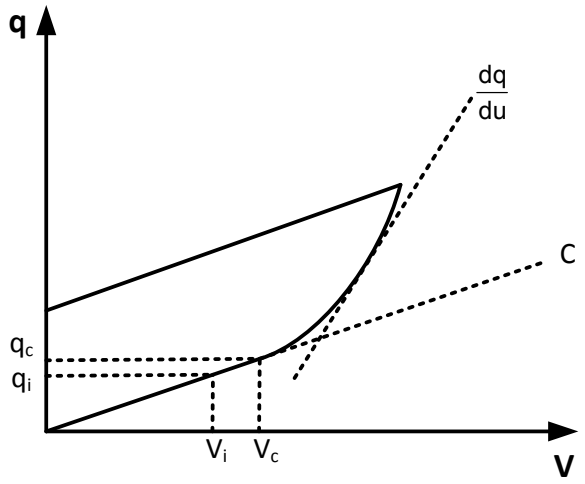

Figure 3-5: Typical q-V characteristic for a line conductor, adapted from [95]

Generally the modelling of the corona phenomenon can be divided into macroscopic models, which reproduce a measured or calculated q-V-curve [98], [100], [102], [107], [119], [121], or microscopic models, such as space-charge models [120], [122]. Despite the older piecewise models [97], [123], [124] and other approaches [102], [105], [109], [115], [118], [125]–[127], the Skilling/ Umoto model [104], [107], [108], [112], [113], Gary model [106], [110]–[112] and Siliciu-model [100], [123] and their variations [102], [108], [127] are mostly used in electromagnetic transient simulations for transmission lines in corona.

Derived from the literature above, it is concluded that a state-of-the-art corona model features a dynamic voltage-dependent corona capacitance as well as a dynamic corona inception voltage with a set of polarity parameters, which covers the range of slow to fast front transients due to the range of steepness of lightning strokes, such as positive slow front lightning strokes or negative fast-front subsequent lightning strokes. As measurements of q-V- curves and corona losses of the conductors used in this piece of work (see appendix B.5) are not available a generic corona model is needed.

In this respect, a comparison of the requirements above and prevalent used corona models shows, that the Skilling/Umoto model features no separate parameter sets for positive and negative polarity and the model input constants, such as the corona attenuation constant σ_C, have to be extracted from measurements. The Siliciu model is based on a fitting method to a measured q-V curve. In contrast to the mentioned restrictions of these two models, the Garry model [98] features a set of parameters for both single and bundled conductors and polarities respectively. Furthermore it is not dependent on a measured q-V-curve and allows the modelling of a continuous corona capacitance after reaching the maximum voltage and continuous changes between positive and negative corona. Due to these facts, it is decided to implement the Garry model and thus is investigated in more detail in the following section.

To derive the additional corona capacitance $C_{c,add}$ Gary's formulation of charge Q_c in equation (3.29) [98], [99] is rewritten to get the additional charge $Q_{c,add}$. The additional corona capacitance $C_{c,add}$ is then derived from equation (3.31) [95] in equation (3.32), which is based on [110] in case a differential capacitance is described.

$$Q_C = \begin{cases} C_0 V & V \le V_i\,,\ \frac{dV}{dt} > 0 \\ C_0 V_i \cdot \left(\frac{V}{V_i}\right)^B & V_i \le V,\ \frac{dV}{dt} > 0 \\ C_0 V_i \cdot \left(\frac{V_m}{V_i}\right)^B - C_0(V_m - V) & 0 \le V \le V_{max}\,, \frac{dV}{dt} < 0 \end{cases} \tag{3.29}$$

$$Q_{c,add} = \begin{cases} 0 & V \le V_i\,,\ \frac{dV}{dt} > 0 \\ C_0 V_i \cdot \left(\frac{V}{V_i}\right)^B - C_0 V & V_i \le V,\ \frac{dV}{dt} > 0 \\ C_0 V_i \cdot \left(\frac{V_m}{V_i}\right)^B - C_0(V_m - V) - C_0 V & 0 \le V \le V_{max}\,, \frac{dV}{dt} < 0 \end{cases} \tag{3.30}$$

$$C_{c,add} = \frac{dQ_{C,add}}{dV} \tag{3.31}$$

$$C_{c,add} = \begin{cases} 0 & V \le V_i\,,\ \frac{dV}{dt} > 0 \\ C_0 \left(B \left(\frac{V}{V_i}\right)^{B-1} - 1\right) & V_i \le V,\ \frac{dV}{dt} > 0 \\ 0 & 0 \le V \le V_{max}\,, \frac{dV}{dt} < 0 \end{cases} \tag{3.32}$$

The geometric capacitance of the line C_0 can be estimated with formula (3.33) in dependency of the conductor radius r and conductor height h above ground [7].

$$C_0 = \frac{10^{-9}}{18\ ln\frac{2h}{r}} \quad \left[\frac{F}{m}\right] \tag{3.33}$$

Parameter *B* is obtained from Gary's measurements [98], [99] and is dependent on the conductor diameter *d* or bundle arrangement with n (2 to 4) conductors in a bundle, reproduced in table 3-3. Another set of formulas for parameter *B* is proposed in [106], [110], summarized in table 3-4.

Table 3-3: Parameter *B* for corona model in dependency of polarity according to [98], [99]

Conductor type	Positive polarity	Negative polarity
Single conductor (*d* in m)	$2.63 \cdot d^{0.153}$	$1.121 + 3.4\,d$
Bundle conductor (*n* in pu)	$1.3 + 0.03 \cdot n$	$0.95 \cdot n^{0.2}$

Table 3-4: Parameter *B* for corona model in dependency of polarity according to [106], [110]

Conductor type	Positive polarity	Negative polarity
Single conductor (*r* in cm)	$0.22 \cdot r + 1.2$	$0.07 \cdot r + 1.12$
Bundle conductor (*n* in pu)	$1.52 - 0.15 \cdot \ln n$	$1.28 - 0.08 \cdot \ln n$

In figure 3-6 and figure 3-7 the results of a comparison of parameter B values from Gary [98], [99] and Naredo/Khadir [106], [110] is performed.

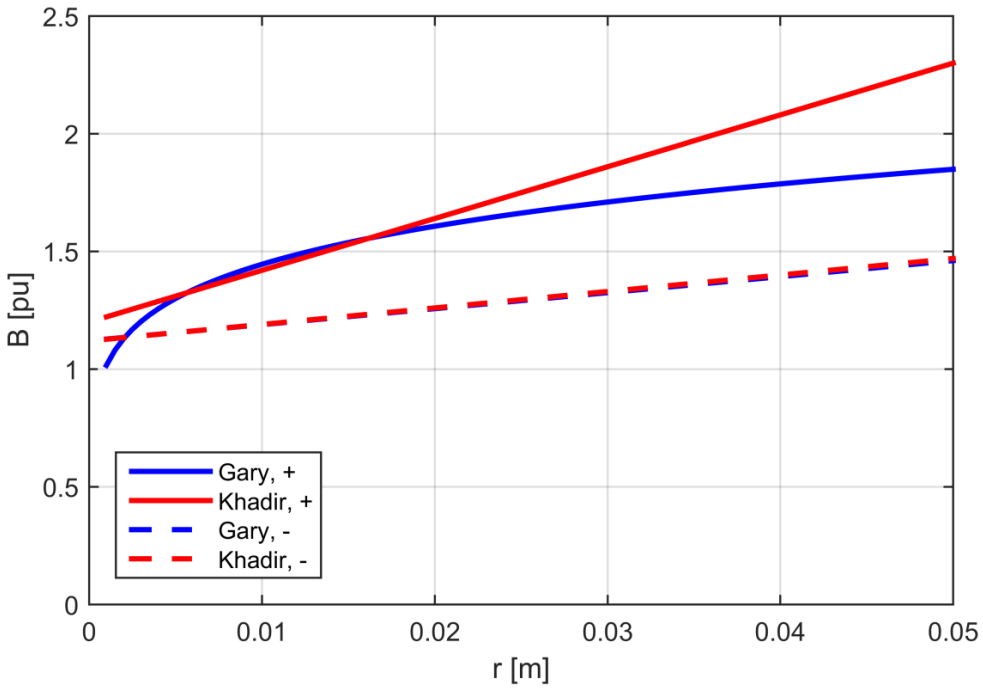

Figure 3-6: Comparison of corona model parameter B values, single conductor

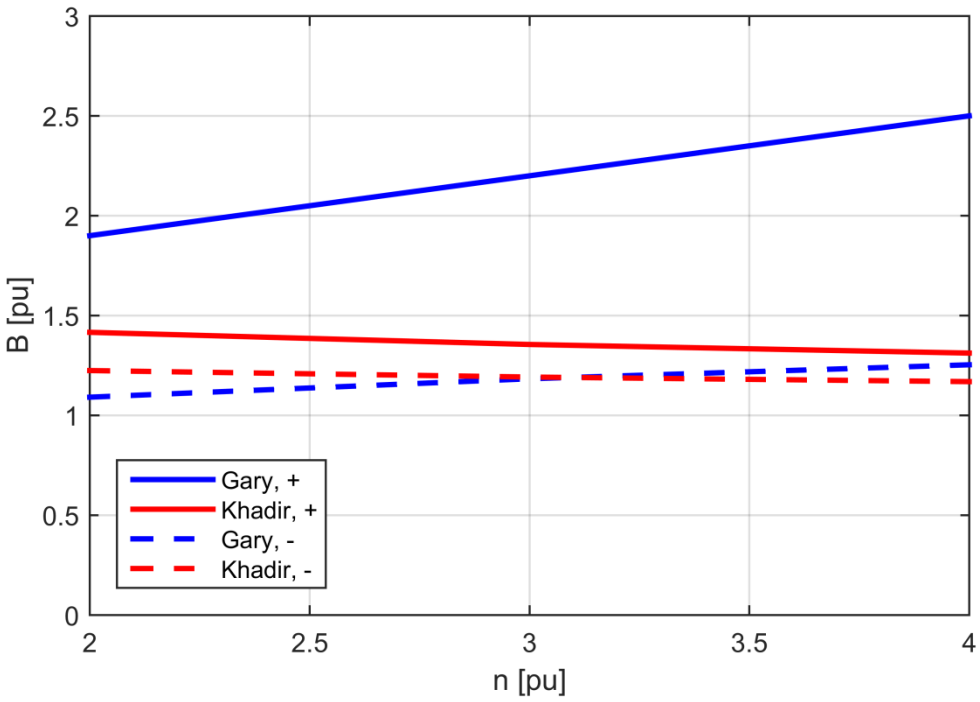

Figure 3-7: Comparison of corona model parameter B values, bundled conductor

The evaluation shows that both parameter formulations match in a reasonable conductor radius range for single conductors and negative corona bundled conductors. For the positive corona bundled conductor Gary's formulation leads to an increased corona capacitance in comparison to Naredo/Khadir's formulation. In this respect, the decision is made to use Gary's original corona formulation with corresponding parameters.

The corona inception voltage V_i can be calculated from equation (3.34) and the critical electric field.

$$V_0 = \frac{2\pi\varepsilon_0 r E_0}{C_0} \tag{3.34}$$

For the critical electric field there exists some experimentally obtained formula with the three well-known ones by CIGRE [24], equation (3.35), Peek [116], equation (3.36) and Skilling [128], equation (3.37), where m is the surface roughness factor of the conductor (0.82 according to [96]), δ is the air density factor (usually set to 1) and r is the conductor radius in cm.

$$E_{0,CIGRE} = 23 \cdot \left(1 + \frac{1.22}{(2r)^{0.37}}\right) \quad \left[\frac{kV}{cm}\right] \tag{3.35}$$

$$E_{0,Peek} = 30 \cdot \mathrm{m} \cdot \delta^{0.67} \left(1 + \frac{0.3}{\sqrt{\delta r}}\right) \quad \left[\frac{kV}{cm}\right] \tag{3.36}$$

$$E_{0,Skilling} = 23 \cdot \mathrm{m} \cdot \delta^{0.67} \left(1 + \frac{0.3}{\sqrt{r}}\right) \quad \left[\frac{kV}{cm}\right] \tag{3.37}$$

The discrepancy between the CIGRE formula and Peek and Skilling formula is quite distinctive. In [106] it is shown that a lower inception voltage, obtained from a lower critical electrical field leads to a higher reduction of steepness of the waveform. In [105] the proposal is given to apply the CIGRE formula for positive and the Peek formula for negative corona, since the positive inception voltage is higher than for negative corona, which is adopted here. Furthermore the inception voltage also depends on the maximum voltage and rise-time of the surge voltage generating corona [94], [98], [99].

Measurement data with regard to the dependency of inception voltage V_i on the wavefront steepness (or maximum surge voltage and front time τ) is limited to references [94], [95], [99] and a general formulation based on voltage steepness $\frac{dV}{dt}$ for corona modelling is not available. Therefore, based on the above mentioned references for an approximately matching conductor size for the earth wire (see appendix B.5), a corona inception formulation depending on voltage steepness $\frac{dV}{dt}$ is proposed. All data is referenced to the peek formulation with $\delta = 1$ and $\mathrm{m} = 0.82$.

For various waveforms the positive and negative corona inception voltage dependent on the square-root of maximum voltage divided by rise-time is extracted from the mentioned references and plotted in figure 3-8 and figure 3-9. There, the maximum voltage of interest is limited by the breakdown voltage of insulators, discussed in the next chapter.

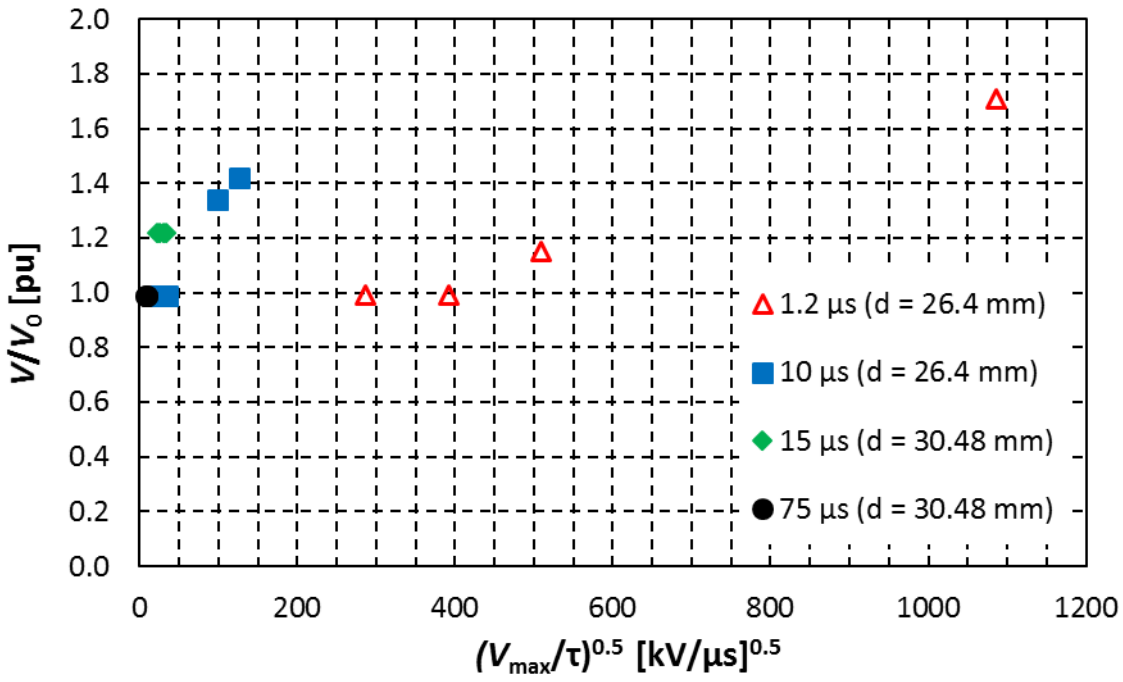

Figure 3-8: **Dependency of inception voltage on maximum voltage and rise-time τ for positive polarity, adapted from** [94], [95], [99]

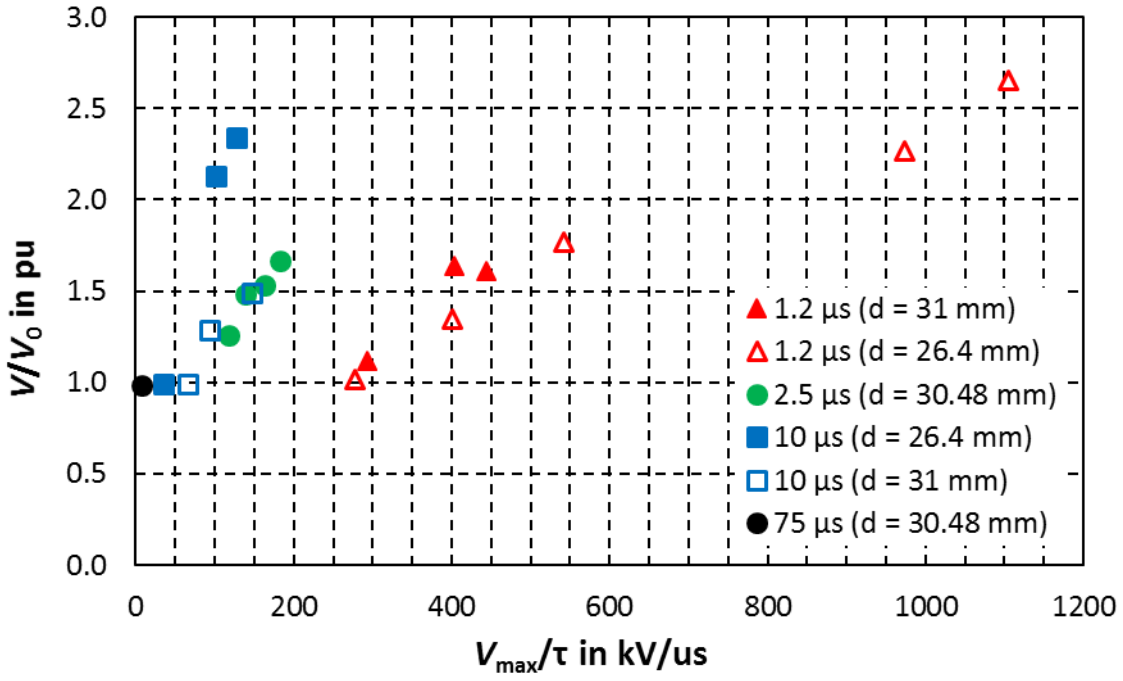

Figure 3-9: **Dependency of inception voltage on maximum voltage and rise-time τ for negative polarity, adapted from** [94], [95], [99]

Apart from variations in the measurements, the following can be derived from figure 3-8 and figure 3-9 and its literature sources:

- the influence of maximum voltage and rise-time is limited to surges with rise-times up to approximately 75 µs for both positive and negative corona

- the inception voltage is higher for negative polarity due to the slower ionization process started by ions
- above the nominal inception voltage V_0 the increase of inception voltage in dependency of the maximum voltage is linear
- above the nominal inception voltage V_0 the increase of inception voltage in dependency of the rise-time is logarithmic

Through adaption of measurement data and a regression analysis, a formula for the inception voltage $\frac{V_i}{V_0}$ for positive and negative corona is derived for this work, which fits the above described behaviour. This is illustrated in figure 3-10 and figure 3-11, where the data points extracted from [94], [95], [99] are transformed into continuous lines through regression analysis. The dashed lines are derived from matching data points with the same maximum voltage and represent the change of $\frac{dV}{dt}$.

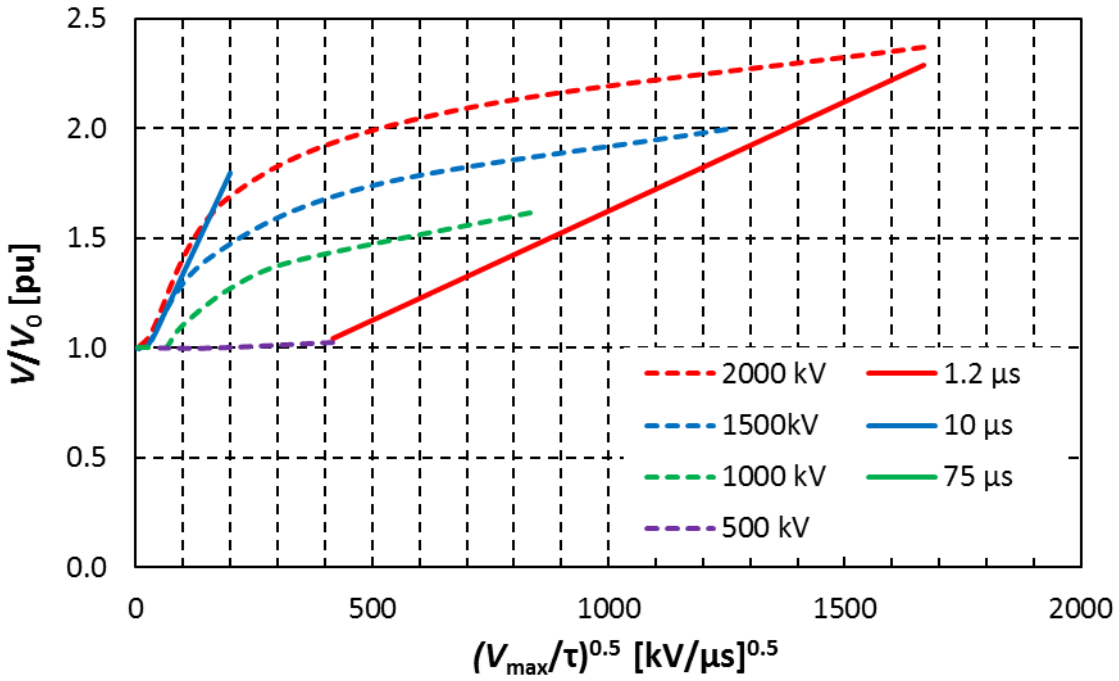

Figure 3-10: Regression analysis of the dependency of inception voltage on maximum voltage and rise-time τ for positive polarity, dashed lines: maximum voltage fixed, continuous line: rise-time fixed

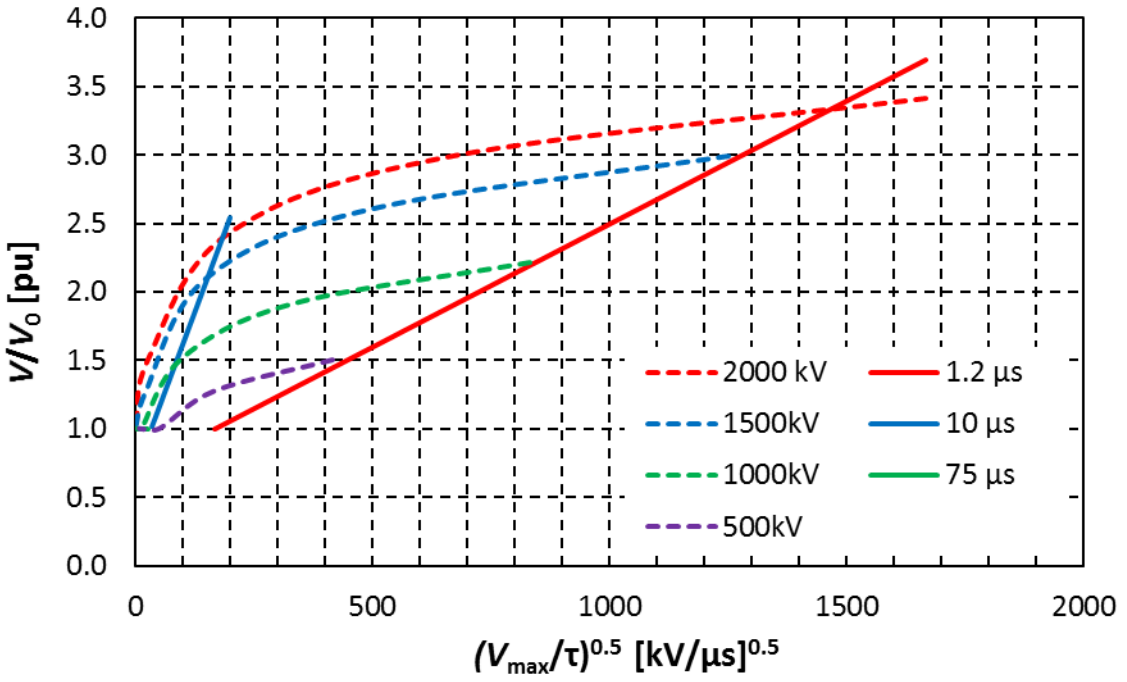

Figure 3-11: Regression analysis of the dependency of inception voltage on maximum voltage and rise-time τ for negative polarity, dashed lines: maximum voltage fixed, continuous line: rise-time fixed

The best fit to the data is obtained with formula (3.38) for positive and (3.39) for negative corona, respectively. However, the lack of measurement data in the region of 10 µs to 75 µs for negative as well as for the whole range for positive corona does not permit a more accurate fitting.

$$\frac{V_{i+}}{V_0} = \begin{cases} 1 & ,0 < V \leq V_{dyn} \\ V_{dyn} = 0.01 \cdot V^{0.4569} ln\left(\frac{dV}{dt}\right) & ,V > V_{dyn} \end{cases} \tag{3.38}$$

$$\frac{V_{i-}}{V_0} = \begin{cases} 1 & ,0 < V \leq V_{dyn} \\ V_{dyn} = 0.017 \cdot V^{0.4346} ln\left(\frac{dV}{dt}\right) & ,V > V_{dyn} \end{cases} \tag{3.39}$$

With these formulas a separate calculation of electric field strength for negative and positive corona as mentioned earlier is not necessary and the base critical electric field strength can be calculated from the Peek formula (3.36).

With the mathematical description of both positive and negative corona effect, a simulation model can be constructed, which features a dynamic corona inception voltage and corona capacitance.

3.2: MODELLING OF TRANSMISSION LINES

As already briefly explained in the introduction to this chapter, various line models can be applied to simulate the transmission line behaviour during lightning stroke conditions. Transmission line models have been improved over the last two decades by many authors to incorporate the different effects as discussed in the previous section, but generally no transmission line model exists, which is suitable for all frequency ranges and phenomena associated with steady-state, slow, fast and very-fast transients. Models have to be adapted for a specific range of frequencies and effects to simulate the dominant behaviour of the transmission line. The basis for each line model is the R-L-C parameters calculation from the line geometry and materials' electrical characteristics. Therefore, the electrical characteristics of a line are briefly discussed, followed by the presentation of different models and their utilization in an example network to show the impact of each physical effect on the voltage waveform, originated from a lightning stroke.

3.2.1: TRANSMISSION LINE CHARACTERISTICS

As shown in the section 3.1, the calculation of the impedance and admittance matrix of a multiphase system is complex. Therefore simulation programs feature a separate or built-in tool to calculate these matrices for a single frequency or a range of frequencies for input to a transmission line model. These tools generally feature some simplifications, such as the already discussed simplifications for stranded conductor, skin-effect and frequency-dependent earth-return and line sag. In this section, the influences of the line characteristics themselves are discussed to improve the understanding of input parameters to the transmission line models.

With the findings from section 3.1, the transmission line characteristics of the considered 400 kV transmission line with data from appendix B.3 to B.5 can be calculated. This is performed using the Line Constant Program (LCP) from PSCAD for low and high soil conductivity, calculation of R-L-C data for each frequency, with either Carson earth return or frequency-dependent earth-return formulation. The input of the line sag is assumed to be 15 m for the phase wires and 10 m for the shielding wire.
In figure 3-12 and figure 3-13, the series and shunt line characteristics of one circuit of the double-circuit line for the frequency range from 1 kHz to 2 MHz for soil resistivity ρ=20000 Ωm and ρ=100 Ωm are depicted.

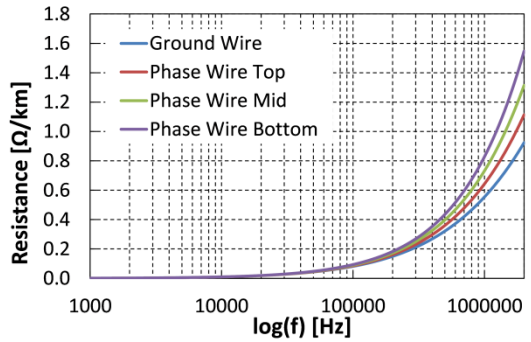

a) Resistance, earth-return with Carson formula

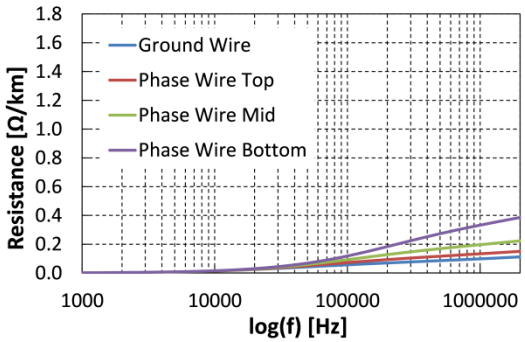

b) Resistance, frequency-dependent earth-return

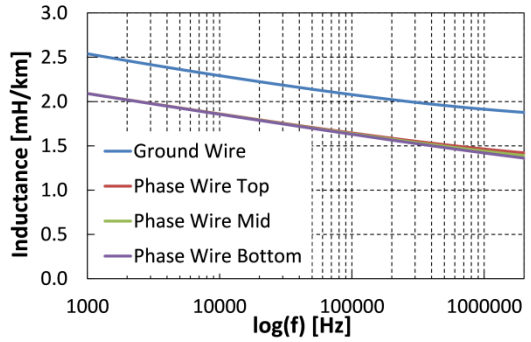

c) Inductance, earth-return with Carson formula

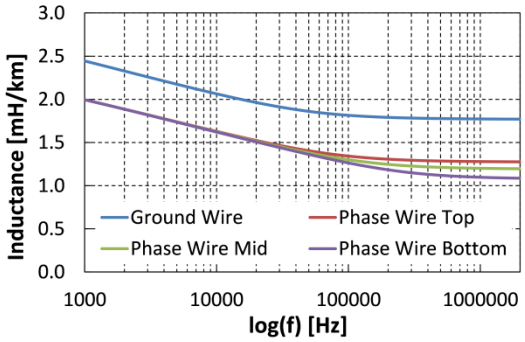

d) Inductance, frequency-dependent earth-return

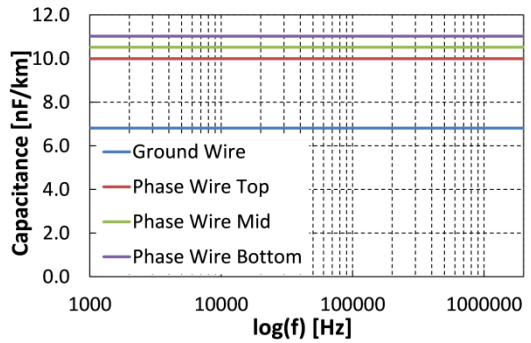

e) Capacitance, earth-return with Carson formula

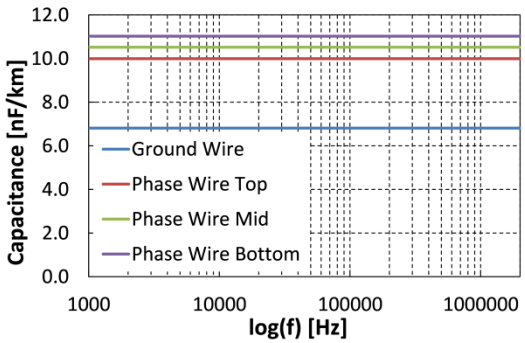

f) Capacitance, frequency-dependent earth-return

Figure 3-12: Series and shunt line characteristics of the considered 400 kV transmission line, low conductive soil ρ=20000 Ωm

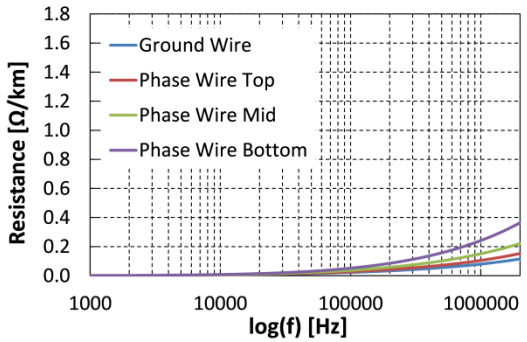

a) Resistance, earth-return with Carson formula

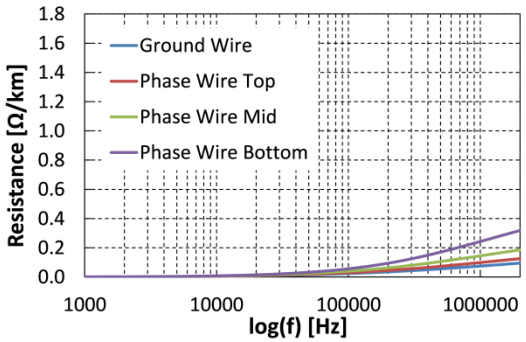

b) Resistance, frequency-dependent earth-return

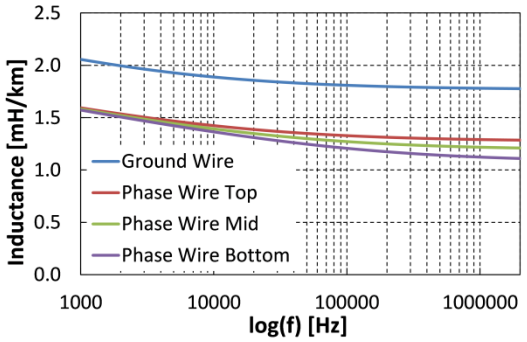

c) Inductance, earth-return with Carson formula

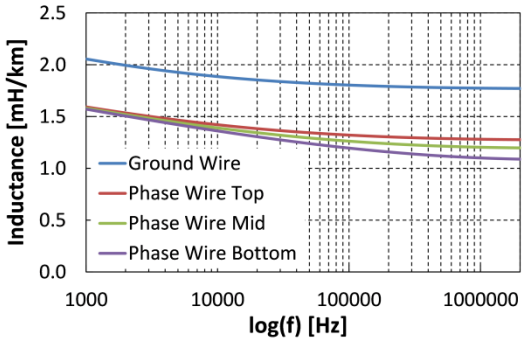

d) Inductance, frequency-dependent earth-return

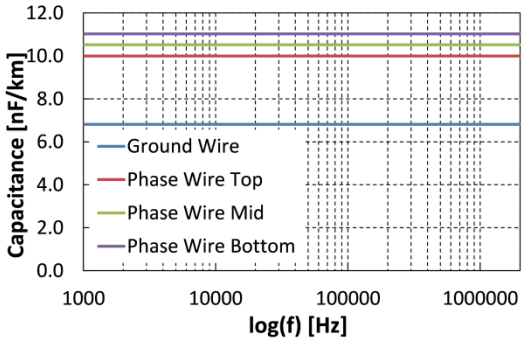

e) Capacitance, earth-return with Carson formula

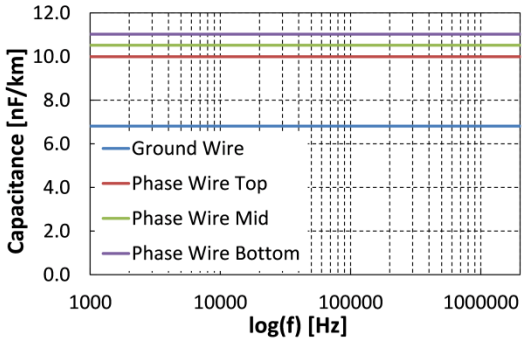

f) Capacitance, frequency-dependent earth-return

Figure 3-13: Series and shunt line characteristics of the considered 400 kV transmission line, high conductive soil ρ=100 Ωm

A comparison of the frequency-response characteristics of series impedance and shunt admittance with and without frequency-dependent earth-return shows that:

- for low conductive soil the line resistance and inductance with frequency-dependent earth-return in the frequency range starting from 10 kHz are reduced in comparison to those with Carson earth-return
- for high conductive soil the effect of frequency-dependent earth-return on line resistance and inductance is minimal

- the shunt-capacitance is not influenced by the earth-return, only by height
- for low conductive soil the line resistance and inductance with frequency-dependent earth-return tends to the behaviour of the line resistance and inductance for high-conductive soil

In both figure 3-12 and figure 3-13, the influence of the conductor height and thus the importance of reasonable assumptions for the conductor sag input can be observed. The shunt capacitance for the ground wire is smaller with increasing height of the conductor above ground, as calculated in equation (3.15). There, D_{ij} includes the absolute value of penetration depth with height above ground in the denominator. For resistance and inductance the earth-return equation (3.14) has to be looked at. The distance of a conductor from its mirror image D_{ij} is complex in this case and therefore includes a complex earth-return, which is frequency-dependent. Although not depicted in the resistance plots, for small frequencies the conductor resistance is bigger with conductor height above ground due to D_{ij} in the enumerator. However, due to the frequency-dependency of the imaginary part of D' for both Carson and frequency-dependent formulation of ground return, the increase of resistance with frequency for greater conductor height above ground is lower. Since the inductance contains the real part of D' in the enumerator, the biggest inductance is calculated with greatest height above ground of a conductor.

After the discussion of the input data, the different models used in simulations are explained, followed by an example, which shows the effect mentioned in the preceding paragraph.

3.2.2: LOSSLESS LINE MODEL

The lossless line or Bergeron line model, first described in [129], can be used for fast-and very fast-front transients, such as lightning, to model the travelling wave phenomenon on transmission lines. The model is based on the internal current sources, characteristic line impedance and time delay τ to model the propagation of waves at the port connections, as shown in the equivalent circuit in figure 3-14.

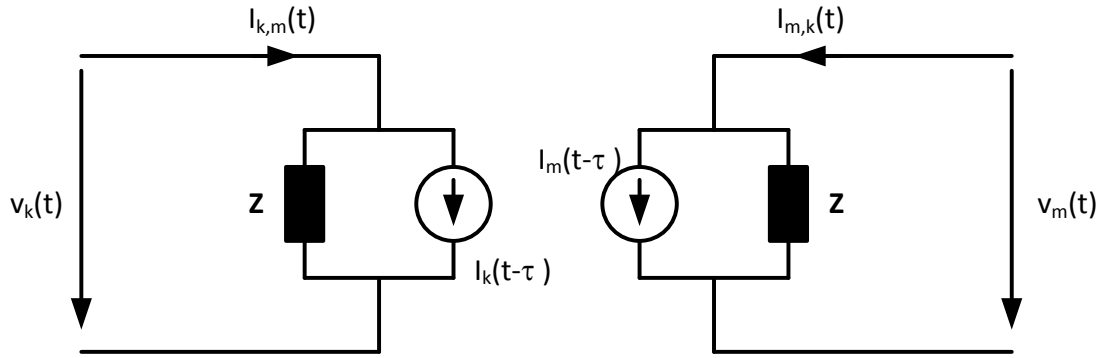

Figure 3-14: Equivalent Circuit of Lossless Line or Bergeron Line Model

The Bergeron model is a single-frequency model, as the characteristic impedance is calculated at a single frequency. Although nowadays, variations of the Bergeron model include single-frequency loss approximations, while the original model features no resistances, frequency-dependent effects, important for the attenuation of travelling waves cannot be included. Therefore this model is depreciated in simulations of transmission lines, however still in use for the simulation of vertical conductors (see chapter 5). The model is readily available in PSCAD/EMTDC and enables fixed damping resistances at the line terminals.

3.2.3: FREQUENCY-DEPENDENT LINE MODEL

The frequency-dependent line model is an elaborated model, which takes travelling waves as well as the skin-effect into account. The model is based on the calculation of R-L-C values for a range of frequencies, as shown in section 3.2.1. These values are transformed into the propagation and characteristic admittance matrix and a rational function approximation fitting algorithm in the frequency domain used to enable frequency-dependent behaviour of the line [130]–[132]. The fitting algorithm is embedded in the LCP of PSCAD/EMTDC and furthermore offers the input of pre-calculated R-L-C parameters, if necessary.

3.2.4: FREQUENCY-DEPENDENT LINE MODEL WITH CORONA-EFFECT

The frequency-dependent line model with corona effect is a combination of the already available frequency-dependent line model and a dynamic resistance and capacitance to ground according to the description in subsection 3.1.4. The implementation of a variable network element is not a straightforward procedure and necessitates background

knowledge of the EMT program structure. The mathematical basics for time discretization and computer implementation of differential equations for capacitances and inductances can be found in [67], [133], [134].

In detail, time-dependent elements, such as inductors and capacitors are represented either by a Thevenin- or Norton-equivalent circuit. The latter is used PSCAD/EMTDC, as illustrated in figure 3-15.

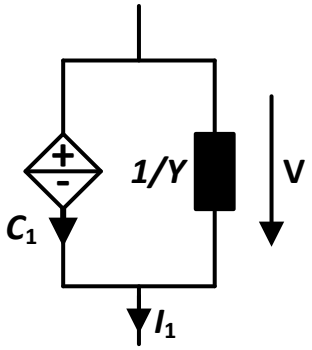

Figure 3-15: Representation of lumped elements in digital computer simulations

For the representation of these elements, the current C_1 and slope Y are needed to calculate the new current I_1 for the next time-step in equation (3.40).

$$I_1 = \mathrm{Y} \cdot \mathrm{V}_1 + C_1, \tag{3.40}$$

To implement a dynamic capacitance for the corona effect with its mathematical description a custom switched type model needs to be created in the EMTDC Fortran section, where calculations are performed in between time-steps of the simulation. The so-called 'GEQ'-interface is utilized to interface with the electric network solution, which enables the direct implementation of the Norton-equivalent on a single-phase basis.
EMTDC offers either a direct call of its so called 'Equivalent Conductance (GEQ) Electric Interface', where a re-triangularization of the conductance matrix at discontinuities has to be performed manually within the code or its 'Custom Current Source and Conductance Interface (CCSC)', which is a user-friendly interface routine of the GEQ. Furthermore, a pre-built variable resistance/inductance/capacitance model is available, but it is not capable of injecting any current and features a one-time-step delay between the control signal transfer and the electric circuit.

For the corona losses, either the conductance Y and current C_1 can be calculated from the derivation of (3.27) with the trapezoidal rule and the "history" current as

$$Y = k_R - k_R \frac{V^2}{V_{co}^2}, \tag{3.41}$$

$$C_1 = C_0 \tag{3.42}$$

to utilize the CCSC or direct GEQ interface or the pre-built variable resistance block can be utilized.

For the corona dynamic capacitance, the differential equation in formula (3.32) for the additional capacitance to ground needs to be transformed into a linear equation with the trapezoidal rule. Since this process is not straight-forward first the linearization of a constant capacitance is investigated.
For a constant capacitance the differential equation in (3.43) is transformed into a linear equation with the trapezoidal rule.

$$\frac{dv}{dt} = \frac{i}{C} \tag{3.43}$$

The variables Y and C_1 for the Norton equivalent circuit can then be determined from

$$Y = \frac{2C}{\Delta t}, \tag{3.44}$$

$$C_1 = -2\mathrm{Y} \cdot \mathrm{V}_0 - C_0 . \tag{3.45}$$

To linearize a variable capacitance, a differential equation has to be linearized. With the first terms of the Taylor series the dynamic capacitance in equation (3.46) can be approximated as a linear equation and Y and C_1 determined, as shown in appendix B.6.

$$\frac{dv}{dt} = \frac{i}{C \cdot \left[B\left(\frac{V}{V_i}\right)^{B-1} - 1\right]}. \tag{3.46}$$

In case a fixed capacitance for each time-step is modelled, the formula in (3.30) needs to solved for a static charge.
The implementation of a capacitance with discontinuities, as in the above case, faces some challenges with regard to numerical stability of the simulation. To avoid numerical instabilities in the change of capacitance, especially at corona inception, where the additional line capacitance jumps from 0 to a value of $C_0 \cdot (B - 1)$, and reach of maximum voltage, strategies including damping of capacitors, such as recommended in

[67], [105] can be employed. However, in the case of capacitance the 'GEQ'-interface features an additional voltage source, which can be used to charge the capacitance to the value of inception voltage at the switch-on of corona.

With the above formula and the formulation of the dynamic inception voltage the corona loss shunt resistance and capacitance is implemented in the corona model with pre-built variable resistance/inductance/capacitance model. Since the corona loss shunt resistance and capacitance cannot be incorporated into the frequency-dependent line model, it is distributed along the line, at each end of a split 10 m frequency-dependent line model.

3.2.5: VERIFICATION OF TRANSMISSION LINE MODELS

After the presentation and brief explanation of the transmission line models, the different physical effects explained in section 3.1 are shown in an example simulation. Furthermore the example simulation is used to verify the model, which is accomplished through a comparison with simulation results from another EMT software in [135].

The example network consists of a 1200 m LV single phase transmission line with shield wire (8.4 m and 7.2 m height, solid copper conductor, radius 5 mm) and nodes every 300 m to measure the shield wire voltage, as depicted in figure 3-16. The transmission line is terminated with its wave impedance of 480 Ω at the injection end. A lightning stroke waveshape with 1 A amplitude, 30% to 90% rise time t_{d30}=0.2 µs and 21 µs time to half value is injected at the earth wire at one end of the line section to produce the voltage wave. Line-to-earth voltage is measured at nodes 'C' and 'E'.

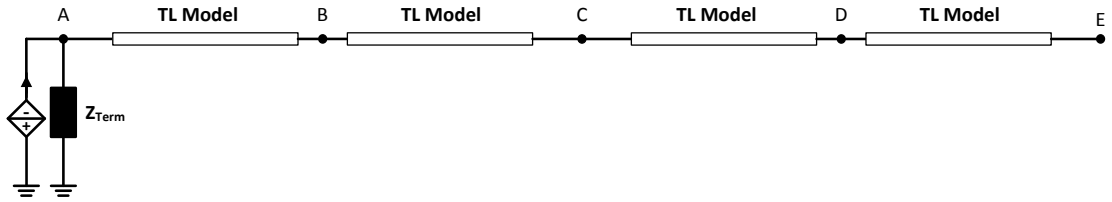

Figure 3-16: Example network of a transmission line (TL) section

The transmission line input parameters are calculated from the above mentioned geometry and conductor data with the internal PSCAD LCP. To show the influence of the frequency-dependent earth-return (see section 3.1.3), a comparison with the Carson earth-return calculation at 0.001 S/m and 0.0001 S/m ground conductivity is made for the frequency-dependent line model, which can be compared to the simulation results in [135] for verification purpose. Additionally the simulations are conducted with the depreciated

Bergeron model for parameters calculated at f = 1 MHz with the Carson earth-return calculation to show the travelling wave phenomena.

The results of the simulations for node voltages ‘C’ and ‘E’ are plotted in appendix B.8 for soil resistivity 1000 Ωm and 10000 Ωm, respectively. A visual comparison of results with those from [135] in appendix B.8 shows a very good agreement for both frequency-dependent line models with Carsons and frequency-dependent (Portela) formulation of the earth-return. Furthermore, results show the travelling wave effect due to the total reflection of waves at point ‘E’ alongside the and skin-effect due to the damping effect of the frequency-dependent resistance along the line. In contrast to the frequency-dependent line model, the Bergeron model features no damping and reflections occur even at the node terminations. The lower voltage encountered at the Bergeron line model is explained with the fixed resistance calculation at 1 MHz, which is overestimated in this case due to the total front and tail time longer than 1 µs. Furthermore, the inclusion of the frequency-dependent earth-return in the frequency-dependent line model reduces the crest voltage and dampens travelling waves.

For the verification of the corona model together with the frequency-dependent line model, the so-called Tidd-Line corona measurement results [101], [136], [137] are utilized. The necessary input data for the Tidd-Line is summarized in appendix B.7. Since no information about the used impulse generator and its internal construction is available, a simple voltage source is used to inject a 1700 kV 1.0/6.0 µs waveform, derived from the plots in [136]. The simulation results of the corona effect are plotted in appendix B.9. As can be seen from the comparison of simulation results in appendix B.9, some deviations in the resulting crest voltage and occurring travelling waves are present. The main cause for this is the simplification of the generation of impregnated voltage and corona model simplifications. However when the voltage delays at the measurement points are compared, a reasonable agreement with the measurement can be found.

Due to the extensive calculation time of the simulation and neglect of corona in various studies, the effect of corona on a common span length of 200 m is assessed for the example 400 kV line’s shield wire at standard height in this work (data from appendix F.1). To avoid travelling waves and surge reflections at the tower footing, the 200 m line is terminated with its surge impedance on both ends, as illustrated in figure 3-17. To

evaluate the influence of corona, a 30 kA first and 12 kA subsequent stroke is injected half-way and a comparison conducted between a line model with and without corona.

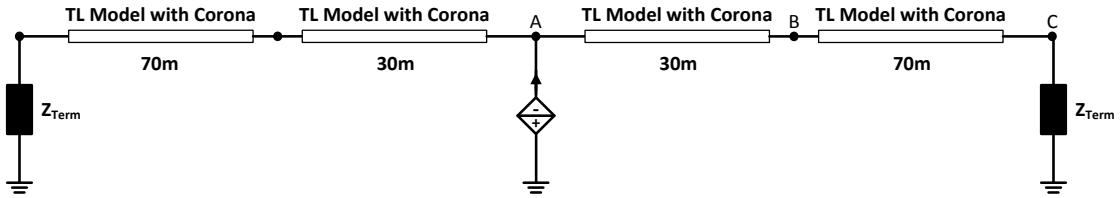

Figure 3-17: Simulation circuit for corona evaluation of a 200 m standard tower span, single shield wire configuration

The simulation results for a first and subsequent negative stroke for the simulation circuit in figure 3-17 are plotted in figure 3-18 and figure 3-19 for the stroke point (node A) and 30 m (node B) and 100 m away (node C).

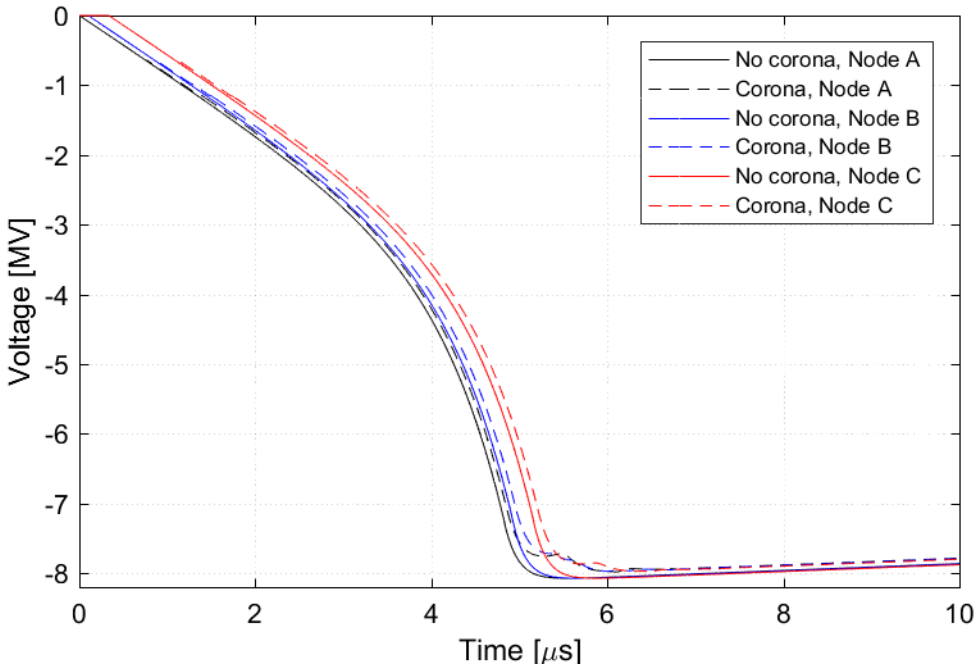

Figure 3-18: Simulation results for a 30 kA first negative stroke for corona evaluation

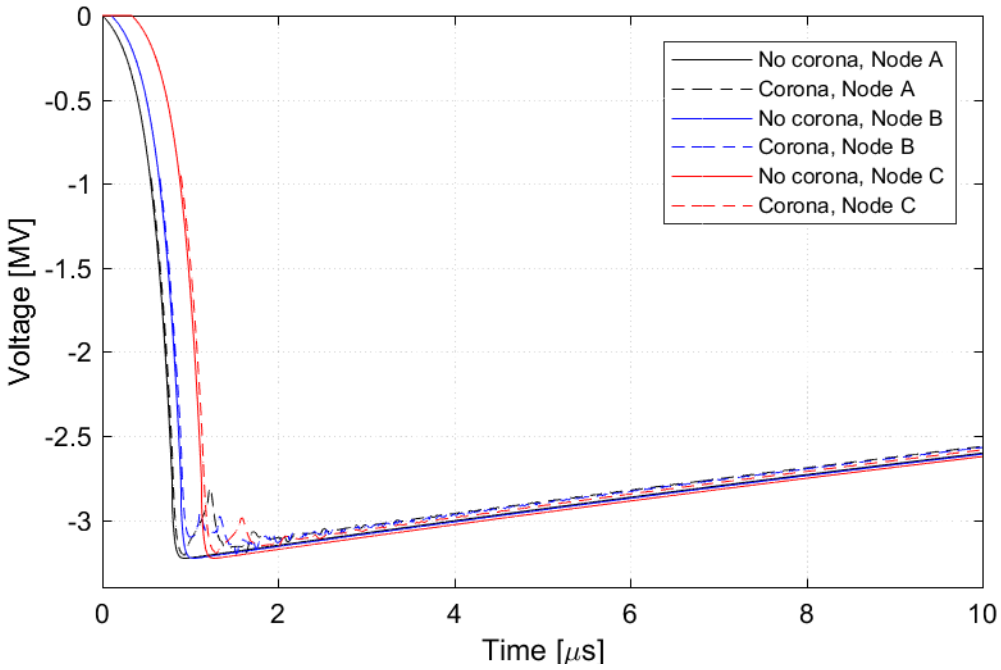

Figure 3-19: Simulation results for a 12 kA subsequent negative stroke for corona evaluation

The results clearly show that corona has an effect on the waveshape, more pronounced at the voltage peak, but overall it is a marginal one, even at 100 m (node C) from the injection point.

In summary, the corona effect has an influence on the wavefront of a voltage surge generated by a lightning stroke, but its influence is dependent on the line length. The effect of corona on the line voltage is marginal in close proximity to the stroke point, but is increased with increasing travelling time and line length, respectively.

3.3: SUMMARY AND CONCLUSION ON TRANSMISSION LINES

In this chapter the occurring physical effects of a transmission line during a lightning stroke and their modelling in a transient simulation are discussed and investigated.

The physical effects of travelling waves, line conductor skin-effect, current earth-return and corona play a decisive role in the simulation of surge voltages originating from a lightning stroke to a transmission line. Travelling waves produce reflections at points of changing surge impedance, which lead to additional maxima and minima of voltage along the line. The skin-effect increases the line conductor resistance due to eddy currents, which reduce the effective conductor size and consequentially increase the damping of fast surges. The inclusion of current earth-return with its soil frequency-dependency

additionally reduces the voltage surge on the line due to its inductive behaviour at higher frequencies. The corona effect can be described as the inclusion of an additional capacitance above an inception voltage, which adds an additional delay effect to a voltage surge along the transmission line. For the corona effect, a dynamic calculation method for the corona inception voltage is developed, based on available corona measurements from the literature, which takes into account the influence of the rise-time of the surge voltage on the corona inception voltage. This improvement helps to increase the corona inception voltage for fast rise-times, mostly encountered at subsequent lightning strokes, and thus delay the start of corona, rather than taking into account a fixed inception voltage for all surge voltage rise-times. As a result, the surge voltages are higher for faster rise-times, leading to a better accuracy in modelling the physical effect of corona.
With a simple example transmission line network, the frequency-dependent model with Carson and frequency-dependent earth-return is verified against simulations in another EMT program, found in the literature. The simulation results show, that the earth-return has an effect on voltages at low-conductive soils depending on the applied transmission line model. For the corona effect, a comparison to measured results is made for model verification purpose, which shows good agreement between the simulated voltage results and the measurements found in the literature. Due to the extensive increase in simulation time when taking corona into account, an investigation into the influence on voltage surges generated by a first and subsequent negative stroke is performed. Results clearly show that corona has a neglectable influence in close proximity to the lightning current injection point. Therefore, the corona effect can be neglected in the simulations of lightning strokes to transmission lines, also because voltage surges generated in close proximity to insulators generate the highest amplitudes and increase the likelihood of a flashover, which is the main interest of this work. In contrast to that, the effect of corona should not be neglected, when surge voltages in substation generated by lightning strokes are investigated, because the effect of corona is increased with increasing line length and travelling time, respectively.

In conclusion to the full simulation model of this work, a frequency-dependent model with frequency-dependent earth-return is applied in the modelling of a transmission line, which includes all relevant physical effects.

CHAPTER 4: THE TRANSMISSION LINE INSULATOR

The breakdown charactersitic of the transmission line insulator string or its coordinated gap (arcing horn) is a key parameter in estimating the back-flashover rate of the transmission line under lightning stroke conditions. Thereby, the dielectric strength of air together with the electrode configuration of the insulated gap between the insulator ends or the arcing horn, if mounted, determines the breakdown characteristic.

In the following, the breakdown process of the air gap as well as the different breakdown criteria based on practical measurements are explained. This is followed by explanation of different methods and models of the breakdown process utilized in EMT simulations, limited to the application of cap-and-pin glass insulators with arcing horns, as used in the 400 kV transmission line example of this work. Based on the review of the models and reported recommendations in the literature, one model is chosen for the implementation into PSCAD/EMTDC and verified with laboratory measurements.

4.1: BREAKDOWN PROCESS OF THE AIR GAP

The breakdown process of the air gap has been investigated since the early days of electric power transmission. [138]. The physical breakdown process of the arc gap or insulator consists of several stages, which sum up to the breakdown time T_B, as shown in equation (4.1) and illustrated in figure 4-1. [139]–[143]

$$T_B = T_P + T_S + T_I + T_L + T_G \tag{4.1}$$

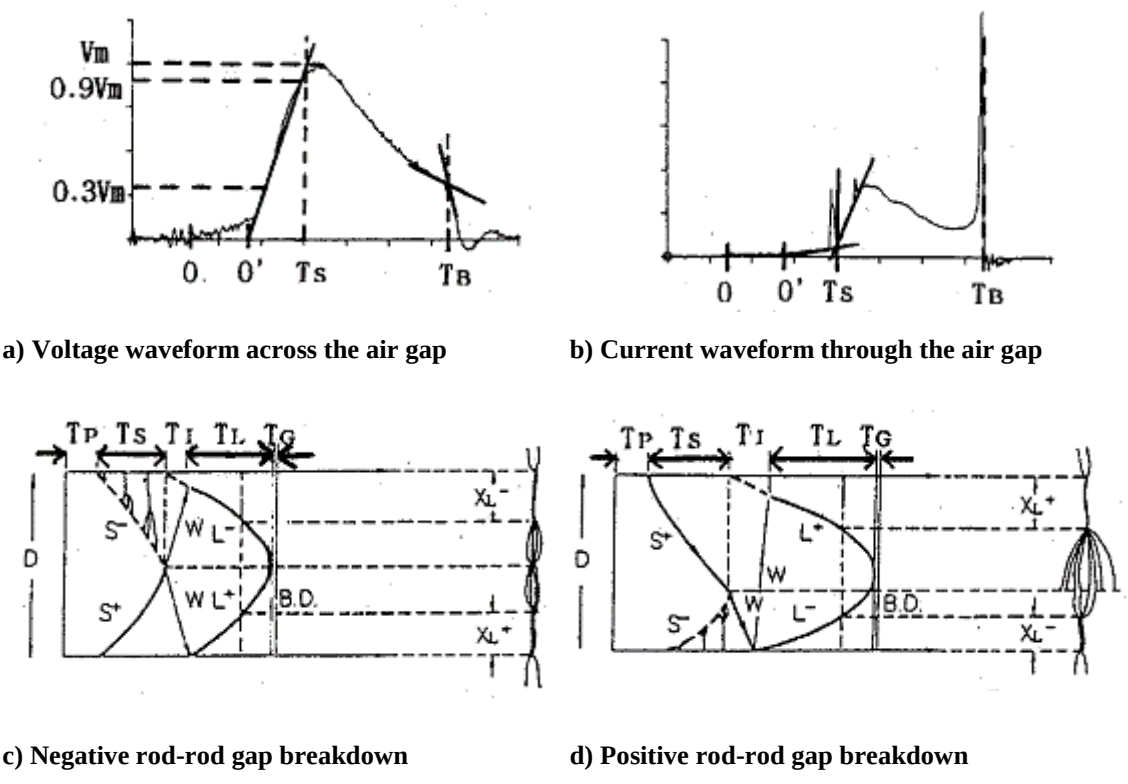

a) Voltage waveform across the air gap **b) Current waveform through the air gap**

c) Negative rod-rod gap breakdown **d) Positive rod-rod gap breakdown**

Figure 4-1: Schematic breakdown process [139]

The breakdown process consists of the streamer inception time T_P, streamer development time T_S, ionization propagation time T_I, leader development time T_L and air heating time T_G as shown in figure 4-1 c) and d) and follows the same physical breakdown process as already mentioned in section 2.1. The applied voltage across the air gap in figure 4-1 a), with its virtual zero at the zero crossing of the straight line from 30% to 90% of the wavefront, results in the pre-discharge current in figure 4-1 b), starting from the end of T_S to the beginning of T_G [144]. For negative lightning impulse the streamers *S* and ionization waves *W* and leader *L* move forward equally across the gap of length *D,* with *X* the leader length until the breakdown *B.D.* occurs at the attachment point in the gap midpoint. For positive lightning impulse, the streamer starts first from the electrode and nearly bridges the whole gap before the attachment occurs near the anode. Thereby the velocity of the attachment process of the leaders is dependent on the applied voltage across the gap above the minimum flashover voltage [142], [145].

4.2: AIR GAP BREAKDOWN CRITERIA

In practical applications of testing the dielectric strength of apparatus under lightning impulses, the crest value of voltage producing a flashover in 50% of its application, called V_{50} and the voltage-time curve, which relates the maximum voltage reached at breakdown

to the time to breakdown as illustrated in figure 4-2, are criteria for the breakdown [146]. This is normally performed with the standard lightning waveshape for testing, called 1.2/50 µs, with a rise time of 1.2 µs to the peak and a tail time of 50 µs to the half-value [147].

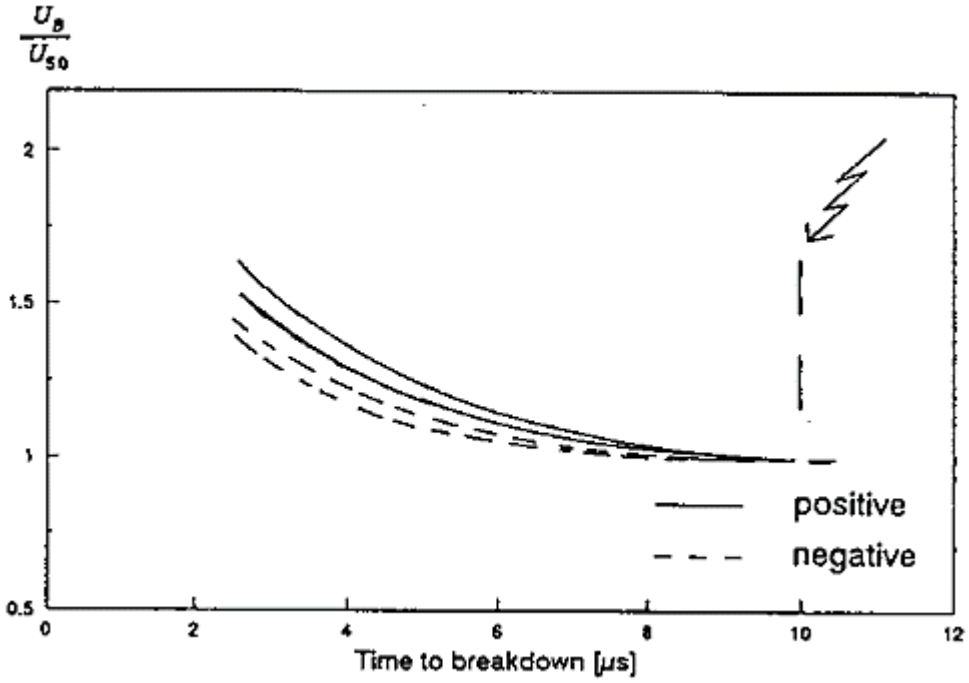

Figure 4-2: Volt-time curves for standard lightning impulses, rod-rod gap 1 m – 6 m [146]

However lightning strokes produce a rather non-standard short tail voltage across the insulator or arcing horn due to reflections at towers, various tower footing resistances and span length [24], [139], [146], [148]–[152]. Furthermore, it is found that the breakdown process is dependent on the gap geometry, applied voltage surge waveshape and polarity [139]–[143], [145], [148], [149]. Therefore the critical flashover voltage V_{50} as well as volt-time curve are only accurate for a given gap configuration and voltage surge waveshape [145], [153]. Consequentially, their application as breakdown criterions for the air gap under lightning stress is limited, but can be used to validate the description of the physical breakdown process [154].

4.3: AIR GAP FLASHOVER MODELS

In the literature several flashover models of the air gap can be found for the determination of the flashover criterion, which are all related to parameters obtained from testing or the physical breakdown process as described in the preceding sections. In the following, different models are presented and their advantages and disadvantages discussed to

enable an informed decision on the model to be implemented in PSCAD/EMTDC for the later simulations of a lightning stroke to a transmission line.

4.3.1: VOLTAGE-THRESHOLD MODEL

In the voltage-threshold model the flashover criterion is solely based on the V_{50}-value of the coordinated gap. The flashover occurs, when the voltage exceeds the threshold voltage V_{50}, as shown in equation (4.2) [155].

$$\begin{matrix} \mathrm{V}_{Flashover} \geq V_{50} & \rightarrow flashover \\ \mathrm{V}_{Flashover} < V_{50} & \rightarrow no\ flashover \end{matrix} \tag{4.2}$$

Albeit the straightforward implementation of this criterion into a transient simulation and readily available flashover parameter V_{50}, this criterion does not feature any representation of the physical breakdown process, voltage-breakdown time dependency nor is it recommended by the relevant standard [153].

4.3.2: VOLTAGE-TIME CURVE MODEL

The voltage-time curve model uses an empirical voltage-time equation to determine the flashover voltage. The criterion for flashover is the same as in equation (4.2). For example, in [156] the flashover voltage is determined with formula (4.3), where L is the length of the insulator or arc gap in m. Time t in µs starts at the moment the surge arrives at the coordinated gap, which is often modelled with a threshold voltage trigger.

$$\mathrm{V}_{Flashover}(kV) = 400 \cdot L + \frac{710 \cdot L}{t^{0.75}} \tag{4.3}$$

Although the model considers the volt-time curve of the arc gap or insulator, its relation to the physical process of the breakdown is weak and its application is limited to the applied waveform, as discussed in section 4.2. The determination of a suitable definition for the volt-time curve for non-standard waveforms, as encountered at the insulator or arc gap terminals during a lightning stroke is difficult. [24].

4.3.3: INTEGRATION METHODS

The integration method, also called severity index- or disruptive effect-method, applies an area criterion to determine the breakdown of the air gap. This method utilizes a

threshold voltage V_0, which must be exceeded to start the integration at time t_0 in equation (4.4). When the volt-time area is greater than the defined area A the breakdown of the arc gap occurs, as illustrated in figure 4-3.

$$A = \int_{t_0}^{t_c} (V(t) - V_0)^n \, dt \tag{4.4}$$

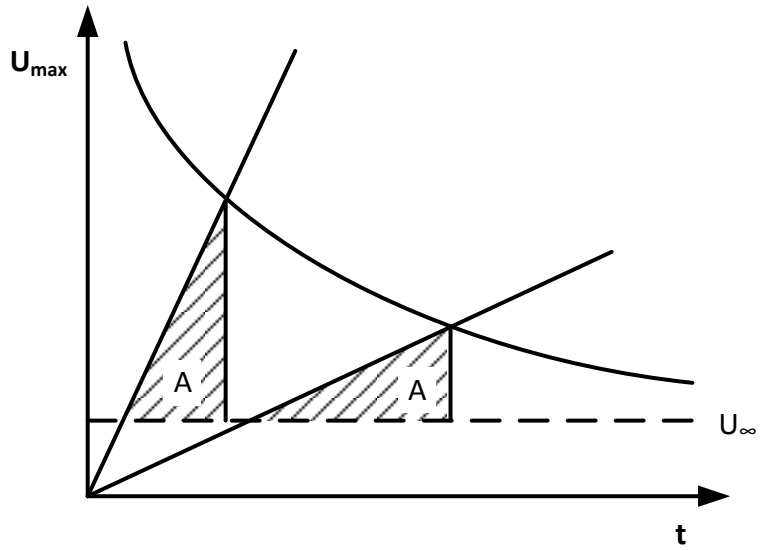

Figure 4-3: Equal-Area Criterion for voltage-time characteristics

The constants V_0 and n are determined based on a fit to a given voltage-time curve. In [148] different values for these constants are given for various gap configurations, where V_0 varies in the range of 90% of V_{50} [24]. A special case is $n = 1$, which is called the equal-area law by Kind [157] and produces a good fit to measured voltage-time curves [148], [158], but V_0 is not related to V_{50}. CIGRE [24], [146], [154], IEEE [156] and IEC [153] recommend the general integration method for modelling the flashover of an air gap, but also report restriction of its application to air gaps smaller than 1.2 m. It's main disadvantage is the relation to specific geometries and waveshapes, since a parameter set is adjusted to fit a specific measured volt-time curve [24].

4.3.4: LEADER-PROGRESSION MODEL

The leader progression model (LPM) is based on a simplified description of the breakdown process in equation (4.1), where the streamer onset time T_P is included into the streamer development time T_S and the ionization propagation time $T_I$and air heating time T_G are neglected due to their short time span [139]–[141], [144], [159]. The breakdown process of the air gap can be described with equation (4.5), whereas T_S is

expressed as the breakdown onset criterion and T_L as a function of leader velocity and gap length, also called leader progression.

$$T_B = T_S + T_L \tag{4.5}$$

In [143] a summary of the formulas for the calculation of the streamer and leader development times for various gap configurations longer than 1 m can be found, determined by laboratory experiments. Due to the LPMs general application to air gaps and good agreement with measurements, CIGRE [24], [146], [154], IEEE [156] and IEC [153] recommend its usage, whereas IEC recommends their usage for long air gaps only [153]. Furthermore in [159] a LPM for short air gaps and transmission line arresters with air gaps (TLA) is described, which shows good agreement with the measured volt-time curves.

Although the older model by Pigini [140], mentioned in both CIGRE [24], [146], [154] and IEC [153] is still in use, the LPM model by Motoyama [139] has become popular in the last decade [143], [160]–[165] due to its independence of V_{50}, eliminating the probability element and the inclusion of the pre-discharge current into the model equivalent circuit [166]. Furthermore, the model is not as conservative with regard to the breakdown, as other models [167].

Due to these advantages, it is concluded to implement Motoyamas LPM into PSCAD/EMTDC. However, as already mentioned in section 4.2, lightning impulses feature a short tail, which is represented in Motoyama's experiments with a decay time to half of 3.2 µs to 3.7 µs (1.2 µs to 1.4 µs front time). This range of waveshapes, as well as testing of rod-rod-gaps without influence of the insulators might limit the model's application with regard to the long wavefront of positive lightning strokes and high current negative strokes (see section 2.2). Therefore a verification of Motoyama's model with other double-exponential waveshapes with a wavefront in the range of 1.2 µs to 5 µs and a wavetail in the rage of 5 µs to 10 µs benefits the models validity and possible fine-tuning of the model parameters for the cap-pin-insulators with arcing horns.

4.4: MODELLING OF THE LEADER PROGRESSION AND ELECTRIC ARC

Prior to the model validation and adjustment of model parameters by measurements, the modelling and implementation of the LPM and electric arc into PSCAD/EMTDC including a verification of the implementation is performed.

The LPM is based on the description in [139] and [163], which also enable modelling of the leader development or pre-discharge current.

In the model the proposed leader onset condition is

$$\frac{1}{T_S}\int_{0,}^{T_S} V(t)\,\mathrm{dt} > V_{AVE}. \tag{4.6}$$

The polarity-dependent average applied voltage V_{AVE} for rod-rod gap configurations is calculated as a function of the gap length D.

$$\begin{matrix} V_{+AVE} \\ V_{-AVE} \end{matrix} > \begin{matrix} \mathrm{k}_{1+} \cdot D + \mathrm{k}_{2+}\ (kV) \\ \mathrm{k}_{1-} \cdot D + \mathrm{k}_{2-}\ (kV) \end{matrix} \tag{4.7}$$

The numerical equivalent of the integral Int, presuming a trapezoidal integration of voltage V, is split in two parts, where indices 1 represents the current and 0 the previous time step

$$Int_1 = \frac{1}{2}(V_1 + V_0)\Delta\mathrm{t}\ + Int_0 \tag{4.8}$$

$$V_{AVE} = \frac{Int_1}{t - t_0} \tag{4.9}$$

The integration start time t_0 can be realized with either a threshold voltage criterion or an area criterion. With regard to the start-up procedure in EMTDC and inclusion of power-frequency voltage for the overall transient simulation, the area criterion in (4.10) is more suitable for these cases. However for test scenarios, such as impulse generator simulations the threshold voltage criterion produces exact starting times of integration.

$$\frac{1}{2}(V_1 + V_0)\Delta\mathrm{t}\ >\ \int_0^{\Delta t} \hat{V}\cos\omega t\,\mathrm{dt} = \frac{\sqrt{2}}{\sqrt{3}} V_{L-L}\sin\omega\Delta t \tag{4.10}$$

The following leader development process is described with the average leader velocity v in m/s and average leader length x_L in m alongside with the linear relationship of leader velocity to the pre-discharge current i in A in (4.11) to (4.13).

$$v = \begin{cases} K_{11} \cdot \left[\frac{V(t)}{D-2x_L} - E_0\right] & 0 \le x_L < \frac{D}{4} \\ K_{12} \cdot \left[\frac{V(t)}{D-2x_L} - E\left(x = \frac{D}{4}\right)\right] + v(x = \frac{D}{4}) & \frac{D}{4} \le x_L < \frac{D}{2} \end{cases} \tag{4.11}$$

$$x_L = \int \mathrm{v}\, dt \tag{4.12}$$

$$i = 2K_0 v \tag{4.13}$$

The above formula for velocity is directly implemented, followed by the numerical equivalent of the leader length calculation in (4.14).

$$x_1 = \frac{1}{2}(v_1 + v_0)\Delta\mathrm{t} + x_0 \tag{4.14}$$

The relationship between the average electric field and the leader development velocity is illustrated in figure 4-4.

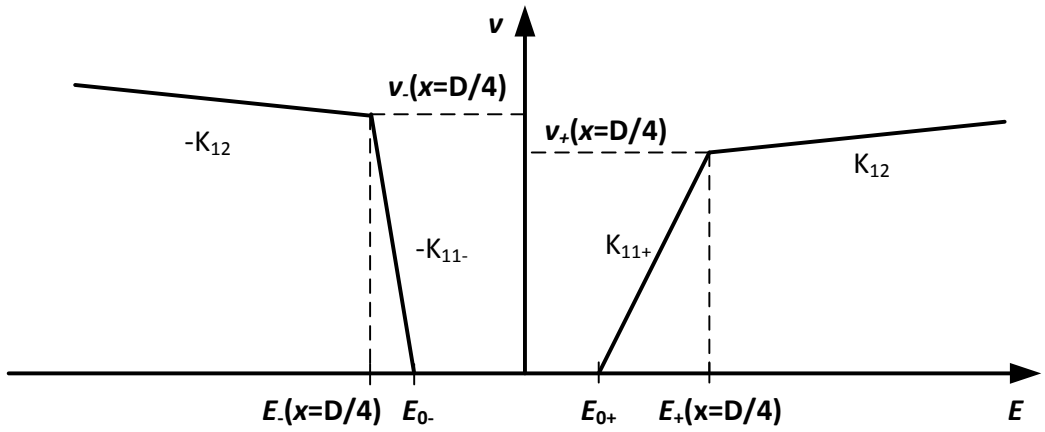

Figure 4-4: Relationship between average electric field and leader development velocity, adapted from [139]

The breakdown occurs when the leader bridges the gap length D in equation (4.15).

$$D \le 2x_L \tag{4.15}$$

The breakdown process is terminated if the applied voltage $V(t)$ becomes smaller than the minimum voltage V_{min} in (4.16), equivalent to the condition that the leader velocity becomes 0.

$$V(t) < V_{min} = E_0 \cdot (D - 2x_L) \text{ or } v < 0 \quad (4.16)$$

For the EMTDC implementation the stop criterion is checked before a new leader length calculation is performed.

For a positive 3 m rod-rod gap LPM Motoyama [139] calculated optimum parameters to fit the measurements. Ametani refined these and added suggestions for negative rod-rod gap parameters, based on Motoyamas work [163]. A summary of these parameters is found in table 4-1 and table 4-2.

Table 4-1: Summary of leader onset parameters

	k_1 (kV/m)	k_2 (kV)
Motoyama [139], positive polarity, air gap	400	50
Motoyama [139], negative polarity, air gap	460	150
Wang [143], positive polarity, porcelain insulator	430	190
Wang [143], negative polarity, porcelain insulator	490	90

Table 4-2: Summary of leader progression model parameters

	E_0 (kV/m)	K_0 (µC/m)	K_{11} (m^2/V·s)	K_{12} (m^2/V·s)
Motoyama [139], positive polarity	750	410	2.5	0.42
Ametani [163] Positive polarity	$V(T_S)/D$	410	3.5	0.4
Ametani [163] Negative polarity	$V(T_S)/D$	410	7.0	0.4
Wang [143], positive polarity	580*	500*	2.9*	
Wang [143], negative polarity	640*	500*	2.5*	

* parameters must be halved to be inputted directly into Motoyama LPM

The electric circuit part of the LPM is consistently implemented as a variable resistance into EMT simulations [139], [143], [159]–[165], [168]. However the representation of the electric arc - after the breakdown has occurred - varies. In the relevant standards [24], [146], [153] the arc is modeled as a constant inductance of 1µH/m gap length. Other

simulation models apply a time-dependent resistance [165], [168], decreasing from 1 kΩ to 1 Ω in 0.1 µs and to 0.1 Ω in 1 s, based on [169] or use a fixed resistance of 0.1 Ω [161].

For the verification the electric circuit implementation of the LPM including the leader development current in PSCAD/EMTDC is performed using the 'GEQ' interface based on the Dommel Norton-equivalent, already mentioned in section 3.2.4. The conductance and history current are implemented as a function of the leader development process as following in equation (4.17), derived in appendix C.2:

$$\begin{array}{lll} G = 0, & I = 0, & \text{before leader development} \\ G = \frac{2K_0K_1}{D-2x}, & I = -2K_0K_1E, & \text{during leader development} \\ G = 1E20, & I = 0, & \text{after breakdown} \end{array} \tag{4.17}$$

Until the streamer criterion is fulfilled, the LPM is a sole high resistance, which changes to a variable resistance during the leader development and a constant low resistance after the breakdown.

The validation of the LPM software implementation is performed by comparison of the leader development current waveshape of the model and the reference [163], where the short tail voltage surge is generated with a simplified test circuit. The test circuit is built in PSCAD and the insulator model set to 3 m length. The results of the short-tail voltage surge flashover test of the insulator are depicted appendix C.3 alongside the results from Ametani [163]. The curve progression of the leader development currents show a very close match.

Additionally, simulations with the mentioned electric arc implementations are shown in figure 4-5. For both the inductive arc and time dependent resistance description a discontinuity at point of the transition from the LPM current/conductance to fixed inductance/ time-dependent conductance exists, which has to be dealt with, when implementing these models instead of a pure resistance model.

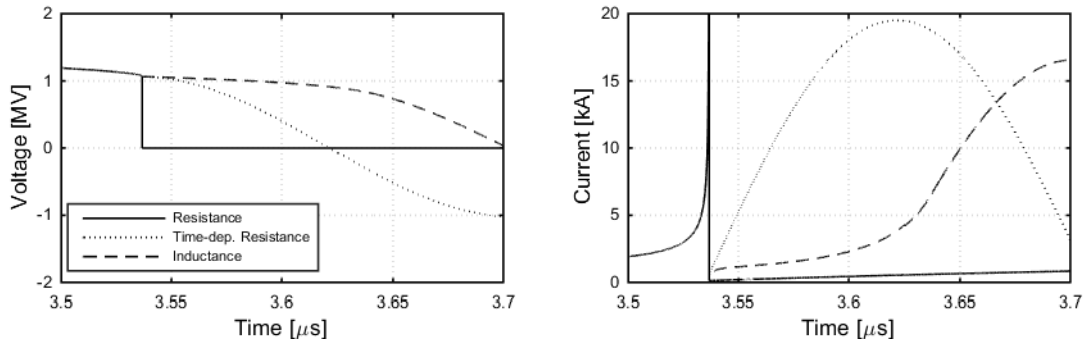

a) Voltage progression after breakdown **b) Current progression after breakdown**

Figure 4-5: Simulation results of electric arc implementation in PSCAD

4.5: VERIFICATION OF THE LEADER PROGRESSION MODEL

The adjustment of the insulator breakdown software model is accomplished by comparison of the voltage-time curve obtained from the simulation model and the experimentally obtained voltage-time curves, as performed by many other researchers [143][151][163]. However, in comparison to these references, tuning of parameters of the software implementation of the LPM is performed with a distributed circuit of the impulse generator in PSCAD/EMTDC including parasitic capacitances and inductances, matching the waveshape of the recorded measurements, because the real impulse generator circuit affects the experimental measured results [160]. Furthermore, to produce a generalized set of parameters for cap-and-pin insulators, which are dependent on the number of discs and arc gap length a generalized formula for the measured V-t-curves needs to be determined.

4.5.1: LABORATORY INVESTIGATION OF THE BREAKDOWN PROCESS

To validate the Motoyama model for cap-and-pin insulators with arcing horns, the critical flashover voltage V_{50} and the volt-time curve for various insulator configurations is measured at the Heriot-Watt University (HWU) and University of Manchester (UoM) high voltage laboratories.

To obtain the actual measurement results at HWU, some preliminary and subsequent work is necessary to ensure that results are reliable, considering the requirements stated in [170], [171]. This includes the determination of the transfer function from the high

voltage divider input to the control room low voltage oscilloscope output as well as the proof of linearity with a sphere gap according to BS EN 60052 [172]. Furthermore post processing of measurements with the transfer function, ambient temperature and pressure correction and filtering of the signal is performed to obtain the HV output signal. At the UoM facilities, impulse generator control as well as measurement and measurement correction is fully automated and accredited, which does not require further actions with respect to processing work.

The transfer function of the measurement track of the HWU impulse generator can be obtained analytically as well as experimentally according to [171], [173], using the frequency- or step-response method. Since the measurement equipment and step-response generator for an experimental determination are not available, the transfer function is determined analytically. This can be performed by calculating the capacitive and resistive voltage dividers of the electric equivalent circuit of the measurement track to obtain the transfer function $H(s)$ in the Laplace-domain as shown in equation (4.18).

$$H(s) = \frac{\mathcal{L}\{V_{LV}(t)\}}{\mathcal{L}\{V_{HV}(t)\}} \tag{4.18}$$

For determination of the transfer function $H(s)$ the short cable connection from the capacitive voltage divider into the control room at HWU is neglected, since this represents predominantly travel time delay, which does not affect the signal itself [173]. The result of the analytical transfer function calculation, found in appendix C.1 together with the impulse generator single line diagram, is presented in equation (4.19).

$$H(s) = \frac{K}{1+sT_2+s^2T_1} = \frac{4.442\cdot10^{-4}}{1+s\cdot47.579\cdot10^{-9}+s^2\cdot2.9587\cdot10^{-16}} \tag{4.19}$$

From the time constant values it can be deducted, that the effect of parasitic inductance is by far negligible and the transfer function can be treated as a standard proportional-delay function, which means the measurement signal at the low-voltage side is damped and divided down. Due to the small value of time constant T_1 it is practical to only multiply the LV signal with the amplification to obtain the HV signal of the measurement for a comparison with the impulse generator software model.
In figure 4-6 and figure 4-7 the recorded raw data at the LV side of a waveform generated with the HWU 800 kV impulse generator and its processed counterpart are shown, which provide an impression of the degree of post-processing.

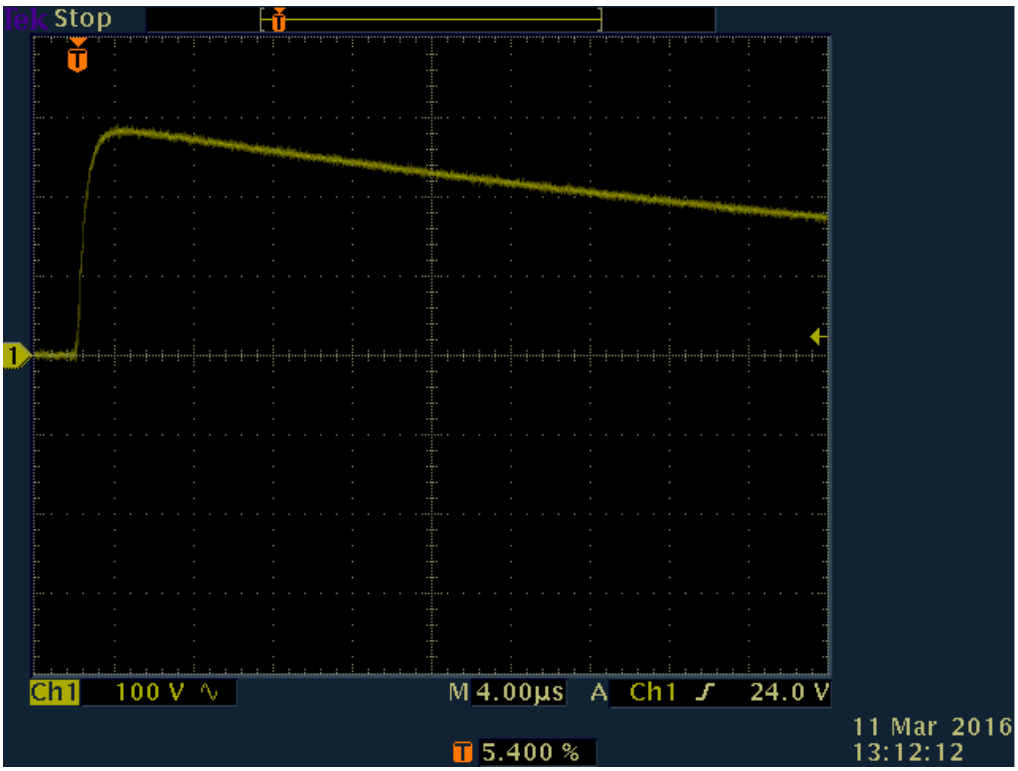

Figure 4-6: Example of raw output at LV side of impulse generator

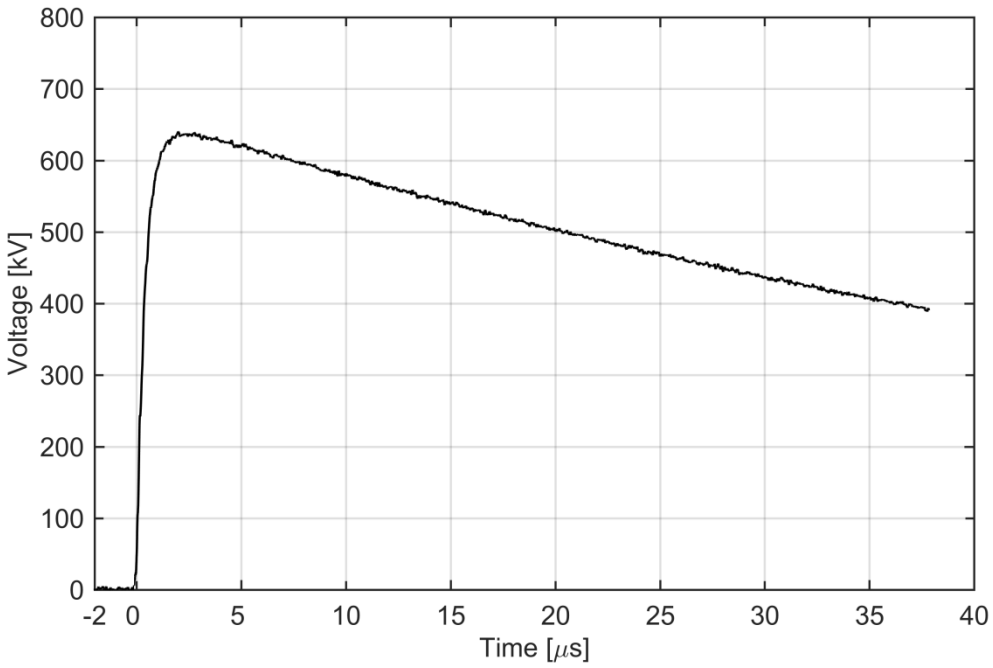

Figure 4-7: Example of processed output at HV side of impulse generator

The determination of the 50% flashover voltage for both positive and negative polarity at HWU and UoM is performed with the up-and-down method according to BS EN 60060-1 [170] with 10 or more flashover samples. A summary of the resulting calculated 50% flashover voltages as a function of number of discs or spacing between arcing horns is plotted in figure 4-8.

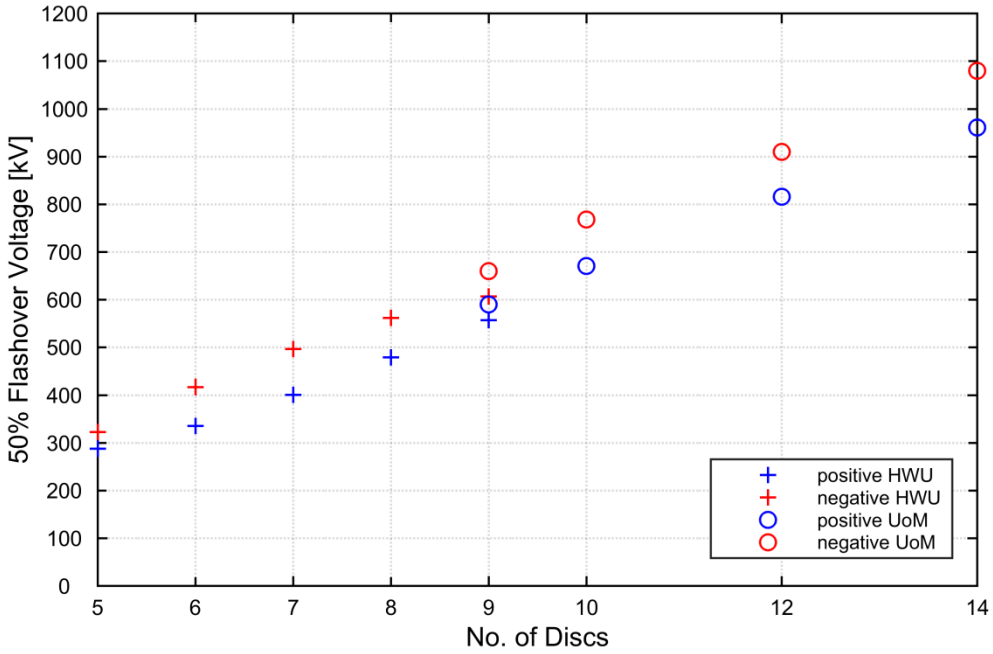

Figure 4-8: **Results of the 50% flashover voltages of cap-and-pin insulator discs with 800 kV impulse generator**

Overall the relationship between 50% flashover voltages and number of discs points out to be a linear function as already observed for longer gaps in [139]. However additional tests with 10 or more discs at higher voltages are necessary to confirm this relationship and compare it to already published results. As expected $V_{50\%}$ for positive polarity is lower than for negative polarity [7].

For determination of the voltage-time-curves of each of the insulator string/arcing horns arrangements, $V_{50\%}$ is taken as a start voltage. The impulse generator voltage is then increased step-wise for each sample. The detailed recordings for both positive and negative polarity can be found in appendix C.4 and C.5. These recordings are digitally processed to calculate the time from waveform start, defined as the x-axis zero crossing of a straight line between 30% and 90% of the peak voltage, to breakdown. Since the breakdown process features a delay until the voltage crosses zero, illustrated in figure 4-9 a dV/dt criterion is applied to determine the end of the breakdown process as shown in figure 4-10.

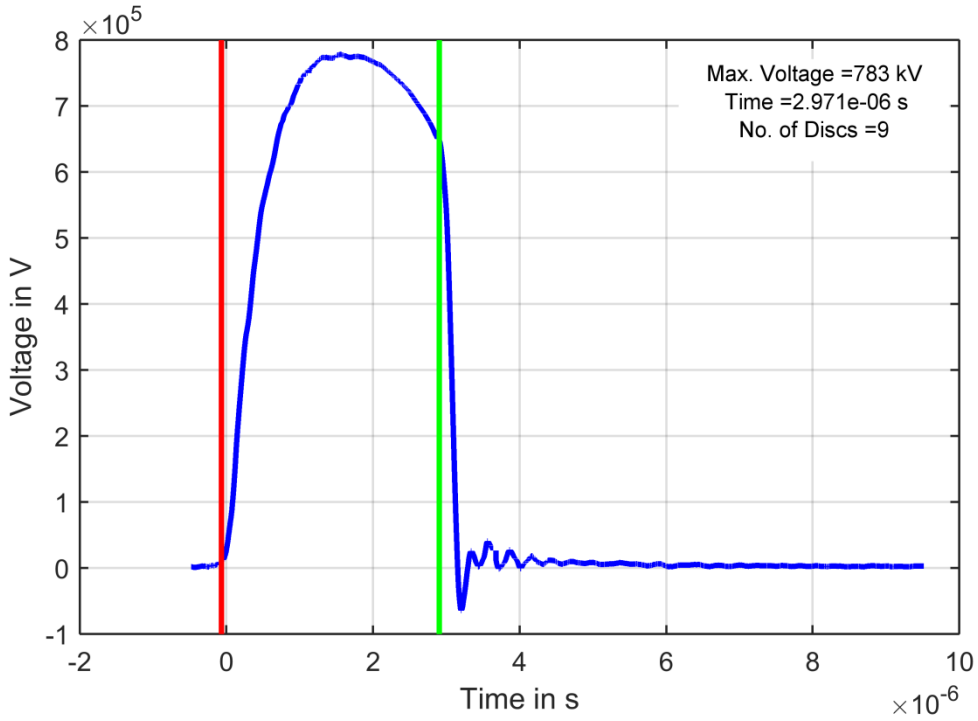

Figure 4-9: Recorded sample of a positive flashover

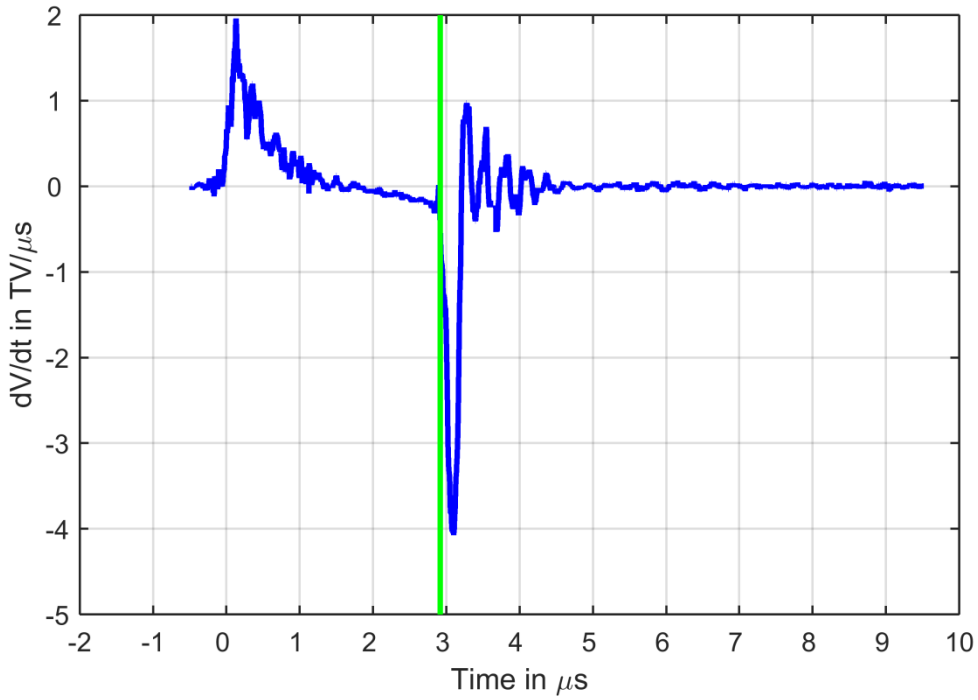

Figure 4-10: dV/dt calculation of recorded sample of a positive flashover

The resulting V-t-curves for both positive and negative polarity are then plotted in figure 4-11 and figure 4-12. These results for V-t-curves generally align with those in tests with air gaps [139]. However, due to the greater obtained size of samples, curve-fitting of the samples to generate functions for each insulator/arcing horn arrangement for further utilization in the software modelling of the flashover phenomenon is necessary.

Additionally a curve-fitting algorithm is applied to the data, which reveals that a power function fits the samples for each insulator/disc arrangement.

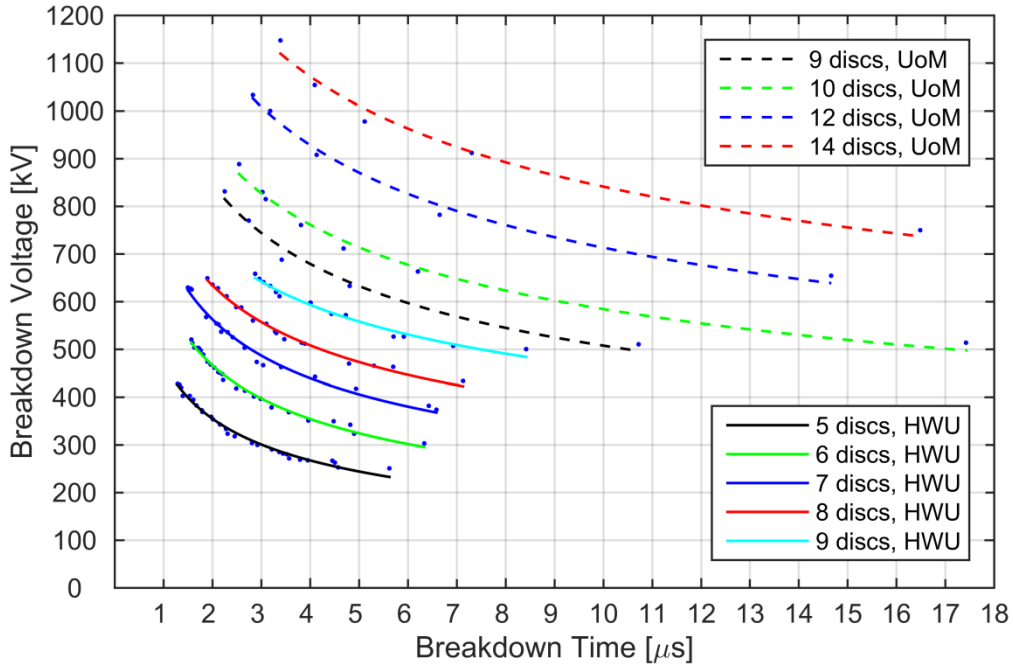

Figure 4-11: Voltage-time curve for positive polarity with curve-fitting

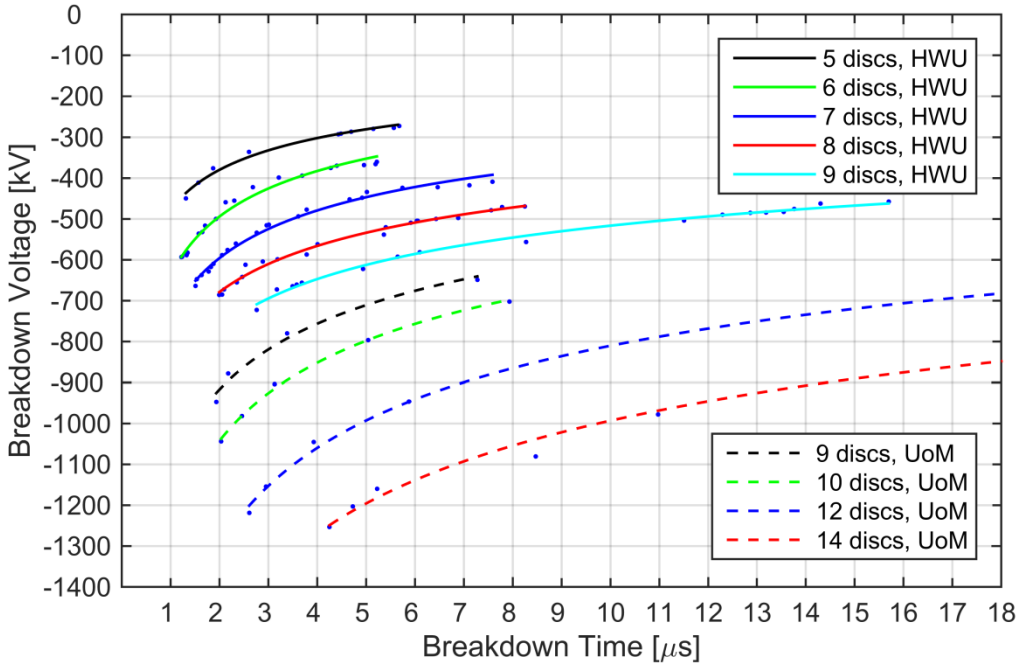

Figure 4-12: Voltage-time curve for negative polarity with curve-fitting

4.5.2: IMPULSE GENERATOR SOFTWARE MODEL

To allow testing and parametrization of the Motoyama model constants with the obtained voltage-time curves from laboratory tests, first a software model of the impulse generator is needed. The tests are performed with an impulse generator at HWU and UoM as illustrated in appendix C.1.

The general behaviour which has to be implemented into an EMT simulation is explained with a single-circuit equivalent as shown in figure 4-13 in the following.

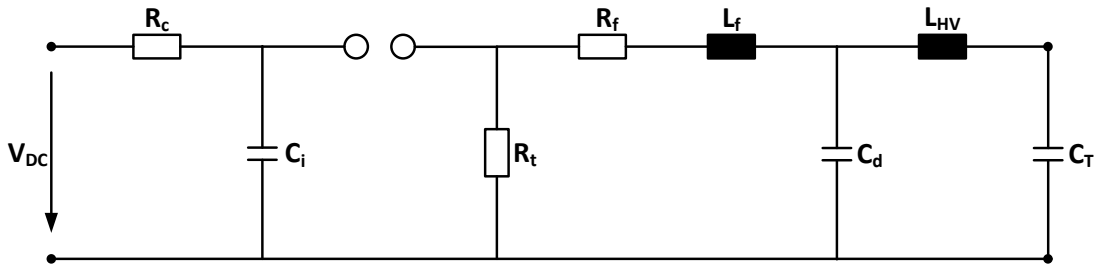

Figure 4-13: Single-equivalent circuit diagram of a single-stage impulse generator

The stage capacitors C_i are slowly charged through the charging resistors $R_c$and then the spark gap triggered to form an RC-circuit with the front and tail resistors R_f and R_t, which generates the desired waveform at the high voltage output. The voltage curve at the test object with capacitance C_t is measured at the voltage divider with capacitance C_d. [12], [147], [174].

Due to the dimensions of an impulse generator with several stages, the inductances of the earth return loops of the connection to the voltage divider L_d and test object L_{HV} as well as parasitic earth capacitances cannot be disregarded.

Therefore RLC values for the EMT implementation of the impulse generator are taken from the manual and where not available calculated according to [174] or by means of an iterative process by comparing EMT simulation and laboratory waveform sample outputs. The results of this process are illustrated in figure 4-14 for the impulse generator at HWU, where several measured recorded and simulated waveforms are compared and in figure 4-15 for the impulse generator at UoM.

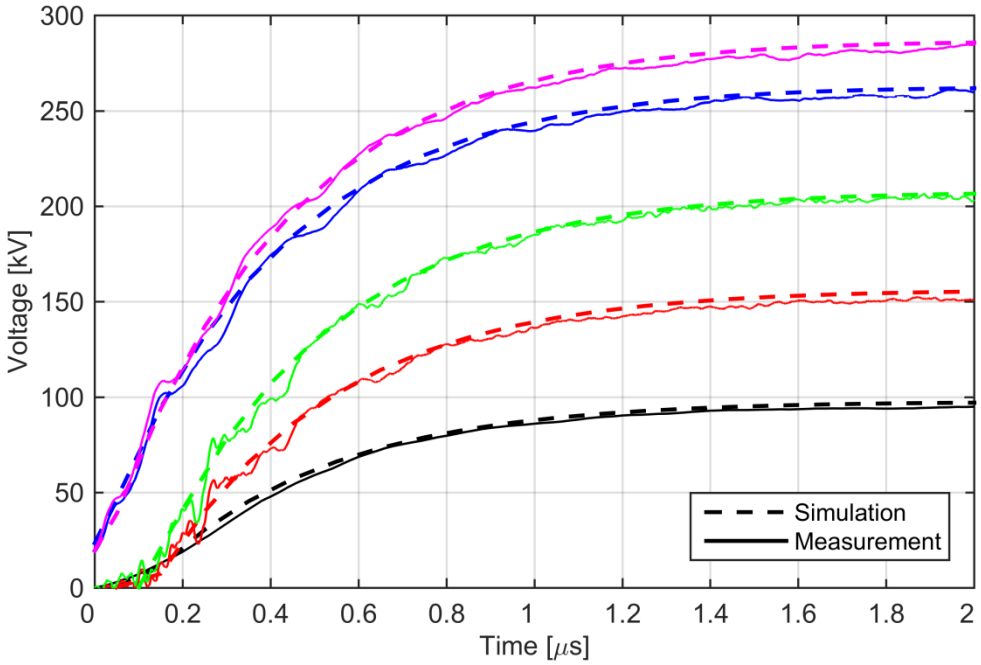

Figure 4-14: Comparison of software model and measurements, 800 kV impulse generator at HWU

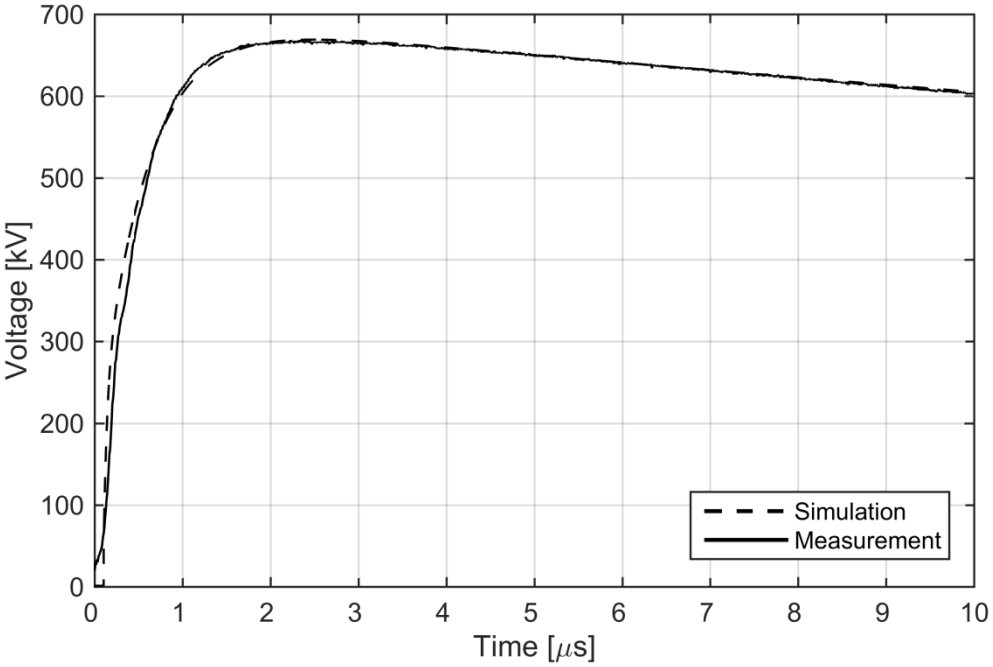

Figure 4-15: Comparison of software model and measurements, 2000 kV impulse generator at UoM

In comparison to the simulated 1.2/50 µs waveform for the impulse generator at HWU, the measured recorded waveform of the impulse generator features an oscillation superimposed on the wavefront, which is intensified with increasing voltage output. These oscillations stem from the breakdown of the spark gaps of each stage and associated

transients due to the discharge of each stage RLC circuit. However these oscillations do not influence investigations of the breakdown process of insulators with arcing horns, since the earliest breakdown of arcing horns occurs near the crest of the wavefront. For the measurement at UoM these oscillations are marginal due to a tuned measurement system and measurement and simulations agree well. Therefore the software model of the impulse generator is valid for investigations of the breakdown process of insulators.

4.5.3: FITTING OF SOFTWARE MODEL TO MEASUREMENT DATA

In general, the LPM parameters are directly determined with measured current and leader velocity, see [139], [143] and a set of various waveforms. As reported in [139], [140], [143] short-tail waveshapes, as encountered during a lightning strike at the insulator, lead to a higher voltage withstand capability than the 1.2/50 µs standard waveshape. However, for most impulse generators, resistor kits are only available for standard waveshapes, such as 250/2500 µs for switching and 1.2/50 µs for lightning impulse, which restrict testing to these waveshapes. Nevertheless, in [139] it is reported, that obtained LPM parameters from short-tail impulses also fit the breakdown characteristics of standard lightning impulses. This leads to the conclusion that LPM parameters obtained with a 1.2/50 µs waveshape represent a worst-case for the breakdown behaviour of the tested insulator/ arcing horn arrangement, which adds a safety margin in the assessment of the lightning performance. Therefore, it is decided to conduct a parameter study and determine parameters based on the best fit to the V-t-curve measurements.

At first, the parameter set from Motoyama in table 4-1 is compared to the measured V-t-curves to identify the differences for a start point of the parameter study. To record both the voltage at breakdown and time to breakdown, an implementation of the dV/dt-criterion, explained in section 4.5.1 is implemented to align the evaluation procedure of simulation and measurement.

In figure 4-16 to figure 4-19 the V-t-curves resulting from simulations with the 800 kV and 2000 kV impulse generator at HWU and UoM are plotted together with the V-t-curves resulting from the experiments.

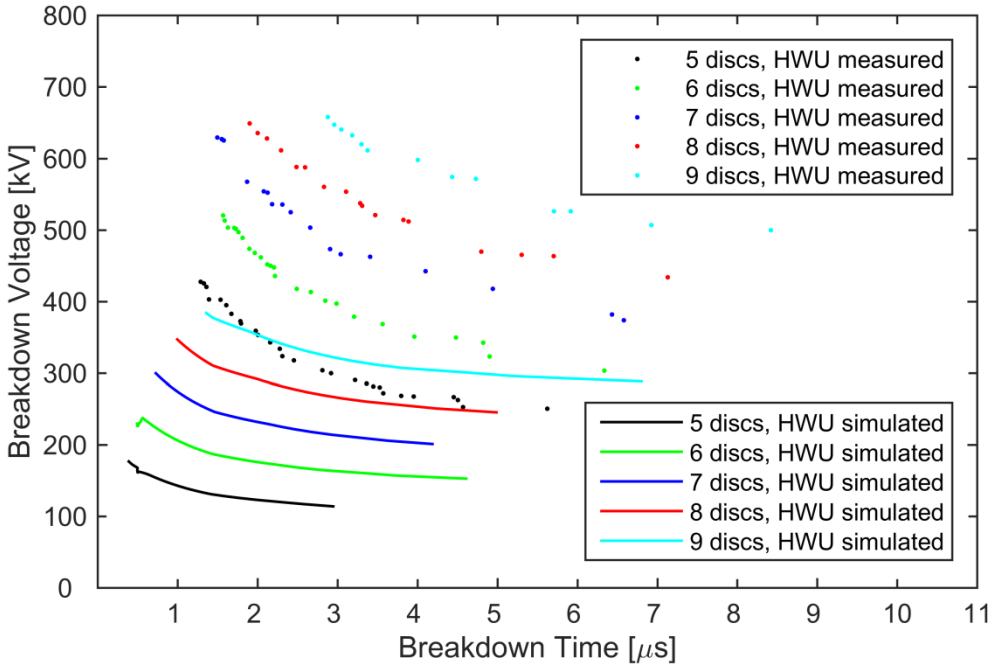

Figure 4-16: Voltage-time curve comparison of measurements and simulation for positive polarity, 800 kV impulse generator HWU, Motoyama parameters

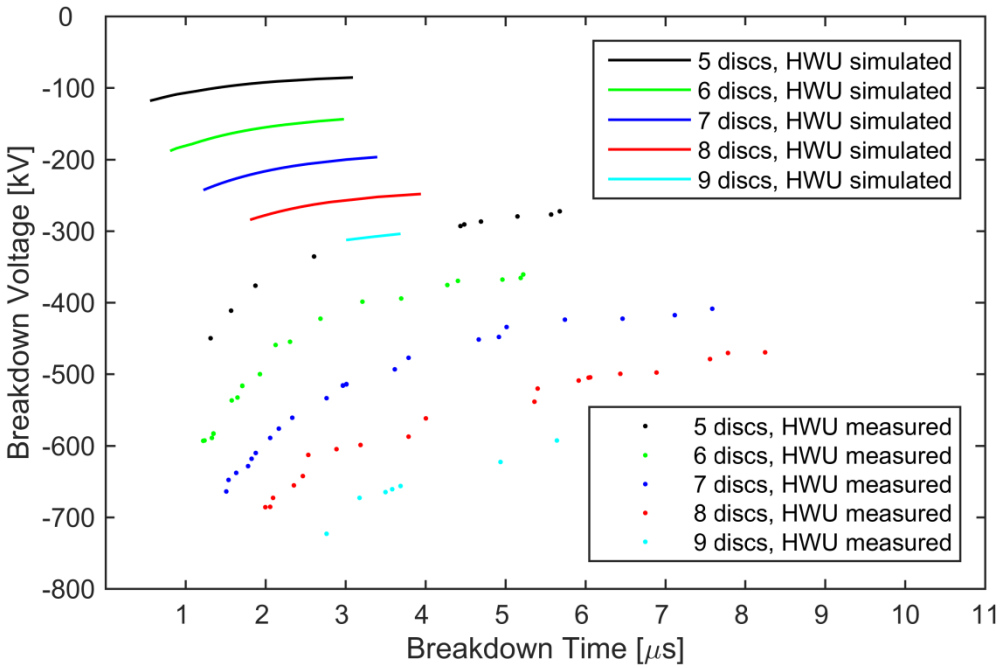

Figure 4-17: Voltage-time curve comparison of measurements and simulation for negative polarity, 800 kV impulse generator HWU, Motoyama parameters

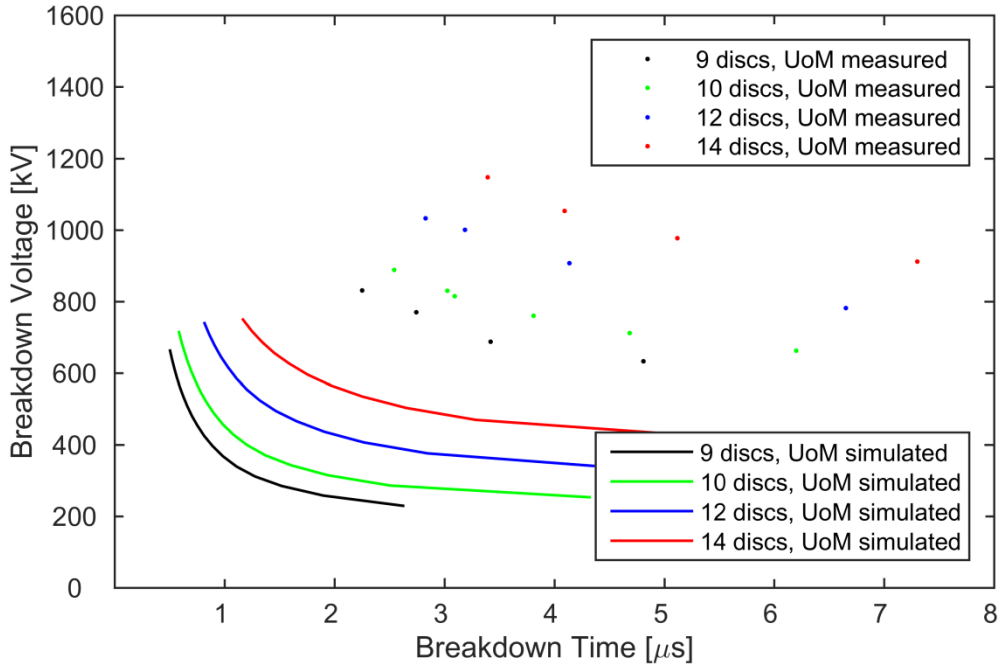

Figure 4-18: **Voltage-time curve comparison of measurements and simulation for positive polarity, 2000 kV impulse generator UoM, Motoyama parameters**

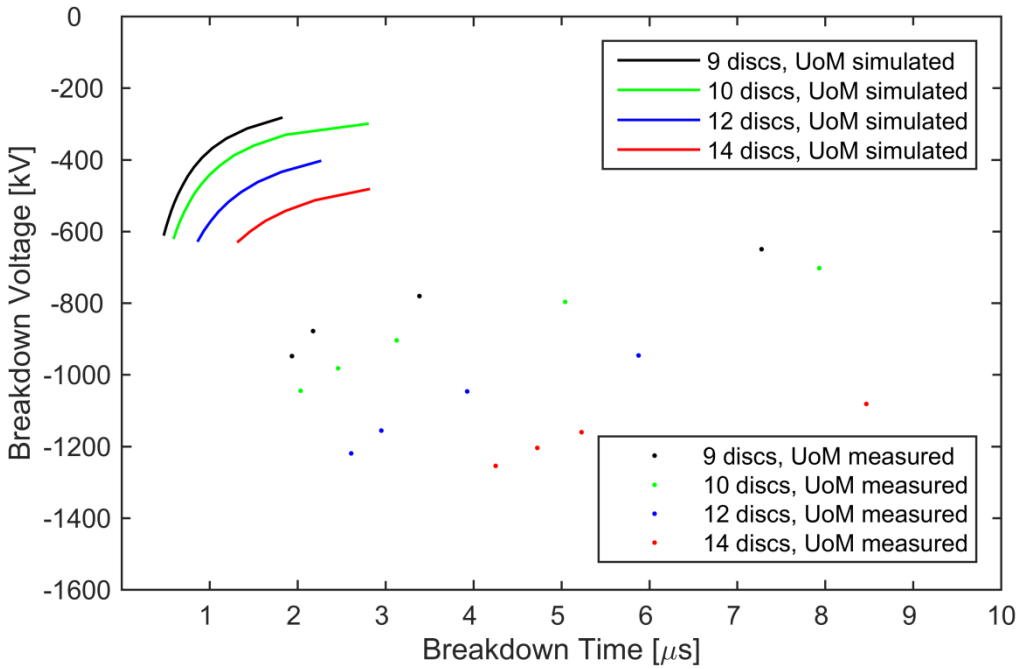

Figure 4-19: **Voltage-time curve comparison of measurements and simulation for negative polarity, 2000 kV impulse generator UoM, Motoyama parameters**

A comparison of the V-t-curves shows, that the Motoyama parameters underestimate the real performance of the cap-and-pin glass insulators with arcing horns and need to be adjusted. Wang's parameters [143] lead to no flashovers in all cases. In this respect, a systematic approach to determine the influence of each parameter in the LPM on the

simulated V-t-curve is taken. The result of this approach is depicted in figure 4-20, which reveals that each parameter from equations (4.7),(4.11) and (4.13) features a dominant influence on a property of the V-t-curve, and a minor influence on the whole shape of the V-t-curve.

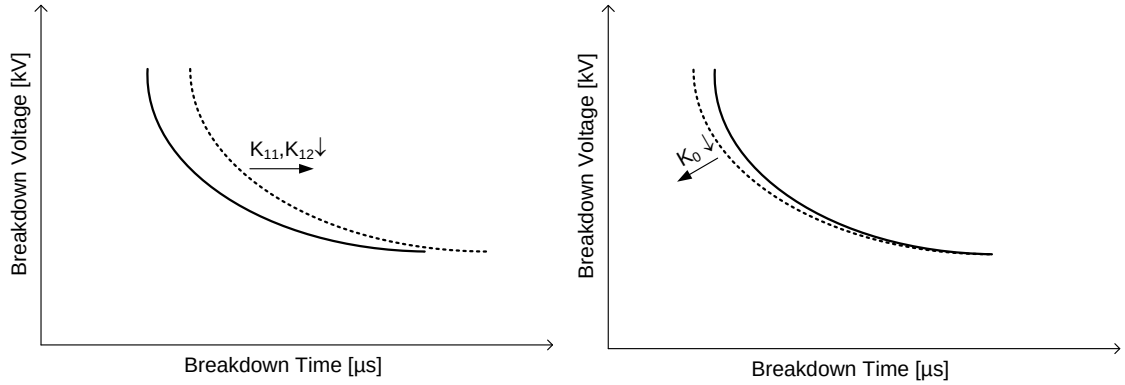

a) Main influence of parameter K_{11} and K_{12} **b) Main influence of parameter K_0**

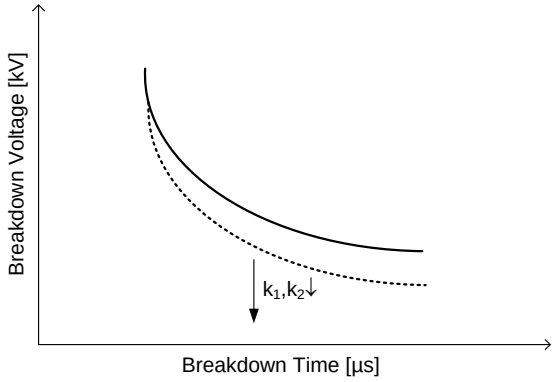

c) Main influence of parameter k_1 and k_2

Figure 4-20: Influence of LPM parameters on V-t-curve

The velocity parameters K_{11} and K_{12} shift the V-t-curve to longer breakdown times in case of decreasing their values, but also stretch the curve to longer breakdown times. The charge parameter K_0, which mainly determines the pre-discharge current, decreases the slope of the V-t-curve, but also the maximum peak voltage, when it is decreased. Parameters k_1 and k_2 shift the curve to lower breakdown voltages, but also compress the V-t-curve to lower breakdown time values when decreased.

Furthermore, it is found that there exists a range of parameter sets to fit the measured V-t-curve, which demands for further criteria for curve fitting. Since the information available is limited to the measured voltage and breakdown measurements, only the criterion of maximum voltage is available. Concluding from the influence of parameter

K_0 on the peak voltage in the previous paragraph, the maximum voltage - breakdown time (V_{max}-t) –Curve is utilized in addition to the V-t-curve for a parameter fitting of the LPM.

For a first parameter determination, the numbers of variables to be adjusted is reduced in setting parameter $K_{12} = K_{11}$. A manual adjustment can readily be performed in the following steps:

- Adjust k_1 and k_2 to get an approximate fit for the horizontal line of the V-t-curve
- Adjust K_{11} to shift the V-t-curve vertically
- Adjust K_0 to get a fit for the upper part of the V-t-curve
- Iterate above step until a reasonable fit is achieved

In figure 4-21 and figure 4-23 a reasonable fit for the measured positive and negative V-t-curve is found with parameters K_{12}=K_{11}=0.7 m^2/V·s, K_0=100 µC/m, k_1=350 kV/m, k_2=190 kV and K_{12}=K_{11}=0.85 m^2/V·s, K_0=100 µC/m, k_1=350 kV/m, k_2=190 kV, respectively. The importance of the inclusion of the V_{max}-t-curve is highlighted in figure 4-22 and figure 4-24, where measured and simulated curves do not match. In this case however, no further improvements are possible.

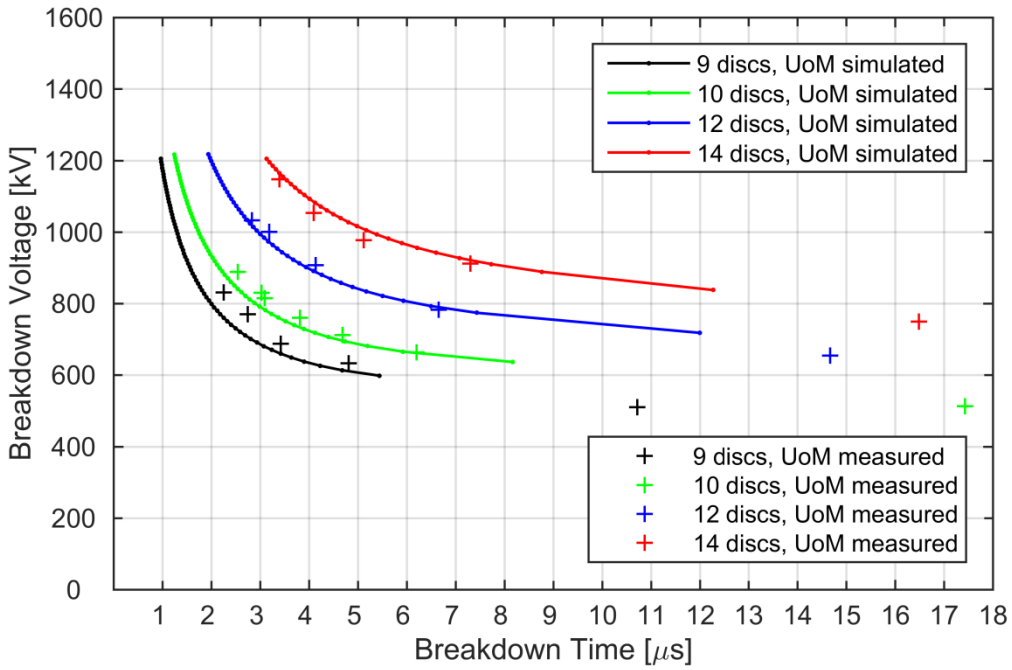

Figure 4-21: Voltage-time curve comparison of measurements and simulation for positive polarity, 2000 kV impulse generator UoM, K_{12}=K_{11}=0.7 m^2/V·s, K_0=100 µC/m, k_1=350 kV/m, k_2=190 kV

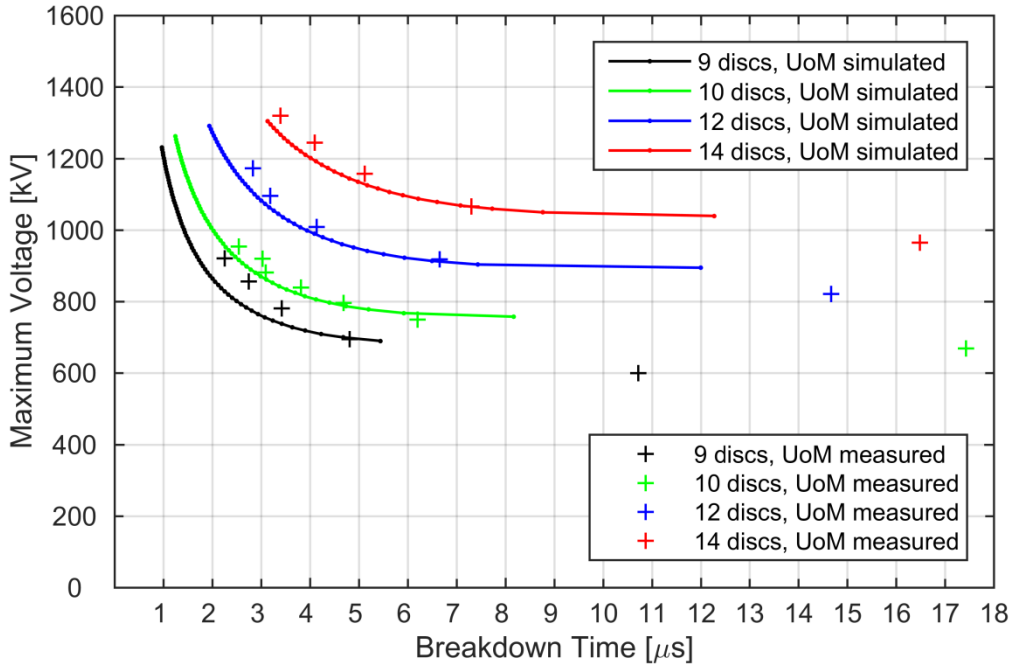

Figure 4-22: **Maximum Voltage-time curve comparison of measurements and simulation for positive polarity, 2000 kV impulse generator UoM, K_{12}=K_{11}=0.7 m^2/V·s, K_0=100 µC/m, k_1=350 kV/m, k_2=190 kV**

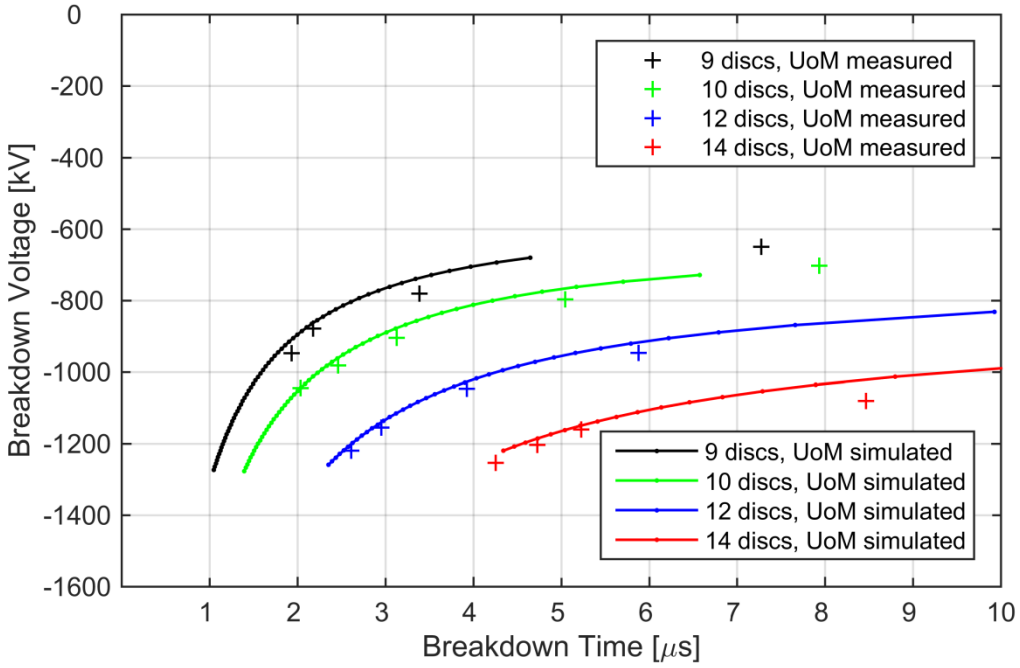

Figure 4-23: **Voltage-time curve comparison of measurements and simulation for negative polarity, 2000 kV impulse generator UoM, K_{12}=K_{11}=0.65 m^2/V·s, K_0=100 µC/m, k_1=440 kV/m, k_2=150 kV**

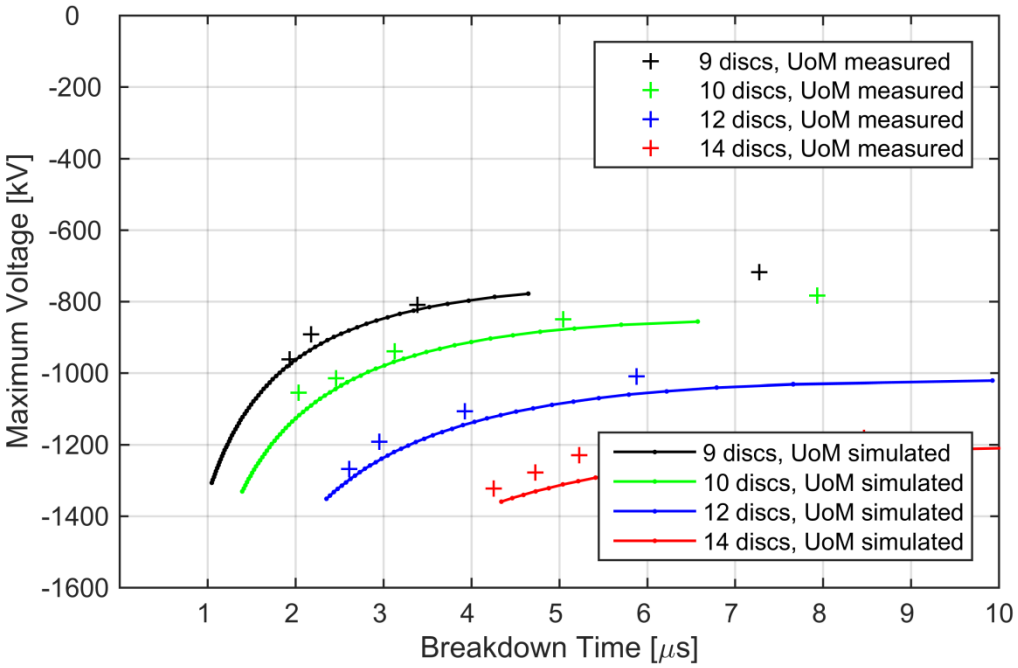

Figure 4-24: Maximum Voltage-time curve comparison of measurements and simulation for negative polarity, 2000 kV impulse generator UoM, K_{12}=K_{11}=0.65 m^2/V·s, K_0=100 µC/m, k_1=440 kV/m, k_2=150 kV

To improve the fit to the measured V-t- and V_{max}-t-curve the variable $K_{12} \neq K_{11}$ is taken into consideration in the simulations and the previously described procedure repeated. In figure 4-25 to figure 4-28 the results of the curve-fitting procedure are plotted for both positive and negative polarity with parameter values of K_{11}=0.85 m^2/V·s, K_{12}= 0.05 m^2/V·s, K_0=100 µC/m, k_1=350 kV/m, k_2=190 kV and K_{11}=0.7 m^2/V·s, K_{12}= 0.05 m^2/V·s, K_0=100 µC/m, k_1=440 kV/m, k_2=150 kV.

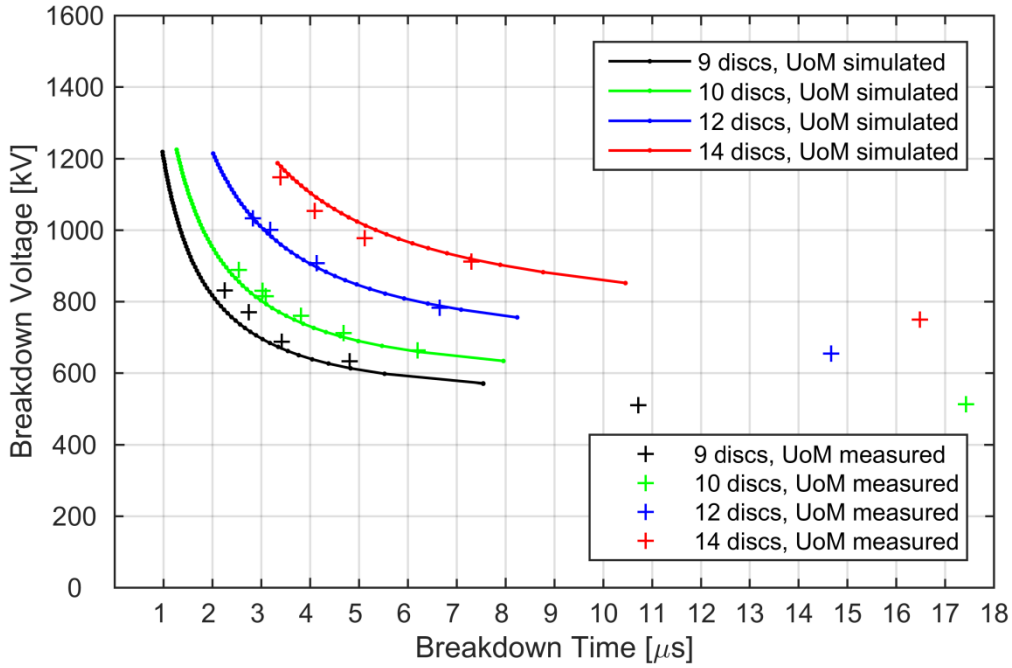

Figure 4-25: **Voltage-time curve comparison of measurements and simulation for positive polarity, 2000 kV impulse generator UoM, K_{11}=0.85 m^2/V·s, K_{12}= 0.05m^2/V·s, K_0=100 µC/m, k_1=350 kV/m, k_2=190 kV**

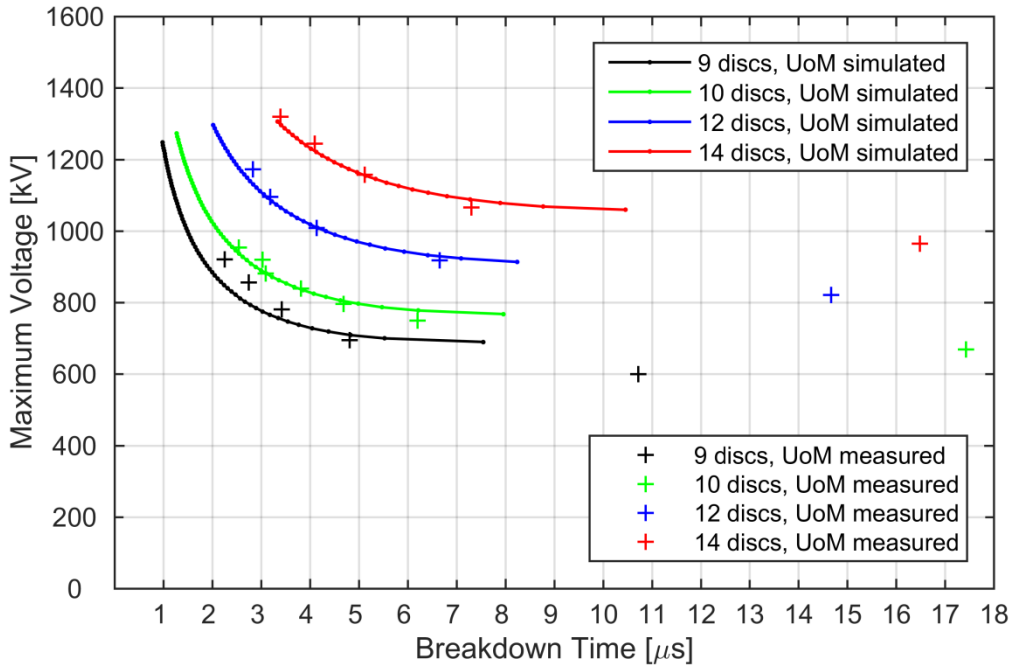

Figure 4-26: **Maximum voltage-time curve comparison of measurements and simulation for positive polarity, 2000 kV impulse generator UoM, K_{11}=0.85 m^2/V·s, K_{12}= 0.05m^2/V·s, K_0=100 µC/m, k_1=350 kV/m, k_2=190 kV**

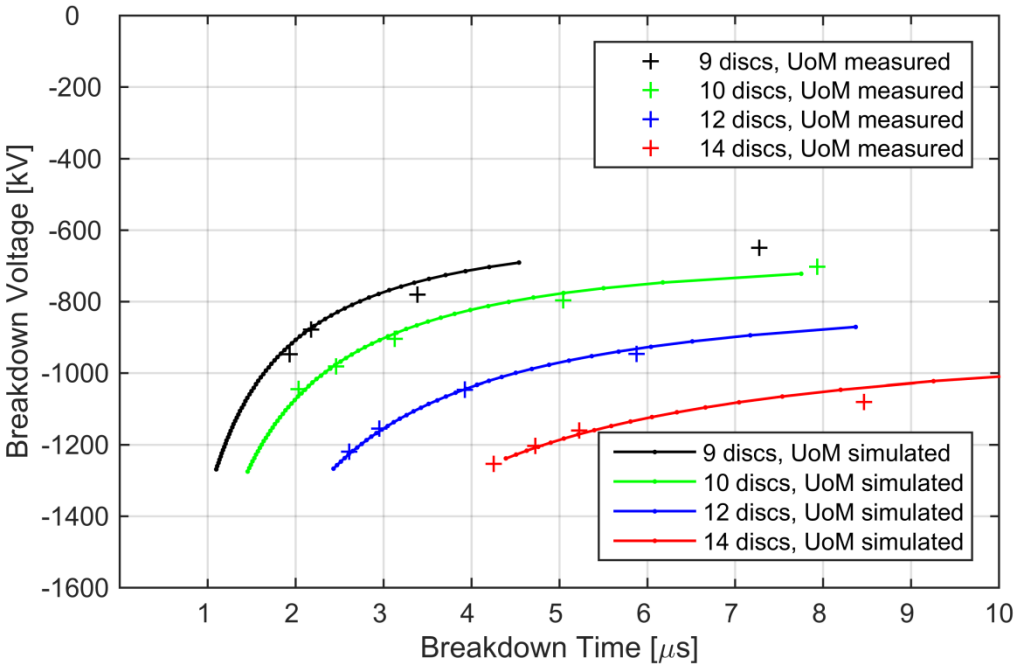

Figure 4-27: **Voltage-time curve comparison of measurements and simulation for negative polarity, 2000 kV impulse generator UoM, K_{11}=0.7 m^2/V·s, K_{12}= 0.05m^2/V·s, K_0=100 µC/m, k_1=440 kV/m, k_2=150 kV**

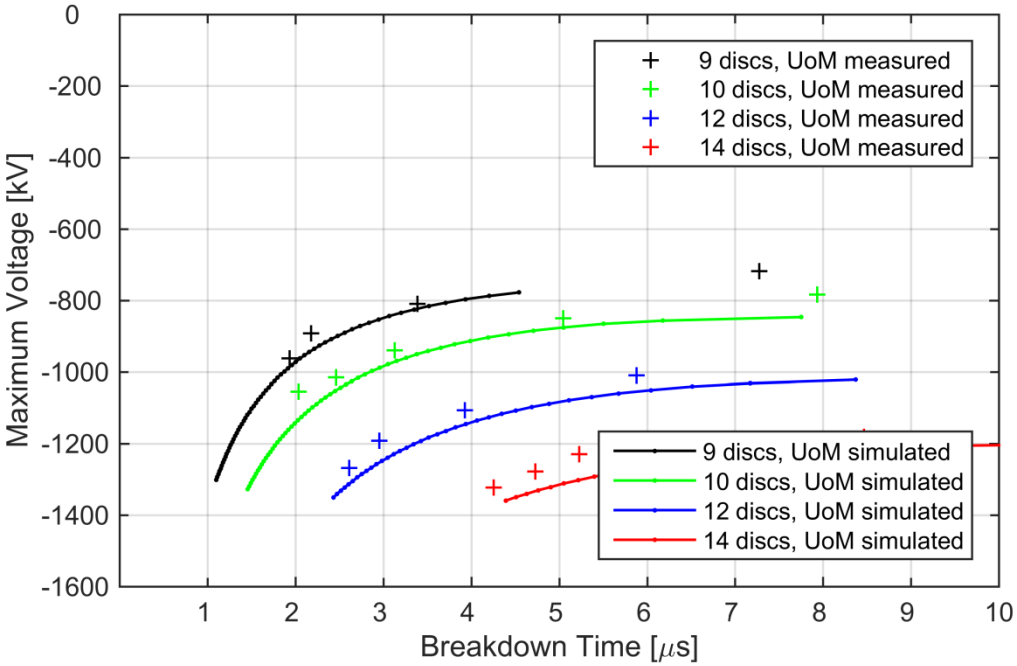

Figure 4-28: **Maximum Voltage-time curve comparison of measurements and simulation for negative polarity, 2000 kV impulse generator UoM, K_{11}=0.7 m^2/V·s, K_{12}= 0.05m^2/V·s, K_0=100 µC/m, k_1=440 kV/m, k_2=150 kV**

With respect to the LPM parameters, determined with the curve-fitting procedure, a comparison of table 4-1 and table 4-2 (Wang's measurements) to table 4-3 and table 4-4 shows similarities to the parameters determined for a porcelain insulator without arcing

horns. However due to the arcing horns, the leader onset voltage is lower. The charge value K_0 and velocity parameter K_{11} is in the same range as in Wang's measurements [143]. The parameters determined through curve-fitting as well as Wang's parameters both show, that the cap-and-pin insulators alter the arc gap behaviour in comparison to Motoyama's measurements of an air gap. Furthermore, the inclusion of the velocity parameter K_{12} only effects lower breakdown voltages in the curve-fitting procedure.

Table 4-3: Summary of leader onset parameters from curve-fitting procedure

	k_1 (kV/m)	k_2 (kV)
Positive polarity $K_{12}=K_{11}$	350	190
Positive polarity $K_{12}\neq K_{11}$	350	190
Negative polarity $K_{12}=K_{11}$	440	150
Negative polarity $K_{12}\neq K_{11}$	440	150

Table 4-4: Summary of leader progression model parameters from curve-fitting procedure

	E_0 (kV/m)	K_0 (µC/m)	K_{11} (m^2/V·s)	K_{12} (m^2/V·s)
Positive polarity $K_{12}=K_{11}$	$V(T_S)/D$	100	0.7	-
Positive polarity $K_{12}\neq K_{11}$	$V(T_S)/D$	100	0.85	0.05
Negative polarity $K_{12}=K_{11}$	$V(T_S)/D$	100	0.65	-
Negative polarity $K_{12}\neq K_{11}$	$V(T_S)/D$	100	0.7	0.05

Although a reasonable fit for both the breakdown voltage-time-curve and maximum voltage-time-curve can be found, deviations from the measured curves still exist. The main problem of curve-fitting is that no definite criterion for the breakdown can be determined. The dV/dt-criterion used may be the best option to determine the breakdown time, but due to the pre-discharge current, where no fast cut-off of voltage in the plots exists, the determination of breakdown voltage leaves some degree of freedom as seen in figure 4-9. Furthermore, inductive effects during the breakdown process and the electric arc itself cannot be modelled in detail, which adds some further inaccuracy to the determination of the LPM parameters, when velocity and current measurement during the breakdown process are not available. However, as reported in [139], [140], [143] short-tail waveshapes as encountered during a lightning stroke at the insulator with arcing horns

have higher breakdown voltage than the 1.2/50µs waveshape, applied in this work, which adds some safety margin. Although breakdown experiments are conducted only for arcing horn length up to 1.70 m, the equidistant shift of the V-t-curves in dependency of the number of insulator discs, justifies the LPM parameter usage for longer arcing horn length, in this work the full 400 kV cap-and-pin insulators with arcing horns.

4.6: SUMMARY AND CONCLUSION ON INSULATORS

In this chapter the breakdown process of air gaps with respect to HV insulators is investigated and the physical process of streamer and leader propagation leading to an electric connection between the electrodes explained. Several models for this process are available in the literature, which range from simple voltage-threshold models using the 50% flashover voltage value as a criterion for breakdown, over voltage-time-curve and integration methods, which use a mathematical description of measured V-t-curves as a breakdown criterion, to physical models of the leader progression.

It is decided to utilize Motoyamas leader progression model and implement it via the PSCAD/EMTDC Fortran code alongside its verification with standard parameters. Since model parameters are only available for pure air gaps, a comparison of the behaviour of the cap-and-pin insulators with arcing horns is necessary. Therefore laboratory flashover tests at the high voltage laboratory at HWU with a 800 kV and at UoM with a 2000 kV impulse generator are performed to determine both the 50% flashover voltage as well as the voltage-time-curve of various length of cap-and-pin insulators with arcing horns. The conducted tests show, that the performance is depending on the test setup, but the general behaviour of the insulators with arcing horns is the same.

To compare the behaviour of the Motoyama LPM with standard parameters for air gaps and the measured behaviour of the insulator with arcing horns, a software model of the impulse generators is built. The impulse generators voltage output of measured 1.2/50µs curves is compared to the simulated ones to verify the impulse generator software models. Then, the simulation of the breakdown tests of the insulators with arcing horns is performed with standard Motoyama parameters. The comparison of measured and simulated voltage-time-curves with 0.99 m to 1.69 m arcing gap shows, that the simulation with standard parameters underestimates the real performance of the insulators and an adjustment of the parameters is necessary. As only measurements of the voltage are available, it is decided to iteratively determine the LPM parameters to fit to the measurements. In this iterative process of curve-fitting it is found, that additionally to the

breakdown voltage – breakdown time- curve the maximum voltage – breakdown time curve can be used for a better curve fitting procedure. Although parameter sets for both positive and negative polarity leading to a relatively good fit to the measured V-t-curves are determined, it is known that the real flashover performance may be even better due to short-tail impulses encountered at insulators during a lightning stroke, in contrast to the relatively long 50 µs tail in the applied V-t-curve-fitting procedure. However, this introduces a safety margin for the simulations and later evaluation of the flashover rate.

Finally it has to be mentioned, that no arc model after breakdown is applied, because for the later evaluation of the flashover rate the voltages and currents after breakdown bring no benefit. Also, the flashover might be affected by transient electromagnetic coupling between the lightning channel, tower and phase conductor, which cannot be included in an EMT simulation [175], which leads to a steeper rise and amplitude of voltages after the back-flashover [161].

CHAPTER 5: THE TRANSMISSION TOWER

In the subject of a transmission line tower struck by lightning, the terms of tower surge response or impulse characteristic are used, which both basically describe the approach of the determination of the behaviour of a transmission tower excited with an impulse current.
In the following, the different methods to determine the surge impedance are discussed, as this is the basis for the subsequent characterization of the surge response as well as the tower modelling.

5.1: DETERMINATION OF TOWER SURGE RESPONSE

The determination of the tower surge response contains the propagation velocity, attenuation and characteristic surge impedance of a transmission tower. Approaches to quantify these parameters can be categorized in theoretical, experimental and simulation.

Theoretical investigations are based on a simplified geometry of a transmission tower, such as a cone or cylinder. There, the surge impedance can readily be calculated from electromagnetic field [176]–[180], or circuit/transmission line theory [181]–[183]. Due to their simplicity this calculation method is included in relevant standards [24], [153], [154], [156], also because a good safety margin for the determination of the lightning performance is included.

Experimental investigations of the surge response of transmission towers are performed on actual towers [184]–[189] and scaled models [190], [191]. The surge impedance and travel time is either determined with the “direct method”, where current is injected into the tower top and voltage and current measured or the time-domain reflectometry method for scale models. For the inclusion in an EMT simulation, the experimental setup is built in the software and values determined iteratively to match the actual measurement records.

In the last decade the determination of the surge response of transmission towers based on finite element or finite difference time domain (FTDT) simulation [161], [183], [192]–[198] has become popular, which is a numerical electromagnetic method to solve the

electric field equations directly. Whereby the surge response results from measurements and FTDT calculation agree well [192]–[194], [196]–[198], which makes the FTDT method an efficient and economic approach to determine the surge impedance of a transmission tower.

5.2: CHARACTERISTICS OF TOWER SURGE RESPONSE

The findings of all of these approaches are summarized in the following and outline the principle characteristics of the tower surge response.

- The surge impedance is a function of tower height [176], [181], [187], [188]
- The surge impedance is dependent on the angle of current injection at the tower top due to the mutual coupling effects of tower and injection wire (or lightning channel) [186]–[188], [198] and is greater for a vertical return-stroke (direct hit of tower) than for a horizontal return stroke (span hit of earth wire) [178], [186]. In a comparison of a FTDT simulation and an actual tower measurement it is shown that the surge impedance difference of horizontal to vertical current injection is approximately 30% [196]. However in [186] it is mentioned that the influence of angle of current injection derived from experiments on an actual tower with earth wires has a minor influence on the archorn voltages.
- The surge impedance decreases over time, which is caused by the reflections at the tower top [187], [188], [199].
- The cross bracing /slanted bars add capacitance and decrease the surge impedance in comparison to a simplified geometric structure [177], [187], [188], [198].
- The surge impedance is frequency-dependent [163], [183], [200]. However in [181] it is shown that the attenuation constant α of the propagation constant $\Gamma = \alpha + j\beta$ is heavily frequency-dependent under the assumption that $\omega L \gg R$. As a result the attenuation α is directly proportional to resistance R and the surge impedance is independent of frequency.
- Experimental results on actual towers show that the surge velocity in a tower is around 90% of the speed of light [164], [184], [185], [187], [196]. In comparison to a cone model of the tower, there the propagation is assumed to be equal to the speed of light, the cross-arms increase the total travel time by augmenting the average path length taken by the return stroke [177], [198], [199].

5.3: MODELLING OF TRANSMISSION TOWERS

5.3.1: DISCUSSION ON MODEL APPLICATION

As can be seen in the previous two sections, each method for determining the surge characteristics of a transmission tower features its pros and cons. In this context, a discussion of the various models for the evaluation of the lightning performance of a whole transmission line with an EMT simulation and their limitations with regard to the real characteristics, as pointed out in the previous section, is necessary.

A critical review on the experimental determination is found in [200], which states the problems of the definition of surge impedance with regard to the excitation waveform as well as various definitions of experimentally obtained voltage-current ratios. Additionally, the experimental results cannot be generalized to a form that fits various tower heights and tower configurations [184]. In this respect, the well-known EMT software model of a 500 kV multistory tower [185], [201], [202] needs to be mentioned as an example (see figure 5-1), which is derived from a comparison of experimental and simulation results through a trial-and-error analysis. The model incorporates the attenuation change of the reflected waves at tower base, which is accomplished with R-L parallel circuits and is valid for direct hits of the tower. The surge propagation is assumed to be speed of light. Another study shows that the model shows a good agreement with FTDT simulations of the transient behaviour until the back-flashover occurs [161]. However the model is restricted to the use of fixed resistance or inductance tower footing models [165], [168], [202]. In [164], [184], [203] it is reported that the model is not suitable for smaller towers and needs to be modified and aligned to measurements for other tower structures. In this respect, the same arguments are valid for FTDT simulations of towers, because simulations are performed for a single tower only due to their complexity and the voltage-current-ratio used to calculate the surge impedance.

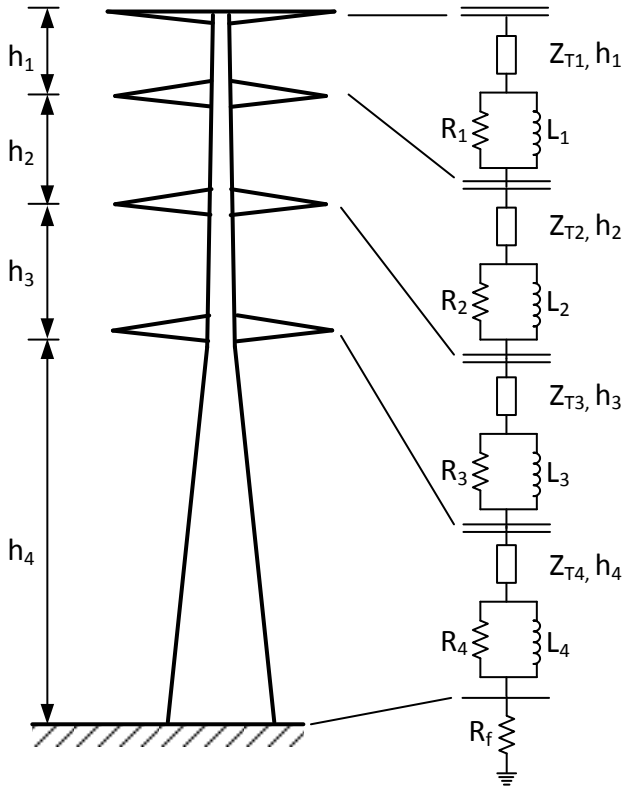

Figure 5-1: Multistory transmission tower model, adapted from [202]

Analytical formulas to calculate the surge impedance often use simplifications, such as perfectly conducting earth, surge velocity equal to the speed of light or neglect of attenuation and are based on simplified geometries of the tower [204]. These simplifications may be justified for some tower configurations, e.g. low and medium tower heights, where the attenuation and height-dependent effects do not contribute significantly [184]. However analytical non-uniform multistory tower models show good agreement with experimental results throughout [181], [183], [185], [204] and are widely adaptable to cover various tower heights and geometries [181].

Finally, the restrictions of the simulation point of view need to be discussed. In [200] it is stated that it is generally advised to obtain an understanding of the limits of the applied tower simulation model to avoid unrealistic results. Furthermore it has to be noted that EMT simulations are based on the transversal electromagnetic (TEM) mode, which limits the description of the real behaviour of a tower during a lightning stroke. In [161] it is shown through a comparison of an EMF FTDT and EMT simulation that the TEM mode is sufficient to describe the transients until a flashover occurs. However due to actual dynamic electromagnetic fields initiated at the instant of flashover, which includes non-TEM coupling, the simulation results differ after the flashover. As a result multiple flashovers cannot be estimated accurately.

The conclusion to the discussion above, keeping in mind the main goal of this work to determine the lightning performance of a whole transmission line in an EMT simulation, is that only the analytical formula for multistory tower models offer the required flexibility for various tower heights and configurations. Although, it is possible to differ between horizontal and vertical current injection with different formulas, only vertical stroke tower models are taken into account, since the stroke angle has a minor influence on the archorn voltages. Although analytical formulas have proven their accuracy, a random sampling with FTDT measurements may further justify their application.

5.3.2: SURGE IMPEDANCE MODELS

As already mentioned in the previous section, simplified formulas for the determination of the tower surge impedance can be applied. These formulas are based on the assumption that earth is a perfect conductor and propagation velocity is speed of light and are either valid for horizontal or vertical current injection at the tower top [176], [177], [199]. Furthermore, the formula used has to fit the tower geometry to achieve a good estimation of the average surge impedance, as illustrated in figure 5-2.

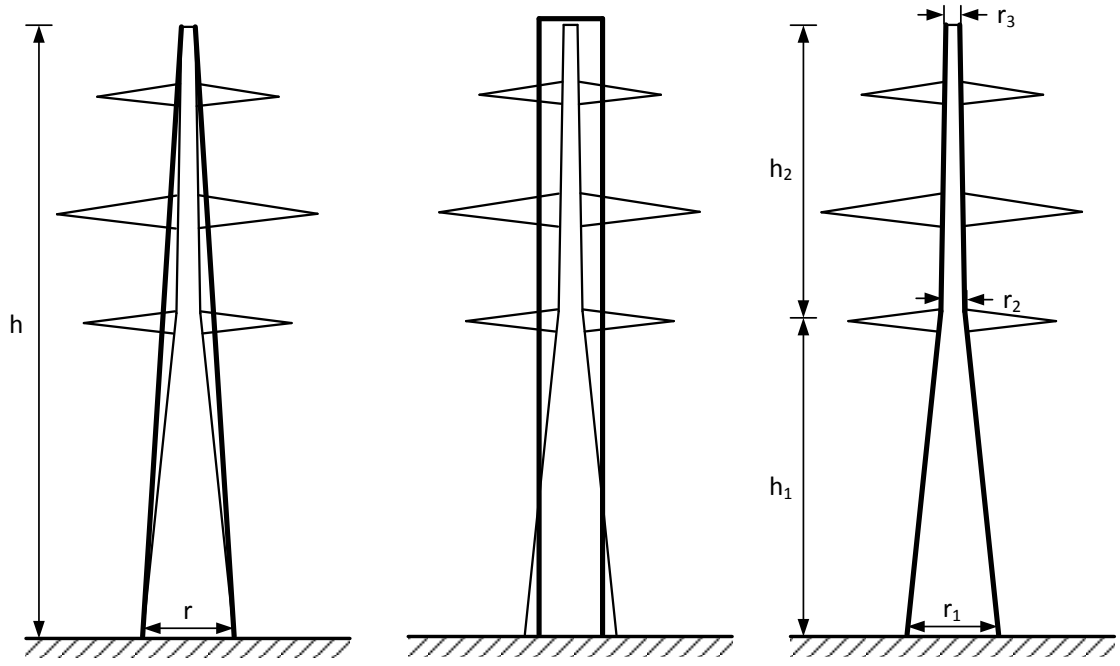

Figure 5-2: Comparison of conical and cylindrical approximations of steel-lattice towers, adapted from [188]

For vertical current injection – direct stroke to a tower – a double-circuit steel lattice tower can be reduced to a cone shape and the surge impedance calculated with formula (5.1) in accordance with measurements in [176], but not taking cross-arms into account. There

the surge impedance is independent of waveform, but dependent on the tower base radius r and height h.

$$Z_{cone,vertical} = 60 \cdot \ln\left(\sqrt{2}\frac{\sqrt{r^2+h^2}}{r}\right) \tag{5.1}$$

For a cylindrical tower shape formula (5.2) with the same assumptions [176] provides an estimation of the surge impedance.

$$Z_{cylinder,vertical} = 60 \cdot \ln\left(\sqrt{2}\frac{2h}{r}\right) - 60 \tag{5.2}$$

For horizontal current injection to the towers simplified as a cone formula (5.3) from [177] and for a cylinder in formula (5.4) can be used to calculate the surge impedance.

$$Z_{cone,horizontal} = 60 \cdot \ln\left[\cot\left(\frac{\tan^{-1}\left(\frac{r}{h}\right)}{2}\right)\right] \tag{5.3}$$

$$Z_{cylinder,horizontal} = 60 \cdot \ln\left[\cot\left(\frac{\tan^{-1}\left(\frac{r}{h}\right)}{2}\right)\right] - 60 \tag{5.4}$$

Furthermore, CIGRE/IEEE [24] recommends formula (5.5) for a wasted tower shape with a weighted radius r_{avg}, as illustrated in figure 5-2 for horizontal current injection according to [177].

$$Z_{CIGRE} = 60 \cdot \ln\left(\cot\left(0.5 \cdot \tan^{-1}\left(\frac{r_{avg}}{h}\right)\right)\right) \tag{5.5}$$

$$r_{avg} = \frac{r_1 h_1 + r_2 h + r_3 h_2}{h} \tag{5.6}$$

Furthermore, in [181] a formula for vertical conductors from [205] is applied, known as 'Jordan's formula', written in (5.7).

$$Z_{Jordan} = 60 \cdot \ln\left(\frac{h}{r}\right) - 60 \tag{5.7}$$

For all the formula above the equivalent radius for a square is needed, which can be calculated from the geometrical mean radius of the square in formula (5.8), where r is the radius of conductors forming the square and d, the distance between adjacent conductors.

$$r_{eq,square} = \sqrt[4]{\sqrt{2} \cdot r \cdot d^3} \tag{5.8}$$

For L-shaped sections with thickness much smaller than length, such as the steel-lattice main supports, the geometric mean radius can be approximated with two lines in 90 degree angle in formula (5.9) [6].

$$r_{eq,L} = 0.692\text{d} \tag{5.9}$$

To obtain average radii for cylinders, formula (5.10) is applied, as suggested in [181].

$$r_{eq,avg,cylinder} = \sqrt[n-1]{1 \cdot 2 \cdot \ldots \cdot n} \tag{5.10}$$

To estimate the travel time and propagation velocity of a tower including the tower cross-arm delay effects, a calculation method based on tower capacitance and surface area from [177] can be utilized. However, the set of formulae is highly dependent on the surge impedance value calculated from the formulae above and may result in unrealistic propagation velocities. Since the surge impedance is slightly reduced when taking cross-arms into account as mentioned in section 5.2, the decrease in propagation velocity can be neglected [24]. As pointed out in [24], [177], [199] cross-arms can be included and treated as short horizontal transmission lines.

In figure 5-3 a comparison of the various formulae above is presented for the 400 kV suspension tower in appendix B.3 with variation of tower height and tower base edge length.

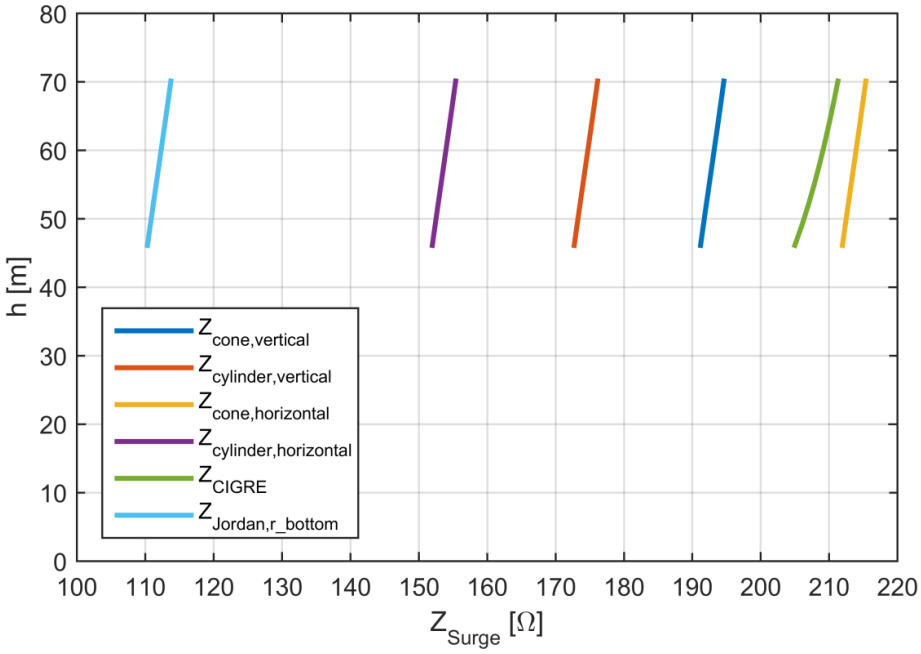

Figure 5-3: Comparison of tower surge impedance formula

The plotted curves show that the relationship between average tower surge impedance and height is approximately linear over a broad range, but also that there is no consistency in the different formulas. In this respect it has to be mentioned that the formulas are based on average impedances in the form of equation (5.11), which can lead to variations dependent on tower geometry, such an extensive tower base paired with a thin top structure.

$$Z_{avg} = \frac{1}{h}\int_0^h Z(h)dh \tag{5.11}$$

A comparison of measurements to the formulae from above in [181] shows that the CIGRE as well as the horizontal cone formula show a pronounced deviation from measurement results. Furthermore, measurements in [178], [186] show that the impedance for vertical current injection is higher than for horizontal current injection, which further supports the results in [181]. However, this behaviour of tower surge impedance in dependency of the angle of current injection is shown in the cylinder formula and Jordan's formula, which also give much lower values for tower surge impedance. To get a further improvement of the calculation of tower surge impedance, the tower structure can be represented with a distributed surge impedance model, which is an improved version of equation (5.11) [181].

5.3.3: DISTRIBUTED TOWER SURGE IMPEDANCE MODEL

To improve the tower representation in the evaluation of the lightning performance of a transmission line, the tower and the tower cross-arms respectively have to be represented with a distributed line model [179]. Ametani et al. present a method of calculating the surge impedances of tower parts, which includes the penetration depth of soil and shows a good approximation of a range of tower sizes, but lacks the frequency-dependent behaviour [181]. However, since the frequency-dependent effect of a tower has a minor effect when the tower grounding system is modelled as a variable resistance or inductive branch [164], which will be discussed in the next chapter, the frequency-dependent effect can be neglected.

Ametani et al. represent the tower with a set of cylinders, either for each leg or merged into a single stack of cylinders, as shown in figure 5-4 [181]. Through an evaluation of the influence of the penetration depth of soil, it is shown that the calculations can be performed with sufficient accuracy taking into account a perfectly conducting ground.

For a four leg model in figure 5-4, (a), the mutual impedances have to be taken into account (see equation (5.12)).

$$Z_S = \frac{Z_{11}+2\cdot Z_{12}+Z_{13}}{4} \tag{5.12}$$

The general formula for self and mutual surge impedance is written in equation (5.13) and (5.14), whereas in the self-impedance case and for the cylinder representation in figure 5-4, (b), $d = r$ and the case of the bottom of the conductor on the earth surface $X = h$.

$$Z_{ij} = 60 \cdot P_{ij} \tag{5.13}$$

$$P_{ij} = \ln\left[\frac{\left(\sqrt{d^2+X^2}+X\right)\cdot\left(\sqrt{d^2+4(h-X)^2}+2(h-X)\right)}{d\cdot\left(\sqrt{d^2+(2h-X)^2}\right)+(2h-X)}\right] + \frac{h}{X}\cdot\ln\left[\frac{\left(\sqrt{d^2+(2h-X)^2}+(2h-X)\right)^2}{\sqrt{d^2+4h^2}+2h}\cdot\right.$$

$$\left.\left(\sqrt{d^2+4(h-X)^2}+2(h-X)\right)\right] + \frac{1}{2X}\left(2d+\sqrt{d^2+4h^2}+\sqrt{d^2+4(h-X)^2}-\right.$$

$$\left.2\sqrt{d^2+X^2}-2\sqrt{d^2+(2h-X)^2}\right) \tag{5.14}$$

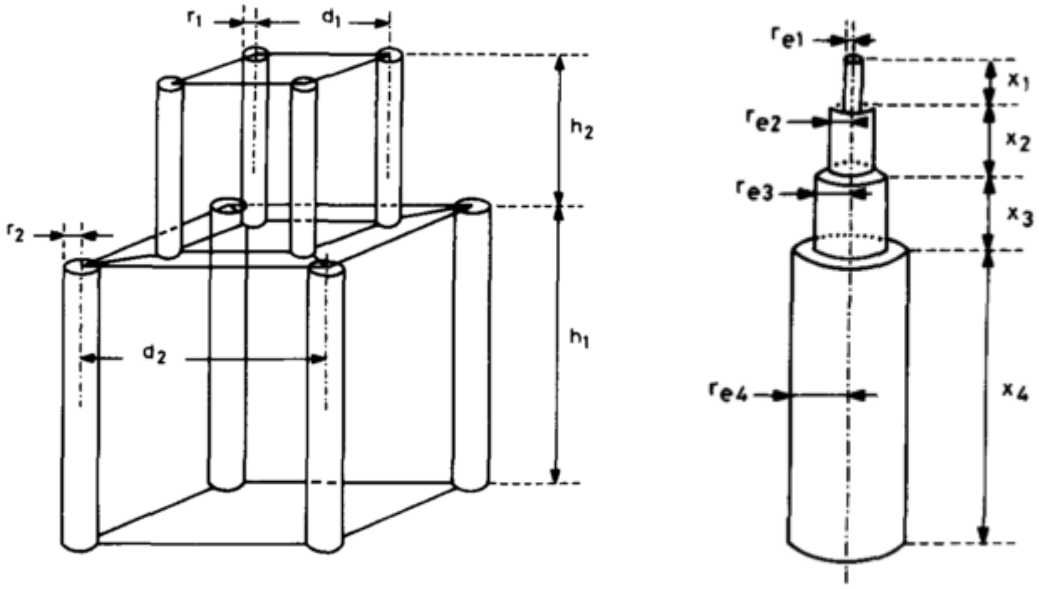

a) Two stair/ four leg model **b) Four stair/ equivalent cylinder model**

Figure 5-4: Multistair transmission tower models [181]

For the 400 kV suspension and tension tower in appendix B.3 with variation of tower height and tower base edge length an evaluation of the distributed line impedances is

performed in figure 5-5 and figure 5-6. Thereby the towers are cut into a number of sections and the calculated impedance is compared to assess the variation of surge impedance with the number of stairs and tower height. In this respect, certain calculation methods are applied for the equivalent radii of the cylinders (see equation (5.8) to (5.10)).

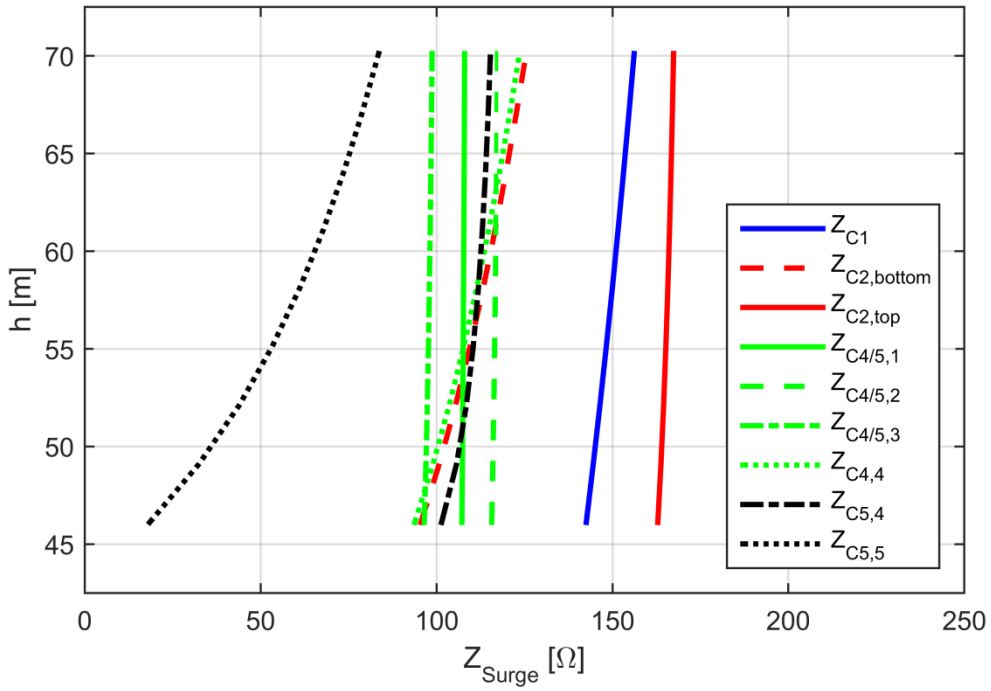

Figure 5-5: Results of suspension tower impedance calculation

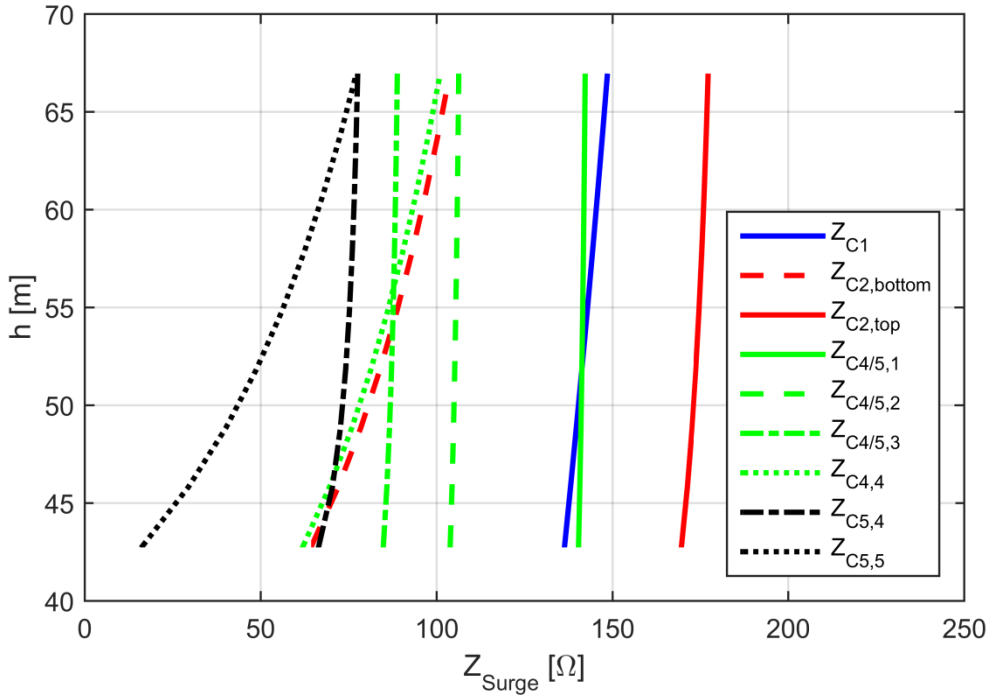

Figure 5-6: Results of tension tower impedance calculation

The results for both the suspension and tension tower align with the results obtained in [181] related to the comparison of a single cylinder Z_{C1}, top and bottom cylinder $Z_{C2,top}$ and $Z_{C2,bottom}$for upper and lower tower section and the four cylinders $Z_{C4,1}$ to $Z_{C4,4}$ for the tower with cross-arms. In addition to the findings in [181], the investigated dependency of surge impedance with tower height for the two tower configurations shows a more pronounced dependency for the single and bottom cylinder approximations (Z_{C1},$Z_{C2,bottom}$, $Z_{C4,4}$), which originates from the increasing edge length with tower height. Since the tower structure top part of the investigated suspension and tension tower remains unchanged, only a minor variation of the surge impedance with tower height is observed for the four cylinder approximation, which ranges from 0.7% for $Z_{C4,1}$ to 2.3% for $Z_{C4,3}$ for the suspension tower and 1% for $Z_{C4,1}$ to 4.7% for $Z_{C4,3}$ for the tension tower. Therefore and with regard to the modelling of a whole transmission line it is practical to fix $Z_{C4,1}$ to $Z_{C4,3}$ to medium values for the four cylinder approximation. Since the variation of surge impedance of the bottom tower structure decreases with increasing tower height, as seen at $Z_{C4,4}$ for both suspension and tension tower, a further sectioning of the bottom part $Z_{C4,4}$ into a fixed part $Z_{C5,4}$ and a variable part $Z_{C5,5}$ is investigated. It is found that the variation of $Z_{C5,4}$ with tower height is in the range of up to 17.3% for suspension and 16.5% tension tower, similar to $Z_{C4,4}$, and the variation of $Z_{C5,5}$ is even more pronounced due to its short length and wide footing radius. This leads to the conclusion that a four cylinder tower with three fixed and one height-dependent variable impedance is sufficient for practical tower modelling.

5.4: SUMMARY AND CONCLUSION ON TRANSMISSION TOWERS

In this chapter a literature review on the methods of determination of the transmission tower surge impedance, tower surge response characteristics and tower modelling has been conducted. The tower surge response can either be determined through experimental tests on towers, EMF simulation, such as FTDT methods or analytically from simplified tower structures.

The tower surge characteristics obtained from these methods are tower height dependent, whereas the surge impedance is independent of the frequency. Various effects, such as the tower meshed structure lead to an increased travelling distance from the tower top to

ground, which is equivalent to a decrease in surge velocity, which is found to be in the region of 90% speed of light. For very high towers (h > 100 m) the attenuation of travelling waves cannot be neglected, but is insignificant for small and medium tower structures.

When modelling transmission towers in EMT simulations, application restrictions originating from the determination method of the surge response have to be considered. Models developed from measurements and FTDT simulations are found to be only valid for the measured tower configuration, but may feature the measured transfer function from top of the tower to ground including attenuation. In contrast to that analytically derived models consist of calculated surge impedance and fixed surge velocity and therefore lack attenuation. Since attenuation is only noticeable at very high towers, analytical derived non-uniform multistory tower models show good agreement with various measurements and are adaptable to various tower heights and geometries.
An investigation on analytical tower modelling with formulas for vertical and horizontal current injection shows a broad variation of the calculated surge impedance values, in which the tower impedance for vertical current injection is higher than for horizontal current injection. Since formulas for vertical current injection lead to higher overvoltages due to the higher tower impedance and the fact that the injection angle has a minor influence on the archorn voltages, it is concluded to use formulas for vertical current injection for tower modelling. A further investigation on an analytically derived non-uniform multistory tower model with partitioning of the transmission towers in appendix B.3 in two to five cylinder parts shows, that the tension and suspension tower structure can be modelled with three fixed upper and one lower end tower height-dependent surge impedance.

Derived from the performed literature review and investigation on the analytical multistory tower model it is concluded that modelling of the suspension and tension tower can be performed with the analytically derived multistory tower models for suspension and tension tower without further verification. The surge velocity is fixed to 90% of the speed of light to take into account the extended lightning surge path length due to slants and cross-arms. Due to the limited tower height below 100 m and investigations with grounding electrode models in the simulations, attenuation and distortion, in form of R-L-circuits in between surge impedance models, are not considered. With regard to the application of the multistory tower model in the later EMT simulation it is concluded to

deploy one tower lower end height-dependent surge impedance in combination with three fixed surge impedances as a practical solution.

CHAPTER 6: TOWER EARTHING SYSTEMS

In this chapter, the fundamental physical behaviour of a tower earthing system in the transient time domain is presented, followed by the boundaries of current verification measurements and the models for simulation.

6.1: ELECTRICAL BEHAVIOUR OF TOWER EARTHING SYSTEMS

The earthing system of a transmission line tower, also called tower footing, generally comprises an earth electrode, such as rods, ring networks or strips connected to the tower foot, and the surrounding soil, backfill and possible enhanced compounds [1]. The grounding system performance is often associated with its power-frequency "tower footing resistance", obtained from low-frequency earth measurements [206]. Requirements for the limit of footing resistance are employed to keep the power-frequency ground potential rise (GPR) and step-voltage during line faults below hazardous limits [207], but the footing resistance is also utilized as a limit value with respect to the lightning protection in international standards [208]. The electrical behaviour of earthing systems has been studied since the early days of high voltage power transmission (see references [77], [87], [209]–[229] and references therein), both for power frequency as well as lightning transients. As is known for decades, the earthing system behaviour with respect to lightning is rather represented with an impedance for both the earthing electrode and soil [230], which demands for different requirements for the earthing system performance with respect to fast front transients [208]. Various studies ([189], [231]–[235]) show that the representation of the tower footing as an impedance including physical effects in the transient time domain has a major effect on the $BFOR$ of insulators and the lightning performance of a transmission line, respectively.

Although there is a broad consensus on the general behaviour, a rigorous analysis of current distribution to earth remains difficult because the soil under the earth surface is by no means homogeneous [207] and soil properties vary due to environmental impacts [236]–[239].

6.1.1: PROPAGATION AND ATTENUATION EFFECTS OF ELECTRODES

In general the electrical behaviour of the tower earthing system is dependent on the soil-penetrating current waveform and current density [216]. Researchers found that the earthing system, especially long buried conductors and rods, feature travelling wave behaviour and are subject to rise-time dependent damping effects [183], [189], [207], [209], [216], [224], [225], [230], [240]–[244] with a fast decrease of velocity in earth [207]. Due to the current dispersion to earth, the current and voltage wave is highly attenuated along its propagation path [216], [245], as illustrated in figure 6-1.

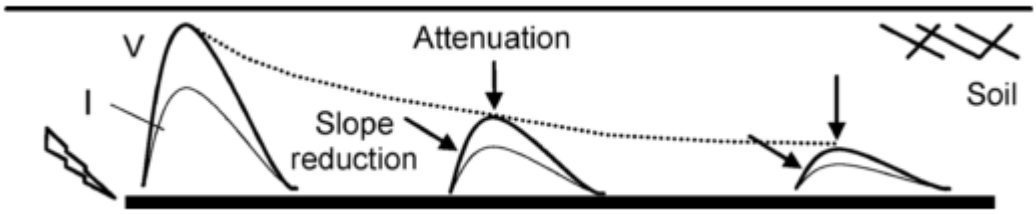

Figure 6-1: Attenuation of current and voltage wave along a buried wire, adapted from [216]

In this context, the concept of effective length of impulse impedance L_{eff} from [246] has to be mentioned, which is connected to the attenuation. With the decreasing dispersion of current to soil along the propagation path of the electrode, the impulse impedance $Z_P = \frac{V}{I}$ decreases with electrode length, as depicted in figure 6-2 for various soil resistivity and also with shorter front times of current waveshapes. At the point where no more current is impressed into the soil the impulse impedance remains constant, which represents the effective length. An extension of the electrode length still reduces the power-frequency resistance of the earthing system, but has no effect on impulse currents [216].

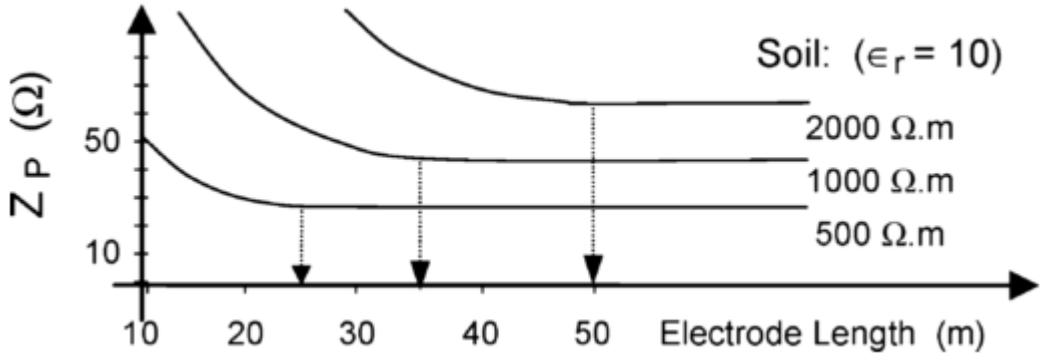

Figure 6-2: Definition of the effective length from impulsive impedance curves, adapted from [216]

6.1.2: LOW-CURRENT IMPULSE RESPONSE OF EARTHING SYSTEMS

With respect to the current density impregnated to earth, it has to be distinguished between a low-current and high-current impulse response [210]. With the example of a hemisphere ground electrode in figure 6-3, the electrical behaviour of an earthing system with regard to the above mentioned separation of effects is explained. Thereby it is assumed that the soil surrounding the electrode is homogenous.

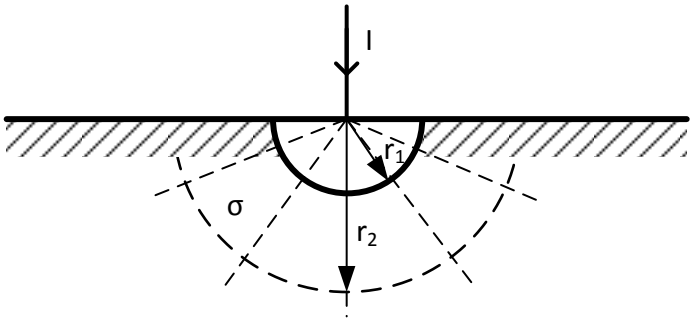

Figure 6-3: Sphere ground electrode

For the low-current response of soil, various researchers found that soil is heavily frequency-dependent [77], [87], [91], [212], [214], [216], [218], [221], [222], [224], [225], [227]–[229], as already mentioned in chapter 3.1.3. To show the frequency-dependency of the example in figure 6-3, measurement curve-fitted formulas for soil resistivity and permittivity from [225] in formula (6.1) and (6.2) are utilized.

$$\rho = \rho_0 \rho_r = \rho_0 \{1 + [1.2 \cdot 10^{-6} \cdot {\rho_0}^{0.73}] \cdot [(f - 100)^{0.65}]\}^{-1} \tag{6.1}$$

$$\varepsilon_r = 7.6 \cdot 10^3 f^{-0.4} + 1.3 \tag{6.2}$$

The impedance of the sphere electrode is calculated with equation (6.3) and (6.4).

$$\underline{\sigma} = \frac{1}{\rho} + j\omega\varepsilon_0\varepsilon_r \tag{6.3}$$

$$\underline{Z} = \frac{1}{2\pi\underline{\sigma}}\left(\frac{1}{r_1} - \frac{1}{x}\right) \tag{6.4}$$

In figure 6-4 and figure 6-5 the impedance, represented as the commonly used impulse coefficient and the corresponding phase angle are plotted for the sphere electrode.
The graphs show that for power-frequency the reactive effects are negligible and the soil can be treated with a constant potential approach [216]. With increasing frequency the

contribution of capacitance to the impedance becomes more distinct. For high soil resistivity this is even more pronounced, as can be seen from the impulse coefficient.

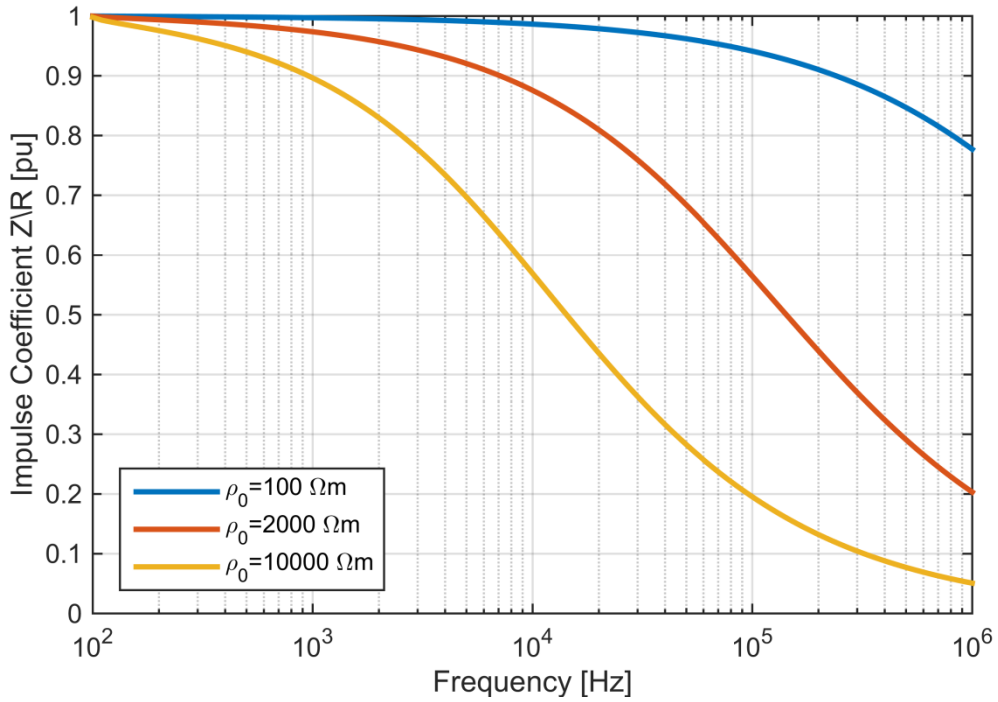

Figure 6-4: Impulse coefficients of various soils

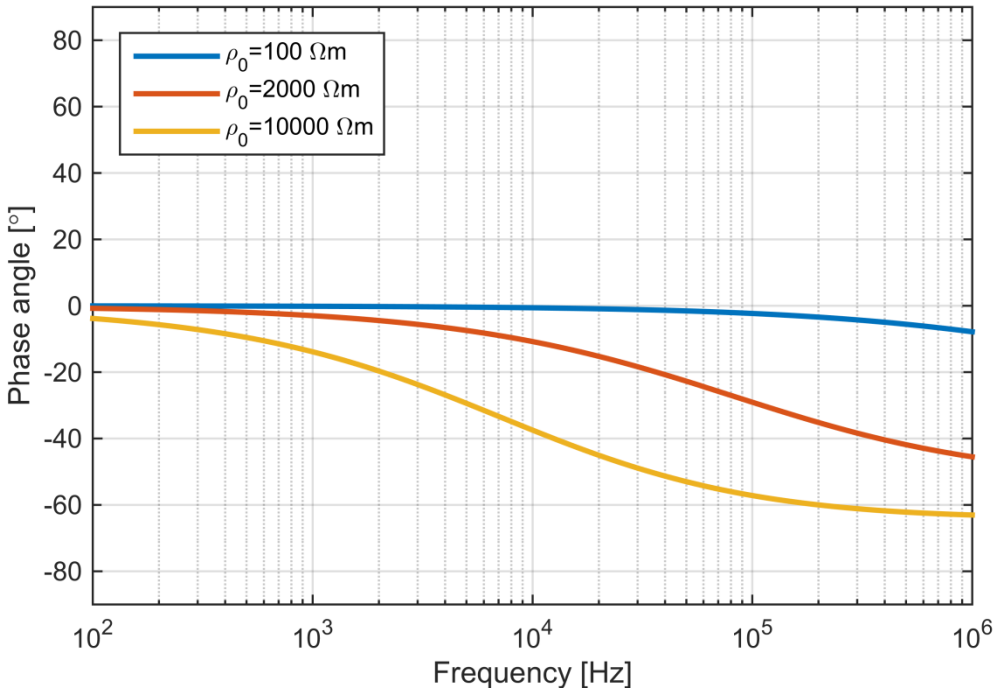

Figure 6-5: Impulse coefficient angle of various soils

Several studies show that the frequency-dependency of soil has a major influence on the back-flashover rate of insulators and therefore should be included in simulations [232]–[235].

6.1.3: HIGH-CURRENT IMPULSE RESPONSE OF GROUNDING SYSTEMS

When a current is discharged into a grounding system and the resulting field strength at the electrode surface exceeds the critical breakdown field strength of the surrounding soil, an ionization process in soil takes place [189], [207], [209], [211], [213], [215], [217], [223], [226], [228], [247]–[249], as depicted in figure 6-6. This process is preceded by a thermal process, there soil particles are heated up through the I^2R losses and as a consequence moisture evaporated, leaving voids in soil. The thermal process varies with soil moisture and is not present for dry materials [217]. The thermal process is followed by an air breakdown process in the voids, leaving ionized paths in soil [215].

The ionization process starts at the sphere electrode surface, where the current density is the highest and streamers propagate in the direction away from the electrode until the electric field strength drops below the breakdown value [211]. The ionized zones in soil around the electrode decrease the grounding system's surge impedance [189], [207] and effectively increase the electrode's radius [249]. For high soil resistivity the ionization process is more pronounced than for low soil resistivity [216]. Furthermore, the intensity of the ionization effect is dependent on the type of electrode used for earthing a transmission tower. In [250], performed measurements show that long horizontal buried electrodes feature a smaller ionization effect than short horizontal electrodes, in which the ionization effect is predominant at the injection point.

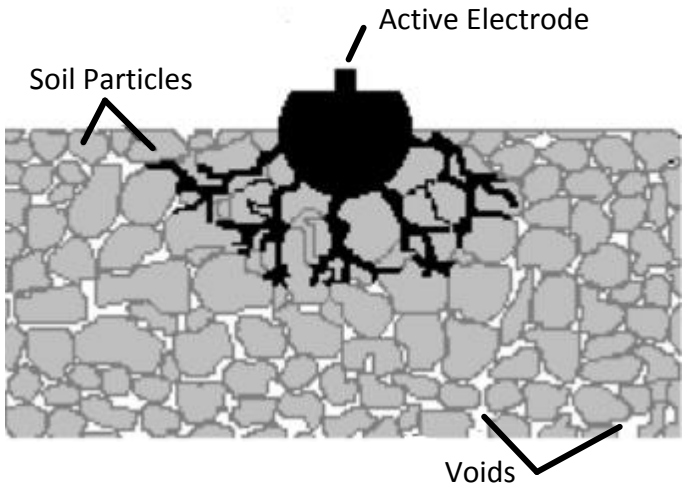

Figure 6-6: Ionization process for a sphere electrode, adapted from [215]

The determination of a generalized approach for the breakdown electric field strength remains difficult [219] as it is dependent on soil properties, whereas investigation results

range from 200 to 1700 kV/m [211]. However several researchers [211], [213], [251] suggest the application of a value in the range of 300 kV/m to 400 kV/m, which is the recommendation by CIGRE [249].

Several studies show that the lightning performance of a tower and the outage rate of a transmission line, respectively, is very sensitive to the ionization process [169], [223]. Therefore this effect should also be included in simulations of lightning strokes to transmission lines.

6.2: APPLICATION RANGE OF EARTHING SYSTEM MODELS

With regard to the difficulties of finding a consistent theory and description of all the above effects of travelling wave, frequency-dependency of soil and ionization effects, it is necessary to evaluate the application range of earthing system models based on available measurement data and determine areas subject to further research. Therefore an overview of more recent performed measurements and test-setups is given in the following.

Measurements on soil ionization can be divided into laboratory-scale and large scale tests, whereas most tests are focused on rods and hemispheres in a sandy soil mix. A summary in table 6-1 provides a list of the electrode types and low-frequency (DC or up to 100 Hz) soil resistivity.

Table 6-1: Summary of soil ionization tests

Reference	Waveshape	Current/ Voltage Range	Electrode Type	Soil low-frequency resistivity
[210]	6-16/18-54 μs	1 kA - 20 kA	rod arrangements hemisphere sparking connection to ground	50 Ωm – 3100 Ωm
[247]	-	-	rod arrangements hemisphere horizontal wires in soil	50 Ωm – 2000 Ωm
[211]	-	0.1 kA - 27 kA	rod arrangements hemisphere rock footing	100 Ωm – 1000 Ωm
[213]		up to 40 kA	rods	200 Ωm – 1000 Ωm
[215]	-	up to 5 kA	hemisphere	-
[220], [223], [252]	various, such as 4.5/13 μs 8.2/36 μs	up to 9kA	horizontal buried wire tower footing	200 Ωm
[226]	1.2/50 μs	up to 50 kV	2 to 4 rods interconnected	780 Ωm

In this respect, the tests on a tower foot, discussed in [220], [223], [252] have to be highlighted as the only test-setup for a tower base. The description and layout of the test-setup is illustrated in figure 6-7. For the injection of impulse currents an impulse generator rated 20 kJ, 20 kA is utilized. Connection to the tower base is made through a overhead line consisting of a bundle of two 30 m-long insulated copper wires, supported by 1.7 m-high wood poles. The current return electrode consists of a 60 m- diameter ring buried at a depth of 0.3 m and connected to eight 16mm-diameter rods, driven to a depth of 2.4 m. In contrast to other test setups such as in [226], which use a single rod as return electrode (see figure 6-8), the ring offers a more even collection.

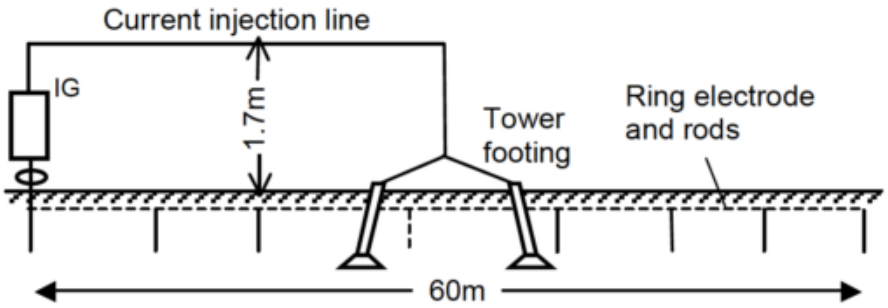

a) Elevated view

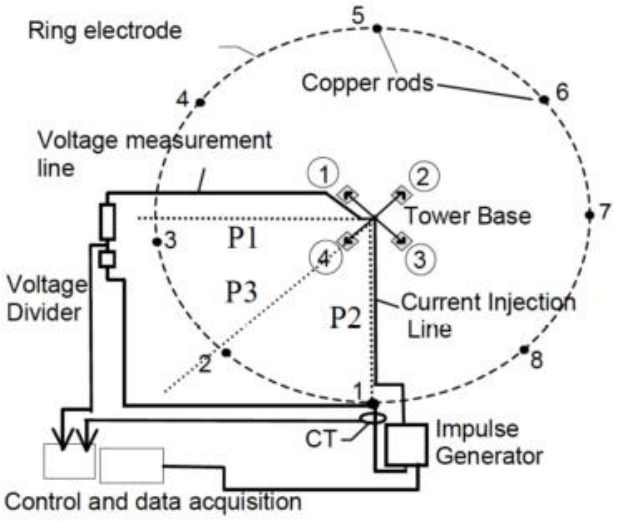

b) Plan view

Figure 6-7: Low- and high-current impulse measurement test setup of a 275 kV tower [252]

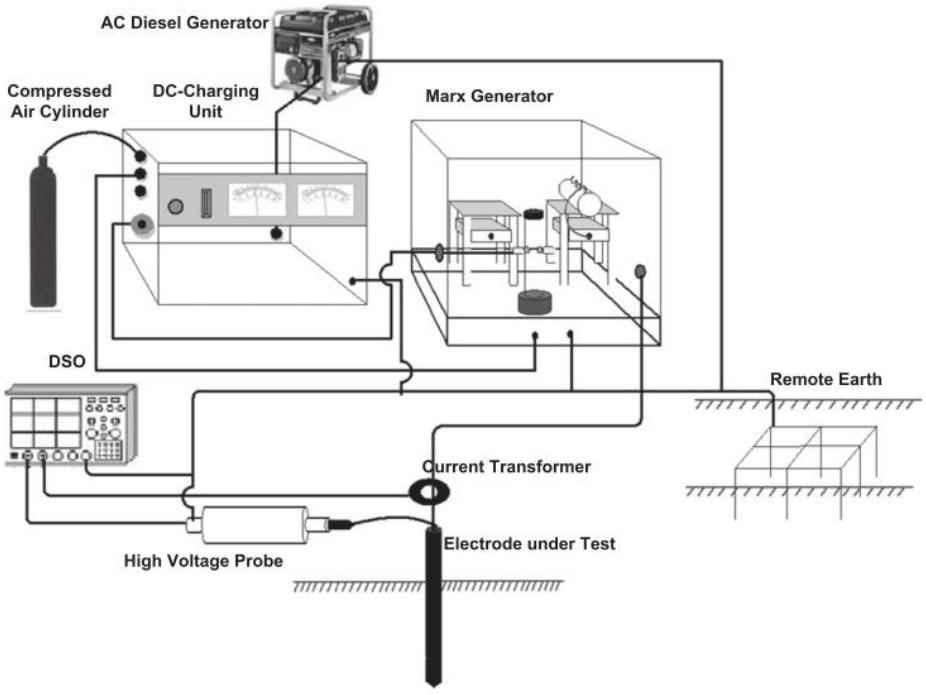

Figure 6-8: Low- and high-current impulse measurement test setup of 2 to 4 rod configurations [226]

Although there are many references on low-current injection measurements of grounding systems, an approach to determine the frequency-dependency of an earthing system is provided in [242], [244] using various impulses, such as 8.2/36 µs or 4.9/13 µs for vertical rods ranging between l.2 m and 4.8 m length, and horizontal electrodes of up to 88 m long buried 30 cm below ground surface, and the already mentioned 275 kV tower footing with the test setup in figure 6-9.

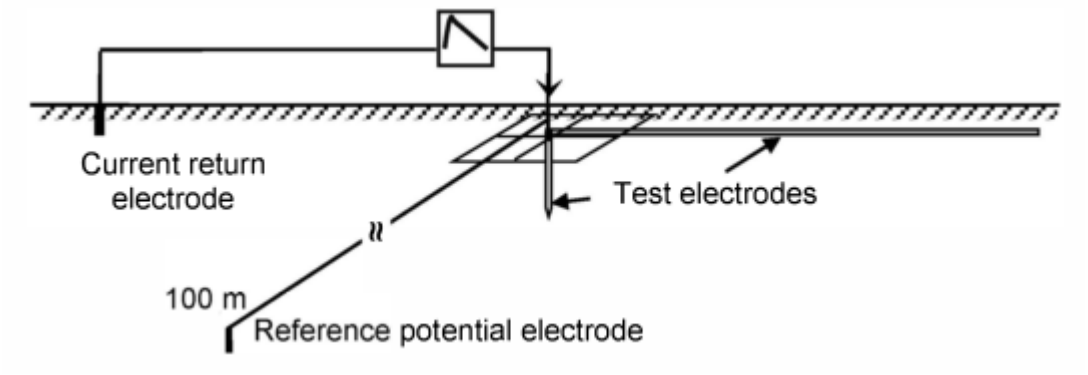

Figure 6-9: Low-current impulse measurement test setup [242]

A systematic approach to determine the formulas for the frequency-dependency of soil is provided in [77], [218], [224], [225], [234], [243], where a 0.6 kV low-current impulse generator was used to inject 0.1/10 µs, 0.2/100 µs and 20/10000 µs current waveforms on a buried hemispheric electrode in sequence. Tests are performed on different soils ranging from 50 Ωm to 9100 Ωm DC resistance. The current return electrode is composed of four interconnected 70 cm- long rods, placed 30 m away, as shown in figure 6-10.

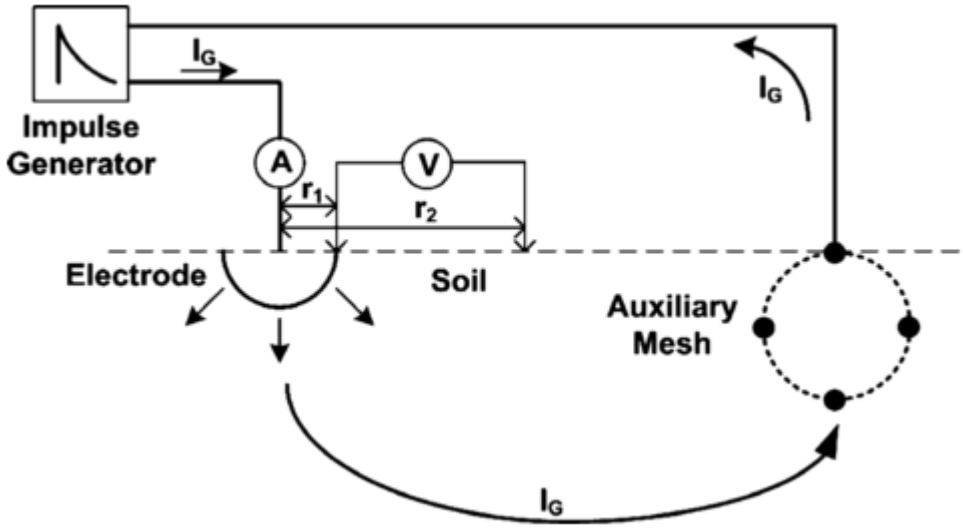

Figure 6-10: Low-current impulse measurement test setup [87]

With regard to the suite of towers and soil resistivity investigated in this work, such as encountered at the 400 kV sample line in the Scottish Highlands, where a vast number of

towers feature a measured low-frequency soil resistivity of 2000 Ωm to 11000 Ωm, the systematic approach in [77], [218], [224], [225], [234], [243] matches the application range. However in the matter of soil ionization, which is distinctive for high soil resistivity, the application range is limited to values up to 3100 Ωm and rod earthing systems. As the utilization of rods in rocky soil is too expensive, either copper strips or short rock footings are normally selected. The literature review reveals that there exist no measurements up to date for these kinds of electrodes in high soil resistivity, which can verify earthing system transient simulation models in this range. In comparison to lower resistive soils, where the assumption of a uniform ionized area surrounding the electrode is still justifiable, ionization paths are presumably confined to cracks in rock or loose areas in rocky soil. Consequentially the extrapolation of ionization measurement results and application of associated developed simulation models would lead to great uncertainties in the prediction of flashovers on a transmission line.

In this context, further measurements on this application range would be necessary to gain knowledge and confidence that modelling assumptions still hold or have to be changed respectively. These measurements may be performed with a similar test setup as shown in figure 6-7 with various current magnitudes and waveshapes. However practical challenges arise with regard to the reference potential electrode to be placed in low-soil resistivity as well as the configuration of the current return electrode in outdoor tests on a tower base.

6.3: MODELLING OF TOWER EARTHING SYSTEMS

To simulate the behaviour of an earthing system subject to lightning impulses as outlined in chapter 6.1, models available in the literature are either based on electromagnetic field theory [253]–[258], such as finite element methods (FEM) and Method of Moments (MoM), transmission line (TL) [259]–[262] or circuit theory [215], [245], [258], [262]–[275]. Although EMF-based methods are the most accurate, computation time and complexity hinders the fast and simple simulation of a whole transmission line [264], but they are often used to verify circuit approaches or derive parameters for circuit elements, such as the pi-circuit based on EMF simulation results fitting in [263], [266], [270], [271], [276].

In general, modelling is dependent on the earthing systems electrode configuration, the soil resistivity and impulse front time, in which travelling wave and attenuation effects, also associated with an electrodes effective length, are pronounced for long buried

horizontal electrodes, in contrast to short vertical electrodes. The capacitive frequency-dependent effect dominates at high soil resistivity, in contrast to inductive effects at low soil resistivity, whereas the overall frequency-dependent effect is more pronounced at short impulses. Soil ionization is only considered at high currents and higher soil-resistivity respectively. [264]

As in this work an EMT circuit approach is taken, only transmission and circuit approach models are applied. Due to the complexity of models, soil ionization models and frequency-dependent soil models are separated in most simulation models, either as a variable resistance or voltage/current source [269], [271], [275]. Although sole ionization models based on R-L-C circuits, such as in [215], [272] feature a closer fit to some measurements, the overall performance differs only slightly from variable resistance models [265], [272]. Therefore only variable resistance models compatible to be included into circuits for frequency-dependency are considered.

6.3.1: RESISTANCE MODELS

In the majority of studies performed to determine the lightning performance of a transmission line a simple resistance model or variable resistance model is used [24], [50], [61], [154], [164], [165], [168], [179], [277]–[285]. This originates from the fact that in practice transmission codes state tower footing requirements (combined soil and electrode) as a resistance at power frequency resistance. Using formulas, such as from [286], the combined resistance of a tower earthing system and soil resistivity taken from measurements can be calculated. Furthermore this type of model leads to conservative results due to the underestimation of the performance of the earthing system [258].
A commonly used variable resistance model, such as proposed by Weck and adopted by CIGRE [24], takes into account the soil ionization effect in equation (6.5) and (6.6), where R_0 is the normal tower footing resistance, I is the instantaneous current through the resistance and E_c the breakdown electric field value.

$$R_F = \frac{R_0}{\sqrt{1+\frac{I}{I_c}}} \tag{6.5}$$

$$I_c = \frac{E_c \rho}{2\pi {R_0}^2} \tag{6.6}$$

The model is developed for earthing rods and not meant to be for extensive earthing networks of more than 30m [249]. The determination of a generalized approach for the breakdown electric field strength remains difficult. In [247], various measurements are summarized and re-evaluated, which leads to a resistivity-dependent breakdown electric field strength ranging from 400 kV/m for 10 Ωm to 1750 kV/m for 10000 Ωm. For (1) an average of 1000 kV/m or the resistivity-dependent breakdown electric field strength from [247] is proposed. In [211] an investigation into previous experiments reported breakdown electric field strength is performed, which concludes to apply a value in the range of 300 kV/m to 400 kV/m. Other researchers [213], [251] confirm a value in the range of 300 kV/m to 400 kV/m, which is also the recommendation by CIGRE [249].

Another variable resistance model for a single rod, mentioned in [287], is based on Korsuncev similarity method with the dimensionless factors in (6.7) and (6.8).

$$\Pi_1 = \frac{sR_0}{\rho} \tag{6.7}$$

$$\Pi_2 = \frac{\rho I}{E_c s^2} \tag{6.8}$$

There, s is the distance between the centre and the outermost point of the metallic structure in m, R_0 is the footing resistance in Ω, ρ is the soil resistivity in Ωm, I is the instantaneous current in kA and E_c is the breakdown electric field strength. It is shown that a rod shaped electrode can be modelled as a hemispherical electrode shape with reasonable accuracy in (6.9), where A is the electrode surface area in m^2.

$$\Pi_1^0 = 0.4517 + \frac{1}{2\pi} ln\left(\frac{s^2}{A}\right) \tag{6.9}$$

Furthermore, above a critical distance, the ionized zone can be simplified with a sphere electrode shape, where the correlation between Π_1 and Π_2 in the range of 0.3 to 10 for Π_2 in (6.10) can be applied.

$$\Pi_1 = 0.2631 \cdot \Pi_2^{-0.3082} \tag{6.10}$$

The initial resistive behaviour can then be established with (6.7) and (6.9) until Π_1 in (6.10) is greater than Π_1^0 in (6.9). For a four rod arrangement, the total resistance can calculated with equations provided in [210], [286] for input in with (6.7). The resulting

variable footing resistance as well as the derived critical current are calculated with (6.11) and (6.12), dependent on a previously calculated total footing resistance R_0.

$$R_F = 0.2631 \frac{\rho}{s} \left(\frac{\rho I}{E_c l^2} \right)^{-0.3082} \tag{6.11}$$

$$\mathrm{I}_C = \frac{E_c s^2}{\rho} \left(\frac{\Pi_1}{0.2631} \right)^{\frac{1}{-0.3082}} \tag{6.12}$$

A more elaborate soil ionization model for rods is based on the simplified physical description of the formation of the ionization zone in the form of conductive shells around the rod, as illustrated in figure 6-11, originally published by Liew et al. [210] and later adapted and simplified by Nixon [288] or changed to be purely based on physical constants by Cooray et al. [240].

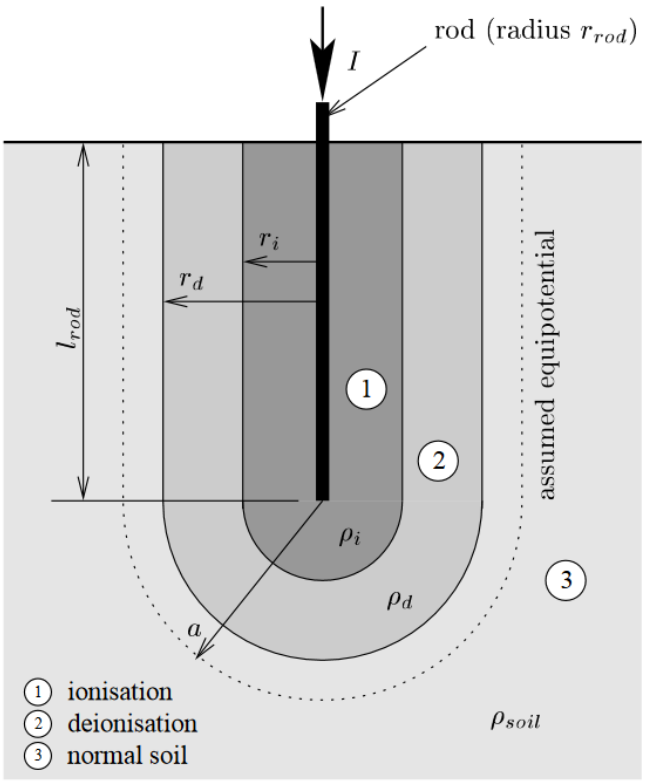

Figure 6-11: Illustration of ionization and de-ionization zones of a rod electrode [288]

In general the following assumptions are made, excerpted from [288]:

- The soil surrounding the driven rod is homogeneous and isotropic with resistivity ρ_{soil}.
- An injected impulse current I results in equipotential surfaces that can be approximated by a cylindrical and hemispherical portion, as shown in figure 6-11.
- The current density, J, in the soil at a radial distance, r, from the center of the driven rod can be approximated by equation (6.13).

$$J = \frac{I}{2\pi(r^2 + r l_{rod})} \tag{6.13}$$

- Breakdown by ionization occurs in the soil where the current density exceeds a critical value of current density, J_c, given by equation (6.14).

$$J_c = \frac{E_c}{\rho_{soil}} \tag{6.14}$$

- The regions of ionization and de-ionisation are assumed to be uniform as shown in figure 6-11 and the resistivity in these regions is time-varying.

Due to the more realistic waveshapes used by Nixon [288] to validate his model (3.5-5/10-14 µs) at 5/29 kA, in contrast to 15/25µs at 11 kA by Cooray et al. [240], there is good agreement with original results from Liew et al. [210] for soil resistivities in the range of 50 Ωm to 3100 Ωm and available EMT validated model in [288], this model is chosen for implementation into PSCAD/EMTDC as an advanced variable resistance soil ionization model. The mathematical description of a shell with thickness a in equation (6.15) together with the various soil resistivities of each region in the following enables the calculation of a total variable resistance in

$$dR = \frac{\rho}{2\pi l_{rod}}\left(\frac{1}{r} - \frac{1}{a + l_{rod}}\right) \tag{6.15}$$

Region 1: Ionisation occurs for $J \geq J_c$ and $r_{rod} < r \leq r_i$ with t_i the onset time of ionization and τ_i the ionization constant with the soil resistivity in equation (6.16).

$$\rho_i = \rho_{soil} \cdot e^{\frac{-t_i}{\tau_i}} \tag{6.16}$$

Region 2: De-ionization occurs for $J < J_c$ and $r_i < r \leq r_d$ with t_d the de-ionisation onset time, τ_d the de-ionization constant and ρ_m the soil resistivity at the onset of de-ionization in equation (6.16). The corresponding formula for the soil resistivity in equation (6.17) is:

$$\rho_d = \rho_m + (\rho_{soil} - \rho_m)\left(1 - e^{\frac{-t_d}{\tau_d}}\right)\left(1 - \frac{J}{J_c}\right) \tag{6.17}$$

Region 3: The soil resistivity features no ionization effect at $J < J_c$ and $r > r_d$ and therefore soil resistivity is ρ_{soil}.

The total resistance can then be expressed as during the ionization process:

$$R = \int_{r_{rod}}^{\infty} dR = \frac{\rho_i}{2\pi l_{rod}} \ln \frac{r_i(r_{rod}+l_{rod})}{r_{rod}(r_i+l_{rod})} + \frac{\rho_d}{2\pi l_{rod}} \ln \frac{r_d(r_i+l_{rod})}{r_i(r_d+l_{rod})} + \frac{\rho_{soil}}{2\pi l_{rod}} \ln \frac{r_d+l_{rod}}{r_d} \tag{6.18}$$

In case no ionization exists, the steady-state resistance is given by equation (6.19).

$$R = \frac{\rho_{soil}}{2\pi l_{rod}} \ln \frac{r_{rod}+l_{rod}}{r_{rod}} \tag{6.19}$$

In contrast to the two previously presented current-dependent ionization models, this model features an additional time- or waveshape-dependency.

To validate the PSCAD/EMTDC implementation of Nixon's model and investigate the difference to the CIGRE soil ionization model, simulations of Nixon's test circuit is performed for the described rod geometry and model parameters given in table 6-2.

Table 6-2: Parameter values for rod ionisation model [288]

Soil parameters:	
ρ in Ωm	139
E_0 in kV/m	300
τ_i in µs	2.0
τ_d in µs	4.5
Electrode Parameters	
r_{rod} in mm	7.95
l_{rod} in mm	2667

Nixon verified his model with two applied current waveforms, as depicted in appendix D.1. The resulting resistance of the model and, for comparison, the CIGRE model is plotted in appendix D.1.

A comparison of Nixon's simulation results in appendix D.1 show, that only marginal differences to the PSCAD/EMTDC implementation exist with are attributed to the differences in the generated waveform. Furthermore, a comparison of CIGRE and Nixon model resistance calculation reveals that the CIGRE models initial resistance decrease is more progressive than in Nixon's model. However, the overall resistance reduction is more pronounced in Nixon's model afterwards. Both the behaviour for the lower increase and slower decrease in resistance afterwards are a result of the modelling of the ionization and de-ionization process.

To model a whole tower foot with four rods, first the power-frequency resistance of this arrangement needs to be calculated and a mathematical description and model for the ionization zones developed. The initial resistance of a four rod in a square arrangement can be calculated with(6.20) to (6.23) [286], where $R_{F,s}$ is the resistance of a single rod in (6.21) and $R_{F,m1}$ and $R_{F,m2}$ are the mutual resistances, where l is the length of a rod in m and d is the distance of rods in a square.

$$R_F = \frac{1}{4} R_{F,s} + R_{F,m1} + R_{F,m2} \tag{6.20}$$

$$R_{F,s} = \frac{\rho}{2\pi l}\left(\ln\left(\frac{4l}{r_{rod}}\right) - 1\right) \tag{6.21}$$

$$R_{F,m1} = \frac{\rho}{4\pi l}\left(\ln\left(\frac{2l+\sqrt{d^2+4l^2}}{d}\right) + \frac{d}{2l} - \frac{\sqrt{d^2+4l^2}}{2l}\right) \tag{6.22}$$

$$R_{F,m2} = \frac{\rho}{8\pi l}\left(\ln\left(\frac{2l+\sqrt{(\sqrt{2}d)^2+4l^2}}{(\sqrt{2}d)}\right) + \frac{(\sqrt{2}d)}{2l} - \frac{\sqrt{(\sqrt{2}d)^2+4l^2}}{2l}\right) \tag{6.23}$$

Another way to calculate the footing resistance is proposed in [210] in (6.24), based on an area criterion in (6.25), which gives similar results as in (6.20) [210].

$$R_F = \frac{1}{4}\int_{r_0}^{\infty} \frac{\rho}{A_1 + A_2}\, dr \tag{6.24}$$

$$\begin{array}{lll} A_1 = 2\pi rl & A_2 = 2\pi r^2 & r_0 < r \leq d/2 \\ A_1 = (2\pi - 4\theta)rl & A_2 = 2\pi r^2 \cos\theta & d/2 < r \leq \sqrt{2}d/2 \\ A_1 = \left(\frac{3}{2}\pi - 2\theta\right)rl & A_2 = 2\pi r^2 \cos\theta + r^2\theta(\sin\theta - \cos\theta) & \frac{\sqrt{2}d}{2} < r \leq \infty \end{array}$$

(6.25)

Both the formulas to calculate the footing resistance show that it can be distinguished between the self-resistance of each rod and the mutual resistance. When ionization takes place, each rod can be modelled as a single rod with regard to the ionization, thus (6.18) replaces (6.21) in the total resistance. From measurements of a four rod arrangement [213], it is known, that the mutual resistance is only reduced slightly. Therefore, it is concluded as a worst-case approximation that the mutual impedance remains constant.

However for the ionization radius the mathematical description in [210] has to be adapted and extended with a dynamic ionization radius for implementation into PSCAD/EMTDC, because ionization zones merge at an ionization radius of quarter the distance of tower feet, as illustrated in figure 6-12.

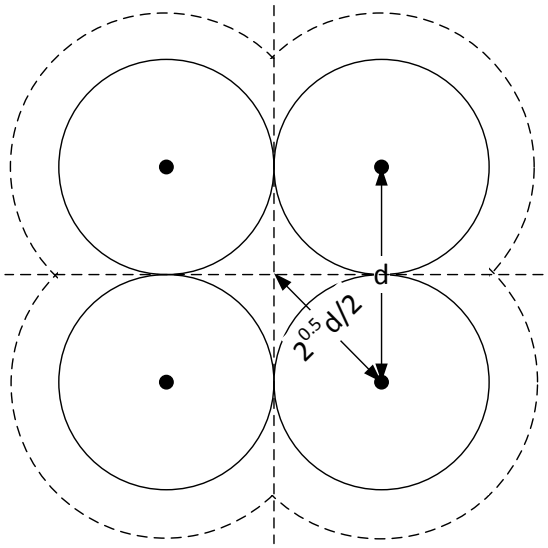

Figure 6-12: Soil ionization radius for four rods in parallel, adapted from [210]

To determine the ionization radius equation (6.26) needs to be solved for the three cases of the ionized area of each rod in equation (6.25), where $\theta = \cos^{-1}\frac{d}{2r}$.

$$J_{ion} = \frac{I}{A} \xrightarrow{yields} J_{ion} = \frac{I}{4 \cdot A_{rod}} \xrightarrow{yields} J_{ion} = \frac{I}{4 \cdot (A_1 + A_2)} \tag{6.26}$$

Up to $d/2$, where d is the distance between tower feet, the ionization radius is calculated for each rod separately. At $d/2$ the ionization areas merge and thus the ionization area needs to be adjusted. From $\sqrt{2}d/2$ onwards the total ionization area only expands at the outer borders until infinity.

To calculate the radius for the expansion of the ionized area, equation (6.26) needs to be solved for the radius r with the three cases in equation (6.25). For the case of $r_0 < r \leq d/2$, the radius can easily be determined solving the 2nd order equation.

$$r_1 = \frac{1}{2}\left(-l + \sqrt{l^2 + \frac{I}{2\pi J_{ion}}}\right). \tag{6.27}$$

For $d/2 < r \leq \sqrt{2}d/2$ the resulting equation cannot be solved in a straightforward way due to the arccosine description of the angle θ. Therefore the expression $\theta = \cos^{-1}(d/2r)$ needs to be approximated and linearized. It is found that a good fit to the original description can be found with a linearization of points at $d/2$ and $\sqrt{2}d/2$ in appendix D.

Furthermore, for $r > \sqrt{2}d/2$ a linearization of the equation to solve for radius r is necessary. From a numerical viewpoint, the development of a linearization including ∞ is not possible. Therefore, the starting values of angle θ are applied and the distance d is used for a second point for linearization.

A graphical illustration of the equivalent ionization radii comprised of the cylinder and sphere parts is shown in figure 6-13. The illustration shows the effect of the merge of the four different ionization zones, as from the intersection of radius r_1 and r_2 nearly no increase of the radius is achieved. At a point where all four ionization zones fully merged into one, the increase is approximately equivalent to the increase of a bigger single rod.

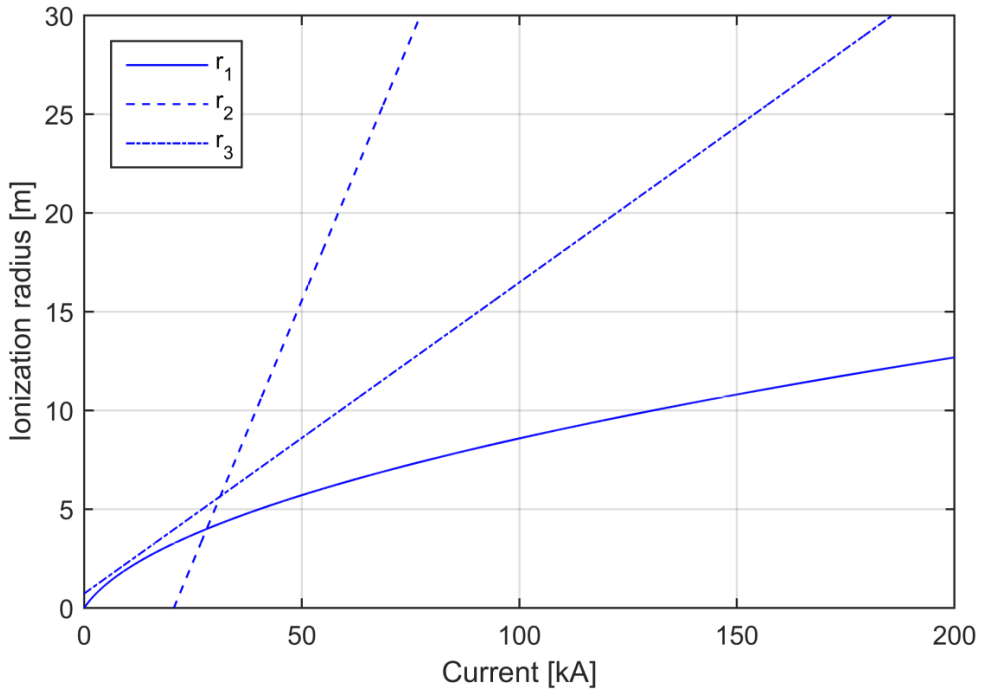

Figure 6-13: **Soil ionization surface area vs radius for four rods in parallel, d=8 m, r_{rod}=0.1 m, l_{rod}=3 m, ρ_{soil}=10000 Ωm and E_c=400 kV/m**

6.3.2: R-C-CIRCUIT MODEL

In [275] modelling of the frequency-dependency of soil for rod geometries with an R-C-circuit is performed. The R-C-circuit, depicted in figure 6-14 is based on the impulse response, calculated from a low-frequency electrode resistance. The circuit comprises an R-C-element for low- and high-frequency-response of soil as well as a resistance for the initial impulse response. The travelling wave phenomenon is neglected due to the short length of rods, but the initial surge response is included.

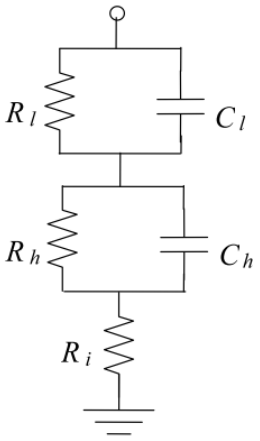

Figure 6-14: **Equivalent RC-circuit for frequency-dependent low-current earthing system modelling**

The calculation of the circuits parameters is readily performed with the geometry factor for rods in [286], using solely the soil low-frequency resistivity and rod geometry values. First, the steady-state parameters including the surge impedance are calculated in (6.28) to (6.32).

$$K = \frac{1}{2\pi l} \ln \frac{2l}{r} \tag{6.28}$$

$$R_0 = \rho \mathrm{K} \tag{6.29}$$

$$C_0 = \varepsilon \mathrm{K}^{-1} \tag{6.30}$$

$$L_0 = \mu_0 l^2 K \tag{6.31}$$

$$Z_0 = \sqrt{\frac{L_0}{C_0}} \tag{6.32}$$

The impulse resistance is calculated according to [273], [275] for the case of the sending end voltage neglecting damping for short rod arrangements in (6.33).

$$R_i = 3Z_0 \cdot \left(\exp\left(-\frac{Z_0}{R_0}\right)\right)^2 \tag{6.33}$$

The high-frequency circuit is calculated with equation (6.34) to (6.36) at $f_h = 100$ kHz due to the range of rise-times of lightning stroke current in the microsecond range using the frequency-dependent soil formulas from equation (6.1) (6.2) to determine soil resistivity $\rho_r(f_h)$ and permittivity $\varepsilon_r(f_h)$.

$$\tau_h = \rho_0 \rho_r(f_h) \varepsilon_0 \varepsilon_r(f_h) \tag{6.34}$$

$$R_h = R_0 \cdot \rho_r(f_h) - R_i \tag{6.35}$$

$$C_h = \frac{\tau_h}{R_h} \tag{6.36}$$

The low-frequency circuit is calculated with equation (6.37) to (6.39) at $f_l = 100$ Hz, the lowest possible value for equation in (6.1) and (6.2) for determination of $\rho_r(f_l)$ and $\varepsilon_r(f_l)$.

$$\tau_l = \rho_0 \varepsilon_0 \varepsilon_r(f_l) \tag{6.37}$$

$$R_l = R_0 - R_i - R_h \tag{6.38}$$

$$C_l = \frac{\tau_l}{R_l} \tag{6.39}$$

In figure 6-15, the step response for a rod with $l = 1.5$ m and $r = 0.007$ m and $Z_0 = 75\ \Omega$ for three different soil resistivities, 143 Ωm, 495 Ωm and 949 Ωm from [275] shows a good agreement with measured values.

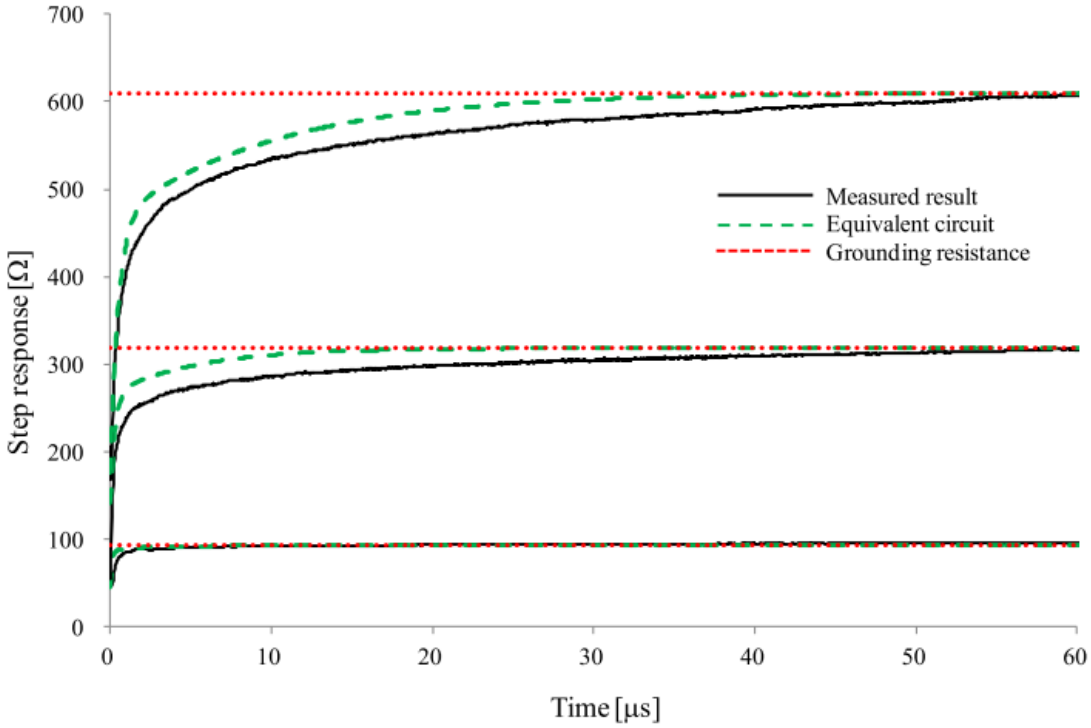

Figure 6-15: Calculated step-response from equivalent RC-circuit for frequency-dependent soil low-current rod earthing system [275]

The author of [275] mentions that soil ionization, as described in equation (6.5) and (6.6) can be included in the initial surge resistance R_i. However, the presented ionization models in section 6.3.1 are all based on the calculation of the steady-state resistance, rather than the surge resistance. Therefore, a decrease of R_i will not result in the same degree of voltage reduction as a decrease of the steady-state resistance R_0. To incorporate soil ionization into the R-C-circuit model, a dynamic calculation and variable resistance and capacitance elements have to be included in PSCAD/EMTDC in a custom model with Fortran code.

For the verification of the described frequency-dependent circuit in combination with the Nixon ionization model in the low current impulse range, measurement results of an earthing rod in [213] are utilized. The corresponding simulation parameters are summarized in table 6-3.

For the generation of lightning impulses, the current generator circuit used in the measurements is modelled according to [289]. The simulation results for a single rod in 160 Ωm soil subject to lightning impulses with current amplitudes of 0.51 kA/ 0.81 kA/1.13 kA are depicted in appendix D.2.

Table 6-3: Soil and electrode parameters in Sekiok's lab experiements [213]

Soil parameters:	
ρ in Ωm	160
E_0 in kV/m	300
τ_i in µs	2.0
τ_d in µs	4.5
Electrode Parameters	
r_{rod} in mm	7
l_{rod} in mm	1500

A comparison of the PSCAD/EMTDC simulation results to the reference [213] in appendix D.2 shows a good agreement. Therefore, it can be concluded, that the adjusted frequency-dependent model in combination with the Nixon ionization model can be used to model both soil ionization and frequency-dependent behaviour of single rods. Furthermore, this represents a further verification of the Nixon ionization model with measurements.

Although measurements of the ionization and frequency-dependent behaviour of four rods in a square in [213] are conducted, the soil resistivity is too low to result in a merging of the ionization zones. Therefore, only verification on the basis of similarity to the CIGRE and similarity approach model can be accomplished and the overall influence on resulting voltage assessed. The simulation results for a negative first and subsequent stroke [47], applied to the developed model of merging ionization zones of a practical tower footing configuration are shown in figure 6-16 and figure 6-17.

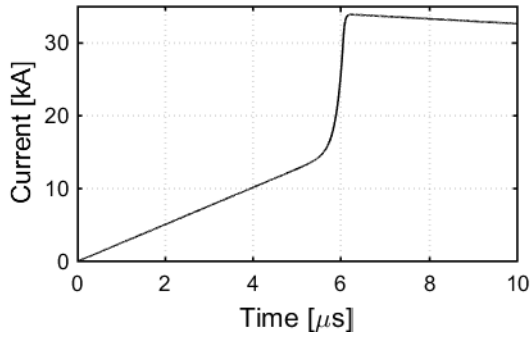

a) Current waveform, first stroke

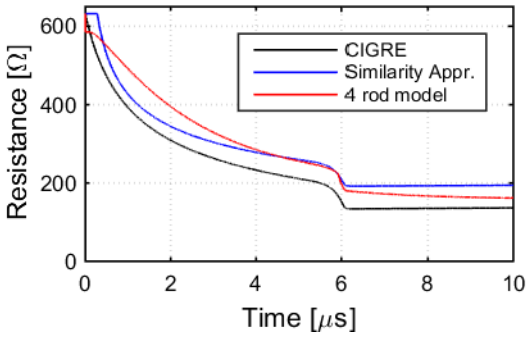

b) Resistance progression, first stroke

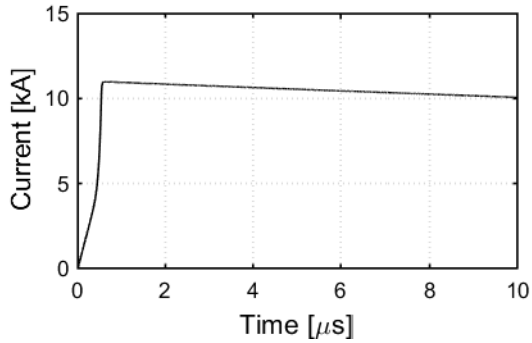

c) Current waveform, subsequent stroke

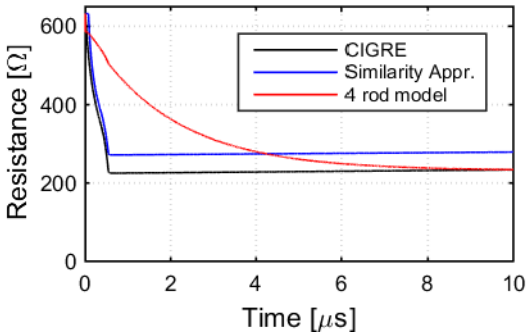

d) Resistance progression, subsequent stroke

Figure 6-16: Simulation results of median strokes to frequency-dependent model with ionization for four rods in parallel, r_{rod}=0.1 m, l_{rod}=3 m, d=8 m, ρ=10000 Ωm

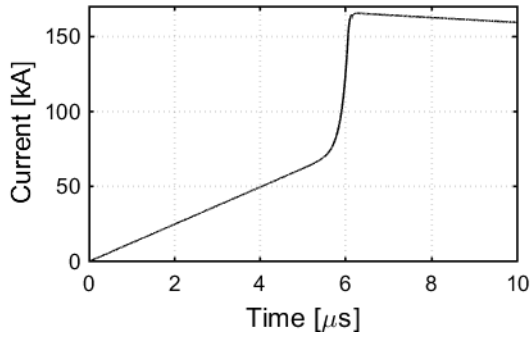

a) Current waveform, first stroke

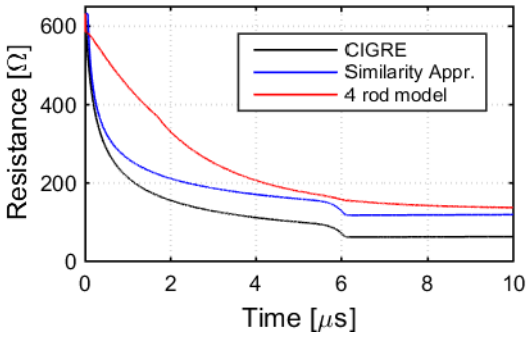

b) Resistance progression, first stroke

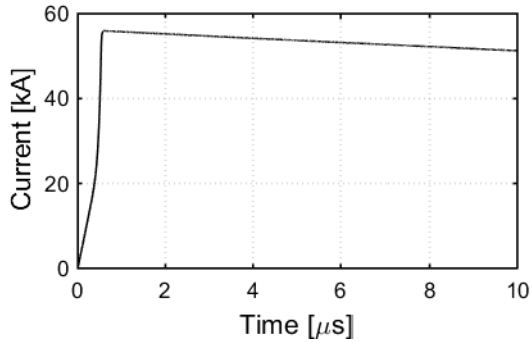

c) Current waveform, subsequent stroke

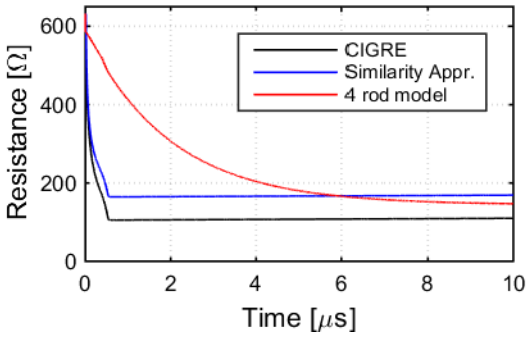

d) Resistance progression, subsequent stroke

Figure 6-17: Simulation results of severe strokes to frequency-dependent model with ionization for four rods in parallel, r_{rod}=0.1 m, l_{rod}=3 m, d=8 m, ρ=10000 Ωm

The comparison of progression of resistance for CIGRE, similarity approach and the developed model for a negative first stroke shows a very similar behavior. For the negative subsequent stroke the time delay in the Nixon model is more dominant, leading to a slower reduction in resistance over time. However the minimum resistance value is very similar to the other models. Furthermore, the resistance progression of the similarity approach and the developed model converge with increasing current, as seen in the case of severe strokes in figure 6-17. The reason for this is that with increasing current the merging of ionization zones forms a hemispherical area, which is both taken into account in the similarity approach and the developed model. For subsequent strokes the minimum resistance value during ionization is also very similar for all three models, but due to the incorporated time delay in the developed ionization model, the reduction of resistance is slower and thus overvoltages at insulators are consequentially higher. In conclusion, the developed model offers a more conservative approach to the grounding system behavior than the CIGRE and similarity approach model.

6.3.3: TRANSMISSION LINE MODELS

Modelling of an earthing system with transmission line models to include the travelling wave phenomena for long buried electrodes is achieved by calculation of the surge impedance and admittance matrix and propagation constant respectively. For the calculation of G-L-C parameters [260]–[262] or direct calculation of impedance, admittance and propagation [259] various formulas are available, but their implementation into an EMT model is difficult due the general simplification of ground admittance to curve-fitting procedures. Furthermore, an implementation of these formulas into EMT line model calculation programs is still missing and calculations have to be performed externally [259], [267]. In this respect, PSCAD/EMTDC offers an input of impedance and admittance in form of a text file, which is utilized to create a transmission model.

In [259], formulas for the calculation of the surge impedance and admittance without soil frequency-dependency are compared, which are valid for buried wires. A simplified but efficient formula is chosen for calculations as written in (6.40) to (6.43), with R_{ab} the radius, d the depth and a the horizontal distance of the buried wire in case mutual coupling of wires is calculated.

$$\gamma_g = \sqrt{\mathrm{j}\omega\mu_0\left(\sigma_g + j\omega\varepsilon_g\right)} \tag{6.40}$$

$$\sigma_g = \sigma_0\sigma_s \quad , \varepsilon_g = \varepsilon_0\varepsilon_s \tag{6.41}$$

$$Z = \frac{\mathrm{j}\omega\mu_0}{2\pi}\left\{\ln\left(\frac{1+\gamma_g R_{ab}}{\gamma_g R_{ab}}\right) + \left(\frac{2e^{-2d|\gamma_g|}}{4+{\gamma_g}^2 {R_{ab}}^2}\right)\right\} \tag{6.42}$$

$$Y = \frac{{\gamma_g}^2}{Z} \tag{6.43}$$

$$Z_m = \frac{\mathrm{j}\omega\mu_0}{2\pi}\left\{\ln\left(\frac{1+\gamma_g a}{\gamma_g a}\right) + \left(\frac{2e^{-2d|\gamma_g|}}{4+{\gamma_g}^2 a^2}\right)\right\} \tag{6.44}$$

$$Y_m = \frac{{\gamma_g}^2}{Z_m} \tag{6.45}$$

Soil frequency-dependency can be considered with formulas for σ_s and ε_s in [82] (see section 3.1.3).

To validate the transmission line model, a comparison of measurements presented in [290] with simulations in PSCAD/EMTDC is performed. The horizontal electrode to be

simulated is made of a 15 m long 116 mm^2 copper wire buried 0.6 m in soil with 70 Ωm and is subject to an impulse with 35 A and 0.6 µs rise time to crest value.

Since no information about the test setup is available, a current source, generating the current to be injected into the electrode, is directly connected to the transmission line model of the buried electrode. Equation (6.42) and (6.43) alongside the frequency-dependent parameters of soil are used in a Matlab script to calculate the magnitude of impedance and admittance, plotted in figure 6-18 and figure 6-19. These values are inputted into the curve-fitting algorithm of the PSCAD/EMTDC LCP through an undocumented interface to generate a transmission line model.

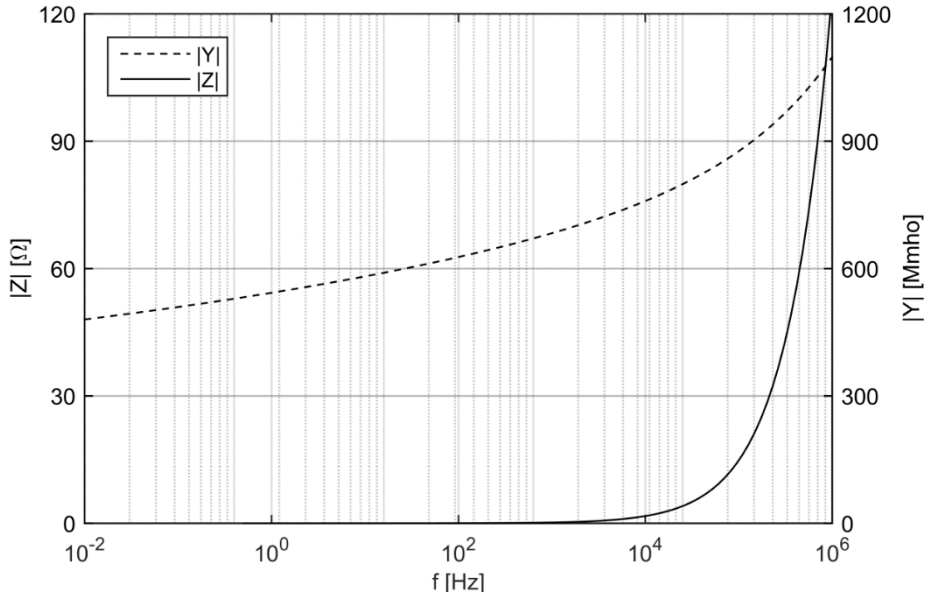

Figure 6-18: Magnitude of impedance and admittance response of 15 m long, 116 mm^2 copper wire, 0.6 m buried in 70 Ωm soil

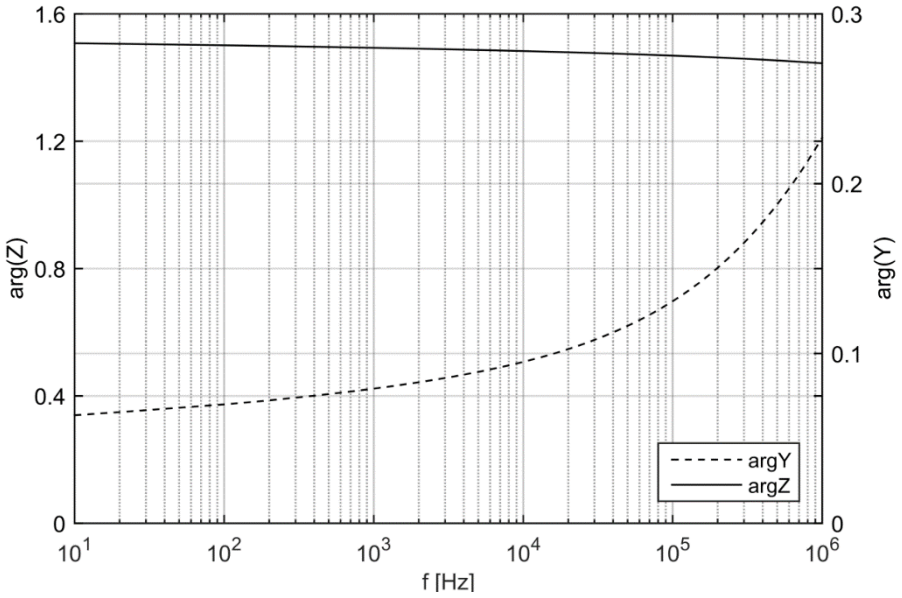

Figure 6-19: Magnitude of impedance and admittance phase response (rad) of 15 m long, 116 mm² copper wire, 0.6 m buried in 70 Ωm soil

The simulation results of the injected current and resulting voltage at the beginning of the 15 m buried wire are plotted in appendix D.4. A comparison of the measurements and the PSCAD/EMTDC counterpart in appendix D.4 show an overall good agreement. However, since no information about the test setup is available and the PSCAD/EMTDC model is simplified and therefore overlaying travelling waves are missing in the PSCAD/ETMDC simulations.

To simulate more complex earthing arrangements, such as counterpoise, illustrated in figure 6-20, mutual coupling needs to be taken into account. Since the transmission line input data can only be fed into one line model without coupling in PSCAD/EMTDC, the earthing arrangement has to be consolidated into one transmission line model, which includes coupling. In [262], [267] a method to merge self-and mutual coupling impedance of the counterpoise arrangement in figure 6-20 is described, resulting in equation (6.46) for the calculation of the total impedance.

$$Z_{total} = \frac{Z+Z_m}{4} \tag{6.46}$$

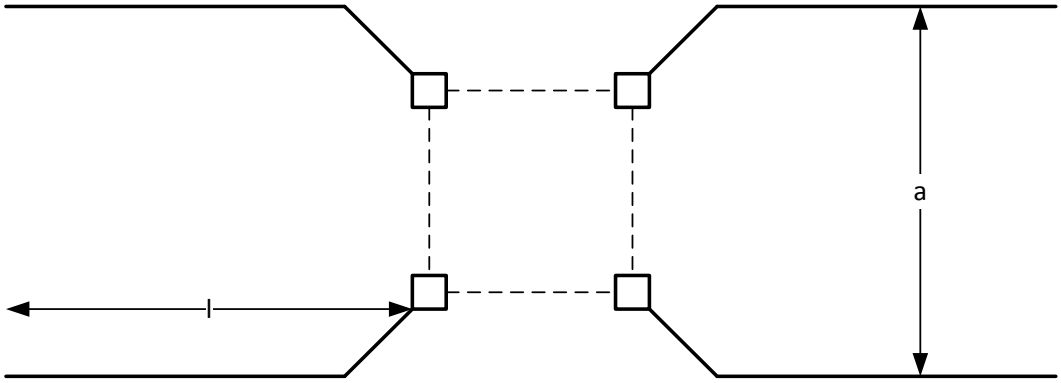

Figure 6-20: Counterpoise earthing arrangement of a transmission tower

To verify the developed procedure of calculation of impedance and admittance matrix of buried wires and modelling of a frequency-dependent transmission line model of buried wires with frequency-dependent soil parameters, a comparison with results in [262] is performed. There, the injection of a subsequent stroke with 12 kA amplitude into a counterpoise with electrodes of radius 2.5 mm, buried in the depth of 0.5 m, length 30 m and distance 30 m in 2400 Ωm soil is simulated. However, the calculation of matrix values in [262] is not taking frequency-dependent soil parameters into account. In appendix D.5 the original transient response to a first and subsequent stroke is depicted for a comparison to the PSCAD/EMTDC model, where soil-frequency dependency is excluded in the Matlab calculation.

The comparison of voltage responses in appendix D.5 shows a perfect match of results for first and subsequent strokes, which proves that the PSCAD/EMTDC implementation alongside the calculation of impedance and admittance is correct. However, since no frequency-dependent soil is taken into account in [262], a comparison to the inclusion of frequency-dependent soil can be made. The results clearly show that the frequency-dependent phenomenon of soil reduces voltages, being more pronounced for faster impulses, such as subsequent strokes, where the initial voltage rise is halved in comparison to the exclusion of the phenomenon.

6.4: SUMMARY AND CONCLUSION ON TOWER EARTHING SYSTEMS

In this chapter the physical behaviour of tower earthing systems subject to lightning strokes alongside the application range of earthing system models and modelling of

electrode arrangements are discussed. In this respect modelling is focused on practical earthing systems to be deployed in medium to high soil resistivities.

The earthing system behaviour with respect to lightning is depending on the type of electrode and waveform and maximum amplitude of injected current. When high currents penetrate the soil, ionization of the soil surrounding the electrode occurs, which reduces the overall earthing system resistance. This behaviour is more pronounced for short earthing rods and higher soil resistivities, where a higher current density is present. At low currents, the soil features a distinctive frequency-dependency, leading to a rather capacitive behaviour of the earthing system at fast impulses. This phenomenon is generally associated with long buried wires, such as counterpoise due to the lower resistance even at higher soil resistivities. Furthermore the travelling wave phenomenon and rise-time dependent damping effects are pronounced in this case.

To determine the application range of models with regard to the described physical effects, a review of more recent measurements is performed, which reveals that soil models are available in the range up to 9100 Ωm. However measurements of buried wires and rod earthing arrangements are only available up to 2000 Ωm and 3100 Ωm respectively. With regard to the assessment of the example transmission line in this work, where the soil resistivity ranges from 2000 Ωm to 11000 Ωm, some uncertainties in the prediction of flashovers on a transmission line exist when extrapolating results, especially for soil ionization in high resistive soils. However, it has to be noted that in practice the type of tower earthing is dependent on the local nature of soil and part of the tower foundations, such as concrete steel reinforcements or solid steel rods. To achieve a certain level of low-frequency tower earthing resistance, the earthing system area has to increase with increasing soil resistivity. Therefore, from a technical point of view, rod type earthing systems are employed at lower soil resistivities and earthing strips, such as counterpoise or ring networks at higher soil resistivities to cover a wider area. Thereby it is assumed that with increasing soil resistivity the density of soil increases (from gravel over rocky soil to solid rock). However from a cost and environmental point of view, covering a wider area with an earthing system is not favorable and the earthing system is normally limited to the tower foundation.

Since only practical earthing arrangements are considered, the literature review of current EMT transmission and circuit approach models is focused on rod and buried wire

arrangements. The review revealed that circuit and transmission models are either adjusted to match EMF simulation or measurement results, or lack ionization effect, frequency-dependent soil effect or travelling wave and attenuation phenomena.

Therefore, starting from the simplified resistance model of a tower earthing system, the above mentioned effects are introduced by extending the model circuit. The fixed resistance model using the 50 Hz measured earthing resistance, often used in simulations to achieve worst case conditions is first extended to a variable resistance model to include ionization effect. Ionization is taken into account either by the general CIGRE model, which reduces the resistance in dependency of the current or the so-called Nixon model, which is a physical model of ionization, taking into account ionization delay and de-ionization area surrounding the electrode. A comparison with measurements of an earthing rod subject to high currents is made, which shows that the Nixon model produces a good match to the measurements. The CIGRE model initially shows a faster reduction of footing resistance than the Nixon model. Although the Nixon model is therefore more conservative, the comparison to measurements and the inclusion of the physical delay of ionization leads to a more realistic behaviour. Next, a more advanced model of a double R-C-circuit to take the frequency-dependency of soil into account is investigated and combined with both the CIGRE and Nixon ionization model. Unlike the author's recommendation to include ionization in an additional resistance to ground, which does lead to an underestimation of ionization, the model is refined by using three variable resistances. A comparison of results with rod earthing system measurements shows a clear improvement of the model and a good agreement with measurement results. To model a complete tower base, the Nixon ionization model is extended to four rods, which demands for a new mathematical description of the radius. To implement the extended model, a linearization of the radius description is developed, which is readily implemented in the EMT simulation software. Furthermore, a more general R-L-C model for buried wires is investigated, which takes ionization effects with the CIGRE model into account. Its application range is however limited to soil resistivities of less than 1000 Ωm and wire length of 30 m and does not take attenuation and travelling wave effects into account. Based on the assumption that the frequency-dependent effect determines the pre-dominant behaviour of buried wires, a procedure is developed to model a buried wire with a transmission line model including frequency-dependent soil effects. The procedure is verified with measurements and EMF simulation results for a single buried wire as well as a counterpoise arrangement found in the literature. In this respect, the inclusion of the

frequency-dependent soil effect for long buried electrodes shows its importance in reducing the voltages at the current injection point.

For practical earthing arrangements of tower grounding the improved double RC for short rods and tower foot anchor points and the transmission line model for counterpoise can then be applied for the later simulations. Finally it has to be noted, that a considerable degree of simplifications is unavoidable when modelling practical earthing system. This stems from the complexity of the different types of tower foundations and their steel reinforcement structure, which resembles an integrated earthing system. When modelling these earthing systems, it is concentrated on the conductive steel part of the foundation and the surrounding soil, which introduces a safety margin in the simulations.

CHAPTER 7: LIGHTNING PERFORMANCE IMPROVEMENT MEASURES

Apart from the general protection of a transmission line against overvoltages caused by lightning, such as shield wires, minimum standard length of insulators and standard design of grounding systems, there exist several additional mitigation measures to improve the lightning performance of a transmission line taking the standard transmission line design as a basis. These measures are generally taken when the local lightning stroke density is exceptionally high, there exist local unfavorable grounding conditions or high soil resistivity, respectively, or there is a high demand of reliability of the line. Therefore measures can be divided into standard measures and advanced measures. Standard measures to improve the lightning performance of a line include

- the up-rating of the insulator BIL by increase of the insulator length,
- improvement of the tower grounding system, additional earthing rods or tower foot bonding to decrease the tower footing impedance,
- increase of the shield wire diameter to decrease its resistance and consequentially reduce the voltage at the insulator.

As outlined in the IEEE standard [50], other tested measures, here called advanced measures, include

- the deployment of transmission line arresters (TLAs),
- additional underbuilt shield wires,
- guy wires on transmission towers,
- ground wires on separate structures,
- unbalanced insulation on double-circuit lines and
- active air terminals as well as
- counterpoise arrangements.

Furthermore, an improved grounding system with counterpoise as an advanced guy wire method is proposed in [291]. In case longer parts of the line route feature a low lightning stroke performance, deviation from the standard transmission line design, e.g. two shielding wire tower or low-profile tower design, can also be considered.

In this chapter, some advanced measures to improve the lightning performance of a transmission line are investigated alongside their modelling in an EMT simulation, which are feasible in practical applications.

7.1: TRANSMISSION LINE ARRESTER

The deployment of transmission line arresters on towers is one method to prevent back-flashovers and improve the lightning performance of transmission lines [277], [292], [293]. Transmission line arresters are made of metal oxide discs and can be paired with an air gap to prevent any continuous current. They are installed in parallel to an insulator and provide a controlled conducting path at high voltages, thus decreasing the voltage across the insulator and prevent a flashover. In this work it is solely focused on metal oxide arresters without air gap, whose characteristics are explained in the next subsection, followed by the EMT modelling.

7.1.1: SURGE ARRESTER CHARACTERISTICS

The characteristics of a surge arrester can be explained with its voltage-current curve, derived from measurements, as depicted in figure 7-1. The curve can be divided into three regions according to [7]:

- In the maximum continuous operating voltage (MCOV) region, normally in the power-frequency region, where only a small capacitive current (< 1mA) flows through the arrester,
- The transient overvoltage and switching surge region, where a primarily resistive current between 1 mA and 1 to 2 kA flows through the arrester, where special care with regard to heating and energy dissipation has to be taken,
- And the lightning surge region, where currents reach values up to 100 kA.

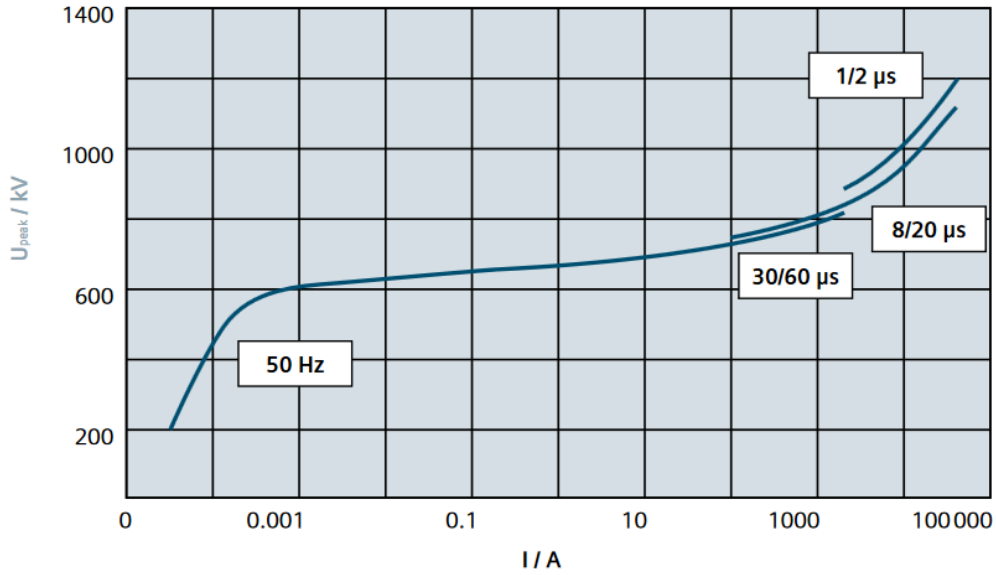

Figure 7-1: Typical voltage-current curve of a 550 kV arrester, adapted from [294]

In general, arresters are type tested according to [170], [295] with three different current waveshapes 30/60 µs for switching and 8/20 µs and 1/2 µs for lightning alongside the continuing current and current amplitudes of 2.5 kA, 5 kA, 10 kA, 20 kA and 40 kA. Datasheets often refer to the maximum residual voltage at 500 A 30/60 µs, 1 kA 30/60 µs, 2 kA 30/60 µs, 5 kA 8/20 µs, 10 kA 8/20 µs, 10 kA 1/2 µs, 20 kA 8/20 µs and 40 kA 8/20 µs to construct a V-I-curve. From these characteristics the conclusion is drawn that metal oxide surge arresters are frequency-dependent devices, where the voltage across the arrester is both a function of current magnitude and rate of rise.

7.1.2: MODELLING OF TOWER LINE ARRESTERS

Since the behaviour of a surge arrester is frequency-dependent, various models have been proposed, depending on the available input data [296]–[299]. In the following the two most prominent and applied models in the literature for high voltage application are discussed [297], [299]–[302], which use datasheets and measurement results as input data.

An IEEE working group made an in-depth investigation on modelling of arresters in [296] and has proposed to model the frequency-dependent behaviour with two R-L-circuits and two variable resistances, as shown in figure 7-2, which is valid in the range of time-to-crest of 5 µs to 40 µs, when parameters are determined correctly.

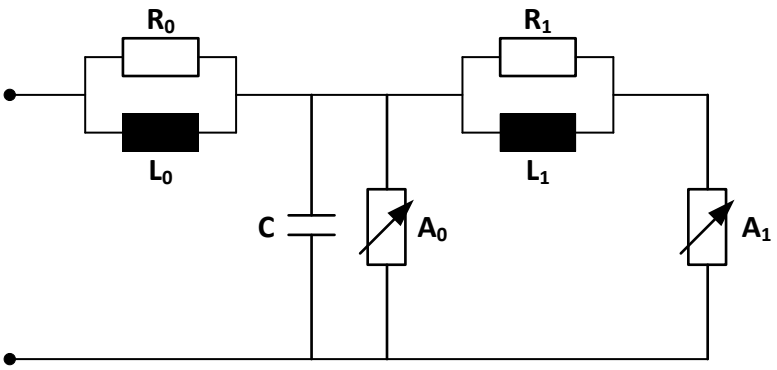

Figure 7-2: Frequency-dependent arrester model [296]

The parameters in figure 7-2 are chosen dependent on the overall arrester height d and number parallel columns of metal oxide discs n, in which R_1 and L_1 comprise the filter between the two variable resistances in equation (7.1) and (7.2). It is noted that the model does not include the influence of the connection leads inductive effect and stray capacitance effect, which should be modelled separately [302].

$$L_1 = 15\frac{d}{n}\ [\mu H] \tag{7.1}$$

$$R_1 = 65\frac{d}{n}\ [\Omega] \tag{7.2}$$

In [300] an optimization of the parameters is made, which concludes that a value of $L_1 = 5\ d/n$ fits better the measurements results. The terminal capacitance of the arrester is calculated with (7.3) and L_0 and R_0 represent the magnetic fields in the vicinity of the arrester and numerical damping measures, respectively.

$$C = 100\frac{n}{d}\ [\text{pF}] \tag{7.3}$$

$$L_0 = 0.2\frac{d}{n}\ [\mu H] \tag{7.4}$$

$$R_0 = 100\frac{d}{n}\ [\Omega] \tag{7.5}$$

A_1 and A_0 can be estimated using the volt-time curve, e.g. 30/60 µs values for A_1 and 8/20 µs values for A_0.

The authors of [296] state that these values not always lead to the best match of the measured behaviour and value L_1 has the biggest impact on it. Therefore they recommend the following procedure:

1. Determine parameters with formula (7.1) to (7.5) and A_1 and A_0 according to the volt-time curve
2. Adjust characteristics of A_1 and A_0 to get a better approximation of the discharge voltages associated with the switching surge currents (300/1000 µs)
3. Adjust L_1 to get a better approximation of the discharge voltages associated with the lightning surge currents 8/20 µs

Although accurate modelling of the arrester behaviour can be achieved with the procedure above, it is a time-consuming and complex method to determine the above stated parameters. Therefore a simplified version of the circuit in figure 7-2 is proposed in [298], which is based on the requirements, that the manufacturers datasheet is available, no iterative process to determine the parameters is used and the model behaves as the real device in the simulations. The model is valid in a time range from 1 µs to 30 µs.
The frequency-dependent model from [296] in figure 7-3 is simplified in that the capacitance is eliminated due to its negligible effects and the two resistances are eliminated and replaced with one at the terminals to damp out numerical effects.

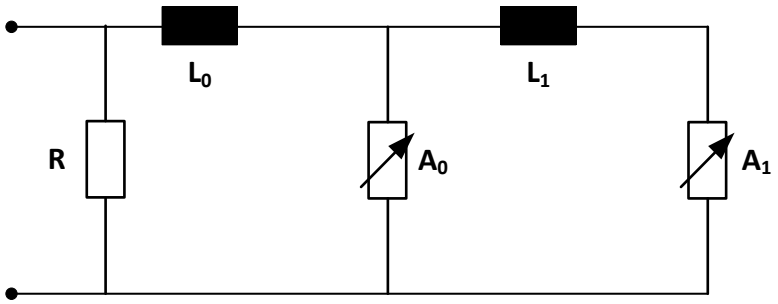

Figure 7-3: Simplified frequency-dependent arrester model [298]

The resistance of the model is chosen in the range of 1 MΩ to prevent any numerical oscillations. However in [300], it is found that a value in the range of 1 kΩ gives better overall results, but care has to be taken with numerical oscillations. Similar to the calculation in [296], the parameters A_1 and A_0 are taken from the normalized curve in figure 7-4, in which the parameters are multiplied with the maximum residual voltage of the 8/20µs waveshape at 10 kA.

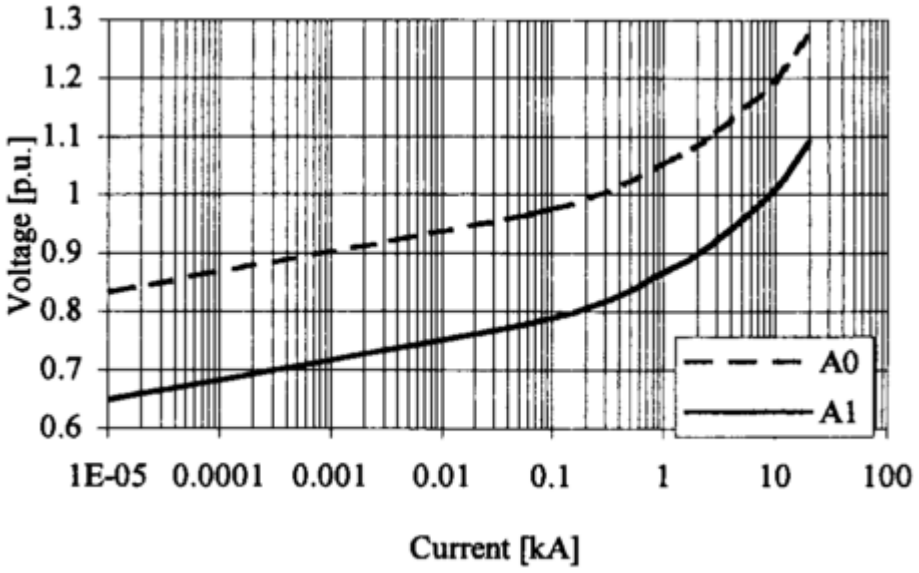

Figure 7-4: Static characteristics of the non-linear elements with the voltage in p.u. referred to the residual voltage V_r of 8/20µs waveshape at 10 kA [298]

The inductances L_0 and L_1 are calculated with formula (7.6) and (7.7), where V_n is the arrester rated voltage, V_{r1/T_2} is the residual voltage at the 10 kA fast front current and $V_{r8/20}$ is the residual voltage at 10 kA current surge with the 8/20 µs waveshape.

$$L_1 = \frac{1}{4} \cdot \frac{V_{r1/T_2} - V_{r8/20}}{V_{r8/20}} \cdot V_n \ [\mu H] \tag{7.6}$$

$$L_0 = \frac{1}{12} \cdot \frac{V_{r1/T_2} - V_{r8/20}}{V_{r8/20}} \cdot V_n \ [\mu H] \tag{7.7}$$

The authors of [298] state, that a comparison with various arrester measurements shows good agreement, but the curves in figure 7-4 may be adjusted for a better accuracy.

For the simulations to determine the lightning stroke performance of the line, one model needs to be selected based on the available input data. Since the model in [298] is solely based on the electrical parameters of the arrester, rather than a measured V-I-curve paired with an iterative process in [296], the simplified arrester model is chosen and verified with an EMT implementation and comparison with the results from [298].

For the comparison the data provided in the appendix of [298] is used and inputted into the arrester model created in PSCAC/EMTDC. For the generation of the 8/20 µs waveshape a single Heidler-function model as described in subsection 2.3.2 is employed.

The simulation results from [298] and the PSCAD simulation from this work are depicted in APPENDIX E.

A comparison of results shows that the crest amplitude of both simulations matches within a 0.1 kV margin. However, the curve progressions in the PSCAD simulation deviate slightly from that in [298]. This is due to the inputted current waveshape in the PSCAD simulation. Although in both the reference and the PSCAD simulation an 8/20 µs waveshape is applied, there exists a certain degree of freedom in the steepness and slope. As the differences are traceable and explainable, the model itself can be acknowledged as verified.

7.2: SHIELD WIRES

Another method to improve the lightning performance of a transmission line is the installation of additional shield wires of some kind other than the installation of additional shield wires on top of the towers. As mentioned in [50], these are underbuilt wires or guy wires located at the tower. In the following, these methods are explained in more detail, both investigating their advantages as well as modelling of these methods.

7.2.1: UNDERBUILT WIRES

The idea behind underbuilt wires is to install additional metallic wires below the phase conductors, maintaining clearance, connected to the tower and adjacent towers, as illustrated in figure 7-5. These wires reduce the overvoltages encountered during a lightning stroke due to their coupling effect to the phase wires and divert the stroke current, which would otherwise flow into the grounding system.

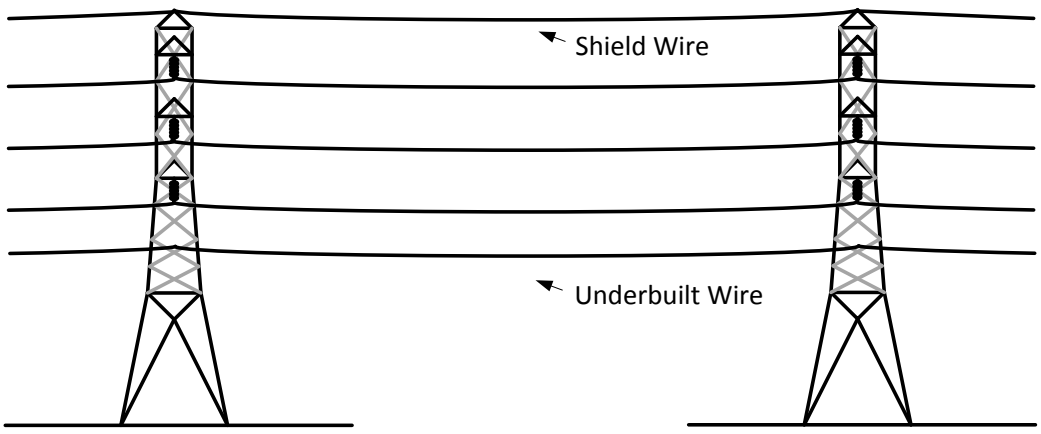

Figure 7-5: Example of underbuilt wires

Although publications on this type of technique are rare, the authors of [303] and previous work in the references within, perform a study on their effectiveness. The technique is recommended when the reduction of tower footing resistance is not readily achievable and the installation of surge arresters to prevent flashovers is excluded. The results of their investigation show that the effectiveness of the underbuilt wires to reduce overvoltages increases with increasing grounding resistance, up to 44% at a grounding resistance of 80 Ω at a 230 kV tower. The effect can furthermore increase when adjacent towers feature a lower grounding resistance. Similar results are obtained for a medium voltage line in [304]. In [305] the installation of additional underbuilt wires in between the phase wires at a multi-circuit 500/220 kV line is discussed, in which the most effective configuration is the installation of two underbuilt wires at the top and bottom traverse.

Modelling of underbuilt wires is accomplished in the same way as normal transmission line modelling in chapter 3 and no limitations exist. Therefore no further investigation into modelling of these is necessary.

7.2.2: GUY WIRES

As mentioned in [50], another method of improving the lightning performance of transmission lines is the installation of guy wires at the tower below the phase wires, as illustrated in figure 7-6. Although figure 7-6 shows an advanced version of this technique, where the guy wires are connected to counterpoise or an aerial cable and further connected to buried electrodes, the basic idea behind this method is the diversion of lightning current to ground, preferably to locations with lower soil resistivity, rather than the sole penetration of the tower foot. Therefore, it is often combined with additional earthing measures.

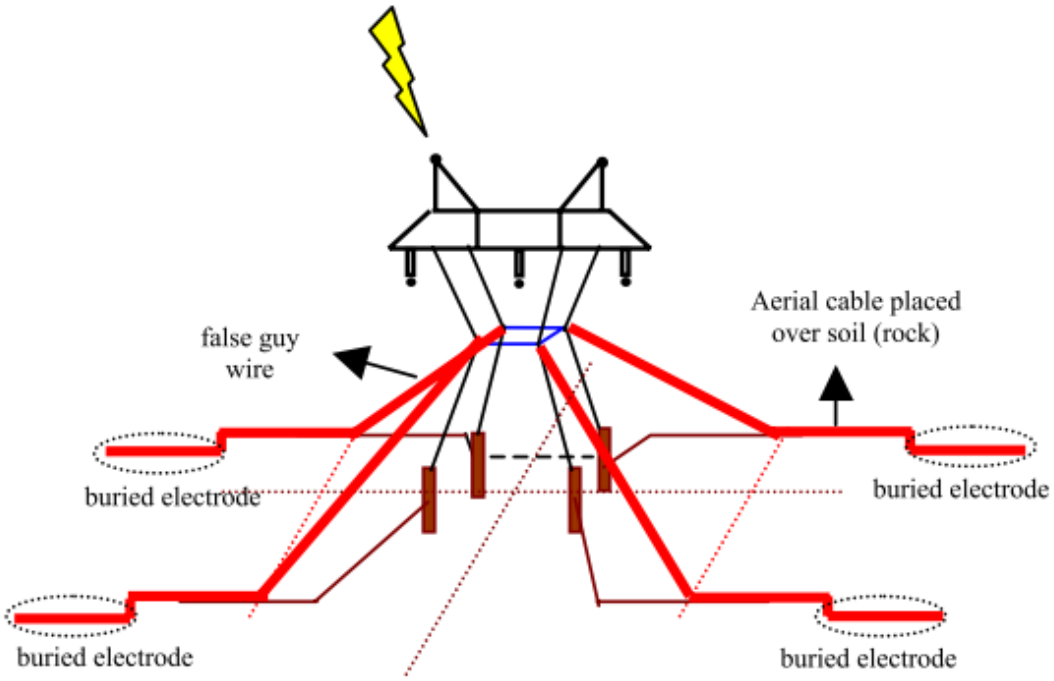

Figure 7-6: Example of a false guy wire configuration [306]

Also for this technique, reported experience in the literature is rare. A study in [306] is performed to investigate the improvement of the lightning performance of a 230 kV transmission line, where the lightning performance is dominated by some hot spots, such as single towers placed on rocky hill tops, which feature a high soil resistivity although long counterpoise is already installed. The authors mention that installation of arresters is not possible in this case due to the remote location and resulting high efforts for maintenance work. The results of their study show that overvoltages at the insulators could be reduced to 40% of their original value without guy wires and buried electrodes at the end of the counterpoise. The paper further reports the implementation of this technique at 26 critical towers and a reduction of outages from 7 outages per year to 0.

Modelling of this technique including the long counterpoise and buried electrodes has its challenges, as already reported in section 6.3. The guy wires can be modelled with calculation methods described in section 5.3 for vertical conductors. Buried electrodes can be modelled as concentrated hemispherical electrodes, as discussed in section 6.3, but the travelling wave and lossy line effects of counterpoise buried in soil can only be roughly estimated as outlined in section 6.3.3.

7.3: IMPROVED EARTHING

In general earthing of transmission line towers is accomplished by encasing the tower feet into concrete, rock anchors or other means. Any additional measure, such as driven ground rods, ring or line electrodes and counterpoise can be seen as an improved grounding measure. However, as discussed in section 6.1, the effectiveness of the grounding system for lightning is different from those for power-frequency and associated ground potential rise. Therefore, favorable measures to increase the effectiveness can be contradictory for lightning and power frequency. As in this work the focus is on transmission lines passing through areas with high soil resistivity, only effective techniques such as counterpoise or line electrodes are discussed in the following.

As discussed in section 6.1, long electrodes or counterpoise feature a maximum effective length dependent on the soil resistance, in which the transient impedance drops until a maximum length is reached, in comparison to a further decrease of the power-frequency resistance. A graphical representation of the effective length in dependency of the soil resistivity based on a 1.2/50 µs lightning impulse, adapted from [216], is illustrated in figure 7-7.

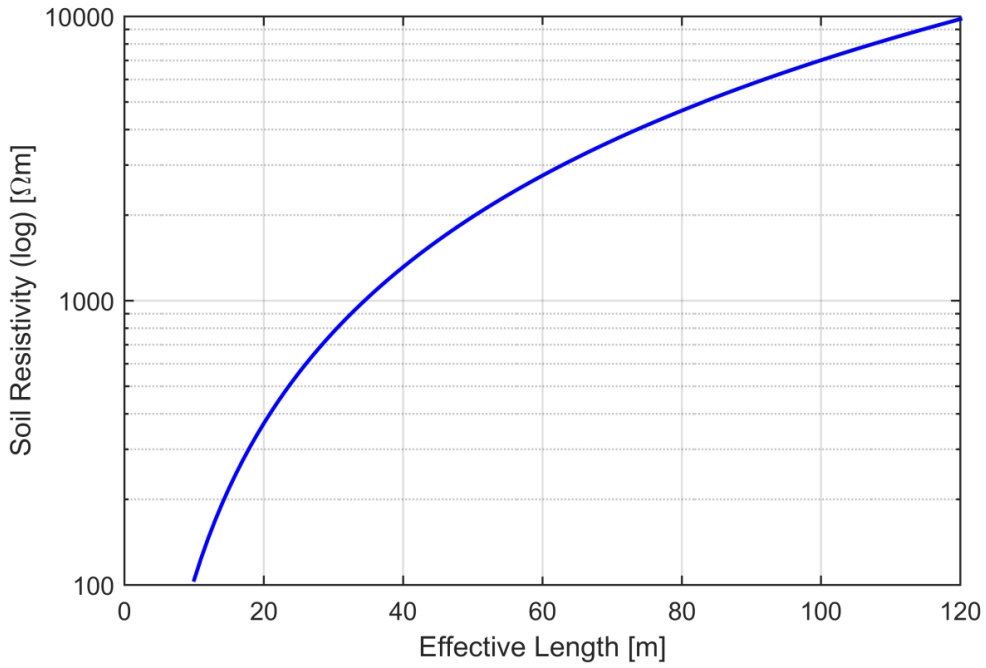

Figure 7-7: Effective length of a long buried wire in dependency of the soil resistivity, adapted from [216]

To overcome this issue, the authors of [291] propose an arrangement as illustrated in figure 7-8, which uses a line on wooden poles on each side of the tower to distribute the

lightning current to an additional counterpoise system. The simulated results of this 230 kV tower arrangement show that a reduction in the impedance of 30% in the range of 0.5 µs to 1.5 µs at 5000 Ωm soil resistivity.

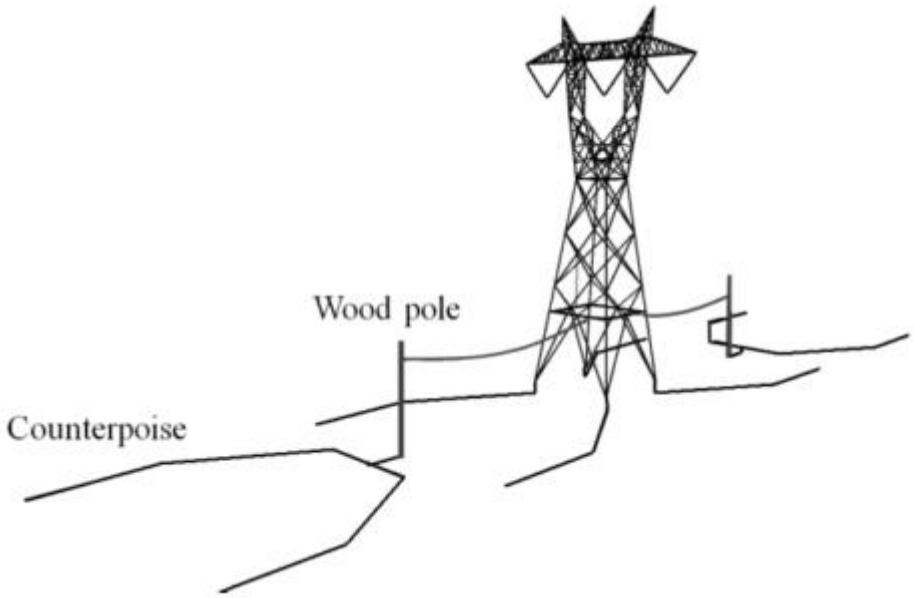

Figure 7-8: Counterpoise arrangement to overcome the effective length issue [291]

Furthermore, when the effective length is longer than the span length due to high soil resistivity, a continuous line electrode, either aerial or buried can be connected at the towers foot. In [306] a reduction of 40% of overvoltages of continuous counterpoise is reported for a 230 kV line, which shows the effectiveness of this technique.

With respect to modelling of the additional counterpoise, the same method as discussed in section 6.3 can be applied. The additional overhead transmission line is modelled with standard methods through the CLP in PSCAD/EMTDC. The short connection of the wooden pole is either neglected or modelled with tower surge impedance formulas in subsection 5.3.2.

7.4: SUMMARY AND CONCLUSION ON LIGHTNING PERFORMANCE IMPROVEMENT MEASURES

In this chapter various measures to improve the lightning performance of a transmission line are presented and discussed. Furthermore, modelling of improvement measures, which are not covered by the previous chapters is presented.

In summary the advantages and disadvantages of the mentioned lightning performance improvement measures are tabulated in table 7-1 to provide a basis for selection of

measures to be applied in the later following simulations for comparison of improvement measures.

Table 7-1: Summary of advantages and disadvantages of lightning performance improvement measures

Measure	Advantage	Disadvantage
Increase of insulator length	Higher insulation level	Taller towers due to clearance
Unbalanced insulator length on double circuit tower	Higher insulation level for one circuit, reduce likelihood of double-circuit flashovers	Taller towers due to clearance
Double shield wires	Improve shielding of phase wires	Increased attraction of lightning
Tower line arresters	Conducting path to reduce insulator overvoltages	Increase failure rate at high winds and ice loading
Underbuilt shield wires	Improved dispersion of lightning currents to ground	Higher mechanical tower strength needed
Guy Wires	Improved dispersion of lightning currents to ground	Increase failure rate at high winds and ice loading
Ground Wires on separate structure	Improved dispersion of lightning currents to ground	Increased footprint of line route
Counterpoise	Improved dispersion of lightning currents to ground	Increased footprint of tower foot
Guy wires and counterpoise	Improved dispersion of lightning currents to ground	Increased footprint of tower foot and failure rate at high winds and ice loading

In addition to the above technical disadvantages, other factors, such as environmental and economic impact of an improvement measure must to be considered. In many cases these

carry more weight in the selection of a lightning performance improvement measure than the sole technical impact.

Scotlands strong commitment to preserve the landscape and environment, the visual impact of overhead lines and the extend of groundwork undertaken limits the application of certain lightning improvement measures. This involves tower height as well as tower visibility. Therefore, guy wires, ground wires on separate structures, increased insulator length, combinations of guy wires with counterpoise or improved earthing are not pursued further. Although counterpoise involves more groundwork and cannot be laid openly on rock due to health and safety reasons, it is not as intrusive to the landscape due to its laying depth of 0.5 m compared to a tower foot mini-pile or shoe foundation. The additional visibility effect of one additional wire - underbuilt or double-shield wires - as well as tower line arresters is generally deemed acceptable. In conclusion, counterpoise, tower line arresters, underbuilt and double shield wires are applied in the following simulations to investigate their impact on the lightning performance of transmission lines.

CHAPTER 8: SIMULATION METHODOLOGY OF LIGHTNING STROKES TO TRANSMISSION LINES

8.1: PRECONSIDERATIONS

For the composition of a complete simulation model, conduction of simulations and the subsequent evaluation of the lightning performance of a transmission line, some modelling aspects, not addressed in the previous chapters, have to be investigated and discussed. This involves the power-frequency voltage on the line, lightning stroke attachment locations, line flashover rate calculation and simulation procedure.

8.1.1: POWER-FREQUENCY SOURCE VOLTAGE

Although the inclusion of system voltage prior to a lightning stroke is not necessarily needed due to the small voltage amplitude in comparison to the lightning stroke surge voltage, it is implemented in most of the conducted lightning simulations [153], [164], [278], [307], [308]. The power-frequency voltage, which adds or subtracts to the insulator withstand voltage during a lightning stroke to a shielding wire or to the surge voltage caused by a direct stroke to a phase wire may have an impact on the flash-over of insulators. To improve the accuracy of the back-flashover rate estimation, the power-frequency voltage needs to be included in the lightning stroke equivalent circuit. As the lightning stroke steep rise and half-time only lasts for some micro-seconds, a constant DC power-frequency voltage may be applied. In [24] it is proposed to use an average value of power-frequency voltage, such as 0.827 times the line-to-earth crest value for a single-circuit horizontally-configured line, 0.551 times for a double-circuit vertically-configured line or a general conservative factor of 0.83, rather than considering a variation of instantaneous values. The probability distribution of voltage is assumed uniform.

For the inclusion of power-frequency into the lightning stroke simulation model, one has to distinguish between shielding and phase wire lightning strokes.

For a phase wire lightning stroke the voltage source may be placed at one end of the line, as depicted in figure 8-1. The line has to be terminated with its wave-impedance to prevent any wave-reflection and thus resulting in the application of two times the power-frequency voltage to generate one time power frequency voltage at the line. For three-phase circuits the voltage source has to be connected to each phase separately taking into account the 120° phase shift. The current source for the lightning stroke is placed in front of the surge impedance termination.

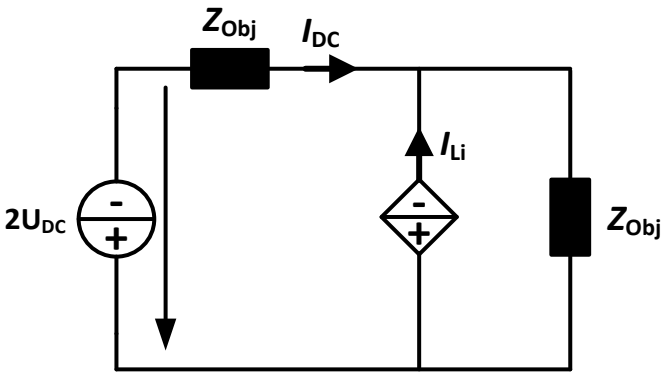

Figure 8-1: Single-phase equivalent circuit of an engineering model of a lightning stroke to a phase wire

However, the application of a voltage source at the overhead line end inherits some disadvantages, depending on the overhead transmission line model used (see chapter 3) and the aim of the simulation.

When a lossless line model is applied the resistive losses of the line are disregarded and the above described approach may be applied. For other line models, which take into account the lines resistance, a second source may be placed at the other end of the line to maintain power-frequency voltage. This is illustrated in figure 8-2, where a simplified single-phase equivalent circuit of a lightning stroke to a phase wire is sketched.

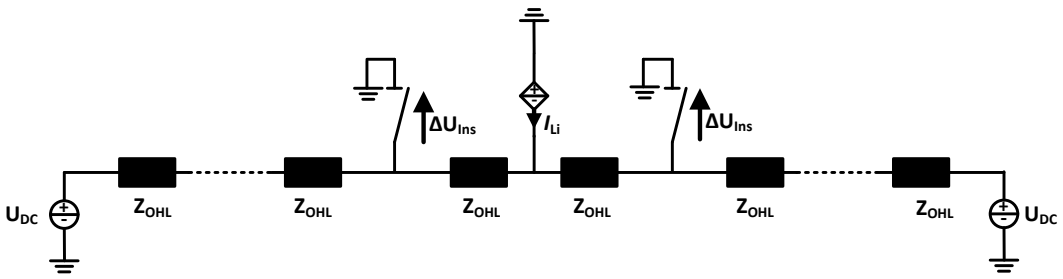

Figure 8-2: Simplified single-phase equivalent circuit of a lightning stroke to a phase wire

Here, the overhead line parts between two towers are represented with the lumped impedance Z_{OHL}, insulator strings as switches and towers as earthed objects. The DC

voltage source at each line end provides the power-frequency voltage resulting in a voltage $\Delta U_{Ins} = U_{DC} - \mathrm{n} \cdot \Delta U_{OHL}$ across the insulator strings before the lightning stroke is initiated. The voltage source amplitude may be adjusted to amount for the resistive line losses.

For lightning strokes to a shielding wire the same approach may be adopted with an extended impedance network, as drawn in figure 8-3. Additionally to the phase wire in figure 8-2, the shielding (earth) wire and tower impedance are added to the simplified equivalent circuit of a lightning stroke to a shielding wire in figure 8-3.

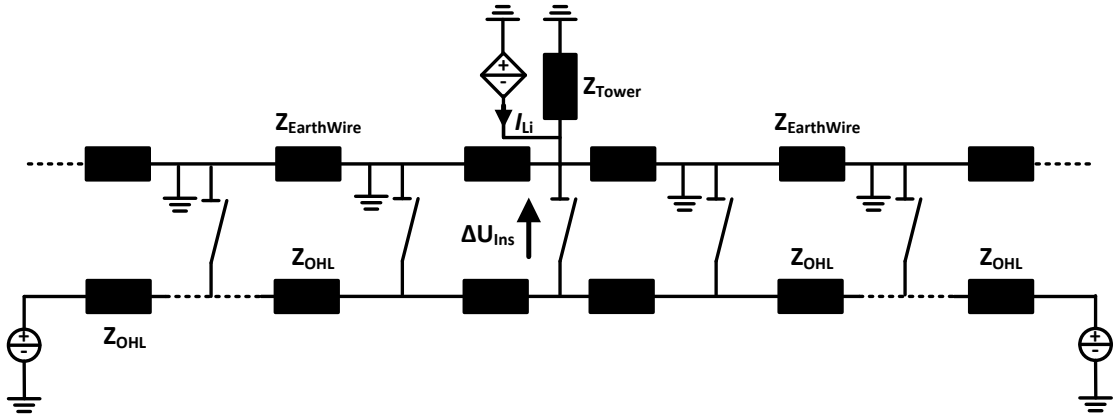

Figure 8-3: Simplified single-phase equivalent circuit of a lightning stroke to a shielding wire

Although the application of a single voltage source may be sufficient in some cases to ensure a conservative approach for the calculation of back-flashover of insulators or where a substation approach is modelled and only one voltage source can be placed at the line end, the more sophisticated power-frequency source model with two voltage sources can be implemented in computational simulations as shown above, especially where a whole line is investigated.

An example of a power frequency voltage source model implementation is shown in figure 8-4. The DC voltage source is placed behind a resistance - matching the wave impedance of the connected transmission line – and can be connected at the transmission line termination.

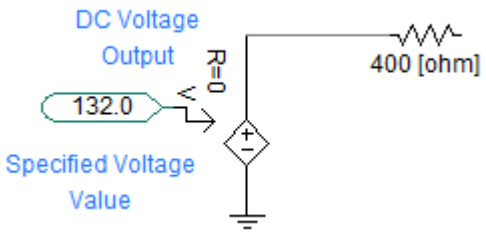

Figure 8-4: Power-frequency block in PSCAD

In figure 8-5, a simple example of the implementation of both the lightning stroke waveshape and power-frequency block with two source voltages are illustrated. The blocks are connected to a simplified network of resistances to show their application in the later lightning stroke simulations. A power-frequency voltage of 132 kV is applied, as seen in the small voltage offset at the measurement points in figure 8-6, before the lightning stroke is initiated.

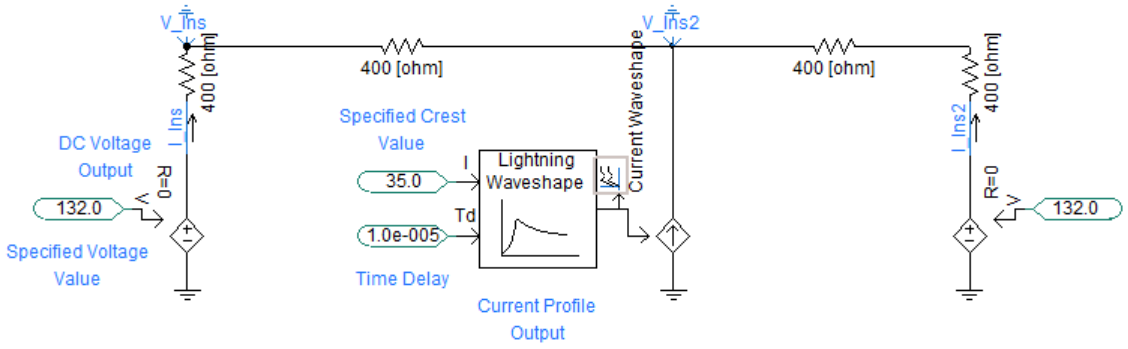

Figure 8-5: Lightning stroke waveshape and power-frequency block in PSCAD

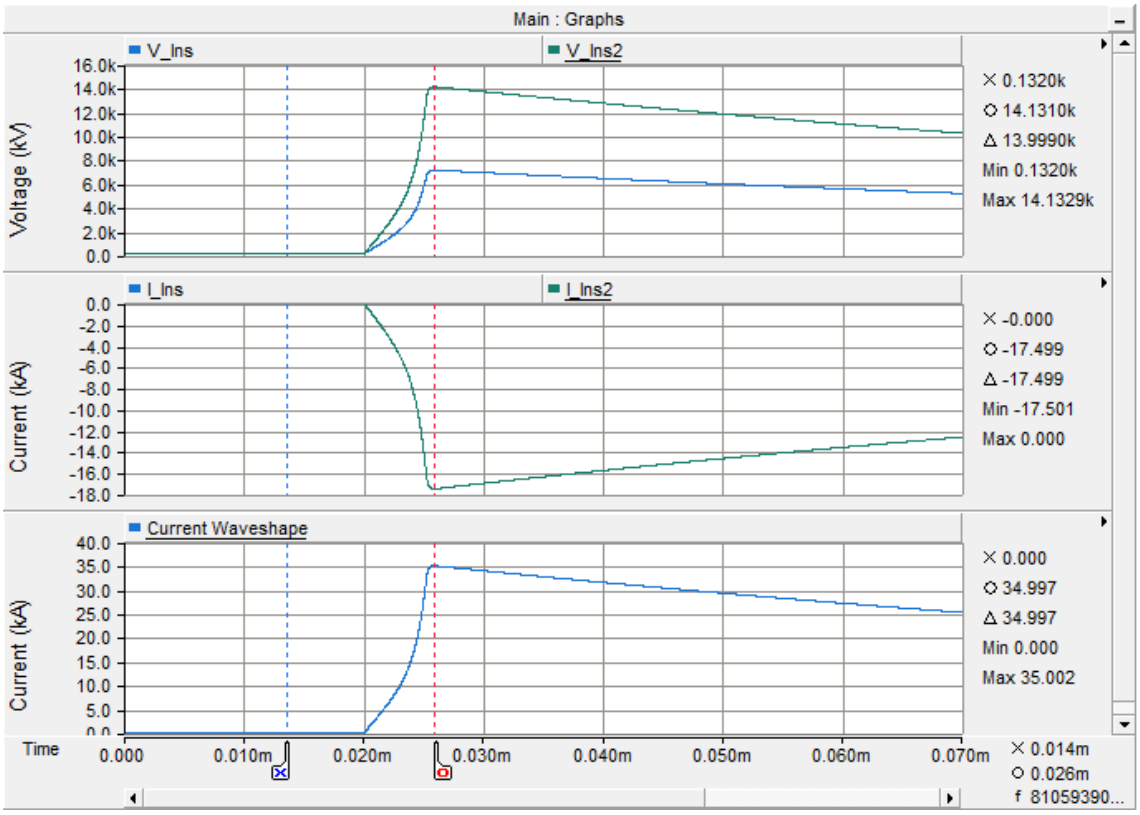

Figure 8-6: Example curve progression of a negative first stroke simulation with power-frequency voltage, peak current 35 kA, lighting initiation at 20 µs

As expected, the lightning stroke current is equally divided, measuring 17.5 kA on both measurement signals ‘I_Ins’ and ‘I_Ins2’, because of the equal distribution of resistances

on both sides of the stroke point. Therefore the line-to-earth voltage at one lines end (measurement point 'V_ins') is 14132 kV. At the stroke point the lightning stroke faces a resistance of 400 Ω and thus a line-to-earth voltage of 28132 kV is measured at 'V_ins2'.

8.1.2: LIGHTNING ATTACHMENT TO TRANSMISSION LINES

For the simulations of lightning strokes to transmission lines as well as in the evaluation process to determine the outage rate, the lightning stroke attachment to the transmission line is of major importance. As already explained in section 2.1 and 2.2, the lightning stroke attachment has a probabilistic element with respect to the stroke location, which is either a direct hit to the tower or within the span. Concerning the occurrence of a back-flashover, the highest insulation strength is at mid-span, the lowest at the tower and insulators respectively. As shown in [24] there exists the possibility of flashovers within the span, but they are insignificant to those at the towers. Therefore, only flashovers at the transmission line insulators are taken into consideration in the simulations.

With regard to the stroke location, a direct hit to the tower represents the worst-case scenario, but the sole consideration of this stroke location consequently leads to an increased back-flashover rate of the whole line in the evaluation [7] due to the confined number of stroke locations. Therefore it is recommended to correct the BFOR with a factor of 0.6 [24]. However measurements of strokes to real lines, such as in table 6-3, show that approximately 65% of lightning strokes hit the span when taking towers with one earth wire into consideration [149], [309].

Table 8-1: Lightning stroke attachment number distribution [149]

	Ground Wire Number			
Impact Point	**0**	**1**	**2**	**3**
Tower [%]	55	35	20	10
Span [%]	45	65	80	90

Therefore, to include this distribution of stroke locations, it is decided to consider two strokes within the span, additionally to a direct hit to the tower. This increases the number of strokes to the line in the later evaluation and hence reduces the BFOR, similar to the factor correction, mentioned above. However, this approach is more accurate due to the

inclusion of the real lines parameters, setting, topographical location, local lightning stroke distribution, etc., rather than the general reduction of the $BFOR$.

To evaluate whether a lightning stroke hits the shielding wire or phase wire, different lightning stroke attachment models, such as the electro-geometric model (EGM), Eriksson's, statistical or generic model are generally used [310]. Furthermore, research is performed to apply leader-progression models [311], but these are dependent on leader velocity and charge. Since both IEEE [282] and CIGRE [24] working groups recommend the EGM, it is used in this work for differentiation of the attachment to shield or phase wire.

The EGM is based solely on the stroke current amplitude in equation (8.1), in which several publications discuss the input parameters A and b. A summary of these is given in [310]. In this work, the IEEE recommendation $A = 8$ and $b = 0.65$ for both shielding to phase as well as phase to earth is applied.

$$r = \mathrm{A} \cdot \mathrm{I}^{b} \tag{8.1}$$

The EGM is based on a vertical lightning stroke attachment, which means that the attachment process of the downward leader and the upward leader is assumed to be a straight line.

In figure 8-7, the results of a shielding analysis of the minimum and maximum setups of the span data in appendix F.1 is performed.

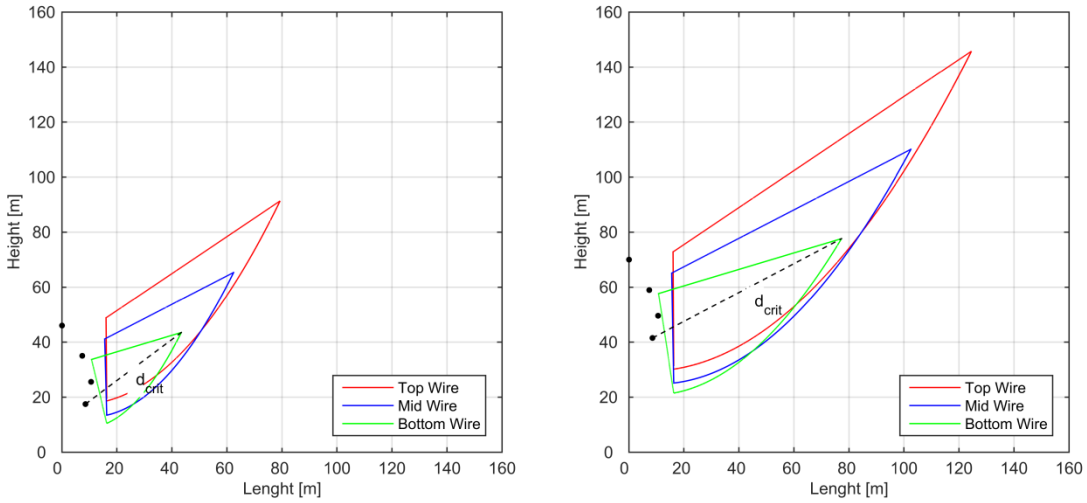

a) Minimum conductor height setup **b) Maximum conductor height setup**

Figure 8-7: Shielding analysis with electro-geometric model of example 400 kV transmission lines

The graphs show the unshielded area of each phase conductor, created by the perpendicular line, composed of the interception points of circles with radius r in equation (8.1) of ground wire and phase wire, and the interception point of the circles with radius r in equation (8.1) of phase wire and ground with height of radius r. This means that lightning strokes up to the distance d_{crit} (conductor position to interception point of circle of ground wire and ground) or a specific current I_{crit}, calculated with equation (8.1), hit the top line wire. In the example for minimum and maximum conductor height the critical distance or current is 91 m and 146 m, 42 kA and 87 kA respectively. It has to be mentioned that these critical current values are much higher than normally encountered in 400 kV transmission lines due to the single shielding wire [24]. In case the tower arrangement in appendix F.1 is changed to a dual shielding wire arrangement 5 m apart from the center at the same height, as depicted in figure 8-8, the critical distance is reduced to 51 m and 82 m and 17 kA and 36 kA, respectively.

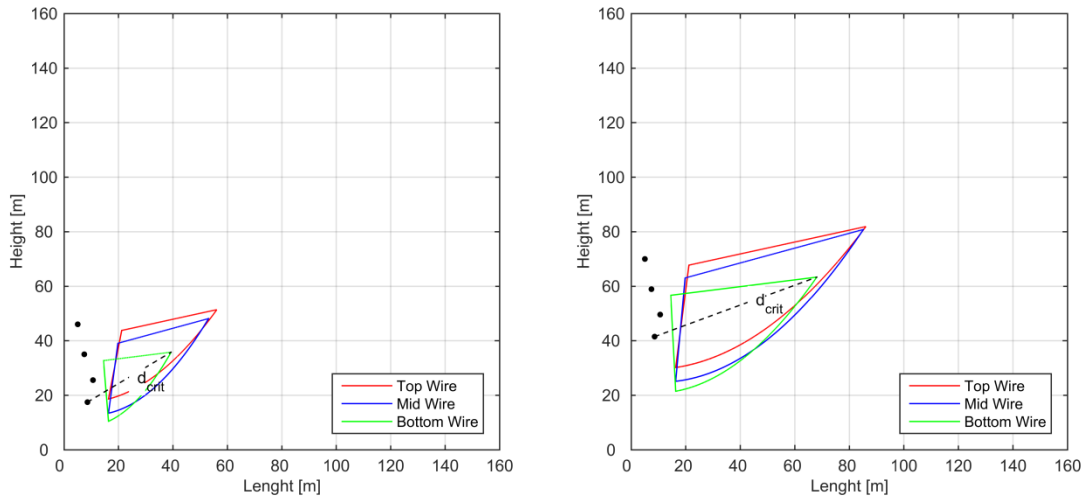

a) Minimum conductor height setup **b) Maximum conductor height setup**

Figure 8-8: Shielding analysis with electro-geometric model of example 400 kV transmission lines with dual shield wire, 5 m from centre

With respect to the simulation of lightning strokes to a transmission line the above described approach and shielding analysis of the span conclude to simulate only strokes to the ground/shield wire and the top line wire. The range of currents considered for the simulation of strokes to the phase wire ranges from the lowest value 3 kA to the critical current calculated in the shielding analysis and from 3 kA to the 99.9% limit of the probability distribution of the stroke current.

However, due to experience with the above described approach and comparison with real shielding failure rates of transmission lines, already reported in 1969 [309], the simple assumption that all leaders are vertical is replaced with the inclusion of the lightning stroke attachment angle, measured from the vertical, as a probability function [279], [312], [313]. The probability of the attachment angle distribution in (8.2) assumes that no leader approaches from below the horizontal, in which the authors of [309] suggest parameters $m = 2$ and $K_2 = \frac{2}{\pi}$ as a result of visual observations.

$$p(\Psi) = \begin{cases} 0, & \Psi < -\pi/2 \\ K_m \cos^m \Psi, & -\pi/2 \leq \Psi \leq \pi/2 \\ 0, & \pi/2 < \Psi \end{cases} \tag{8.2}$$

Therefore the probability of stroke angles in the plane area sums up to 1, as plotted in figure 8-9 for the above mentioned parameters applied to equation (8.3), which means that the probability of a stroke to a shielding wire is much more likely than for a phase wire.

$$P(\Psi) = \int_{-\pi/2}^{\pi/2} K_m \cos^m \Psi \, d\Psi = 1 \tag{8.3}$$

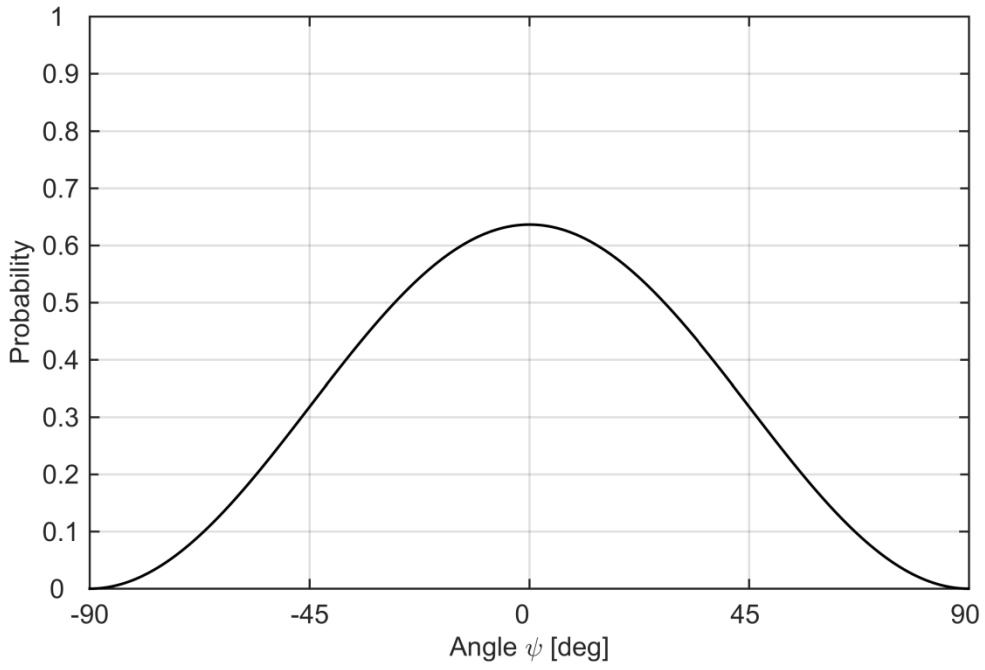

Figure 8-9: Probability density function of stroke angle

In comparison to the standard EGM shielding analysis with regard to the simulations, the range of currents considered for the simulation of strokes now includes a second

probability element, namely the attachment angle ψ. The impact of this element is shown in figure 8-10, where it is now distinguished between lightning attachment to earth, shield wire and three phase wires, rather than the sole consideration of strokes to shield wire and top phase wire. As a result, the critical distance between conductor position and interception point of the perpendicular line with the line-ground curve is reduced, which also reduces the current injection amplitude in the simulation.

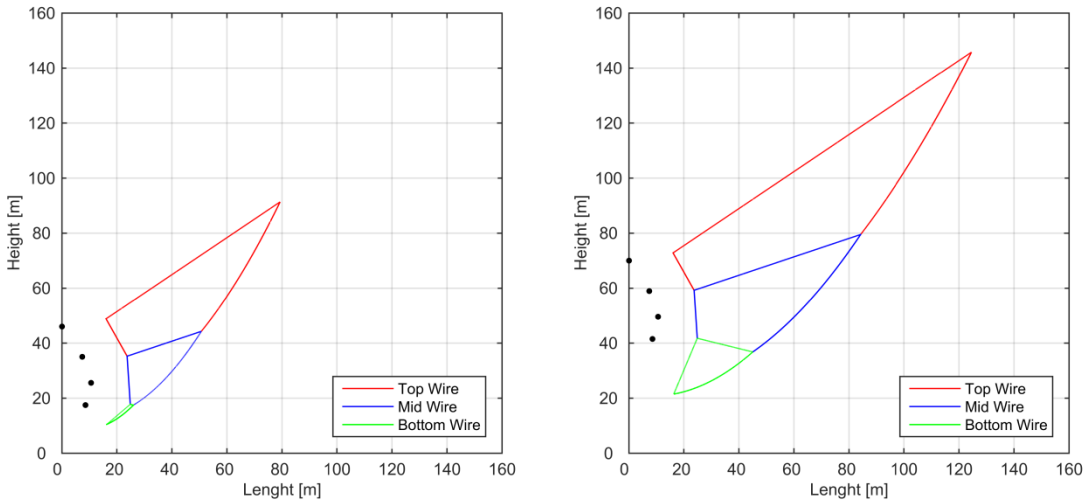

a) Minimum conductor height setup **b) Maximum conductor height setup**

Figure 8-10: Shielding analysis with electro-geometric model with attachment angle of example 400 kV transmission lines

The change to a dual shielding wire arrangement 5 m apart from the center at the same height as shown before reduces the critical are of the top phase wire, as depicted in figure 8-11.

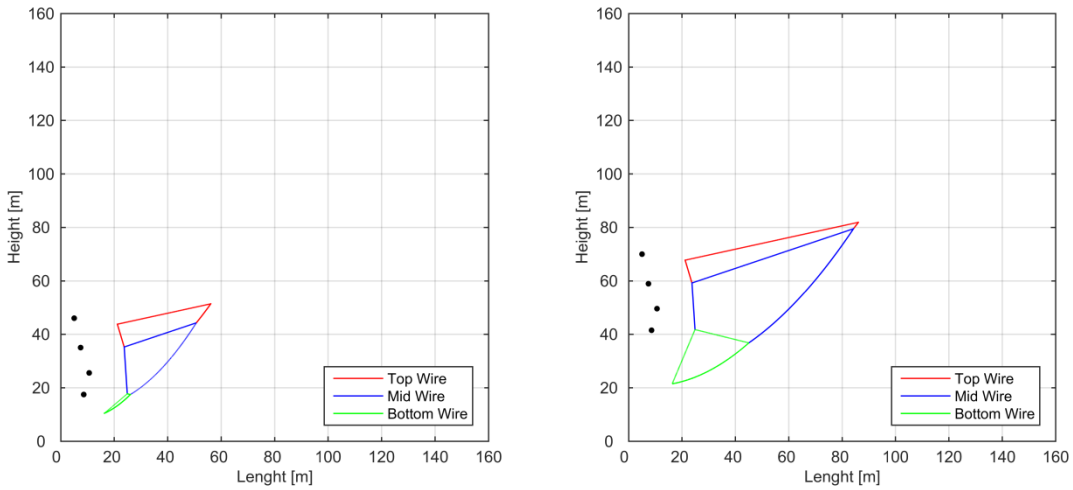

a) Minimum conductor height setup **b) Maximum conductor height setup**

Figure 8-11: Shielding analysis with electro-geometric model with attachment angle of example 400 kV transmission lines with dual shield wire, 5 m from centre

To distinguish which conductor is hit by the lightning stroke in the EMT simulations, an evaluation procedure has to be employed, taking stroke amplitude and angle into consideration. In the literature, a method for a single line tower geometry is proposed, taking into account a horizontal conductor arrangement, one shield wire and one phase wire respectively [279], [312]. However, as shown in figure 8-10, all three phases need to be included in such a method. Therefore a new calculation procedure for this tower arrangement is developed.

First, the coordinates for the stroke point are defined, as depicted in figure 8-12 and equations (8.4) and (8.5).

$$y_{SP} = r_g \tag{8.4}$$

$$x_{SP} = \frac{y_{SP}}{\tan\left(\frac{\pi}{2} - \Psi\right)} \tag{8.5}$$

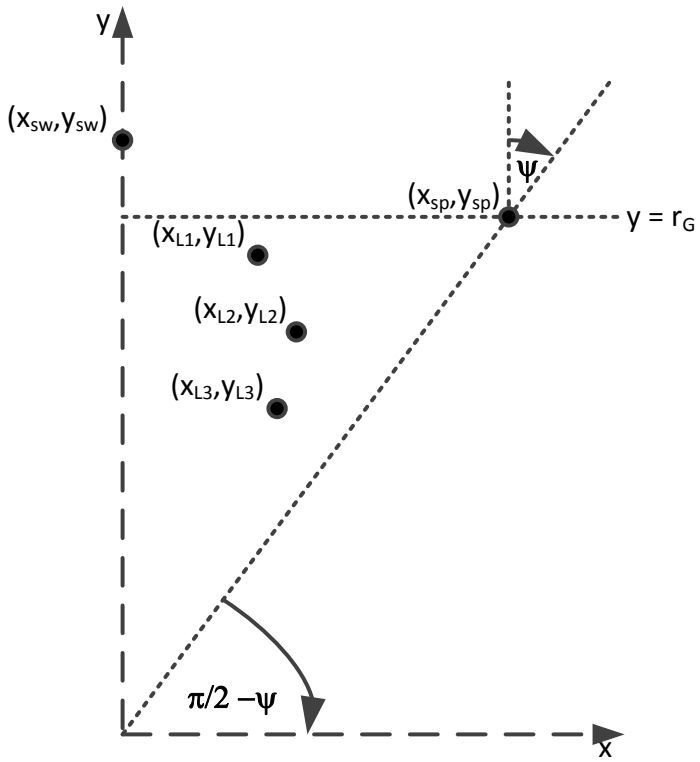

Figure 8-12: Definition of shielding angle and coordinate definition of developed EGM procedure

Then, the attachment area of each conductor is calculated with the interception points of each conductor attachment radius and ground attachment height and conductor attachment radi, as shown in in the four examples for the maximum conductor height setup of the example 400 kV transmission line span with various stroke currents and leader attachment angles in figure 8-12. At last the distances between the stroke point and the areas are compared to determine the conductor the lightning stroke attaches to. A full description of the procedure can be found in appendix F.2.

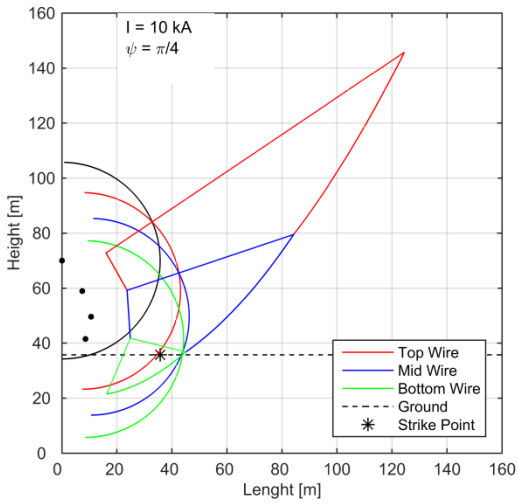

a) Lightning attachment to phase wire L3

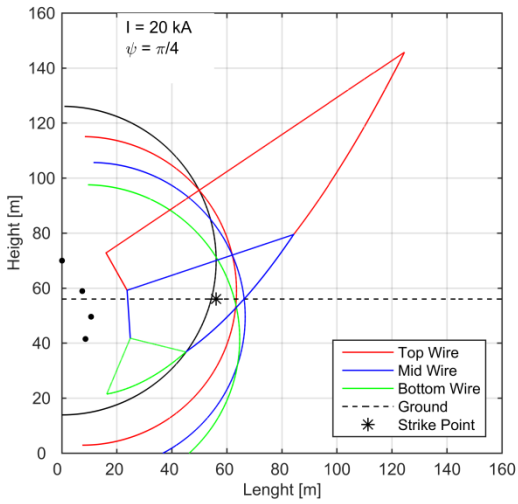

b) Lightning attachment to phase wire L2

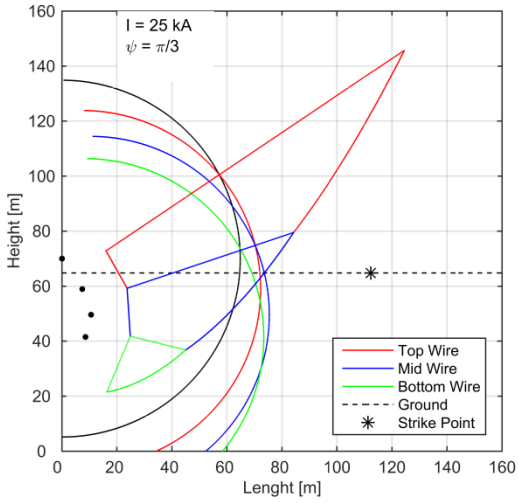

c) Lightning attachment to ground

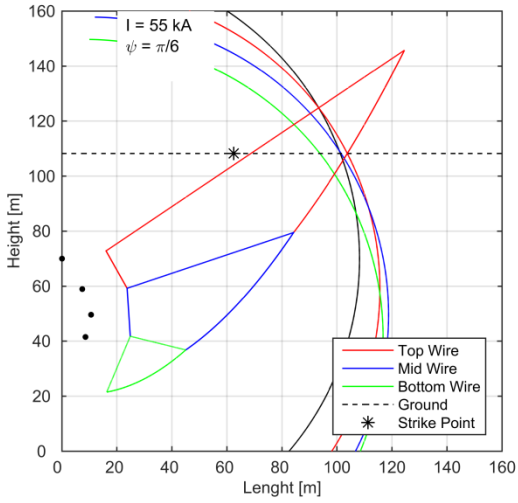

d) Lightning attachment to shield wire

Figure 8-13: New shielding analysis procedure with electro-geometric model with attachment angle of example 400 kV transmission lines, maximum conductor height setup

8.1.3: CALCULATION OF FLASHOVER RATES

In the general case, a measure for the assessment of the lightning performance of a transmission line is the lightning flashover rate, abbreviated LFOR in flashes per 100 kilometer per year. As already pointed out, in subsection 8.1.2, there exist three possibilities of stroke termination, ground, shield wire or phase wire. For the calculation of the LFOR it is therefore distinguished between the shielding failure flashover rate (SFFOR), which is the flashover of a line insulator caused by a lightning stroke to a phase

wire, and the back-flashover rate (BFOR), which is a flashover due to a stroke to the shielding wire or transmission line tower [7], [24].

The calculation of the SFFOR is related to the exposed area of the phase conductor and therefore a result of the application of the EGM, discussed in subsection 8.1.2 and the stroke current distribution in section 2.2. The SFFOR is a limitation of the case of the shielding failure rate (SFR) in equation (8.6), which is the measure of strokes to a phase wire.

$$SFR = 2N_G L \int_3^{I_m} D_C f(I)\, dI \tag{8.6}$$

The SFR (related to the line length L in flashes per 100 km-year) is calculated from N_G, the ground flash density in units of flashes per 100 square km-year, $L \cdot 2D_C$, the exposed area of the phase conductor, which may collect a flash and $P(I) = \int f(I)dI$, the probability of a current that will occur. The product $L \cdot 2D_C$ consists of the length of the line L multiplied with the exposed unshielded horizontal distance D_C on both sides of the span (see figure 8-14). Since D_C decreases with increasing current (see section 8.1.2) until distances r_c of the shielding wire, phase wire and r_c of the lightning ground attachment radius meet, a maximum shielding failure current I_m can be calculated. Therefore the distance D_C is part of the integral calculation together with the stroke current probability function. The lowest value of current to occur is set to 3 kA, derived from the CIGRE distribution of current, see section 2.2 for stroke current distributions.[7]

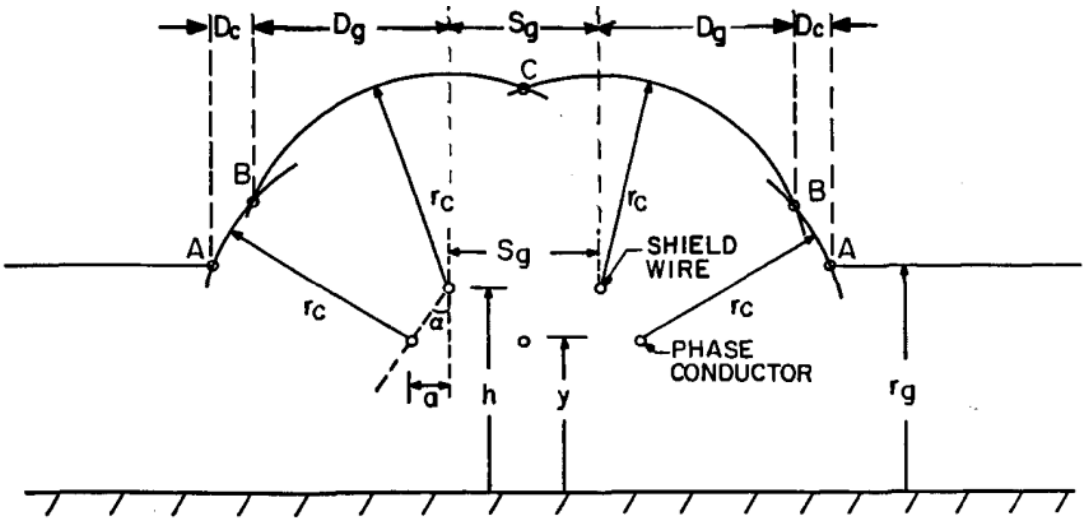

Figure 8-14: The geometric model, definitions of angles and distances [7]

The SFFOR is a limitation of this minimum or critical current at and above a flashover occurs, as written in equation (8.7).

$$SFFOR = 2N_G L \int_{I_c}^{I_m} D_C f(I)\, dI \tag{8.7}$$

The calculation of the BFOR follows this method of a critical current, as seen in equation (8.9) for the probability of a stroke current at I_c or above leading to a flashover multiplied with the collection area $2D'_g L$.

$$D'_g = D_g + \frac{1}{2} S_g \tag{8.8}$$

$$BFOR = 2LN_G \int_{I_c}^{\infty} D'_g f(I) dI \tag{8.9}$$

The resulting flashover rate then is a simple addition of the SFFOR and BFOR in equation (8.10).

$$LFOR = \text{SFFOR} + \text{BFOR} \tag{8.10}$$

With respect to a simulation approach, the stroke current I_c needs to be determined to calculate the LFOR. In this case, the stroke current needs to be increased from the minimum value until a breakdown of the insulator arc gap is present. However, in the literature no differentiation between positive, negative first and negative subsequent strokes is made, because historically only negative first strokes are investigated. This is overcome in the simulation approach with a Monte-Carlo procedure, explained in the next section. There, the calculation of SFFOR and BFOR per 1 km of the line can be simplified to equation (8.11) and (8.12), where N_G is the ground flash density in flashes/ 100km^2/year and d is the maximum width of impact area, which is considered separately for strokes to each phase and shield wire. F_P/N and F_G/N respectively are the ratios of simulations, which lead to a flashover divided by the total number of simulations.

$$SFFOR = N_G \cdot 100 \cdot d \cdot \frac{F_P}{N} \tag{8.11}$$

$$BFR = N_G \cdot 100 \cdot d \cdot \frac{F_G}{N} \tag{8.12}$$

In contrast to the standard approach, where the critical current is determined, the Monte-Carlo method allows the variation of stroke polarity among others, because only the flashover itself is taken as a criterion rather than the stroke current.

In contrast to [314], where a fixed width d, based on the highest current value leading to a flashover, is applied, a new procedure adapted from the standard calculation with critical currents in equation (8.7) and (8.9) is applied. Since the lightning attachment angle is taken into account in the Monte-Carlo method, it is derived from the standard calculation method that the distance d is different for each phase. This is furthermore justified, because the attachment area (see figure 8-13) is smaller for the lower phase wires. Therefore, for each phase the highest current leading to a flashover in the simulation is taken and the distance d calculated with the EGM for each phase and the shield wire respectively. This leads to smaller distances d_{PW} for phase wires in comparison to the distance d_{SW} for the shield wire.

8.2: MONTE-CARLO SIMULATION PROCEDURE

As the phenomenon of lightning strokes with respect to waveshape, stroke location and attachment to a transmission line features a random behaviour, it can only be described with a probabilistic approach as pointed out in the previous section to calculate the LFOR. Therefore many researchers applied a Monte-Carlo procedure to estimate the lightning performance of a transmission line [279]–[281], [284], [314]–[317]. In this work subsequent strokes are considered as well, due to a major impact on the flashover rate [318], [319].

In a Monte-Carlo procedure, probability distributions are used to generate random values within their limits. In computer applications either a maximum number of generated values or a stop criterion based on a comparison of the generated density functions to their theoretical functions is applied.

For the simulations of lightning strokes to a transmission line the following distributions are included, although authors in [279]–[281], [284], [314]–[317] use variations or exclude certain distributions:

- Current amplitude I_F, log-normal distribution (see section 2.2)
- Stroke polarity and subsequent strokes, uniform distribution (see subsection 2.2.7)
- Attachment angle Ψ, quasi normal distribution (see subsection 8.1.2)
- Power frequency voltage, uniform distribution (see subsection 8.1.1)

- Location within the span, uniform distribution (see subsection 8.1.2)

In contrast to other authors, no explicit variation of the steepnesses of waveshapes is performed, but is included as a dependency of the current amplitude I_F for each stroke type.

In the literature, implementations of the Monte-Carlo procedure into an EMT program are limited to ATP/EMTP or their derivatives, which use a combination of Matlab random parameter generation, EGM calculation, simulation in EMT and evaluation in Matlab [283], [314], [316], [320], as illustrated in figure 8-15.

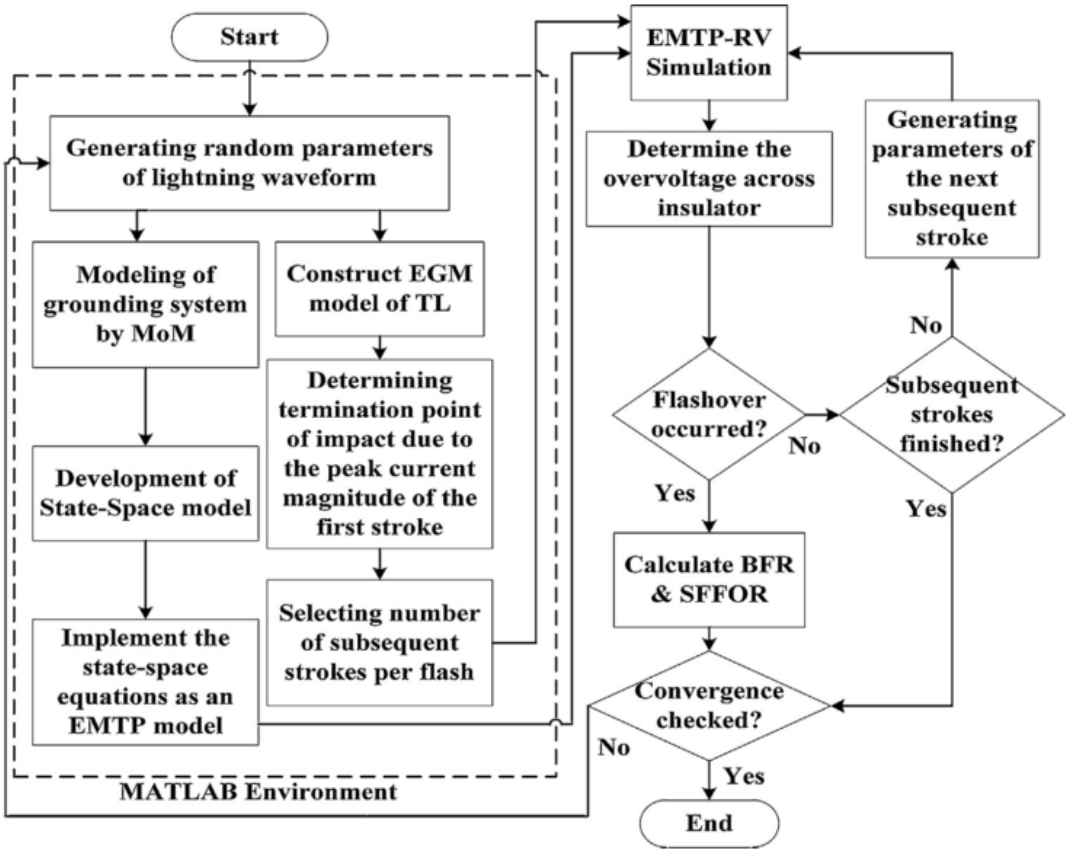

Figure 8-15: Example of Monte-Carlo method implementation in a Matlab – EMTP procedure [314]

However due to the program capability of PSCAD/EMTDC, used in this work, the simulation control can be programmed within PSCAD, which calls Matlab scripts to enable outsourcing of calculations. Therefore, the generation of random values, construction of the EGM model and stroke termination calculation is performed in a Matlab script and called from a PSCAD/EMTDC control simulation. Furthermore this enables the run of simulations in parallel and batch mode to speed up simulations. The

evaluation of the BFOR and SFFOR as well as the convergence check of probability distributions for the randomly generated simulation input values is conducted similar to the random value generation as a Matlab script. A schematic overview of the simulation procedure developed in this study is shown in figure 8-16.

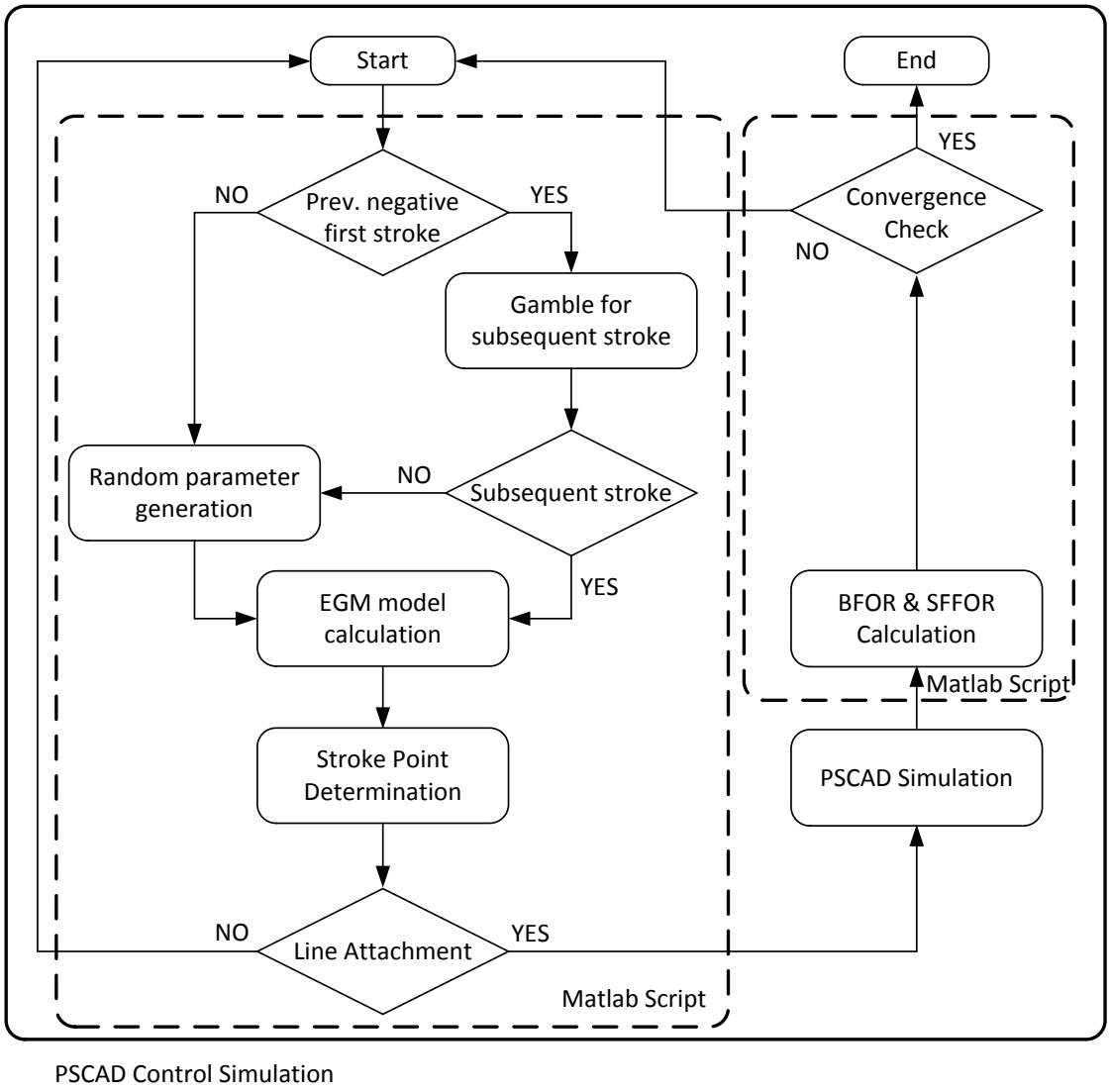

Figure 8-16: Schematic overview of simulation procedure in PSCAD/EMTDC

First, a Matlab script is called and the stored randomly generated parameters are checked on the existence of a first negative stroke in the last simulation. If this is the case a random generator is used to "gamble" for the occurrence of a negative subsequent stroke. The Matlab script furthermore checks with an EGM calculation if a stroke hits the shield wire, phase wire or ground. In case the calculation result is no attachment, the control simulation is called again. Otherwise a PSCAD simulation is called with the randomly generated parameters. At the end of the PSCAD simulation an evaluation script is called from the control simulation to calculate the back-flashover rate and shielding failure flashover rate. To generate a stop signal, a convergence check is programmed in the

parameter generation procedure, which is conducted through the calculation of the respective distribution from the generated values. For power frequency angle, polarity and location the discrete normal distributions of natural numbers can be calculated using (8.13) and (8.14), where n is the number of values.

$$\mu = \frac{n+1}{2} \tag{8.13}$$

$$\sigma = \sqrt{\frac{n^2-1}{12}} \tag{8.14}$$

For the logarithmic standard deviation of the stroke current, based on a row of values, the median M is calculation with the geometric mean GM and the logarithmic standard deviation with the geometric standard deviation GSD in (8.15) and (8.16).

$$M = e^{\mu} = GM(X) = e^{\left(\frac{1}{n}\sum_{i=1}^{n} ln(a_i)\right)} \tag{8.15}$$

$$\sigma = \ln\big(GSD(X)\big) = \sqrt{\frac{\sum_{i=1}^{n}\left(ln\left(\frac{a_i}{\mu}\right)\right)^2}{n}} \tag{8.16}$$

The attachment angle distribution is approximated with a normal distribution and thus the random sample mean and deviation is calculated in (8.17) and (8.18).

$$\mu = \frac{1}{n}\sum_{i=1}^{n} a_i \tag{8.17}$$

$$\sigma = \sqrt{\frac{1}{n}\sum_{i=1}^{n}(a_i - \mu)^2} \tag{8.18}$$

The associated criteria for convergence of distributions paired with the allowance of a deviation of $\pm$5% are input parameter dependent [314], [315]. For the power frequency angle a range of 1 to 360 degree is chosen, which results in the mean and deviation of $\mu = 180.5$ and $\sigma = 103.92$. To reflect the percentage of strokes to be positive or negative, the polarity is randomly varied in the range of 1 and 100 in percent, which results in $\mu = 50.5$ and $\sigma = 28.87$. The stroke location is randomly varied between 1 and 15, derived from 3 possible stroke locations (in front of tower, tower, behind tower) multiplied with the number of towers simulated, in this case 5, which calculates to $\mu = 8$ and $\sigma = 4.32$. For the stroke current, the inputted median and log-normal deviation is

used. Since the attachment angle is approximated as a uniform distribution, $\mu = 0$ and $\sigma = 0.57$ are applied.

Once the criteria are met, a full simulation stop is programmed, writing out results to text files including the number of simulations and number of simulations resulting in back-flashovers and shielding failure flashover.

8.3: SIMULATION SCENARIOS

To investigate several mitigation methods for improving the lightning performance of a transmission line and fulfill the goal of determination of suitable techniques in dependency of the soil resistivity, several scenarios are simulated. A summary of general variations is provided in figure 8-17.

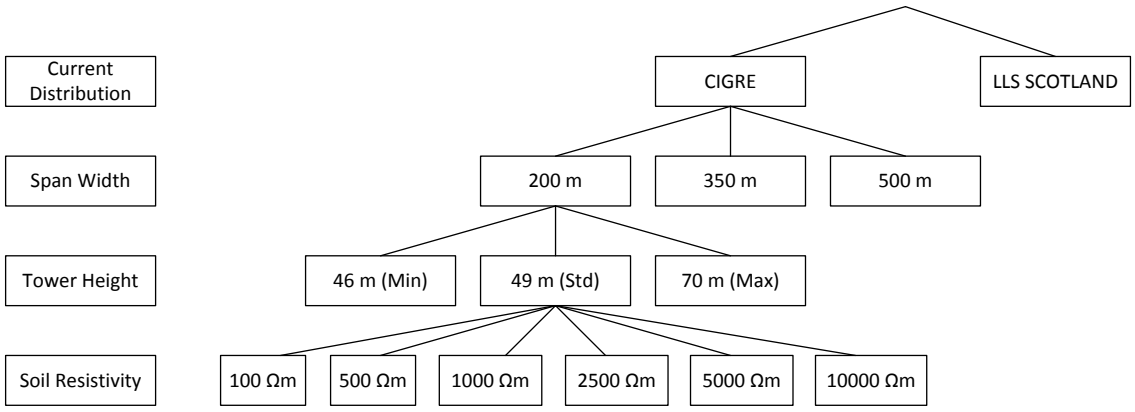

Figure 8-17: Summary of general simulation variations

To cover worst-case scenarios and with regard to the variation of lightning activity, as discussed in subsection 2.2.7, additionally to the current distributions of peak currents of lightning strokes obtained through the LLS evaluation, the CIGRE current distribution is taken into account. To cover variations of tower and line configurations, the standard 400 kV tower design is considered with minimum, standard and maximum tower height and three span lengths for a range of soil resistivities, informed by the soil measurements of the sample line in section 1.4. With regard to a criterion for the effectiveness of a flashover mitigation method, either the critical current value or the ratio of flashovers to the total number of strokes can be applied, as outlined in subsection 8.1.3. Therefore, an evaluation is carried out for simulations of lightning strokes to a single tower as part of a span with regard to the critical current as well as simulations of lightning strokes to a 1 km span with the Monte Carlo method with regard to the ratio of number of flashovers to total simulations.

8.3.1: BASE SCENARIOS

First of all, base scenarios have to be established to enable a comparison to any lightning performance improvement method. To investigate improvements in modelling the tower foot or earthing system respectively, the simple tower footing resistance (see chapter 6) is applied for all base cases. In practice, various methods to fix the towers to ground are used, such as shallow pad and column foundations, rock anchor foundations, mini-pile or pile-cap foundations. However, the most commonly used foundations on the sample line in this work have a similar geometry in that each tower leg foundation a steel-reinforced core with length between 1 and 4 m and an average thickness of 200 mm or equivalent. To cover this majority of cases for the 400 kV tower earthing arrangements, it is decided to use a range of rod length from 1 m to 4 m with a 200 mm diameter rod and 6 m to 8m foot distance arrangements. For the calculation of the low-frequency tower footing resistance for rods equation (6.19) is applied. For the base cases this results in a range of 5 Ω to 455 Ω for the tower footing resistance, which matches the range of measured footing resistances of the sample line.

As the stroke current amplitude is linearly increased in the simulations of lightning strokes to a single tower as part of a span, no lightning stroke distributions are needed for these cases. For the simulations with the Monte-Carlo method, a summary of the different parameters varied in the base cases is given below in table 8-2.

Table 8-2: Summary of simulation base scenarios, stroke current distributions

	Negative First Stroke Peak Current Distribution		Negative Subsequent Stroke Peak Current Distribution		Positive Stroke Peak Current Distribution		Multiplicity of Negative Stroke Distribution		Percentage of Positive Strokes
	M [kA]	σ	M [kA]	σ	M [kA]	σ	M [kA]	σ	
CIGRE	31	0.484	12.4	0.53	35	1.195	1.241	1.127	10
LLS Scotland	13.5	0.456	12.4	0.53	25.2	0.985	1.241	1.127	29

To investigate the improvements in tower earthing modelling, the fixed footing resistance is replaced with the frequency-dependent rod model with ionization effects, described in subsection 6.3.2. In these cases, the impedance of the four rods is calculated from the frequency-dependent soil resistivity.

8.3.2: MITIGATION METHOD SCENARIOS

To assess the effectiveness of any mitigation method, simulations of lightning strokes to a single tower as part of a span with regard to the critical current as well as simulations of lightning strokes to a 1 km span with the Monte Carlo method are performed. However, cases where the simulation results of base scenarios already show a sufficient lightning performance are excluded.
As outlined in section 7.4, the following mitigation methods are investigated:

- Underbuilt shield wire
- Double shield wire on tower
- Counterpoise earthing
- Transmission line arresters

For simulations of an underbuilt shield wire, an identical shield wire is placed at the lower end of the bottom traverse, because it is recommended in [303] to achieve a minimum distance to the phase wires and top shield wire.

For the double shield wire arrangement, a Y-tower shape is chosen and the top part of the towers replaced to achieve a location at 5 m from the center line of the towers at the same height of the normal tower design (see appendix F.1).

With regard to counterpoise earthing, although, there exist several counterpoise layouts, the predominantly used H-design in figure 6-20 is applied, where the length of the wires is set to the effective length in dependency of the soil resistivity in figure 7-7.

For transmission line arresters, it is known that placement on all phases reduces the SFFOR and BFOR to zero. However from an economical viewpoint a reduction of the number of arresters is preferable. In [321] a similar tower configuration with one shield wire is investigated with a variety of arrester placements on the tower. The results of a literature investigation show that placement of an arrester at the top phase improves the SFFOR and BFOR significantly. In case two arresters per system are employed, the mid phase should be protected to mainly decrease shielding failures. In conclusion to the simulations in this work, the configuration with two arresters at top and mid phase per system is investigated due to the results in the electro-geometric model evaluation of

lightning attachment to phase wires, which reveals a significant exposure of the top and mid phase.

8.4: THE COMPLETE SIMULATION MODEL

To assess the line flashover rate of the scenarios set out in section 8.3 a full simulation model is built in PSCAD/EMTDC with the models for lightning strokes, lines, insulators, towers and earthing systems as presented and discussed in the previous chapter 2 to chapter 7 and the pre-considerations in section 8.1 and the Monte-Carlo-procedure in section 8.2. For both the simulations of lightning strokes to a single tower as part of a span and the simulations of lightning strokes to a 1 km span with the Monte Carlo method, the same simulation model is utilized with the exception of the control workspace and automation of simulations. In the sections, supported by the input data summary flowchart in figure 8-18, the complete simulation model is explained.

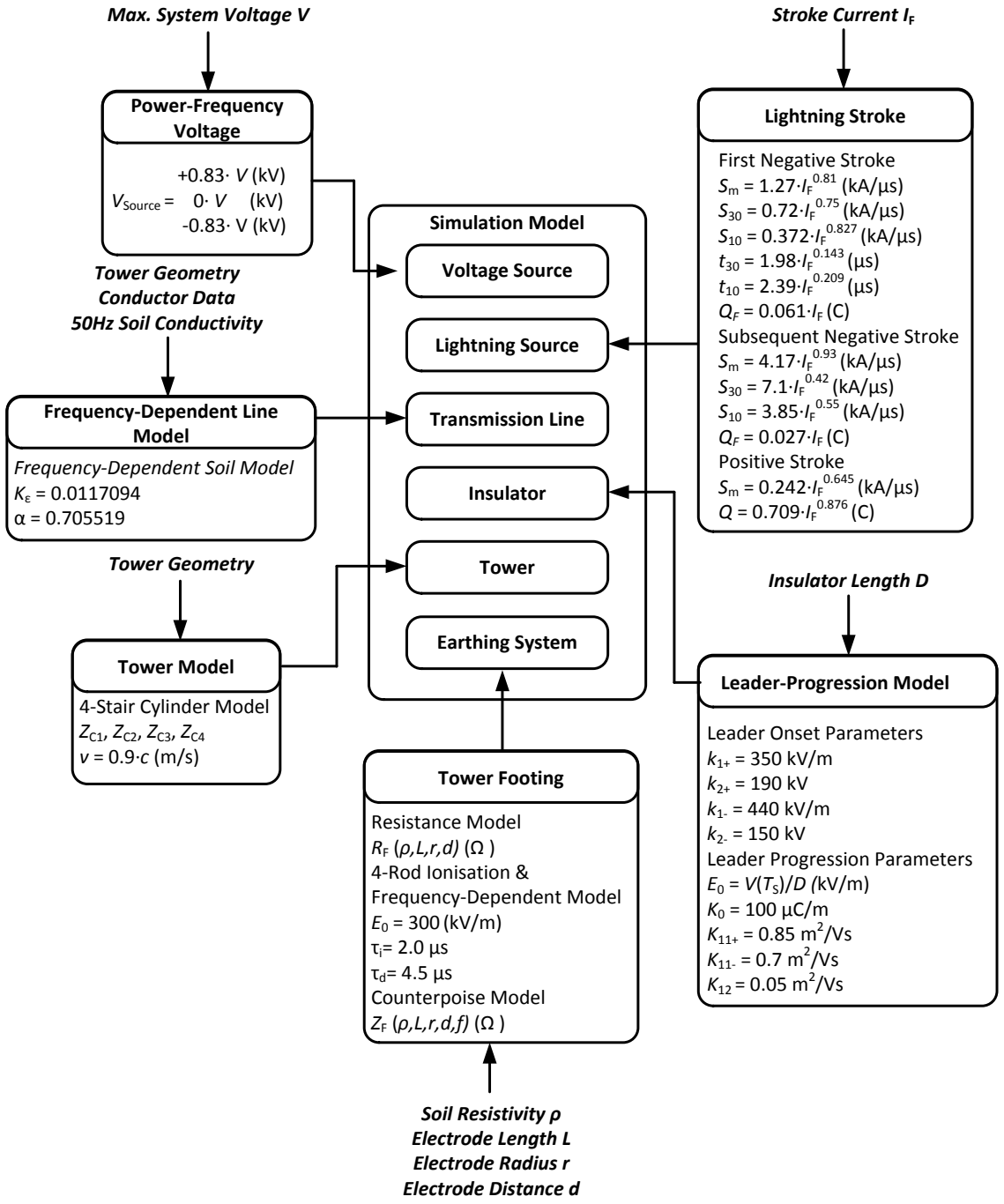

Figure 8-18: Summary flowchart of model input data

8.4.1: MODEL OVERVIEW

In reality the span length and height as well as the soil resistivity and possible lightning attachment points vary along a line route. However, to derive more general conclusions for various tower heights and soil resistivities as summarized in section 8.3, the investigation of an idealized line route piece is performed. In total, three idealized pieces of a whole transmission line, consisting of either two tension and three suspension towers with a span length of 200 m as illustrated in figure 8-19, two tension and one suspension

tower with a span length of 350 m as illustrated in figure 8-20, which is the average span length of the 400 kV sample line, or three tension towers with a span length of 500 m, depicted in figure 8-21 for maximum tower height are investigated. Possible lightning attachment locations are put on each connection of the line to the towers or insulator HV sides and 30 m away from each side of the tower, marked with red dots. This is derived from table 8-1, where approximately 33% of lightning strokes hit the transmission towers when one shield wire is employed. To compare results for the 350 m and 500 m span, a reduced number of attachment points is considered as for the 200 m span. The simulations regarding the critical current are conducted with stroke locations at the mid suspension tower.

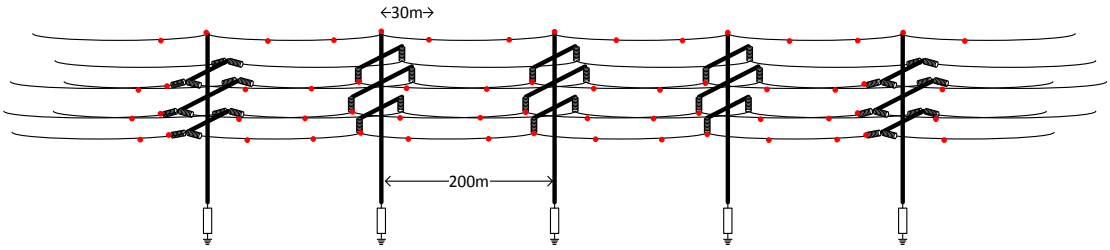

Figure 8-19: Complete simulation model, main transmission line, span width 200 m

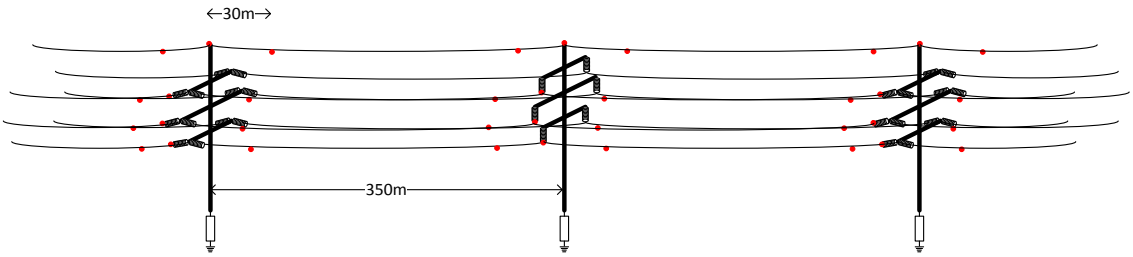

Figure 8-20: Complete simulation model, main transmission line, span width 350 m

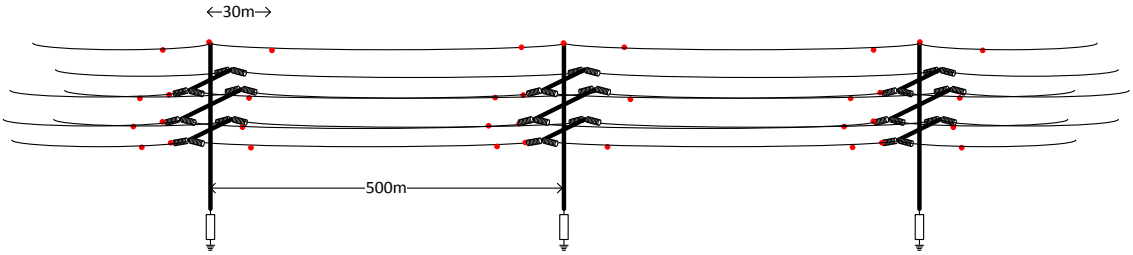

Figure 8-21: Complete simulation model, main transmission line, span width 500 m

The line is terminated on both ends with another three suspension tower spans with 200 m span length or one suspension tower for 350 m and one tension tower for 500 m span length, respectively, and a terminating PI-circuit with matching surge impedances and DC voltage sources to impregnate the power-frequency voltage as explained in subsection 8.1.1, depicted in figure 8-22, figure 8-23 or figure 8-24.

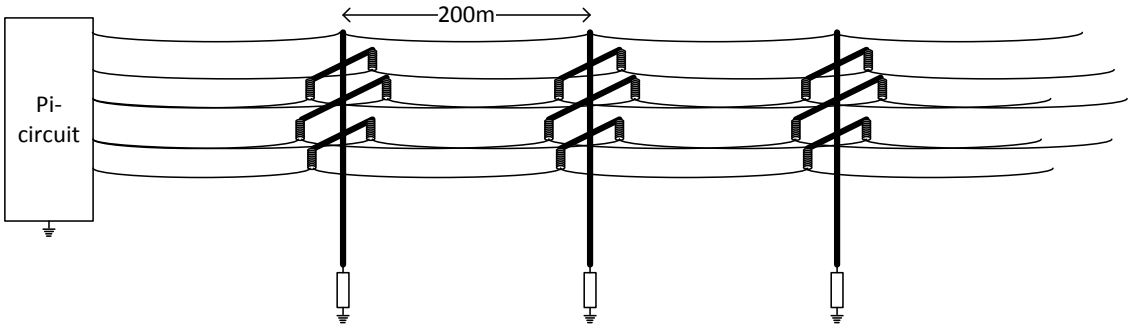

Figure 8-22: Complete simulation model termination, span width 200 m

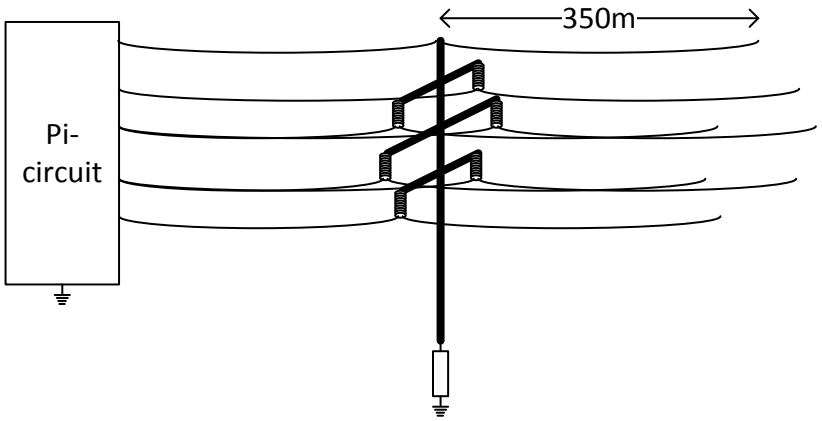

Figure 8-23: Complete simulation model termination, span width 350 m

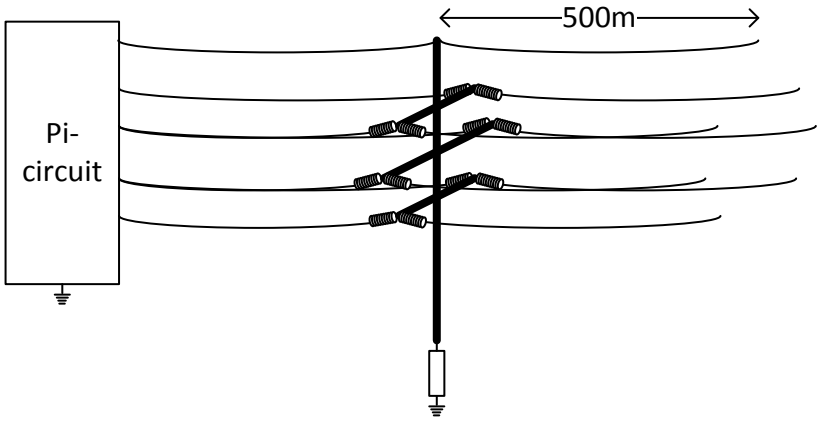

Figure 8-24: Complete simulation model termination, span width 500 m

The main reason behind that arrangement is to enable travelling waves to have an effect on the tension towers insulator voltages and provide a more realistic voltage distribution at the tower footings. Furthermore, due to the frequency-dependency of the line model, it is impossible to terminate the line with the exact surge impedance to avoid reflections at the Pi-circuit termination. The travel time delay of the additional three suspension tower spans with 200 span widths, suspension with 350 m or one tension tower with 500 m span width ensures that any reflections at the Pi-circuit are delayed and damped out before arriving at the tension tower insulator. In simulations with the Monte-Carlo Method,

additionally the power-frequency voltage in form of a DC voltage, as discussed in subsection 8.1.1, is implemented.

8.4.2: LIGHTNING STROKE MODEL

For the injection of the lightning current stroke waveform, the current source model described in subsection 2.3.1 is applied. The connection to the specific lightning attachment point is made through a set of switches in PSCAD/EMTDC. For the generation of the waveform shape, the improved double exponential description in subsection 2.3.4 to 2.3.6 for negative first, negative subsequent and positive stroke is implemented. For the description of negative first strokes the parameter sets from Takami (Japanese parameter set) in table 2-3 and table 2-4 and the impulse charge for the first 100 µs in table 2-6 is used. For negative subsequent strokes the parameter set from CIGRE in table 2-7 and the impulse charge parameter for the first 50 µs in table 2-9 is implemented. For positive stroke parameters the set from Berger provided in table 2-12 is inputted in the mathematical description.

8.4.3: TRANSMISSION LINE SPAN MODEL

To model a transmission line span, taking the lightning attachment locations into account, four connected 7-port frequency-dependent line models with frequency-dependent earth-return, as concluded in section 3.3, are utilized. The necessary input data to the LCP is taken from the conductor data sheets in appendix B.4 and B.5 and the necessary heights and sag from appendix F.1 for the minimum, standard and maximum tower height of the sample 400 kV line. To include the frequency-dependent earth-return, experimental frequency-dependent soil data from Portela in table 3-2 is applied.
With regard to the flashover mitigation methods described in section 7.2 and 7.3, where underbuilt shield wires and guy wires have to be modelled, the available shield wire data from appendix B.4 is applied.

8.4.4: CAP-AND PIN INSULATOR STRING WITH ARCING HORNS

As outlined in chapter 4, the Motoyama leader progression model in combination with the parameter set from table 4-3 and table 4-4, determined from flashover tests, is used to model the cap-and-pin insulator strings with arcing horns. The arc gap length is taken

from appendix B.4 and is equal for both tension and suspension strings. However, due to the double insulator string arrangement for tension strings on a tension tower, some simplifications have to be made. Although, a double string still contains one set of arcing horns, two sets of strings are mounted on a tension tower, electrically connected in parallel. Since the pre-discharge current of an arc gap reduces the applied voltage, it can be deducted, that two parallel arc gaps encounter both a lower voltage across the gap due to two possible paths for the pre-discharge current to flow. Under this assumption, the double string arrangement of a tension tower is modelled as a single string featuring an additional safety margin for the assessment of the flashover rates.

8.4.5: TOWER MODELS

For modelling of tension and suspension towers, the distributed line tower model in subsection 5.3.3 alongside the according surge impedance calculation is applied, following the conclusion in section 5.4 to reduce surge velocity to 90% of the speed of light to take into account the towers slanted structure. The calculated values for the three tower heights are summarized in appendix F.1. Furthermore it has to be noted, that as a result of the calculation and modelling process to model each tower story as a single cylinder, only one electrical connection at the tower foot is available to connect an earthing system model, instead of modelling all four tower feet.

8.4.6: EARTHING SYSTEM MODELS

With regard to the modelling of the typical earthing systems used for 400 kV towers of the sample line and further for the mitigation methods to be investigated, a decision on applicable models based on the earthing arrangements geometry is made.

In general, a standard tower footing consists of four foundations, which comprise some sort of rod shape electrode. Therefore, the simple resistance model, applicable to rod and hemispherical electrode shapes is applied, which comprises a noticeable safety margin. Therefore, also the developed improved earthing modelling with ionization and frequency-dependent effects in subsection 6.3.2 is applied for a whole tower foundation. For an advanced earthing method, the counterpoise earthing strip model from section 6.3 is utilized.

Due to the single node restriction imposed by the tower model, superposition is employed for modelling earthing systems connected to each foot of the tower. This principle is described for the four rod and counterpoise models in subsection 6.3.1 and 6.3.3. For all

base scenario simulations, an equivalent rod model with 4 m length and 0.2 m thickness for each tower foundation is assumed. In dependency of the soil resistivity, this leads to a low-frequency footing resistance in the range of measured values of the sample line, summarized in table 8-3.

Table 8-3: Equivalent resistance for 4 parallel 4 m long 0.2 m thick rod in square distance of 8 m

ρ in Ωm	100	500	1000	2500	5000	10000
R in Ω	4.5	22.75	45.5	113.75	227.5	455

For counterpoise, data from the example in subsection 6.3.3 is used. This is a 2.5 mm copper wire buried 0.5 m in soil. To form a counterpoise as in figure 6-20, two wires are run in parallel at a distance 22 m apart on each side of the tower in the direction of the line route. The length of the counterpoise wires is set to the effective length in dependency of the soil resistivity, derived from figure 7-7, summarized for the investigated soil resistivities in table 8-4.

Table 8-4: Effective length of counterpoise in dependency of the soil resistivity

ρ in Ωm	100	500	1000	2500	5000	10000
L in m	10	24	34	57	83	121

8.4.7: ARRESTER MODEL

The tower line arresters are modelled with the simplified arrester model in subsection 7.1.2, taking only the residual voltage value at 1/2 µs/10kA and 8/20 µs / 10 kA into account, since the scale parameters for arresters in [298] are employed to create the V-I-curve. The continuous operating voltage V_C of the arresters should be at least 5 % higher than the maximum power frequency line-to-earth voltage $V_H/\sqrt{3}$ of the system. With a maximum system voltage of 420 kV, values close to V_C are chosen, summarized in table 6-3. The stray inductances of the arrester are calculated according to equation (7.6) and (7.7).

Table 8-5: Tower line arrester data

V_C [kV]	267
U_R(1/2µs, 10kA) [kV]	932
U_R(8/20µs, 10kA) [kV]	855

8.4.8: REMARKS ON SAFETY MARGINS IN THE COMPLETE MODEL

As already outlined in the summary and conclusion of chapter 2 to chapter 7, modelling and simulation of lightning strokes to transmissions lines necessitates a certain degree of simplification. This is ascribed partly to the kind of simulation approach, namely the electromagnetic transient approach, which features no natural electromagnetic coupling between modelled elements, but mainly to the derivation of EMT models from a limited number of measurements and general simplifications when modelling physical behaviour of apparatus. In this respect, the engineering approach to employ safety margins, where uncertainties in the modelling exist, is applied.

In the following, a list of major simplifications is provided:

Lightning Stroke Model:

- Neglect of lightning channel impedance leads to higher injected currents
- Lightning stroke waveforms based on limited amount of measurements, especially for positive strokes
- Lightning stroke waveform shape solely dependent on stroke current amplitude

Transmission Line Model:

- Neglect of corona phenomenon, however influence is negligible
- Current earth-return frequency-dependent soil model based on averaged soil measurements
- Simplification and worst-case approximation of conductor sagging

Insulator with Arcing Horns Model:

- Leader progression model based on tests with 1.2/50 µs waveshape, but lightning strokes generally feature shorter tails, which leads to a better flashover performance in reality
- Neglect of changing environmental conditions, such as rain, air pressure and humidity

Transmission Line Towers:

- Attenuation and distortion of travelling waves due to slanted structure of pylons are neglected
- Tower feet are summarized in one connection to grounding system
- Electromagnetic coupling of lightning channel and tower are neglected

Tower Earthing System:

- Simplification of foundations modelled as single rods, worst-case assumption
- Ionization parameters independent of soil properties
- Horizontal wire (counterpoise) soil ionization neglected
- Frequency-dependent soil model based on averaged soil measurements

Monte-Carlo-Method:

- Electro-geometric model to decide attachment to shield/phase wire based solely on stroke current amplitude
- Division of strokes to span and tower based on limited measurement data

CHAPTER 9: SIMULATION RESULTS AND EVALUATION

This chapter presents the simulation results and evaluation of the lightning performance of a transmission line, either with the critical current I_c, used in CIGRE [24] or the ratio of simulations leading to a flashover to the total number of simulations F/N in the Monte-Carlo procedure in section 8.2. Therefore, as discussed in section 8.3, simulation scenarios, simulations are performed to determine the current for shield and phase wires, at and above a flashover occurs, called the critical current I_c, as well as simulations using the Monte-Carlo method to take into account the randomness of lightning. Since both these values, which are dependent on the transmission system and line route layout, are a main input to the flashover ratio calculation, they are also criteria for measuring the general performance of a transmission line system and thus a measure for any flashover mitigation method.

In the following, first the simulation results for critical current determination, both for base cases and flashover mitigation cases are presented, followed by the associated evaluation of the flashover rates. Second, the results for the flashover ratio F/N, determined with Monte-Carlo method simulations and the evaluation of flashover ratios are discussed. At last, a comparison of both critical current determination and the Monte-Carlo method results is conducted and conclusions drawn on the advantages and disadvantages of each mitigation method.

With regard to acceptable design limits for $SFFOR$ and $BFOR$, [7] recommends a value of 0.05 flashovers/ 100km-year for the $SFFOR$ for the critical current determination method and attachment calculation with the EGM. For $BFOR$ design limits, no explicit recommendations are found, but since the $BFOR$ is dependent on the lightning flash density as well as tower earthing conditions, transmission and distribution system operators use values between 0.2 to 4 flashovers/ 100km-year [7], [279], [315] based on operation experience.

9.1: CRITICAL CURRENT DETERMINATION METHOD

9.1.1: SIMULATION RESULTS OF BASE SCENARIOS

The critical current values are obtained from simulations with a variety of soil resistivities (100 Ωm to 10000 Ωm), tower height (minimum 'MIN', standard 'STD' and maximum 'MAX') and span length of the transmission system (200 m to 500 m). Direct hits to the tower and phase wires with positive and first negative and negative subsequent lightning strikes are simulated and the stroke current amplitude increased in each simulation until a flashover occurs.

A summary of critical current results for base cases, stroke to shield wire, with a simple resistance representation of the tower earthing system, as well as an earthing rod model representation with frequency-dependent and soil ionization behaviour is given in figure 9-1 to figure 9-6. Tables of simulation results are provided in appendix G.1. For all cases the maximum simulated current is 1003 kA.

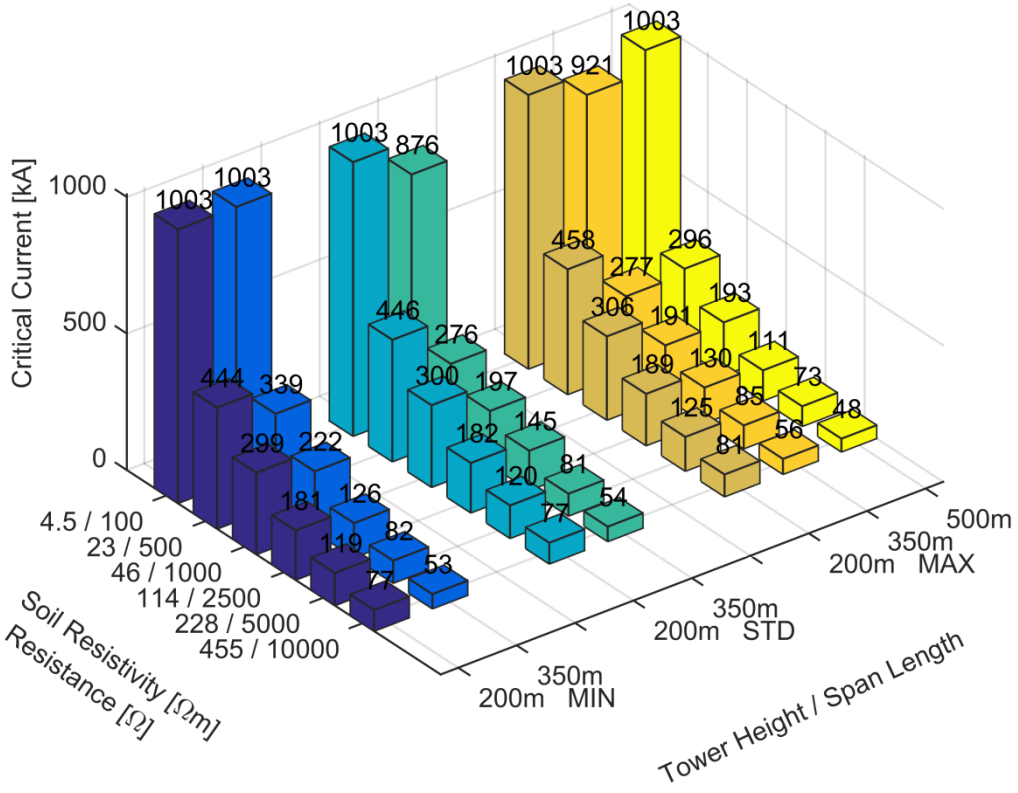

Figure 9-1: Results of critical current determination for shield wire, positive stroke polarity, base scenarios with simple resistance tower earthing representation

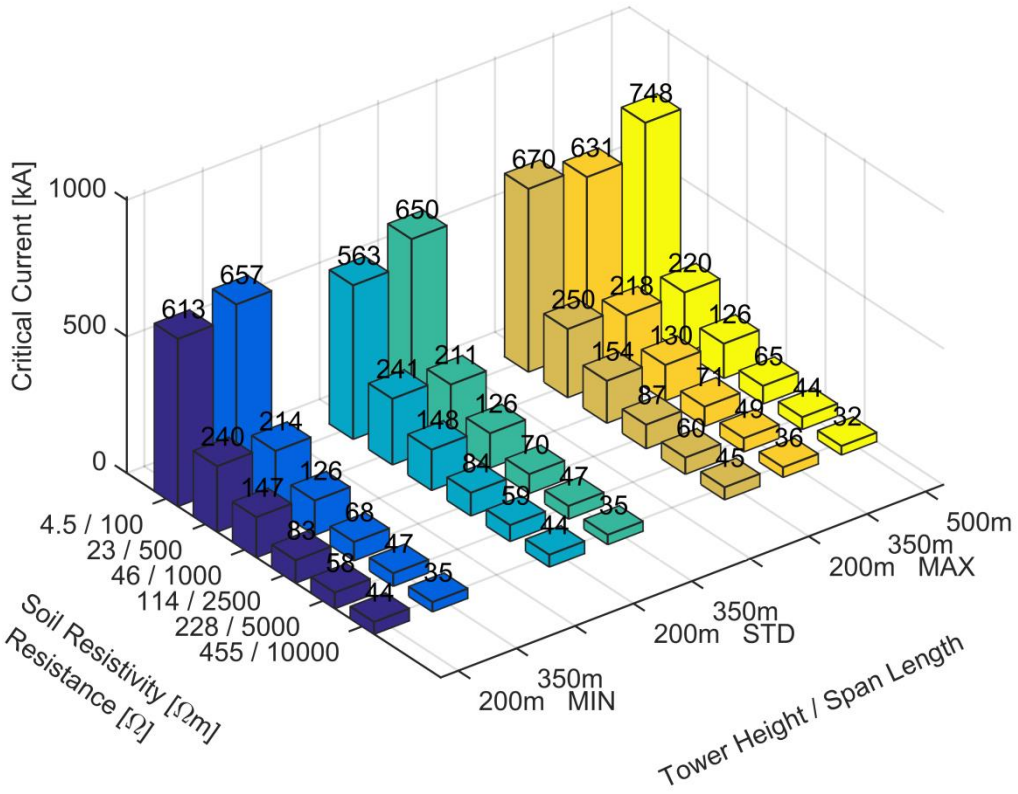

Figure 9-2: **Results of critical current determination for shield wire, negative stroke polarity, base scenarios with simple resistance tower earthing representation**

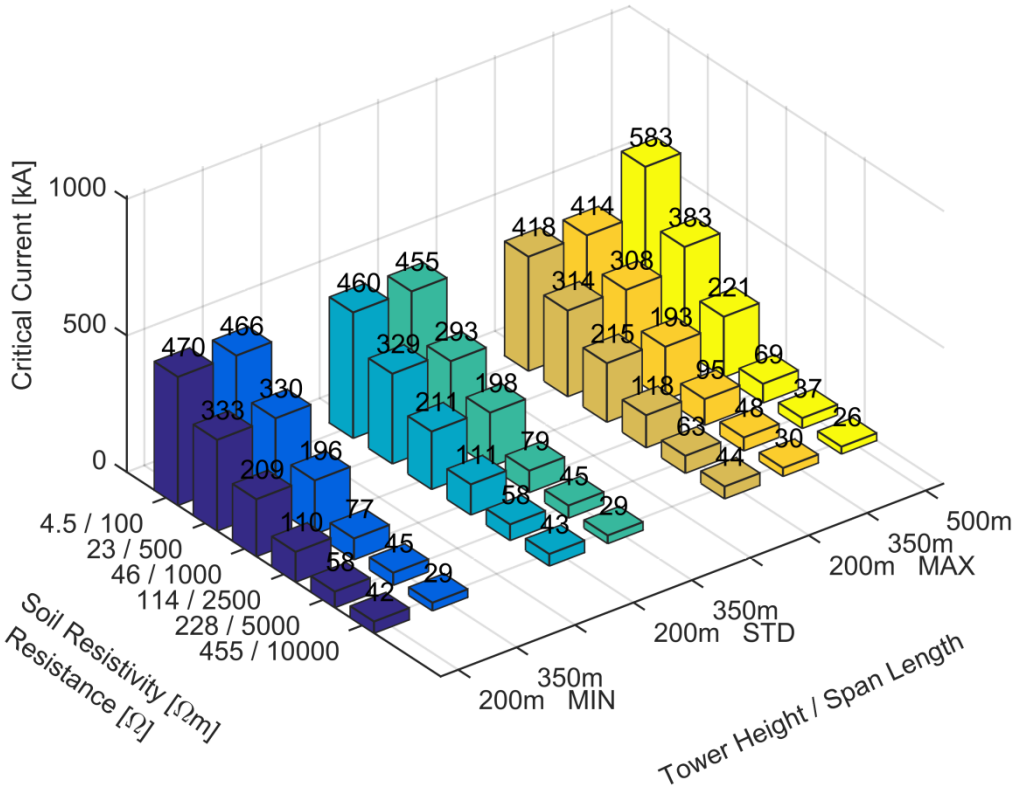

Figure 9-3: **Results of critical current determination for shield wire, negative subsequent stroke polarity, base scenarios with simple resistance tower earthing representation**

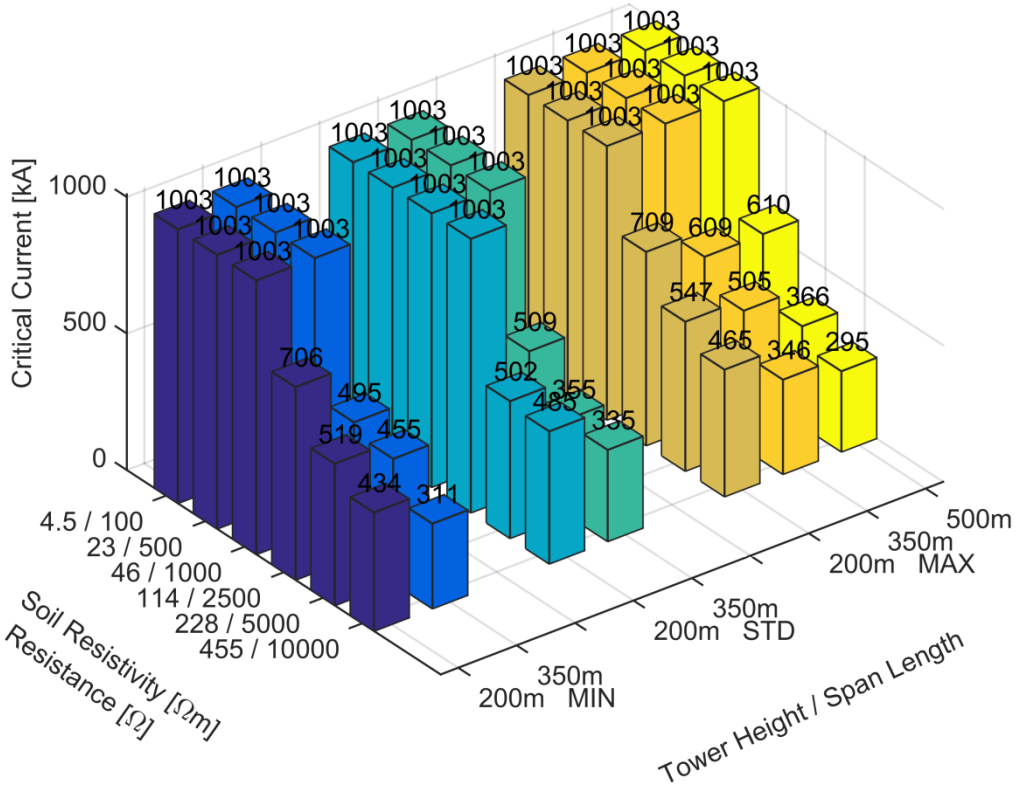

Figure 9-4: **Results of critical current determination for shield wire, positive stroke polarity, base scenarios with improved tower earthing model representation**

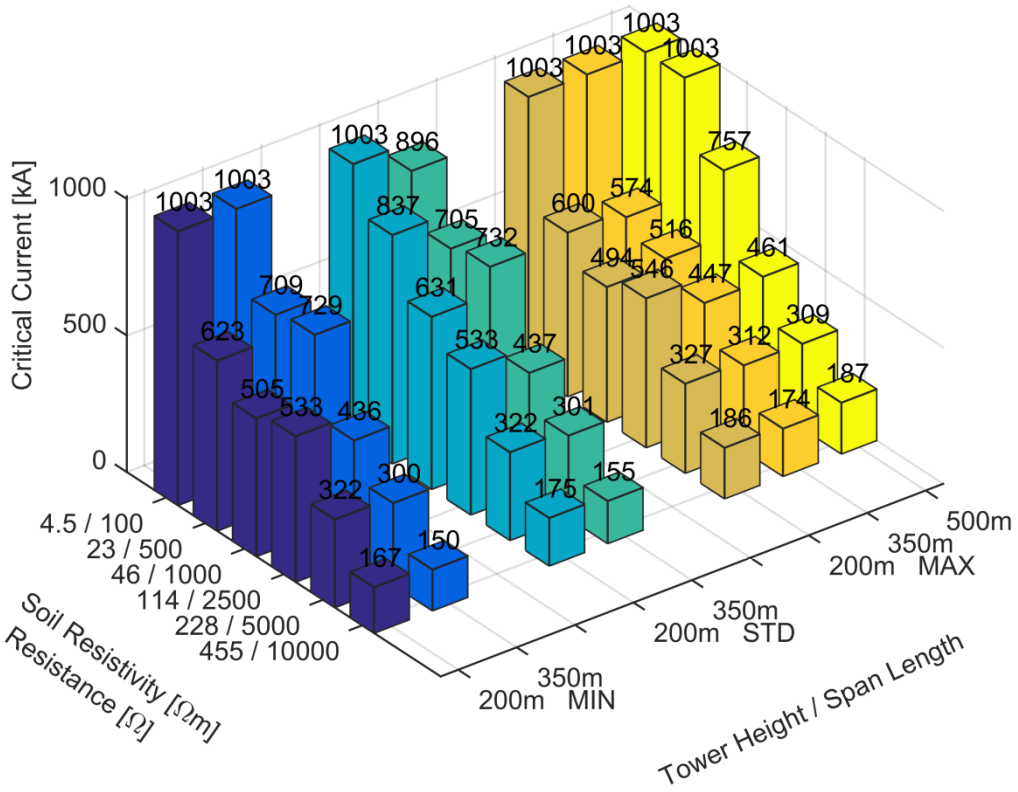

Figure 9-5: **Results of critical current determination for shield wire, negative stroke polarity, base scenarios with improved tower earthing model representation**

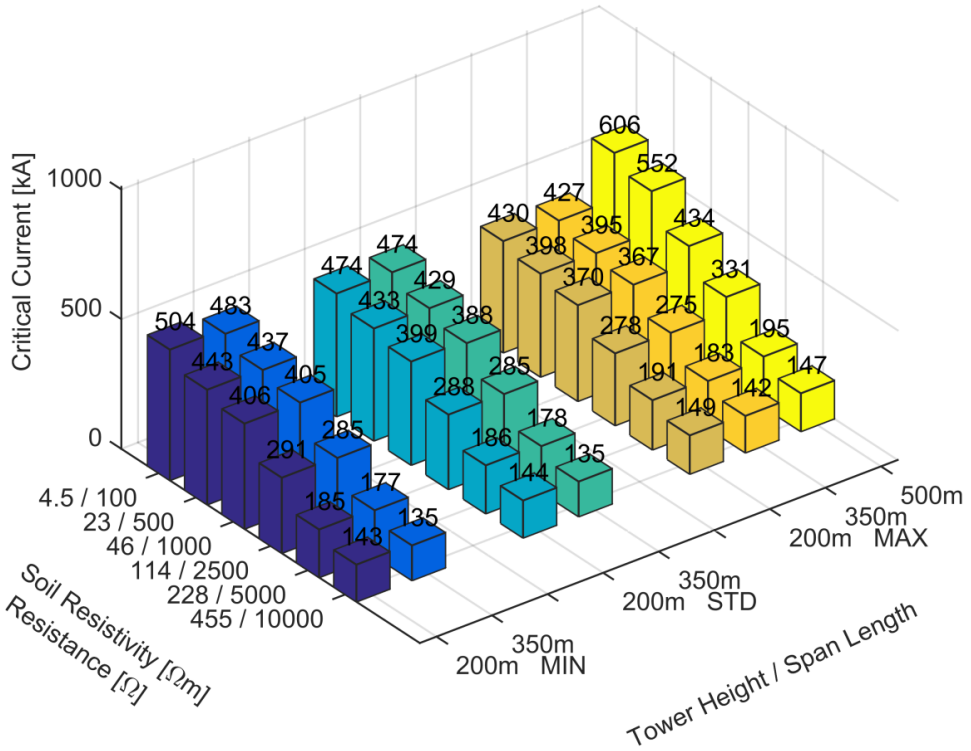

Figure 9-6: Results of critical current determination for shield wire, negative subsequent stroke polarity, base scenarios with improved tower earthing model representation

In general the simulation results with respect to back-flashovers show that:

- The critical current decreases with increasing soil resistivity,
- the critical current decreases with increasing span length,
- the tower height of the sample transmission line suite has a minor influence on the critical current independent of the stroke polarity and
- overall highest critical currents are seen at positive strokes, followed by first negative and subsequent negative strokes.

A comparison of the resistive and improved earthing system model shows that the effect of the variable impedance and foremost the ionization effect has a major impact on critical currents. The ionization effect is especially pronounced for strokes of negative polarity when the span length is increased to 500 m due to the smaller number of earthing points, which leads to a higher current density and a further increase of ionization effect and lower resistance respectively.

Following the determination of critical currents for hits to the shield wire, a summary of the results for direct hits to the upper phase wire is presented in figure 9-7 to figure 9-12 for base scenarios with simple resistance tower earthing and improved tower earthing representation. The whole simulation results are provided in appendix G.1.

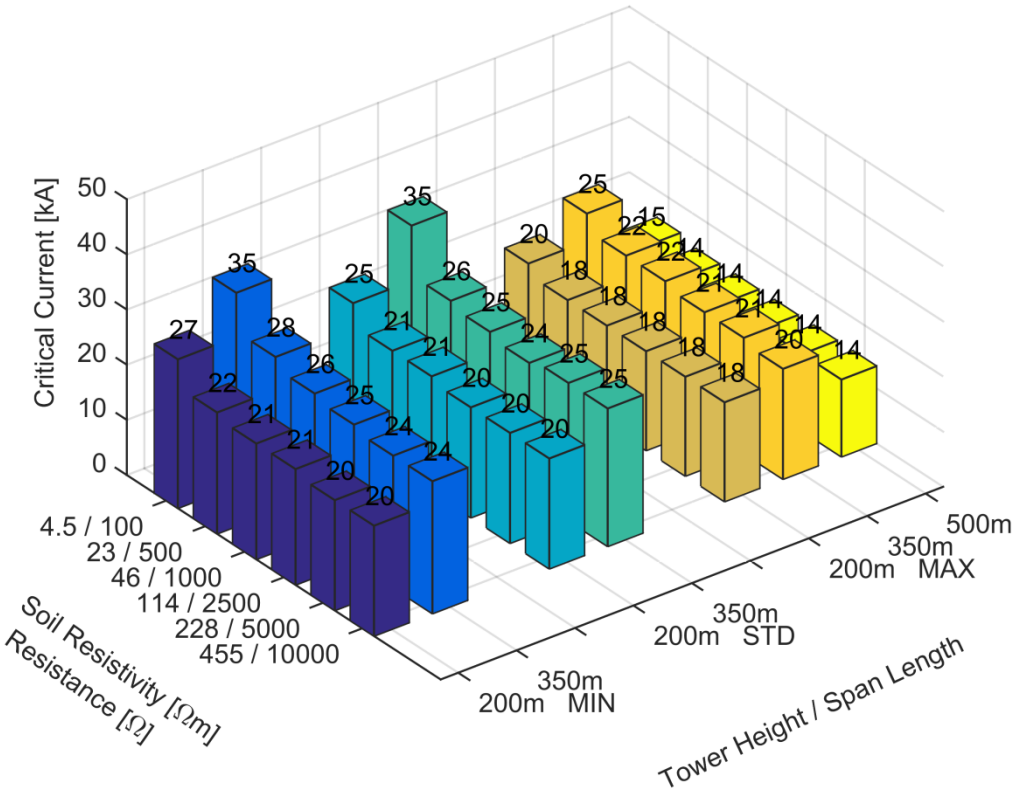

Figure 9-7: **Results of critical current determination for top phase wire, positive stroke polarity, base scenarios with simple resistance tower earthing representation**

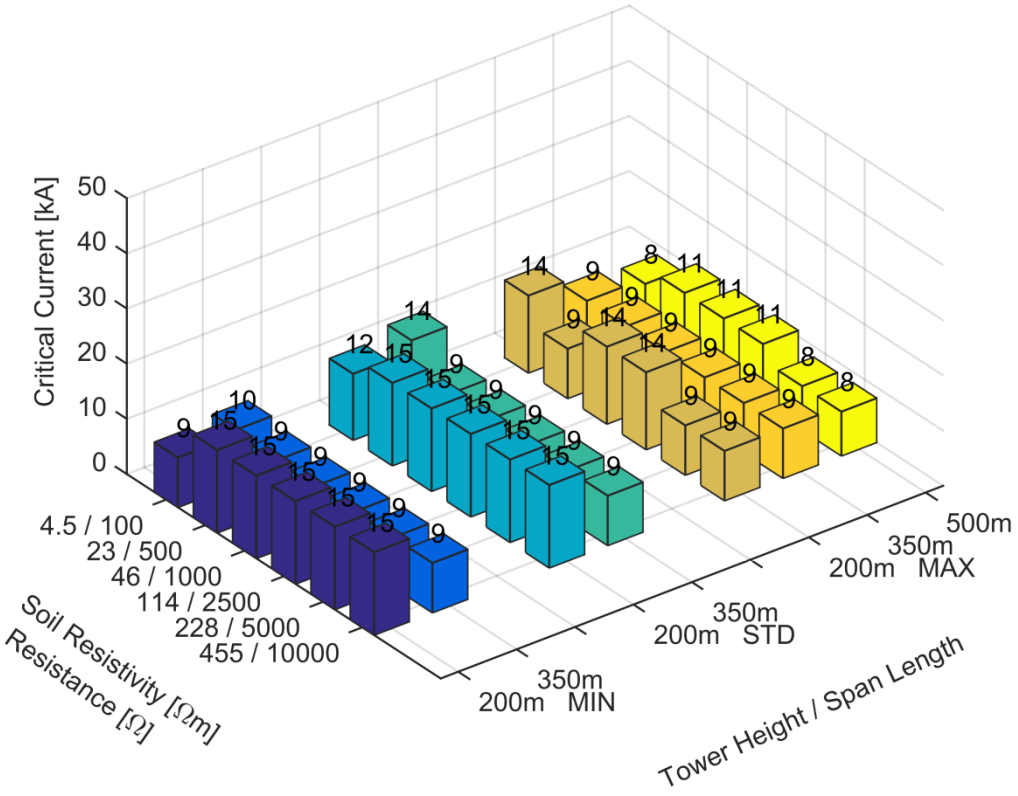

Figure 9-8: **Results of critical current determination for top phase wire, negative stroke polarity, base scenarios with simple resistance tower earthing representation**

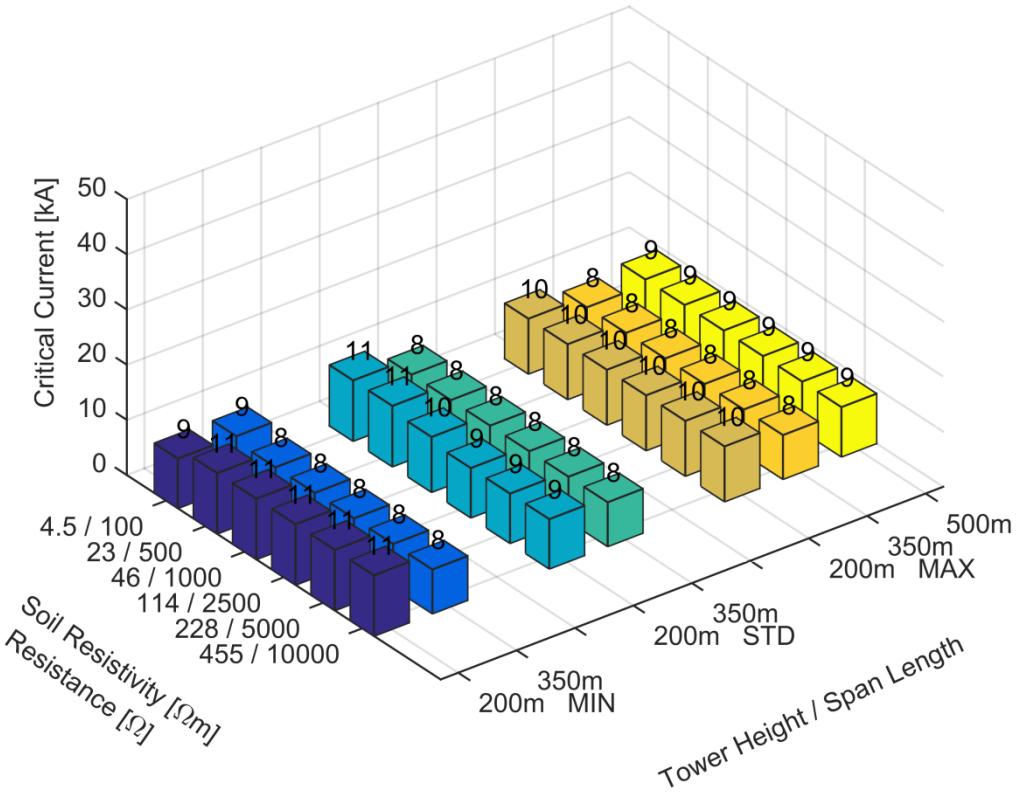

Figure 9-9: **Results of critical current determination for top phase wire, subsequent negative stroke polarity, base scenarios with simple resistance tower earthing representation**

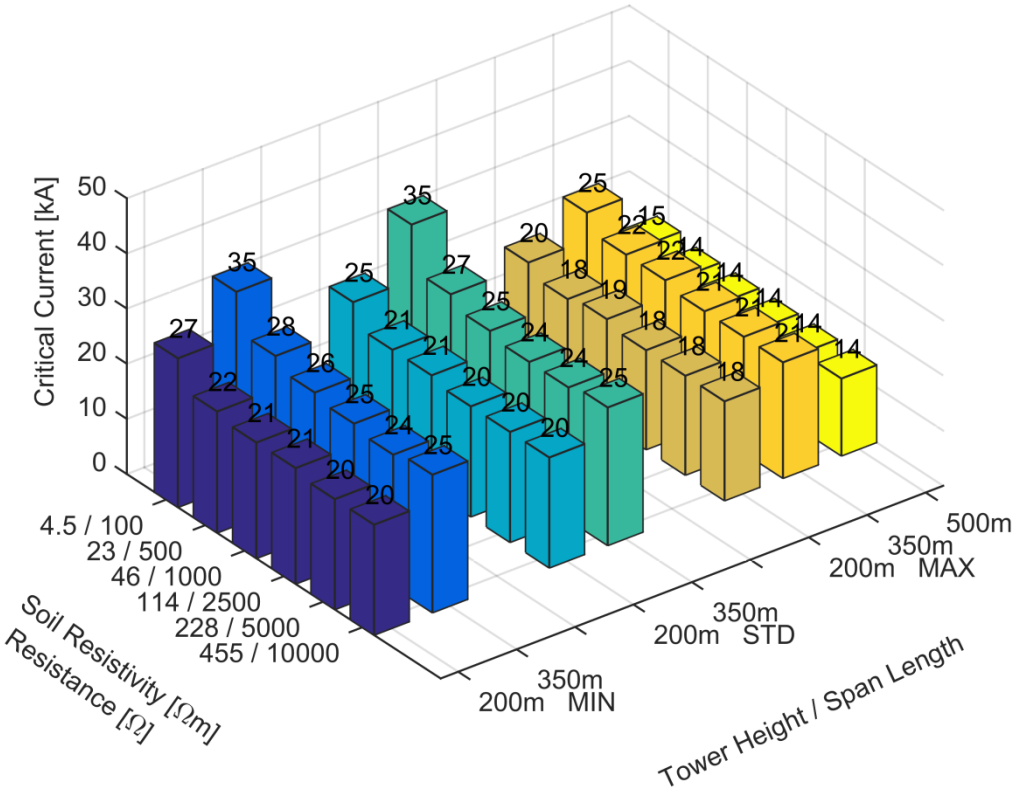

Figure 9-10: **Results of critical current determination for top phase wire, positive stroke polarity, base scenarios with improved tower earthing model representation**

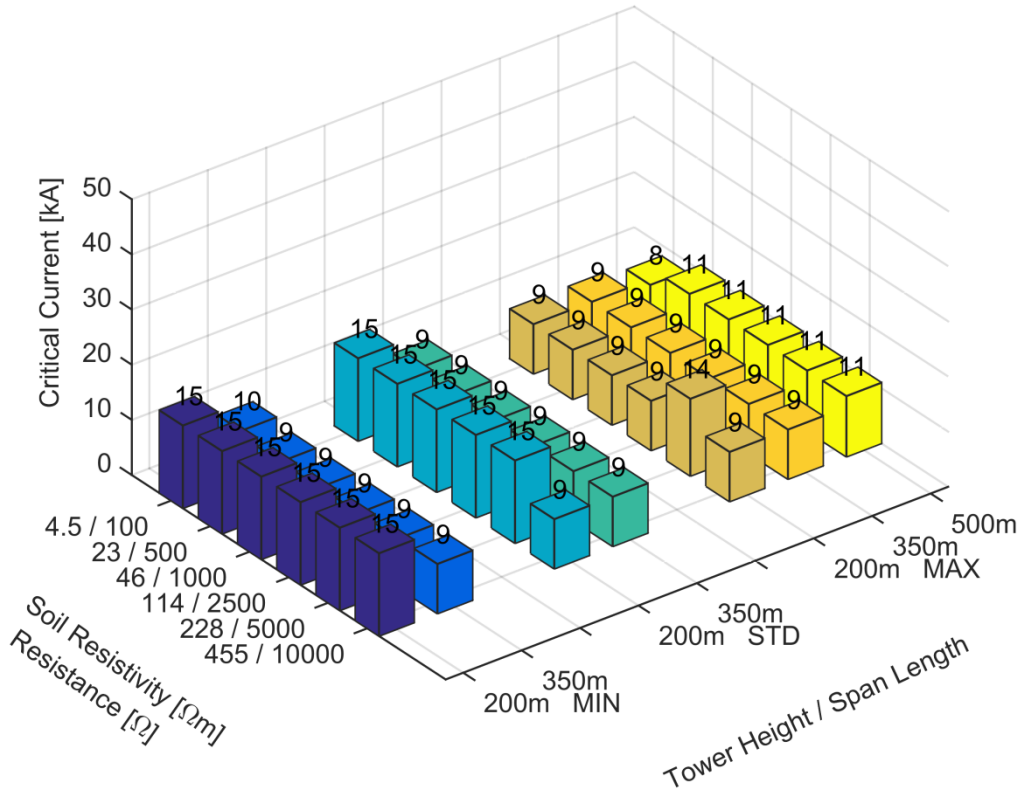

Figure 9-11: **Results of critical current determination for top phase wire, negative stroke polarity, base scenarios with improved tower earthing model representation**

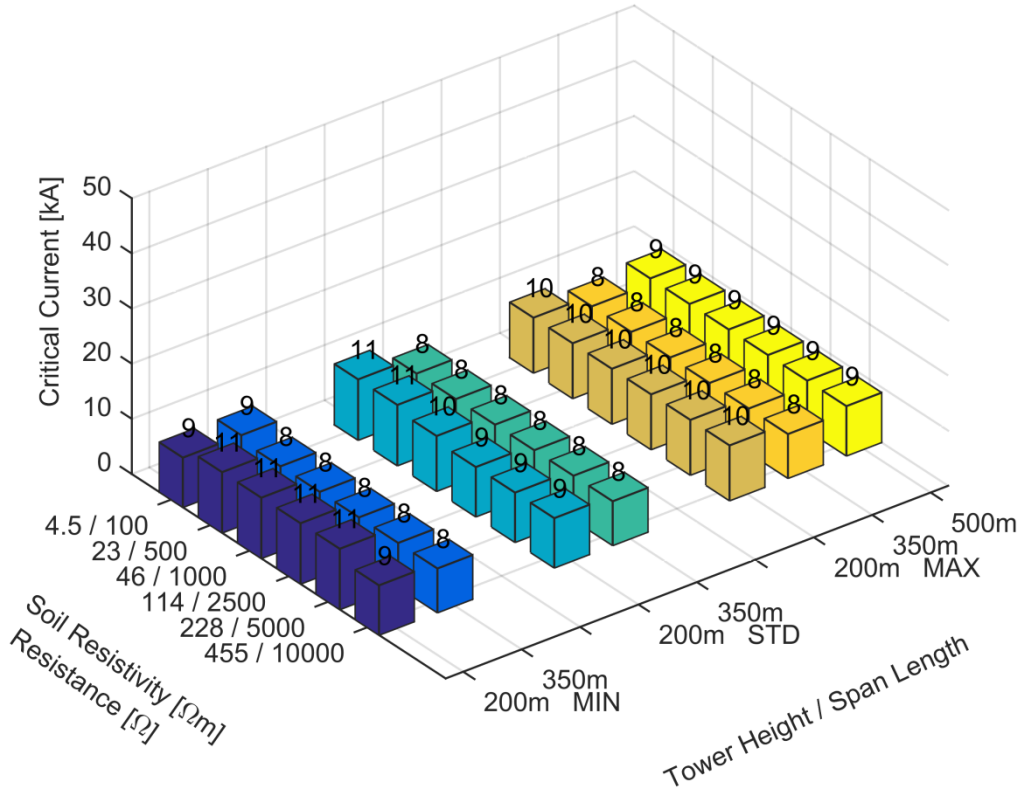

Figure 9-12: **Results of critical current determination for top phase wire, subsequent negative stroke polarity, base scenarios with improved tower earthing model representation**

The simulation results for direct strokes to the phase wires reveal that

- critical current values for different phases, tower heights, span length and soil resistivities differ only marginally (in the range of 3 kA) for negative polarity with an average of 9 kA,
- critical current values for negative first and subsequent strokes do not differ within the resolution of the parameter,
- critical current values for positive strokes are slightly decreasing with increasing soil resistivity, but decreasing with increasing tower height in the range of 20 to 40 kA and
- improving the tower earthing model does not change the critical current results.

9.1.2: EVALUATION OF FLASHOVER RATES CALCULATED FROM CRITICAL CURRENTS OF BASE SCENARIOS

The calculation of flashover rates based on the critical current assumes that only vertical first strokes occur and the attachment angle is not taken into consideration. To calculate the $SFFOR$ with equation (8.7), the critical distance D_C for strokes to the top phase wire as well as D_g' in formula (8.9) for the $BFOR$ need to be determined. Furthermore, to compare results for the various scenarios investigated, some simplifications in equation (8.7) and (8.8) are made in equation (9.1) and (9.2). The equations are divided by the line length L, multiplied by 100 and the ground flash density is recalculated to flashes per square-km per year. The $SFFOR$ and $BFOR$ are therefore expressed in flashes per 100 km per year. In general, strokes within the span have to be taken into consideration as well. In [7], it is found that due to the attenuation of surges along the transmission line, the actual $BFOR$ can be calculated from the $BFOR$ determined with critical currents from direct hits to the tower by a multiplication of the factor 0.6. Although it is not explicitly written in [7], the same argument is valid for the $SFFOR$. Therefore the same factor is applied as well.

$$SFFOR = 0.6 \cdot 2N_G \int_{I_c}^{I_m} D_C f(I)\, dI \tag{9.1}$$

$$BFOR = 0.6 \cdot 2N_G \int_{I_c}^{\infty} D_g' f(I) dI \tag{9.2}$$

To consider both stroke polarities, the line flashover rate is calculated from a sum of $SFFOR$ and BFRs of each polarity and their ground flash densities from

table 2-15 respectively. As already noted, subsequent strokes are neglected in this type of calculation. The maximum current for an attachment to the shield wire I_m and distances D_C and D'_g are calculated with the EGM in section 8.1.2. The associated probability of the stroke currents is calculated with both the CIGRE and LLS Scotland distribution in table 2-14 and

table 2-15. The ground flash density N_G is based on the LLS Scotland data. The resulting flashover rate calculation results are illustrated in figure 9-13 to figure 9-24.

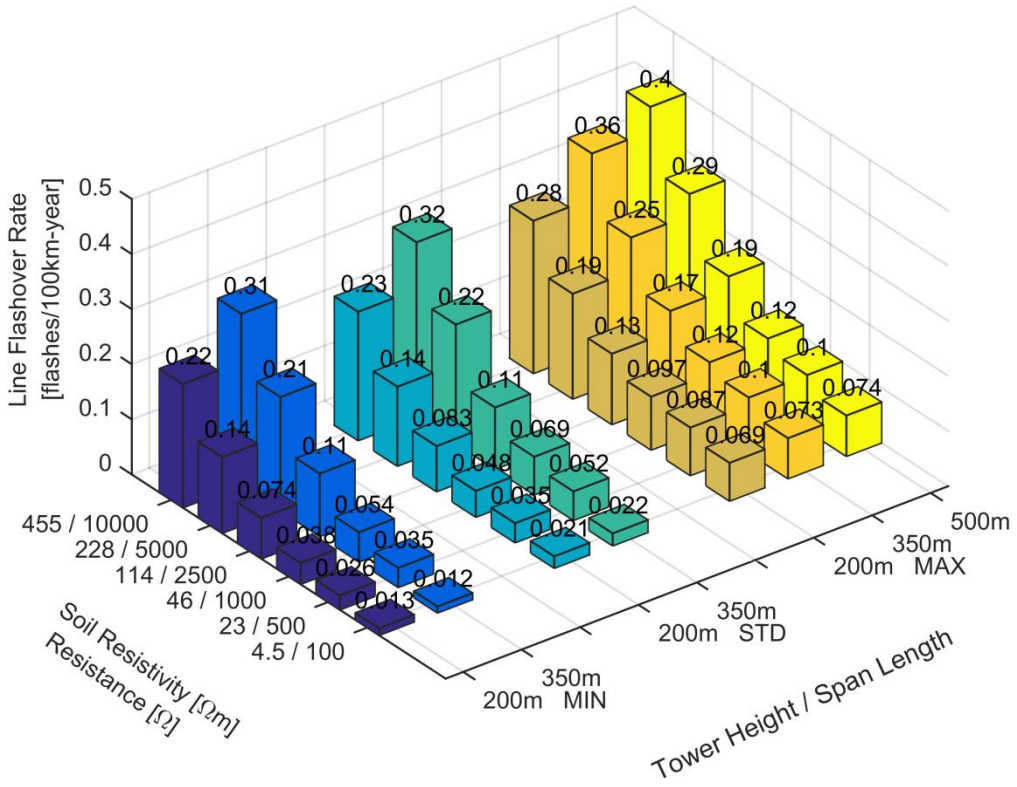

Figure 9-13: Line flashover rate from critical current determination, base scenarios with simple resistance tower earthing representation, CIGRE stroke distribution

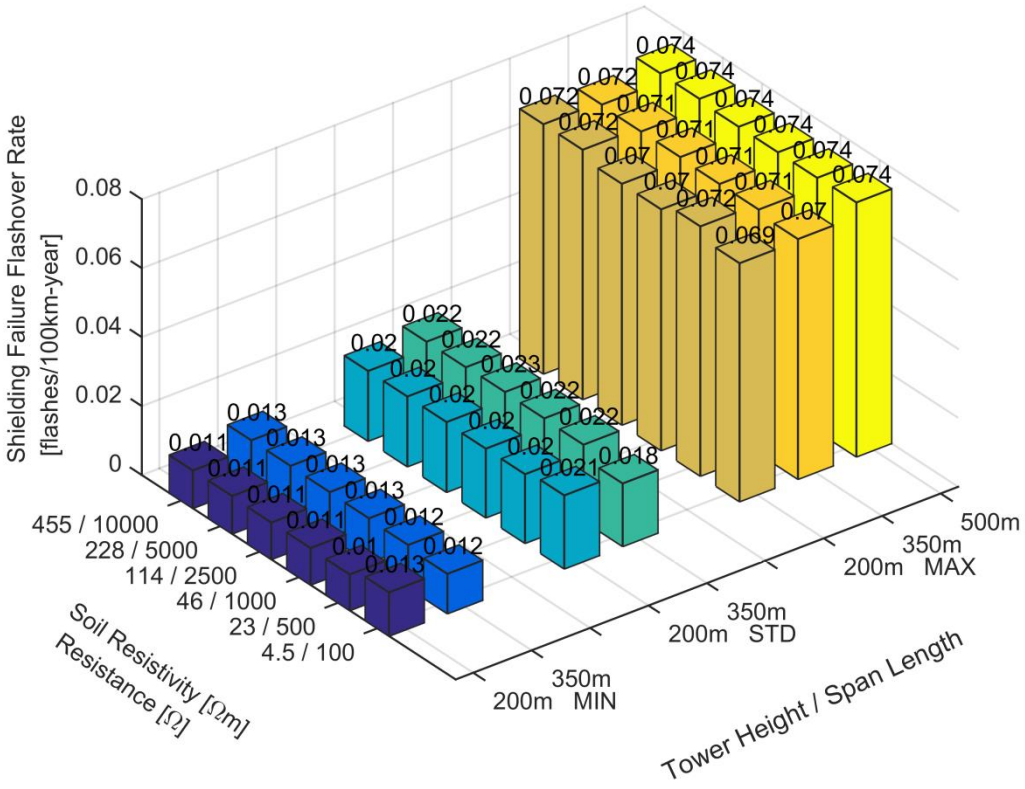

Figure 9-14: Shielding failure flashover rate from critical current determination, base scenarios with simple resistance tower earthing representation, CIGRE stroke distribution

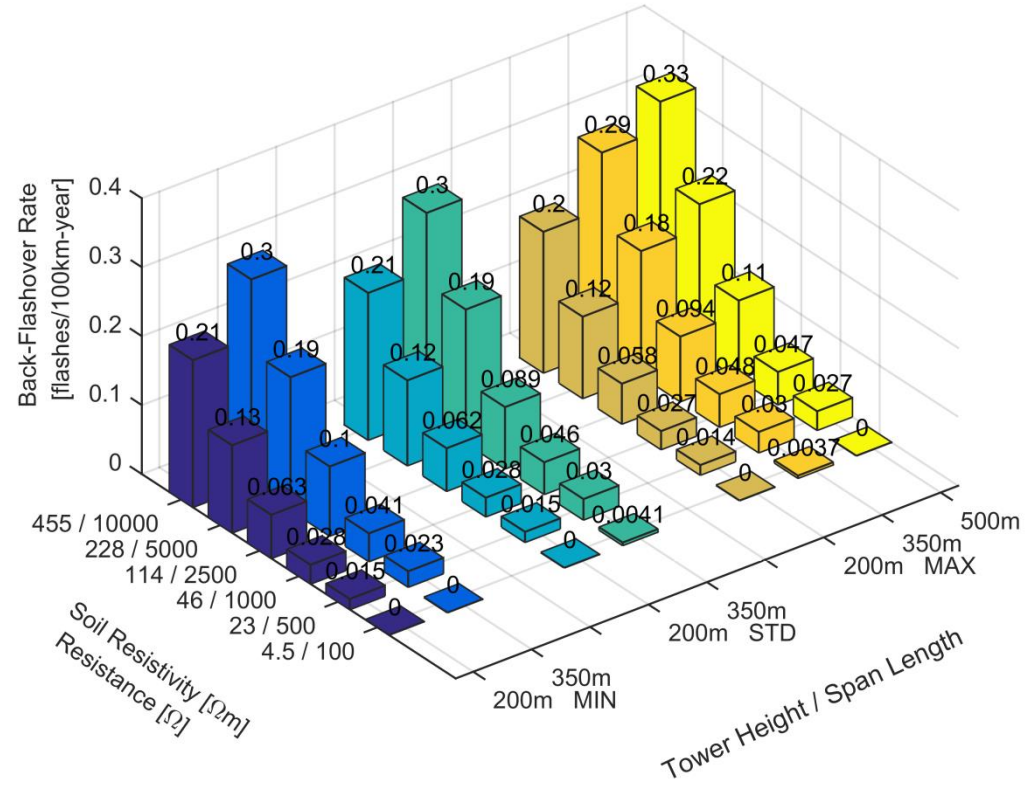

Figure 9-15: Back-flashover rate from critical current determination, base scenarios with simple resistance tower earthing representation, CIGRE stroke distribution

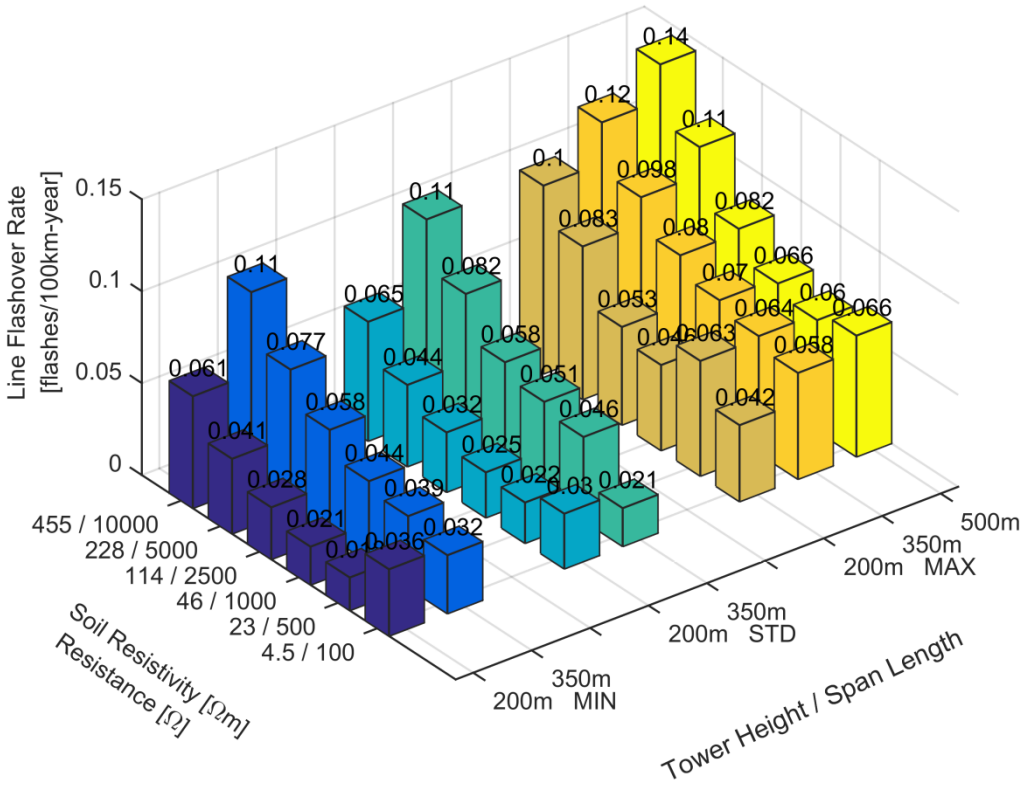

Figure 9-16: Line flashover rate from critical current determination, base scenarios with simple resistance tower earthing representation, LLS Scotland stroke distribution

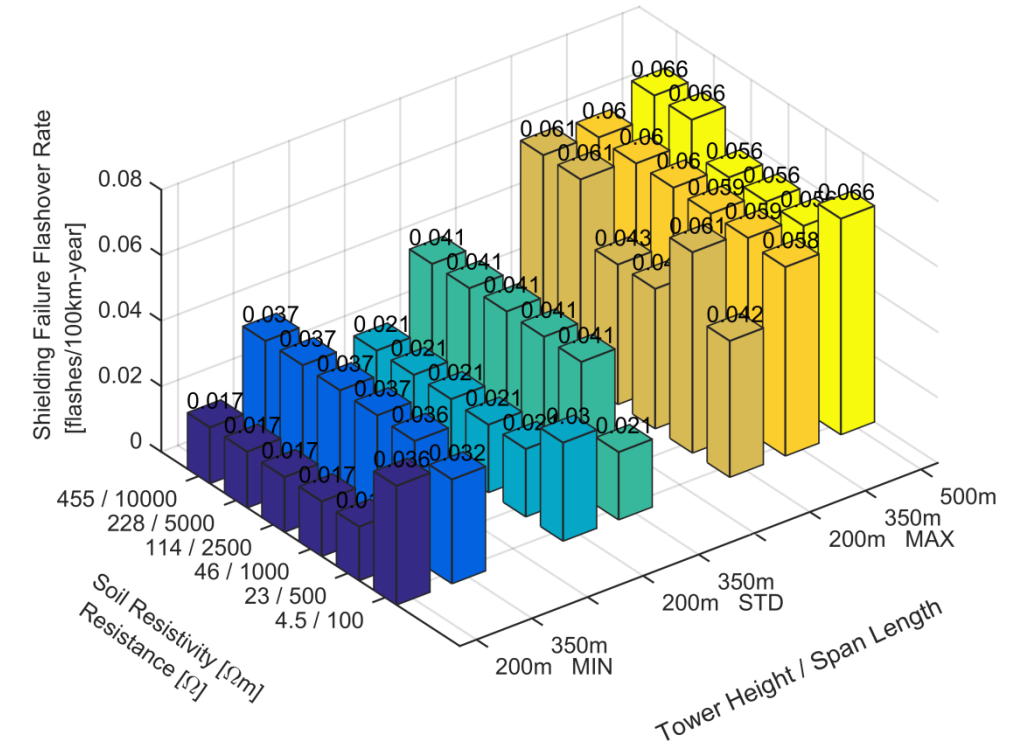

Figure 9-17: Shielding failure flashover rate from critical current determination, base scenarios with simple resistance tower earthing representation, LLS Scotland stroke distribution

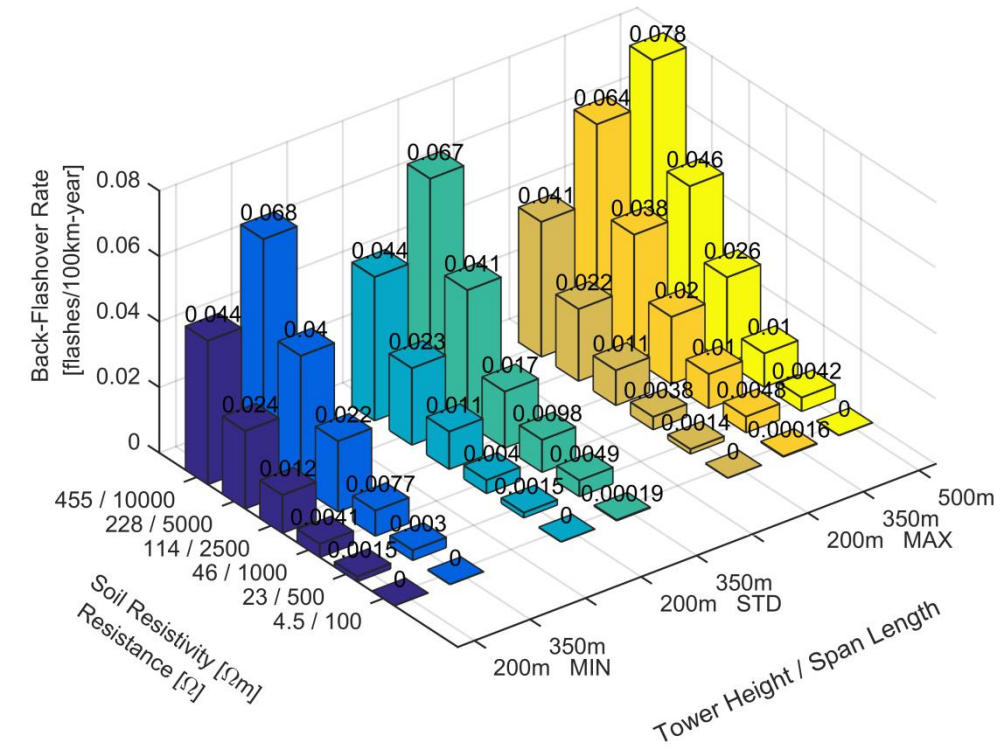

Figure 9-18: Back-flashover rate from critical current determination, base scenarios with simple resistance tower earthing representation, LLS Scotland stroke distribution

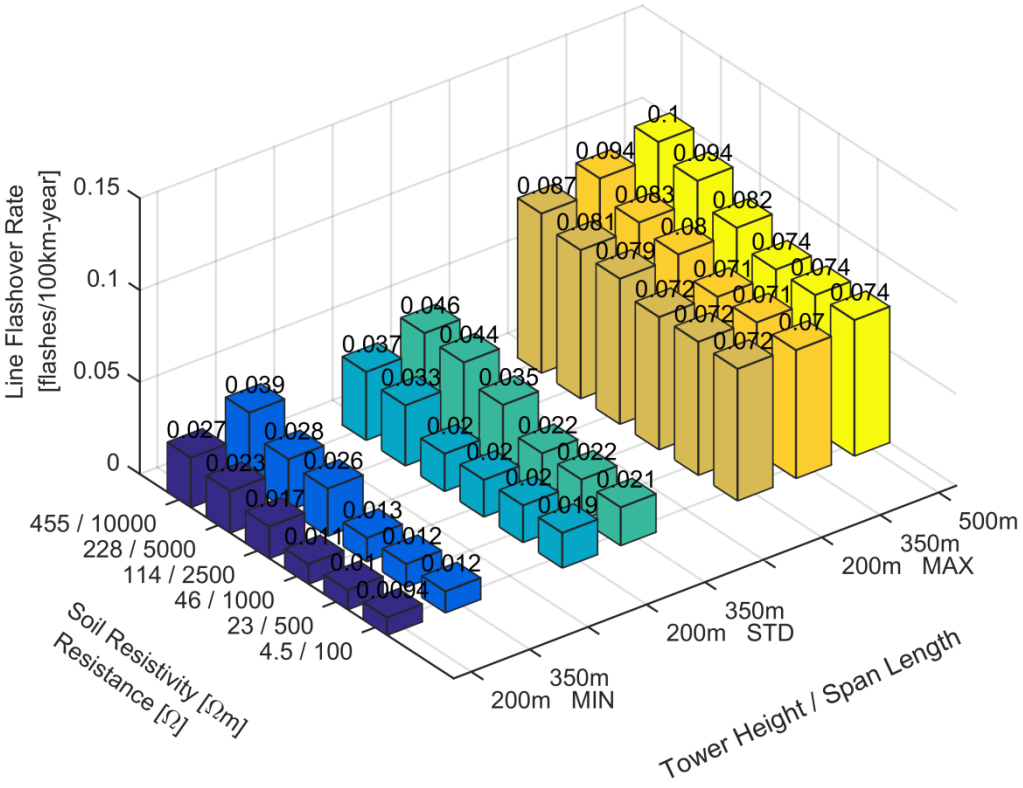

Figure 9-19: Line flashover rate from critical current determination, base scenarios with improved tower earthing model representation, CIGRE stroke distribution

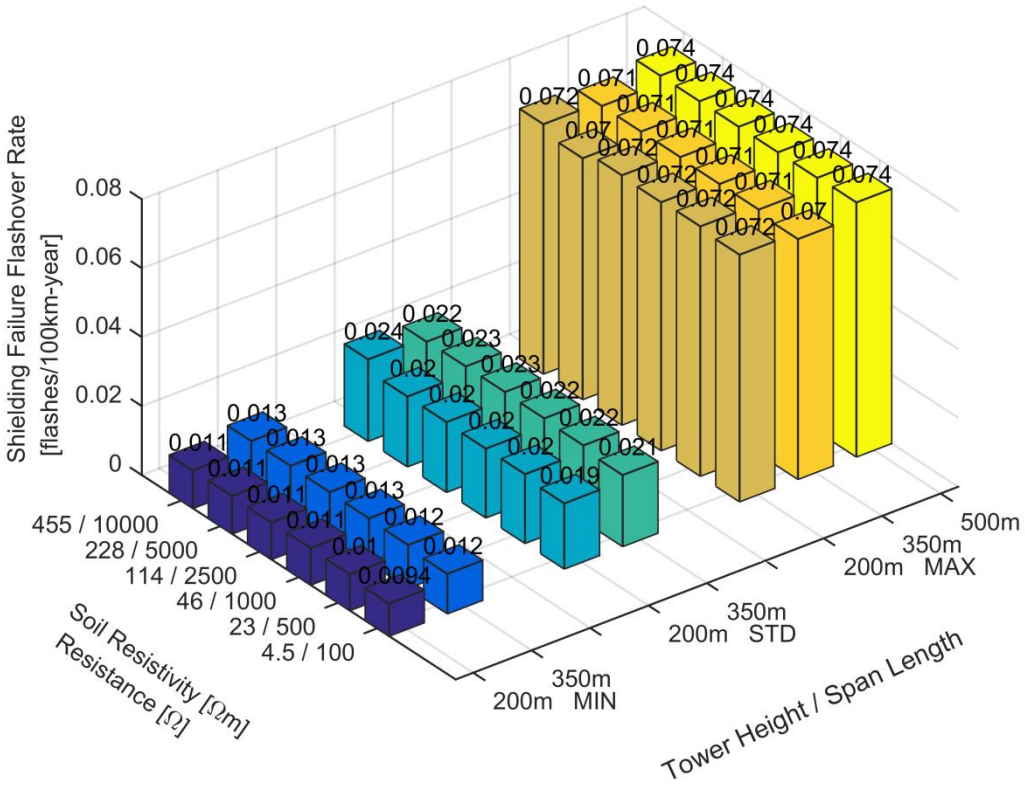

Figure 9-20: Shielding failure flashover rate from critical current determination, base scenarios with improved tower earthing model representation, CIGRE stroke distribution

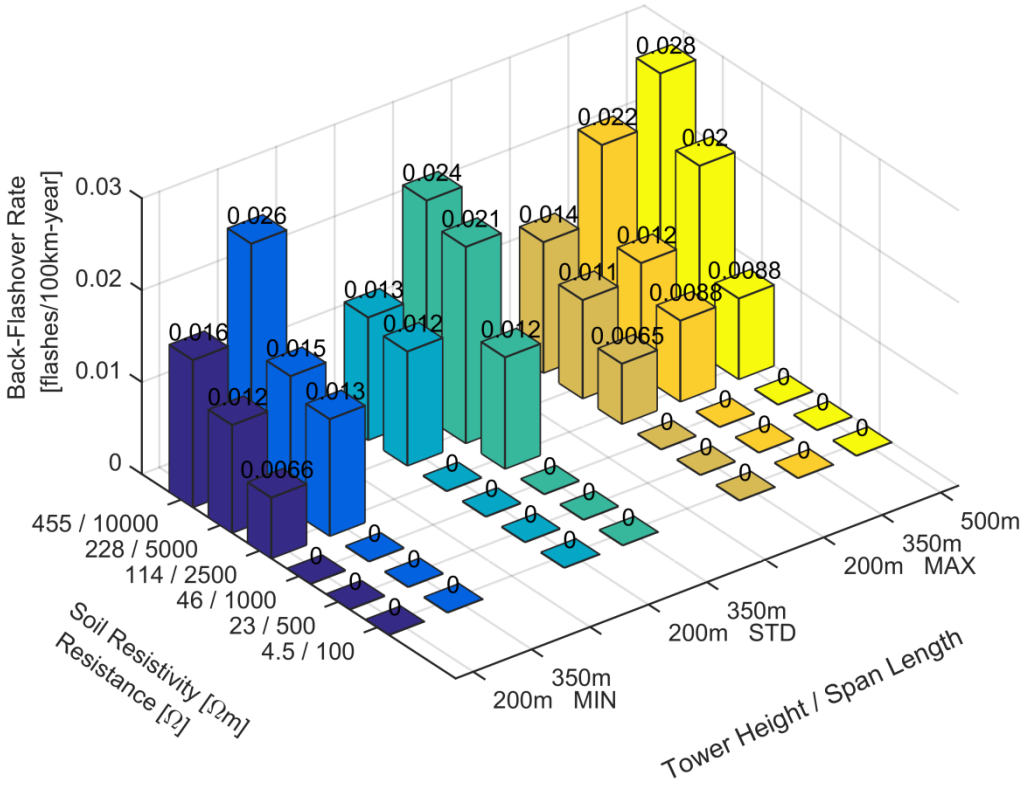

Figure 9-21: Back-flashover rate from critical current determination, base scenarios with improved tower earthing model representation, CIGRE stroke distribution

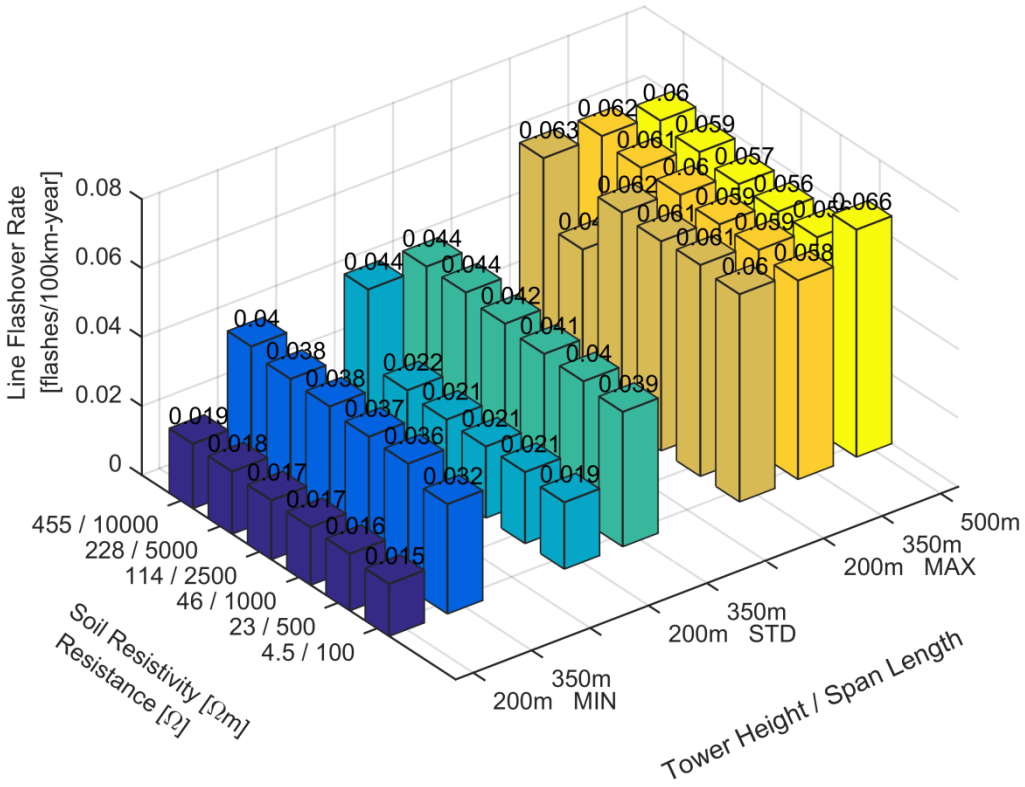

Figure 9-22: Line flashover rate from critical current determination, base scenarios with improved tower earthing model representation, LLS Scotland stroke distribution

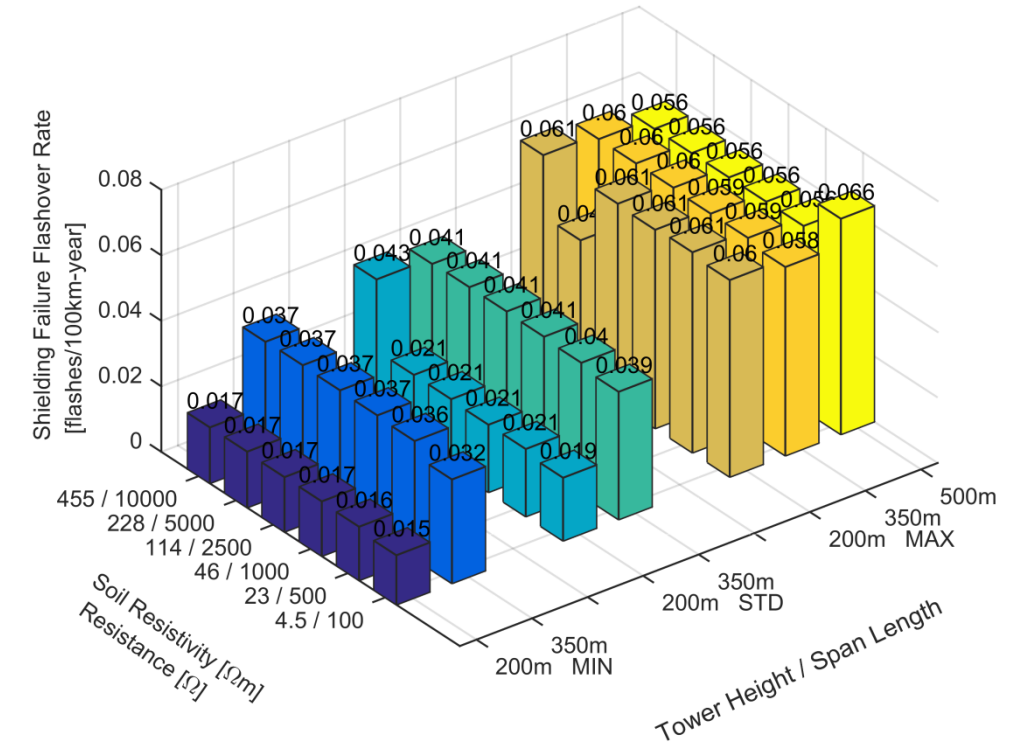

Figure 9-23: Shielding failure flashover rate from critical current determination, base scenarios with improved tower earthing model representation, LLS Scotland stroke distribution

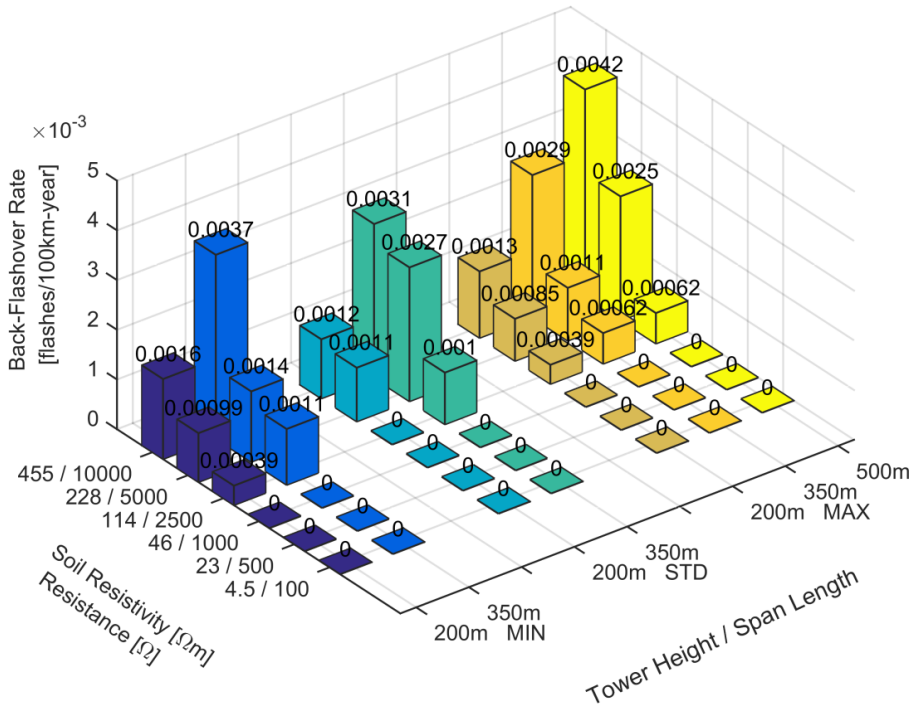

Figure 9-24: Back-flashover rate from critical current determination, base scenarios with improved tower earthing model representation, LLS Scotland stroke distribution

The evaluation of simulation results for the critical current determination and flashover ratio calculation clearly shows the impact of different stroke current distributions as well as an improved earthing.

- The $BFOR$ dominates the $LFOR$, with a maximum of 0.4 flashes per 100 km-year at a line span of 500 m and maximum tower height for CIGRE stroke distribution, basic scenarios and simple tower footing resistance.
- The flashover and back-flashover ratio increases equally with the increase in critical currents for increasing span length and soil resistivities.
- The $SFFOR$ is solely dependent on the tower geometry and height, respectively, where the EGM shows an bigger exposed area of the top shield wire at higher tower height and has a rather constant value for variation of span length and soil resistivity, approximately 0.07 flashes per 100 km-year.
- For the LLS Scotland distribution, a decrease in the $LFOR$, $BFOR$ and $SFFOR$ is present, which is a result of the lower median values of the stroke distribution with the worst-case for maximum tower height and maximum span length being 0.14 flashovers per 100 km-year for the $LFOR$ the worst-case value.

- However, due to these lower median values, the $SFFOR$ increases for minimum and standard tower height and furthermore is the dominant factor of the $LFOR$ for lower tower footing resistances and soil resistivities, respectively.
- For higher values of tower footing resistance, the $BFOR$ increases to equal values of flashover ratio related to the $SFFOR$.
- The inclusion of the frequency- and soil ionization dependent impedance as an earthing system with regard to the CIGRE stroke distribution leads to a significant drop of $LFOR$ (worst-case of 0.1 flashovers per 100 km-year), and $BFOR$ in all scenarios,
- but the $SFFOR$ remains at the same level as for the basic scenario with simple tower footing resistance due to the fact that the shielding failure calculation is independent of the earthing system.
- For all variations of span length, tower height and soil resistivity, the $BFOR$ features lower values than the $SFFOR$.
- For the LLS Scotland distribution, the $BFOR$ is furthermore decreased to insignificant values and the $LFOR$ (worst-case of 0.06 flashovers per 100 km-year) is clearly dominated by the $SFFOR$.
- With regards to the suggested $SFFOR$ and $BFOR$ limits in the beginning of this chapter, the calculation for all scenarios with the LLS Scotland stroke distribution and furthermore with improved earthing show that a limit of approximately 0.1 flashovers per 100 km-year can be maintained for all cases.
- For the base cases with the CIGRE stroke distribution, this is achieved for scenarios with a soil resistivity up to 1000 Ωm or 46Ω tower footing resistance respectively.

In conclusion to the selection of scenarios to be simulated with flashover mitigation methods, the evaluation of the base scenarios shows, that the tower height has a minor influence on simulation results, in which worst-case scenarios are for maximum tower height. Therefore, only the maximum tower height needs to be investigated for mitigation scenarios. The improved tower earthing model, especially the soil ionization, leads to far better results than the simple resistance model. However, due to the variety of tower foundations in the practical case and unknown behaviour of the intensity of soil ionization, these cases are not investigated further. In the evaluation, it has to be kept in

mind that the effectiveness of the tower earthing is better than that of a solely resistive representation of the earthing system.

9.1.3: SIMULATION RESULTS OF FLASHOVER MITIGATION SCENARIOS

For the chosen mitigation methods, arresters installed at top and mid phase of each system, double shield wire, counterpoise and underbuilt wire, the simulation of the critical current are performed in the same way as for the base scenarios, but limited to the simple resistive earthing system representation concluded from the base scenarios. A summary of the results for positive, negative and negative subsequent strokes to one shield wire and the top phase wire are given in figure 9-25 to figure 9-30.

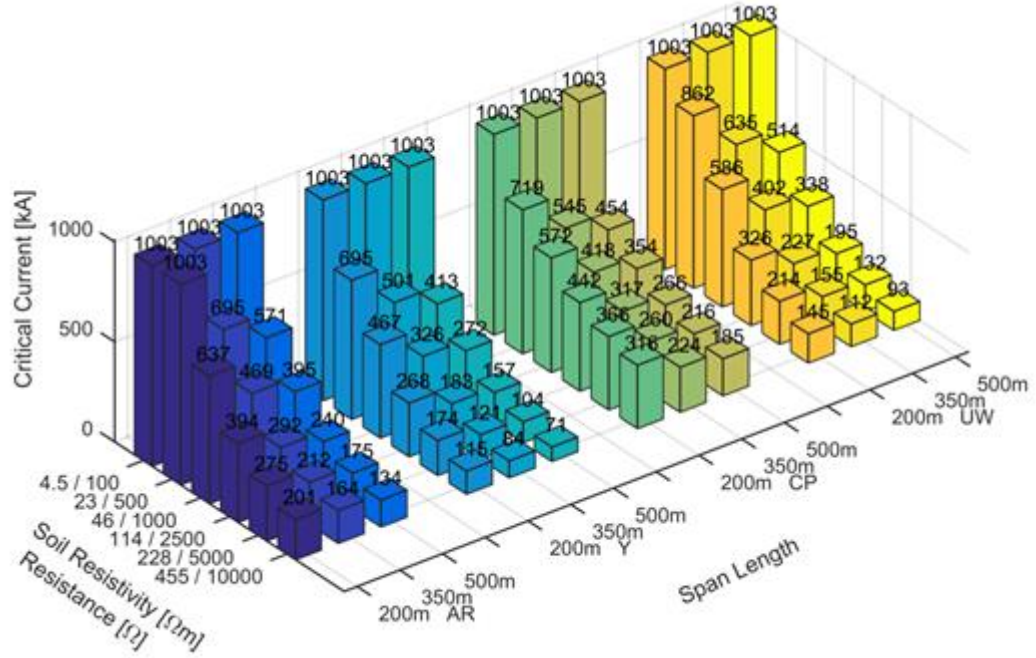

Figure 9-25: Results of critical current determination for shield wire, positive stroke polarity, mitigation scenarios with simple resistance tower earthing representation (AR: arresters, Y: double shield wire, CP: counterpoise, UW: underbuilt wire)

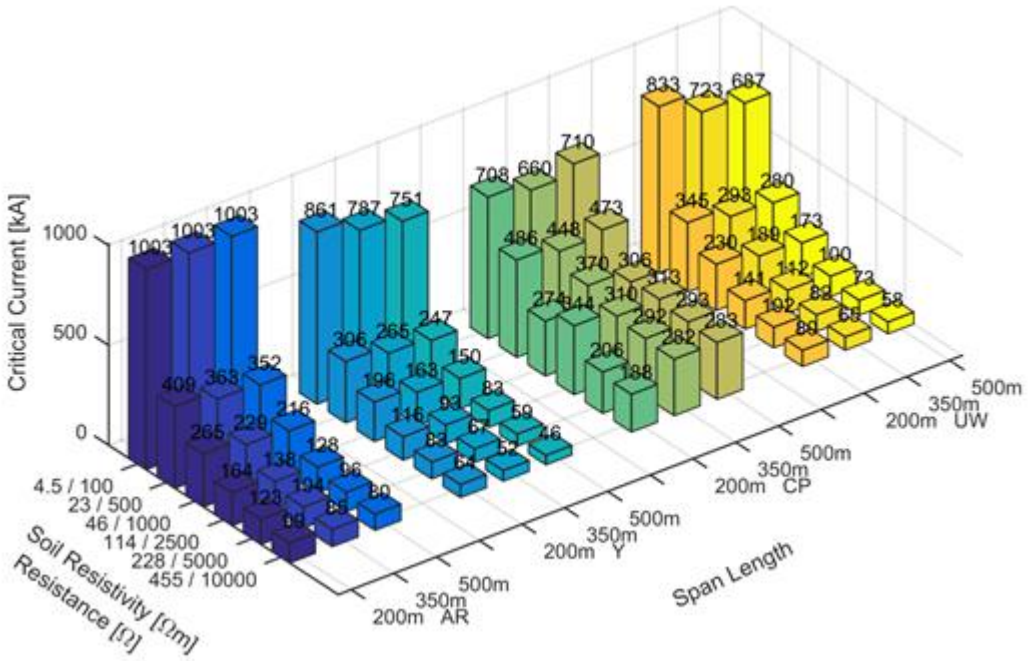

Figure 9-26: Results of critical current determination for shield wire, negative stroke polarity, mitigation scenarios with simple resistance tower earthing representation (AR: arresters, Y: double shield wire, CP: counterpoise, UW: underbuilt wire)

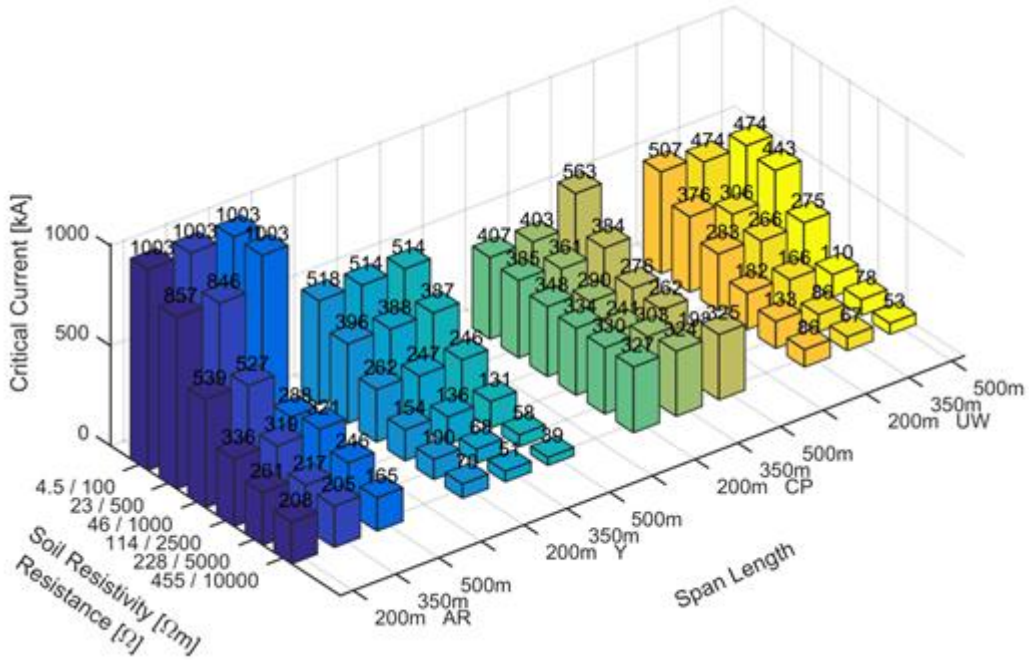

Figure 9-27: Results of critical current determination for shield wire, negative subsequent stroke polarity, mitigation scenarios with simple resistance tower earthing representation (AR: arresters, Y: double shield wire, CP: counterpoise, UW: underbuilt wire)

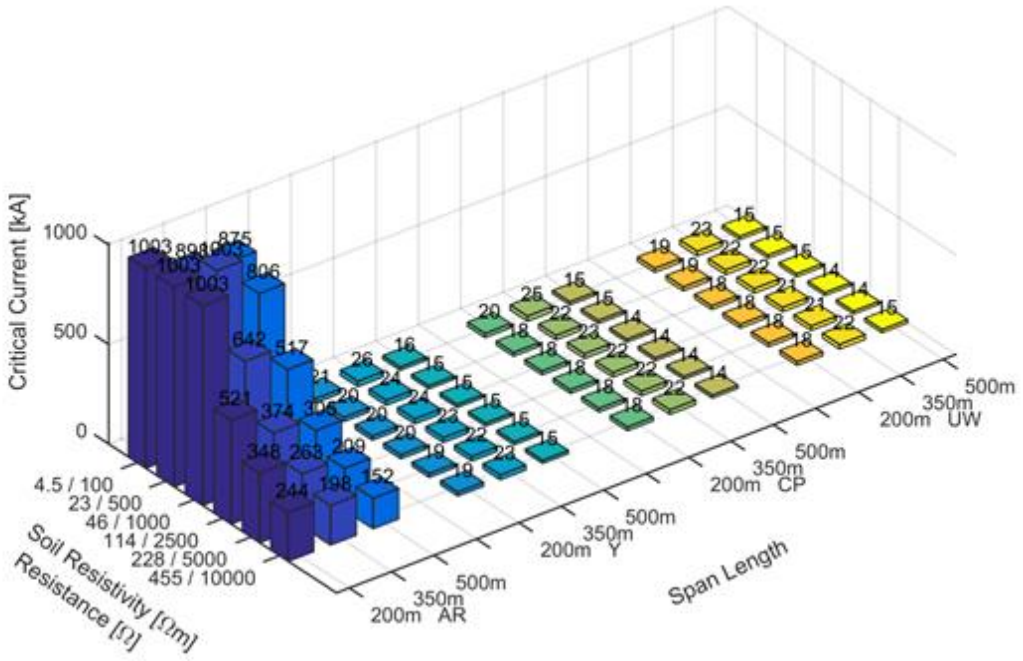

Figure 9-28: Results of critical current determination for top phase wire, positive stroke polarity, mitigation scenarios with simple resistance tower earthing representation (AR: arresters, Y: double shield wire, CP: counterpoise, UW: underbuilt wire)

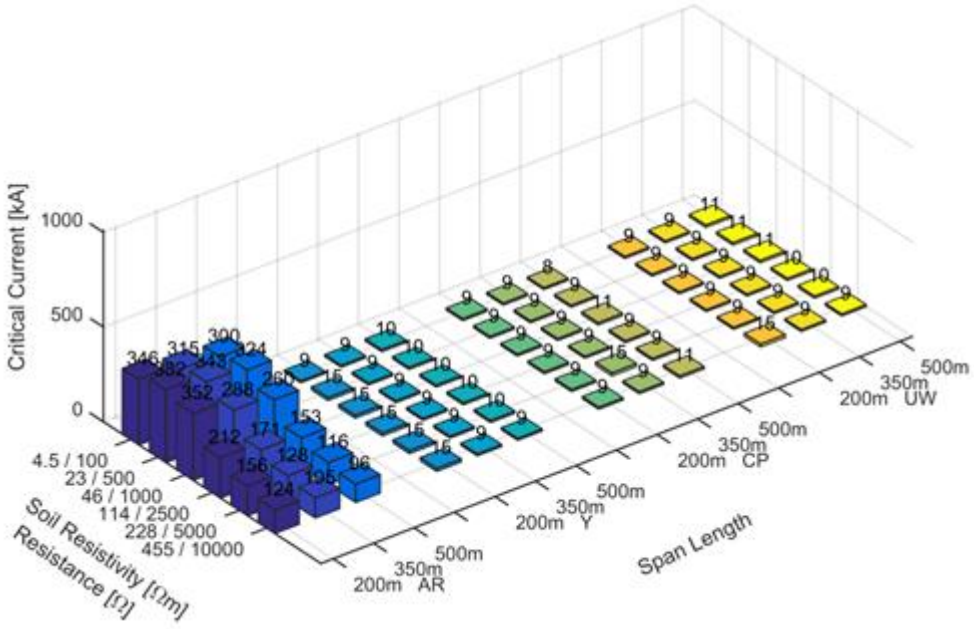

Figure 9-29: Results of critical current determination for top phase wire, negative stroke polarity, mitigation scenarios with simple resistance tower earthing representation (AR: arresters, Y: double shield wire, CP: counterpoise, UW: underbuilt wire)

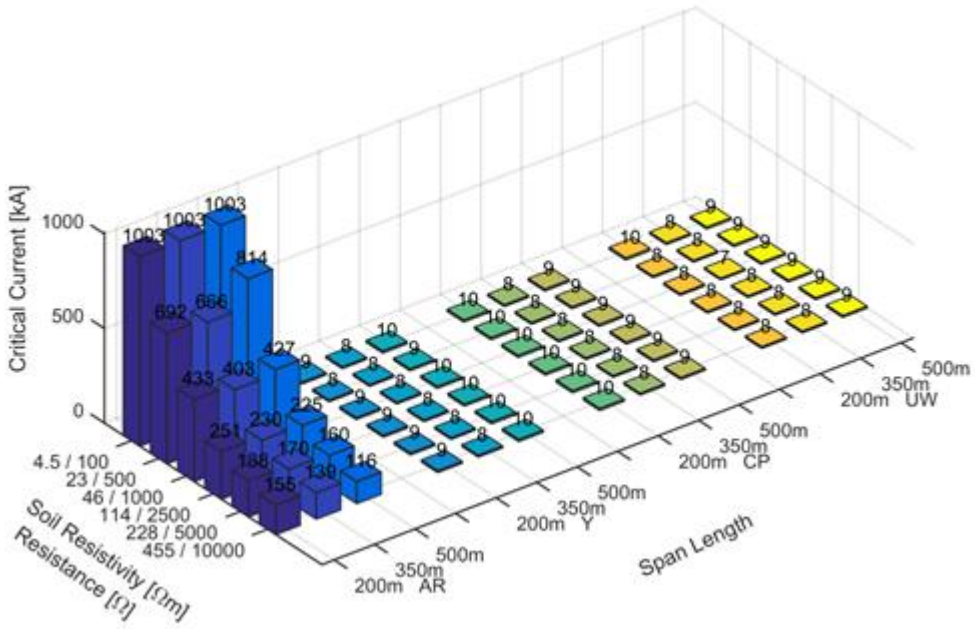

Figure 9-30: Results of critical current determination for top phase wire, negative subsequent stroke polarity, mitigation scenarios with simple resistance tower earthing representation (AR: arresters, Y: double shield wire, CP: counterpoise, UW: underbuilt wire)

In comparison to the base scenario results for the critical current determination for the shield wire, all mitigation methods increase the critical current for hits to the shield wire. The effectiveness, however, varies. The highest critical currents are achieved with counterpoise for all stroke polarities, where the length of the buried wires is increased with soil resistivity, maintaining a rather constant critical current for all soil resistivities, which is in the range of 1000 Ωm or 46Ω footing resistance respectively. Second in effectiveness of increasing the critical current is the application of arresters. Due to the lack of arrester on the bottom phase wire, the critical current decreases with increasing soil resistivity, but critical current values are more than doubled in comparison to the base scenario simulations. The flashover mitigation methods of double shield wire and underbuilt wire approximately feature the same performance, where the critical current values are nearly doubled in comparison to the base scenario simulations.

With regard to hits to the top shield wire, the critical currents remain the same as in the base scenarios, expect for the arrester mitigation method, where critical currents increase to values similar to results for the shield wire. Therefore, arresters are the sole mitigation method to improve the critical current of a phase wire.

9.1.4: EVALUATION OF FLASHOVER RATES CALCULATED FROM CRITICAL CURRENTS OF MITIGATION SCENARIOS

The associated flashover rates for the different mitigation methods, calculated from the determined critical currents for the CIGRE and the LLS Scotland distribution are illustrated in figure 9-31 to figure 9-36. Tabulated results are summarized in appendix G.1.

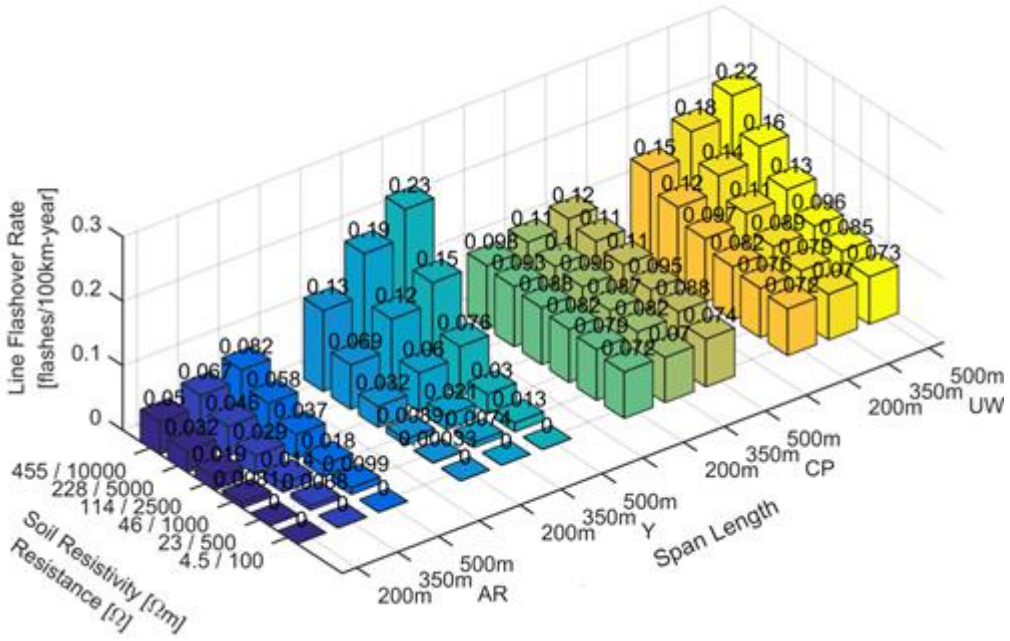

Figure 9-31: Line flashover rate from critical current determination, mitigation scenarios with simple resistance tower earthing representation, CIGRE stroke distribution (AR: arresters, Y: double shield wire, CP: counterpoise, UW: underbuilt wire)

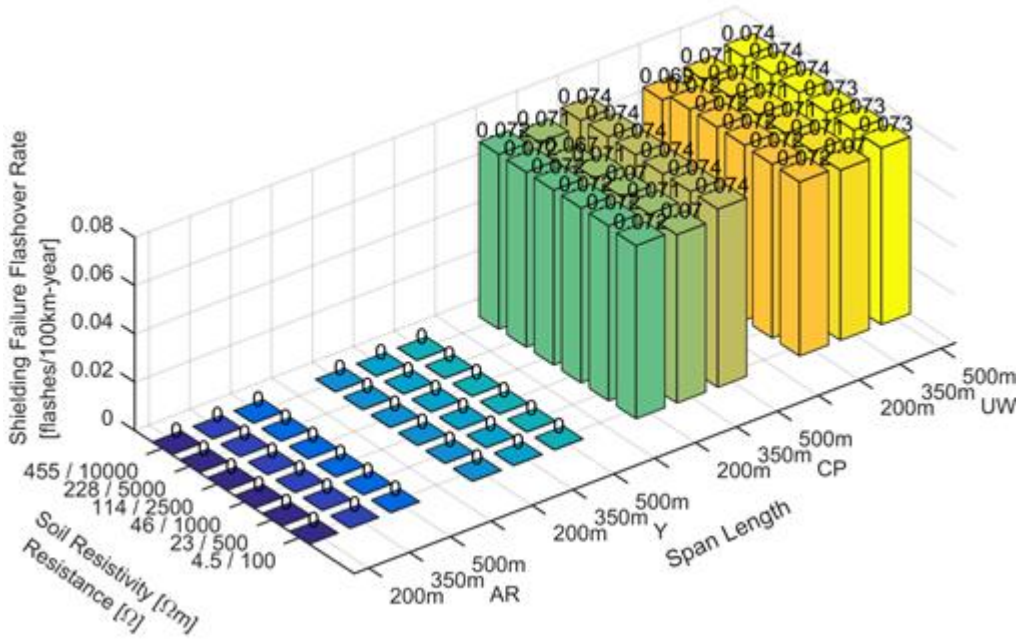

Figure 9-32: Shielding failure flashover rate from critical current determination, mitigation scenarios with simple resistance tower earthing representation, CIGRE stroke distribution (AR: arresters, Y: double shield wire, CP: counterpoise, UW: underbuilt wire)

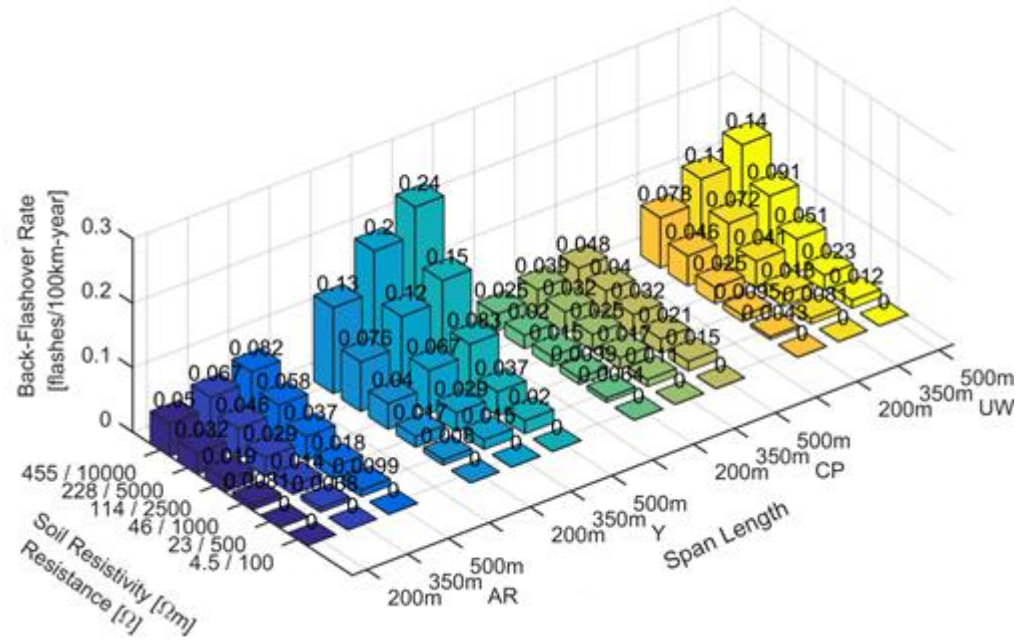

Figure 9-33: Back-flashover rate from critical current determination, mitigation scenarios with simple resistance tower earthing representation, CIGRE stroke distribution (AR: arresters, Y: double shield wire, CP: counterpoise, UW: underbuilt wire)

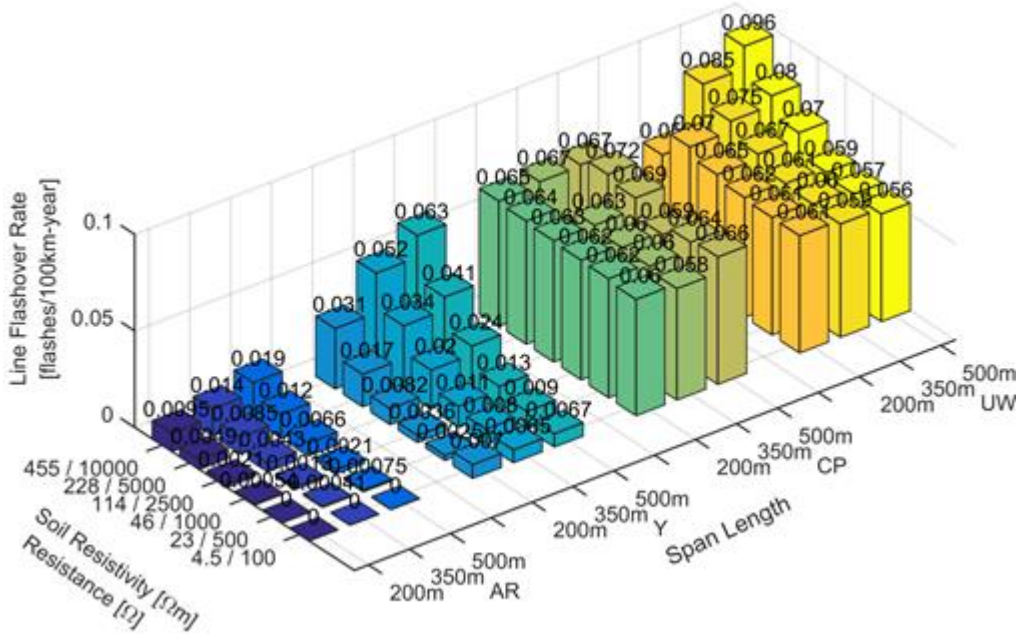

Figure 9-34: Line flashover rate from critical current determination, mitigation scenarios with simple resistance tower earthing representation, LLS Scotland stroke distribution (AR: arresters, Y: double shield wire, CP: counterpoise, UW: underbuilt wire)

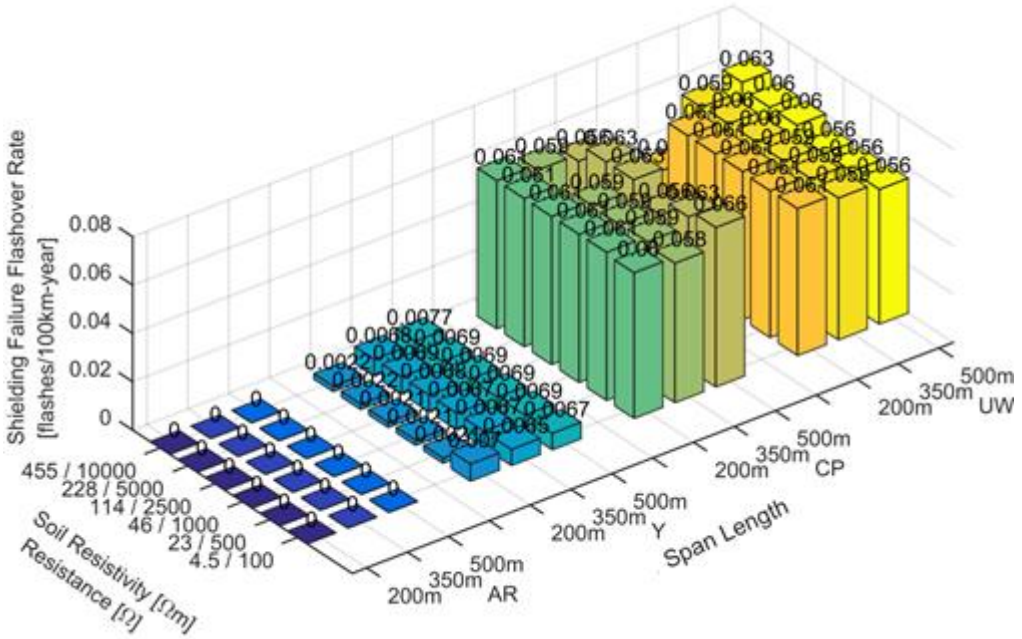

Figure 9-35: Shielding failure flashover rate from critical current determination, mitigation scenarios with simple resistance tower earthing representation, LLS Scotland stroke distribution (AR: arresters, Y: double shield wire, CP: counterpoise, UW: underbuilt wire)

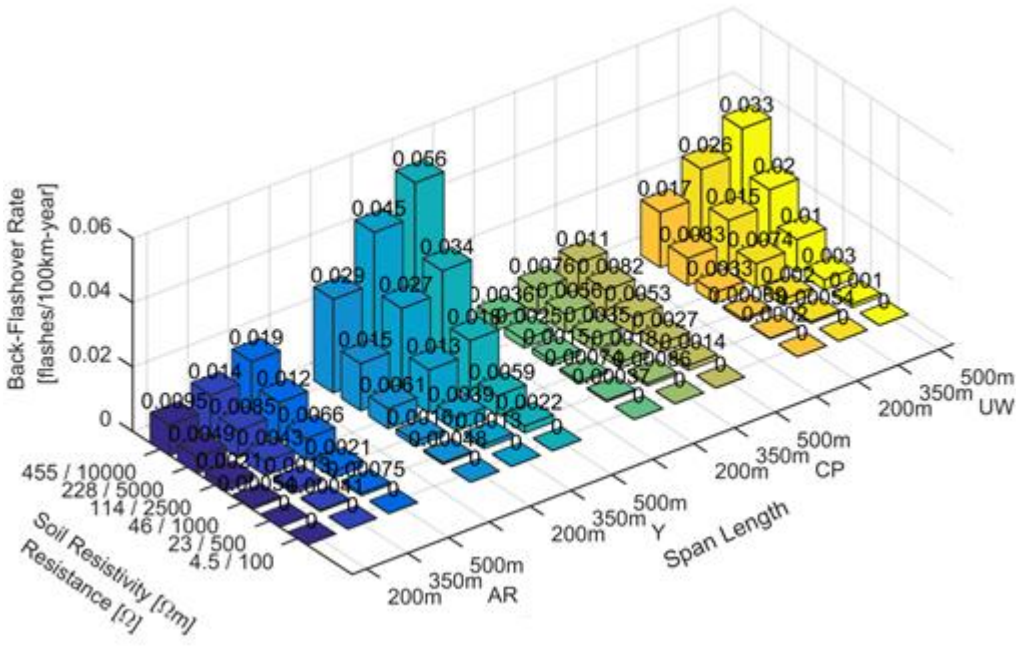

Figure 9-36: Back-flashover rate from critical current determination, mitigation scenarios with simple resistance tower earthing representation, LLS Scotland stroke distribution (AR: arresters, Y: double shield wire, CP: counterpoise, UW: underbuilt wire)

Overall, all the investigated flashover mitigation methods for the CIGRE stroke distribution show a significant decrease of the $LFOR$, with arresters and double-shield wires also reducing the $SFFOR$. With regard to the effectiveness, arresters decrease both the $SFFOR$ and $BFOR$, and thus are the most effective method with a worst-case $LFOR$ of 0.08 flashes per 100 km-year. Since the counterpoise length is adjusted with soil resistivity, the $BFOR$ and $LFOR$ respectively are dramatically reduced, making it the second best option with a $LFOR$ 0.12 flashes per 100 km-year. For double shield wires and underbuilt wires similar values of $LFOR$ can be achieved, in the worst-case halving the values from the base scenario to an $LFOR$ of 0.22 flashes per 100 km-year. However, the underbuilt wire features a better $BFOR$ performance than the double shield wire due to the smaller lightning attraction area formed by the shield wire. As previously mentioned, values smaller than 0.05 flashes per 100 km-year are rounded to 0. Therefore the $SFFOR$ for the double shield wire configuration is zero, although a neglectable value of $SFFOR$ is calculated.

Results for the LLS Scotland stroke distribution show a further drop of flashover values for all mitigation methods. Due to the lower median currents and resulting reduction of back-flashover possibilities, the $SFFOR$ reduction becomes the dominant factor for decreasing the $LFOR$. Therefore the order of effectiveness changes, with arresters and double shield wire being first and second choice. Due to the same $SFFOR$ performance

of counterpoise and underbuilt wire, the greater reduction in $BFOR$ for the counterpoise, leads to lower $LFOR$ values than for the underbuilt wire. However, the worst-case $LFOR$ for the underbuilt wire mitigation method is still below 0.1 flashes per 100 km-year.

9.2: MONTE-CARLO METHOD

9.2.1: SIMULATION RESULTS OF BASE SCENARIOS

The ratio of simulations leading to a flashover to the total number of simulations F/N obtained with the Monte-Carlo procedure are determined for varying soil resistivity, tower height, span length and lightning stroke distribution (CIGRE and LLS Scotland) of a 1 km piece of a transmission line route. In contrast to fixed stroke locations at the tower in the critical current determination, power-frequency voltage and the randomness of lightning is taken into account with several randomized factors, such as stroke polarity, current amplitude, lightning stroke attachment angle, stroke location, etc. (see section 8.2). The whole simulation results are provided in a tabulated form in appendix G.2, in which a summary of results for base cases with a simple resistance representation of the tower earthing system, as well as an earthing rod model representation with frequency-dependent and soil ionization behaviour is given in figure 9-37 to figure 9-42. The results are rounded to one digit, which results in ratios below 0.05% to be 0%.

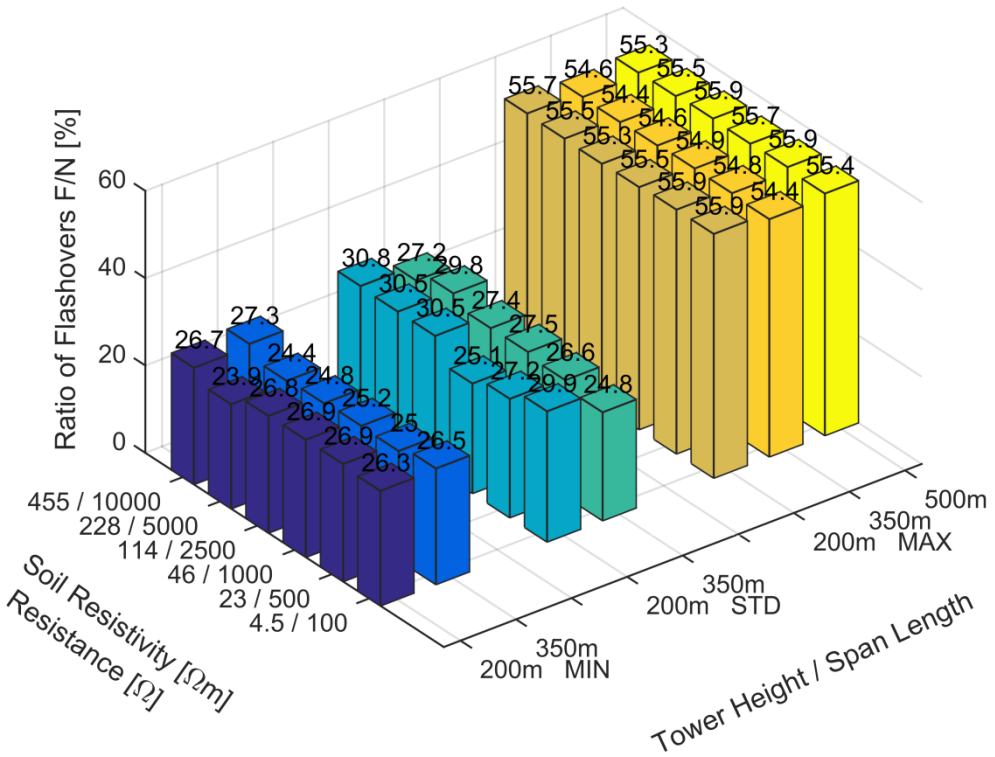

Figure 9-37: **Results of shielding failure flashover ratio F/N determination with Monte-Carlo method, CIGRE lightning stroke distributions, base scenarios with simple resistance tower earthing representation**

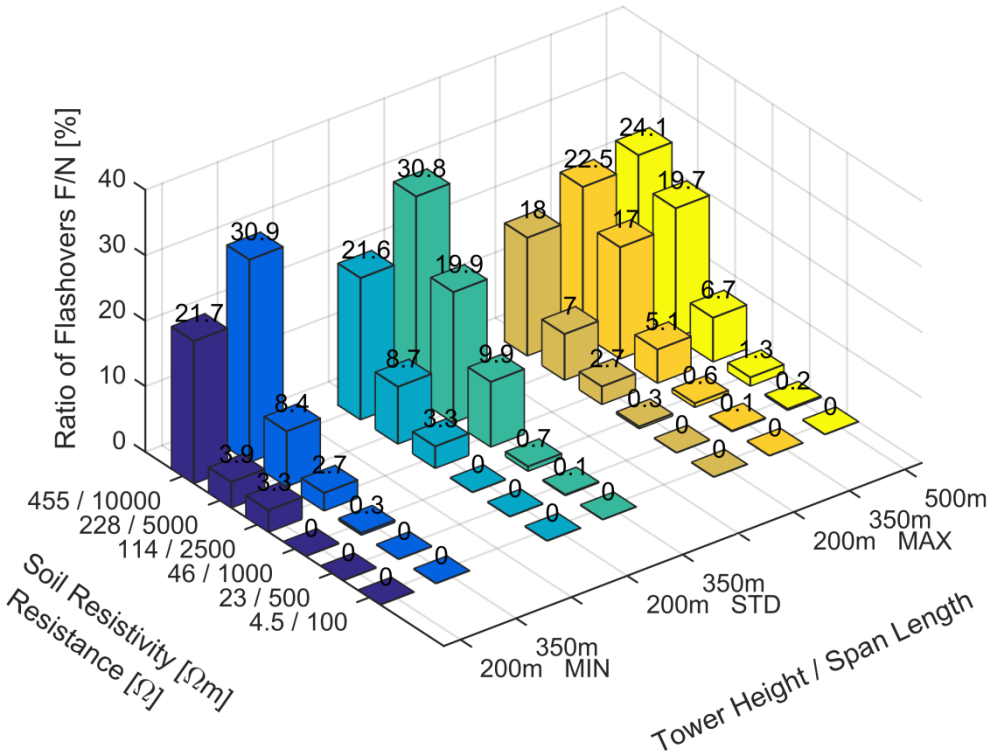

Figure 9-38: **Results of back-flashover ratio F/N determination with Monte-Carlo method, CIGRE lightning stroke distributions, base scenarios with simple resistance tower earthing representation**

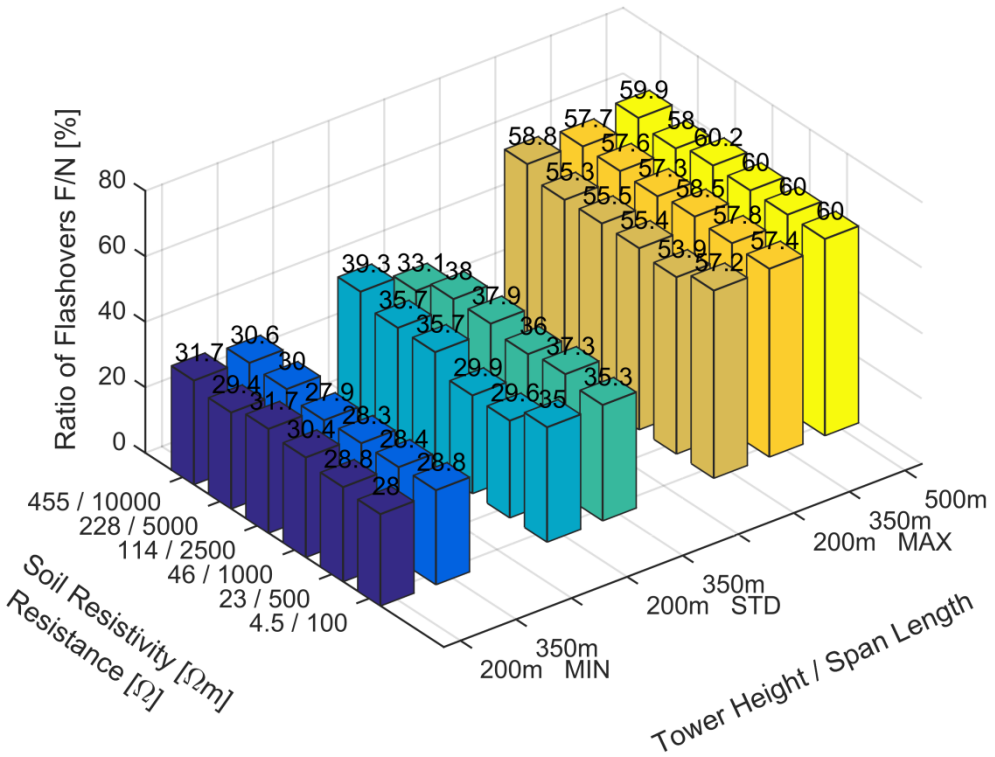

Figure 9-39: **Results of shielding failure flashover ratio F/N determination with Monte-Carlo method, LLS Scotland lightning stroke distributions, base scenarios with simple resistance tower earthing representation**

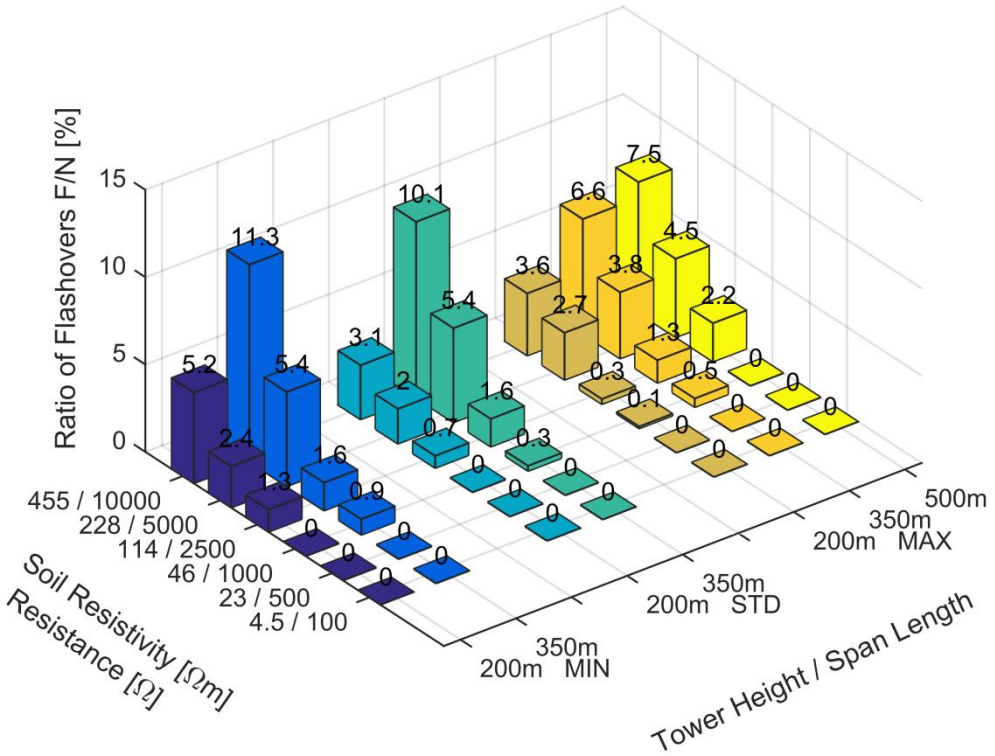

Figure 9-40: **Results of back-flashover ratio F/N determination with Monte-Carlo method, LLS Scotland lightning stroke distributions, base scenarios with simple resistance tower earthing representation**

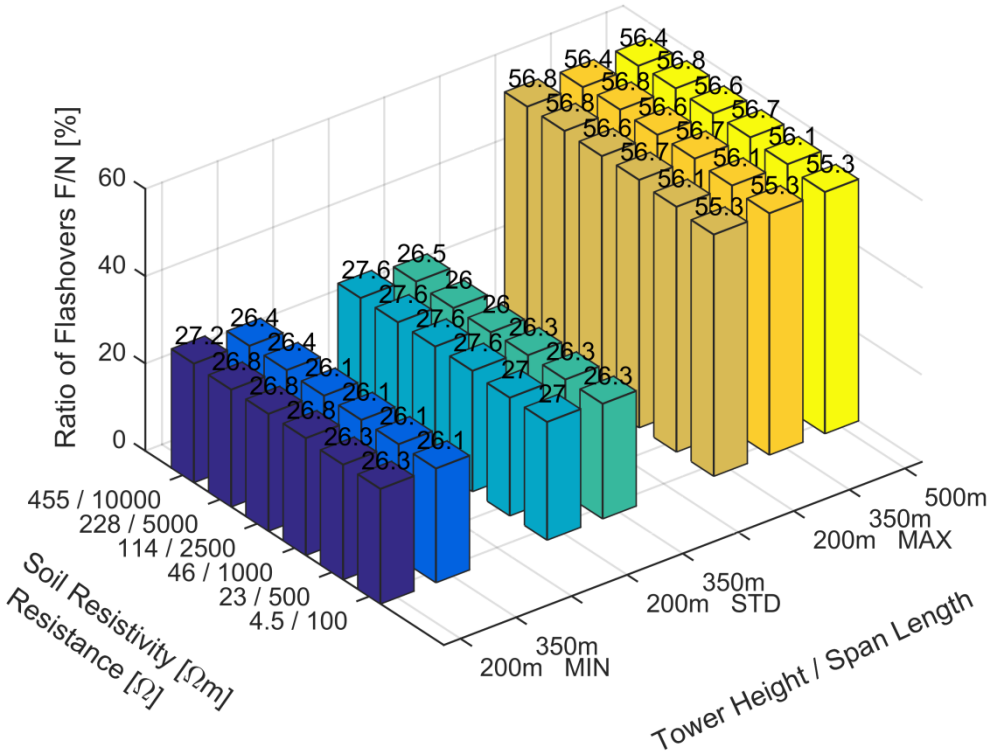

Figure 9-41: **Results of shielding failure flashover ratio F/N determination with Monte-Carlo method, CIGRE lightning stroke distributions, base scenarios with improved tower earthing model representation**

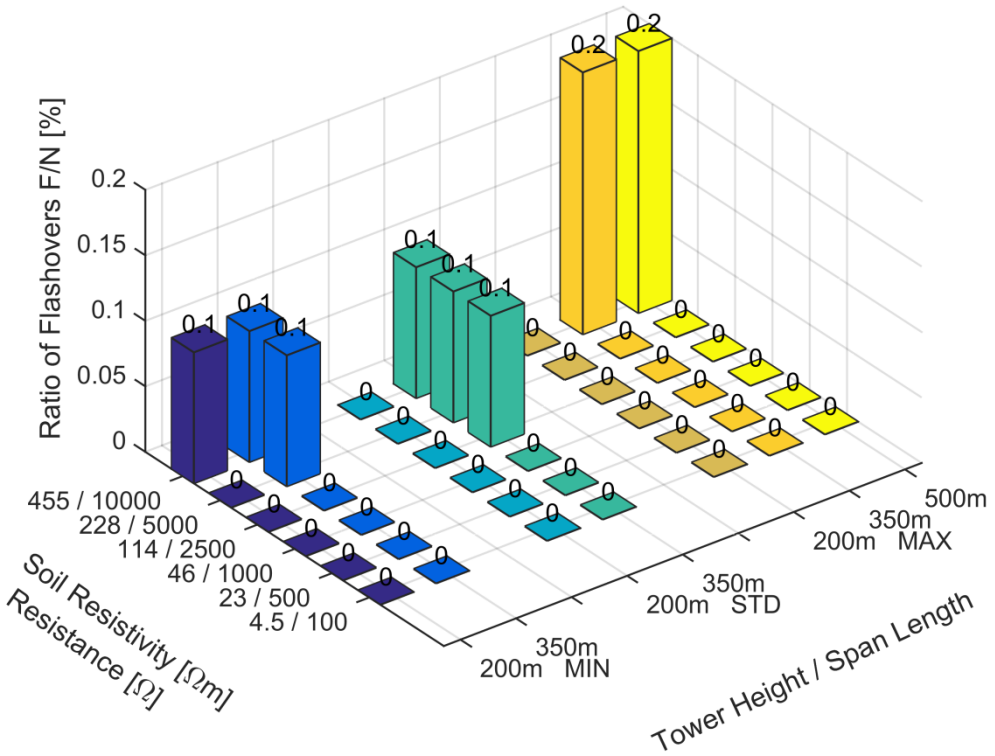

Figure 9-42: **Results of back-flashover ratio F/N determination with Monte-Carlo method, CIGRE lightning stroke distributions, base scenarios with improved tower earthing model representation**

Generally the simulation results for the base scenarios can be summarized as follows:

- The shielding failure flashover ratio and back-flashover ratio increase with increasing tower height,
- the back-flashover ratio increase with increasing span length and increasing soil resistivity,
- the shielding failure flashover ratio is independent of the soil resitivity,
- the back-flashover ratio features negligible values for soil resistivities up to 1000 Ωm,
- lightning stroke distributions have a major impact on the line flashover ratio, shielding failure flashover ratio and back-flashover ratio when the CIGRE and LLS Scotland distribution are compared,
- the lower median values of the LLS Scotland distribution lead to a significant reduction of back-flashover ratio, but shielding failure flashover ratios are increased,
- improved modeling of the earthing system leads a neglectable back-flashover ratio for all soil resistivities.

The simulation results for the base scenarios with improved earthing, considering frequency-dependency and soil ionization, show that the back-flashover ratio is below 0.05%, thus approximately 0. In the case for maximum tower height and 350 m span length, CIGRE lightning stroke distribution, some statistical outliers lead to the increased flashover ratio of 0.3%.

9.2.2: EVALUATION OF FLASHOVER RATES CALCULATED FROM FLASHOVER RATIOS FOR BASE SCENARIOS

With the ratio of simulations leading to a flashover to the total number of simulations F/N in the Monte-Carlo procedure the flashover rates can be determined according to formula (8.11) and (8.12). However, a decision on the width d, which is the band or corridor along a line route where lightning may hit the line has to be made. In the literature, either a fixed width in the range of 400 m to 1 km or a variable width dependent on the maximum stroke current peak value leading to a flashover generated in the Monte-Carlo simulation is taken into account [279], [314], [322]. To align with the standard calculation method for critical current determination, the corridor is determined on the

basis of D_g', calculated separately for shield wire failure and back-flashover failure, dependent on the maximum current in the simulation leading to a flashover. Since each phase wire features its own lightning attraction area, the maximum stroke current peak value leading to a shielding failure for a respective phase is determined to calculate D_g' for each phase seperately. Therefore the shielding failure flashover rate consists of a sum of each phases' shielding failure flashover rate.

The resulting flashover rates are illustrated in figure 9-43 to figure 9-51 for both the CIGRE and LLS Scotland stroke distribution and with simple resistance and impedance tower earthing representation for the variations of tower height and span length.

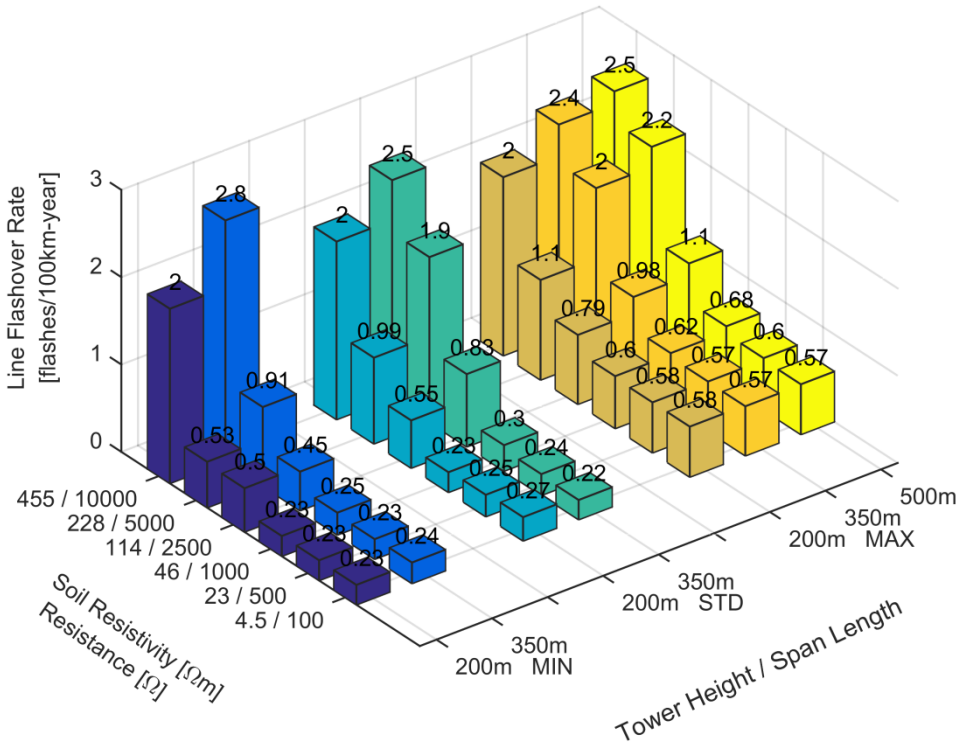

Figure 9-43: Line flashover rate from Monte-Carlo method, base scenarios with simple resistance tower earthing representation, CIGRE stroke distribution

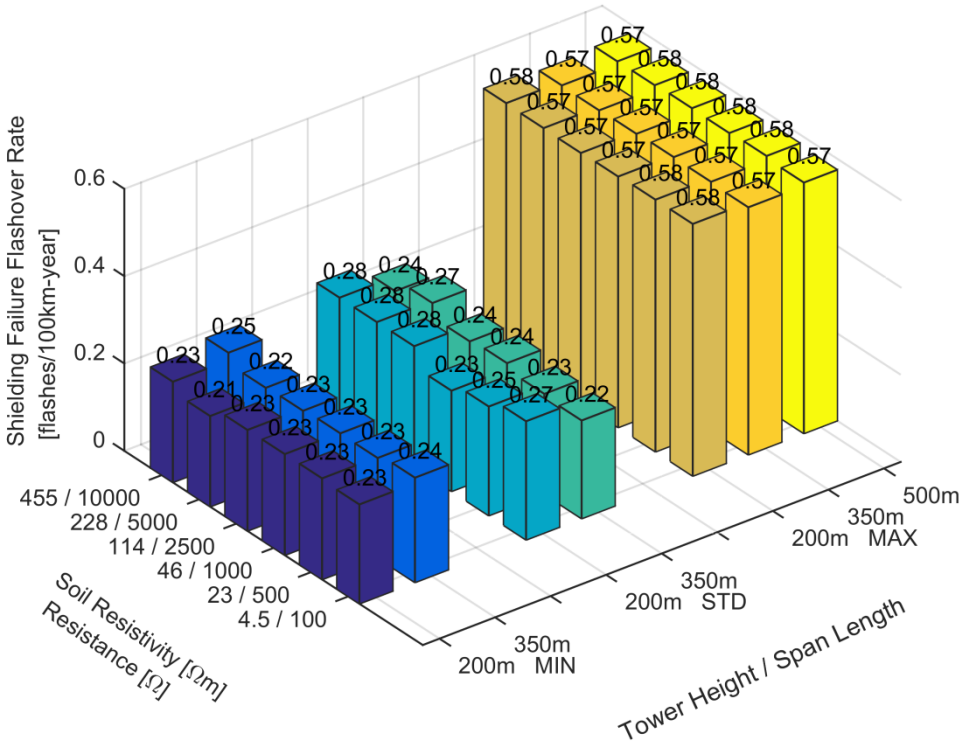

Figure 9-44: Shielding failure flashover rate from Monte-Carlo method, base scenarios with simple resistance tower earthing representation, CIGRE stroke distribution

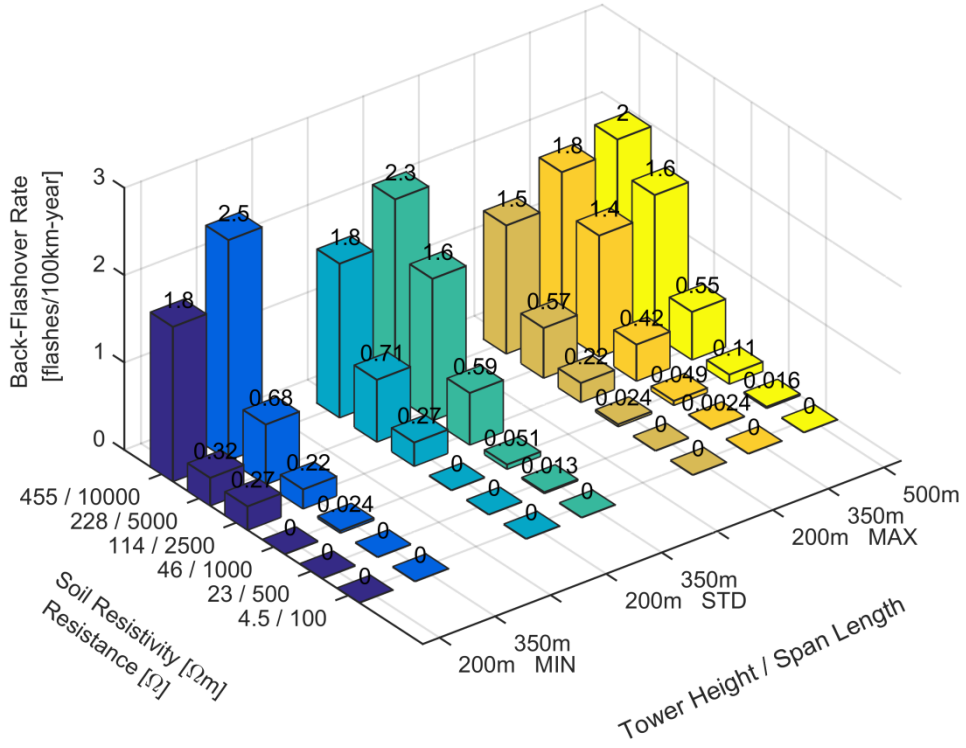

Figure 9-45: Back- flashover rate from Monte-Carlo method, base scenarios with simple resistance tower earthing representation, CIGRE stroke distribution

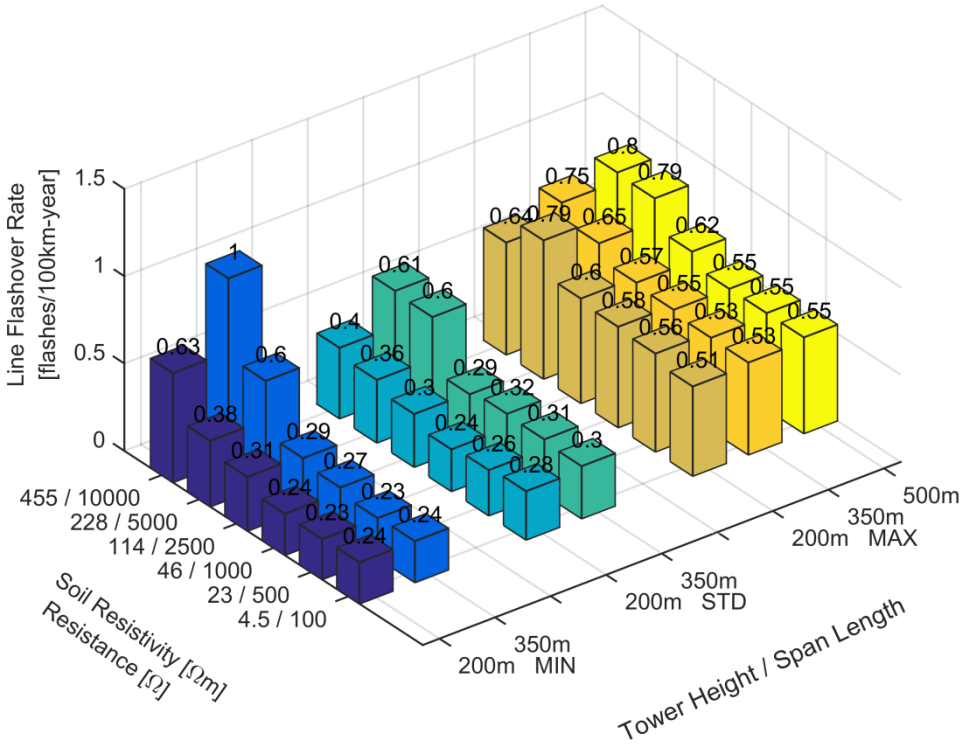

Figure 9-46: Line flashover rate from Monte-Carlo method, base scenarios with simple resistance tower earthing representation, LLS Scotland stroke distribution

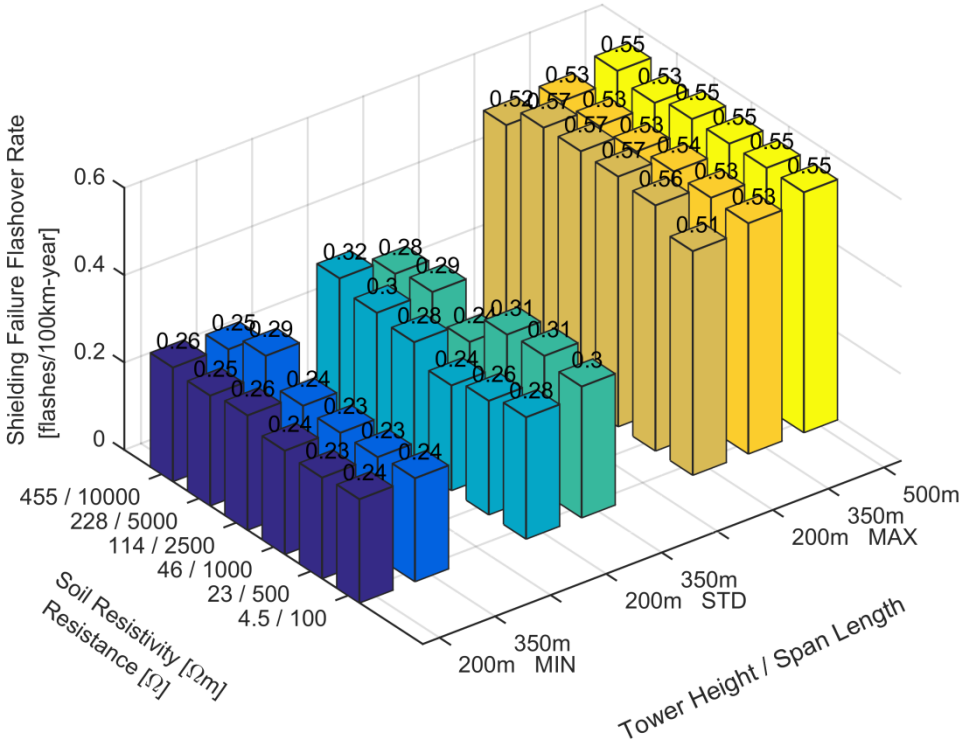

Figure 9-47: Shielding failure flashover rate from Monte-Carlo method, base scenarios with simple resistance tower earthing representation, LLS Scotland stroke distribution

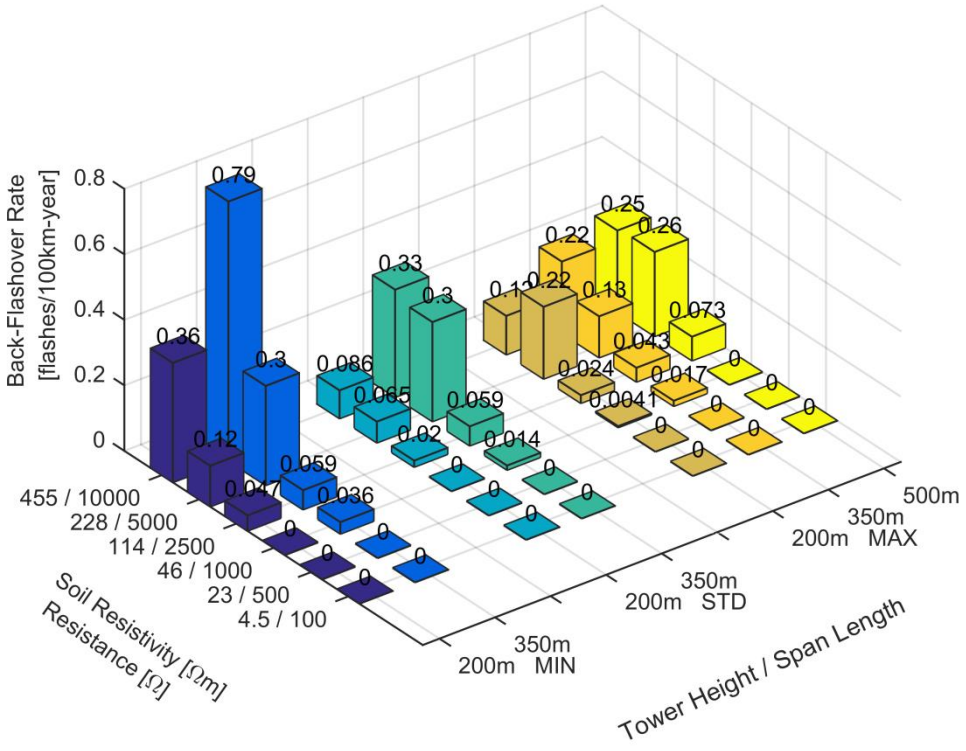

Figure 9-48: Back- flashover rate from Monte-Carlo method, base scenarios with simple resistance tower earthing representation, LLS Scotland stroke distribution

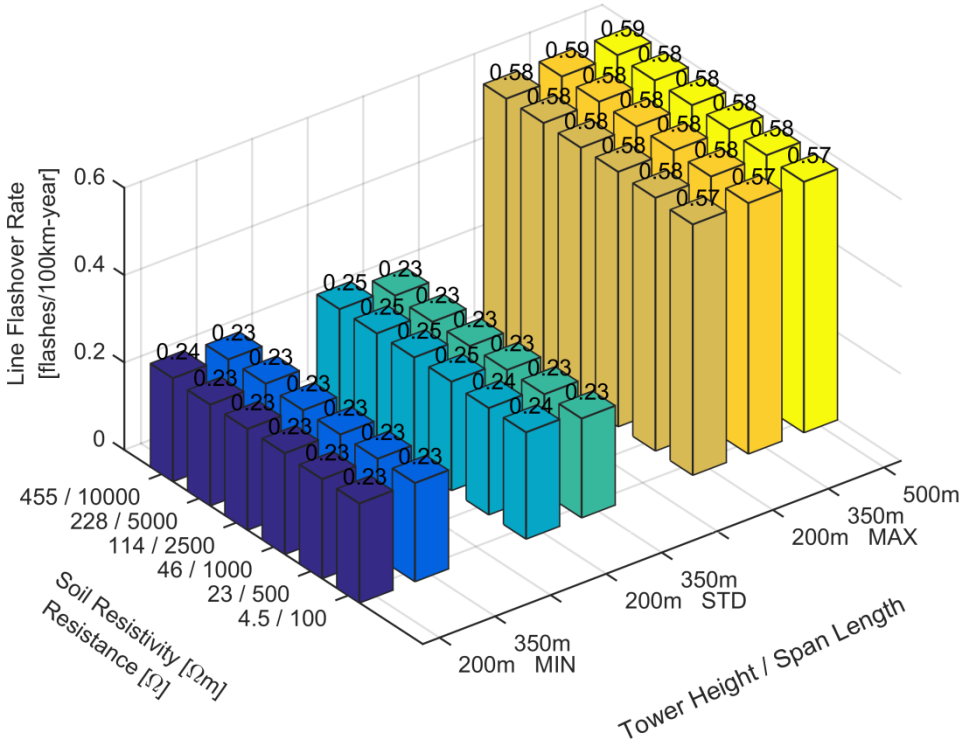

Figure 9-49: Line flashover rate from Monte-Carlo method, base scenarios with impedance tower earthing representation, CIGRE stroke distribution

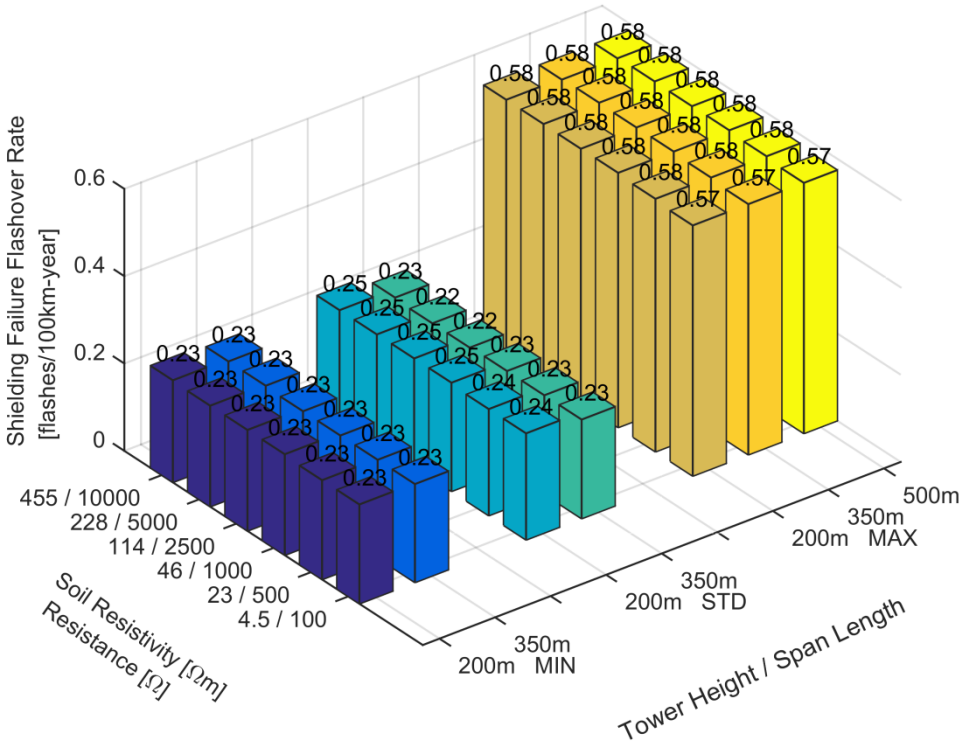

Figure 9-50: Shielding failure flashover rate from Monte-Carlo method, base scenarios with impedance tower earthing representation, CIGRE stroke distribution

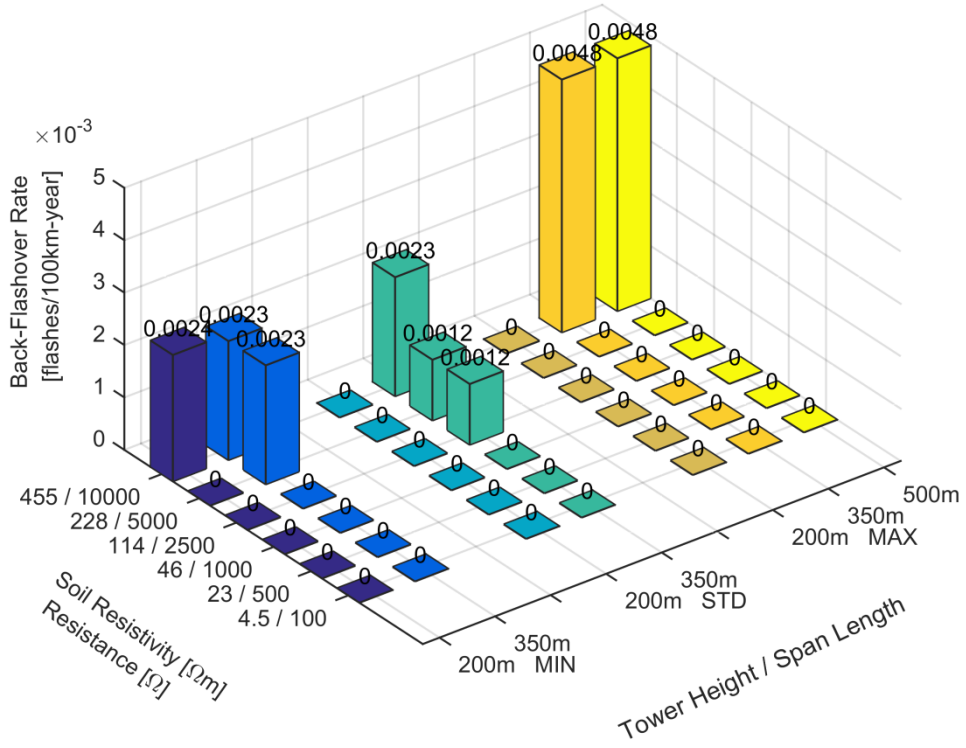

Figure 9-51: Back- flashover rate from Monte-Carlo method, base scenarios with impedance tower earthing representation, CIGRE stroke distribution

In general, the results of the flashover rate calculations can be summarized in the following points:

- The shielding failure flashover rate and back-flashover ratio increase with increasing tower height,
- the back-flashover rate increase with increasing span length and increasing soil resistivity,
- the shielding failure flashover rate is independent of the soil resitivity,
- the back-flashover rate features neglectable values for soil resistivities up to 1000 Ωm for both CIGRE and LLS Scotland distribution with the simple resistive earthing model,
- lightning stroke distributions have a major impact on the back-flashover rate when the CIGRE and LLS Scotland distribution are compared,
- the lower median values of the LLS Scotland distribution lead to a significant reduction of back-flashover rate,
- improved modeling of the earthing system leads a neglectable back-flashover ratio for all soil resistivities.

The most remarkable evaluation results is, that both, the calculation results for the $LFOR$ with CIGRE and LLS Scotland distribution show a sharp increase in flashover rate values above 1000 Ωm or 46 Ω footing resistance respectively, with originates from a significant increase in the $BFOR$ above this value. However at and below this tower footing resistance value, the $LFOR$ is dominated by the $SFFOR$ with 0.6 flashes per 100 km-year, with negligible $BFOR$ values (below 0.1 flashes per 100 km-year. It also has to be noted that the existing variations in the flashover rate results are caused by the varying maximum current leading to a flashover in each simulation set.

Furthermore, the evaluation of the flashover rates with regard to the stroke current distribution shows, that a decrease in the median current (LLS Scotland) does not lead to an increase in the $SFFOR$, which remains at 0.6 flashes per 100 km-year. This is due to the calculation procedure of the $SFFOR$. At a lower median current, the likelihood of a shielding failure is increased, but due to the lower maximum stroke current values, the resulting exposed lightning attachment area is decreased, which leads to a nullification of these effects.

With regard to the magnitude of flashover rates, these are in the same range as values reported in the literature for 400 kV lines [279]. At maximum tower height and span length of 500 m for the CIGRE stroke distribution a $LFOR$ worst-case value of 2.5 flashes per 100 km-year is reached, which is mainly to a $BFOR$ of 2.0 flashes per 100 km-year. For the LLS Scotland distribution these values are significantly reduced to 0.8 flashes per 100 km-year for the $LFOR$ and 0.26 flashes per 100 km-year for the $BFOR$.

At last, from the evaluation it is deducted that mitigation methods are investigated for the base scenario with simple resistive tower footing representation and CIGRE stroke distribution as a worst-case.

9.2.3: SIMULATION RESULTS OF FLASHOVER MITIGATION SCENARIOS

The simulations for the mitigation methods arresters, double shield wire, counterpoise and underbuilt wire are conducted with the Monte-Carlo method to determine the flashover ratios F/N. The results of the simulations are presented in figure 9-52 and figure 9-53, with a tabulated summary in appendix G.2.

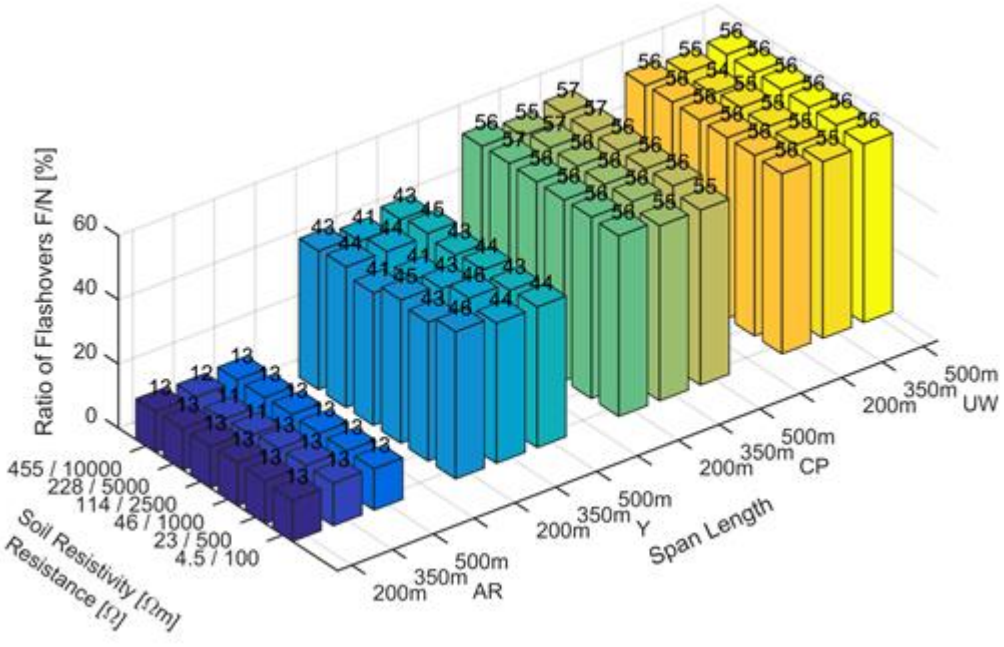

Figure 9-52: Results of shielding failure flashover ratio F/N determination with Monte-Carlo method, CIGRE lightning stroke distributions, mitigation scenarios with simple resistance tower earthing representation (AR: arresters, Y: double shield wire, CP: counterpoise, UW: underbuilt wire)

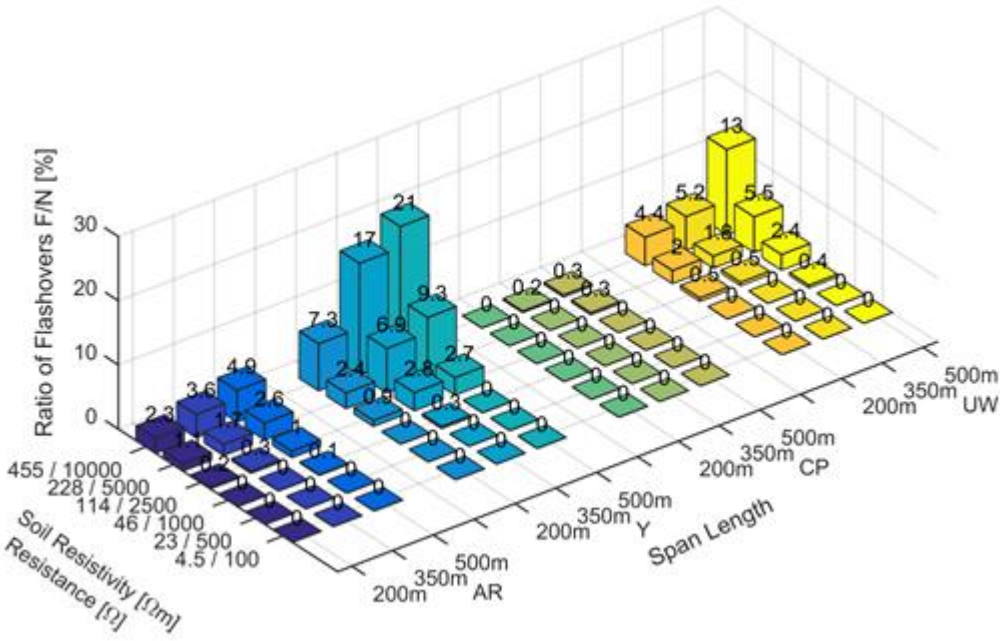

Figure 9-53: Results of back-flashover ratio F/N determination with Monte-Carlo method, CIGRE lightning stroke distributions, mitigation scenarios with simple resistance tower earthing representation (AR: arresters, Y: double shield wire, CP: counterpoise, UW: underbuilt wire)

The results of the back-flashover ratios for the mitigation methods show a similar picture as the base scenarios, as the flashover ratios feature a steep increase above the soil resistivity of 1000 Ωm or 46 Ω tower footing resistance, respectively. For arresters as well as counterpoise, the ratio is zero for back-flashovers. It is however remarkable that the flashover ratios from the simulations of a double shield wire tower configuration are higher than for an underbuilt wire. This can however be explained with the greater attraction area of a double shield wire configuration. Furthermore, the positive effect of a double shield wire arrangement on the $SFFOR$ can be seen then comparing the ratios to the underbuilt wire and base scenario cases with CIGRE stroke distribution. Due to the possibility of strokes to the unprotected bottom phase, the shielding failure ratio for arresters is not zero. Another notable result is the back-flashover ratio of the underbuilt wire mitigation method, which nearly halves the back-flashover ratio in comparison to the base scenario.

9.2.4: EVALUATION OF FLASHOVER RATES CALCULATED FROM FLASHOVER RATIOS FOR MITIGATION SCENARIOS

The resulting flashover rates, calculated from the results in the last subsection for the mitigation scenarios, are illustrated in figure 9-54 to figure 9-56. Detailed values are tabulated in appendix G.2.

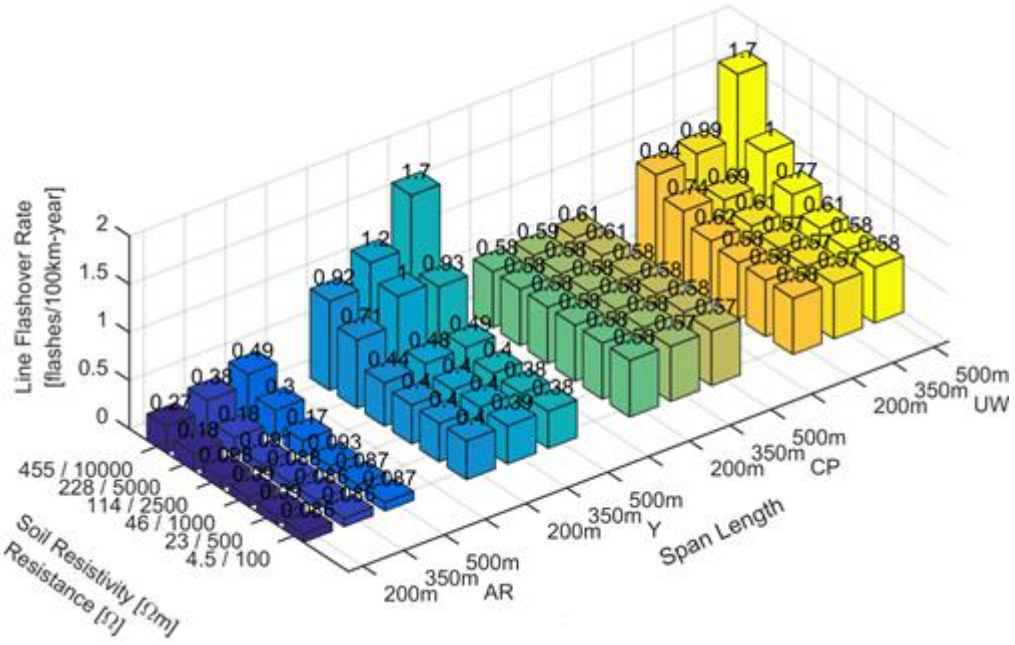

Figure 9-54: Line flashover rate from Monte-Carlo method, mitigation scenarios with simple resistance tower earthing representation, CIGRE stroke distribution (AR: arresters, Y: double shield wire, CP: counterpoise, UW: underbuilt wire)

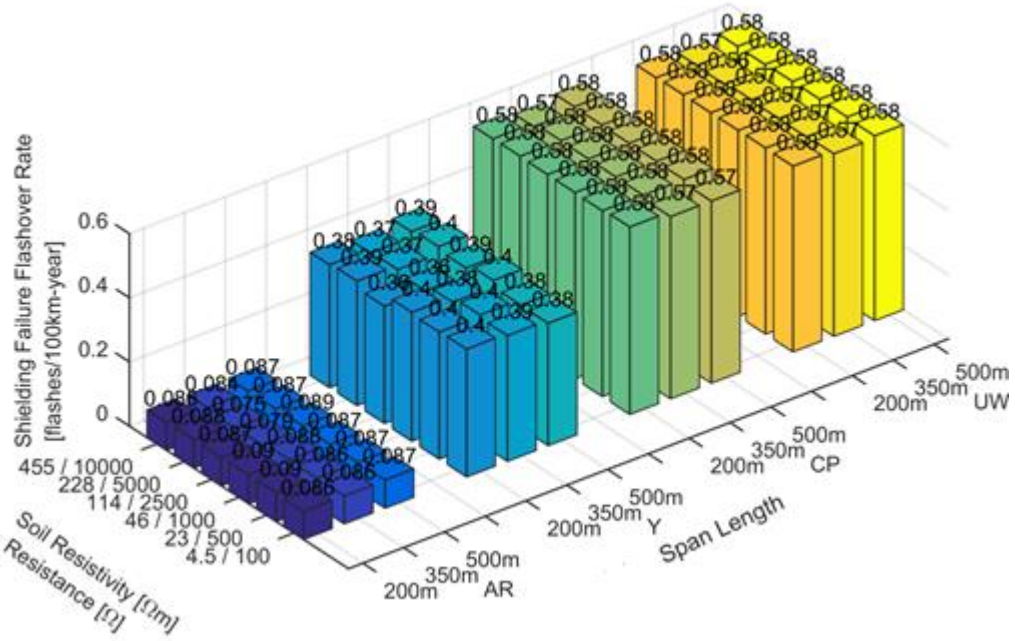

Figure 9-55: Shielding failure flashover rate from Monte-Carlo method, mitigation scenarios with simple resistance tower earthing representation, CIGRE stroke distribution (AR: arresters, Y: double shield wire, CP: counterpoise, UW: underbuilt wire)

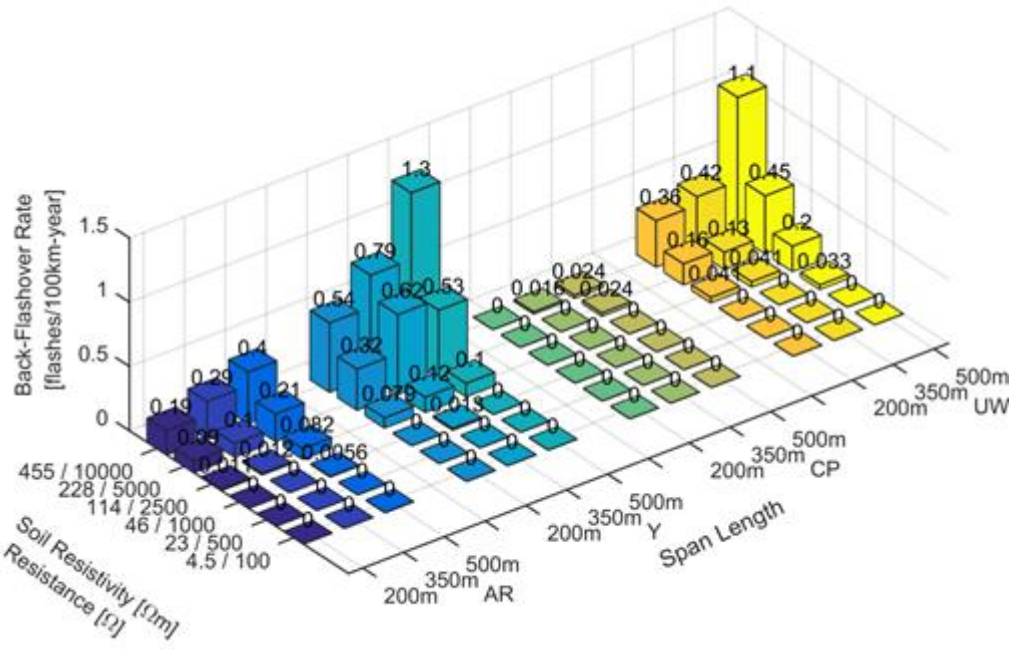

Figure 9-56: Back-flashover rate from Monte-Carlo method, mitigation scenarios with simple resistance tower earthing representation, CIGRE stroke distribution (AR: arresters, Y: double shield wire, CP: counterpoise, UW: underbuilt wire)

The results of the flashover rates match the results of the flashover ratios in the last subsection and partly of the results for the base scenarios in the following:

- Below 1000 Ωm or 46 Ω tower footing resistance, respectively, the $BFOR$ is neglectable for all mitigation methods,
- for arresters as well as counterpoise, the $BFOR$ is zero for all soil resistivities,
- for double shield wire and underbuilt wire the $BFOR$ is halved in comparison to the base scenarios,
- for the $SFFOR$, only arresters and double shield wires decrease the flashover rate,
- for a reduction of the $LFOR$, the most effective method is arresters, followed by counterpoise and
- for the reduction of the $BFOR$, the most effective method is counterpoise followed by arresters, underbuilt wires and double shield wire.

A notable results with regard to the reduction of the $BFOR$ is the flashover mitigation performance of the underbuilt wire, as a cost-effective method. Up to a tower footing impedance of 114 Ω features a maximum rate of 0.2 flashes per 100 km-year for the worst-case, which is at the lower end of design criterion.
In worst-case earthing conditions, only arresters and counterpoise reduce the $BFOR$ to acceptable limits. However from a practical point of view, a counterpoise configuration with 120 m long earthing strips on each side of the tower in the 10000 Ωm case in rocky soil is hardly achievable. Therefore only arresters are a practical flashover mitigation method at these earthing conditions.

9.3: SUMMARY AND CONCLUSIONS ON THE EVALUATION OF SIMULATION RESULTS

In this chapter the evaluation of the simulation results is conducted, based on the simulations of various scenarios, summarized in section 8.3. To ensure simulation results are valid and trustworthy, two different methods to obtain the $LFOR$ are applied.
In the critical current determination method, the minimum or critical current at and above a flashover occurs is determined for direct hits to the tower shield and top phase wire, and $LFOR$ calculated with the probability and stroke distance at and above the critical current.
In the Monte-Carlo method, the randomness of lightning is taken into account and stroke locations to the span and all phase wires included. The $LFOR$ is then calculated based on the ratio of simulations where a flashover occurs to the total number of simulations, in

which the stroke distance in the flashover rate is calculated from the highest current leading to a flashover for each phase in the simulation.

With regard to recommended design values for $SFFOR$ and $BFOR$, for the critical current determination method, recommendations for the $SFFOR$ found in the literature state a design limit of 0.05 flashes per 100 km-year [7]. For the $BFOR$ only values from TSO's experience exist, which are between 0.2 to 4 flashovers/ 100km-year [7], [279], [315]. Furthermore, these values depend on tower design, lightning activity and the necessary reliability of a line. Therefore, recommendations for values are derived from the following results of all scenarios.

The most important results from both methods with regard to the base scenarios are:

- The lightning stroke distribution applied in the calculation of the flashover rates has a major influence on results,
- In which the lower median current in the LLS Scotland distribution leads to a significant reduction in the $BFOR$ in comparison the CIGRE distribution, where worst-case values for 10000 Ωm/455 Ω soil resistivity/footing resistance, maximum tower height and 500 m span length are 0.33 to 0.08 flashes per 100 km-year for current determination and 2.0 to 0.25 flashes per 100 km-year for the Monte-Carlo method.
- The $SFFOR$ is solely dependent on tower geometry and thus tower height, with minor influence of the lightning stroke distribution, where the worst-case is 0.074 flashes per 100 km-year and 0.064 flashes per 100 km-year for CIGRE and LLS Scotland distribution, respectively for the current determination method and 0.074 flashes per 100 km-year for the Monte-Carlo method.
- Up to 1000 Ωm/46 Ω soil resistivity/footing resistance, the $BFOR$ features neglectable values, 0.05 flashes per 100 km-year and 0.01 flashes per 100 km-year for CIGRE and LLS Scotland distribution for the current determination method and 0.11 flashes per 100 km-year and 0.01 flashes per 100 km-year for the Monte-Carlo method, respectively.
- Inclusion of the physical effects of the tower earthing system and representation as impedance with frequency-dependency and ionization effect leads to neglectable values of the $BFOR$.

The most important results with regard to the flashover mitigation scenarios are:

- All flashover mitigation methods reduce the $LFOR$ and $BFOR$, however only arresters and double shield wires reduce the $SFFOR$,
- where the order of effectiveness is arresters, counterpoise, double shield wires and underbuilt wires for $LFOR$, and
- arresters, counterpoise, underbuilt wires and double shield wires for $BFOR$ for the CIGRE stroke distribution.
- Double shield wires reduce the $SFFOR$, but this comes at the cost of an increased $BFOR$ due to the greater lightning attraction radius.

There also exist major differences in the method used to obtain the flashover rates. The critical current determination method is solely based on the EGM and only takes into account first strokes as well as a single value, the critical current, for the calculation of flashover rates. The Monte-Carlo method includes the randomness of lighting, which is various stroke locations, attachment angle and as the most significant difference, all three phase wire locations. Therefore, the flashover rate results differ significantly in their values. However, the general conclusion drawn above are the same for both methods. With regard to a comparison of calculated flashover rate values to values from experience, the Monte-Carlo method offers a better fit.

As previously mentioned, flashover rate limits are normally based on operational experience. Since the Monte-Carlo results show a constant value of approximately 0.6 flashes per 100 km-year for the $SFFOR$ based on the current UK/SSE 400 kV tower design with the flash density for Scotland, this can be regarded as a design limit. For the $BFOR$, results from both the critical current and Monte-Carlo method show that a value of 0.1 flashes per 100 km-year is achievable up to 46 Ω tower footing resistance, which is also below the lower end of reported values in the literature. Therefore this value can be taken as a design limit for the $BFOR$, although values of 0.2 flashes per 100 km-year would be acceptable. These values are then applied to the following recommendations.

CHAPTER 10: DISCUSSION

As it is the intention of this thesis to provide recommendations and guidance to design engineers for the lightning protection of transmission lines based on state-of-the art and developed novel methods and models, first the novelty of this work is discussed with a comparison to general practice in the assessment of the lightning protection of transmission lines. Second, the most important findings for modelling of lightning strokes to a transmission line are presented, followed by the discussion on the simulation and evaluation of simulation results. Since the thesis aims to demonstrate the applicability of this work in an industrial context, finally recommendations are developed for the current UK/SSE 400 kV tower design and OHL arrangements with lightning data from Scotland. Since the assessment of the lightning performance of a transmission line is based on the line flashover rate are dependent on the lightning flash density, recommendations have limited applicability in areas with different lightning density. However, recommendations based on the calculated flashover ratios are generally applicable, because they are not dependent on the lightning flash density, but solely on the overhead line properties.

10.1: NOVELTY OF THIS WORK

To evaluate the lightning performance of a transmission line with updated data, methods, and simulations models, the following novel advancements are accomplished:

CHAPTER 2: The Lightning Flash

Valid standards and technical brochures [24], [153], [282] base the evaluation on the assumption that positive lightning strokes are neglected due to the low probability of occurrence. Furthermore, a general lightning stroke distribution comprised of data sets from various locations (CIGRE distribution) is applied. Although [18] recommends to apply local data for the evaluation of lightning strokes to transmission lines, no data for Scotland is available in the public domain nor any recommendations on their reliability and sample size.

Therefore, in section 2.2.7: Regional Lightning Data, through a developed tool to query a LLS database, novel data for lightning stroke density and log-normal return-stroke amplitude and multiplicity for Scotland is obtained [59], which is the first data set

available for Scotland in the public domain. Furthermore, recommendations on the applicability with regard to sample size and area are developed.

Furthermore it has to be noted that valid standards and technical brochures neglected negative subsequent and positive strokes or models for them are only available for a fixed waveshape and amplitude, e.g. in [47]. However the novel data set for Scotland necessitates scalable waveforms for both negative and positive strokes, in section 2.3.4 to 2.3.6 a novel mathematical model for the generation of first and subsequent negative and first positive strokes is developed, which features the advantage of utilizing initial steepness of first strokes as well as scalability of first and subsequent negative and first positive strokes with current amplitude [323].

CHAPTER 4: The Transmission Line Insulator

Various investigations into the assessment of the lightning performance [143], [160]–[165] are conducted using the LPM model by Motoyama [139], who provides a set of parameters for air gaps.

However, as in this work the flashover behaviour of cap-and-pin insulators with arcing horns is assessed, and no data for this type of string arrangement is available in the literature, laboratory investigations are performed to determine the real flashover performance and compare the results with the LPM model and parameters by Motoyama. In this respect, novel data in the form of V-t-curves and 50% flashover voltages for a 1.2/50 µs waveshape are generated, which represent a worst-case approximation for lightning return-stroke waveshapes with shorter tail. For the EMT implementation of the measured V-t-curves, a curve-fitting procedure is developed to generate a novel worst-case LPM parameter set for cap-and-pin insulators with arcing horns [324].

CHAPTER 6: Tower Earthing Systems

Available earthing system simulation models in the literature for EMT simulations are often based on measurements or accurate finite element methods (FEM) and Method of Moments (MoM) of a specific electrode geometry and therefore lack an ease of implementation in form of circuit models or differing electrode geometry. Additionally, due to the complexity of models, soil ionization models and frequency-dependent soil models are separated in most simulation models.

As a result of these restrictions, a novel circuit model of a tower footing based on a four-rod in a square arrangement with variable geometry is developed, which features soil

ionization as well as frequency dependency [325]. The model takes into account the merging of ionization zones of the four rods which is especially important at very high soil resistivities or high injected currents, as well as the time delay of forming of the ionization area, which has an impact on the resulting voltages with regard to subsequent strokes.

CHAPTER 9: Simulation Results and Evaluation

Various studies of the assessment of the lightning performance of transmission lines are available, either conducted with the 'classic' critical current or the Monte-Carlo method. However, as conducted in this work, a more detailed assessment, taking the specific flashover behaviour of cap-and-pin insulators with arcing horns into account as well as actual lightning data from Scotland is made. The novelty in this case lies in the BFOR and SFFOR data, specific for Scottish 400 kV transmission lines, published for the first time in the literature [326], [327] and in a more usable form for other lightning densities in the determined critical currents I_c and the ratio of simulations leading to a flashover to the total number of simulations F/N. The later can be used to calculate the $LFOR$ for other flash densities.

10.2: MAIN FINDINGS

CHAPTER 2: The Lightning Flash

The most important piece of information for the assessment of the lightning performance of a transmission line is lightning data. As is evident from the evaluation of the lightning location data, there exist remarkable differences in resulting lightning parameter distributions and flash density dependent on the investigated area. It is found that the percentage of positive strokes is approximately 30%, which shows that positive strokes cannot be disregarded. Furthermore the median current amplitude is much lower than the global CIGRE distribution, 13.5 kA in comparison to 31 kA for negative strokes, and 25 kA in comparison to 35 kA for positive strokes. The average number of strokes per flash is 1.24 for negative strokes and 1.06 for positive strokes, which leads to the conclusion that positive subsequent strokes can be neglected.

With regard to the selection of an appropriate search area for lightning strokes to be considered in an evaluation, it is found that the search area is dependent on the sample size available in a LLS database, but also on topographical circumstances. The conducted research shows that the lightning activity in Scotland is very low and therefore the number

of samples is generally poor. However it is also discovered that lightning hot-spot regions exist, which feature a high number of samples, but also deviating lightning stroke probability and density compared to a wider search area. Consequentially, investigations of small areas, such as a line corridor, feature greater uncertainties with regard to the information value. Therefore, it is concluded to use average values based on 100 square-kilometer search grids rather than 1 km broad line corridors for Scotland.

CHAPTER 3: The Transmission Line

The physical effects of skin effect, travelling wave, current earth-return and corona effect of a transmission line under lightning stroke conditions all reduce the generated surge voltages on a transmission line. Therefore their inclusion is essential in modelling of a transmission line subject to lightning surges. In the literature, as well as in standards and technical reports [24], [164], [314], [316] it is common practice to neglect corona and the frequency-dependent current earth return. Consequentially, the resulting surge voltages are higher leading to a worst-case approximation with a safety margin.

As in this work, it is the aim to improve the modelling, an assessment of the current earth-return and corona effect is performed. Results show, that the current earth-return should be included, especially for higher soil resistivities. For the corona effect, for the commonly simulated first negative strokes, the dynamic corona inception does not influence the results, especially for higher lightning stroke currents due to the higher rise-time. However for negative subsequent strokes, which also lead to back-flashovers [319], [328], it is found that the dynamic corona inception voltage plays an important role.

CHAPTER 4: The Transmission Line Insulator

The flashover process of insulators with or without arcing horns has a major impact on the overall results when evaluating the lightning performance of a transmission line. Various models for the flashover criterion are found in the literature, in which the physical model of leader progression is recommended by standards and technical reports [24], [146], [153], [154], [156] due to its general application to air gaps. A comparison of the measured V-t-curve of cap-and-pin insulators with arcing horns and the one produced with LPM parameters from an air gap reveals that the parameter set for the air gap from the literature underestimates the flashover performance of cap-and-pin insulators with arcing horns. Therefore a new set of LPM parameters, specific for cap-and-pin insulators has to be applied to get closer to the real flashover performance.

CHAPTER 6: Tower Earthing Systems

The tower earthing system and the soil resistivity also have a major impact on the lightning performance of a transmission line, where soil ionization is the dominant effect for short electrode configurations and frequency-dependency of soil and travelling waves are the two main effects for long electrode configurations to be considered for lightning return-stroke currents. It is found that measurements are limited to soil resistivities in the range of 3100 Ωm and therefore uncertainties exist in the earthing system behaviour above this value. Therefore in many studies, a conservative approach to the modeling of the earthing system is taken, in which a simple fixed low-frequency resistance is applied, which does not include any of the above effects. In case these effects are included, especially in conjunction with high soil resistivities, the resulting voltages at the tower footing are highly decreased. As a result of the development of a novel tower footing model for four rods in a square, it is found that the merging of ionization zones of each rod does not decrease the total tower footing resistance as much and leads to higher footing voltages, especially at higher currents and soil resistivities. Additionally, the inclusion of the ionization delay with regard to subsequent strokes results in higher voltages at the tower footing as well. In conclusion to this, both these features have to be included in the modeling of tower earthing systems with respect to the lightning phenomena to ensure a conservative modelling approach.

CHAPTER 9: Simulation Results and Evaluation

The simulation results for both the critical current and Monte-Carlo method reveal that up to a footing resistance of 46 Ω the back-flashover rate is negligible and furthermore that there is a high risk of shielding failures due to the standard tower design with one shield wire. The investigation into flashover mitigation methods shows that arresters and counterpoise are the most effective methods to decrease the back-flashover rate. However underbuilt wires can also reduce the back-flashover to acceptable values with the advantage of lower installation and maintenance cost. A tower design with two shield wires would reduce the shielding failure flashover rate, but also leads to an increase of the back-flashover rate due to the bigger attraction area of the two shield wires. From a comparison of the two methods to determine the flashover rates it is concluded that the critical current determination method underestimates the real flashover performance when comparing results with those found in the literature. From the wealth of simulation results and the evaluation recommendations are developed, which are outlined in the following sections.

10.3: RECOMMENDATIONS WITH REGARD TO THE TOWER EARTHING DESIGN

Recommendations for the design of a transmission tower earthing system are twofold, because the design is generally focused on the reduction of the ground potential rise encountered during transmission line faults on a power-frequency basis, which is associated with the low-frequency tower footing resistance. However, the earthing system also needs to be designed to sufficiently disperse lightning stroke currents into the ground to avoid back-flashovers of insulators. In this respect, the physical phenomena in soil associated with the fast lightning surges demand for a different, sometimes contradictory design of the earthing system at challenging soil resistivities, because the earthing behaviour has the nature of an impedance [206][329][330][331] [332][333].

Due to the findings of the investigated 400 kV transmission line scenarios with lightning data for Scotland, it is concluded that the general requirement of a 10 Ω low frequency tower footing resistance or the goal to reduce the resistance as far as possible, neglecting the actual lightning activity and associated phenomena in soil, is too conservative. Instead, a requirement for the line flashover rate or back-flashover rate, taking into account lightning activity and soil properties should be employed. In this respect investigations employing the lightning activity for Scotland show, that a tower footing resistance of approximately 50 Ω still maintains an appropriate lightning protection of the transmission line with a $BFOR$ of 0.1 flashes per 100 km-year.

Furthermore, at high soil resistivities and stroke currents in the kilo-ampere range, frequency-dependency of soil and soil ionization are important factors in enhancing the dispersion of currents into ground. Although the degree of ionization on actual tower footing foundations cannot be quantified due to the complexity of actual pile, anchor or block foundations, it leads to a decrease of the resistive part of the earthing impedance during lightning conditions, especially at high soil resistivities. To improve the situation further, concrete as a backfill material for rod electrode arrangements increases this effect due to its earthing enhancement properties [238]. Therefore, the mentioned low-frequency tower footing value of 50 Ω effectively comprises additional safety margins due to the neglect of soil frequency-dependency and ionization effect.

In cases where long buried electrodes, such as counterpoise, are employed, the concept of potential equalization does not apply to fast lightning surges [216]. Due to damping and attenuation effects of high-frequency surges, the potential rise is more concentrated

at the stroke current injection point and thus not equal along the electrode. In practice this means, that an increase in electrode length decreases the low-frequency tower footing resistance, but does not decrease the high-frequency impedance any further when reaching the effective electrode length for lightning protection. An initial estimation of the effective length with regard to the soil resistivity is provided in figure 10-1 (for details see section 7.3).

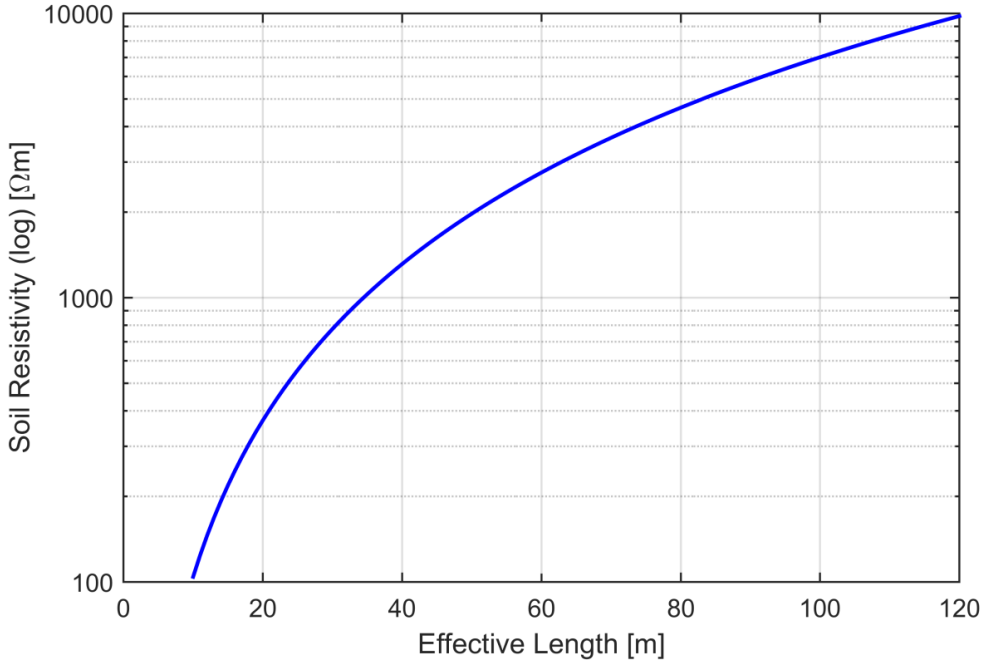

Figure 10-1: Effective length of a long buried wire in dependency of the soil resistivity, adapted from [216]

10.4: RECOMMENDATIONS FOR LIGHTNING PROTECTION WITH REGARD TO TRANSMISSION LINE DESIGN

The guidelines for engineers on the design and policies regarding lightning protection for transmission lines in Scotland are provided, deduced from the investigations of several scenarios of transmission line layouts and earthing conditions.

As already discussed in the evaluation of simulation results, specifically the shielding failure analysis, the tower design with a single shield wire contains a noticeable risk of shielding failures. In the literature a value of 0.05 flashes per 100 km-year is recommended using the critical current method with the electro-geometric lightning attachment model, which is exceeded with the standard tower design at maximum tower height. The only option to reduce the shielding failure flashover rate apart from arresters is the use of double shield wires. However, as shown in the evaluation, this comes at the expense of an increased back-flashover rate due to the greater attraction area and the fact that soil resistivity and tower earthing system improvements do not affect the shielding failure rate. Therefore in the case of standard tower design with a single shield wire it is recommended to keep the tower height along the line to a minimum as long as clearance to ground is maintained without shortening the insulator length at any point along the line.

With regard to the back-flashover rate, the evaluation clearly revealed that the lightning stroke distribution as well as the tower footing impedance is a design input parameter for the transmission line design. Generally a sufficient lightning protection against back-flashovers can be achieved in cases where soil resistivities are small, but also where the lightning activity and lightning flash density is low. The results with the CIGRE stroke distribution with 31 kA median negative current and LLS Scotland stroke distribution with 13.5 kA negative current and the LLS Scotland lightning flash density clearly show that the back-flashover rate remains reasonably low up to values of 46 Ω tower footing resistance in the worst-case scenarios, which equals a $BFOR$ of 0.1 flashes per 100 km-year. Furthermore, back-flashover rate values for the LLS Scotland stroke distribution are marginal, in worst-cases 0.25 flashes per 100 km-year. As a result, back-flashover mitigation methods, such as arresters, counterpoise or underbuilt wires only have to be

employed at high tower footing resistances and higher lightning stroke distributions or flash densities.

Overall, the back-flashover rate remains reasonably low at low soil resistivities and tower footing resistances, but also at low lightning stroke current distributions and flash densities. Deduced from the simulation results and a back-flashover rate limit of 0.2 flashes per 100 km-year, the following Flashover Mitigation Selection Scheme (FMSS) for future transmission line design is proposed in figure 10-2.

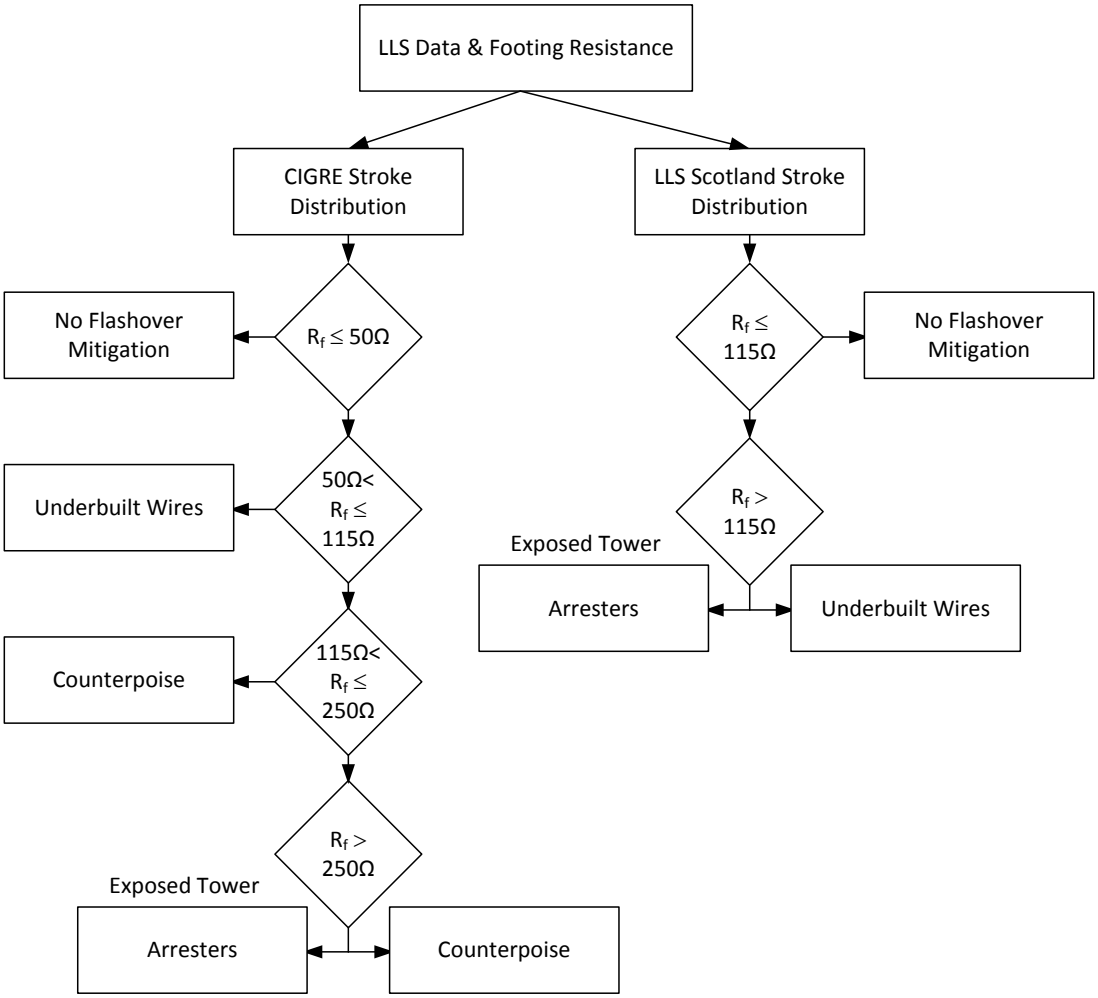

Figure 10-2: Flashover mitigation selection scheme (FFMS) based on lightning flash density for Scotland and BFOR=0.2 flashes/100km-year

The scheme takes into account the lightning stroke current and flash density distribution as well as the tower footing resistance to categorize the application of flashover mitigation methods. For exposed tower locations, such as on mountain ridges, arresters are favoured over counterpoise due to installation cost. It has to be noted, that a further safety margin is included, because the more accurate representation of the tower earthing system as impedance with ionization effect is not taken into account. Additionally, values for LLS

Scotland distribution above 115 Ω are only slightly above the set limit of 0.2 flashes/100km-year.

Once the lightning flash density and stroke current distributions are obtained from a lightning location system or known for an area and the expected tower footing resistance is calculated from soil measurements or measured, the scheme can be applied to charts as in figure 10-3 for the sample 400 kV line route through the Scottish Highlands.

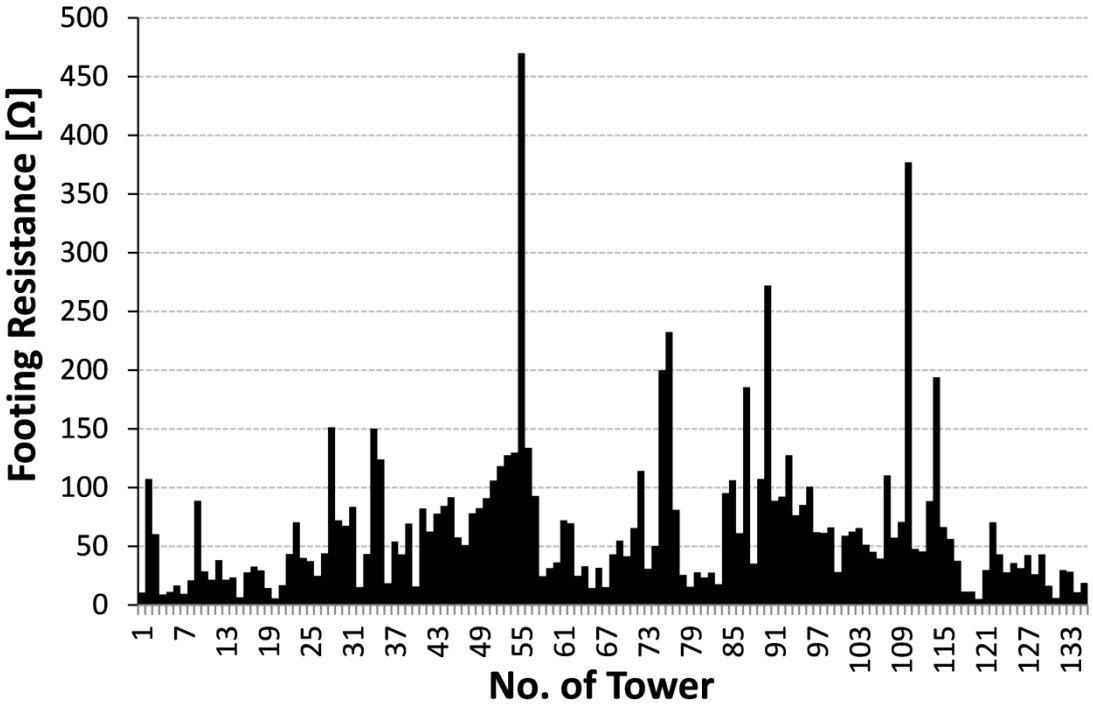

Figure 10-3: Excerpt of measured tower footing resistance of 400 kV line route through the Scottish Highlands

Using the scheme in figure 10-2 for the LLS Scotland stroke distribution, three tower locations (54, 90 and 110) are identified where flashover mitigation methods must be employed. For other locations in the range of 115 Ω to 250 Ω an underbuilt wire may be employed. However, due to the fact that the tower locations left and right of these identified locations feature a much lower footing resistance, an underbuilt wire needs not to be employed necessarily, also because soil frequency-dependency and ionization effects are not taken into account.

In this respect, although the proposed scheme offers an initial recommendation on the line route design with regard to the lightning protection on the safe side, an assessment of the lightning protection of critical sections of a transmission line using the simulation

approach taken in this work could determine the lightning performance more accurately and possibly avoid mitigation methods and reduce cost.

CHAPTER 11: CONCLUSION

Since it is the overall objective of this work to investigate the current UK/SSE 400 kV tower design and overhead line arrangements with regard to the lightning performance of a whole transmission line, it is chosen to use an electro-magnetic transient simulation approach as a state-of-the-art technique. This enables the investigation of a variety of tower and overhead line arrangements, soil conditions and earthing designs, as well as the evaluation of various measures to improve the lightning performance of a transmission line. To undertake this approach, detailed lightning data needs to be sourced and transmission line equipment models for the lightning, overhead line, insulators, transmission towers, earthing systems and flashover mitigation methods describing their physical behaviour in lightning stroke conditions need to be developed.

For the lightning an extensive literature review of the physics and characteristics alongside available lightning stroke waveshape data is performed to describe both positive and negative flashes.

Lightning data is sourced from a lightning location system to evaluate the frequency of occurrence for each span of a transmission line as well as whole areas, in this work Scotland. The evaluation of LLS data shows that the stroke amplitude distributions and local flash density for Scotland is by far less than the global average and strokes with positive polarity cannot be neglected. For a line route through the Scottish Low- and Highlands, the evaluation reveals that the stroke amplitude distributions and local flash density are by far overestimated due to the low sample size. Therefore stroke amplitude distributions and local flash density for a bigger area should be used for the assessment of the lightning protection of overhead lines. Furthermore the accuracy and reliability of LLS data is dependent on the number of measurement stations for lightning stroke localization. Consequentially the LLS with the most measurement stations in the considered area should be utilized in any evaluation of lightning data.

To incorporate the different types of lightning stroke waveshapes into the simulation, a mathematical description of positive, negative first and negative subsequent strokes is developed due to a lack of mathematical description considering new available waveshape parameters in the literature.

For modelling of transmission lines, the physical effects of travelling waves, skin-effect, current earth return and corona effect occurring during a lightning stroke attachment to the line are reviewed. It is found that all these effects reduce the overvoltages generated by a lightning stroke to a transmission line, in which the frequency-dependency of soil has an effect not be neglected for high-resistive soils. As available transmission line models in the used EMT software already include the effects of travelling waves, frequency-dependency of conductor and current earth return, only an analysis of the relevant input data, processing of data and model verification with available data and measurements in the literature is performed. The analysis reveals that the input data of conductor height over ground as well as the sagging of conductors has a relevant influence on the surge impedance inputted into transmission line models and assumptions, such as an average height for the whole line, can lead to great deviations from the real line impedance. As the effect of corona is not included in the available transmission line models, a literature review on available measurements and corona models is performed. The review shows, that the corona inception voltage for very fast rise times of lightning generated overvoltages is underestimated, which can be coped with a dynamic inception voltage. Using available measurements, formulas for positive and negative dynamic corona inception voltage are developed and implemented in the available mathematical description of the corona effect. Following the implementation of the corona effect and verification with available measurements, an evaluation of its impact on the lightning waveshapes and generated overvoltages is performed. The results show, that corona can be neglected for strokes in the vicinity of the towers and thus in the simulations.

For transmission line insulators with arcing horns a literature review on the breakdown criterion of the arcing horns, the physical process and the associated models is performed. From the literature review of models, a physical streamer-leader progression model is selected, which is based on air-gap breakdown measurements. To verify the physical model and assess the capacitive influence of the cap-and-pin insulators, laboratory breakdown test on cap-and-pin insulator strings with arcing horns are performed and compared to a transient simulation model of the impulse generator in combination with the streamer-leader progression model in order to determine the insulator/arcing-horn model parameters. Measurement results at Heriot-Watt and University of Manchester show that the resulting voltage-time-curves of cap-and-pin insulators with arcing horns perform better than a standard rod-rod arrangement found in the literature. Therefore the

parameter inputs of the physical model are adjusted to fit the measurements and ensure a more realistic breakdown process in the simulations.

For the transmission line tower a literature review on the impulse-response is conducted alongside the various approaches on modelling. It is discovered that a general model from measurements for a variety of tower geometries cannot be deduced. However theoretical approaches, especially distributed-line approaches show good agreement to measurements and a variety of tower geometries. An evaluation of the dependency of a chosen distributed-line model on tower height shows that except for the tower base impedance, fixed impedances for each section independent of tower height can be applied.

For the tower earthing system a literature review on the basic physical effects of impulse currents on earthing systems and available measurements is performed. It is found that the effects of travelling waves, soil ionization and frequency- dependency all play an important role but their significance is dependent on the type of earthing system and soil-resistivity. Furthermore it is discovered that low-frequency soil resistivity measurements cannot be used to quantify the real earthing system capability with regard to lightning. For lightning, the earthing system has to be described with its impedance at high frequencies, also taking into account low- and high-current waveshapes. Although measurements for average soil resistivity are widely available, a blank spot with regard to the soil ionization at high soil resistivity is discovered.

The literature review of tower earthing models reveals that there are currently no circuit models available, which take into account the soil ionization and frequency-dependent effect of soil. Therefore, for the two most common earthing systems, earthing rods and earthing strips, models are developed and validated with measurements available in the literature. For earthing rods, an ionization model for single rods taking into account the ionization delay is combined with a circuit model for the frequency-dependency of soil, both found in the literature are taken and a new model developed for the typical four tower feet rod arrangement. For horizontal wires used in counterpoise, a calculation procedure for wires in soil is adapted, which takes the frequency-dependency into account, and an interface created to implement the resulting transmission line model into the EMT software. Finally, a verification of the models is performed with available measurements in the literature.

With the obtained models a complete simulation model of a lightning stroke to a transmission line is created and various scenarios are investigated. This includes various soil resistivities, tower heights, span length, global and Scottish local lightning stroke distribution, representation of the earthing system as resistance and impedance including soil ionization as well as flashover mitigation methods of arresters, double shield wire, counterpoise and underbuilt wire. The line flashover rate of each scenario is determined with two different methods. In the critical current method, the minimum or critical current above which flashovers occur is determined with simulations and the flashover rates calculated using the probability of a lightning stroke exceeding a stroke current value. This method only takes vertical strokes to the shield and top phase wire into account. The current state-of-the-art Monte-Carlo method randomly generates stroke parameters and stroke locations to determine the ratio of number of simulations leading to a flashover to the total number of simulations. This method takes also strokes with an angle to the horizontal into account, enabling an attachment of lightning to the mid and bottom phase wire.

The evaluation of these simulations reveals that a reasonable lightning protection with the standard tower design is maintained for tower footing resistances up to approximately 50 Ω. Above this value, mitigation methods have to be employed to keep the back-flashover rate within reasonable limits, depending on the lightning stroke current distribution and soil resistivity or tower footing resistance, respectively. In this respect, a flashover mitigation selection scheme for 400 kV lines in Scotland is developed. In detail, underbuilt wires are suitable for high soil resistivities in the range up to 115 Ω tower footing resistance. Above that, only arresters and counterpoise with increasing copper strip length are an effective method.

Estimation of the Lightning Performance of Transmission Lines with Focus on Mitigation of Flashovers

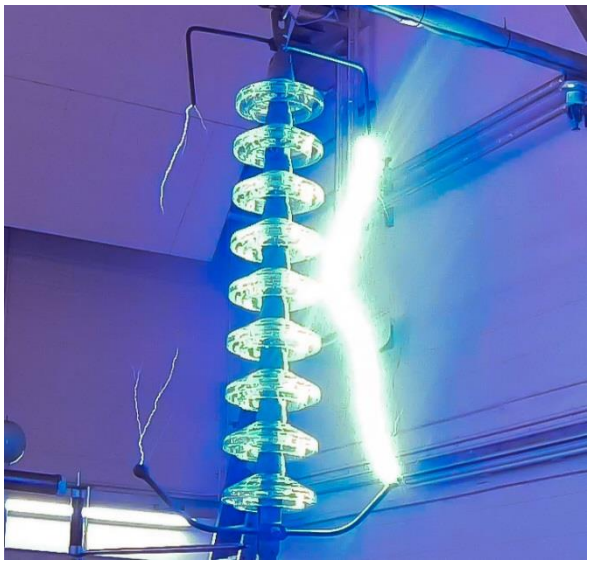

Volume 2 of 2

Fabian Matthias Koehler

Submitted for the degree of Doctor of Philosophy

Heriot-Watt University

School of Engineering & Physical Sciences

Institute of Mechanical, Process and Energy Engineering

August 2018

ABSTRACT

The growth of transmission networks into remote areas due to renewable generation features new challenges with regard to the lightning protection of transmission systems. Up to now, standard transmission line designs kept outages resulting from lightning strokes to reasonable limits with minor impacts on the power grid stability. However, due to emerging problematic earthing conditions at towers, topographically exposed transmission towers and varying lightning activity, such as encountered at the 400 kV Beauly-Denny transmission line in Scotland, the assessment of the lightning performance of transmission lines in operation and in planning emerges as an important aspect in system planning and operations.

Therefore, a fresh approach is taken to the assessment of the lightning performance of transmission lines in planning and construction, as well as possible lightning performance improvements in more detail, based on the current UK/Scottish and Southern Energy 400 kV tower design and overhead line arrangements. The approach employs electro-magnetic transient simulations where a novel mathematical description for positive, negative and negative subsequent lightning strokes, which are all scalable with stroke current, is applied. Furtermore, a novel tower foot earthing system model which combines soil ionisation and soil frequency-dependent effect is used. Novel lightning stroke distribution data for Scotland as well as novel cap-and-pin insulators with arcing horn flashover data derived from laboratory experiments are applied. For overhead lines, transmission towers, and flashover mitigation methods describing their physical behaviour in lightning stroke conditions state-of-the-art models are utilised. The investigation features a variety of tower and overhead line arrangements, soil conditions and earthing designs, as well as the evaluation of various measures to improve the performance. Results show that the lightning performance of a transmission line is less dependent on the tower earthing conditions, but more dependent on the degree of lightning activity and stroke amplitude distribution. The assessment of flashover mitigation methods shows that cost-effective and maintenance free solutions, such as underbuilt wires can effectively replace a costly improvement of the tower earthing system. However, in locations where challenging earthing conditions prevail, tower line arresters or counterpoise are the only options to maintain an effective lightning protection.

TABLE OF CONTENTS

VOLUME 1

REFERENCES

[1] F. Kießling, P. Nefzger, and U. Kaintzyk, *Freileitungen: Planung, Berechnung, Ausführung*. Springer-Verlag Berlin Heidelberg GmbH, 2001.

[2] European Network of Transmission System Operators for Electricity (ENTSO-E), "Nordic Grid Disturbance Statistics 2012." 2013.

[3] A. A. Chowdhury, L. Bertling, and B. P. Glover, "Causal and seasonal analysis of bulk transmission line forced outages using the MAPP outage database," in *2006 9th International Conference on Probabilistic Methods Applied to Power Systems, PMAPS, June 11, 2006 - June 15, 2006*, 2006.

[4] C. G. Price and D. Rind, "Possible implications of global climate change on global lightning distributions and frequencies," *Journal of Geophysical Research*, vol. 99. pp. 10823–10831, 1994.

[5] D. M. Romps, J. T. Seeley, D. Vollaro, and J. Molinari, "Projected increase in lightning strikes in the United States due to global warming," *Science*, vol. 346, no. 621, pp. 851–853, 2014.

[6] D. Oeding and B. Oswald, *Elektrische Kraftwerke und Netze*. Springer-Verlag Berlin Heidelberg, 2011.

[7] A. R. Hileman, *Insulation Coordination for Power Systems*. Taylor & Francis, 1999.

[8] Manitoba HVDC Research Centre, "PSCAD User's Guide." 2010.

[9] Manitoba HVDC Research Centre, "EMTDC User's Guide." 2010.

[10] J. R. Dwyer and M. A. Uman, "The physics of lightning," *Physics Reports*, vol. 534, no. 4, pp. 147–241, 2014.

[11] D. R. Poelman, "On the Science of Lightning : An Overview," *Royal Meteorological Institute of Belgium*, 2010.

[12] A. Küchler, *Hochspannungstechnik*. Berlin, Heidelberg: Springer Berlin Heidelberg, 2009.

[13] P. D. Hinrichsen, "Hochspannungstechnik: Der elektrische Durchschlag von Gasen," Darmstadt, 2010.

[14] V. Rakov, "The Physics of Lightning," *Surveys in Geophysics*, vol. 34, no. 6, pp. 701–729, 2013.

[15] V. Rakov and M. Uman, "Long continuing current in negative lightning ground flashes," *Journal of Geophysical Research*, vol. 95, no. D5, p. 5455, 1990.

[16] V. Rakov, "Transient response of a tall object to lightning," *IEEE Transactions on Electromagnetic Compatibility*, vol. 43, no. 4, pp. 654–661, 2001.

[17] L. Z. S. Campos, M. M. F. Saba, O. Pinto, and M. G. Ballarotti, "Waveshapes of continuing currents and properties of M-components in natural negative cloud-to-ground lightning from high-speed video observations," *Atmospheric Research*, vol. 84, no. 4, pp. 302–310, Jun. 2007.

[18] CIGRE Working Group C4.407, "Lightning Parameters for Engineering

Applications," 2013.

[19] K. Berger, "Blitzstrom-Parameter von Aufwärtsblitzen," *Bulletin SEV/VSE*, vol. 69, pp. 353–369, 1978.

[20] F. Heidler and J. Cvetic, "A Class of Analytical Functions to Study the Lightning Effects Associated With the Current Front," *ETEP*, vol. 12, no. 2, pp. 141–150, 2002.

[21] K. Berger, "Parameters of Lightning Flashes," *ELECTRA*, vol. 41, 1975.

[22] R. Anderson and A. Eriksson, "A summary of lightning parameters for engineering applications," *ELECTRA*, vol. 69, 1980.

[23] R. B. Anderson, "Summary of lightning parameters for engineering applications," *International Conference on Large High Voltage Electric Systems*, vol. 2, no. Paper 33-0, 1980.

[24] CIGRE Working Group 33.01, "Guide to procedures for estimating the lightning performance of transmission lines," 1991.

[25] J. Takami, S. Okabe, and A. O. Sites, "Observational Results of Lightning Current on Transmission Towers," *IEEE Transactions on Power Delivery*, vol. 22, no. 1, pp. 547–556, 2007.

[26] T. Narita, T. Yamada, a. Mochizuki, E. Zaima, and M. Ishii, "Observation of current waveshapes of lightning strokes on transmission towers," *IEEE Transactions on Power Delivery*, vol. 15, no. 1, pp. 429–435, 2000.

[27] F. Heidler, M. Manhardt, and K. Stimper, "Upward positive lightning measured at the Peissenberg Tower, Germany," *2013 International Symposium on Lightning Protection (XII SIPDA)*, pp. 82–90, Oct. 2013.

[28] R. Fisher, G. Schnetzer, R. Thottappillil, V. Rakov, M. Uman, and J. Goldberg, "Parameters of triggered-lightning flashes in Florida and Alabama," *Journal of Geophysical Research*, vol. 98, no. D12, p. 22887, 1993.

[29] V. Cooray and H. Pérez, "Some features of lightning flashes observed in Sweden," *Journal of Geophysical Research*, vol. 99, no. D5, p. 10683, 1994.

[30] S. Visacro, A. J. Soares, M. Schroeder, L. Cherchiglia, and V. J. de Sousa, "Statistical analysis of lightning current parameters: Measurements at Morro do Cachimbo Station," *Journal of Geophysical Research*, vol. 109, no. D1, p. D01105, 2004.

[31] K. Berger and E. Garabagnati, "Lightning current parameters," *International Union of Radio Scienctist Conference*, 1984.

[32] Lightning and Insulator Subcommitee of the T&D Commitee, "Parameters of Lightning Strokes : A Review," *IEEE Transactions on Power Delivery*, vol. 20, no. 1, pp. 346–358, 2005.

[33] J. Schoene, M. Uman, V. Rakov, K. Rambo, J. Jerauld, C. Mata, A. Mata, D. Jordan, and G. Schnetzer, "Characterization of return-stroke currents in rocket-triggered lightning," *Journal of Geophysical Research*, vol. 114, no. D3, p. D03106, Feb. 2009.

[34] V. Rakov and M. Uman, "Some properties of negative cloud-to-ground lightning flashes versus stroke order," *Journal of Geophysical Research*, vol. 95, no. D5, p. 5447, 1990.

[35] M. G. Ballarotti, C. Medeiros, M. M. F. Saba, W. Schulz, and O. Pinto, "Frequency distributions of some parameters of negative downward lightning flashes based on accurate-stroke-count studies," *Journal of Geophysical Research: Atmospheres*, vol. 117, no. D6, p. D06112, 2012.

[36] A. C. V Saraiva, M. M. F. Saba, O. Pinto, K. L. Cummins, E. P. Krider, and L. Z. S. Campos, "A comparative study of negative cloud-to-ground lightning characteristics in São Paulo (Brazil) and Arizona (United States) based on high-speed video observations," *Journal of Geophysical Research: Atmospheres*, vol. 115, no. D11, p. D11102, 2010.

[37] C. Leteinturier, J. H. Hamelin, S. Member, and A. Eybert-berard, "Submicrosecond Characteristics of Lightning Return-Stroke Currents," *IEEE Transactions on Electromagnetic Compatibility*, vol. 33, no. 4, 1991.

[38] J. Yang, X. Qie, G. Zhang, Q. Zhang, G. Feng, Y. Zhao, and R. Jiang, "Characteristics of channel base currents and close magnetic fields in triggered flashes in SHATLE," *Journal of Geophysical Research: Atmospheres*, vol. 115, no. D23, p. D23102, 2010.

[39] V. Cooray, V. Rakov, and N. Theethayi, "The lightning striking distance—Revisited," *Journal of Electrostatics*, vol. 65, no. 5–6, pp. 296–306, 2007.

[40] J. Schoene, M. Uman, and V. Rakov, "Return stroke peak current versus charge transfer in rocket-triggered lightning," *Journal of Geophysical Research*, vol. 115, no. D12, p. D12107, Jun. 2010.

[41] M. M. F. Saba, O. Pinto, and M. G. Ballarotti, "Relation between lightning return stroke peak current and following continuing current," *Geophysical Research Letters*, vol. 33, no. 23, p. L23807, Dec. 2006.

[42] A. Nag and V. Rakov, "Positive lightning: An overview, new observations, and inferences," *Journal of Geophysical Research*, vol. 117, no. D8, p. D08109, Apr. 2012.

[43] A. Nag and V. Rakov, "Parameters of Electric Field Waveforms Produced by Positive Lightning Return Strokes," *IEEE Transactions on Electromagnetic Compatibility*, vol. 56, no. 4, pp. 932–939, Aug. 2014.

[44] T. Gakuin, "Electrical characteristics of winter lightning," *Journal of Atmospheric and Terrestrial Physics*, vol. 57, no. 5, pp. 449–458, 1995.

[45] V. Rakov, "A Review of Positive and Bipolar Lightning Discharges," *Bulletin of the American Meteorological Society*, vol. 84, no. 6, pp. 767–776, Jun. 2003.

[46] K. Miyakc, T. Suzuki, K. Shinjou, and K. Miyake, "Characteristics of winter lightning current on Japan Sea coast," *IEEE Transactions on Power Delivery*, vol. 7, no. 3, pp. 1450–1457, 1992.

[47] W. Gamerota, J. Elism, M. Uman, and V. Rakov, "Current Waveforms for Lightning Simulation," *IEEE Transactions on Electromagnetic Compatibility*, vol. 54, no. 4, pp. 880–888, 2012.

[48] M. Lees, "Lightning activity in the UK," *IEE Half-day Colloquium on Lightning Protection of Wind Turbines*, pp. 2–4, 1997.

[49] V. Rakov, A. Borghetti, C. Bouquegneau, W. Chisholm, V. Cooray, K. Cummins, G. Diendorfer, F. Heidler, M. Ishii, C. Nucci, A. Piantini, O. Pinto, X. Qie, F. Rachidi, M. Saba, T. Shindo, W. Schulz, S. Visacro, and W. Zischank,

"CIGRE Technical Brochure on Lightning Parameters for Engineering Applications," pp. 373–377, 2013.

[50] Transmission and Distribution Committee of the IEEE Power Engineering Society, *IEEE Std 1243-1997: IEEE Guide For Improving The lightning Performance of Transmission Lines*. 1997, pp. 1–44.

[51] A. Greenwood, *Electrical transients in power systems*. John Wiley & Sons, Ltd, 1991.

[52] C. F. Wagner and A. Hileman, "Surge impedance and its application to the Lightning Stroke," *Transactions of the American Institute of Electrical Engineers. Part III: Power Apparatus and Systems*, no. 2, pp. 1011–1020, 1961.

[53] K. Cummins, "A Review of Lightning Information for Power Systems Analysis," pp. 1072–1076.

[54] F. Heidler, J. M. Cvetic, and B. V. Stanic, "Calculation of lightning current parameters," *IEEE Transactions on Power Delivery*, vol. 14, no. 2, pp. 399–404, Apr. 1999.

[55] F. Heidler, "Analytische Blitzstromfunktion zur LEMP-berechnung," *Proc. 18th Int. Conf. Lightning Protection*, 1985.

[56] C. A. Nucci, F. Rachidi, and V. Michel, "Lightning-Induced Voltages on Overhead Lines," *IEEE Transactions on Electromagnetic Compatibility*, vol. 35, no. 9204745, 1993.

[57] A. De Conti and S. Visacro, "Analytical Representation of Single- and Double-Peaked Lightning Current Waveforms," *IEEE Transactions on Electromagnetic Compatibility*, vol. 49, no. 2, pp. 448–451, May 2007.

[58] D. Lovrić, S. Vujević, and T. Modrić, "On the estimation of Heidler function parameters for reproduction of various standardized and recorded lightning current waveshapes," *International Transactions on Electrical Energy Systems*, 2013.

[59] F. Koehler and J. Swingler, "An Evaluation Procedure for Lightning Strike Distributions on Transmission Lines," in *International Conference on Lightning Protection*, 2016.

[60] B. Gustavsen, J. A. Martinez, D. Durbak, B. Johnson, J. Mahseredjian, B. Mork, and R. Walling, "Parameter determination for modeling system transients - Part I: Overhead Lines," *IEEE Transactions on Power Delivery*, vol. 20, no. 3, pp. 2045–2050, 2005.

[61] A. F. Imece, D. W. Durbak, H. Elahi, S. Kolluri, D. Mader, T. E. Mcdermott, A. Morched, A. M. Mousa, R. Natarajan, L. Rugeles, and E. Tarasiewicz, "MODELING GUIDELINES FOR FAST FRONT TRANSIENTS - Report Prepared by the Fast Front Transients Task Force of the IEEE Modeling and Analysis of System Transients Working Group."

[62] E. Jordan and K. Balmain, *Electromagnetic waves and radiating systems*. Prentice Hall Professional, 1968.

[63] L. V. Bewley, "Traveling Waves on Transmission Systems," *Transactions of the American Institute of Electrical Engineers*, vol. 50, pp. 532–550, 1931.

[64] H. W. Johnson and M. Graham, *High-speed Signal Propagation: Advanced Black Magic*. Prentice Hall Professional, 2003.

[65] F. E. Gardiol, *Lossy Transmission Lines*. Artech House, 1987.

[66] A. S. Meliopoulos, "Power System Grounding and Transients-An Introduction," *Mar & Dekker, Inc., New York and Basel*, 1988.

[67] H. W. Dommel, *Electromagnetic Transients Program Theory Book*. Microtran Power System Analysis Corporation, 1986.

[68] G. Herold, *Elektrische Energieversorgung II.: Parameter elektrischer Stromkreise, Leitungen, Transformatoren*. J. Schlembach, 2008.

[69] L. Grigsby, *Electric Power Generation, Transmission and Distribution*. CRC Press, 2012.

[70] J. Martinez-Velasco, *Power System Transients: Parameter Determination*. CRC Press, 2009.

[71] C. Paul, *Analysis of Multiconductor Transmission Lines*. Wiley-IEEE Press, 2008.

[72] J. R. Carson, "Wave Propagation in Overhead Wires with Ground Return," *Bell System Technical Journal*, vol. 5, pp. 539–554, 1926.

[73] A. Deri, G. Tevan, A. Semlyen, and A. Castanheira, "The Complex Ground Return Plane a Simplified Model for Homogeneous and Multi-Layer Earth Return," *IEEE Transactions on Power Apparatus and Systems*, vol. PAS-100, no. 8, pp. 3686–3693, 1981.

[74] C. Medeiros Portela, M. Cristina Tavares, and J. Pissolato Filho, "Accurate representation of soil behaviour for transient studies," *IEE Proceedings - Generation, Transmission and Distribution*, vol. 150, no. 6, p. 736, 2003.

[75] C. Portela, "Frequency and transient behavior of grounding systems. I. Physical and methodological aspects," *IEEE 1997 International Symposium on Electromagnetic Compatibility*, 1997.

[76] C. Portela, "Frequency and transient behavior of grounding systems. II. Practical application examples," *IEEE 1997 International Symposium on Electromagnetic Compatibility*, pp. 385–390, 1997.

[77] R. Alipio and S. Visacro, "Frequency dependence of soil parameters: Effect on the lightning response of grounding electrodes," *IEEE Transactions on Electromagnetic Compatibility*, vol. 55, no. 2, pp. 132–139, 2013.

[78] C. Portela, "Measurement and modeling of soil electromagnetic behavior," *1999 IEEE International Symposium on Electromagnetic Compatability*, vol. 2, pp. 1004–1009, 1999.

[79] Z. Li, J. He, and B. Zhang, "The influence of frequency dependent soil parameters on transmission line," *International Conference on Lightning Protection*, pp. 1010–1013, 2014.

[80] R. Moura, M. Schroeder, P. Menezes, L. Nascimento, and A. Lobato, "Influence of the Soil and Frequency Effects to Evaluate Atmospheric Overvoltages in Overhead Transmission Lines – Part I : The Influence of the Soil in the Transmission Lines Parameters," in *XV International Conference on Atmospheric Electricity*, 2014, no. June, pp. 15–20.

[81] A. de Lima and C. Portela, "Inclusion of frequency-dependent soil parameters in transmission-line modeling," *IEEE Transactions on Power Delivery*, vol. 22, no.

1, pp. 492–499, 2007.

[82] S. Visacro, F. H. Silveira, S. Xavier, and H. B. Ferreira, “Frequency dependence of soil parameters: The influence on the lightning performance of transmission lines,” *International Conference on Lightning Protection*, pp. 1–4, Sep. 2012.

[83] S. Visacro, F. H. Silveira, and R. Alípio, “How the Lightning Performance of Electrical Power Systems is affected by the Frequency Dependence of Soil Parameters,” in *International Conference on Lightning Protection*, 2014, pp. 1267–1271.

[84] A. Semlyen, “Accuracy limits in the computed transients on overhead lines due to inaccurate ground return modeling,” *IEEE Transactions on Power Delivery*, vol. 17, no. 3, pp. 872–878, 2002.

[85] Z. Li and B. Zhang, “Influence of frequency characteristics of soil parameters on ground-return transmission line parameters,” *Electric Power Systems Research*, vol. 139, pp. 127–132, 2016.

[86] R. Moura, M. Schroeder, P. Menezes, L. Nascimento, and A. Lobato, “Influence of the Soil and Frequency Effects to Evaluate Atmospheric Overvoltages in Overhead Transmission Line - Part II : The Influence of the Soil in Atmospheric,” *XV International Conference on Atmospheric Electricity*, no. June, pp. 15–20, 2014.

[87] S. Visacro, R. Alipio, M. H. Murta Vale, and C. Pereira, “The response of grounding electrodes to lightning currents: The effect of frequency-dependent soil resistivity and permittivity,” *IEEE Transactions on Electromagnetic Compatibility*, vol. 53, no. 2, pp. 401–406, 2011.

[88] R. Alipio, “A New Model for the Frequency Dependence of Soil Parameters,” in *International Conference on Lightning Protection*, 2014, pp. 1432–1436.

[89] R. Alipio and S. Visacro, “Modeling the Frequency Dependence of Electrical Parameters of Soil,” *IEEE Transactions on Electromagnetic Compatibility*, vol. 56, no. 5, pp. 1163–1171, 2014.

[90] C. M. Portela, J. B. Gertrudes, M. C. Tavares, and J. Pissolato, “Earth conductivity and permittivity data measurements: Influence in transmission line transient performance,” *Electric Power Systems Research*, vol. 76, pp. 907–915, 2006.

[91] S. Wang, Z. Li, J. Zhang, J. Wang, L. Cheng, T. Yuan, and B. Zhu, “Experimental study on frequency-dependent properties of soil electrical parameters,” *Electric Power Systems Research*, vol. 139, pp. 116–120, 2016.

[92] R. Davis, R. W. E. Cook, and W. G. Standring, “The surge corona discharge,” *Proceedings of the IEE Part C: Monographs*, vol. 108, no. 13, p. 230, 1961.

[93] J. Lucas, “High voltage engineering,” *Colombo, Open University of Sri. Lanka*, 2001.

[94] P. Maruvada, “Corona characteristics of conductor bundles under impulse voltages,” *IEEE Transactions on Power Apparatus and Systems*, vol. 96, no. 1, 1977.

[95] C. Gary, G. Dragan, and D. Critescu, “Attenuation of Traveling Waves caused by Corona,” *CIGRE Technical Brochure*, 1978.

[96] G. V Podporkin and A. Sivaev, “Lightning impulse corona characteristics of

conductors and bundles," *IEEE Transactions on Power Delivery*, vol. 12, no. 4, pp. 1842–1847, 1997.

[97] L. Ganesan and M. J. Thomas, "Studies on the influence of corona on overvoltage surges," *Electric Power Systems Research*, vol. 53, no. 2, pp. 97–103, 2000.

[98] C. Gary, G. Dragan, and I. Langu, "Impulse corona discharge energy around the conductors," *Industry Applications Society Annual Meeting*, pp. 2–4, 1990.

[99] C. Gary, G. Drăgan, and I. Lungu, "Several physical characteristics of impulse-corona discharge around conductors. Part 2: Onset voltage and delay time of corona discharge," *IEE Proceedings Physical Science*, pp. 191–196, 1989.

[100] P. S. Maruvada, D. H. Nguyen, and H. Hamadani-Zadeh, "Studies on Modeling Corona Attenuation of Dynamic Overvoltages," *IEEE Power Engineering Review*, vol. 9, no. 4, pp. 106–106, 1989.

[101] C. Wagner and B. Lloyd, "Effects of corona on traveling waves," *Electrical Engineering*, 1955.

[102] P. Yang, S. M. Chen, and J. He, "Lightning Impulse Corona Characteristic of 1000-kV UHV Transmission Lines and Its Influences on Lightning Overvoltage Analysis Results," *IEEE Transactions on Power Delivery*, vol. 28, no. 4, pp. 2518–2525, 2013.

[103] J. He, X. Zhang, P. Yang, S. Chen, and R. Zeng, "Attenuation and deformation characteristics of lightning impulse corona traveling along bundled transmission lines," *Electric Power Systems Research*, vol. 118, pp. 29–36, 2015.

[104] S. Astinfeshan, A. Gholami, and M. Mohajeri, "Analysis of corona effect on lightning performance of HV overhead transmission line using ATP/EMTP," *ICEE 2012 - 20th Iranian Conference on Electrical Engineering*, pp. 485–488, 2012.

[105] T. J. Gallagher and I. M. Dudurych, "Model of corona for an EMTP study of surge propagation along HV transmission lines," *IEE Proceedings-Generation, Transmission and Distribution*, pp. 61–66, 2004.

[106] M. A. Kadir and W. Ahmad, "The Importance of Corona Effect in Lightning Surge Propagation Studies," *Journal of Applied Sciences*, vol. 8, 2008.

[107] K. C. Lee, "Non-Linear Corona Models in an Electromagnetic Transient Program (EMTP)," *IEEE Transactions on Power Apparatus and Systems*, vol. 0, no. 9, pp. 2936–2942, 1983.

[108] J. M. Li and Y. Zhang, "Improvement on the Corona Model of Ultra High Voltage Alternating Current Transmission Lines," in *Proceedings of 2013 IEEE International Conference on Applied Superconductivity and Electromagnetic Devices*, 2013, pp. 69–75.

[109] Y. Lu, D. Sui, and J. Xu, "Study on the Lightning Withstand Ability of Transmission Line Considering Surge Corona," in *Sixth International Conference on Electromagnetic Field Problems and Applications (ICEF)*, 2012.

[110] J. Naredo, A. Soudack, and J. Marti, "Simulation of transients on transmission lines with corona via the method of characteristics," *IEE Proceedings-Generation, Transmission and Distribution*, p. 7619, 1995.

[111] M. Davila, J. L. Naredo, M. P. Moreno, R. J. Gutierrez, and Z. P. Gomez,

"Analyzing transients on multiconductor lines with corona," *2004 IEEE/PES Transmission and Distribution Conference and Exposition Latin America IEEE*, pp. 236–242, 2004.

[112] M. A. De Freitas, S. Kurokawa, and J. Pissolato Filho, "Corona effect in frequency dependent transmission line models," *2008 IEEE/PES Transmission and Distribution Conference and Exposition: Latin America*, pp. 1–7, 2008.

[113] M. S. Mamis, "Computation of electromagnetic transients on transmission lines with nonlinear components," *IEE Proceedings - Generation, Transmission and Distribution*, vol. 150, no. 2, p. 200, 2003.

[114] T. H. Thang, Y. Baba, N. Nagaoka, A. Ametani, J. Takami, S. Okabe, and V. Rakov, "FDTD simulation of lightning surges on overhead wires in the presence of corona discharge," *IEEE Transactions on Electromagnetic Compatibility*, vol. 54, no. 6, pp. 1234–1243, 2012.

[115] H. Kudyan and C. H-Shih, "A Nonlinear Circuit Model for Transmission Lines in Corona," *IEEE Transactions on Power Apparatus and Systems*, vol. PAS-100, no. 3, pp. 1420–1430, 1981.

[116] F. W. Peek, "The Law of Corona and the Dielectric Strength of Air I-IV," *Transactions of the American Institute of Electrical Engineers*, Jul. 1911.

[117] K. Lee, "Non-Linear Corona Models in an Electromagnetic Transient Program," *Power Apparatus and Systems, IEEE Transactions on*, vol. 0, no. 9, pp. 2936–2942, 1983.

[118] A. Semlyca and H. Wei-Gang, "Corona Modelling for the Calculation of Transients on Transmission Lines," *IEEE Transactions on Power Delivery*, vol. 1, no. 3, pp. 228–239, 1986.

[119] M. Mihailescu-Suliciu and I. Suliciu, "A Rate Type Constitutive Equation for the Description of the Corona Effect," *IEEE Transactions on Power Apparatus and Systems*, vol. PAS-100, no. 8, 1981.

[120] C. de Jesus and M. T. C. de Barros, "Modelling of corona dynamics for surge propagation studies," *IEEE Transactions on Power Delivery*, vol. 9, no. 3, pp. 1564–1569, 1994.

[121] X. Li, O. P. Malik, and Z. Zhao, "A practical mathematical Model of Corona for Calculation of Transients on Transmission Lines," *IEEE Transactions on Power Delivery*, vol. 4, no. 2, pp. 1145–1152, 1989.

[122] M. Al-Tai, H. Elayyan, D. German, A. Haddad, N. Harid, and R. T. Waters, "The simulation of surge corona on transmission lines," *Power Delivery, IEEE Transactions on*, vol. 4, no. 2, pp. 1360–1368, 1989.

[123] J. Carnairo, J. R. Marti, H. W. Dommel, and H. M. Barros, "An Efficient Procedure for the Implementation of Corona Models in Electromagnetic Transient Programs," *IEEE Transactions on Power Delivery*, vol. 9, 1994.

[124] S. Carneiro and J. R. Marti, "Evaluation of corona and line models in electromagnetic transients simulations," *IEEE Transactions on Power Delivery*, vol. 6, no. 1, pp. 334–342, 1991.

[125] T. Noda, N. Nose, N. Nagaoka, and A. Ametani, "A Wave-Front-Time Dependent Corona Model for Transmission-Line Surge Calculations," *Electrical Engineering in Japan*, vol. 129, no. 1, pp. 29–38, 1999.

[126] A. Semlyen and W.-G. Huang, “Computation of Electro-Magnetic Transients on Three-Phase Transmission Lines with Corona and Frequency-Dependent Parameters,” *IEEE Transactions on Power Delivery*, vol. 2, no. 3, pp. 887–898, 1987.

[127] J. Wang and X. Wang, “Lightning transient simulation of transmission lines considering the effects of frequency dependent and impulse corona,” *2011 International Conference on Electrical and Control Engineering, ICECE 2011 - Proceedings*, pp. 696–699, 2011.

[128] H. H. Skilling and P. de K. Dykes, “Distortion of Traveling Waves by Corona,” *Transactions of the American Institute of Electrical Engineers*, vol. 56, no. 7, pp. 850–857, 1937.

[129] L. Bergeron, “Water hammer in hydraulics and wave surges in electricity,” 1961.

[130] B. Gustavsen and A. Semlyen, “Rational approximation of frequency domain responses by vector fitting,” *IEEE Transactions on Power Delivery*, 1999.

[131] A. Morched, B. Gustavsen, and M. Tartibi, “A universal model for accurate calculation of electromagnetic transients on overhead lines and underground cables,” *IEEE Transactions on Power Delivery*, vol. 14, no. 3, pp. 1032–1037, 1999.

[132] B. Gustavsen, “Computer code for rational approximation of frequency dependent admittance matrices,” *IEEE Transactions on Power Delivery*, vol. 17, no. 4, pp. 1093–1098, 2002.

[133] A. M. Miri, *Ausgleichsvorgänge in Elektroenergiesystemen: Mathematische Einführung, elektromagnetische und elektromechanische Vorgänge*. Springer-Verlag, 2013.

[134] H. W. Dommel, “Berechnung elektromagnetischer Ausgleichsvorgaenge in elektrischen Netzen mit Digitalrechnern,” *Bulletin SEV/VSE*, vol. 60, pp. 538–548, 1969.

[135] A. De Conti and R. Alipio, “Lightning Transients on Branched Distribution Lines Considering Frequency-Dependent Ground Parameters,” in *International Conference on Lightning Protection*, 2016.

[136] C. F. Wagner, I. W. Gross, and B. L. Lloyd, “High-Voltage Impulse Tests on Transmission Lines,” *Transactions of the American Institute of Electrical Engineers. Part III: Power Apparatus and Systems*, vol. 73, no. 1, pp. 196–210, 1954.

[137] C. F. Wagner, A. Wagner, E. L. Peterson, and I. W. Gross, “Corona Considerations on High-Voltage Lines and Design Features of Tidd 500-Kv Test Lines,” *Transactions of the American Institute of Electrical Engineers*, vol. 66, no. 1, pp. 1583–1591, 1947.

[138] W. Chisholm, “New challenges in lightning impulse flashover modeling of air gaps and insulators,” *IEEE Electrical Insulation Magazine*, vol. 26, no. 2, pp. 14–25, 2010.

[139] H. Motoyama, “Experimental study and analysis of breakdown characteristics of long air gaps with short tail lightning impulse,” *IEEE Transactions on Power Delivery*, vol. 11, no. 2, pp. 972–979, 1996.

[140] A. Pigini and G. Rizzi, “Performance of large air gaps under lightning

overvoltages: experimental study and analysis of accuracy predetermination methods," *IEEE Transactions on Power Delivery*, 1989.

[141] T. Shindo and T. Suzuki, "A new calculation method of breakdown voltage-time characteristics of long air gaps," *IEEE Transactions on Power Apparatus and Systems*, 1985.

[142] T. Suzuki and K. Miyake, "Experimental study of breakdown voltage-time characteristics of large air gaps with lightning impulses," *IEEE Transactions on Power Apparatus and Systems*, vol. 96, 1977.

[143] X. Wang, Z. Yu, and J. He, "Breakdown Process Experiments of 110- to 500-kV Insulator Strings Under Short Tail Lightning Impulse," *IEEE Transactions on Power Delivery*, vol. 29, no. 5, pp. 2394–2401, 2014.

[144] T. Shindo, Y. Aoshima, I. Kishizima, and T. Harada, "A study of predischarge current characteristics of long air gaps," *IEEE Transactions on Power Apparatus and Systems*, vol. 78, no. 11, pp. 3262–3268, 1985.

[145] C. Wagner and A. Hileman, "Mechanism of breakdown of laboratory gaps," *Transactions of the American Institute of Electrical Engineers - Power Apparatus and Systems, Part III*, vol. 80, pp. 604–618, 1961.

[146] CIGRE Working Group 33.07, "Guidelines for the evaluation of the dielectric strength of external insulation," 1992.

[147] W. Hauschild and E. Lemke, *High-Voltage Test and Measuring Techniques*. Springer-Verlag, 2014.

[148] R. Caldwell and M. Darveniza, "Experimental and analytical studies of the effect of non-standard waveshapes on the impulse strength of external insulation," *IEEE Transactions on Power Apparatus and Systems*, vol. 4, 1973.

[149] C. Gary, R. Garabedian, Z. Zhang, D. Cristescu, and R. Enache, "Breakdown characteristics of insulator strings stressed by short tail waves," *IEE Proceedings Physical Science*, vol. 133, no. 8, 1986.

[150] A. Inoue and S. I. Kanao, "Observation and analysis of multiple-phase grounding faults caused by lightning," *IEEE Transactions on Power Delivery*, vol. 11, no. 1, pp. 353–358, 1996.

[151] M. Kadir, M. Ahmad, and J. Jasni, "Effect of the Non-Standard Lightning Current and Waveshape on Lightning Surge Analysis," *Asian Journal of Applied Science*, 2008.

[152] Y. Matsumoto, O. Sakuma, K. Shinjo, M. Saiki, T. Wakai, T. Sakai, H. Nagasaka, H. Motoyama, and M. Ishii, "Measurement of lightning surges on test transmission line equipped with arresters struck by natural and triggered lightning," *IEEE Transactions on Power Delivery*, vol. 11, no. 2, pp. 996–1002, 1996.

[153] IEC/TR 60071-4: 2004, "Insulation co-ordination - Part 4: Computational guide to insulation co-ordination and modelling of electrical networks," 2004.

[154] CIGRE Working Group 33.02, "Guidelines for Representation of Network Elements when Calculating Transients," 1990.

[155] I. Cotton, A. Kadir, and M. Abidin, "A randomised leader progression model for backflashover studies," *European Transactions on Electrical Power*, vol. 18, pp. 709–724, 2008.

[156] IEEE Task Force on Fast Front Transients, "Modeling guidelines for fast front transients," *IEEE Transactions on Power Delivery*, vol. 11, no. 1, pp. 493–506, 1996.

[157] D. Kind, "Die Aufbaufläche bei Stoßbeanspruchung technischer Elektrodenanordnungen in Luft," *Ph.D. Dissertation TU München*. 1957.

[158] M. Darveniza and A. Vlastos, "Generalized integration method for predicting impulse volt-time characteristics for non-standard wave shapes - a theoretical basis.," *IEEE Transactions on Electrical Insulation*, vol. 23, no. 3, pp. 373–381, 1988.

[159] T. Ueda, S. Neo, and T. Funabashi, "Flashover model for arcing horns and transmission line arresters," *International Conference on Power Systems Transients*, 1995.

[160] Z. Datsios and P. Mikropoulos, "Implementation of leader development models in ATP-EMTP Using a type-94 circuit component," *International Conference on Lightning Protection*, 2014.

[161] T. Mozumi, Y. Baba, M. Ishii, N. Nagaoka, and A. Ametani, "Numerical electromagnetic field analysis of archorn voltages during a back-flashover on a 500-kV twin-circuit line," *IEEE Transactions on Power Delivery*, vol. 18, no. 1, pp. 207–213, 2003.

[162] T. Pham and S. Boggs, "Flashover model of arcing horn in transient simulation," *Conference Record of IEEE International Symposium on Electrical Insulation*, pp. 8–11, 2010.

[163] A. Ametani, N. Nagaoka, K. Ueno, and T. Funabashi, "Investigation of flashover phases in a lightning surge by new archorn and tower models," *IEEE/PES Transmission and Distribution Conference and Exhibition*, vol. 2, pp. 0–5, 2002.

[164] A. Ametani and T. Kawamura, "A method of a lightning surge analysis recommended in Japan using EMTP," *IEEE Transactions on Power Delivery*, vol. 20, no. 2 I, pp. 867–875, 2005.

[165] M. Kizilcay, "Mitigation of Back-Flashovers for 110-kV Lines at Multi-Circuit Overhead Line Towers," *Proceedings of the International Conference on Power Systems Transients*, 2009.

[166] Z. G. Datsios and P. N. Mikropoulos, "Modeling of lightning impulse behavior of long air gaps and insulators including predischarge current: Implications on insulation coordination of overhead transmission lines and substations," *Electric Power Systems Research*, vol. 139, pp. 37–46, 2015.

[167] Z. G. Datsios, P. N. Mikropoulos, and T. E. Tsovilis, "Estimation of the minimum shielding failure flashover current for first and subsequent lightning strokes to overhead transmission lines," *Electric Power Systems Research*, vol. 113, pp. 141–150, 2014.

[168] M. Kizilcay and C. Neumann, "Backflashover Analysis for 110-kV Lines at Multi-Circuit Overhead Line Towers," *International Conference on Power Systems Transients*, pp. 4–9, 2007.

[169] M. Fernandes, M. C. de Barros, and M. Ameida, "Statistical Study of the Lightning Overvoltages at a Gas Insulated Station Transformer," *International Conference on Power Systems Transients*, 1995.

[170] BS EN 60060-1, *High-voltage test techniques – Part 1: General definitions and test requirements*. 2010, p. 154.

[171] BS EN 60060-2, *High-voltage test techniques Part 2 : Measuring systems*. 2011.

[172] BS EN 60052, *Voltage measurement by means of standard air gaps*, vol. 3. 2002.

[173] A. Schwab, *Hochspannungsmesstechnik - Messgeraete und Messverfahren*. Springer Berlin Heidelberg, 2011.

[174] M. Naidu and V. Kamaraju, *High Voltage Engineering*. McGraw-Hill, 2013.

[175] CIGRE Working Group C4.501, "Guideline for Numerical Electromagnetic Analysis Method and its Application to Surge Phenomena," vol. 543. 2013.

[176] M. Sargent and M. Darveniza, "Tower Surge Impedance," *IEEE Transactions on Power Apparatus and Systems*, vol. PAS-88, no. 5, pp. 680–687, May 1969.

[177] W. A. Chisholm, Y. L. Chow, and K. D. Srivastava, "Travel Time of Transmission Towers," *IEEE Transactions on Power Apparatus and Systems*, vol. PAS-104, no. 10, pp. 2922–2928, 1985.

[178] H. Motoyama and H. Matsubara, "Analytical and experimental study on surge response of transmission tower," *IEEE Transactions on Power Delivery*, vol. 15, no. 2, pp. 812–819, 2000.

[179] Z. Lu and D. Li, "The lightning protection performance of back striking for double-circuit transmission line based on the distributed transmission line tower model," in *2011 7th Asia-Pacific International Conference on Lightning, APL2011*, 2011, no. 2, pp. 500–503.

[180] C. F. Wagner and A. R. Hileman, "A New Approach to Calculation of Lightning Performance of Transmission Lines-II," *Transactions of the American Institute of Electrical Engineers. Part III: Power Apparatus and Systems*, vol. 78, no. 4, pp. 996–1020, Dec. 1959.

[181] A. Ametani, Y. Kasa, J. Sawada, A. Mochizuki, and T. Yamada, "Frequency-dependent impedance of vertical conductors and a multiconductor tower model," *IEE Proceedings - Generation, Transmission and Distribution*, vol. 141, no. 4, p. 339, 1994.

[182] J. A. Gutiérrez, R. P. Moreno, J. L. Naredo, J. L. Bermúdez, M. Paolone, C. a. Nucci, and F. Rachidi, "Nonuniform transmission tower model for lightning transient studies," *IEEE Transactions on Power Delivery*, vol. 19, no. 2, pp. 490–496, 2004.

[183] N. Harid, H. Griffiths, and A. Haddad, "A New Frequency-Dependent Surge Impedance Calculation Method for High-Voltage Towers," *IEEE Transactions on Power Delivery*, vol. 21, no. 3, pp. 1430–1437, 2006.

[184] T. Ueda and T. Ito, "A comparison between two tower models for lightning surge analysis of 77 kV system," in *International Conference on Power System Technology*, 2000, vol. 1, pp. 433–437.

[185] T. Yamada, a. Mochizuki, J. Sawada, E. Zaima, T. Kawamura, a. Ametani, M. Ishii, and S. Kato, "Experimental evaluation of a UHV tower model for lightning surge analysis," *IEEE Transactions on Power Delivery*, vol. 10, no. 1, pp. 393–402, 1995.

[186] H. Motoyama, Y. Kinoshita, and K. Nonaka, "Experimental Study on Lightning

Surge Response of 500kV Transmission Tower with Overhead Lines," *IEEE Transactions on Power Delivery*, vol. 23, no. 4, pp. 2488–2495, 2008.

[187] G. Breuer and A. Schultz, "Field studies of the surge response of a 345-kV transmission tower and ground wire," *Transactions of the American Institute of Electrical Engineers. Part III: Power Apparatus and Systems*, vol. 3, no. 76, pp. 1392–1396, 1957.

[188] M. Kawai, "Studies of the Surge Response on a Transmission Line Tower," in *IEEE Summer General Meeting and Nuclear Radiation Effects Conference*, 1964, no. 63–1041, pp. 30–34.

[189] R. Davis and J. E. M. Johnston, "The Surge Characteristics of Tower and Tower-Footing," *Journal of the Institution of Electrical Engineers-Part II: Power Engineering*, vol. 88, no. 5, 1941.

[190] J. Takami, T. Tsuboi, K. Yamamoto, S. Okabe, and Y. Baba, "Lightning surge characteristics on inclined incoming line to substation based on reduced-scale model experiment," *IEEE Transactions on Dielectrics and Electrical Insulation*, vol. 20, no. 3, pp. 739–746, 2013.

[191] J. L. Bermudez, J. A. Gutiérrez, W. A. Chisholm, F. Rachidi, and M. Paolone, "A Reduced-Scale Model to Evaluate the Response of Tall Towers Hit by Lightning," *International Symposium on Power Quality (SICEL)*, 2001.

[192] Y. Ikeda, N. Nagaoka, Y. Baba, and A. Ametani, "A frequency dependent circuit model of a wind turbine tower using transient response calculated by FDTD," *International Conference on Lightning Protection*, vol. 113, pp. 1–6, 2012.

[193] T. Noda, "A Numerical Simulation of Transient Electromagnetic Fields for Obtaining the Step Response of a Transmission Tower Using the FDTD Method," *IEEE Transactions on Power Delivery*, vol. 23, no. 2, pp. 1262–1263, 2008.

[194] T. X. Cao, T. Pham, and S. Boggs, "Computation of Tower Surge Impedance in Transmission," in *2013 Electrical Insulation Conference*, 2013, pp. 77–80.

[195] A. Tatematsu, "Development of a Surge Simulation Code VSTL REV Based on the 3D FDTD Method," in *IEEE International Symposium on Electromagnetic Compatibility (EMC)*, 2015, pp. 1111–1116.

[196] H. Motoyama, Y. Kinoshita, K. Nonaka, and Y. Baba, "Experimental and analytical studies on lightning surge response of 500-kV transmission tower," *IEEE Transactions on Power Delivery*, vol. 24, no. 4, pp. 2232–2239, 2009.

[197] J. Takami, T. Tsuboi, K. Yamamoto, S. Okabe, Y. Baba, and A. Ametani, "Lightning surge response of a double-circuit transmission tower with incoming lines to a substation through FDTD simulation," *IEEE Transactions on Dielectrics and Electrical Insulation*, vol. 21, no. 1, pp. 96–104, 2014.

[198] Y. Baba and M. Ishii, "Numerical electromagnetic field analysis of tower surge response," *IEEE Transactions on Power Delivery*, vol. 12, no. 1, pp. 483–488, 1997.

[199] W. A. Chisholm, Y. L. Chow, and K. D. Srivastava, "Lightning Surge Response of Transmission Towers," *Power Engineering Review, IEEE*, vol. PER-3, no. 9, pp. 56–57, 1983.

[200] L. Grcev and F. Rachidi, "On tower impedances for transient analysis," *IEEE*

Transactions on Power Delivery, vol. 19, no. 3, pp. 1238-- 44, 2004.

[201] H. Motoyama, K. Shinjo, Y. Matsumoto, and N. Itamoto, "Observation and analysis of multiphase back flashover on the Okushishiku Test Transmission Line caused by winter lightning," *IEEE Transactions on Power Delivery*, vol. 13, no. 4, pp. 1391–1398, 1998.

[202] M. Ishii, T. Kawamura, and T. Kouno, "Multistory transmission tower model for lightning surge analysis," *IEEE Transactions on Power Delivery*, vol. 6, no. 3, pp. 1327–1335, 1991.

[203] A. Ametani, N. Nagaoka, T. Funabashi, and N. Inoue, "Tower Structure Effect on a Back-Flashover Phase," in *International Conference on Power Systems Transients (IPST'05)*, 2005, no. IPST05-190.

[204] R. Gutiérrez, P. Moreno, L. Guardado, and J. L. Naredo, "Comparison of transmission tower models for evaluating lightning performance," in *2003 IEEE Bologna PowerTech - Conference Proceedings*, 2003, vol. 4, pp. 339–344.

[205] C. Jordan, "Lightning computations for transmission lines with overhead ground wires," *General Electric Review*, 1934.

[206] S. C. Lim, C. Gomes, and M. Z. A. Ab Kadir, "Electrical earthing in troubled environment," *International Journal of Electrical Power & Energy Systems*, vol. 47, pp. 117–128, 2013.

[207] R. Ruedenberg, "Grounding principles and practice I—Fundamental considerations on ground currents," *Electrical Engineering*, vol. 64, no. 1, pp. 1–13, 1945.

[208] S. C. Lim, M. Z. Abidin Ab Kadir, C. Gomes, and J. Jasni, "Ambiguity of grounding specifications: IEC 62305 revisited," *International Conference on Lightning Protection*, 2012.

[209] L. V. Bewley, "Test and theory of counterpoise," *Transactions of the American Institute of Electrical Engineers*, vol. 53, no. 8, pp. 1163–1172, 1934.

[210] A. C. Liew and M. Darveniza, "Dynamic model of impulse characteristics of concentrated earths," *Proceedings of the Institution of Electrical Engineers*, vol. 121, no. 2, p. 123, 1974.

[211] A. M. Mousa, "The soil ionization gradient associated with discharge of high currents into concentrated electrodes," *IEEE Transactions on Power Delivery*, vol. 9, no. 3, pp. 1669–1677, 1994.

[212] S. Goo, K. Park, and J. Yoon, "Direct Measurement of Frequency Domain Impedance Characteristics of Grounding System," in *Power System Technology*, 2002, pp. 2218–2221.

[213] S. Sekioka, T. Sonoda, and a. Ametani, "Experimental Study of Current-Dependent Grounding Resistance of Rod Electrode," *IEEE Transactions on Power Delivery*, vol. 20, no. 2, pp. 1569–1576, 2005.

[214] H. Motoyama, "Experimental and analytical studies on lightning surge characteristics of a buried bare wire," *Electrical Engineering in Japan*, vol. 126, no. 3, p. 556--561+9, 2006.

[215] N. Mohamad Nor, A. Haddad, and H. Griffiths, "Characterization of ionization phenomena in soils under fast impulses," *IEEE Transactions on Power Delivery*, vol. 21, no. 1, pp. 353–361, 2006.

[216] S. Visacro, “A comprehensive approach to the grounding response to lightning currents,” *IEEE Transactions on Power Delivery*, vol. 22, no. 1, pp. 381–386, 2007.

[217] N. Mohamad Nor and A. M. Ramli, “Electrical properties of dry soil under high impulse currents,” *Journal of Electrostatics*, vol. 65, no. 8, pp. 500–505, 2007.

[218] S. Visacro and R. G, “Response of Grounding Electrodes to Impulsive Currents : An experimental Evaluation,” *IEEE Transactions on Electromagnetic Compatibility*, vol. 51, no. 1, pp. 161–164, 2009.

[219] F. Asimakopoulou, I. F. Gonos, and A. Stathopulos, “Experimental Investigation on Soil Ionization,” in *International Symposium on High Voltage Engineering*, 2009, pp. 1–5.

[220] A. Haddad, H. Griffiths, M. Ahmeda, and N. Harid, “Experimental investigation of the impulse characteristics of practical ground electrode systems,” *High Voltage Engineering and Application ICHVE 2010 International Conference on*, pp. 469–472, 2010.

[221] M. S. Castro, E. G. da Costa, R. C. S. Freire, E. C. T. Macedo, M. a. O. Rodrigues, and L. V. Gomes, “Experimental impulse response of grounding systems,” *2012 IEEE International Power Modulator and High Voltage Conference (IPMHVC)*, pp. 148–151, 2012.

[222] G. Karnas, G. Maslowski, R. Ziemba, and S. Wyderka, “Influence of different multilayer soil models on grounding system resistance,” *International Conference on Lightning Protection*, pp. 1–4, 2012.

[223] N. Harid, H. Griffiths, N. Ullah, M. Ahmeda, and A. Haddad, “Experimental investigation of impulse characteristics of transmission line tower footings,” *Journal of Lightning Research*, pp. 36–44, 2012.

[224] S. Visacro, M. B. Guimarães, and L. S. Araujo, “Experimental impulse response of grounding grids,” *Electric Power Systems Research*, vol. 94, pp. 92–98, 2013.

[225] R. Alipio and S. Visacro, “Frequency dependence of soil parameters: Effect on the lightning response of grounding electrodes,” *IEEE Transactions on Electromagnetic Compatibility*, vol. 55, no. 1, pp. 132–139, 2013.

[226] N. Mohamad Nor, S. Abdullah, R. Rajab, and K. Ramar, “Field tests: Performances of practical earthing systems under lightning impulses,” *International Journal of Electrical Power & Energy Systems*, vol. 45, no. 1, pp. 223–228, 2013.

[227] D. Guo, D. Clark, D. Lathi, N. Harid, H. Griffiths, A. Ainsley, and A. Haddad, “Controlled Large-Scale Tests of Practical Grounding Electrodes 2014;Part I: Test Facility and Measurement of Site Parameters,” *IEEE Transactions on Power Delivery*, vol. 29, no. 3, pp. 1231–1239, 2014.

[228] D. Guo, D. Clark, D. Lathi, N. Harid, H. Griffiths, A. Ainsley, and A. Haddad, “Controlled Large-Scale Tests of Practical Grounding Electrodes 2014;Part II: Comparison of Analytical and Numerical Predictions With Experimental Results,” *IEEE Transactions on Power Delivery*, vol. 29, no. 3, pp. 1231–1239, 2014.

[229] S. Mousa, N. Harid, H. Griffiths, and a. Haddad, “Experimental investigation of high frequency and transient performance of earth rod systems,” *Electric Power Systems Research*, vol. 113, pp. 196–203, 2014.

[230] E. D. Sunde, “Surge Characteristics of a Buried Bare Wire,” *Electrical Engineering*, vol. 59, no. 12, pp. 987–991, 1940.

[231] P. Yadee and S. Premrudeepreechacharn, “Analysis of Tower Footing Resistance Effected Back Flashover Across Insulator in a Transmission System,” *International Conference on Power Systems Transients*, 2007.

[232] F. M. Gatta, A. Geri, S. Lauria, and M. Maccioni, “Effect of corona and non-linear tower grounding system modelling on backflashover simulation,” *International Conference on Lightning Protection*, pp. 220–225, 2014.

[233] S. Visacro and F. H. Silveira, “Lightning performance of grounding of overhead power distribution lines,” *International Conference on Lightning Protection*, vol. 134, no. 2, pp. 91–94, 2014.

[234] S. Visacro, R. Alipio, C. Pereira, M. Guimaraes, and M. A. O. Schroeder, “Lightning Response of Grounding Grids: Simulated and Experimental Results,” *IEEE Transactions on Electromagnetic Compatibility*, vol. 57, no. 1, pp. 121–127, 2015.

[235] S. Visacro and F. H. Silveira, “The Impact of the Frequency Dependence of Soil Parameters on the Lightning Performance of Transmission Lines,” *IEEE Transactions on Electromagnetic Compatibility*, vol. 57, no. 3, pp. 434–441, 2015.

[236] N. M. Guimarães, L. Araujo, R. V. Castro, L. F. D. Santos, M. H. Murta Vale, and S. Visacro, “Impulse response of grounding grids: Experimental versus simulated results,” *International Conference on Lightning Protection*, pp. 6–9, 2012.

[237] A. Samouëlian, I. Cousin, A. Tabbagh, A. Bruand, and G. Richard, “Electrical resistivity survey in soil science: a review,” *Soil and Tillage Research*, vol. 83, no. 2, pp. 173–193, 2005.

[238] V. P. Androvitsaneas, I. F. Gonos, and I. A. Stathopulos, “Experimental study on transient impedance of grounding rods encased in ground enhancing compounds,” *Electric Power Systems Research*, vol. 139, pp. 109–115, 2016.

[239] V. L. Coelho, A. Piantini, H. A. D. Almaguer, R. A. Coelho, W. D. C. Boaventura, and J. O. S. Paulino, “The influence of seasonal soil moisture on the behavior of soil resistivity and power distribution grounding systems,” *Electric Power Systems Research*, vol. 118, pp. 76–82, 2015.

[240] V. Cooray, M. Zitnik, M. Manyahi, R. Montano, M. Rahman, and Y. Liu, “Physical model of surge-current characteristics of buried vertical rods in the presence of soil ionisation,” *Journal of Electrostatics*, vol. 60, no. 2–4, pp. 193–202, 2004.

[241] Y. Liu, N. Theethayi, and R. Thottappillil, “An engineering model for transient analysis of grounding system under lightning strikes: Nonuniform transmission-line approach,” *IEEE Transactions on Power Delivery*, vol. 20, no. 2, pp. 722–730, 2005.

[242] N. Harid, D. Clark, S. Mousa, H. Griffiths, and A. Haddad, “Impulse characterization of ground electrodes,” *International Conference on Lightning Protection*, no. 3, pp. 1418–1423, 2014.

[243] R. Alipio and S. Visacro, “Impulse Efficiency of Grounding Electrodes: Effect of Frequency-Dependent Soil Parameters,” *IEEE Transactions on Power Delivery*,

vol. 29, no. 2, pp. 716–723, 2014.

[244] N. Harid, H. Griffiths, S. Mousa, S. Robson, D. Clark, and A. Haddad, “On the Analysis of Impulse Test Results on Grounding Systems,” *IEEE Transactions on Industry Applications*, vol. 9994, no. c, pp. 1–1, 2015.

[245] J. H. Choi and B. H. Lee, “An analysis of conventional grounding impedance based on the impulsive current distribution of a horizontal electrode,” *Electric Power Systems Research*, vol. 85, pp. 30–37, 2012.

[246] B. R. Gupta and B. Thapar, “Impulse Impedance of Grounding Grids,” *IEEE Transactions on Power Apparatus and Systems*, vol. PAS-99, no. 6, pp. 2357–2362, 1980.

[247] E. E. Oettle, “A new general estimation curve for predicting the impulse impedance of concentrated earth electrodes,” *IEEE Transactions on Power Delivery*, vol. 3, no. 4, pp. 2020–2029, 1988.

[248] Stojkovic Z., “The soil ionozation influence on the lightning performance of transmission lines,” *Electrical Engineering*, vol. 82, pp. 49–58, 1999.

[249] A. Geri, “Behaviour of grounding systems excited by high impulse currents: the model and its validation,” *IEEE Transactions on Power Delivery*, vol. 14, no. 3, pp. 1008–1017, 1999.

[250] K. Otani, Y. Baba, N. Nagaoka, A. Ametani, and N. Itamoto, “FDTD surge analysis of grounding electrodes considering soil ionization,” *Electric Power Systems Research*, vol. 113, pp. 171–179, 2014.

[251] R. E. de Souza, F. H. Silveira, and S. Visacro, “The effect of soil ionization on the lightning performance of transmission lines,” *International Conference on Lightning Protection*, pp. 1307–1311, 2014.

[252] N. Harid, N. Ullah, M. Ahmeda, H. Griffiths, and N. Grid, “Experimental Evaluation of Potential Rise and Step and Touch Voltages At High Voltage Towers Under Lightning Impulses,” no. 1, pp. 1–6, 2009.

[253] L. D. Grcev and F. Dawalibi, “An electromagnetic model for transients in grounding systems,” *IEEE Transactions on Power Delivery*, vol. 5, no. 4, pp. 1773–1781, 1990.

[254] L. D. Grcev, “Computer analysis of transient voltages in large grounding systems,” *IEEE Transactions on Power Delivery*, vol. 11, no. 2, pp. 815–823, 1996.

[255] K. Tanabe and A. Asakawa, “Computer analysis of transient performance of grounding grid element based on the finite-difference time-domain method,” *International Symposium on Electromagnetic Compatibility*, vol. 1, p. 209–212 Vol.1, 2003.

[256] R. Xiong, B. Chen, C. Gao, Y. Yi, and W. Yang, “FDTD calculation model for the transient analyses of grounding systems,” *IEEE Transactions on Electromagnetic Compatibility*, vol. 56, no. 5, pp. 1155–1162, 2014.

[257] J. Wu, B. Zhang, J. He, R. Zeng, and S. Member, “A Comprehensive Approach for Transient Performance of Grounding System in the Time Domain,” *IEEE Transactions on Electromagnetic Compatibility*, vol. 57, no. 2, pp. 250–256, 2015.

[258] J. Wu, J. He, B. Zhang, and R. Zeng, “Influence of grounding impedance model

on lightning protection analysis of transmission system," *Electric Power Systems Research*, vol. 139, no. JANUARY, pp. 133–138, 2016.

[259] N. Theethayi, R. Thottappillil, M. Paolone, C. A. Nucci, and F. Rachidi, "External impedance and admittance of buried horizontal wires for transient studies using transmission line analysis," *IEEE Transactions on Dielectrics and Electrical Insulation*, vol. 14, no. 3, pp. 751–761, 2007.

[260] A. P. C. Magalhães, C. Ufrj, C. Ufrj, M. Teresa, and C. De Barros, "Full-Wave Modelling of a Counterpoise," *International Conference on Lightning Protection*, no. 1, 2016.

[261] R. Alipio, R. M. Costa, and R. N. Dias, "Grounding Modeling Using Transmission Line Theory : Extension to Arrangements Composed of Multiple Electrodes," *International Conference on Lightning Protection*, 2016.

[262] J. Paulino, W. Boaventura, A. Lima, and M. Guimaraes, "Transient voltage response of ground electrodes in the time-domain," in *International Conference on Lightning Protection*, 2012, vol. 2, pp. 1–6.

[263] F. M. Gatta, A. Geri, S. Launa, and M. Maccioni, "Equivalent lumped parameter Pi-network of typical grounding systems for linear and non-linear transient analysis," *2009 IEEE Bucharest PowerTech*, no. JUNE, pp. 1–6, 2009.

[264] L. Grcev, "Time- and frequency-dependent lightning surge characteristics of grounding electrodes," *IEEE Transactions on Power Delivery*, vol. 24, no. 4, pp. 2186–2196, 2009.

[265] E. P. Nicolopoulou, F. E. Asimakopoulou, I. F. Gonos, and I. a. Stathopulos, "Comparison of circuit models for the simulation of soil ionization," *International Conference on Lightning Protection*, no. 1, pp. 1–6, 2012.

[266] F. M. Gatta, A. Geri, S. Lauria, and M. Maccioni, "Simplified HV tower grounding system model for backflashover simulation," *Electric Power Systems Research*, vol. 85, pp. 16–23, 2012.

[267] A. B. Lima, J. O. S. Paulino, W. Do Couto Boaventura, and M. F. Guimarães, "A simplified method for calculating the tower grounding impedance by means of pspice," in *International Conference on Lightning Protection*, 2012, no. 1, pp. 0–3.

[268] G. Celli, E. Ghiani, and F. Pilo, "Behaviour of grounding systems: A quasi-static EMTP model and its validation," *Electric Power Systems Research*, vol. 85, pp. 24–29, 2012.

[269] M. Mokhtari, Z. Abdul-Malek, and Z. Salam, "An Improved Circuit-Based Model of a Grounding Electrode by Considering the Current Rate of Rise and Soil Ionization Factors," *IEEE Transactions on Power Delivery*, vol. PP, no. 99, pp. 1–1, 2014.

[270] F. M. Gatta, A. Geri, S. Lauria, M. Maccioni, and A. Santarpia, "An ATP-EMTP Monte Carlo procedure for backflashover rate evaluation: A comparison with the CIGRE method," *Electric Power Systems Research*, vol. 113, pp. 134–140, 2014.

[271] F. M. Gatta, A. Geri, S. Lauria, and M. Maccioni, "Generalized pi-circuit tower grounding model for direct lightning response simulation," *Electric Power Systems Research*, vol. 116, pp. 330–337, 2014.

[272] E. P. Nicolopoulou, F. E. Asimakopoulou, I. F. Gonos, and I. A. Stathopulos,

"Comparison of equivalent circuit models for the simulation of soil ionization," *Electric Power Systems Research*, vol. 113, pp. 180–187, 2014.

[273] S. Sekioka, M. I. Lorentzou, and N. D. Hatziargyriou, "Approximate formulas for terminal voltages on the grounding conductor," *IEEE Transactions on Electromagnetic Compatibility*, vol. 56, no. 2, pp. 444–453, 2014.

[274] R. A. Correa Altafim, L. Goncalves, R. A. Pisani Altafim, R. C. Creppe, and A. Piantini, "One-port nonlinear electric circuit for simulating grounding systems under impulse current," *Electric Power Systems Research*, vol. 130, pp. 259–265, 2016.

[275] S. Sekioka, "Discussion of Current Dependent Grounding Resistance using an Equivalent Circuit Considering Frequency-dependent Soil Parameters," in *International Conference on Lightning Protection*, 2016.

[276] P. Yutthagowith, "A Modified Pi-Shaped Circuit-Based Model of Grounding Electrodes," in *International Conference on Lightning Protection*, 2016.

[277] S. Bedoui, A. Bayadi, and A. M. Haddad, "Analysis of Lightning Protection with Transmission Line Arrester Using ATP / EMTP : Case of an HV 220kV Double Circuit Line," in *UPEC 2010*, 2010.

[278] L. Colla, F. M. Gatta, A. Geri, and S. Lauria, "Lightning Overvoltages in HV-EHV ' Mixed ' Overhead-Cable Lines," in *International Conference on Power System Transients*, 2007, pp. 1–6.

[279] N. Filipe, C. Cardoso, J. Mendes, D. Duarte, L. Perro, and M. M. Fernandes, "A methodology for estimating transmission lines lightning performance using a statistical approach," in *International Conference on Lightning Protection*, 2016.

[280] I. F. Gonos, L. Ekonomou, F. V Topalis, and I. A. Stathopulos, "Probability of backflashover in transmission lines due to lightning strokes using Monte-Carlo simulation," *Electrical Power and Energy Systems*, vol. 25, pp. 107–111, 2003.

[281] R. Holt and T. T. Nguyen, "Monte Carlo estimation of the rates of lightning strikes on power lines," *Electric Power Systems Research*, vol. 49, no. 3, pp. 201–210, 1999.

[282] IEEE Standards Assocation, "IEEE Guide for Improving the Lightning Performance of Electric Power Overhead Distribution Lines," 2010.

[283] J. A. Martinez and F. Castro-Aranda, "Lightning Performance Analysis of Overhead Transmission Lines Using the EMTP," *IEEE Transactions on Power Delivery*, vol. 20, no. 3, pp. 2200–2210, 2005.

[284] P. Sarajcev, "Monte Carlo method for estimating backflashover rates on high voltage transmission lines," *Electric Power Systems Research*, vol. 119, pp. 247–257, 2015.

[285] C. Teixeira and J. Pinto, "Back-flashover analysis of overhead transmission lines for different tower and lightning models," in *Universities Power Engineering Conference*, 2004, no. I, pp. 238–241.

[286] H. B. Dwight, "Calculation of Resistances to Ground," *Electrical Engineering*, no. December, 1936.

[287] W. A. Chisholm and W. Janischewskyj, "Lightning surge response of ground electrodes," *IEEE Transactions on Power Delivery*, vol. 4, no. 2, pp. 1329–1337, 1989.

[288] K. J. Nixon, “The Lightning Transient Behaviour of a Driven Rod Earth Electrode in Multi-Layer Soil - PhD Thesis,” University of the Witwatersrand, Johannesburg, 2006.

[289] S.Sekioka, T. Hara, and A. Ametani, “Development of a nonlinear model of a concrete pole grounding resistance,” in *International Conference on Power Systems Transients (IPST’05)*, 1995.

[290] L. Grcev, “Impulse efficiency of ground electrodes,” *IEEE Transactions on Power Delivery*, vol. 24, no. 1, pp. 441–451, 2009.

[291] A. B. Lima, J. O. S. Paulino, W. C. Boaventura, C. E. F. Caetano, and E. N. Cardoso, “Transmission line grounding arrangement that overcomes the effective length issue,” in *International Conference on Lightning Protection*, 2016.

[292] C. A. Christodoulou, L. Ekonomou, G. P. Fotis, I. F. Gonos, and I. A. Stathopulos, “Assessment of surge arrester failure rate and application studies in Hellenic high voltage transmission lines,” *Electric Power Systems Research*, vol. 80, no. 2, pp. 176–183, 2010.

[293] N. H. N. Hassan, A. H. A. Bakar, H. Mokhlis, and H. A. Illias, “Analysis of arrester energy for 132kV overhead transmission line due to back flashover and shielding failure,” *2012 IEEE International Conference on Power and Energy*, vol. 1, no. December, pp. 683–688, 2012.

[294] Siemens, “Line surge arresters for increased system reliability.” 2014.

[295] British Standards Association, *BS EN 60099-4: Surge arresters*. 2014.

[296] IEEE Working Group 3.4.11, “Modeling of Metal Oxide Surge Arresters,” *IEEE Transactions on Power Delivery*, vol. 7, no. 1, pp. 302–309, 1992.

[297] F. Fernandez and R. Diaz, “Metal oxide surge arrester model for fast transient simulations,” *The International Conference on Power System Transients*, vol. 1, pp. 0–4, 2001.

[298] M. Giannettoni and P. Pinceti, “A simplified model for zinc oxide surge arresters,” *IEEE Transactions on Power Delivery*, vol. 14, no. 2, pp. 393–398, 1999.

[299] N. Triruttanapiruk and P. Yutthagowith, “A simple surge arrester model extracted from experimental results,” *International Conference on Lightning Protection*, pp. 1616–1620, 2014.

[300] G. D. Peppas, I. A. Naxakis, C. T. Vitsas, and E. C. Pyrgioti, “Surge arresters models for fast transients,” *International Conference on Lightning Protection*, no. 2, 2012.

[301] S. Dau, “Modelling of metal oxide surge arresters as elements of overvoltage protection systems,” *International Conference on Lightning Protection*, pp. 0–4, 2012.

[302] P. M. Miguel, “Comparison of surge arrester models,” *IEEE Transactions on Power Delivery*, vol. 29, no. 1, pp. 21–28, 2014.

[303] S. Visacro, F. H. Silveira, and A. De Conti, “The use of underbuilt wires to improve the lightning performance of transmission lines,” *IEEE Transactions on Power Delivery*, vol. 27, no. 1, pp. 205–213, 2012.

[304] T. Thanasaksiri, “Improving the lightning performance of overhead distribution

lines," *IEEE Region Conference TENCON*, vol. C, pp. 1–6, 2004.

[305] W. Xi, Z. Li, and J. He, "Improving the lightning protection effect of multi-circuit tower by installing coupling ground wire," *Electric Power Systems Research*, vol. 113, pp. 213–219, 2014.

[306] S. Visacro, A. S. Jr, R. Oliveira, M. Felipe, A. Silva, and M. H. M. Vale, "Non-Conventionnal Measures for Improvement of Lightning Performance of Transmission Lines," in *International Conference on Lightning Protection*, 2004.

[307] N. Malcolm and R. K. Aggarwal, "An Analysis of Reducing Back Flashover Faults with Surge Arresters on 69 / 138 kV Double Circuit Transmission Lines Due to Direct Lightning Strikes on the Shield Wires," pp. 1–6.

[308] H. Schmitt and W. Winter, "Simulation of Lightning Overvoltages in Electrical Power Systems," *International Conference on Power Systems Transients*, p. 6, 2001.

[309] G. W. Brown and E. R. Whitehead, "Field and Analytical Studies of Transmission Line Shielding : Part II," *IEEE Transactions on Power Apparatus and Systems*, no. 5, pp. 617–626, 1969.

[310] P. N. Mikropoulos, T. E. Tsovilis, and S. Member, "Lightning Attachment Models and Maximum Shielding Failure Current : Application to Transmission Lines," *IEEE Bucharest Power Tech Conference*, pp. 1–8, 2009.

[311] X. Wang, Z. Yu, X. Peng, and Z. Li, "Comparison of numerical analysis models for shielding failure of transmission lines," *Electric Power Systems Research*, vol. 94, pp. 71–78, 2013.

[312] A. Shafaei, A. Gholami, and R. Shariatinasab, "Probabilistic evaluation of lightning performance of overhead transmission lines, considering non-vertical strokes," *Scientia Iranica*, vol. 19, no. 3, pp. 812–819, 2012.

[313] J. Plesch, T. Hoehn, and S. Pack, "Modelling and analysis of different representations for high voltage tower structures," in *International Conference on Lightning Protection*, 2014, pp. 446–450.

[314] R. Shariatinasab, J. Gholinezhad, K. Sheshyekani, and M. R. Alemi, "The effect of wide band modeling of tower-footing grounding system on the lightning performance of transmission lines: A probabilistic evaluation," *Electric Power Systems Research*, vol. 141, pp. 1–10, 2016.

[315] R. Shariatinasab and J. G. Safar, "Probabilistic evaluation of lightning performance of overhead distribution lines using Monte Carlo method," in *Proceedings of 17th Conference on Electrical Power Distribution Networks (EPDC)*, 2012, pp. 1–7.

[316] F. M. Gatta, A. Geri, S. Lauria, M. Maccioni, and A. Santarpia, "An ATP-EMTP Monte Carlo Procedure for Backflashover Rate Evaluation," in *International Conference on Lightning Protection*, 2012, no. 1.

[317] J. G. Anderson, "Monte Carlo Computer Calculation of Transmission-Line Lightning Performance," *Transactions of the American Institute of Electrical Engineers. Part III: Power Apparatus and Systems*, vol. 80, no. August, 1961.

[318] A. Jiang, Z. Fu, B. Huang, G. Wang, and R. Li, "Backflashover rate of quadruple-circuit transmission lines due to first and subsequent return strokes," *Electric Power Systems Research*, vol. 139, pp. 47–51, 2015.

[319] F. H. Silveira, S. Visacro, and A. De Conti, “Lightning Performance of 138-kV Transmission Lines: The Relevance of Subsequent Strokes,” *IEEE Transactions on Electromagnetic Compatibility*, vol. 55, no. 6, pp. 1195–1200, Dec. 2013.

[320] J. Martínez-Velasco and F. Castro-Aranda, “Emtp Implementation of a Monte Carlo Method for Lightning Performance Analysis of Transmission Lines,” *Ingeniare. Revista chilena de ingeniería*, vol. 16, pp. 169–180, 2008.

[321] J. A. Martinez and F. Castro-Aranda, “Lightning flashover rate of an overhead transmission line protected by surge arresters,” *2007 IEEE Power Engineering Society General Meeting, PES*, pp. 1–6, 2007.

[322] J. Gholinezhad, “The Effect of High Frequency Model of Tower- Footing Grounding Systems on the Back Flashover Rate of Transmission lines,” *International Conference on Lightning Protection*, no. 1, 2016.

[323] F. Koehler and J. Swingler, “Simplified Analytical Representation of Lightning Strike Waveshapes,” *IEEE Transactions on Electromagnetic Compatibility*, vol. 58, no. 1, 2016.

[324] F. Koehler, J. Swingler, and V. Peesapati, “Breakdown Process Experiments of Cap-and-Pin Insulators and their EMT Leader-Progression Model Implementation,” *IET Generation, Transmission & Distribution*, 2017.

[325] F. Koehler and J. Swingler, “Practical Model for Tower Earthing Systems in Lightning Simulations,” *Electric Power Systems Research*, 2018.

[326] F. Koehler and J. Swingler, “Unconventional Flashover Mitigation Measures to Improve the Lightning Performance of Transmission Lines,” in *International Conference on Resilience of Transmission and Distribution Networks*, 2017.

[327] F. Koehler and J. Swingler, “Analysis of Flashover Mitigation Measures to Improve the Lightning Performance of Transmission Line,” in *Universities Power Engineering Conference*, 2018.

[328] F. H. Silveira, S. Visacro, A. De Conti, and C. R. De Mesquita, “Backflashovers of Transmission Lines Due to Subsequent Lightning Strokes,” *IEEE Transactions on Electromagnetic Compatibility*, vol. 54, no. 2, pp. 316–322, Apr. 2012.

[329] A. Rahman, A. Marican, and M. Z. Kadir, “Optimised transmission tower earthing: Experience in design and operation,” *International Conference on Lightning Protection*, pp. 1600–1603, 2014.

[330] S. Visacro and F. H. Silveira, “Lightning Performance of Transmission Lines: Methodology to Design Grounding Electrodes to Ensure an Expected Outage Rate,” *IEEE Transactions on Power Delivery*, vol. 30, no. 1, pp. 1–1, 2014.

[331] J. Liu and Q. Chen, “Optimized design of earthing network with power frequency earthing resistance substituted by effective utilization ratio of earthing network area in the event of lightning strike,” *International Conference on Lightning Protection*, pp. 192–196, 2014.

[332] F. Zhang, A. Chang, Y. Yang, B. Cao, S. Wei, W. Zhou, and S. Yang, “The simulation research on the impulse characteristics of the grounding electrode in the layered soil,” *International Conference on Lightning Protection*, pp. 1625–1628, 2014.

[333] V. P. Androvitsaneas, I. F. Gonos, and I. a. Stathopulos, “Transient impedance of

grounding rods encased in ground enhancing compounds," *International Conference on Lightning Protection*, pp. 359–363, 2014.

APPENDIX A: THE LIGHTNING

A.1: EVALUATION OF ANALYTICAL DESCRIPTION OF LIGHTNING WAVESHAPES

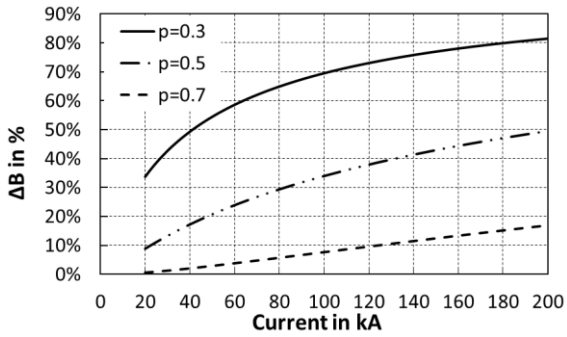

a) Variable B

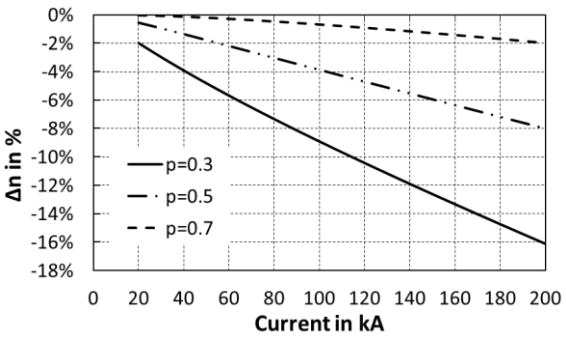

b) Variable n

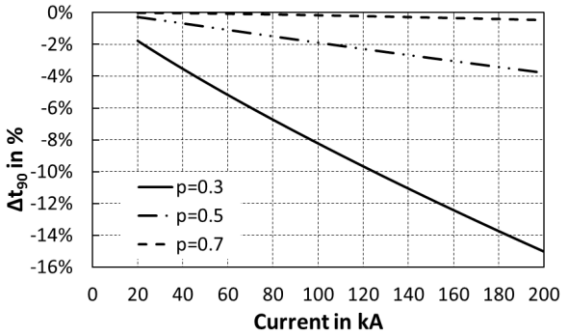

c) Variable t_{90}

Figure A-1: Deviation of analytical wavefront variable calculation from numerical solution in dependency of parameter *p*, CIGRE parameters for negative first strokes

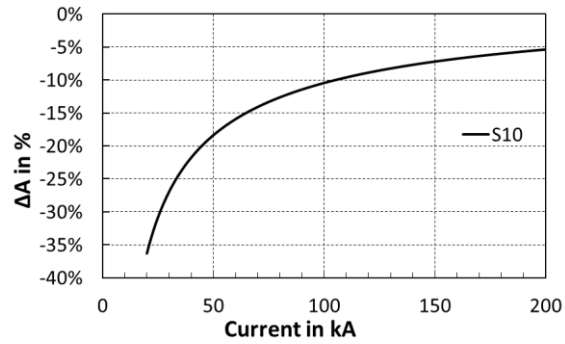

a) Variable A

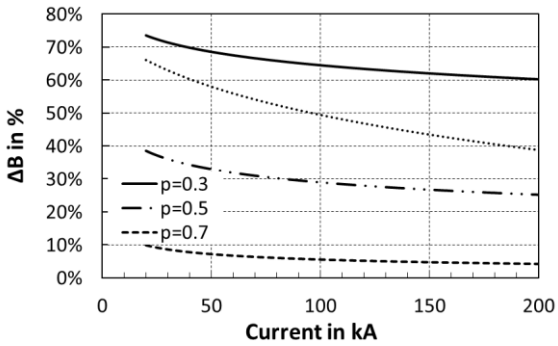

b) Variable B

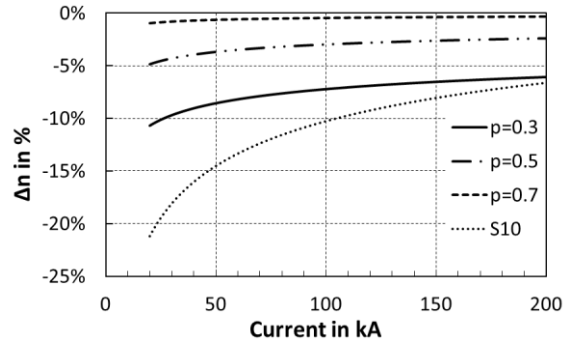

c) Variable n

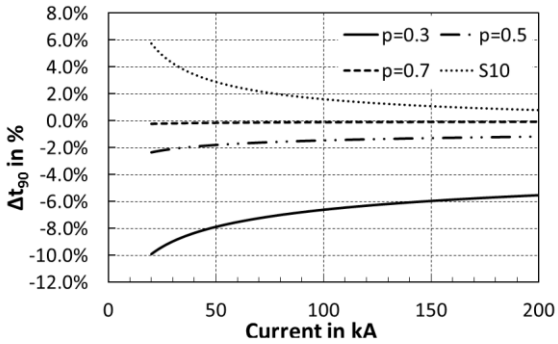

d) Variable t_{90}

Figure A-2: Deviation of analytical wavefront variable calculation from numerical solution in dependency of parameter *p*, Japan parameters for negative first strokes

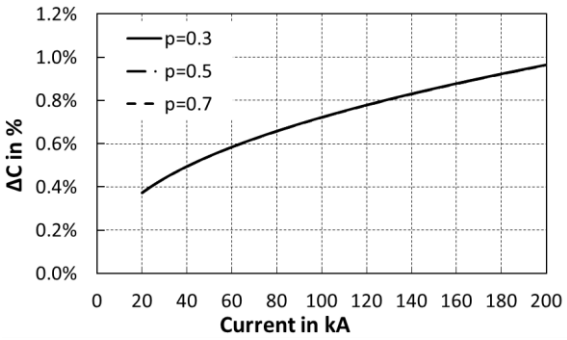

a) Variable C

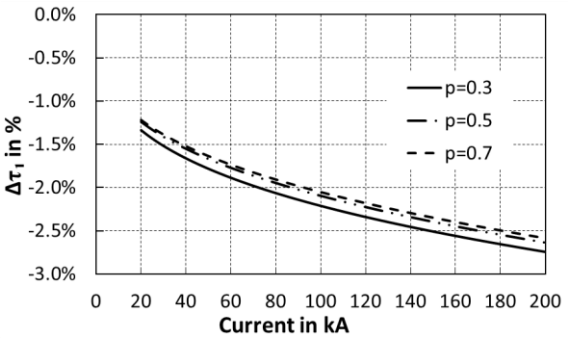

b) Variable τ_1

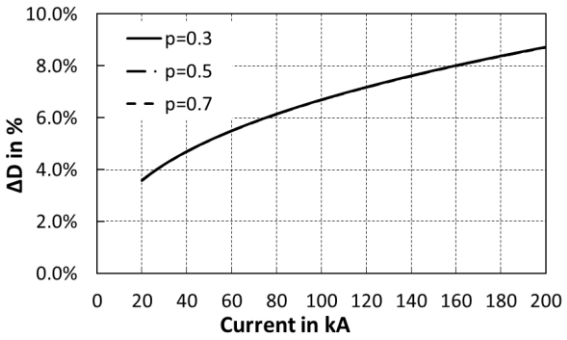

c) Variable D

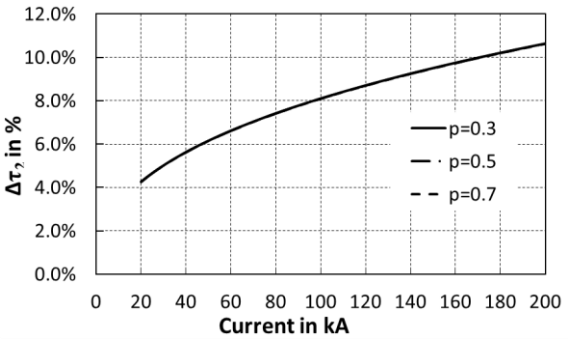

d) Variable τ_2

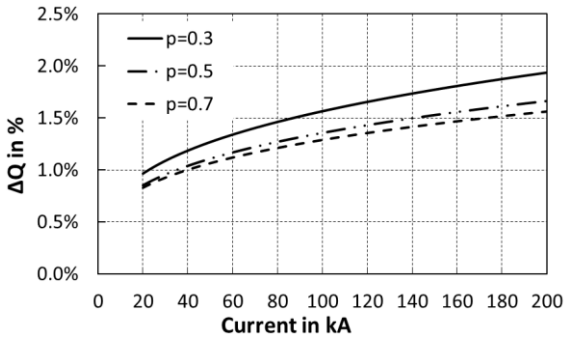

e) Charge Q over 2 ms

Figure A-3: Deviation of analytical wavetail variable calculation from numerical solution, CIGRE parameters for negative first strokes

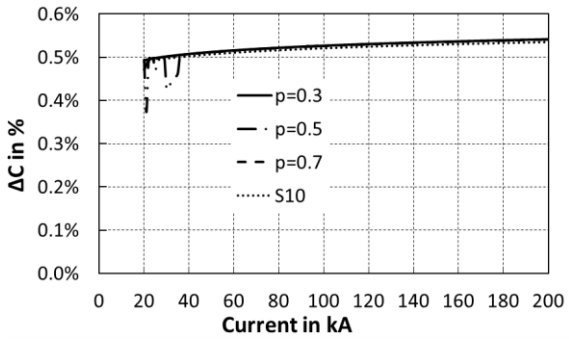

a) Variable C

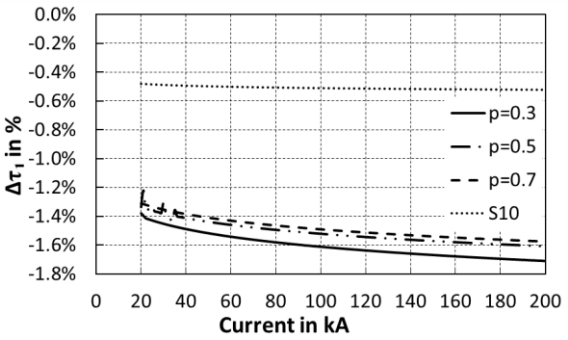

b) Variable τ_1

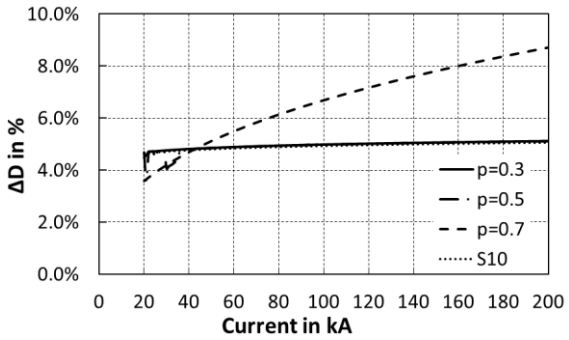

c) Variable D

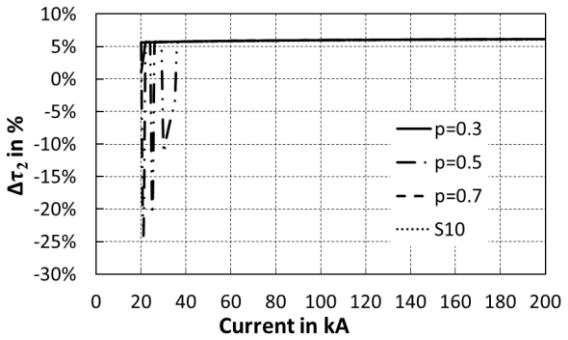

d) Variable τ_2

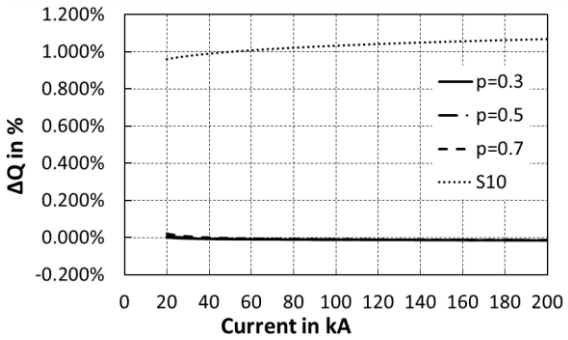

e) Charge Q over 2 ms

Figure A-4: Deviation of analytical wavetail variable calculation from numerical solution, CIGRE parameters for negative first strokes

A.2: LIGHTNING LOCATION SYSTEM DATABASE RESULTS FOR 400 KV LINE ROUTE

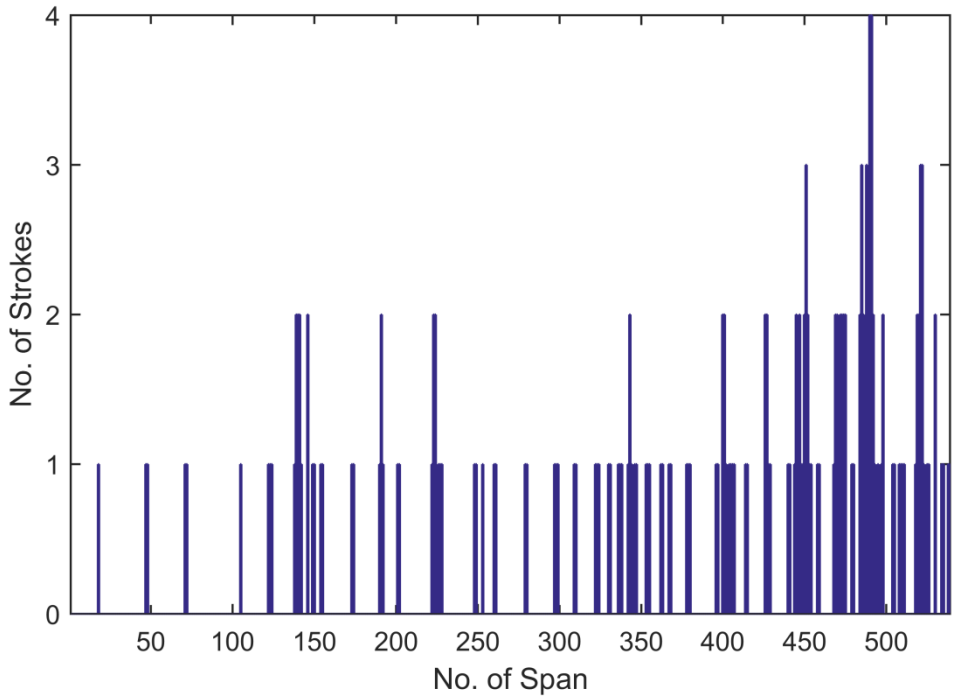

Figure A-5: Evaluation of lightning location system query for 400 kV line route through the Scottish Highlands, number of negative strokes

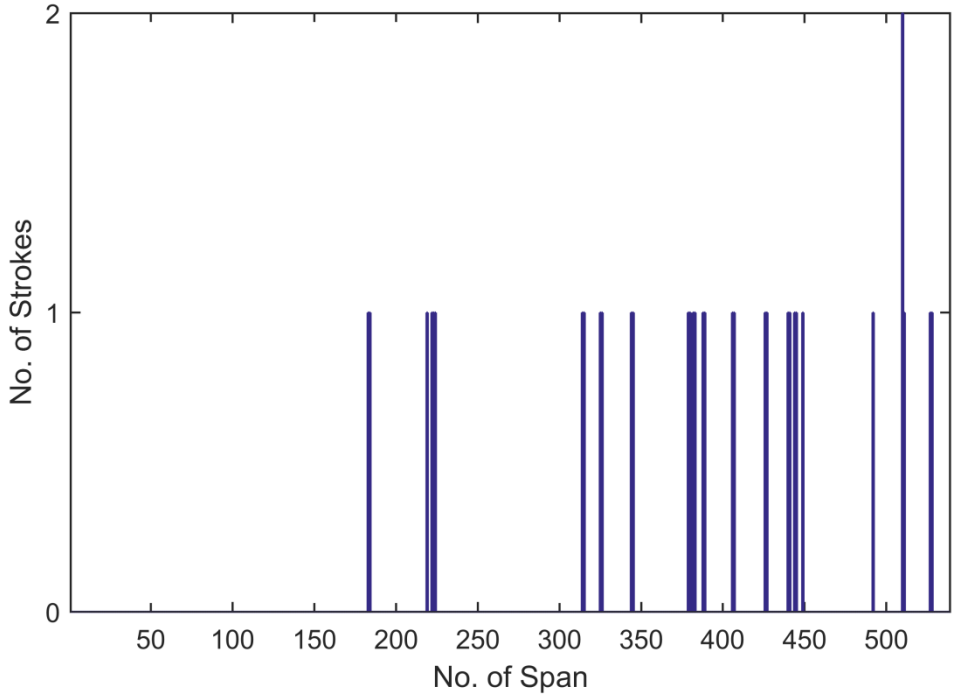

Figure A-6: Evaluation of lightning location system query for 400 kV line route through the Scottish Highlands, number of positive strokes

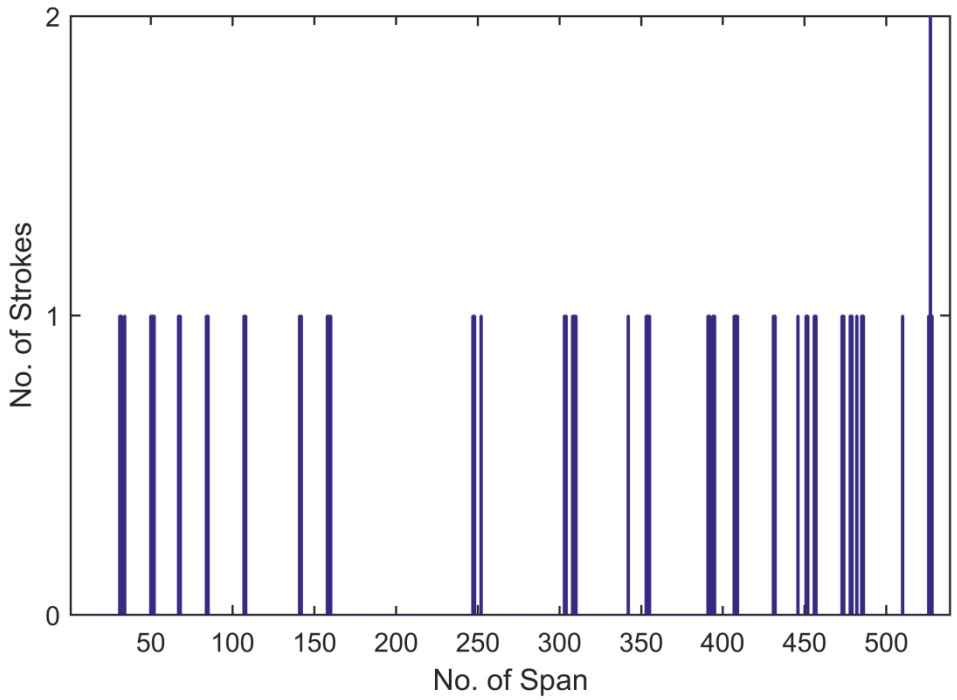

Figure A-7: Evaluation of lightning location system query for 400 kV line route through the Scottish Highlands, number of unknown polarity strokes

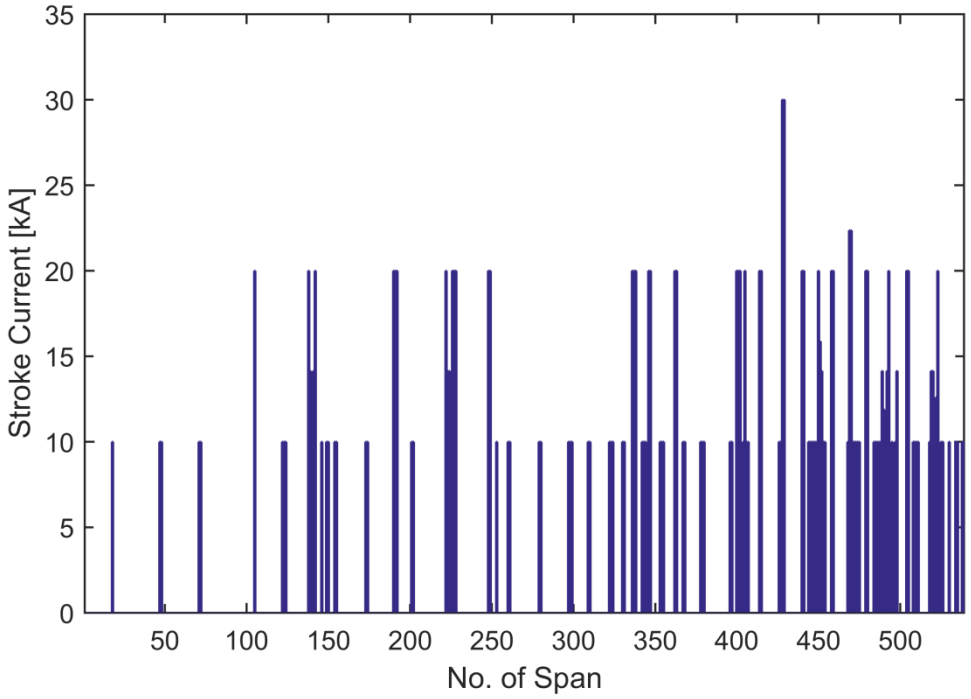

Figure A-8: Evaluation of lightning location system query for 400 kV line route through the Scottish Highlands, negative stroke current

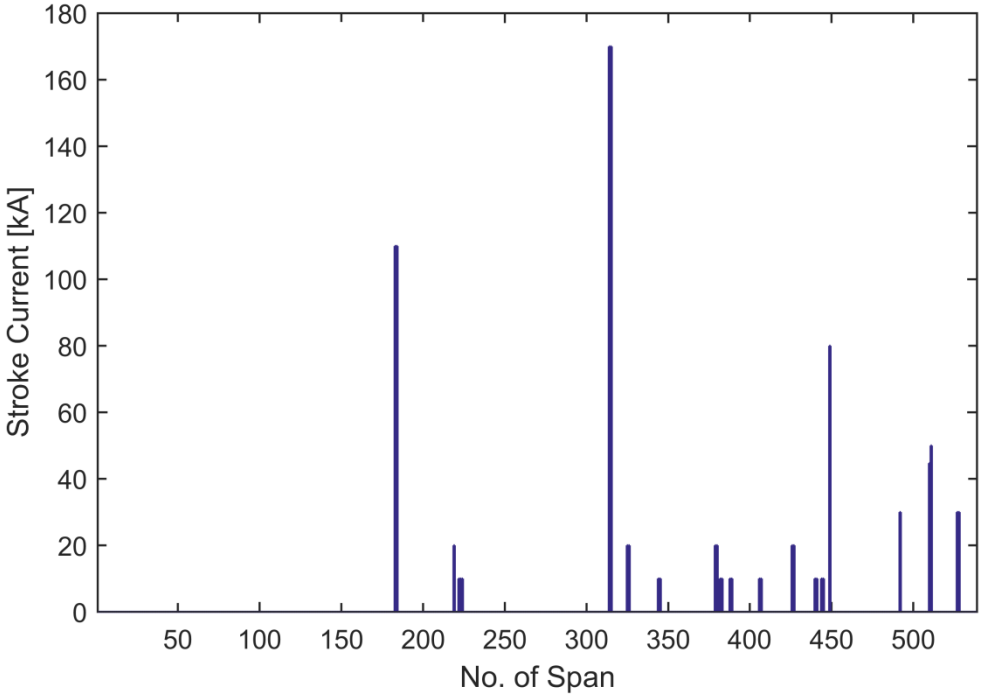

Figure A-9: Evaluation of lightning location system query for 400 kV line route through the Scottish Highlands, positive stroke current

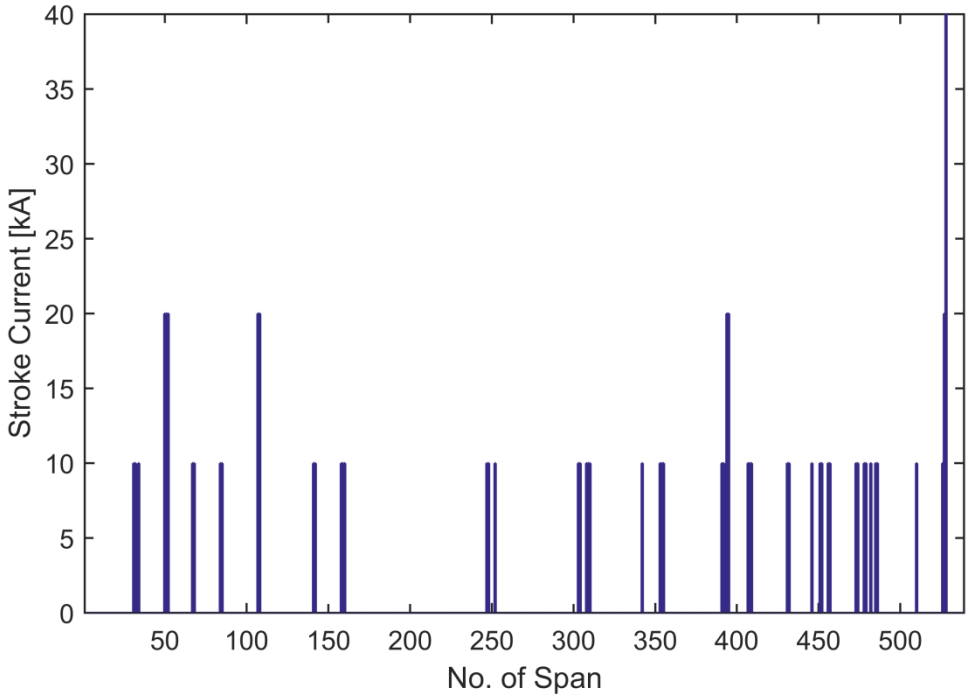

Figure A-10: Evaluation of lightning location system query for 400 kV line route through the Scottish Highlands, unknown polarity stroke current

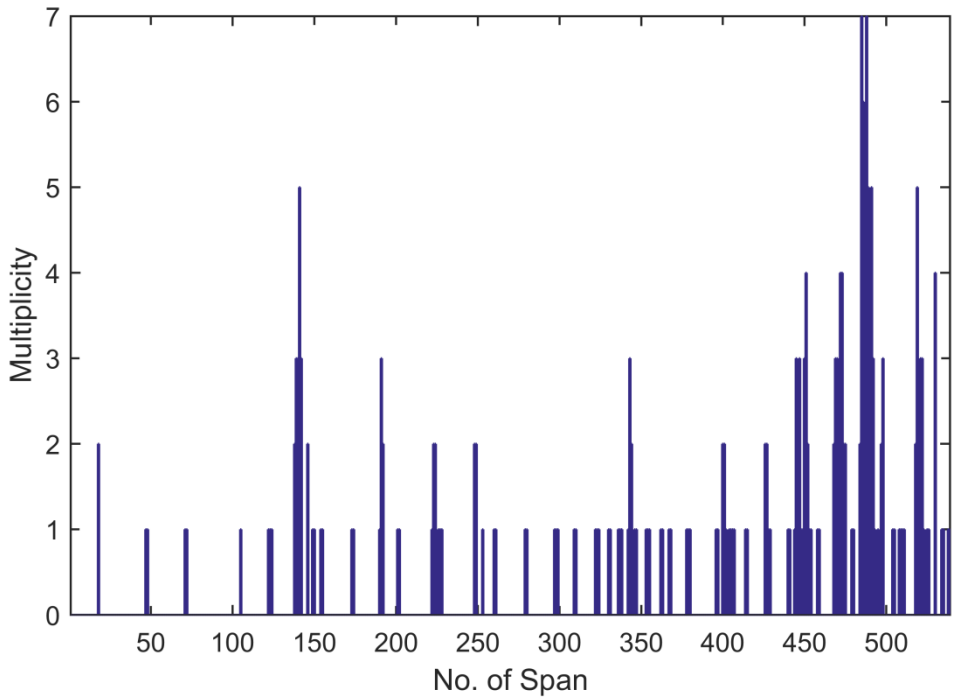

Figure A-11: Evaluation of lightning location system query for 400 kV line route through the Scottish Highlands, negative multiplicity

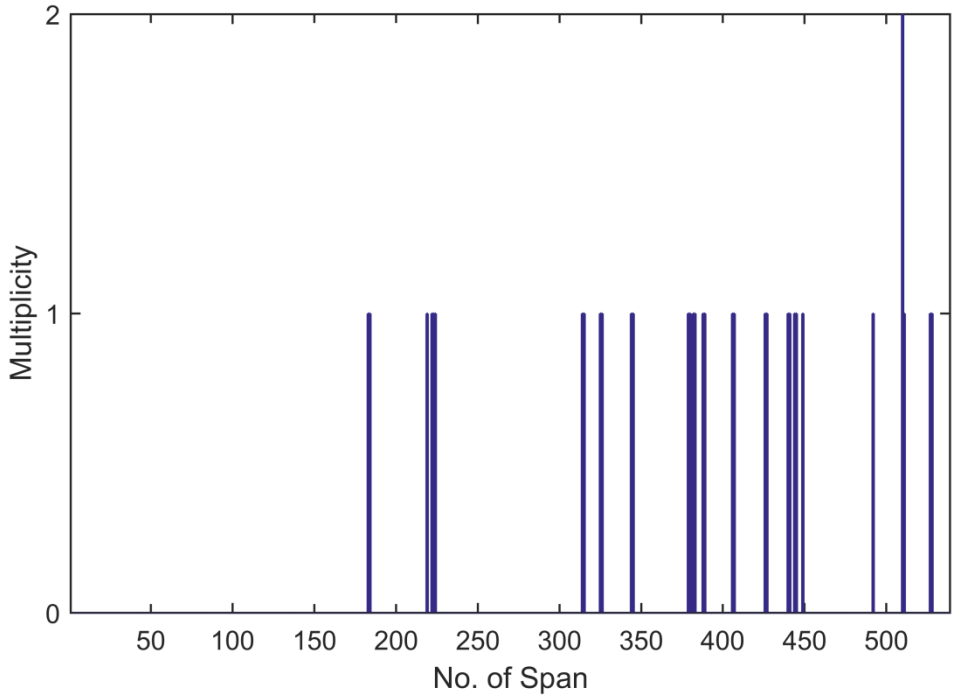

Figure A-12: Evaluation of lightning location system query for 400 kV line route through the Scottish Highlands, positive multiplicity

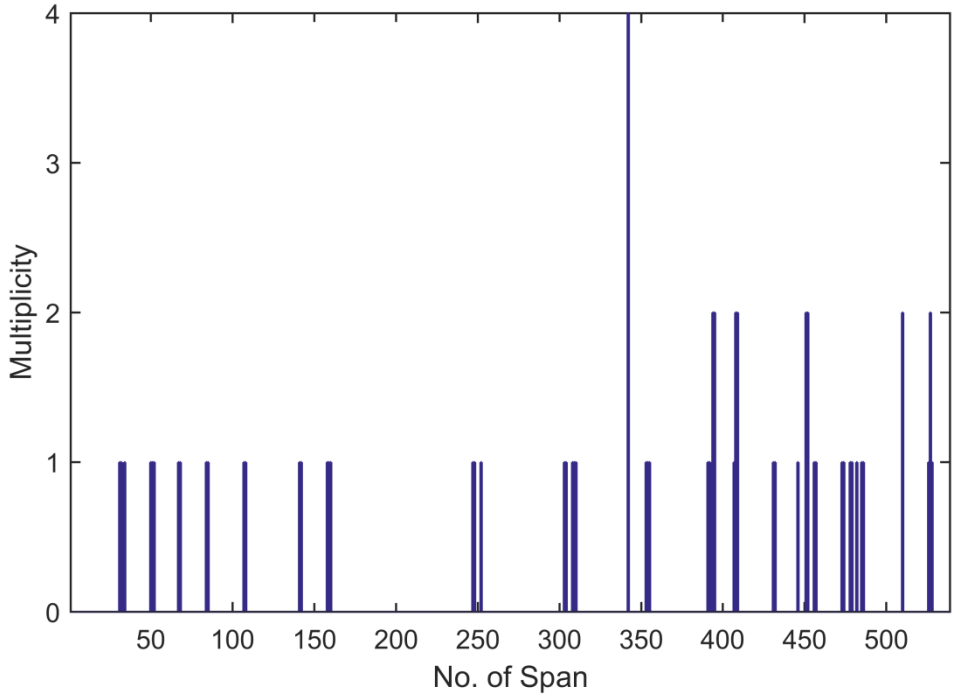

Figure A-13: Evaluation of lightning location system query for 400 kV line route through the Scottish Highlands, unknown polarity multiplicity

APPENDIX B: THE TRANSMISSION LINE

B.1: COMPARISON OF FREQUENCY-DEPENDENT SOIL MODELS

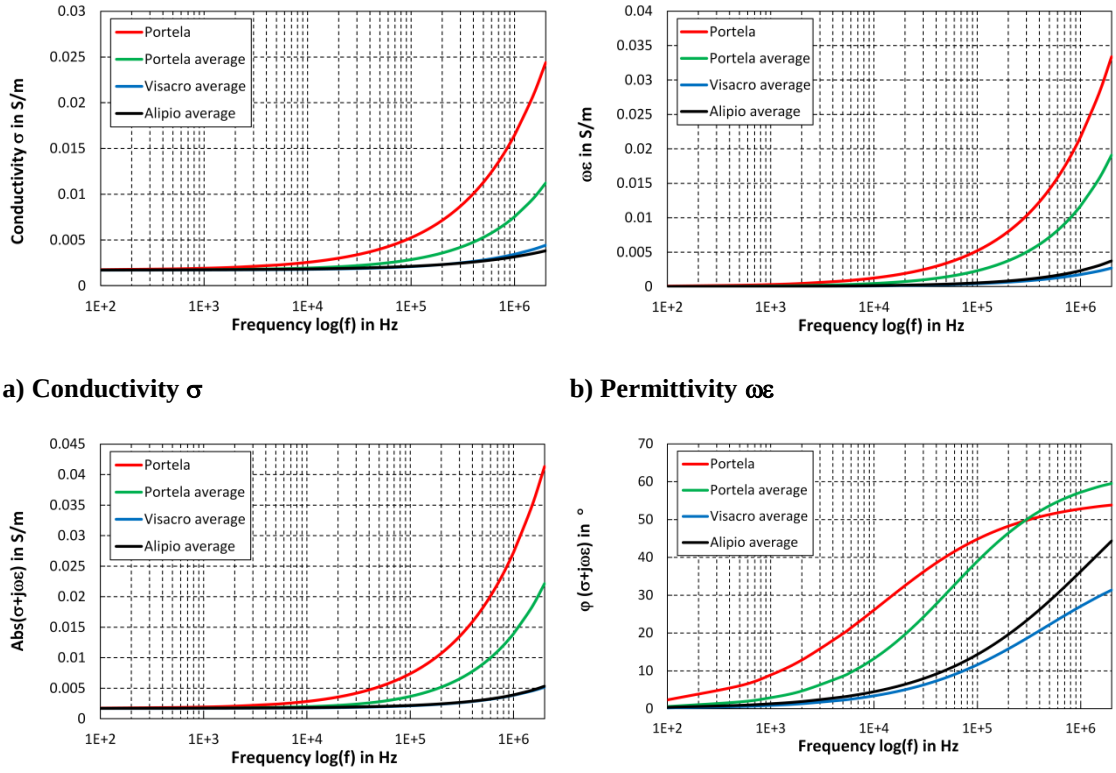

a) Conductivity σ **b) Permittivity ωε**

c) Absolute conductivity Abs(σ+jωε) **d) Phase angle φ(σ+jωε)**

Figure B-1: Comparison of frequency-dependent soil models for σ_0=0.0017 S/m

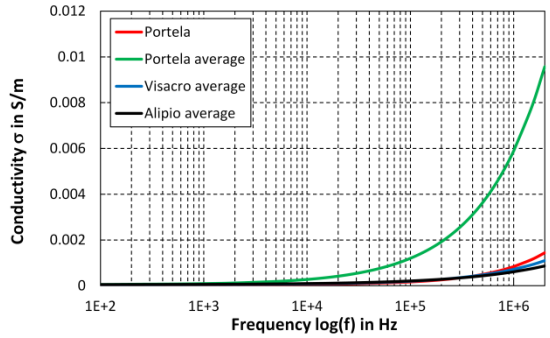

a) Conductivity σ

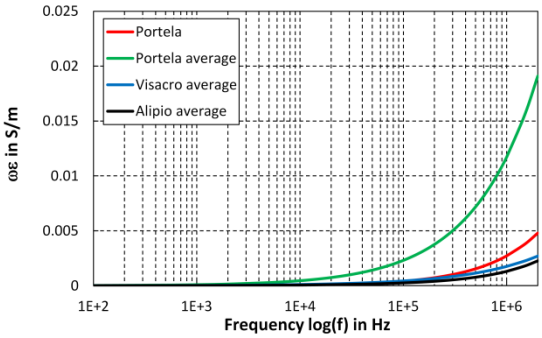

b) Permittivity ωε

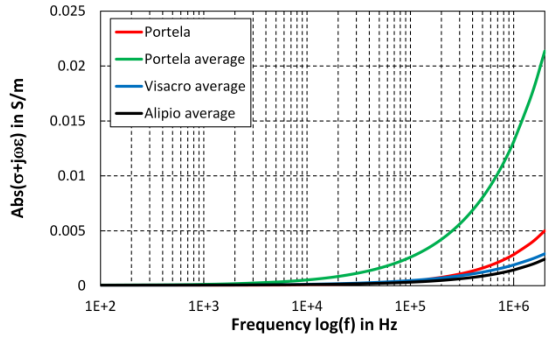

c) Absolute conductivity Abs(σ+jωε)

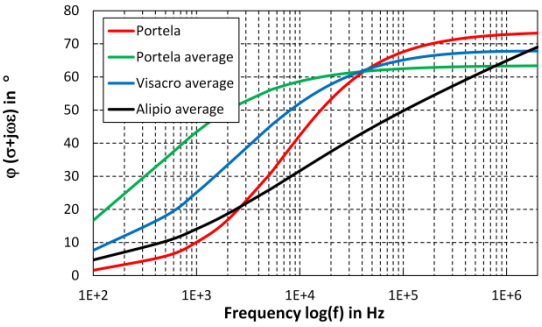

d) Phase angle φ(σ+jωε)

Figure B-2: Comparison of frequency-dependent soil models for σ_0=0.00005 S/m

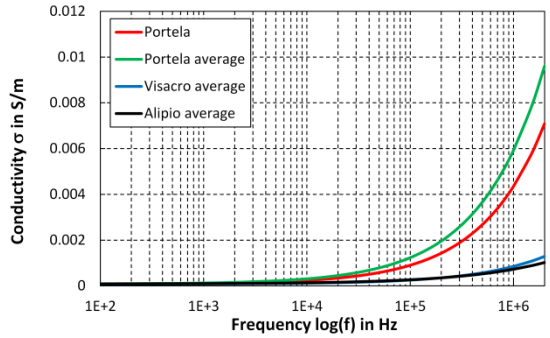

a) Conductivity σ

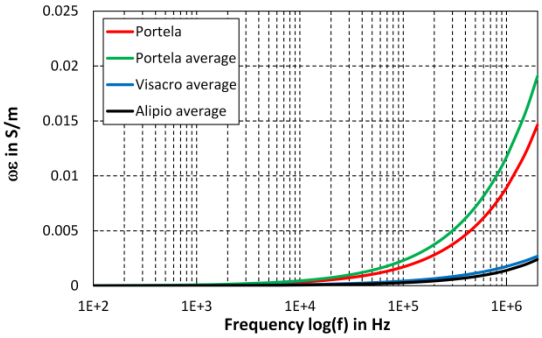

b) Permittivity ωε

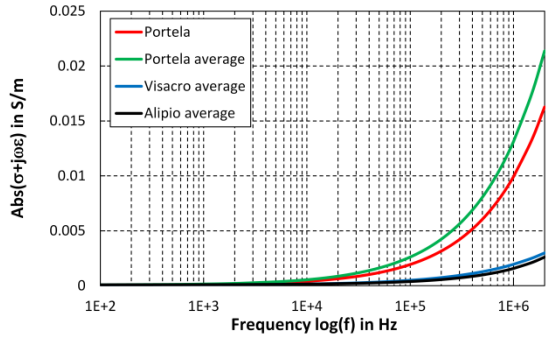

c) Absolute conductivity Abs(σ+jωε)

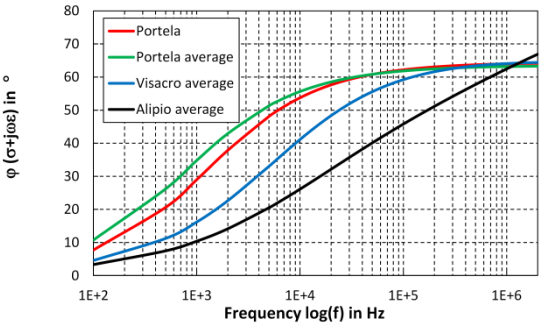

d) Phase angle φ(σ+jωε)

Figure B-3: Comparison of frequency-dependent soil models for σ_0=0.00008416 S/m

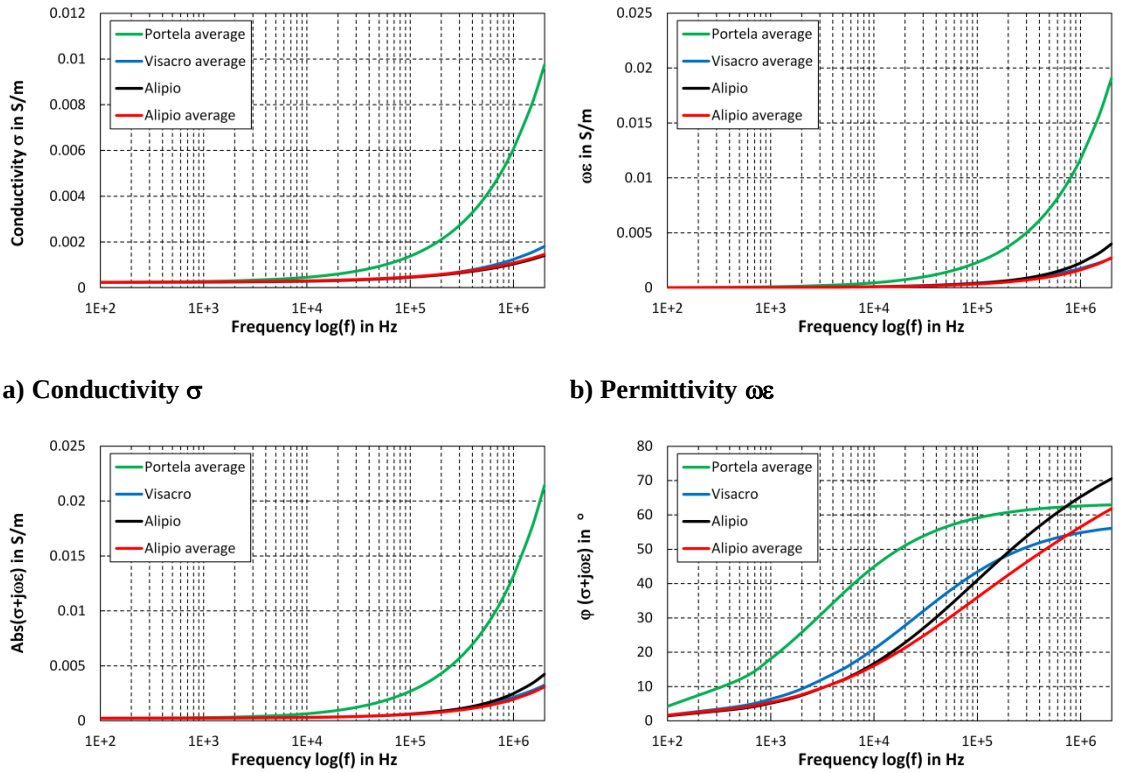

a) Conductivity σ **b) Permittivity ωε**

c) Absolute conductivity Abs(σ+jωε) **d) Phase angle φ(σ+jωε)**

Figure B-4: Comparison of frequency-dependent soil models for σ_0=0.000229 S/m

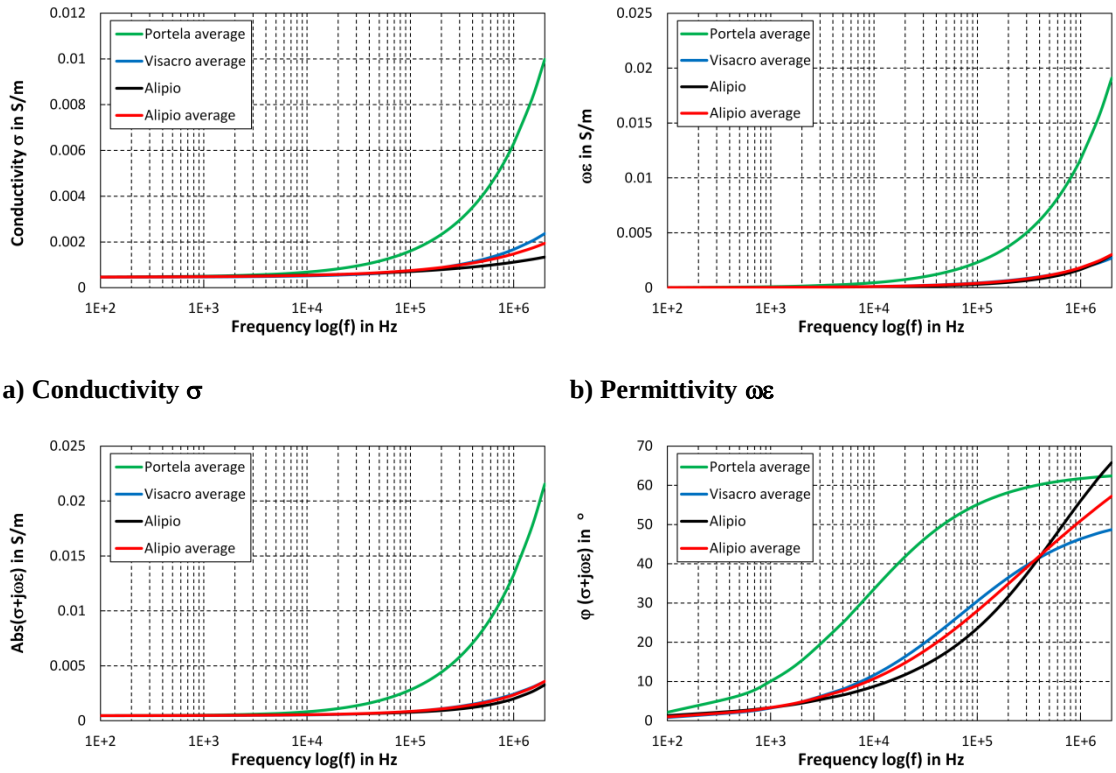

a) Conductivity σ **b) Permittivity ωε**

c) Absolute conductivity Abs(σ+jωε) **d) Phase angle φ(σ+jωε)**

Figure B-5: Comparison of frequency-dependent soil models for σ_0=0.000459 S/m

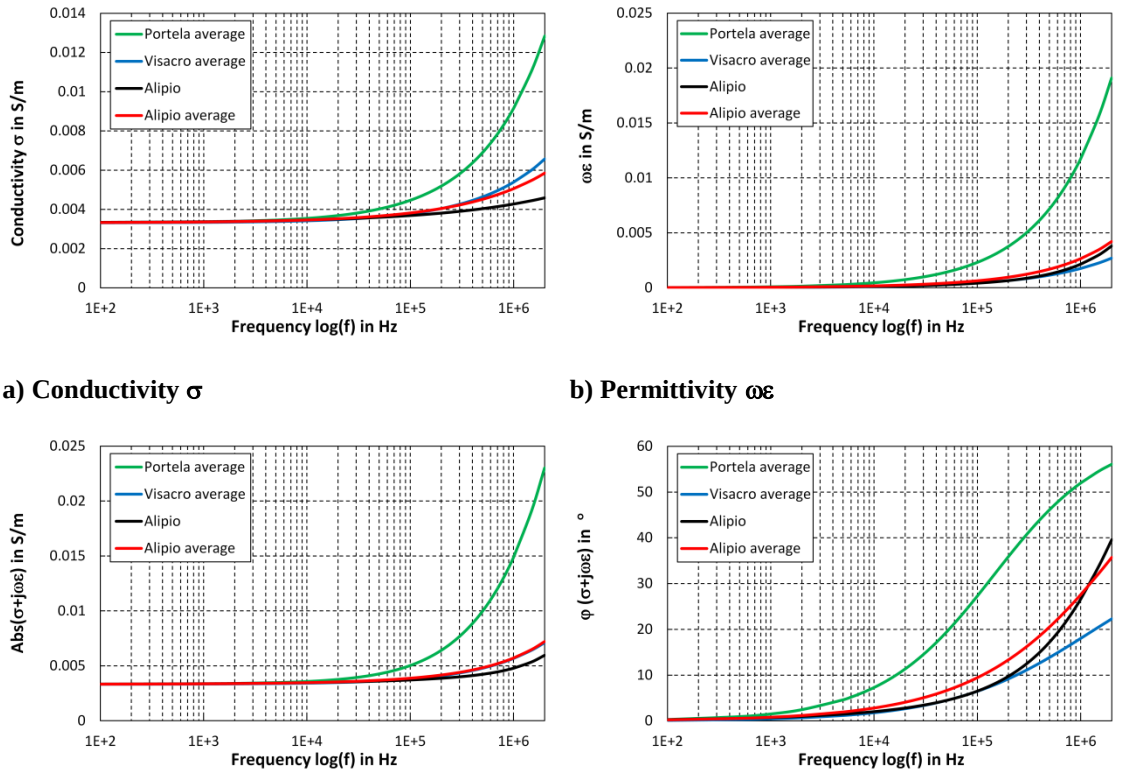

a) Conductivity σ

b) Permittivity ωε

c) Absolute conductivity Abs(σ+jωε)

d) Phase angle φ(σ+jωε)

Figure B-6: Comparison of frequency-dependent soil models for σ_0=0.00332 S/m

B.2: CURVE FITTING OF FREQUENCY-DEPENDENT SOIL MODELS

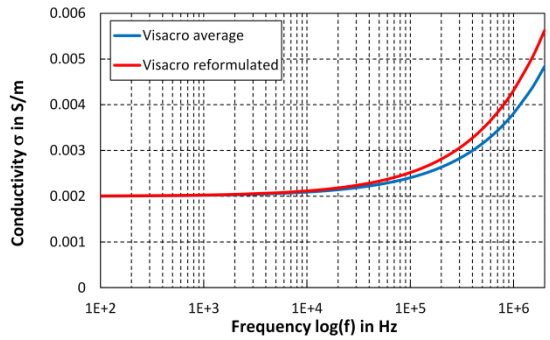

a) Conductivity σ

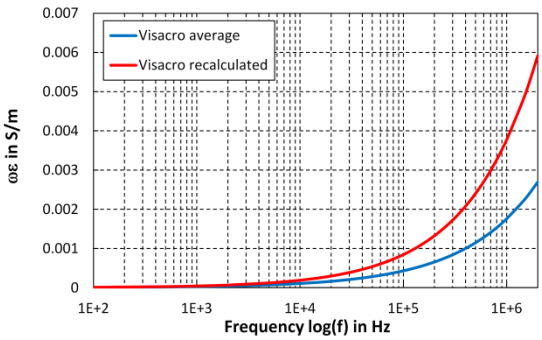

b) Permittivity ωε

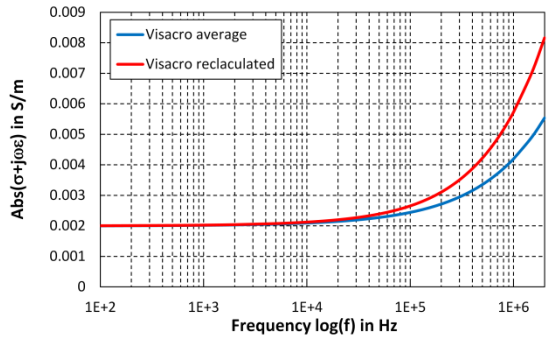

c) Absolute conductivity Abs(σ+jωε)

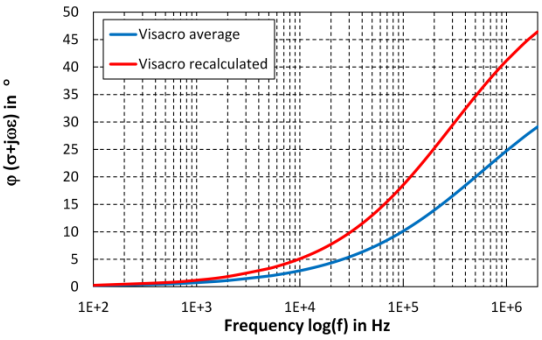

d) Phase angle φ(σ+jωε)

Figure B-7: Curve fitting of Visacro frequency-dependent soil model, σ_0=0.002 S/m

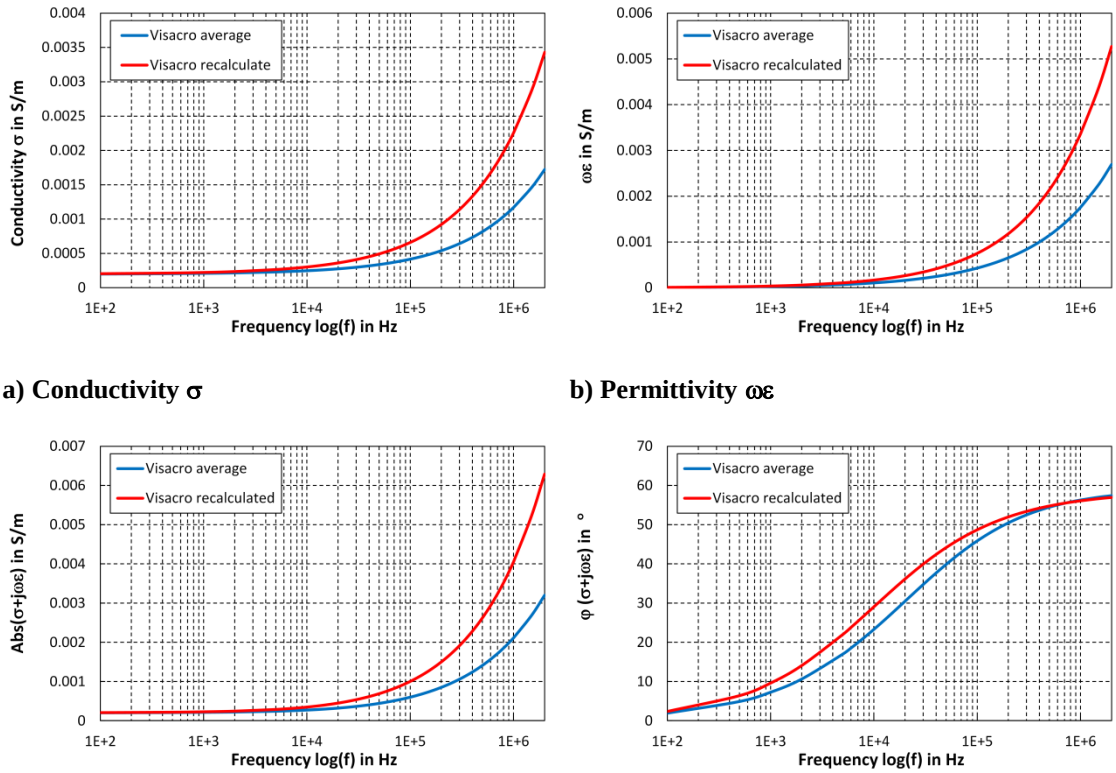

a) Conductivity σ **b) Permittivity ωε**

c) Absolute conductivity Abs(σ+jωε) **d) Phase angle φ(σ+jωε)**

Figure B-8: Curve fitting of Visacro frequency-dependent soil model, σ_0=0.0002 S/m

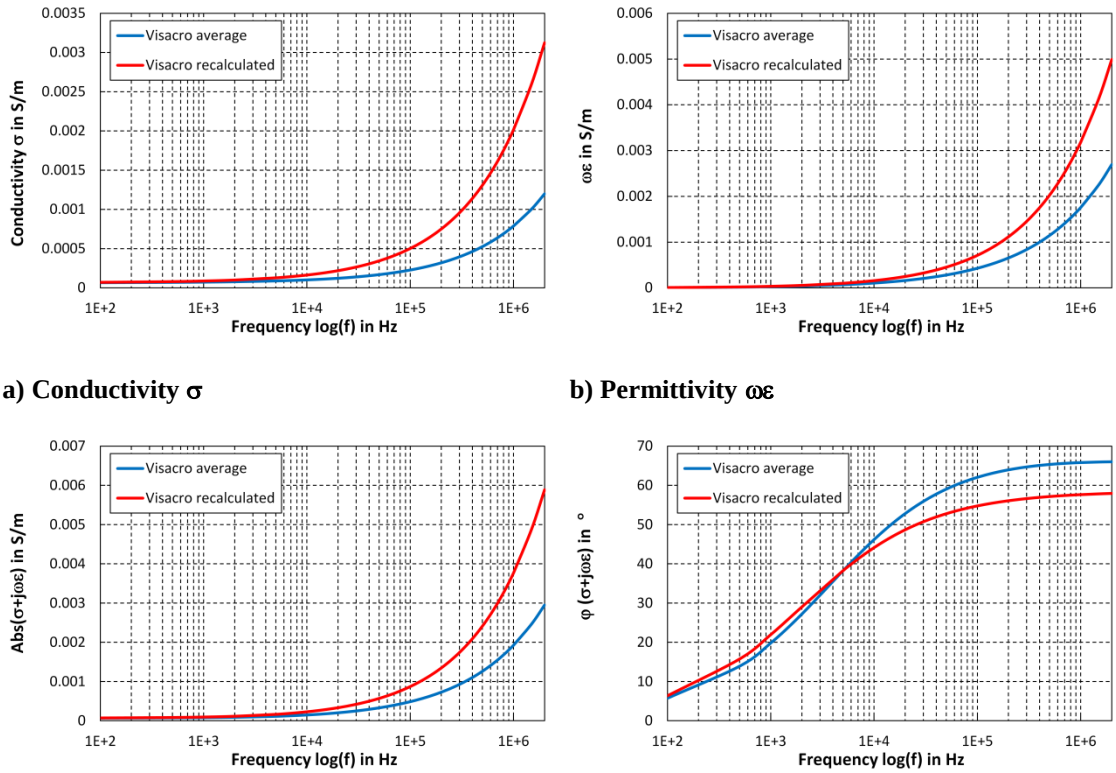

a) Conductivity σ **b) Permittivity ωε**

c) Absolute conductivity Abs(σ+jωε) **d) Phase angle φ(σ+jωε)**

Figure B-9: Curve fitting of Visacro frequency-dependent soil model, σ_0=0.0000667 S/m

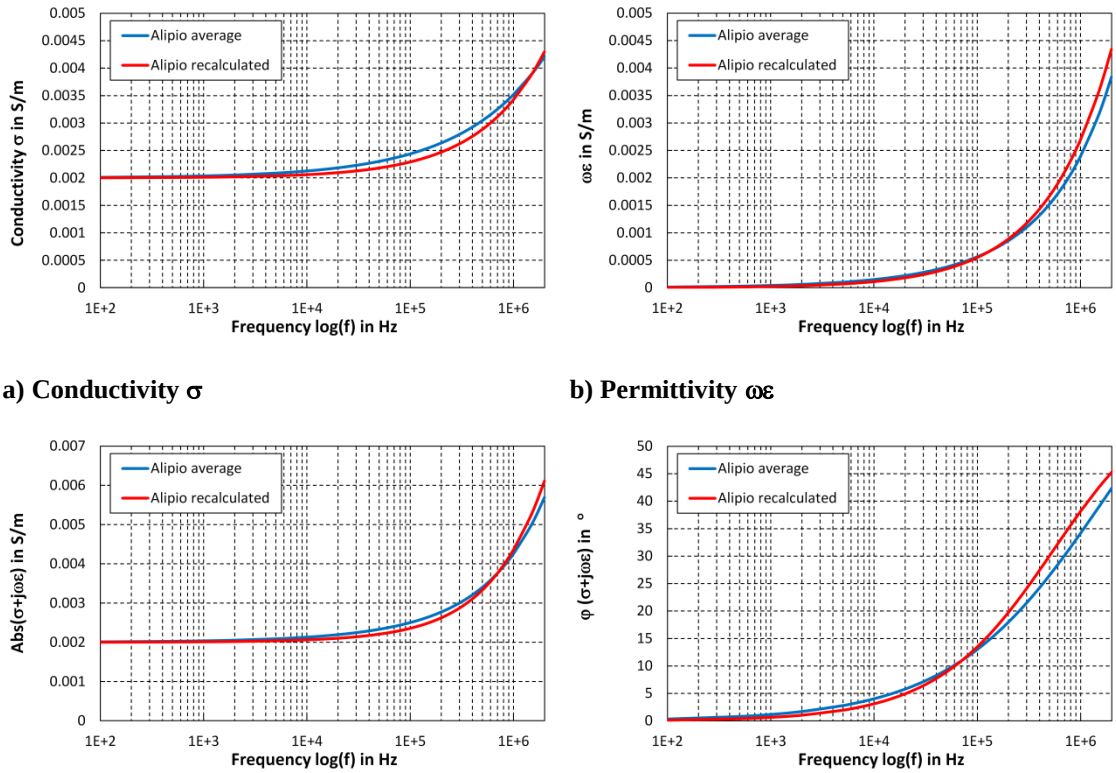

a) Conductivity σ **b) Permittivity ωε**

c) Absolute conductivity Abs(σ+jωε) **d) Phase angle φ(σ+jωε)**

Figure B-10: Curve fitting of Alipio frequency-dependent soil model, σ_0=0.002 S/m

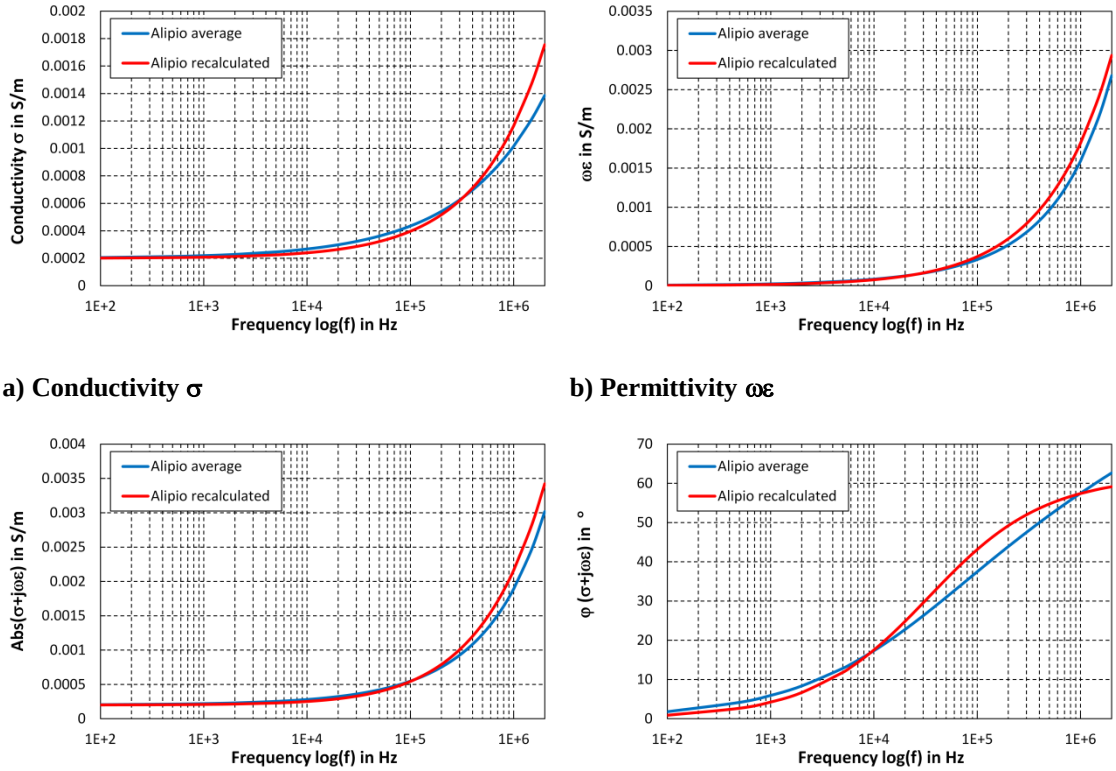

a) Conductivity σ **b) Permittivity ωε**

c) Absolute conductivity Abs(σ+jωε) **d) Phase angle φ(σ+jωε)**

Figure B-11: Curve fitting of Alipio frequency-dependent soil model, σ_0=0.0002 S/m

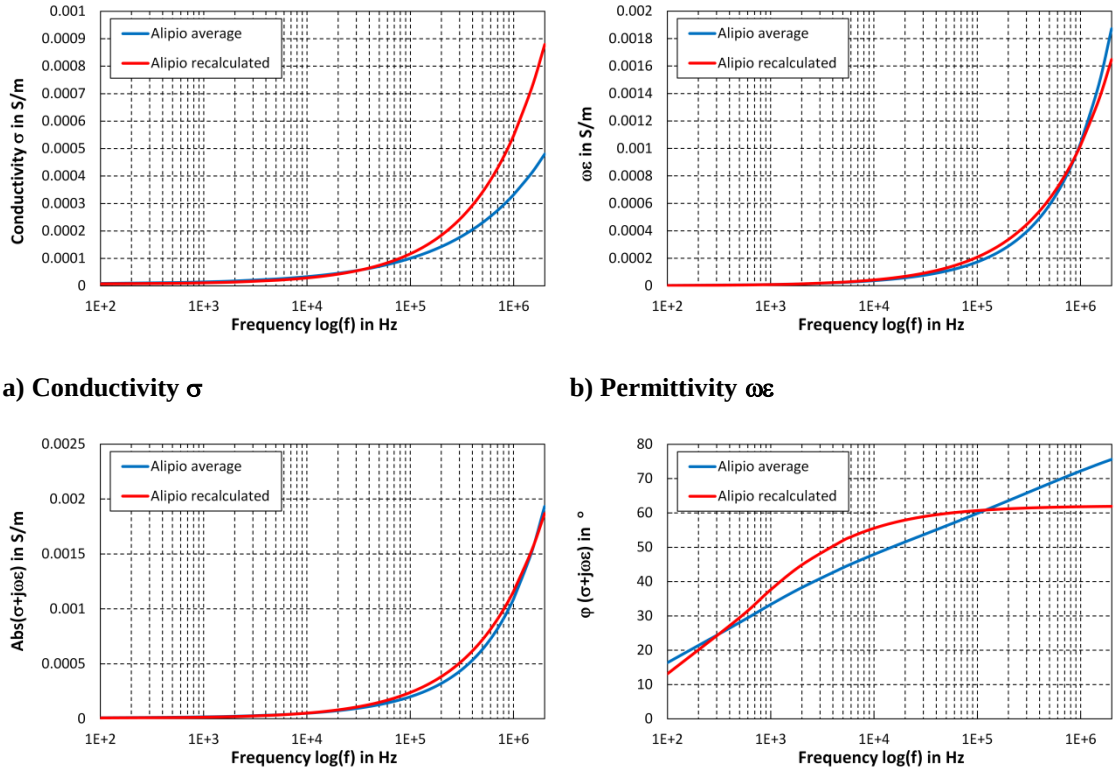

a) Conductivity σ **b) Permittivity ωε**

c) Absolute conductivity Abs(σ+jωε) **d) Phase angle φ(σ+jωε)**

Figure B-12: Curve fitting of Alipio frequency-dependent soil model, σ_0=0.000067 S/m

B.3: TOWER DATA

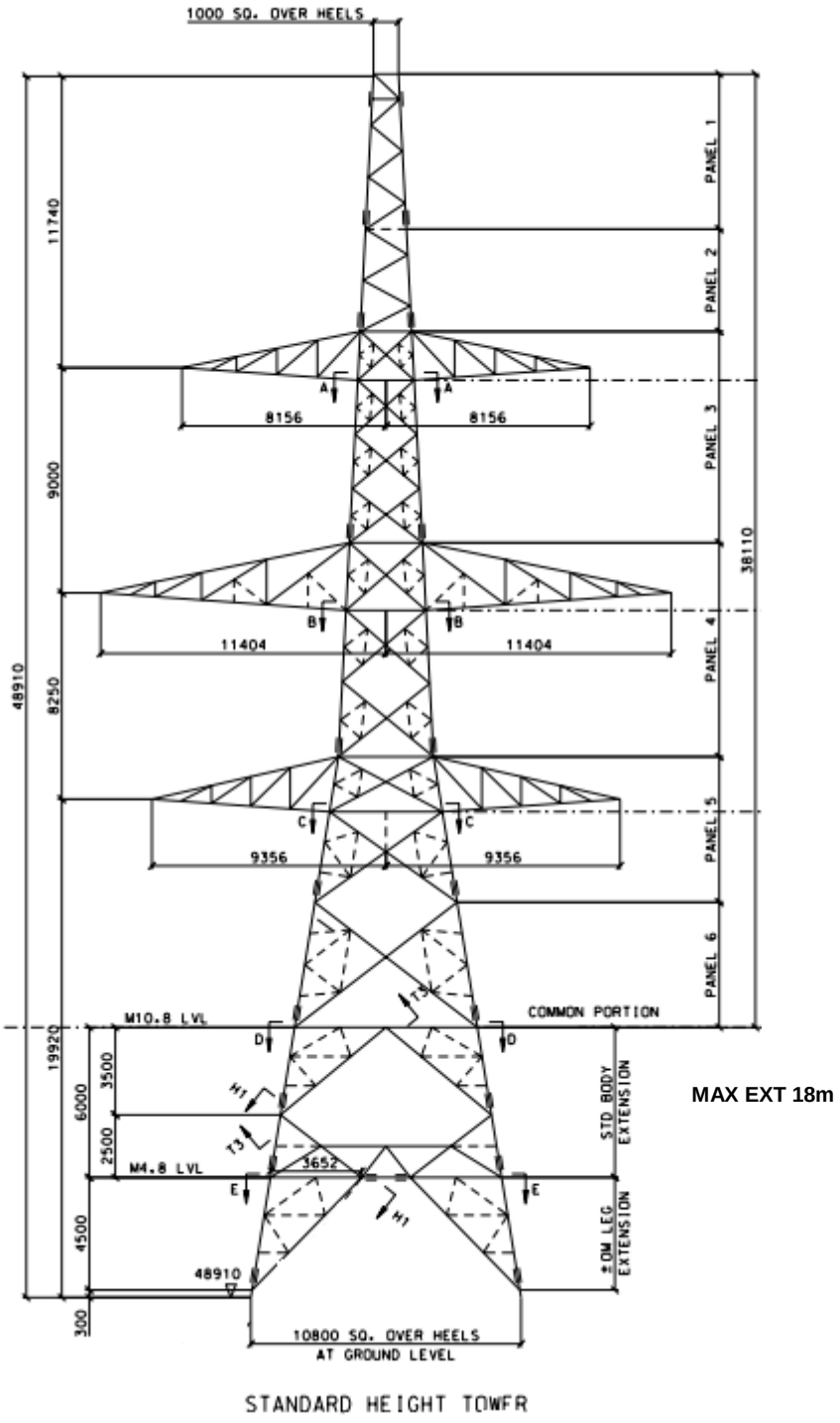

Figure B-13: 400 kV tension tower data

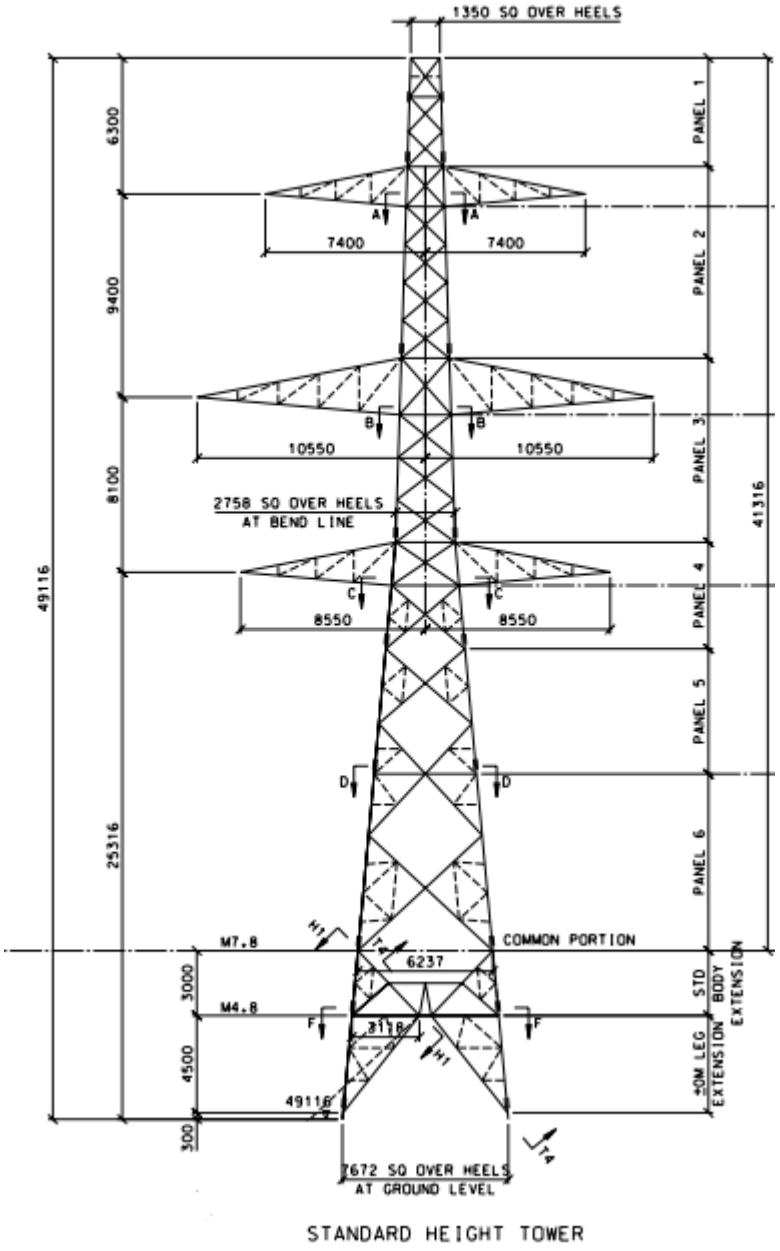

Figure B-14: 400 kV suspension tower data

B.4: INSULATOR DATA

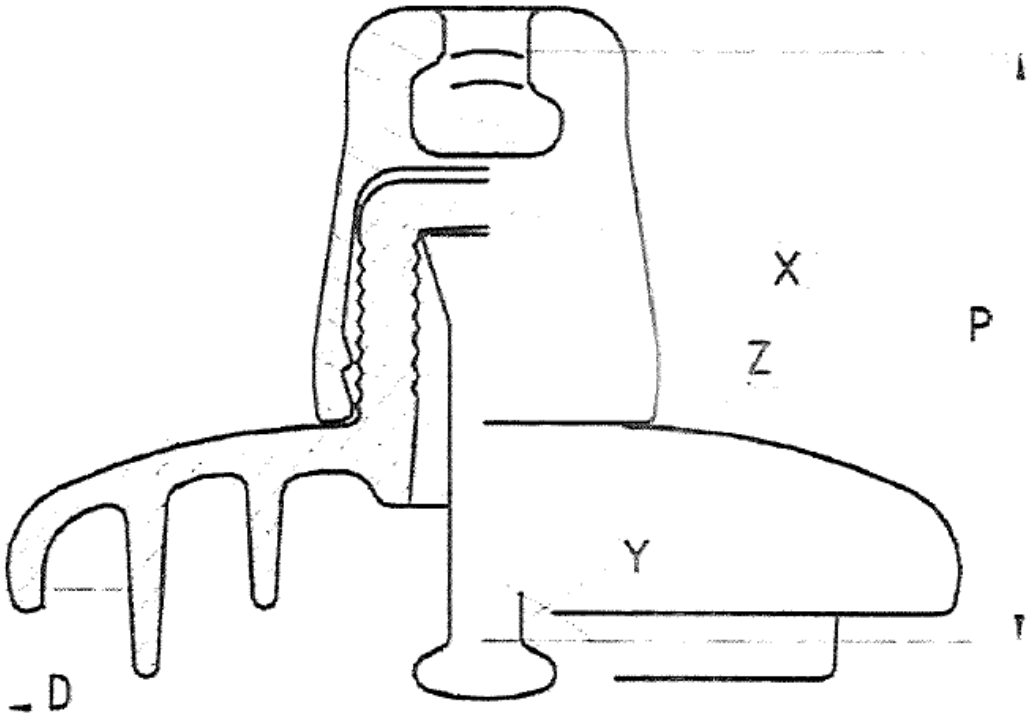

DIMENSIONS

- Diameter of shell (D)	mm	320 ± 14
- Spacing (P)	mm	200
-Minimal creepage distance	mm	480
- Couplings according to IEC 60120 & BS 3288	Size	24
- Approximate net weight	kg	11.1

TECHNICAL DETAILS According to IEC 60383 & NGT TS 3.4.4 & NGT TS 3.4.17

- Power frequency withstand voltage (wet)	kV	50
- Lightning impulse withstand voltage	kV	140
- Minimum puncture voltage	kV	130
- Test voltage for single unit RIV (≤ 52dB)	kV	30
- Minimum mechanical failing load	kN	300

COMPONENT PARTS

-X: Cap	HOT DIP GALVANIZED MALLEABLE CAST IRON EN 1562: EN-GJMB 350-10; EN-GJMB 450-6 EN ISO1461-14713 Suppliers: Safam Zigong (China) – Lince (Spain) – Reliable(China)
- Z: Dielectric shell	TOUGHENED GLASS - Suppliers : SEVES Nusco Italy
- Y: Pin	HOT DIP GALVANIZED FORGED STEEL EN 10083-1 C40E/R; C45E/R; C50E/R; C55E/R ; EN ISO1461-14713 Suppliers: Stevenin (France) –Pernos Y Derivados (Spain) –Electroforja (ex:Usimec Brasil) – Reliable(China) Chengdu(China)
-Cotter key	STAINLESS STEEL EN 10088-1 X5CrNI18-10
-Ciment	ALUMINOUS
Tolerances	*According to IEC 60305 UNLESS OTHERWISE STATED*

Full insulator string with arcing horns: 21 discs@ 195mm spacing, arc gap 2800mm

Figure B-15: 400 kV insulator data

B.5: CONDUCTOR DATA

Type:	Designation:	Composition:	Standard:
Conductor AAAC	700 ARAUCARIA (EHC)	61	NGTS 3.4.2 Ed. 6/11

Description	Unit	Characteristics
1. Aluminium Alloy Wires		
Number of aluminium alloy wires	-	61
Diameter of wires	mm	4,14
Area of the wires	mm^2	13,46
Maximum individuality resistivity	$Ohm.mm^2/m$	0,0315
Maximum medium resistivity	$Ohm.mm^2/m$	0,0305
Minimum tensile strenght (before and after stranding)	N/mm^2	295
Minimum elongation at break (250 mm)	%	3,5
2. Complete Conductor		
Area of conductor	mm^2	821,15
Diameter of conductor	mm	37,26
Total weight of conductor	Kg/Km	2.269
Total weight of conductor with grease	Kg/Km	2.348
Maximum electrical resistance at 20 °C	Ohm/Km	0,038
Final modulus of elasticity	N/mm^2	54.000
Coefficient of linear expansion	1/°C	$23,0x10^{-6}$
Nominal breaking load (NBL)	KN	230
Lay ratios		
All Inner layers	xD	10 to 16
Outer Layer	xD	10 to 14

OBS: the direction of lay of the external layer shall be right hand except when otherwise specified by the purchaser.
Aluminium alloy, according to NGTS 3.4.2 Issue 5/04, specification and with a maximum medium resistivity at 20°C of 3.05 microhm.cm.
The conductor will be greased, except on the outer layer, with Metalube OCG 5000 grease and will be accord. to NGTS 3.4.2 Issue 6/11 specification.
The weight of grease used will be between 59 and 98 g/m.

Cross Sectional Area:

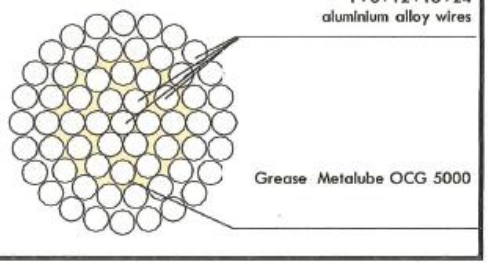

Figure B-16: 400 kV phase conductor data

E-AlMgSi/Stalum 109/209 2C
AACSR/ACS 109/209 2C

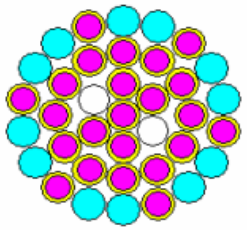

1	x	3,40 mm	Stalum (ACS)
4	x	3,40 mm	Stalum (ACS)
2	x	3,20 mm	Stahlbündelader (Stainless Steel Loose Tube (SLT))
12	x	3,40 mm	Stalum (ACS)
6	x	3,40 mm	Stalum (ACS)
12	x	3,40 mm	E-AlMgSi (Al-Alloy), AL3

Norm	EN 50182/2001		Standard
Schlaglänge	Deviation from Standard		Pitch
Seildurchmesser	23,80	mm	Overall Diameter
Querschnittsfläche E-Al/E-AlMgSi	108,95	sqmm	Area Al/Al-Alloy
Querschnittsfläche Stahl/Stalum	208,82	sqmm	Area Steel/ACS
Gesamtquerschnitt	317,77	sqmm	Cross Sectional Area
Stahl/Stalum - Gewicht	1408	kg/km	Steel/ACS - Weight
E-Al/E-AlMgSi - Gewicht	303	kg/km	Al/Al-Alloy - Weight
Stahlbündelader - Gewicht	40	kg/km	SLT - Weight
Fett - Gewicht	31	kg/km	Grease - Weight
Gesamtgewicht	1782	kg/km	Total - Weight
Elastizitätsmodul	12711	daN/sqmm	Modulus of Elasticity
Rechnerische Bruchkraft	27855	daN	Calculated Breaking Load
Temperaturkoeffizient	1,46 E-05	1/°C	Coeff. Of Linear Expansion
Kurzschlußstrom (0,5 s / 35°C - 160°C)	36,02	kA	Short Current (0,5 s / 35°C - 160°C)
Gleichstromwiderstand bei 20°C	0,1726 *)	Ohm/km	DC - Resistance at 20°C
Faseranzahl	48		Number of Fibers

*) Conductivity of al-alloy wires = 32,00 Sm/sqmm
Greasing to cat. 3 of L38/1 1991

Figure B-17: 400 kV earth conductor data

B.6:: MATHEMATICAL DERIVATION OF CORONA MODEL

$$\frac{dv}{dt} = \frac{i}{C \cdot \left[\left(\frac{v}{V_i}\right)^{B-1} - 1\right]}$$

Taylor-Series with termination after second term:

$$\frac{V_1 - V_0}{\Delta t} = \mathrm{f}(v,i)|_{v=V_0,i=I_0} + \left.\frac{\mathrm{df}}{\mathrm{dv}}\right|_{v=V_0,i=I_0} \cdot (V_1 - V_0) + \left.\frac{\mathrm{df}}{\mathrm{di}}\right|_{v=V_0,i=I_0} \cdot (I_1 - I_0)$$

$$\mathrm{f}(v,i)|_{v=V_0,i=I_0} = \frac{I_0}{C \cdot \left[\left(\frac{V_0}{V_i}\right)^{B-1} - 1\right]}$$

$$\left.\frac{\mathrm{df}}{\mathrm{d}v}\right|_{v=V_0,i=I_0} = -\frac{I_0 \cdot C \cdot \left(\frac{V_0}{V_i}\right)^{B-2} \cdot (B-1) \cdot \frac{1}{V_i}}{\left\{C \cdot \left[\left(\frac{V_0}{V_i}\right)^{B-1} - 1\right]\right\}^2} = -\frac{I_0 \cdot \left(\frac{V_0}{V_i}\right)^{B-2} \cdot (B-1) \cdot \frac{1}{V_i}}{C\left[\left(\frac{V_0}{V_i}\right)^{B-1} - 1\right]^2}$$

$$\left.\frac{\mathrm{df}}{\mathrm{d}i}\right|_{v=V_0,i=I_0} = \frac{1}{C \cdot \left[\left(\frac{V_0}{V_i}\right)^{B-1} - 1\right]}$$

$$\frac{V_1 - V_0}{\Delta t} = \frac{I_0}{C \cdot \left[\left(\frac{V_0}{V_i}\right)^{B-1} - 1\right]} - \frac{I_0 \cdot \left(\frac{V_0}{V_i}\right)^{B-2} \cdot (B-1) \cdot \frac{1}{V_i}}{C \cdot \left[\left(\frac{V_0}{V_i}\right)^{B-1} - 1\right]^2}(V_1 - V_0) + \frac{1}{C \cdot \left[\left(\frac{V_0}{V_i}\right)^{B-1} - 1\right]}(I_1 - I_0)$$

$$\frac{V_1 - V_0}{\Delta t} = \frac{I_0}{C \cdot \left[\left(\frac{V_0}{V_i}\right)^{B-1} - 1\right]} - \frac{I_0 \cdot \left(\frac{V_0}{V_i}\right)^{B-2} \cdot (B-1) \cdot \frac{1}{V_i}}{C \cdot \left[\left(\frac{V_0}{V_i}\right)^{B-1} - 1\right]^2} \cdot V_1 + \frac{I_0 \cdot \left(\frac{V_0}{V_i}\right)^{B-2} \cdot (B-1) \cdot \frac{1}{V_i}}{C \cdot \left[\left(\frac{V_0}{V_i}\right)^{B-1} - 1\right]^2} \cdot V_0$$
$$+ \frac{I_1}{C \cdot \left[\left(\frac{V_0}{V_i}\right)^{B-1} - 1\right]} - \frac{I_0}{C \cdot \left[\left(\frac{V_0}{V_i}\right)^{B-1} - 1\right]}$$

$$\frac{V_1 - V_0}{\Delta t} = -\frac{I_0 \cdot \left(\frac{V_0}{V_i}\right)^{B-2} \cdot (B-1) \cdot \frac{1}{V_i}}{C \cdot \left[\left(\frac{V_0}{V_i}\right)^{B-1} - 1\right]^2} \cdot V_1 + \frac{I_0 \cdot \left(\frac{V_0}{V_i}\right)^{B-2} \cdot (B-1) \cdot \frac{1}{V_i}}{C \cdot \left[\left(\frac{V_0}{V_i}\right)^{B-1} - 1\right]^2} \cdot V_0 + \frac{1}{C \cdot \left[\left(\frac{V_0}{V_i}\right)^{B-1} - 1\right]} \cdot I_1$$

Substitution of constants:

$$C_K = C \cdot \left[\left(\frac{V_0}{V_i}\right)^{B-1} - 1\right]$$

$$\frac{1}{V_K} = \frac{\left(\frac{V_0}{V_i}\right)^{B-2} \cdot (B-1) \cdot \frac{1}{V_i}}{\left[\left(\frac{V_0}{V_i}\right)^{B-1} - 1\right]}$$

$$\frac{V_1 - V_0}{\Delta t} = -\frac{I_0}{C_K} \cdot \frac{1}{V_K} \cdot V_1 + \frac{I_0}{C_K} \cdot \frac{1}{V_K} \cdot V_0 + \frac{1}{C_K} I_1$$

$$V_1 - V_0 = -\frac{\Delta t}{C_K} I_0 \cdot \frac{1}{V_K} \cdot V_1 + \frac{\Delta t}{C_K} I_0 \cdot \frac{1}{V_K} \cdot V_0 + \frac{\Delta t}{C_K} I_1$$

Substitution of next-time-step variables:

$$V_1 = \frac{I_1 - c_1}{Y}$$

$$I_0 = V_0 Y + c_0$$

$$V_1 - V_0 = -\frac{\Delta t}{C_K} I_0 \cdot \frac{1}{V_K} \cdot V_1 + \frac{\Delta t}{C_K} I_1 + \frac{\Delta t}{C_K} I_0 \cdot \frac{V_0}{V_K}$$

$$\frac{I_1 - c_1}{Y} - V_0 = -\frac{\Delta t}{C_K} (V_0 Y + c_0) \cdot \frac{1}{V_K} \cdot \frac{I_1 - c_1}{Y} + \frac{\Delta t}{C_K} (V_0 Y + c_0) \cdot \frac{1}{V_K} \cdot V_0 + \frac{\Delta t}{C_K} I_1$$

$$\frac{I_1}{Y} - \frac{c_1}{Y} - V_0 = -\frac{\Delta t}{C_K} (V_0 Y + c_0) \cdot \frac{1}{V_K} \cdot \frac{I_1}{Y} + \frac{\Delta t}{C_K} (V_0 Y + c_0) \cdot \frac{1}{V_K} \cdot \frac{c_1}{Y} + \frac{\Delta t}{C_K} V_0 Y \cdot \frac{1}{V_K} \cdot V_0 + \frac{\Delta t}{C_K} c_0 \cdot \frac{1}{V_K} \cdot V_0 + \frac{\Delta t}{C_K} I_1$$

$$\frac{I_1}{Y} - \frac{c_1}{Y} - V_0 = \underbrace{-\frac{\Delta t}{C_K} V_0 Y \cdot \frac{1}{V_K} \cdot \frac{I_1}{Y}} \underbrace{-\frac{\Delta t}{C_K} c_0 \cdot \frac{1}{V_K} \cdot \frac{I_1}{Y}} + \frac{\Delta t}{C_K} V_0 Y \cdot \frac{1}{V_K} \cdot \frac{c_1}{Y} + \frac{\Delta t}{C_K} c_0 \cdot \frac{1}{V_K} \cdot \frac{c_1}{Y} + \frac{\Delta t}{C_K} V_0 Y \cdot \frac{1}{V_K} \cdot V_0 + \frac{\Delta t}{C_K} c_0 \cdot \frac{1}{V_K} \cdot V_0 \underbrace{+ \frac{\Delta t}{C_K} I_1}$$

$$\underbrace{\frac{I_1}{Y} + \frac{\Delta t}{C_K} V_0 \cdot \frac{I_1}{V_K} + \frac{\Delta t}{C_K} c_0 \cdot \frac{1}{V_K} \cdot \frac{I_1}{Y} - \frac{\Delta t}{C_K} I_1}_{=0} = \frac{\Delta t}{C_K} V_0 \frac{c_1}{V_K} + \frac{\Delta t}{C_K} c_0 \cdot \frac{1}{V_K} \cdot \frac{c_1}{Y} + \frac{\Delta t}{C_K} V_0 Y \cdot \frac{1}{V_K} \cdot V_0 + \frac{\Delta t}{C_K} c_0 \cdot \frac{1}{V_K} \cdot V_0 + \frac{c_1}{Y} + V_0$$

Condition:

$$\frac{1}{Y}+\frac{\Delta t}{C_K}V_0\cdot\frac{1}{V_K}+\frac{\Delta t}{C_K}c_0\cdot\frac{1}{V_K}\cdot\frac{1}{Y}-\frac{\Delta t}{C_K}=0$$

$$\frac{1}{Y}+\frac{\Delta t}{C_K}c_0\cdot\frac{1}{V_K}\cdot\frac{1}{Y}=-\frac{\Delta t}{C_K}V_0\cdot\frac{1}{V_K}+\frac{\Delta t}{C_K}$$

$$\frac{1}{Y}\left(1+\frac{\Delta t}{C_K}c_0\cdot\frac{1}{V_K}\right)=-\frac{\Delta t}{C_K}V_0\cdot\frac{1}{V_K}+\frac{\Delta t}{C_K}$$

$$\mathrm{Y}=\frac{\left(1+\frac{\Delta t}{C_K}c_0\cdot\frac{1}{V_K}\right)}{-\frac{\Delta t}{C_K}V_0\cdot\frac{1}{V_K}+\frac{\Delta t}{C_K}}=\frac{\left(\frac{C_K}{\Delta t}+\frac{c_0}{V_K}\right)}{-\frac{V_0}{V_K}+1}=-\frac{\left(\frac{C_K}{\Delta t}+\frac{c_0}{V_K}\right)}{\frac{V_0}{V_K}-1}$$

$$0=\underbrace{\frac{\Delta t}{C_K}V_0\frac{c_1}{V_K}}+\underbrace{\frac{\Delta t}{C_K}c_0\cdot\frac{1}{V_K}\cdot\frac{c_1}{Y}}+\frac{\Delta t}{C_K}V_0Y\cdot\frac{1}{V_K}\cdot V_0+\frac{\Delta t}{C_K}c_0\cdot\frac{1}{V_K}\cdot V_0+\underbrace{\frac{c_1}{Y}}+V_0$$

$$-\frac{\Delta t}{C_K}V_0Y\cdot\frac{1}{V_K}\cdot V_0-\frac{\Delta t}{C_K}c_0\cdot\frac{1}{V_K}\cdot V_0-V_0=\frac{\Delta t}{C_K}V_0\frac{c_1}{V_K}+\frac{\Delta t}{C_K}c_0\cdot\frac{1}{V_K}\cdot\frac{c_1}{Y}+\frac{c_1}{Y}$$

$$-\frac{\Delta t}{C_K}V_0Y\cdot\frac{1}{V_K}\cdot V_0-\frac{\Delta t}{C_K}c_0\cdot\frac{1}{V_K}\cdot V_0-V_0=c_1\left(\frac{\Delta t}{C_K}\frac{V_0}{V_K}+\frac{\Delta t}{C_K}c_0\cdot\frac{1}{V_K}\cdot\frac{1}{Y}+\frac{1}{Y}\right)$$

$$-\left(\frac{\Delta t}{C_K}V_0Y\cdot\frac{1}{V_K}\cdot V_0+\frac{\Delta t}{C_K}c_0\cdot\frac{1}{V_K}\cdot V_0+V_0\right)=c_1\left(\frac{\Delta t}{C_K}\frac{V_0}{V_K}+\frac{\Delta t}{C_K}c_0\cdot\frac{1}{V_K}\cdot\frac{1}{Y}+\frac{1}{Y}\right)$$

$$-\left(\frac{\Delta t}{C_K}\frac{V_0}{V_K}\cdot V_0Y+\frac{\Delta t}{C_K}c_0\cdot\frac{1}{V_K}\cdot V_0+V_0\right)=c_1\left(\frac{\Delta t}{C_K}\frac{V_0}{V_K}+\frac{\Delta t}{C_K}c_0\cdot\frac{1}{V_K}\cdot\frac{1}{Y}+\frac{1}{Y}\right)$$

$$-V_0Y\left(\frac{\Delta t}{C_K}\frac{V_0}{V_K}+\frac{\Delta t}{C_K}c_0\cdot\frac{1}{V_K}\cdot\frac{V_0}{V_0Y}+\frac{V_0}{V_0Y}\right)=c_1\left(\frac{\Delta t}{C_K}\frac{V_0}{V_K}+\frac{\Delta t}{C_K}c_0\cdot\frac{1}{V_K}\cdot\frac{1}{Y}+\frac{1}{Y}\right)$$

$$-V_0Y\left(\frac{\Delta t}{C_K}\frac{V_0}{V_K}+\frac{\Delta t}{C_K}c_0\cdot\frac{1}{V_K}\cdot\frac{1}{Y}+\frac{1}{Y}\right)=c_1\left(\frac{\Delta t}{C_K}\frac{V_0}{V_K}+\frac{\Delta t}{C_K}c_0\cdot\frac{1}{V_K}\cdot\frac{1}{Y}+\frac{1}{Y}\right)$$

$$c_1=-V_0Y$$

B.7: TIDD-LINE DATA

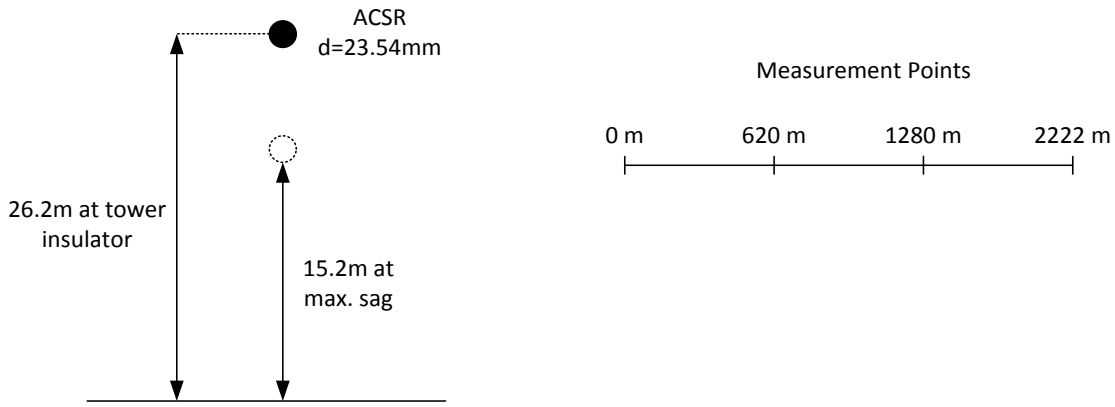

B.8: VERIFICATION OF FREQUENCY-DEPENDENCY OF TRANSMISSION LINE MODELS

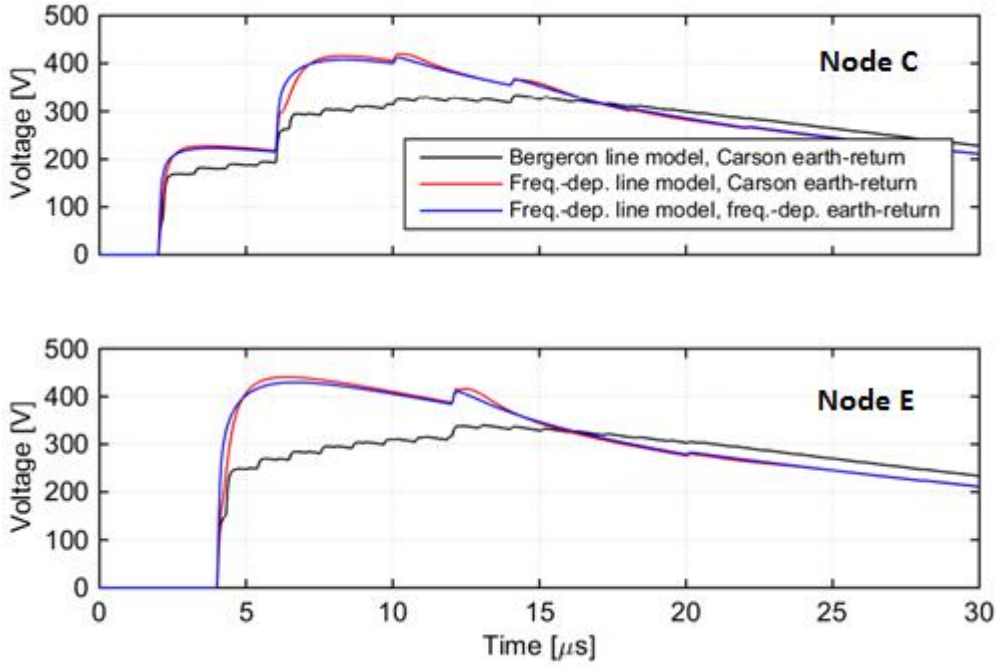

Figure B-18: Simulation results of transmission line models, soil resistance 1000 Ωm, measured voltage at nodes C (top picture) and node E (bottom picture)

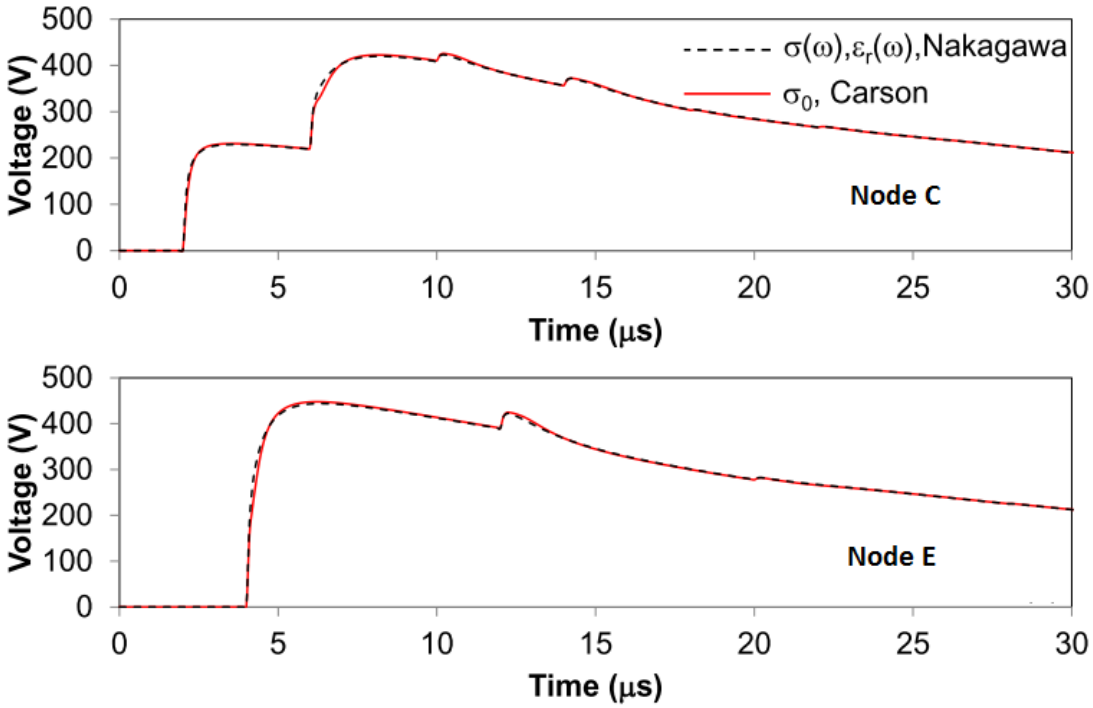

Figure B-19: Simulation results of transmission line models from [135]**, soil resistance 1000 Ωm, measured voltage at nodes C (top picture) and node E (bottom picture)**

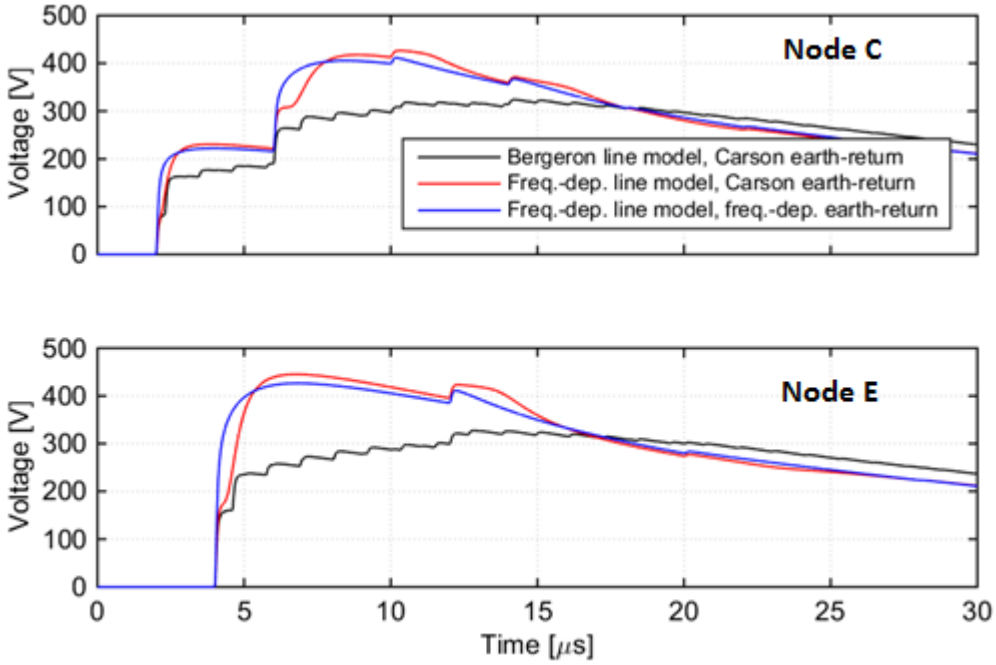

Figure B-20: Simulation results of transmission line models, soil resistance 10000 Ωm, measured voltage at nodes C (top picture) and node E (bottom picture)

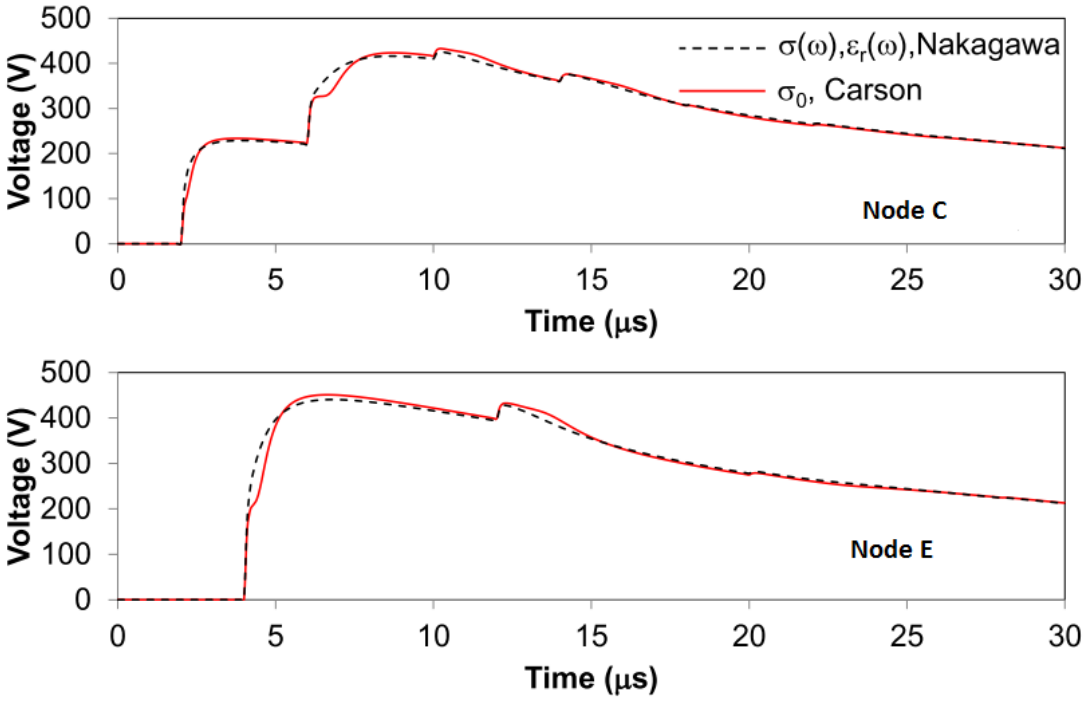

Figure B-21: **Simulation results of transmission line models from** [135]**, soil resistance 10000 Ωm, measured voltage at nodes C (top picture) and node E (bottom picture)**

B.9: VERIFICATION OF TRANSMISSION LINE CORONA MODEL

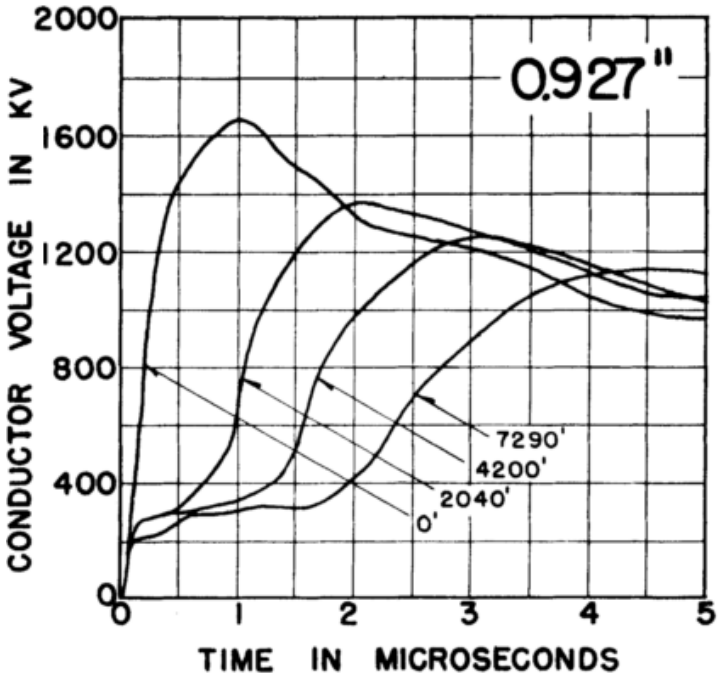

Figure B-22: **Tidd-Line measurement results for single ACSR conductor at various measurement points** [136]

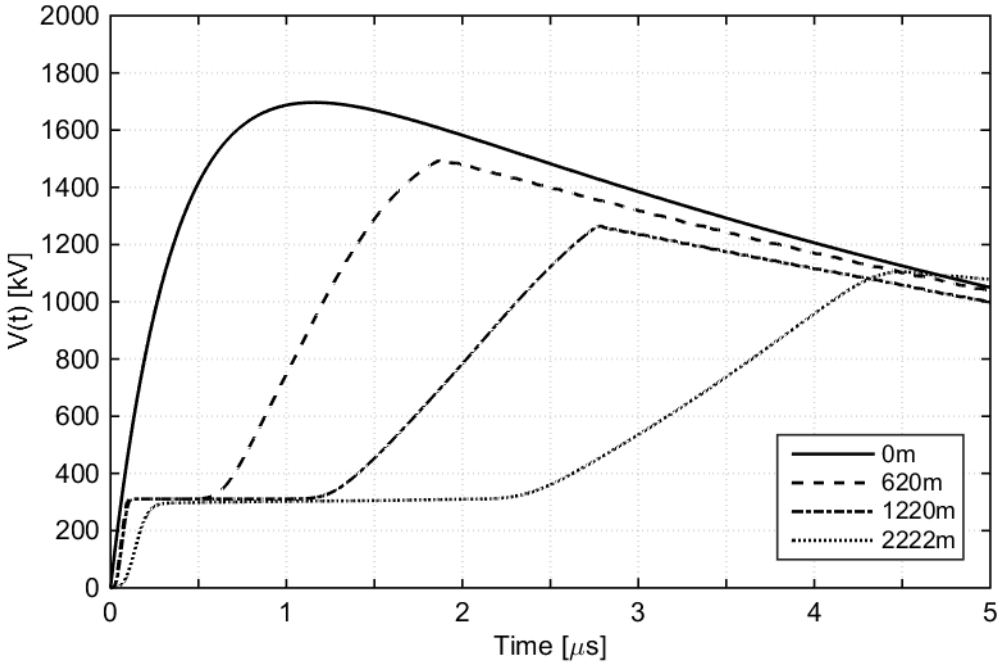

Figure B-23: Tidd-Line PSCAD/EMTDC simulation results for single ACSR conductor at various measurement points with corona model

APPENDIX C: THE TRANSMISSION LINE INSULATORS

C.1: IMPULSE GENERATOR CIRCUITS

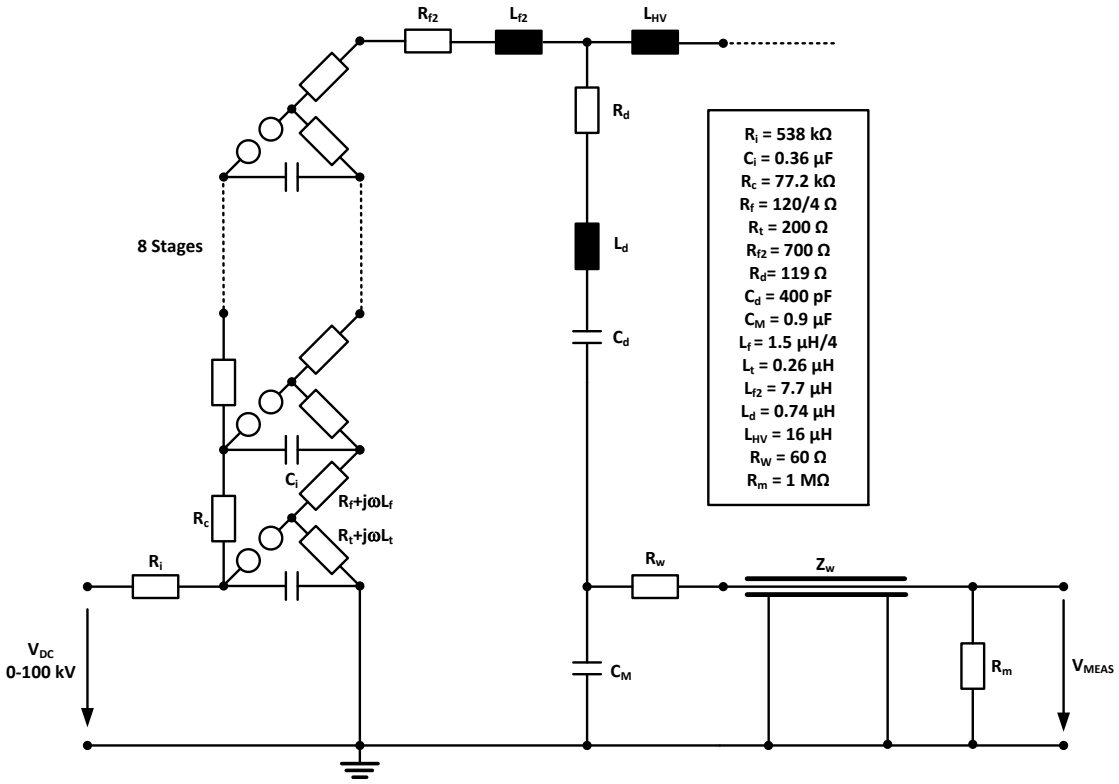

Figure C-1: 8-stage 800 kV impulse generator circuit with parasitic inductances at HWU HV lab

Transfer function (neglecting Z_w):

$$\frac{V_{MEAS}}{V_M} = \frac{R_M}{R_M + R_W}$$

$$Z_M = \frac{1}{sC_M} \qquad Z_d = R_d + sL_d + \frac{1}{sC_d}$$

$$\frac{V_M}{V_{HV}} = \frac{Z_M}{Z_M + Z_d}$$

$$\frac{V_{MEAS}}{V_{HV}} = \frac{R_M}{R_M + R_W} \cdot \frac{Z_M + Z_d}{Z_M}$$

$$\frac{V_M}{V_{HV}} = \frac{\frac{1}{sC_M}}{\frac{1}{sC_M} + R_d + sL_d + \frac{1}{sC_d}} = \frac{1}{1 + sC_M R_d + s^2 L_d C_M + \frac{C_M}{C_d}}$$

$$= \frac{\frac{1}{1 + \frac{C_M}{C_d}}}{1 + s\frac{C_M R_d}{1 + \frac{C_M}{C_d}} + s^2 \frac{L_d C_M}{1 + \frac{C_M}{C_d}}}$$

$$H(s) = \frac{V_{MEAS}}{V_{HV}} = \frac{K}{1 + sT_2 + s^2 T_1}$$

$$K = \frac{R_M}{R_M + R_W} \cdot \frac{1}{1 + \frac{C_M}{C_d}}$$

$$T_1 = \frac{L_d C_M}{1 + \frac{C_M}{C_d}}$$

$$T_2 = \frac{C_M R_d}{1 + \frac{C_M}{C_d}}$$

Neglecting L_d:

$$\frac{V_M}{V_{HV}} = \frac{\frac{1}{sC_M}}{\frac{1}{sC_M} + R_d + \frac{1}{sC_d}} = \frac{1}{1 + sC_M R_d + \frac{C_M}{C_d}} = \frac{\frac{1}{1 + \frac{C_M}{C_d}}}{1 + s\frac{C_M R_d}{1 + \frac{C_M}{C_d}}}$$

$$\frac{V_{MEAS}}{V_{HV}} = \frac{R_M}{R_M + R_W} \cdot \frac{\frac{1}{1 + \frac{C_M}{C_d}}}{1 + s\frac{C_M R_d}{1 + \frac{C_M}{C_d}}}$$

$$H(s) = \frac{V_{MEAS}}{V_{HV}} = \frac{K}{1 + sT}$$

$$K = \frac{R_M}{R_M + R_W} \cdot \frac{1}{1 + \frac{C_M}{C_d}}$$

$$T = \frac{C_M R_d}{1 + \frac{C_M}{C_d}}$$

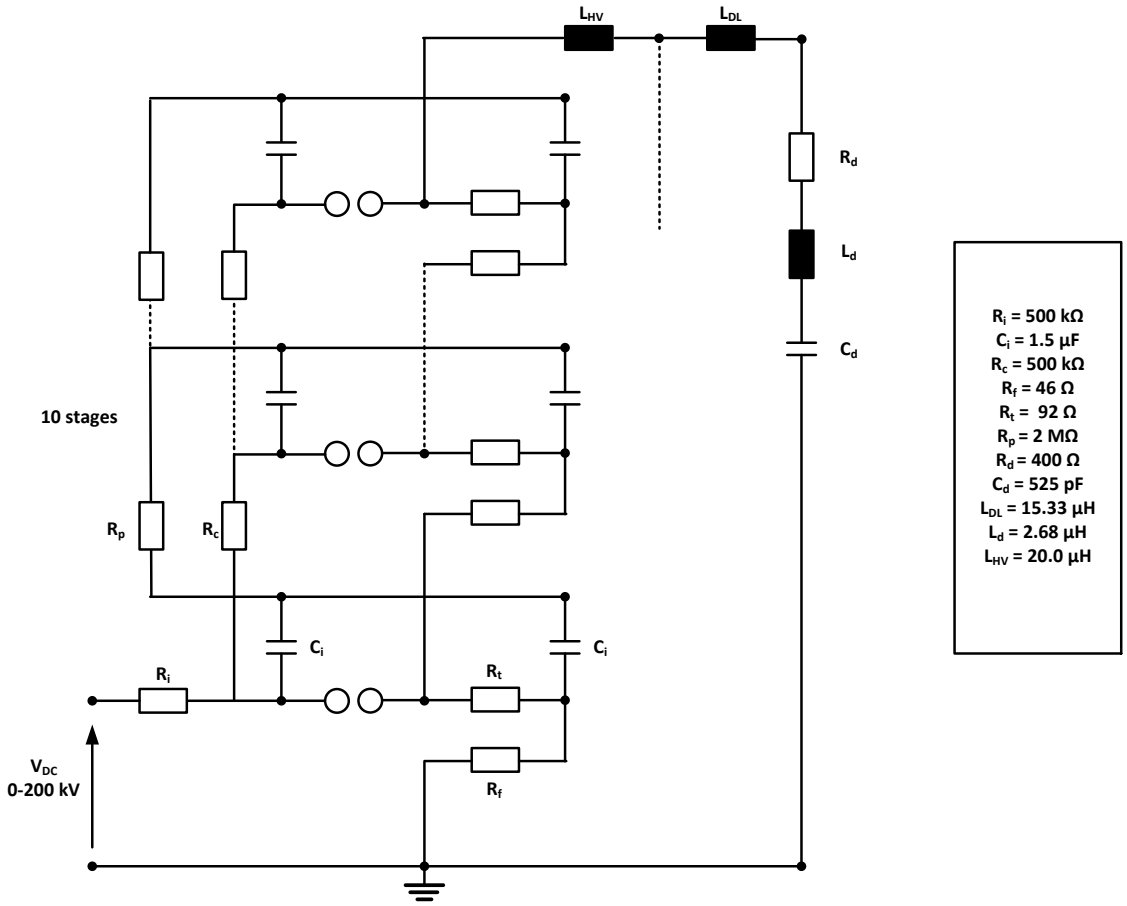

Figure C-2: 10-stage 2000 kV impulse generator circuit at UoM HV lab

C.2: MOTOYAMA MODEL NUMERICAL IMPLEMENTATION

$$I_L = 2K_0 \cdot v_L = 2K_0K_1\left(\frac{V(t)}{D-x_L} - E\right) = \frac{2K_0K_1}{D-x_L}V(t) - 2K_0K_1E$$

$$I_1 = G \cdot V_1 + I_0 \xrightarrow{yields} G = \frac{2K_0K_1}{D-x_L}\ , I_0 = -2K_0K_1E$$

$$\frac{I_1 + I_0}{2} = \frac{2K_0K_1}{D-x_L}\frac{V_1 + V_0}{2} - 2K_0K_1E$$

$$I_1 + I_0 = \frac{2K_0K_1}{D-x_L}V_1 + \frac{2K_0K_1}{D-x_L}V_0 - 4K_0K_1E$$

$$I_1 + I_0 = \frac{2K_0K_1}{D-x_L}\frac{I_1 - c_1}{Y} + \frac{2K_0K_1}{D-x_L}\frac{I_0 - c_0}{Y} - 4K_0K_1E$$

$$\underbrace{I_1 - \frac{2K_0K_1}{D-x_L}\frac{I_1}{Y}}_{0} = -\frac{2K_0K_1}{D-x_L}\frac{c_1}{Y} + \frac{2K_0K_1}{D-x_L}\frac{I_0 - c_0}{Y} - 4K_0K_1E - I_0$$

$$I_1\left(1 - \frac{2K_0K_1}{D-x_L}\frac{1}{Y}\right) = 0$$

$$Y = \frac{2K_0K_1}{D-x_L}$$

$$0 = -\frac{2K_0K_1}{D-x_L}\frac{c_1}{Y} + \frac{2K_0K_1}{D-x_L}\frac{I_0 - c_0}{Y} - 4K_0K_1E - I_0$$

$$0 = -c_1 + I_0 - c_0 - 4K_0K_1E - I_0$$

$$c_1 = -c_0 - 4K_0K_1E$$

For resistance $c_1 = c_0$:

$$2c_1 = -4K_0K_1E$$

$$c_1 = -2K_0K_1E$$

For $E = E_0$ and $K_1 = K_{11}\ x_{L1} > x_{L0} > 0 \xrightarrow{yields} Y_1 > Y_0 > 0, c_1 < 0$

Transition from $K_1 = K_{11}$ to $K_1 = K_{12} \xrightarrow{yields} v_1 = v_0$

$$v_1 = v_0 + K_{12}\left(\frac{V}{D-2x} - E_1\right) \xrightarrow{yields} v_1 = K_{12}\left(\frac{V}{D-2x} - \left(E_1 - \frac{v_0}{K_{12}}\right)\right)$$

C.3: VERIFICATION OF THE LEADER-PROGRESSION-MODEL

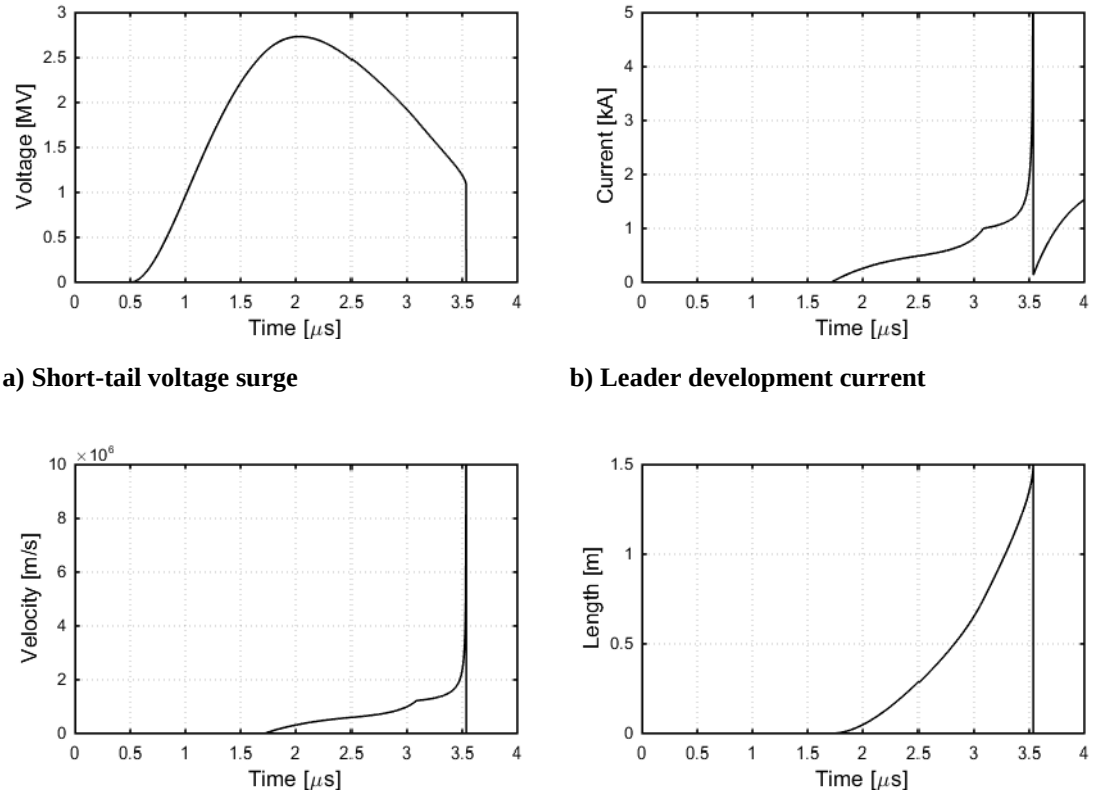

a) Short-tail voltage surge

b) Leader development current

c) Leader velocity

d) Leader length

Figure C-3: Simulation results of the insulator LPM implementation in PSCAD

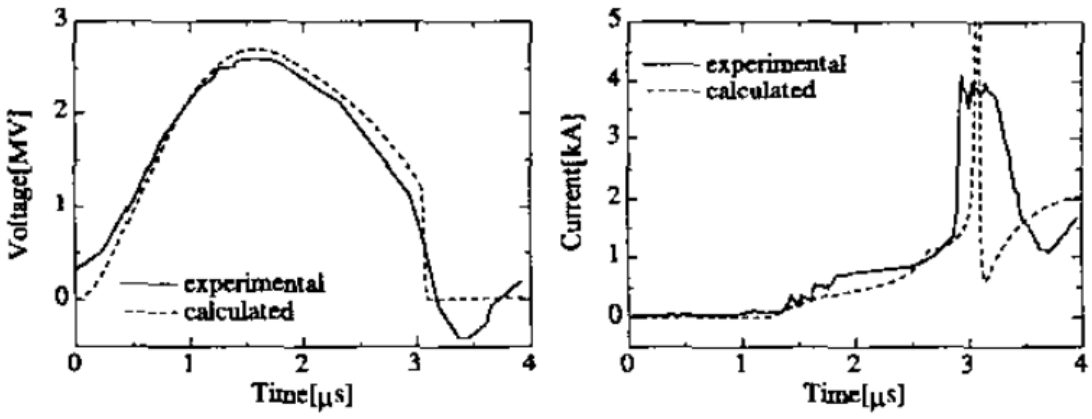

Figure C-4: Experimental and simulation results of the insulator of flashover from [163]

C.4: RESULTS OF FLASHOVER TESTS FOR POSITIVE POLARITY

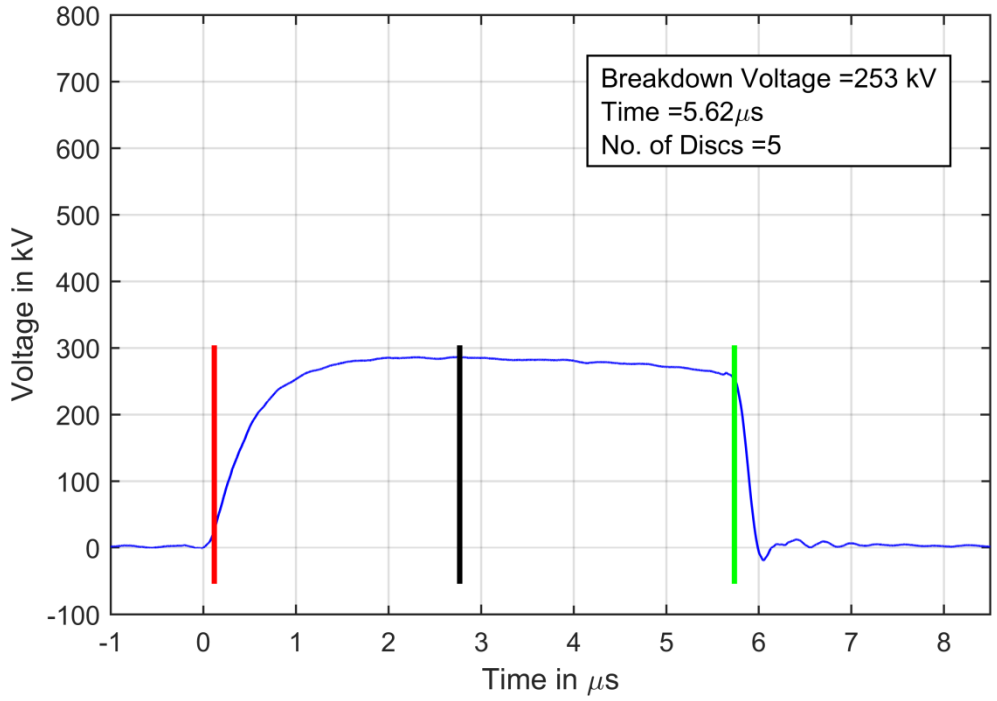

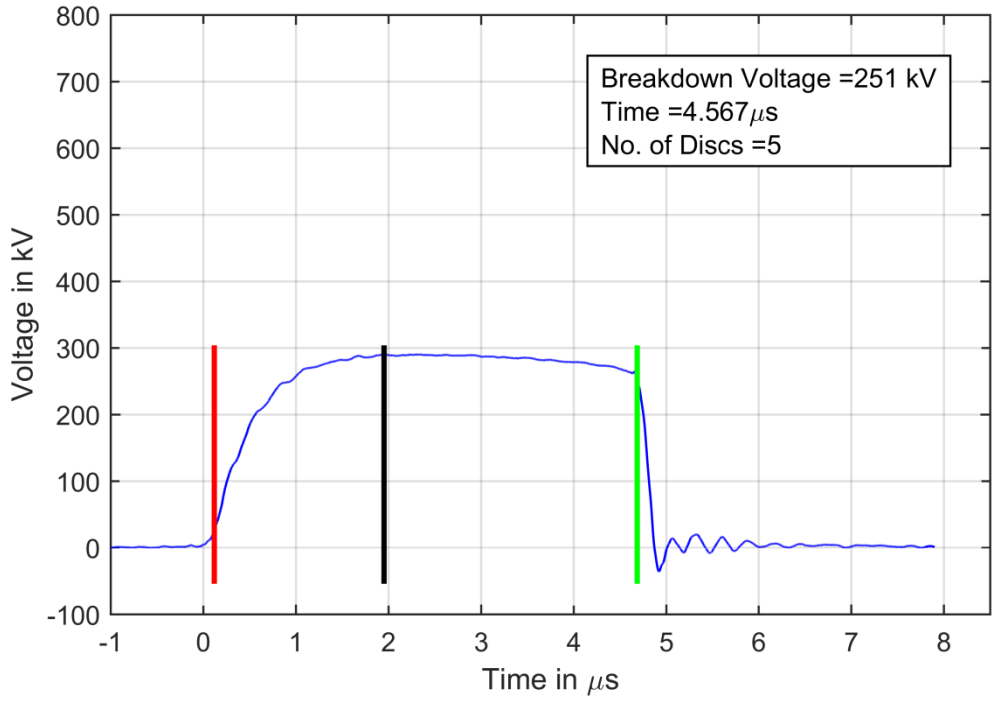

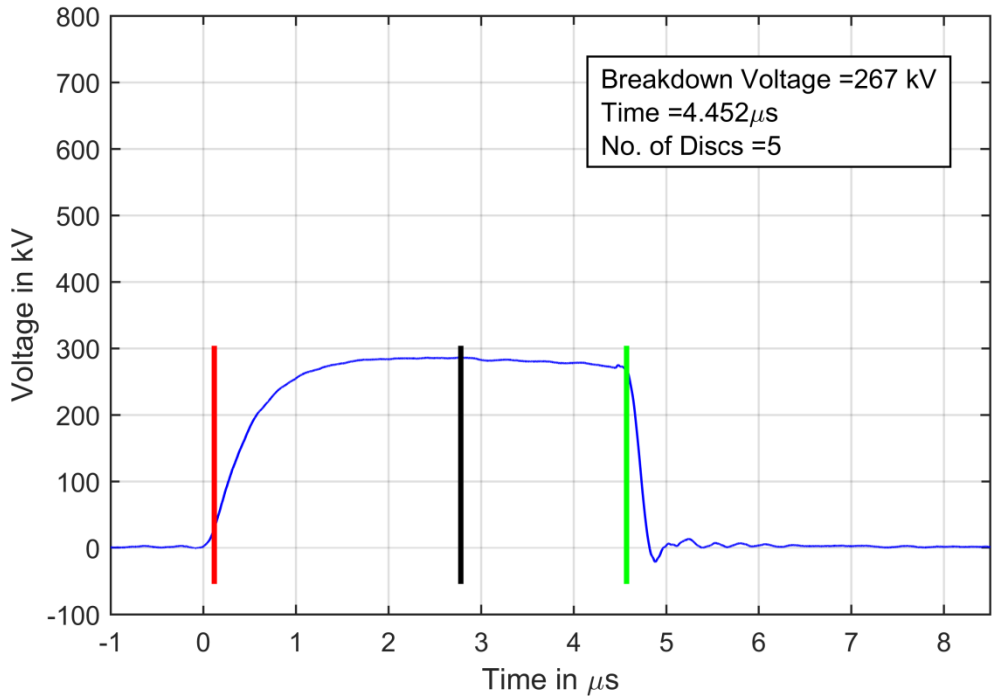
Breakdown Voltage =267 kV
Time =4.452μs
No. of Discs =5
Voltage in kV
Time in μs
800
700
600
500
400
300
200
100
0
-100
-1
0
1
2
3
4
5
6
7
8

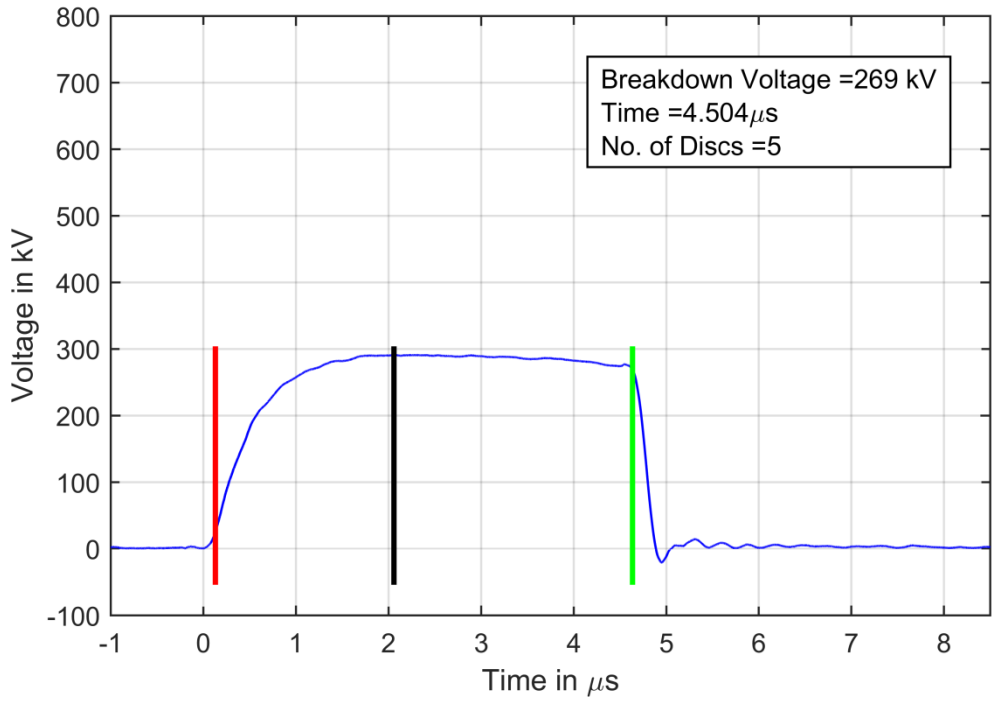
Breakdown Voltage =269 kV
Time =4.504μs
No. of Discs =5
Voltage in kV
Time in μs
800
700
600
500
400
300
200
100
0
-100
-1
0
1
2
3
4
5
6
7
8

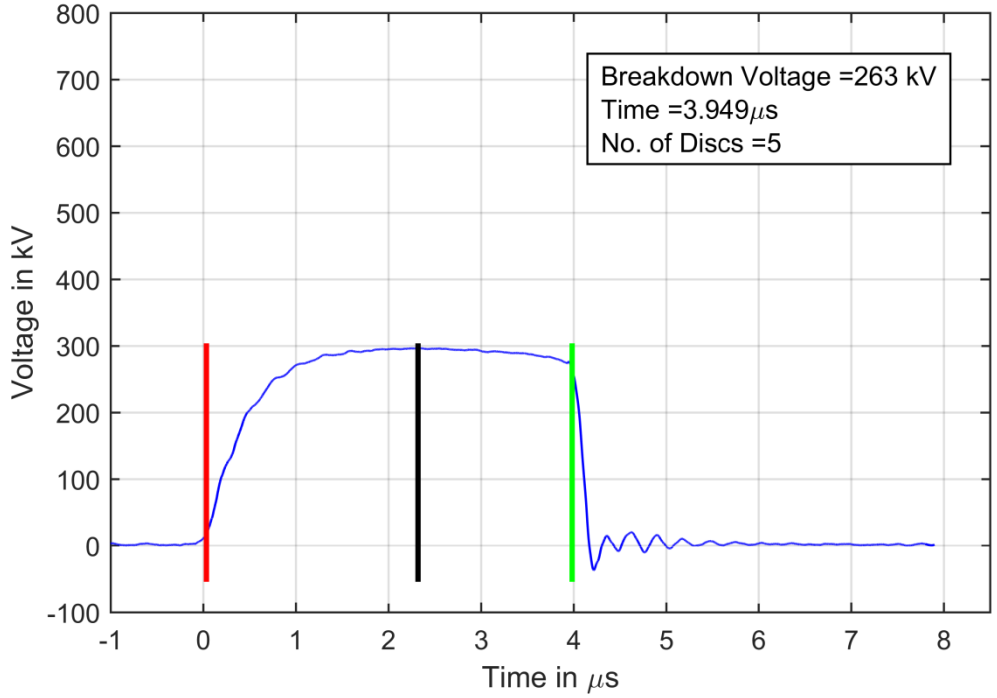
Breakdown Voltage =263 kV
Time =3.949μs
No. of Discs =5
Voltage in kV
Time in μs
800
700
600
500
400
300
200
100
0
-100
-1
0
1
2
3
4
5
6
7
8

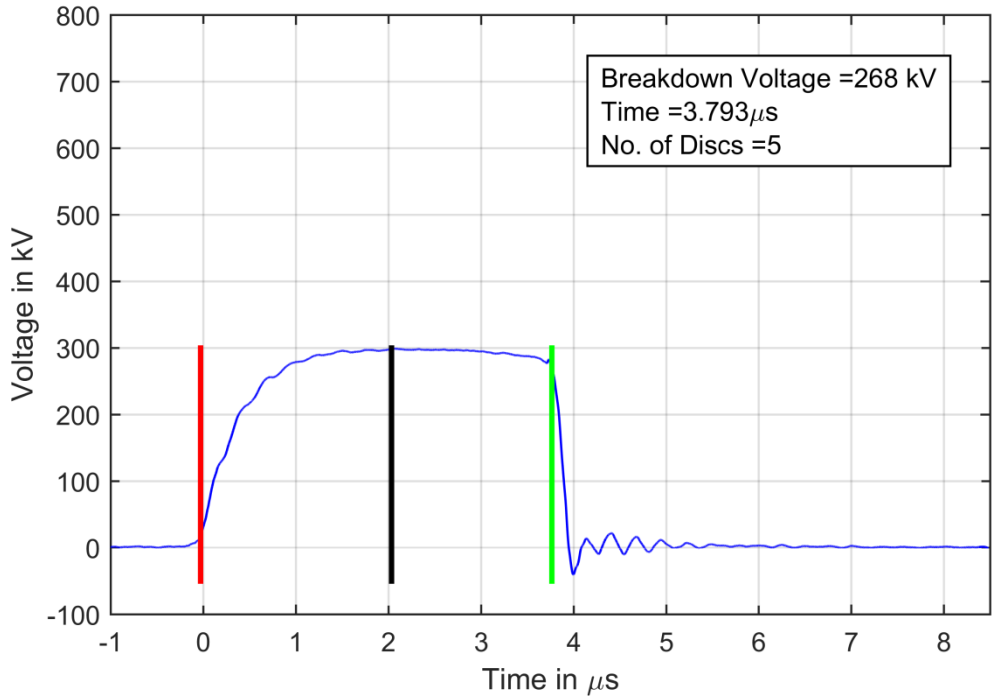
Breakdown Voltage =268 kV
Time =3.793μs
No. of Discs =5
Voltage in kV
Time in μs
800
700
600
500
400
300
200
100
0
-100
-1
0
1
2
3
4
5
6
7
8

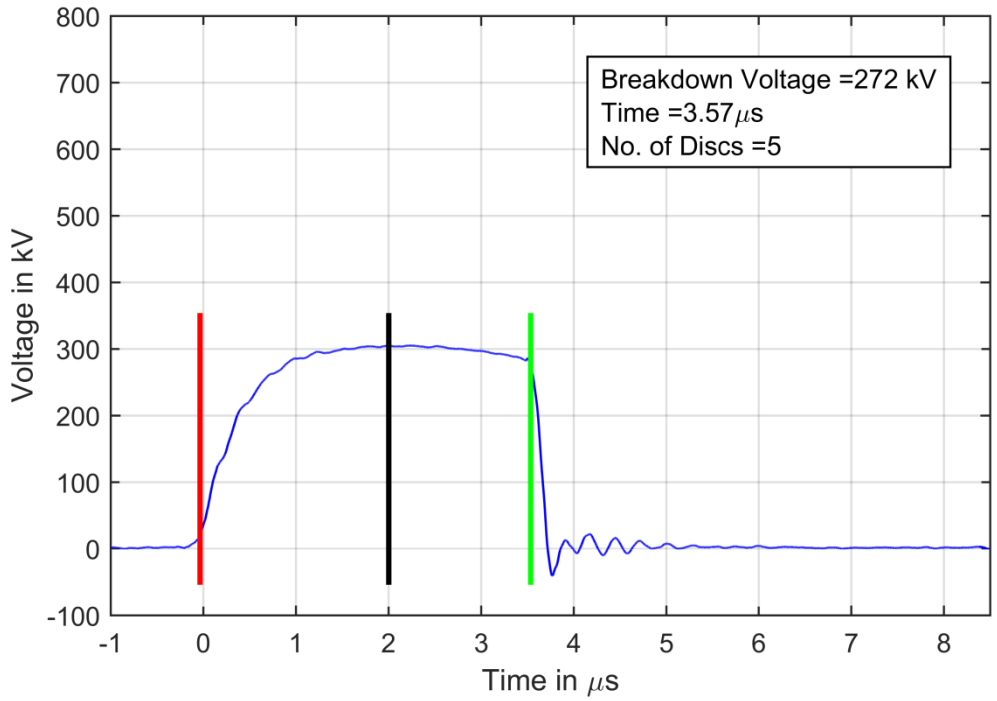
Breakdown Voltage =272 kV
Time =3.57μs
No. of Discs =5
Voltage in kV
Time in μs
800
700
600
500
400
300
200
100
0
-100
-1
0
1
2
3
4
5
6
7
8

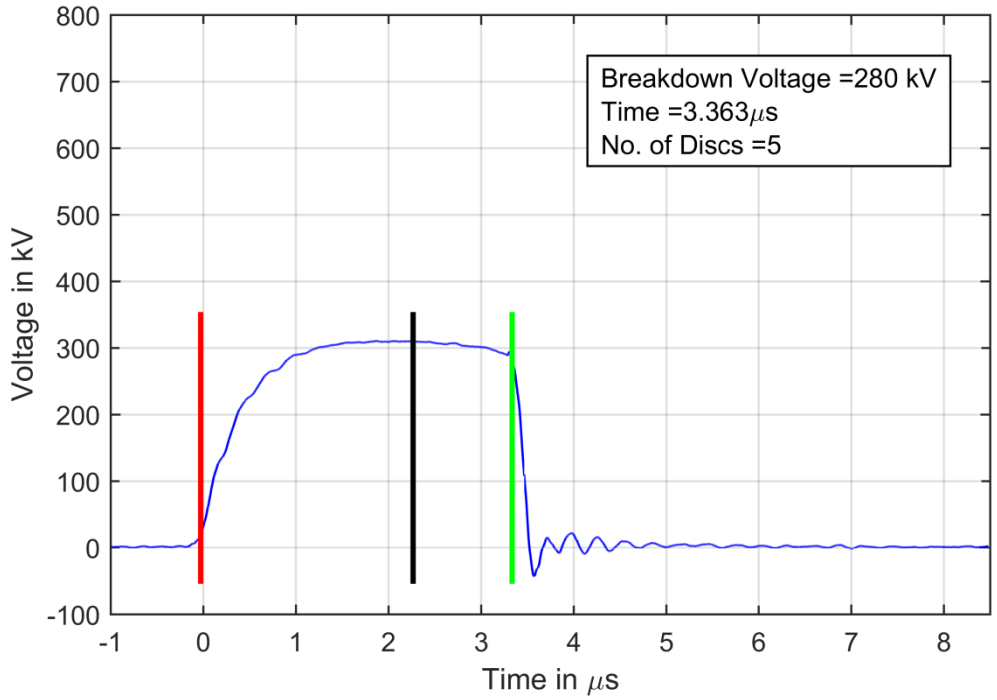
Breakdown Voltage =280 kV
Time =3.363μs
No. of Discs =5
Voltage in kV
Time in μs
800
700
600
500
400
300
200
100
0
-100
-1
0
1
2
3
4
5
6
7
8

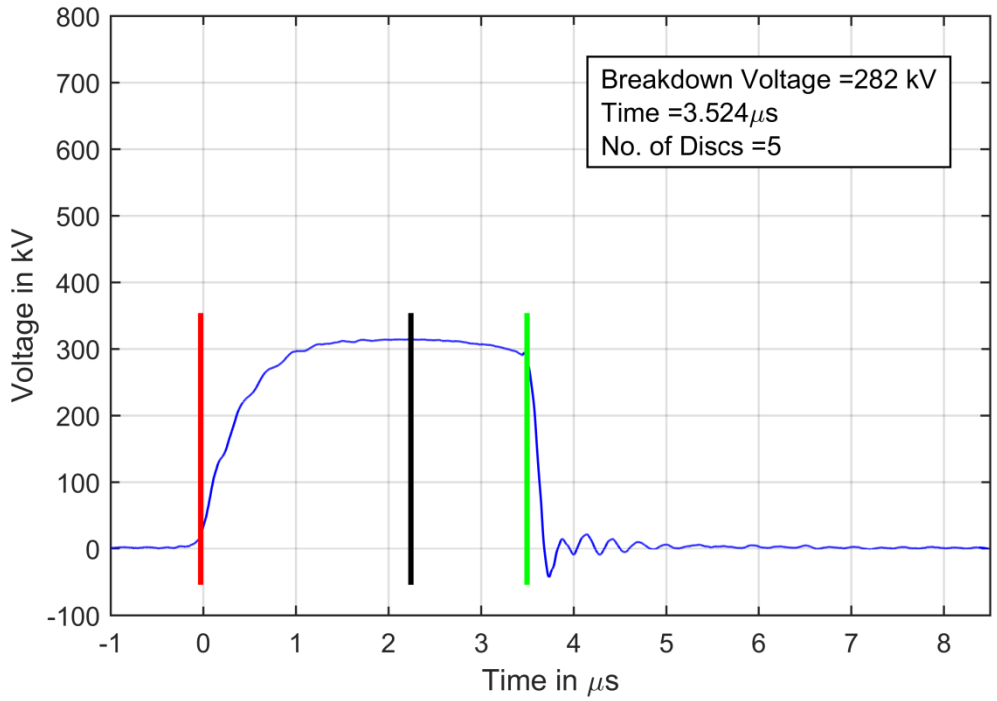
Breakdown Voltage =282 kV
Time =3.524μs
No. of Discs =5
Voltage in kV
Time in μs
800
700
600
500
400
300
200
100
0
-100
-1
0
1
2
3
4
5
6
7
8

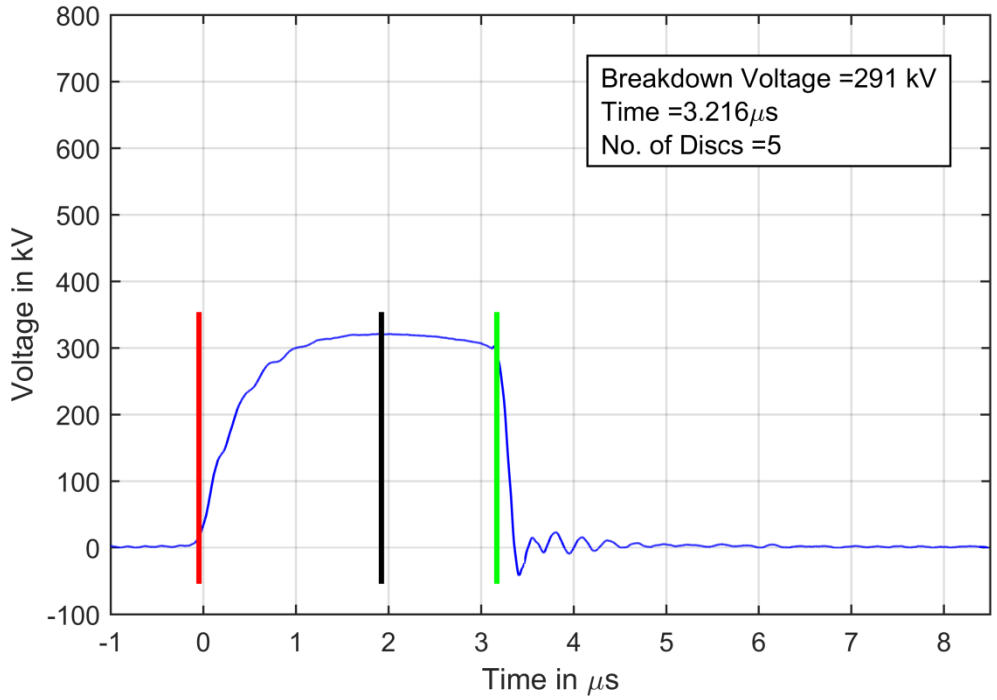
Breakdown Voltage =291 kV
Time =3.216μs
No. of Discs =5
Voltage in kV
Time in μs
800
700
600
500
400
300
200
100
0
-100
-1
0
1
2
3
4
5
6
7
8

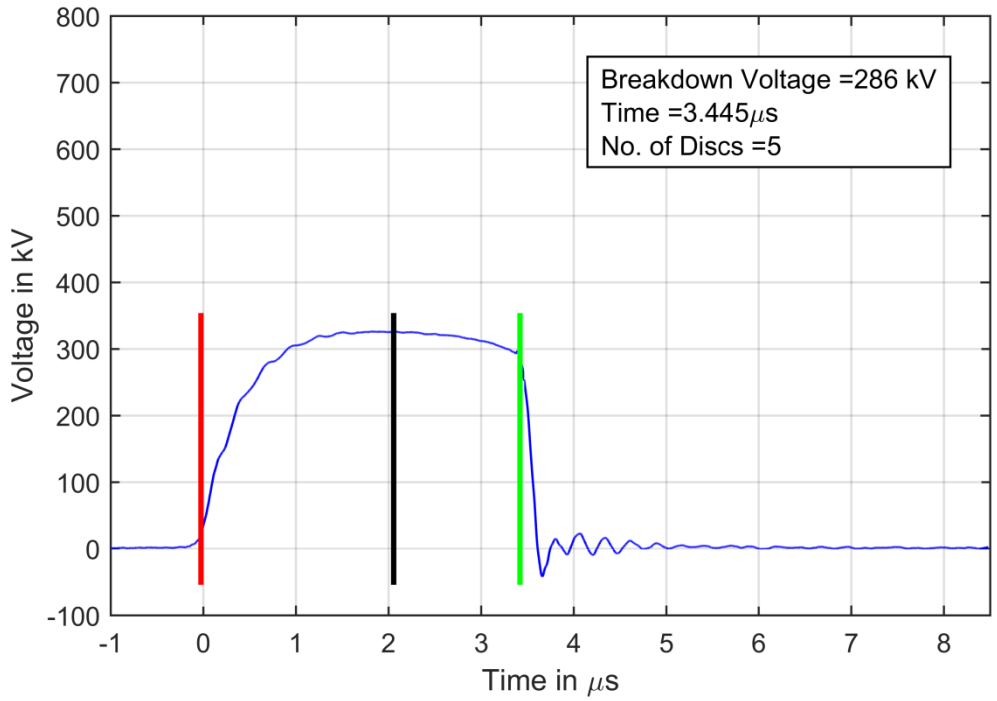
Breakdown Voltage =286 kV
Time =3.445μs
No. of Discs =5
Voltage in kV
Time in μs

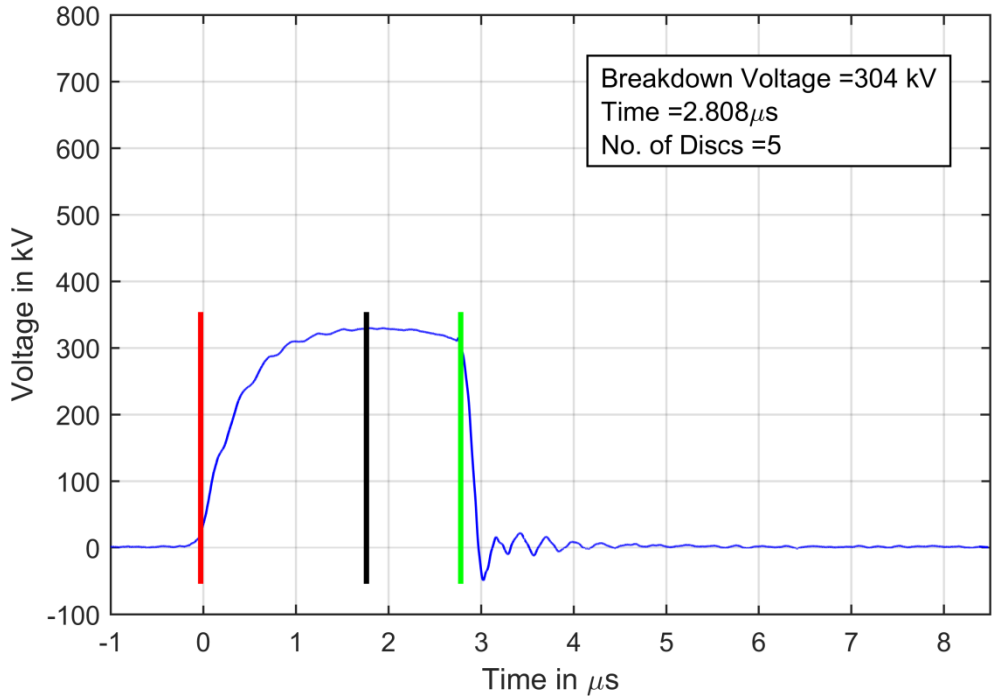
Breakdown Voltage =304 kV
Time =2.808μs
No. of Discs =5
Voltage in kV
Time in μs

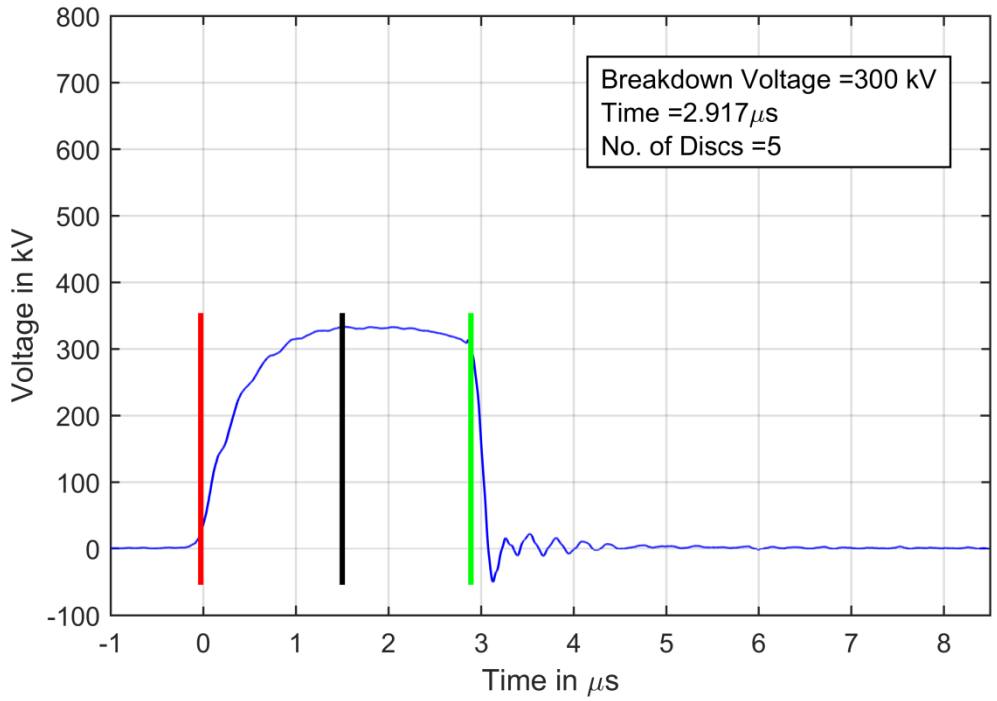
Breakdown Voltage =300 kV
Time =2.917μs
No. of Discs =5
Voltage in kV
Time in μs
800
700
600
500
400
300
200
100
0
-100
-1
0
1
2
3
4
5
6
7
8

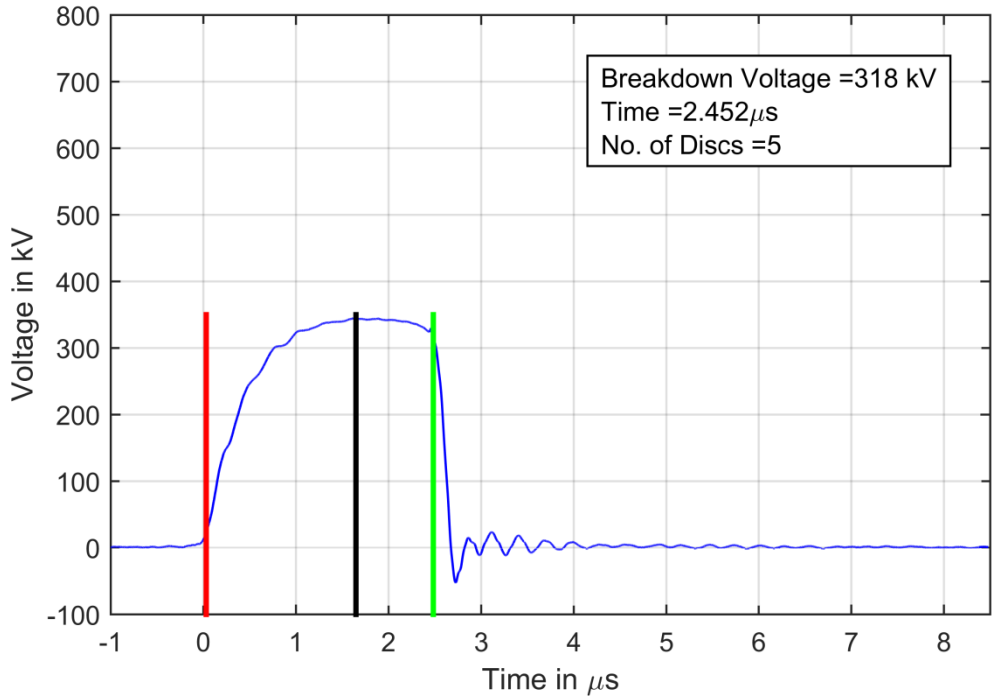
Breakdown Voltage =318 kV
Time =2.452μs
No. of Discs =5
Voltage in kV
Time in μs
800
700
600
500
400
300
200
100
0
-100
-1
0
1
2
3
4
5
6
7
8

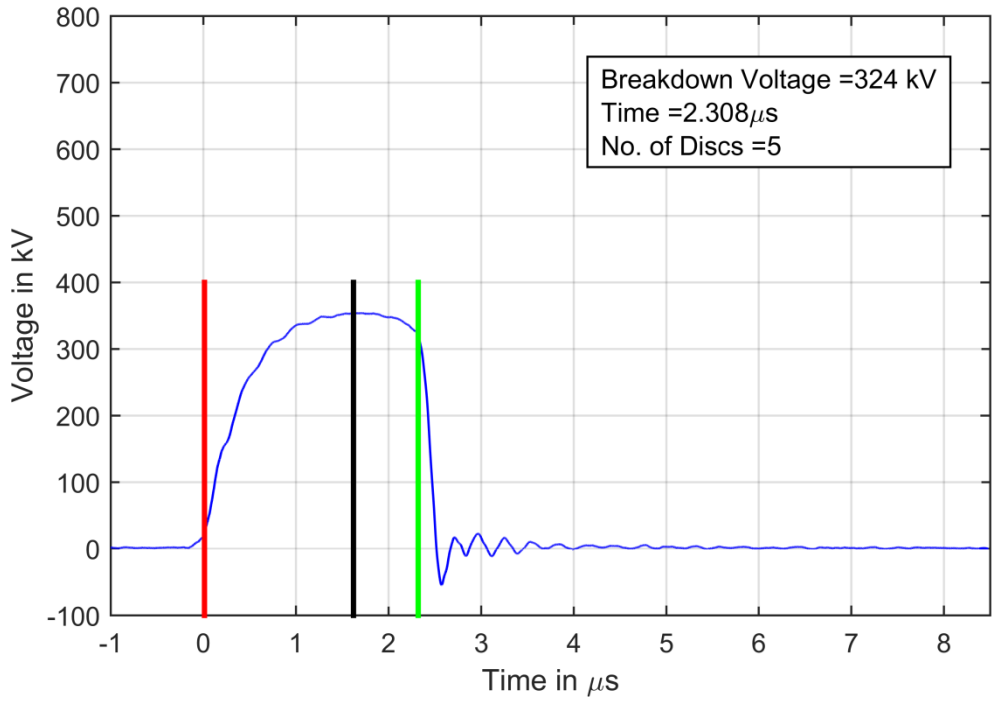
Breakdown Voltage =324 kV
Time =2.308μs
No. of Discs =5
Voltage in kV
Time in μs
800
700
600
500
400
300
200
100
0
-100
-1
0
1
2
3
4
5
6
7
8

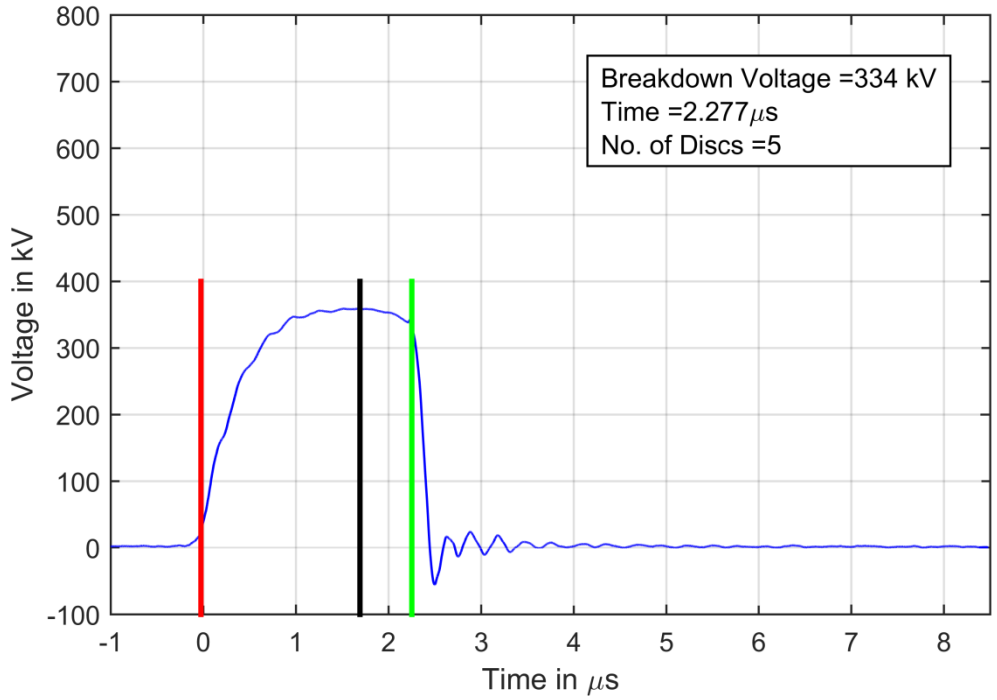
Breakdown Voltage =334 kV
Time =2.277μs
No. of Discs =5
Voltage in kV
Time in μs
800
700
600
500
400
300
200
100
0
-100
-1
0
1
2
3
4
5
6
7
8

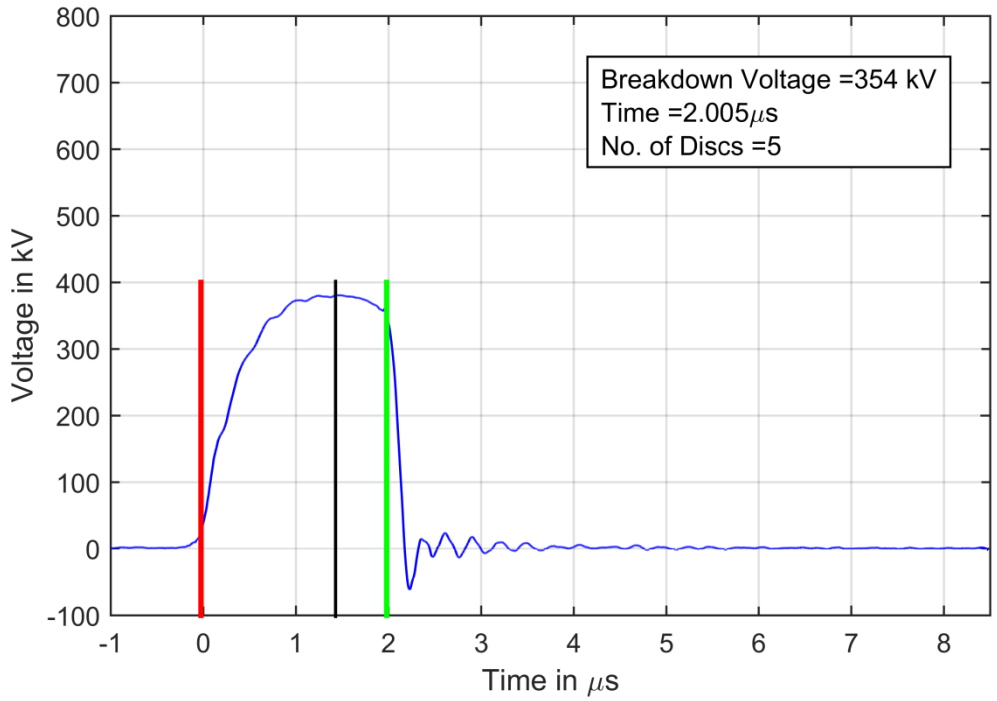
Breakdown Voltage =354 kV
Time =2.005μs
No. of Discs =5
Voltage in kV
Time in μs
800
700
600
500
400
300
200
100
0
-100
-1
0
1
2
3
4
5
6
7
8

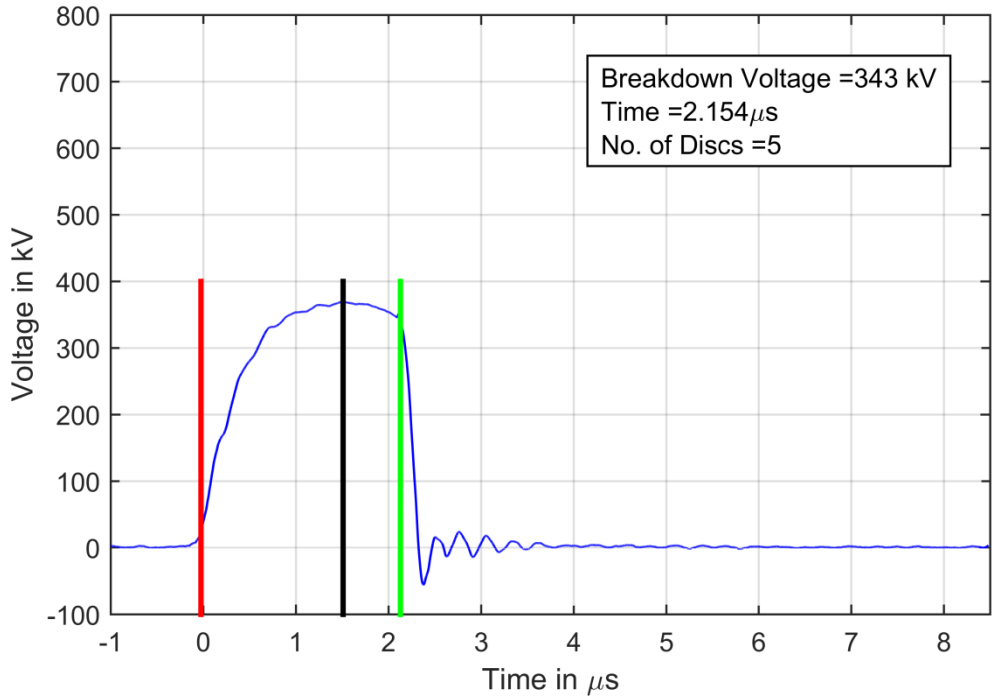
Breakdown Voltage =343 kV
Time =2.154μs
No. of Discs =5
Voltage in kV
Time in μs
800
700
600
500
400
300
200
100
0
-100
-1
0
1
2
3
4
5
6
7
8

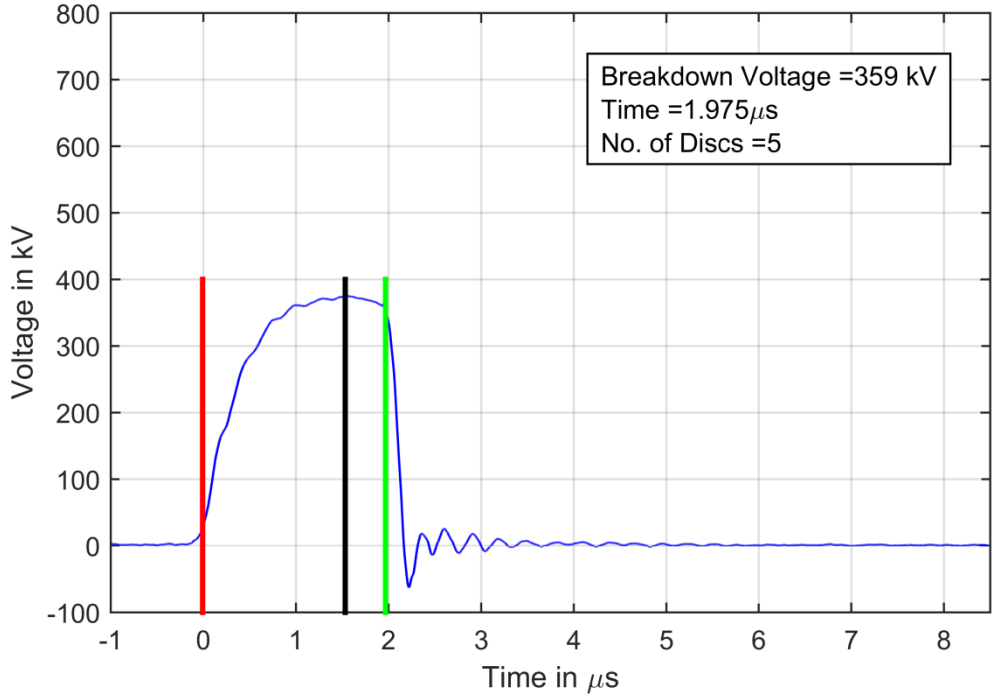
Breakdown Voltage =359 kV
Time =1.975μs
No. of Discs =5
Voltage in kV
Time in μs
800
700
600
500
400
300
200
100
0
-100
-1
0
1
2
3
4
5
6
7
8

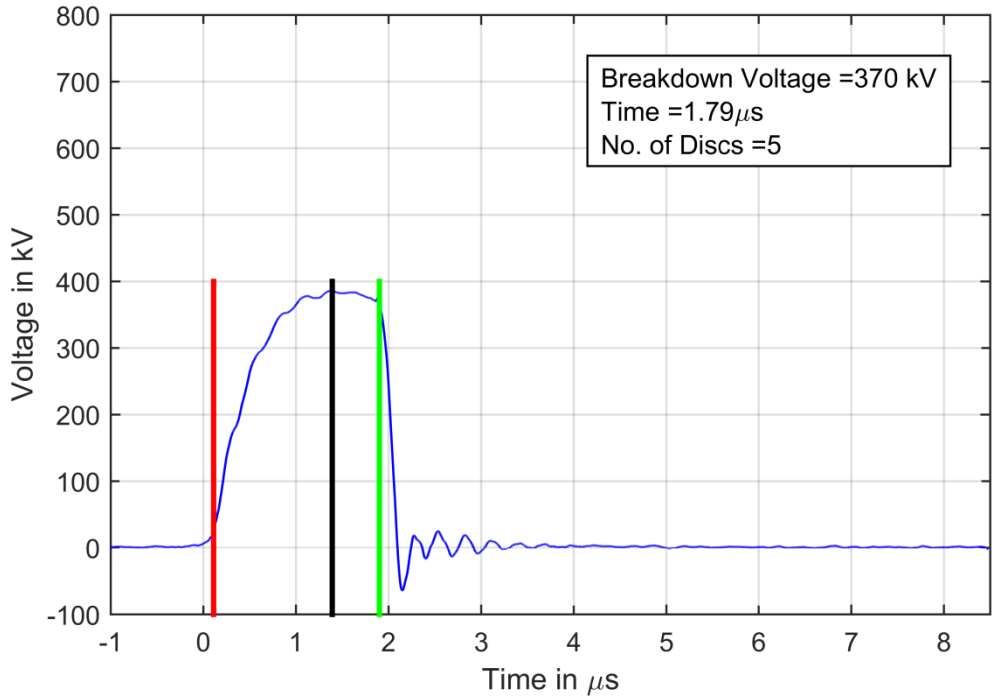
Breakdown Voltage =370 kV
Time =1.79μs
No. of Discs =5
Voltage in kV
Time in μs
800
700
600
500
400
300
200
100
0
-100
-1
0
1
2
3
4
5
6
7
8

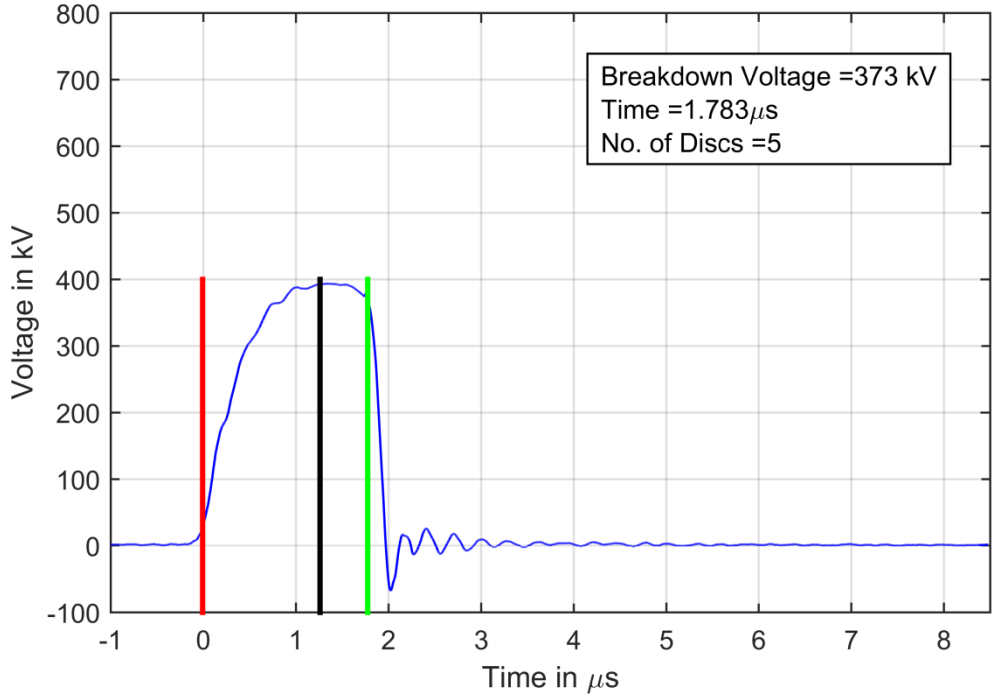
Breakdown Voltage =373 kV
Time =1.783μs
No. of Discs =5
Voltage in kV
Time in μs
800
700
600
500
400
300
200
100
0
-100
-1
0
1
2
3
4
5
6
7
8

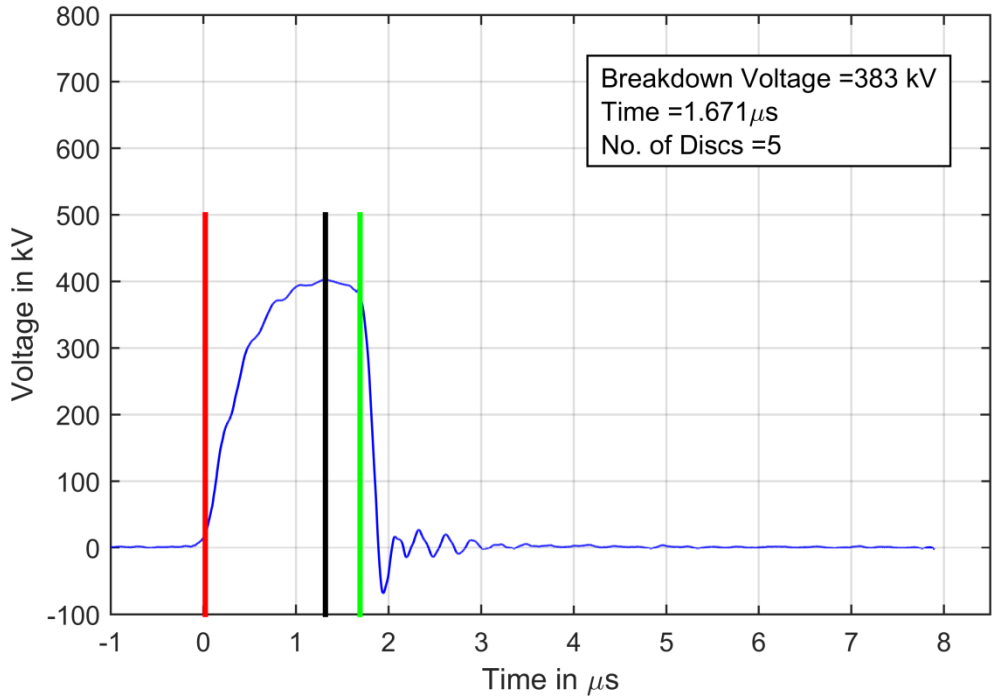
Breakdown Voltage =383 kV
Time =1.671μs
No. of Discs =5
Voltage in kV
Time in μs
800
700
600
500
400
300
200
100
0
-100
-1
0
1
2
3
4
5
6
7
8

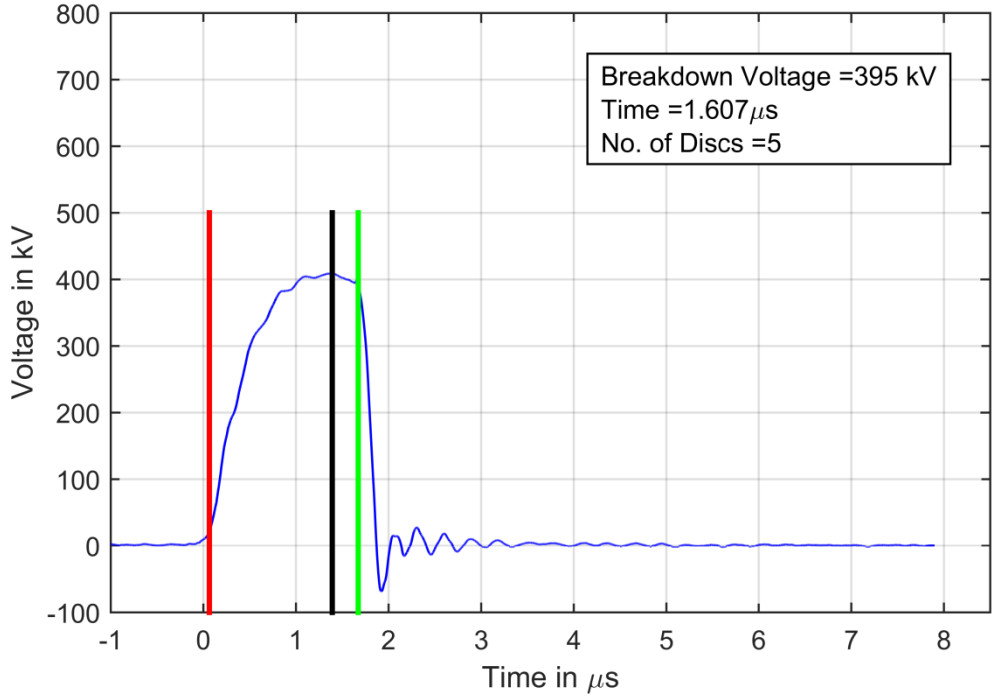
Breakdown Voltage =395 kV
Time =1.607μs
No. of Discs =5
Voltage in kV
Time in μs
800
700
600
500
400
300
200
100
0
-100
-1
0
1
2
3
4
5
6
7
8

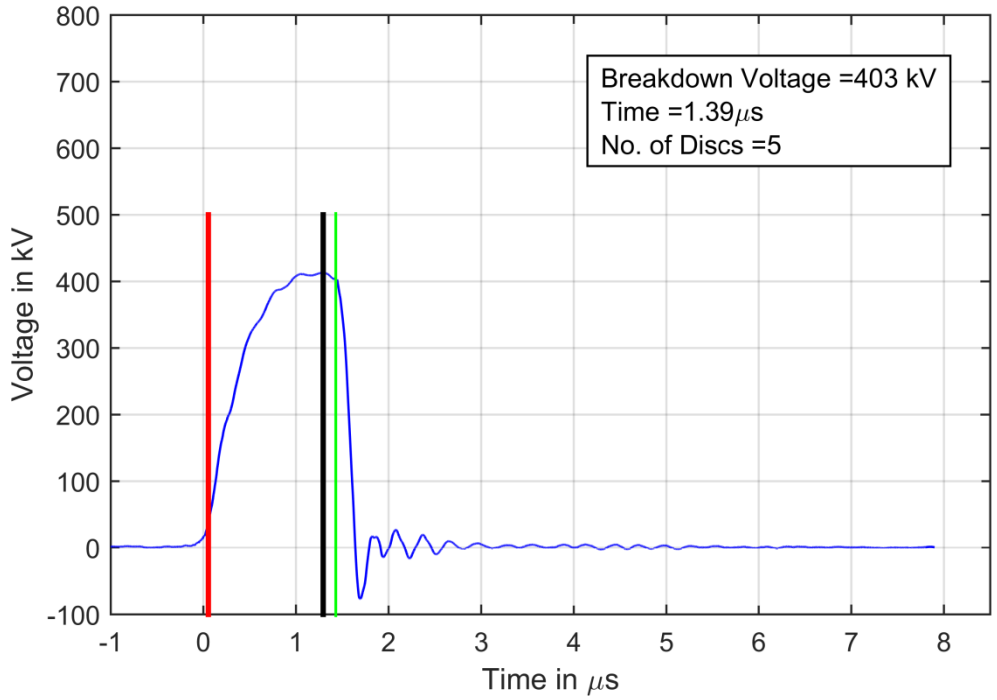
Breakdown Voltage =403 kV
Time =1.39μs
No. of Discs =5
Voltage in kV
Time in μs
800
700
600
500
400
300
200
100
0
-100
-1
0
1
2
3
4
5
6
7
8

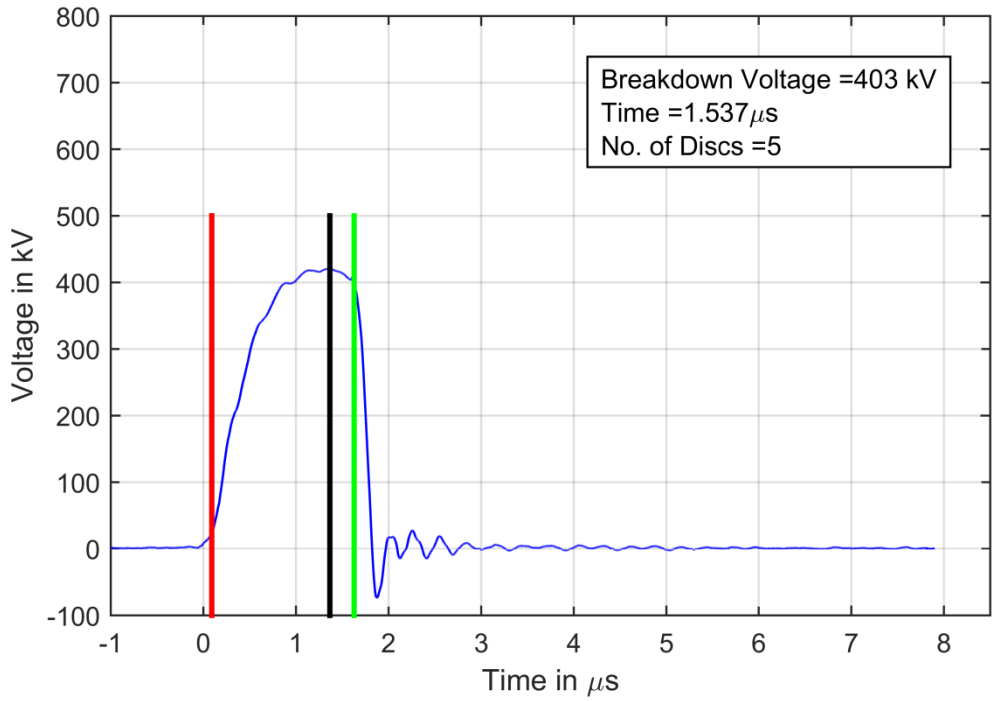
Breakdown Voltage =403 kV
Time =1.537μs
No. of Discs =5
Voltage in kV
Time in μs

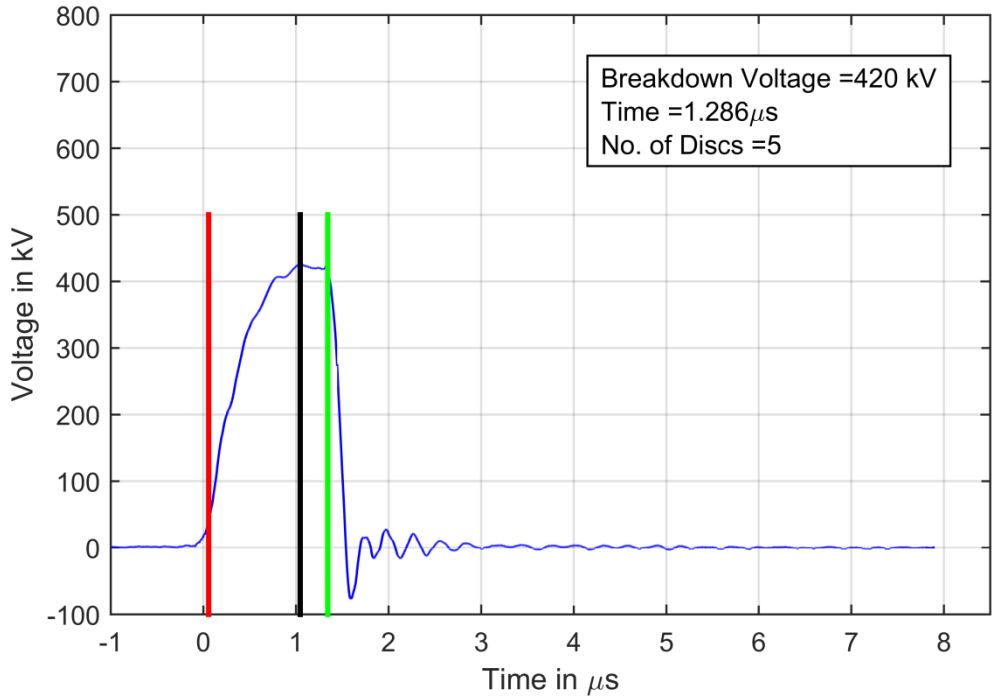
Breakdown Voltage =420 kV
Time =1.286μs
No. of Discs =5
Voltage in kV
Time in μs

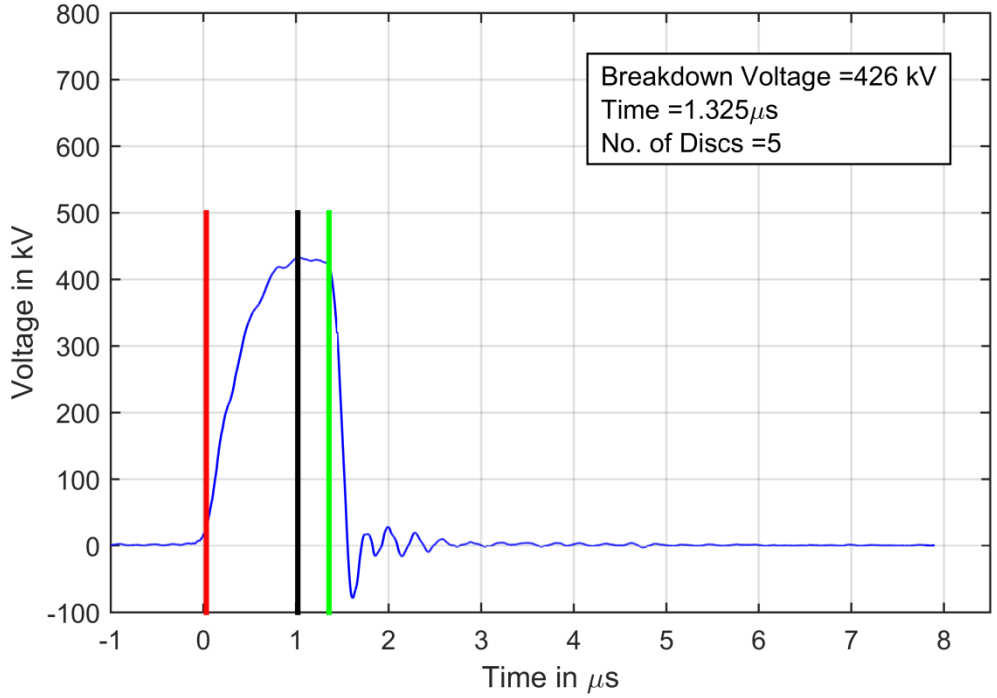
Breakdown Voltage =426 kV
Time =1.325μs
No. of Discs =5
Voltage in kV
Time in μs
800
700
600
500
400
300
200
100
0
-100
-1
0
1
2
3
4
5
6
7
8

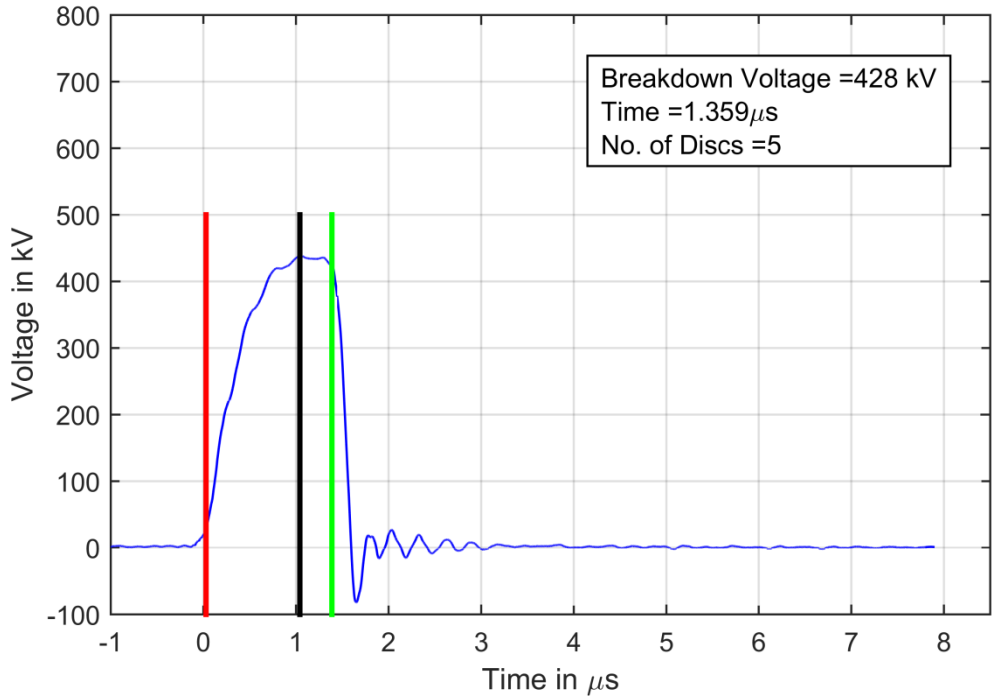
Breakdown Voltage =428 kV
Time =1.359μs
No. of Discs =5
Voltage in kV
Time in μs
800
700
600
500
400
300
200
100
0
-100
-1
0
1
2
3
4
5
6
7
8

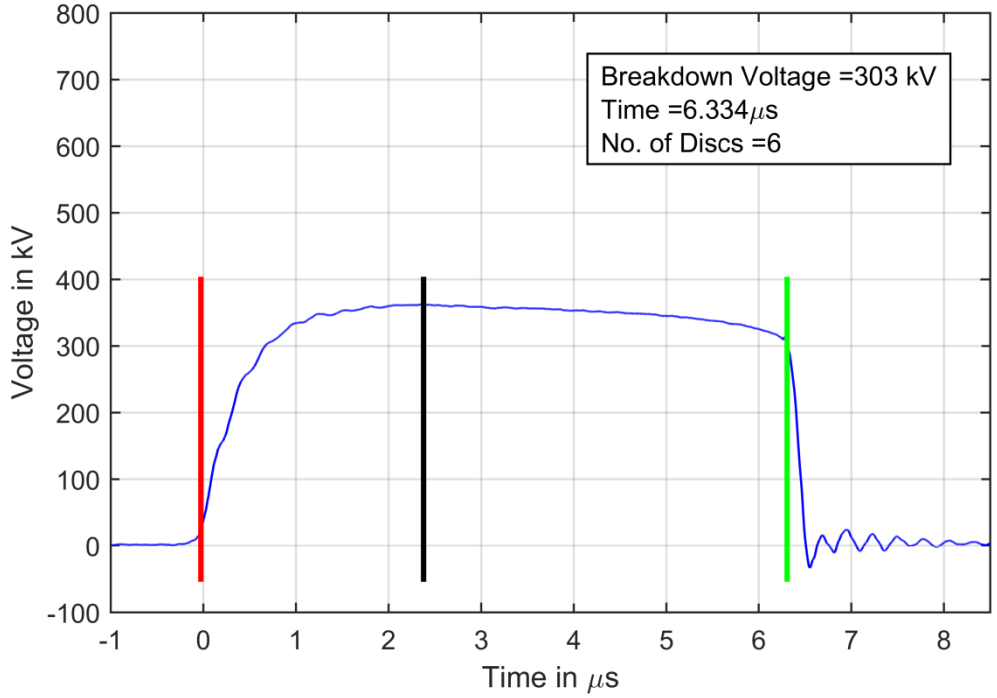
Breakdown Voltage =303 kV
Time =6.334μs
No. of Discs =6
Voltage in kV
Time in μs
800
700
600
500
400
300
200
100
0
-100
-1
0
1
2
3
4
5
6
7
8

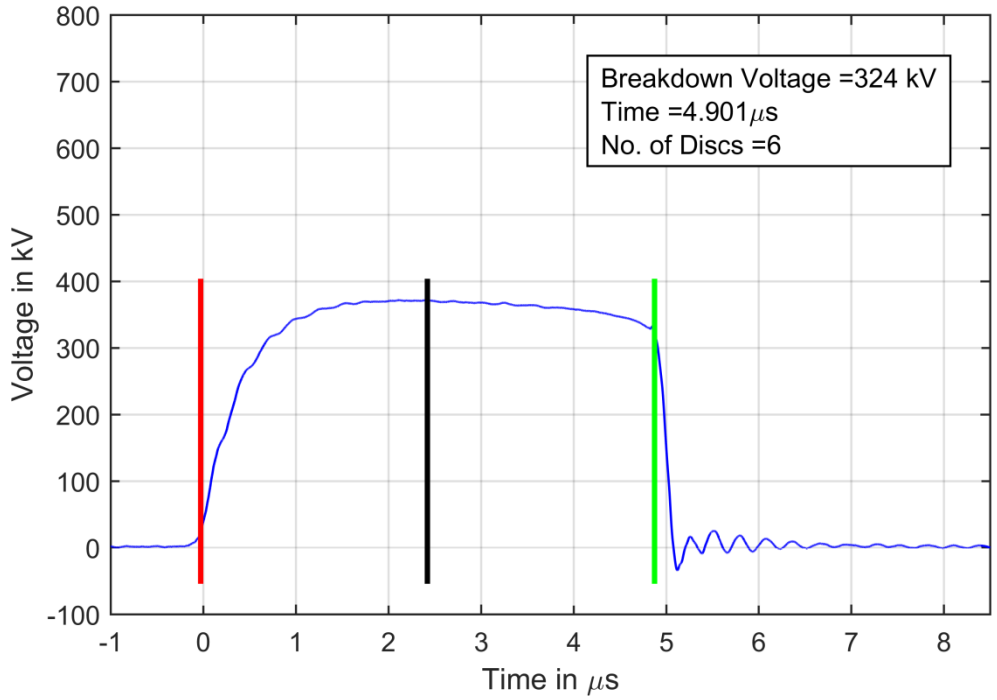
Breakdown Voltage =324 kV
Time =4.901μs
No. of Discs =6
Voltage in kV
Time in μs
800
700
600
500
400
300
200
100
0
-100
-1
0
1
2
3
4
5
6
7
8

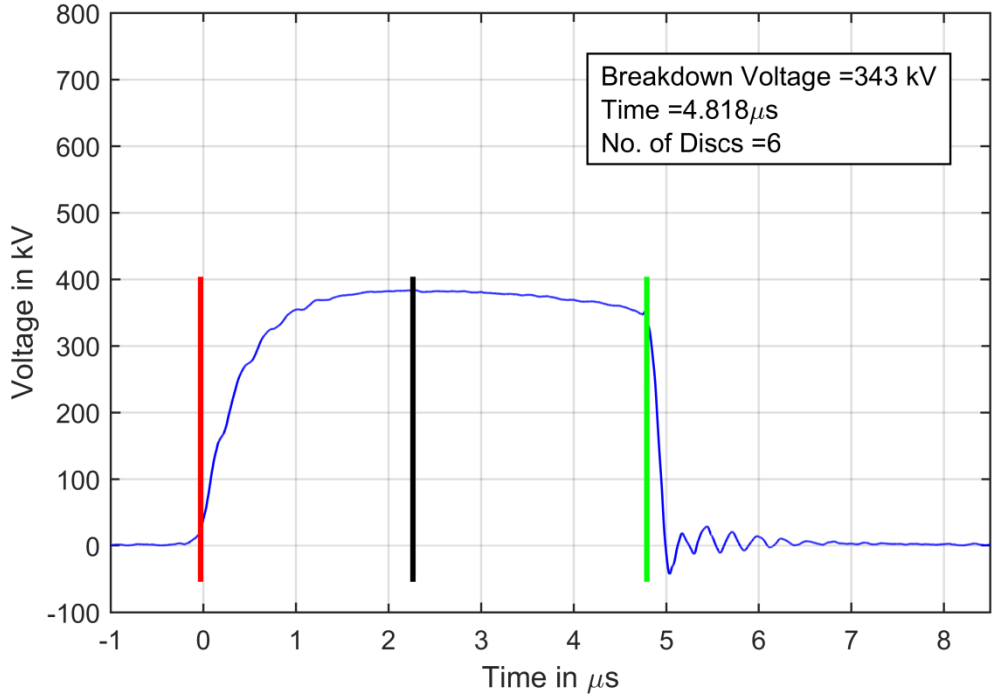
Breakdown Voltage =343 kV
Time =4.818μs
No. of Discs =6
Voltage in kV
Time in μs
800
700
600
500
400
300
200
100
0
-100
-1
0
1
2
3
4
5
6
7
8

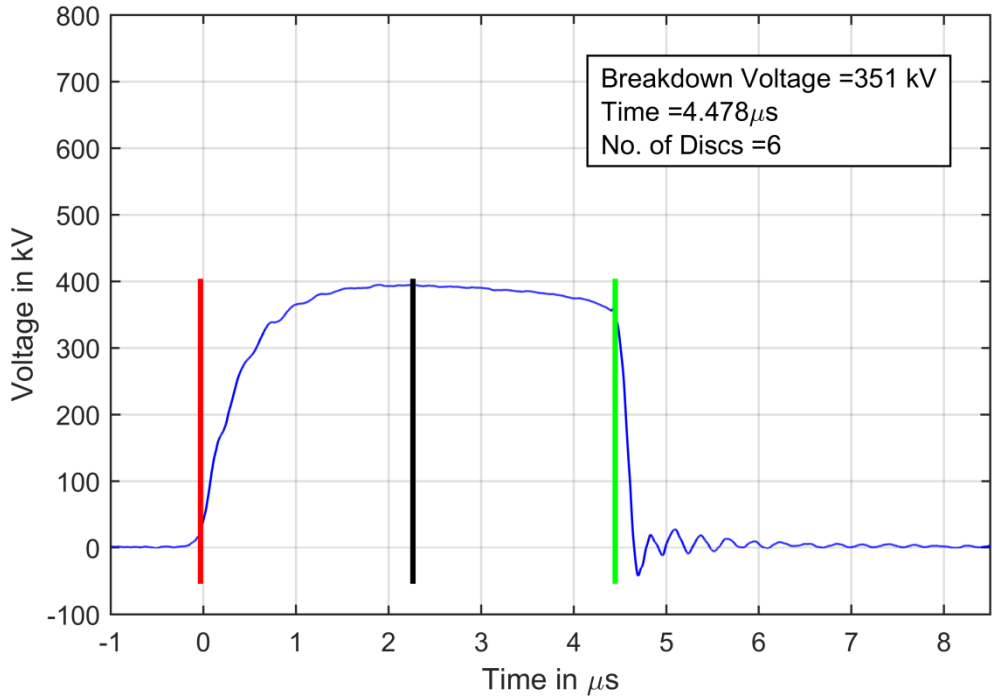
Breakdown Voltage =351 kV
Time =4.478μs
No. of Discs =6
Voltage in kV
Time in μs
800
700
600
500
400
300
200
100
0
-100
-1
0
1
2
3
4
5
6
7
8

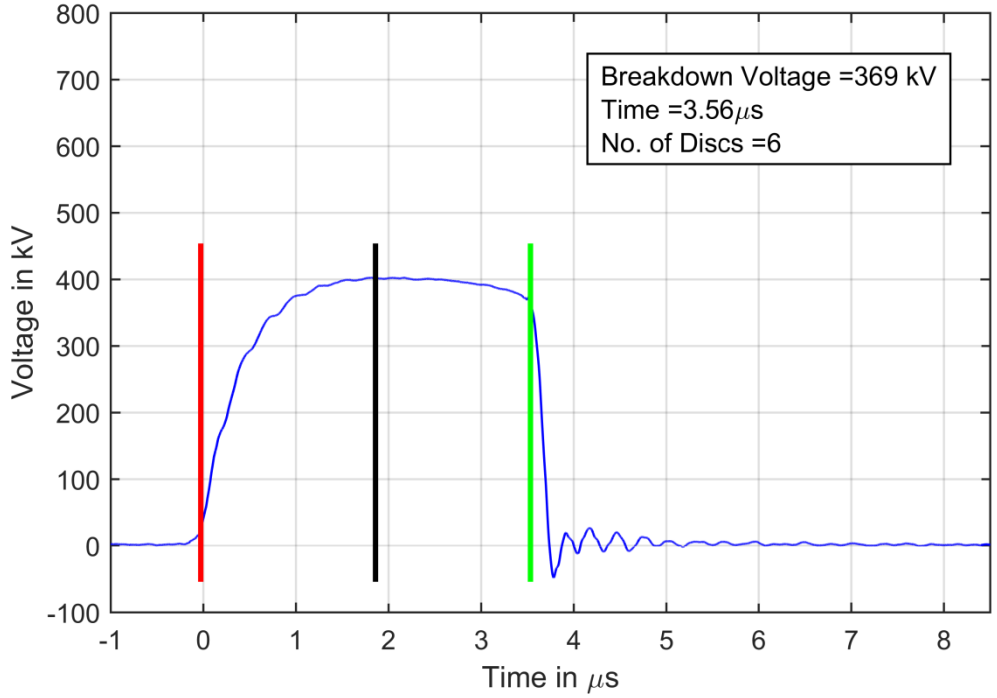
Breakdown Voltage =369 kV
Time =3.56μs
No. of Discs =6
Voltage in kV
Time in μs
800
700
600
500
400
300
200
100
0
-100
-1
0
1
2
3
4
5
6
7
8

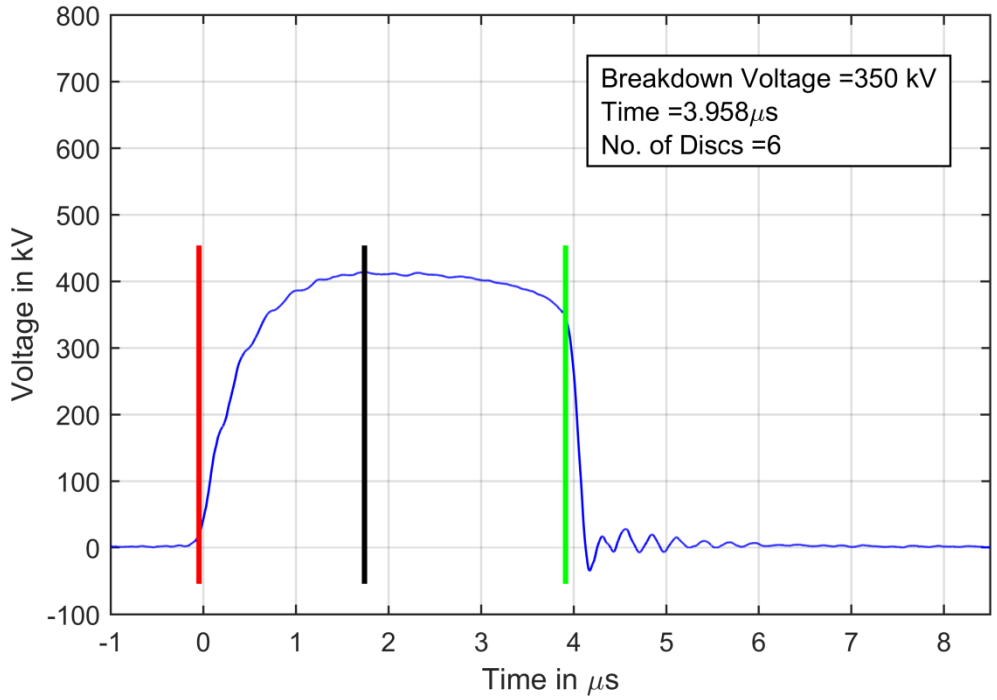
Breakdown Voltage =350 kV
Time =3.958μs
No. of Discs =6
Voltage in kV
Time in μs
800
700
600
500
400
300
200
100
0
-100
-1
0
1
2
3
4
5
6
7
8

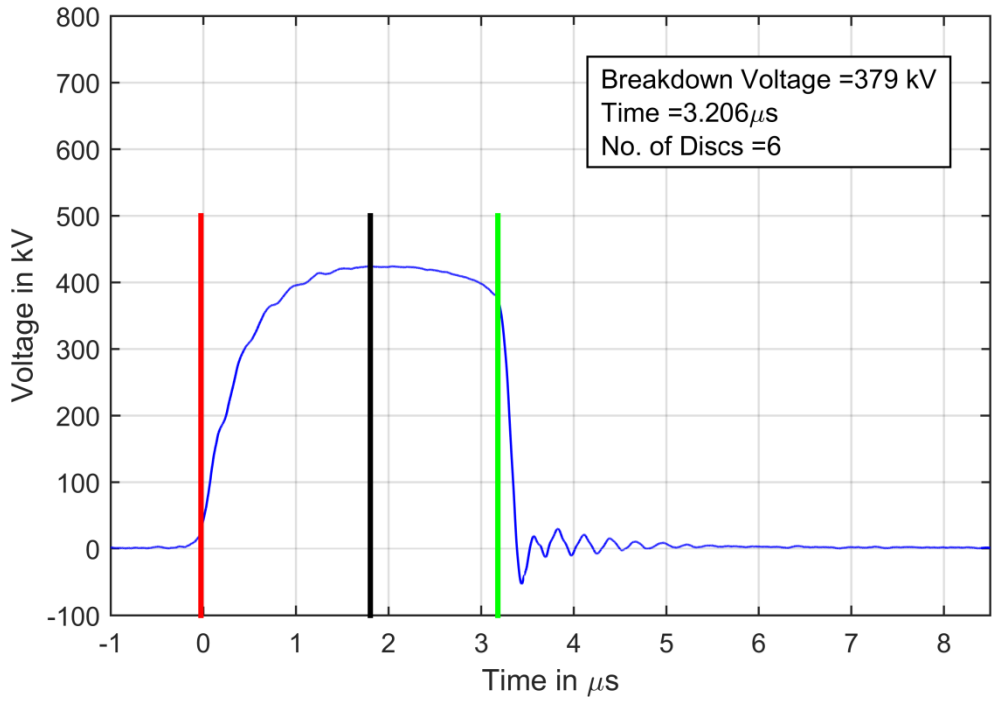
Breakdown Voltage =379 kV
Time =3.206μs
No. of Discs =6
Voltage in kV
Time in μs
800
700
600
500
400
300
200
100
0
-100
-1
0
1
2
3
4
5
6
7
8

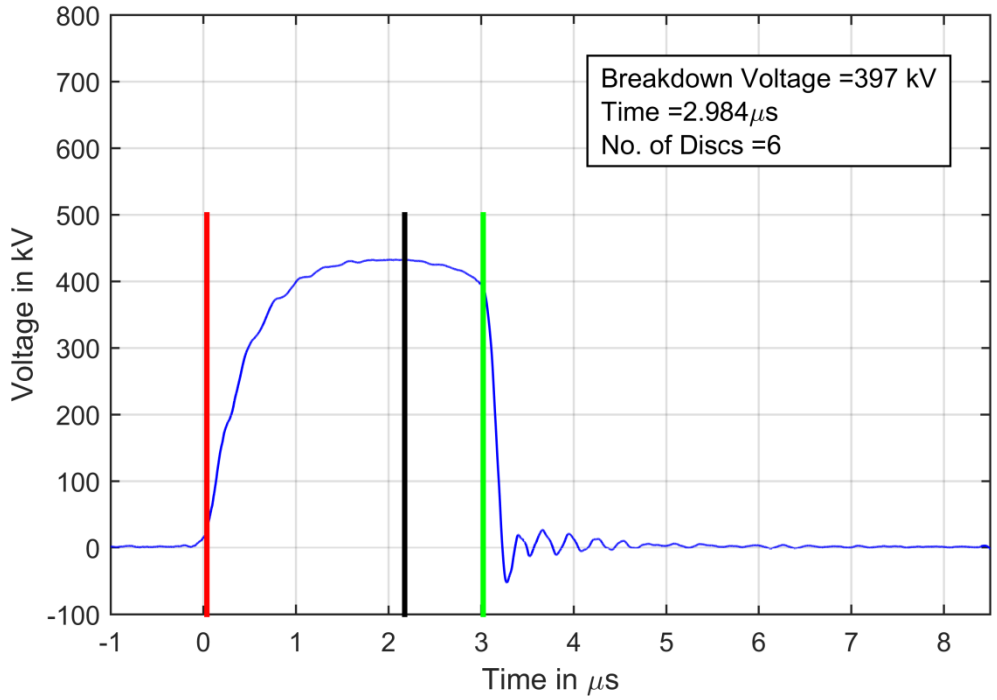
Breakdown Voltage =397 kV
Time =2.984μs
No. of Discs =6
Voltage in kV
Time in μs
800
700
600
500
400
300
200
100
0
-100
-1
0
1
2
3
4
5
6
7
8

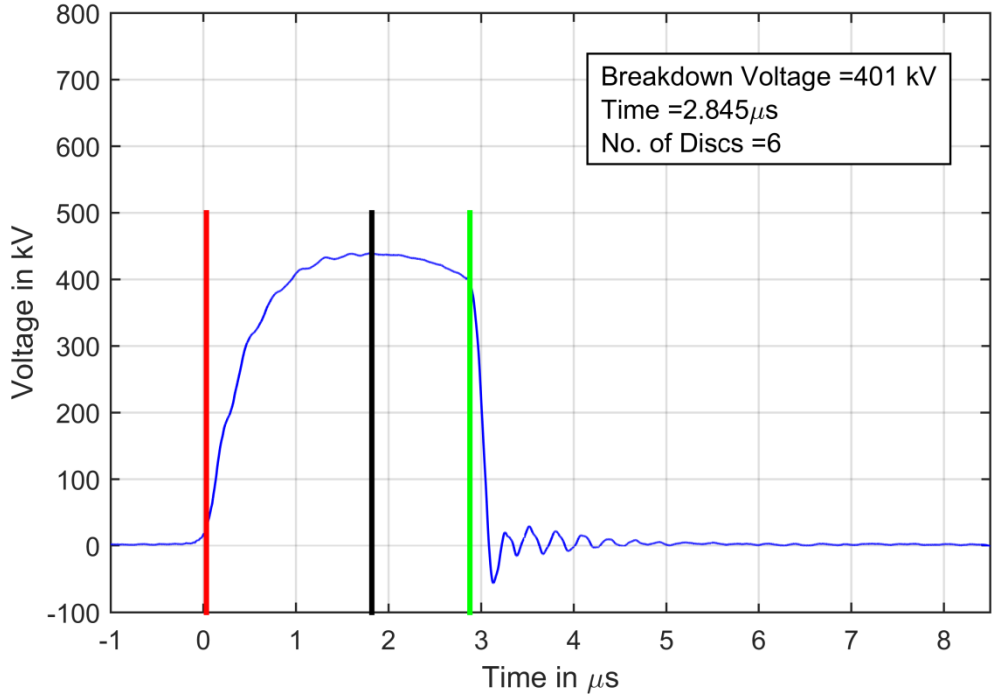
Breakdown Voltage =401 kV
Time =2.845μs
No. of Discs =6
Voltage in kV
Time in μs
800
700
600
500
400
300
200
100
0
-100
-1
0
1
2
3
4
5
6
7
8

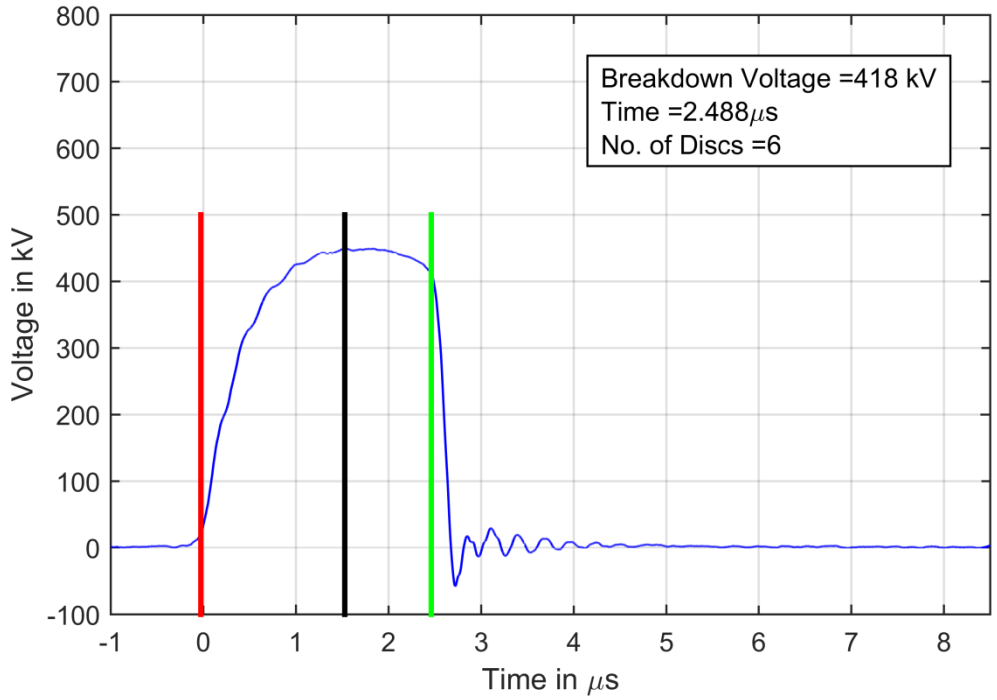
Breakdown Voltage =418 kV
Time =2.488μs
No. of Discs =6
Voltage in kV
Time in μs
800
700
600
500
400
300
200
100
0
-100
-1
0
1
2
3
4
5
6
7
8

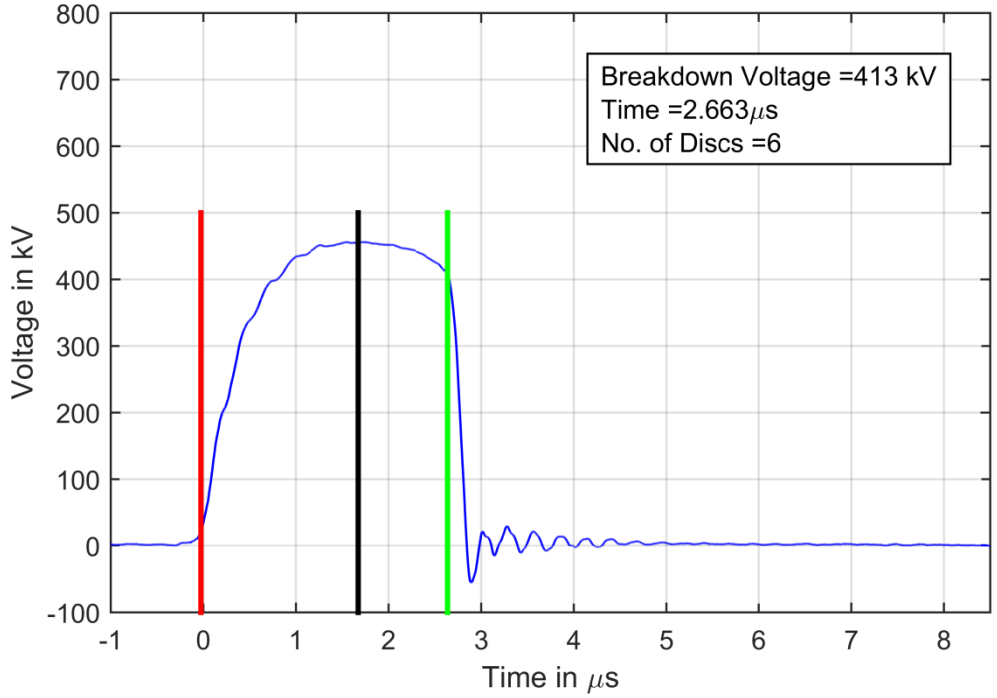
Breakdown Voltage =413 kV
Time =2.663μs
No. of Discs =6
Voltage in kV
Time in μs
800
700
600
500
400
300
200
100
0
-100
-1
0
1
2
3
4
5
6
7
8

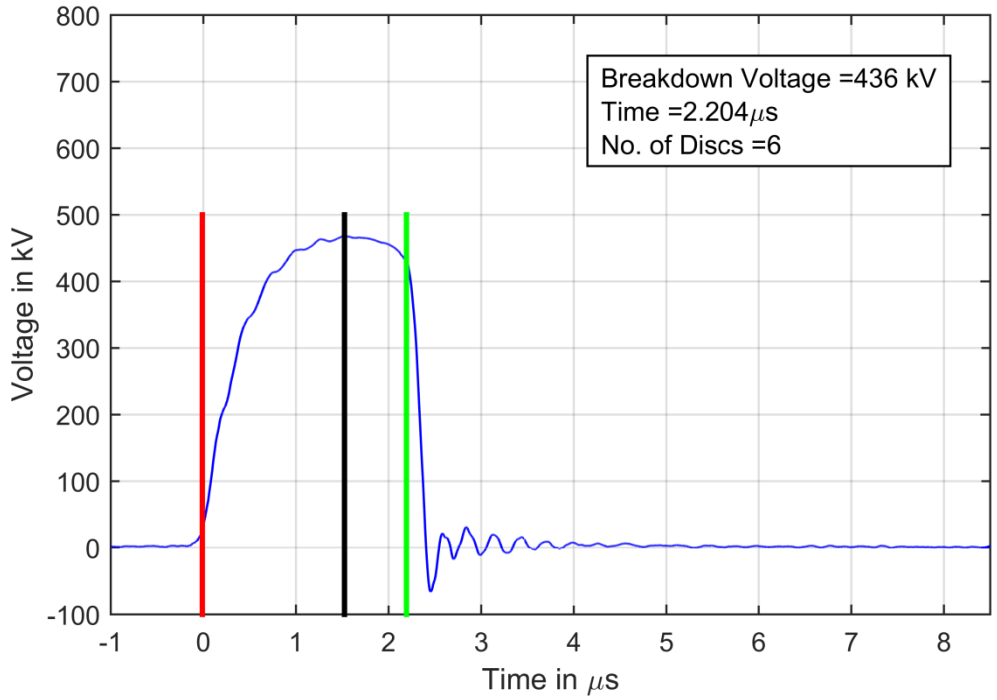
Breakdown Voltage =436 kV
Time =2.204μs
No. of Discs =6
Voltage in kV
Time in μs
800
700
600
500
400
300
200
100
0
-100
-1
0
1
2
3
4
5
6
7
8

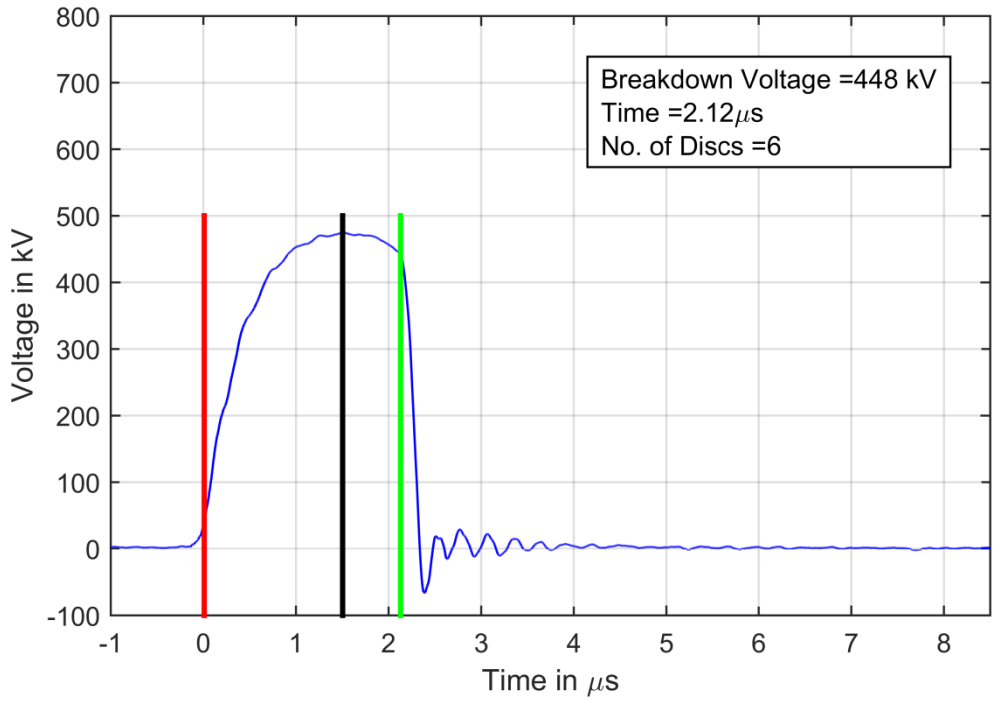
Breakdown Voltage =448 kV
Time =2.12μs
No. of Discs =6
Voltage in kV
Time in μs
800
700
600
500
400
300
200
100
0
-100
-1
0
1
2
3
4
5
6
7
8

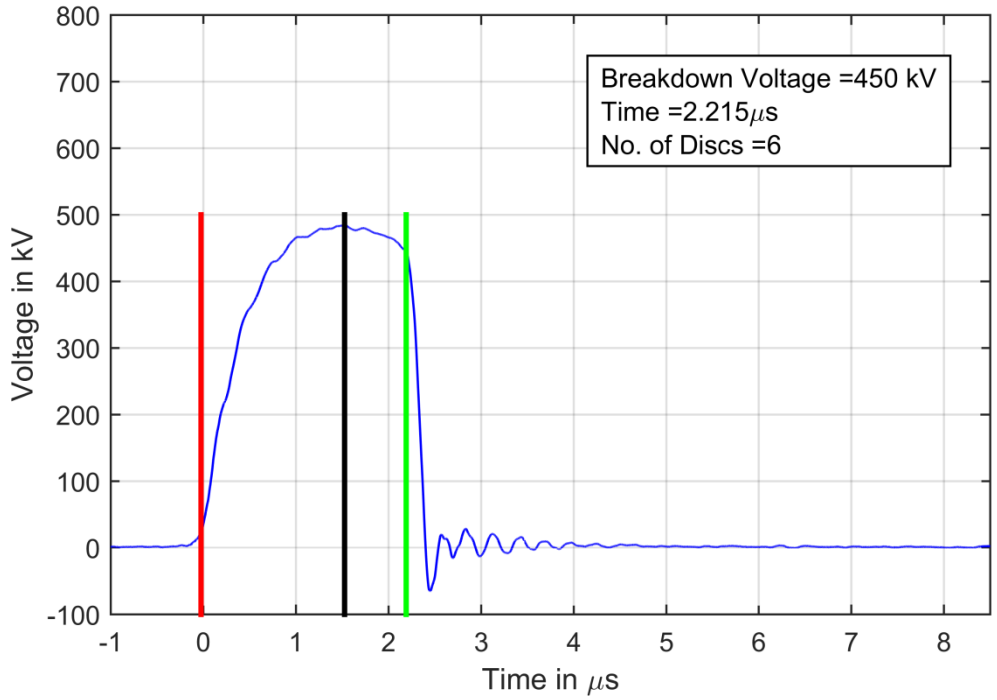
Breakdown Voltage =450 kV
Time =2.215μs
No. of Discs =6
Voltage in kV
Time in μs
800
700
600
500
400
300
200
100
0
-100
-1
0
1
2
3
4
5
6
7
8

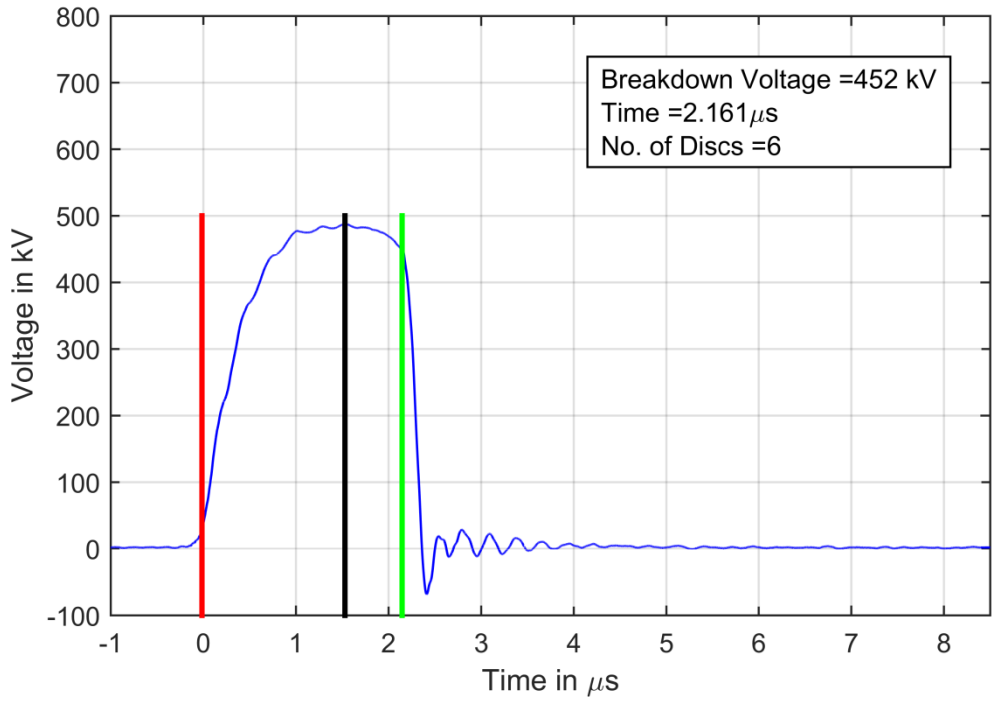
Breakdown Voltage =452 kV
Time =2.161μs
No. of Discs =6
Voltage in kV
Time in μs
800
700
600
500
400
300
200
100
0
-100
-1
0
1
2
3
4
5
6
7
8

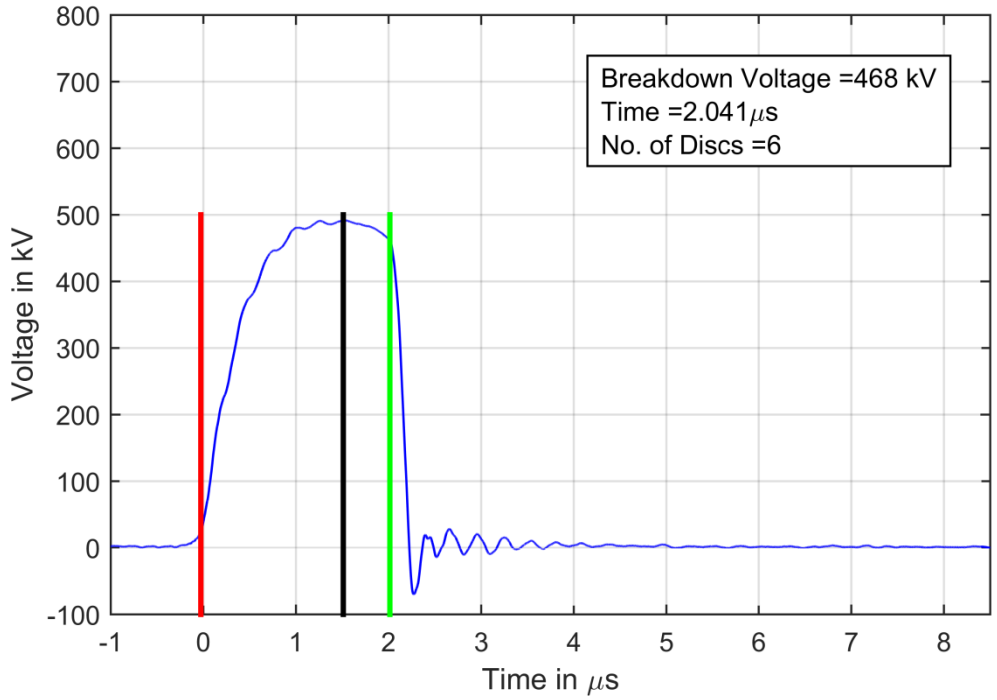
Breakdown Voltage =468 kV
Time =2.041μs
No. of Discs =6
Voltage in kV
Time in μs
800
700
600
500
400
300
200
100
0
-100
-1
0
1
2
3
4
5
6
7
8

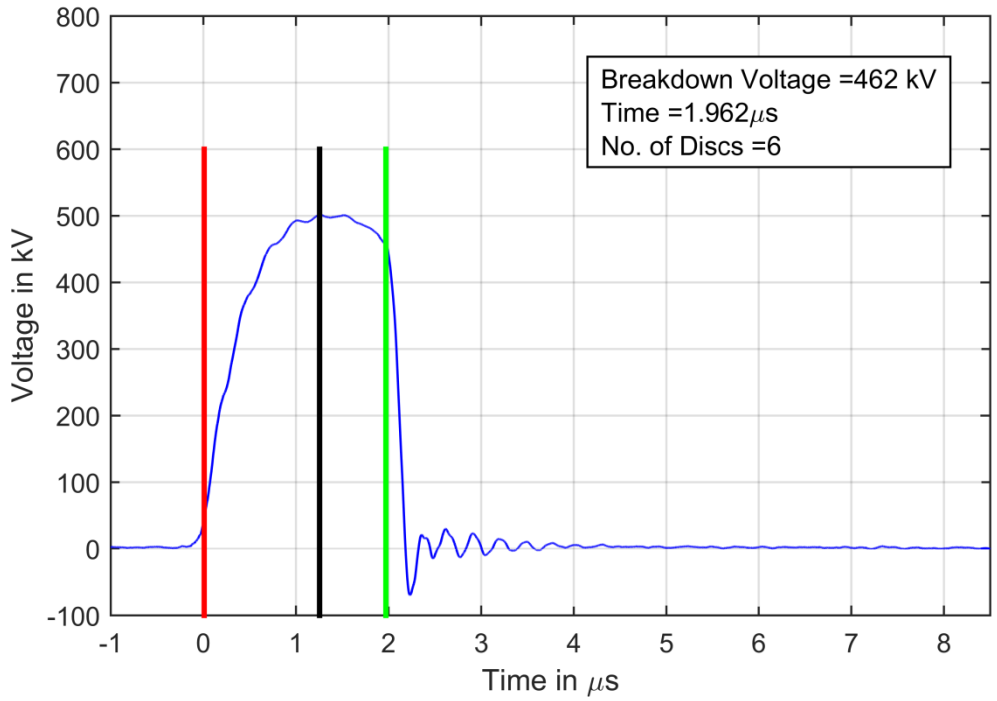
Breakdown Voltage =462 kV
Time =1.962μs
No. of Discs =6
Voltage in kV
Time in μs

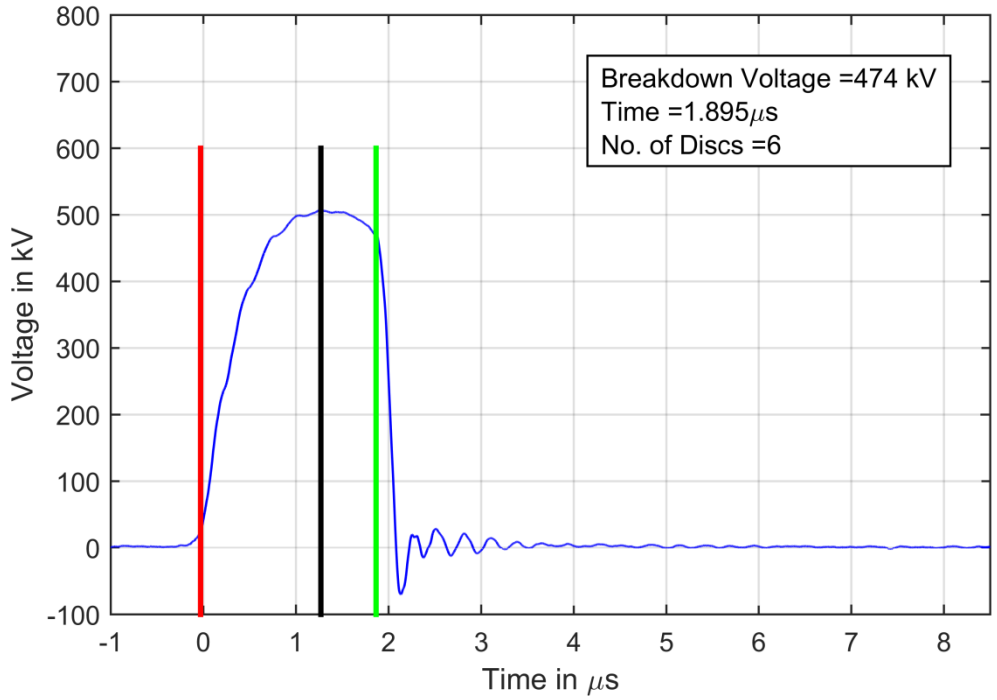
Breakdown Voltage =474 kV
Time =1.895μs
No. of Discs =6
Voltage in kV
Time in μs

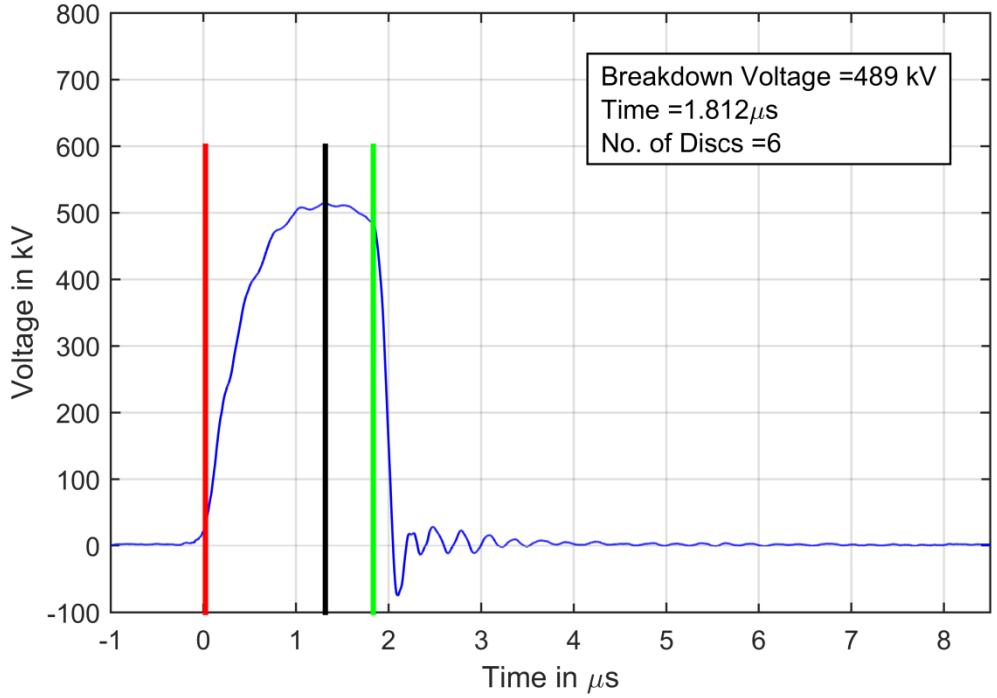
Breakdown Voltage =489 kV
Time =1.812μs
No. of Discs =6
Voltage in kV
Time in μs
800
700
600
500
400
300
200
100
0
-100
-1
0
1
2
3
4
5
6
7
8

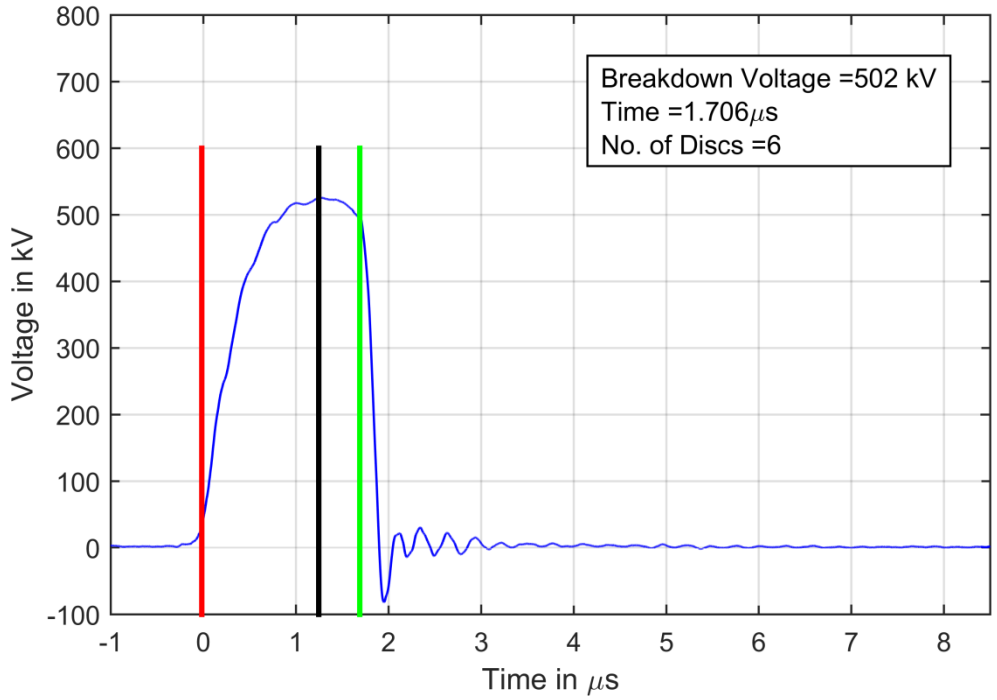
Breakdown Voltage =502 kV
Time =1.706μs
No. of Discs =6
Voltage in kV
Time in μs
800
700
600
500
400
300
200
100
0
-100
-1
0
1
2
3
4
5
6
7
8

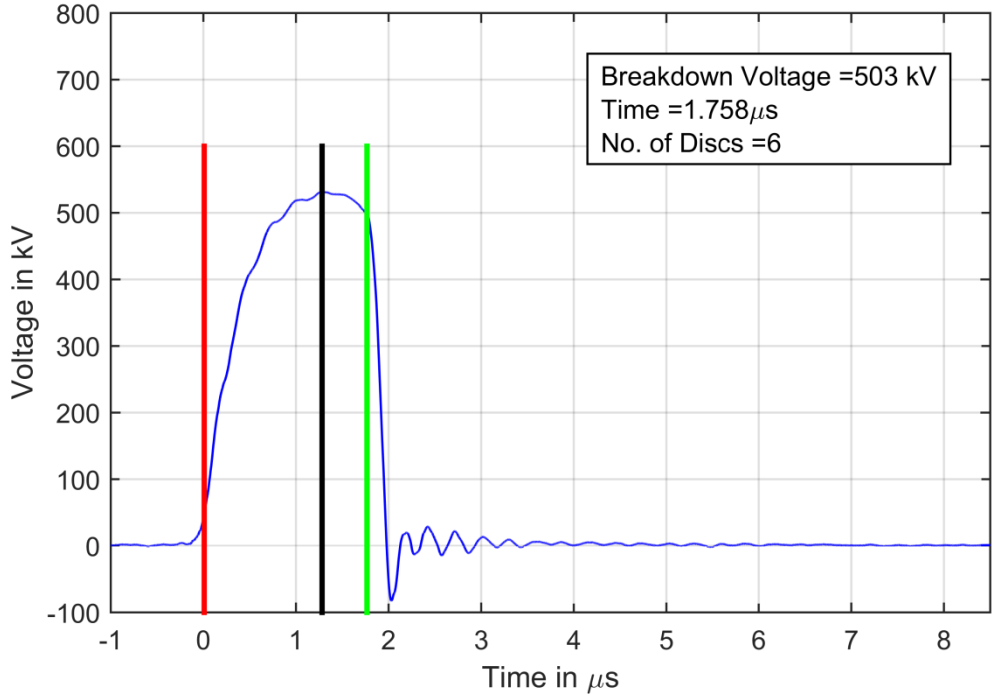
Breakdown Voltage =503 kV
Time =1.758μs
No. of Discs =6
Voltage in kV
Time in μs
800
700
600
500
400
300
200
100
0
-100
-1
0
1
2
3
4
5
6
7
8

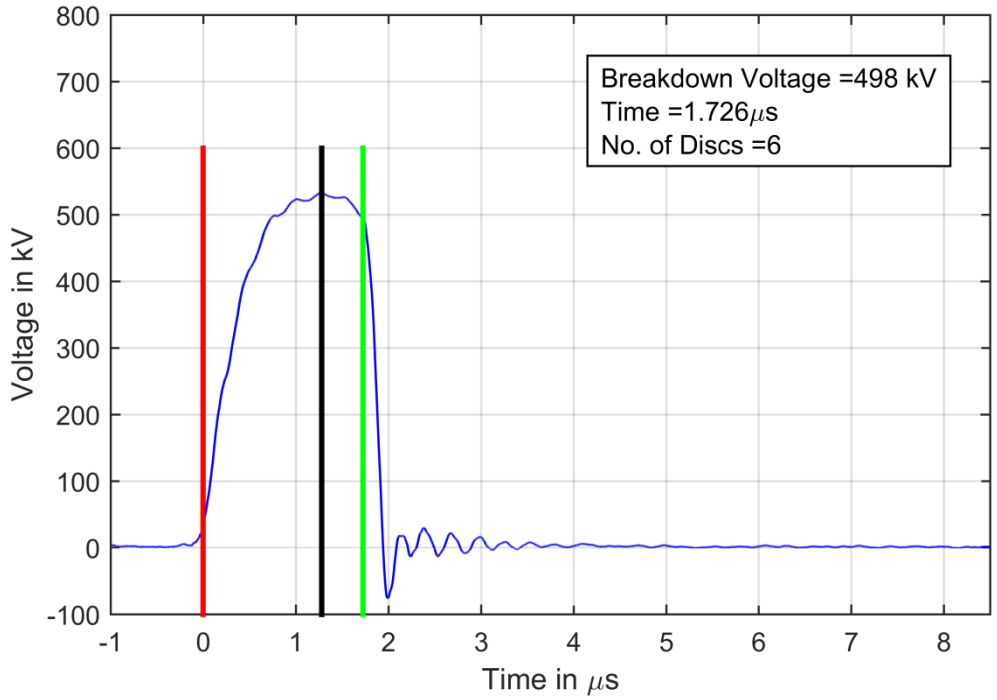
Breakdown Voltage =498 kV
Time =1.726μs
No. of Discs =6
Voltage in kV
Time in μs
800
700
600
500
400
300
200
100
0
-100
-1
0
1
2
3
4
5
6
7
8

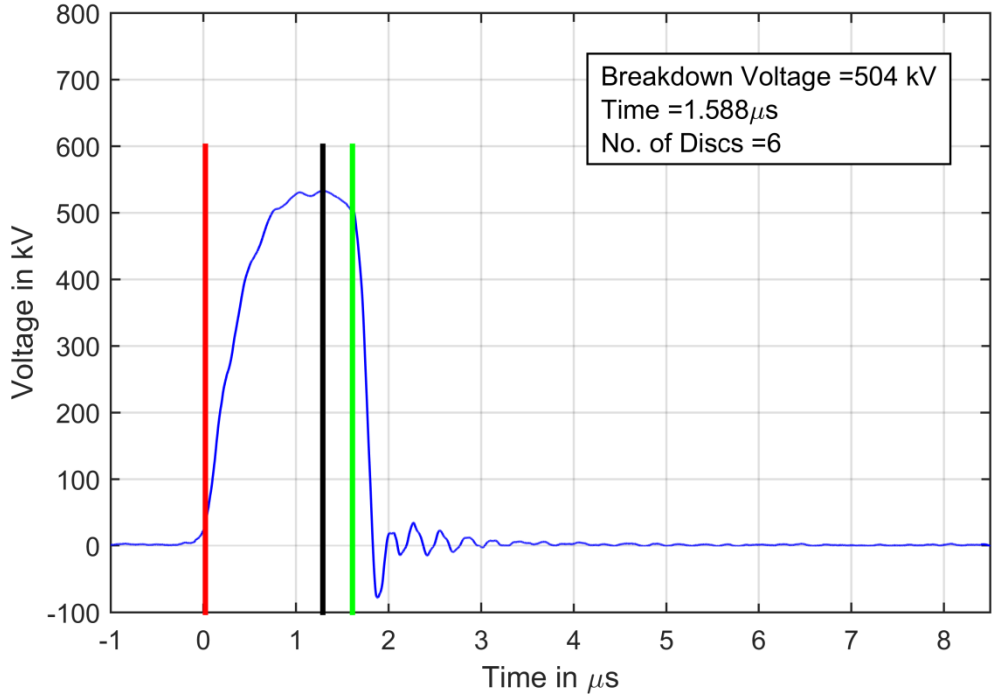
Breakdown Voltage =504 kV
Time =1.588μs
No. of Discs =6
Voltage in kV
Time in μs

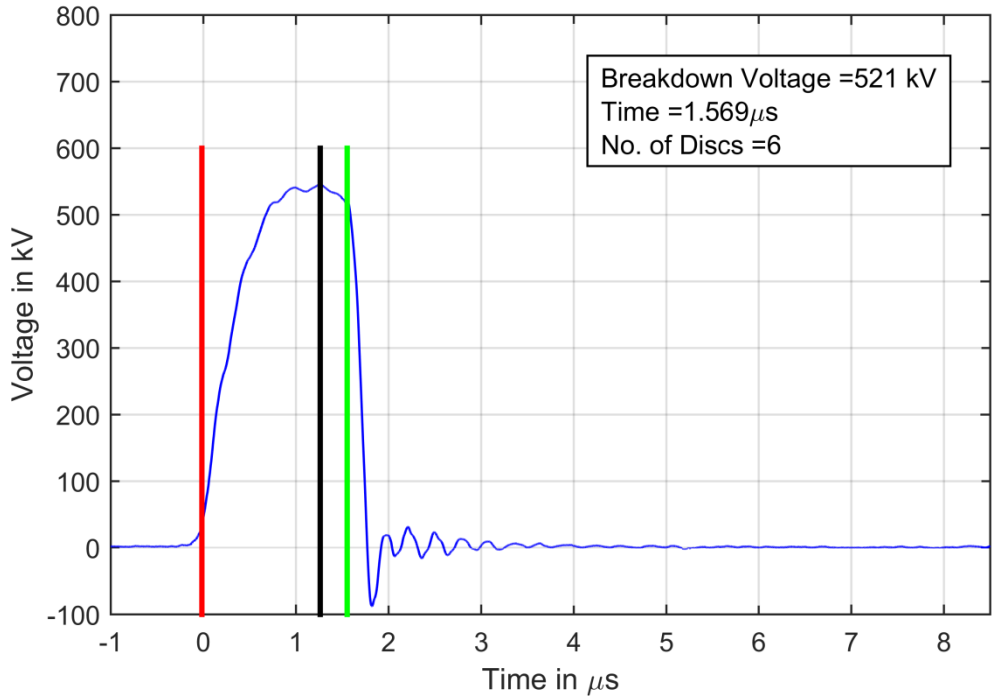
Breakdown Voltage =521 kV
Time =1.569μs
No. of Discs =6
Voltage in kV
Time in μs

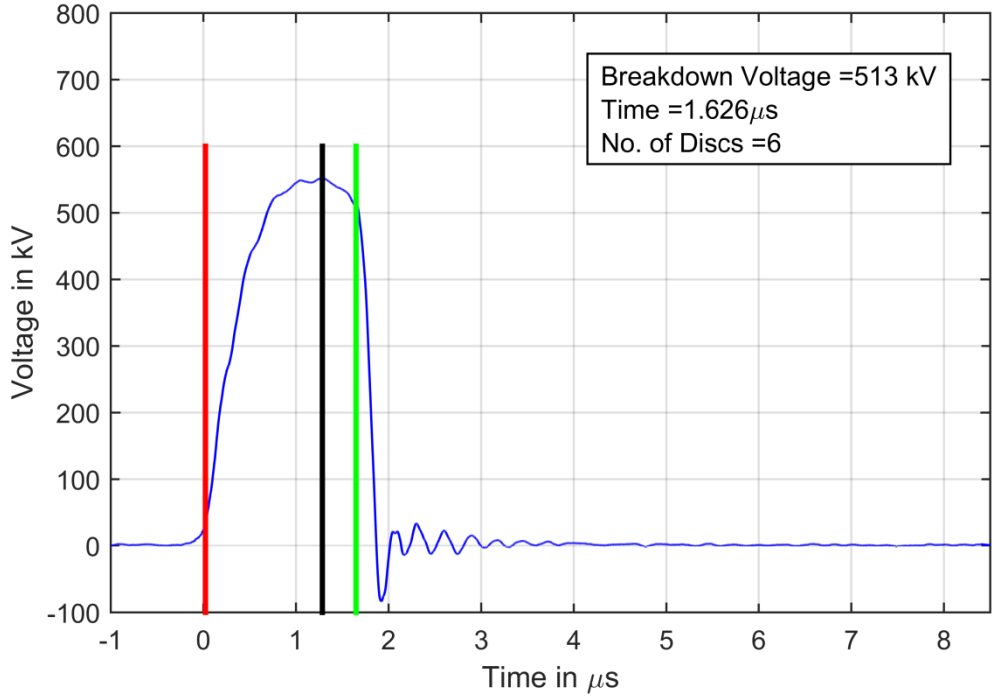
Breakdown Voltage =513 kV
Time =1.626μs
No. of Discs =6
Voltage in kV
Time in μs
800
700
600
500
400
300
200
100
0
-100
-1
0
1
2
3
4
5
6
7
8

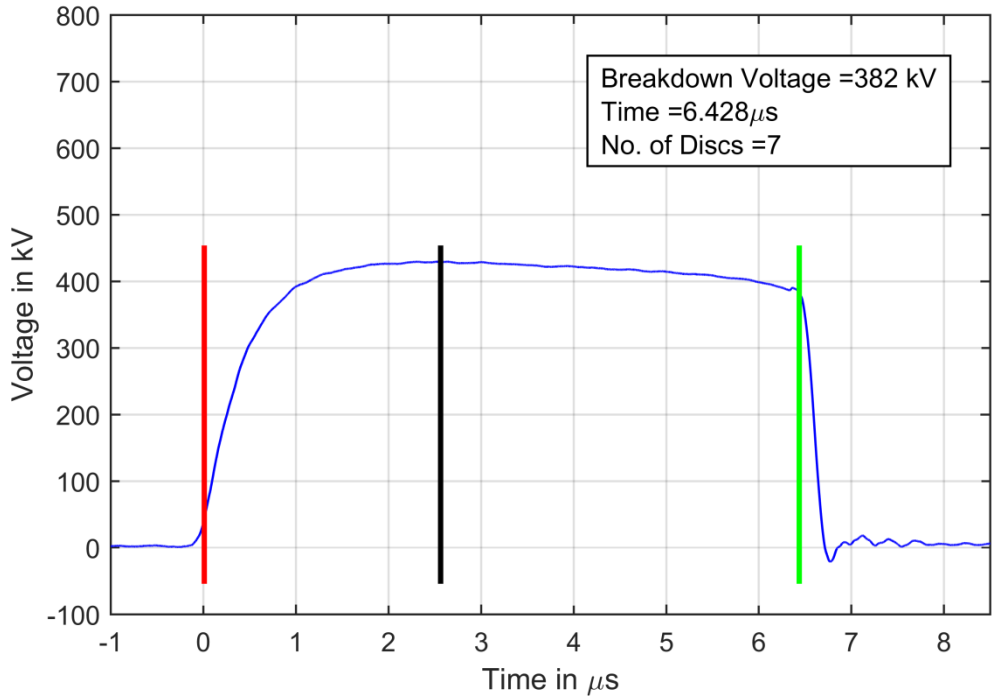
Breakdown Voltage =382 kV
Time =6.428μs
No. of Discs =7
Voltage in kV
Time in μs
800
700
600
500
400
300
200
100
0
-100
-1
0
1
2
3
4
5
6
7
8

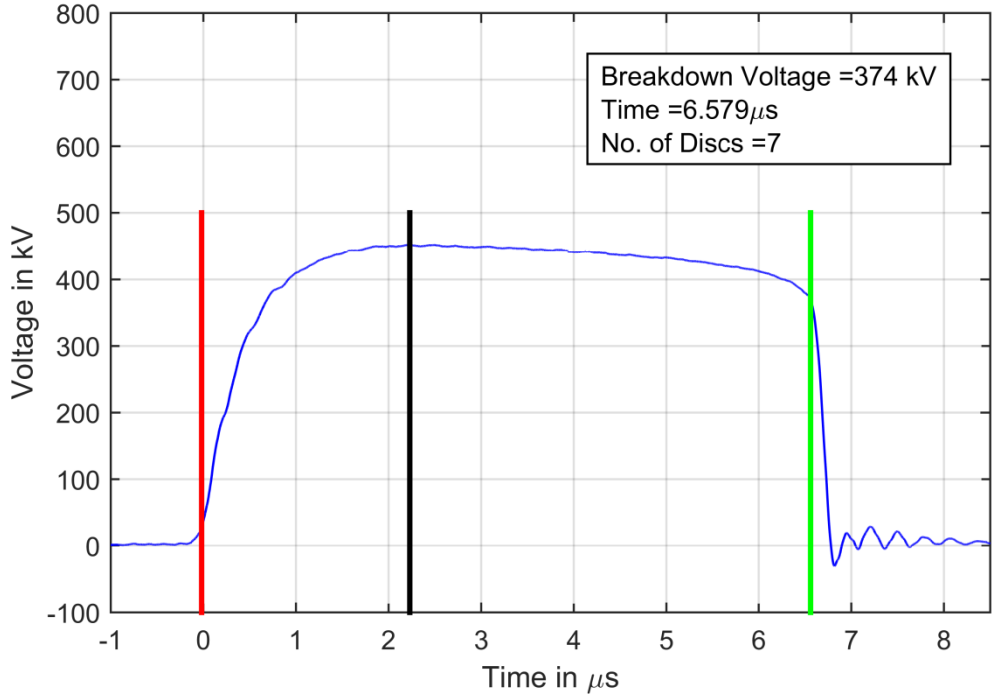
Breakdown Voltage =374 kV
Time =6.579μs
No. of Discs =7
Voltage in kV
Time in μs
800
700
600
500
400
300
200
100
0
-100
-1
0
1
2
3
4
5
6
7
8

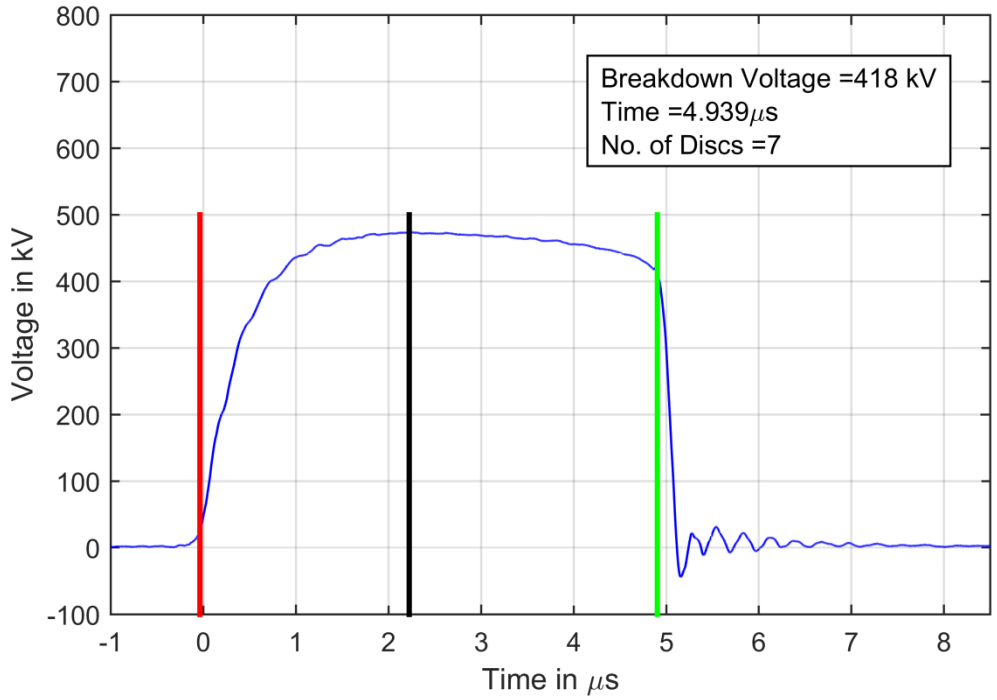
Breakdown Voltage =418 kV
Time =4.939μs
No. of Discs =7
Voltage in kV
Time in μs
800
700
600
500
400
300
200
100
0
-100
-1
0
1
2
3
4
5
6
7
8

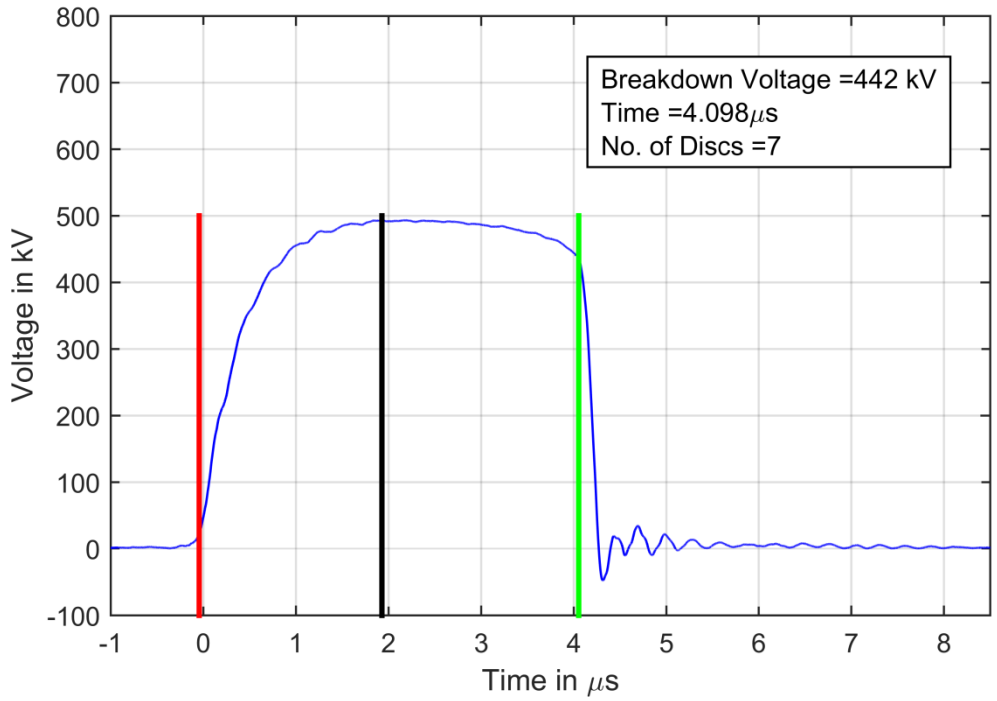
Breakdown Voltage =442 kV
Time =4.098μs
No. of Discs =7
Voltage in kV
Time in μs
800
700
600
500
400
300
200
100
0
-100
-1
0
1
2
3
4
5
6
7
8

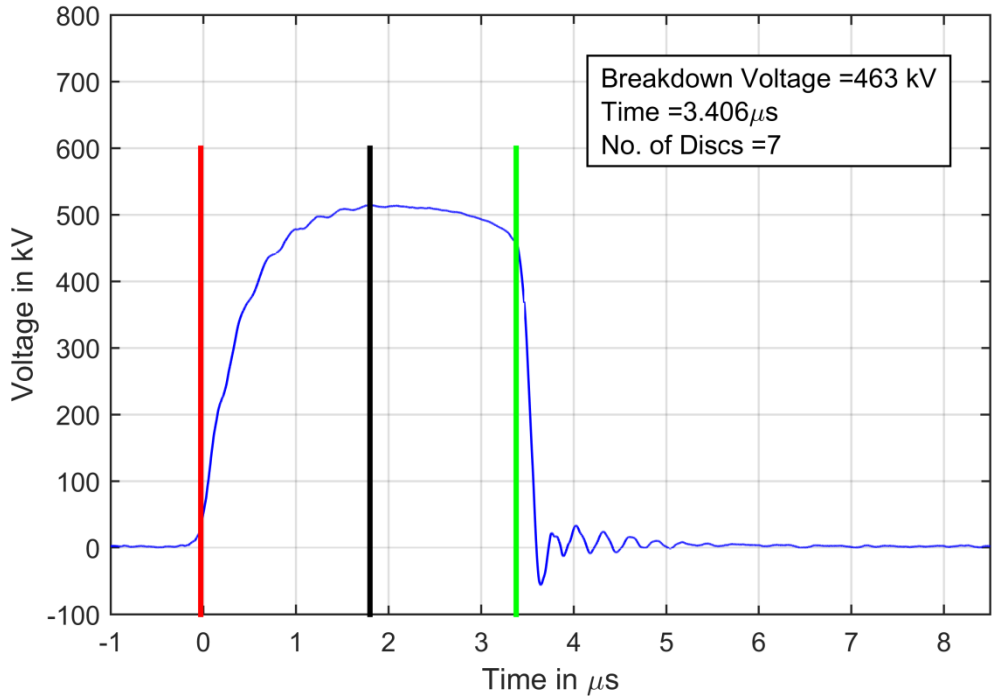
Breakdown Voltage =463 kV
Time =3.406μs
No. of Discs =7
Voltage in kV
Time in μs
800
700
600
500
400
300
200
100
0
-100
-1
0
1
2
3
4
5
6
7
8

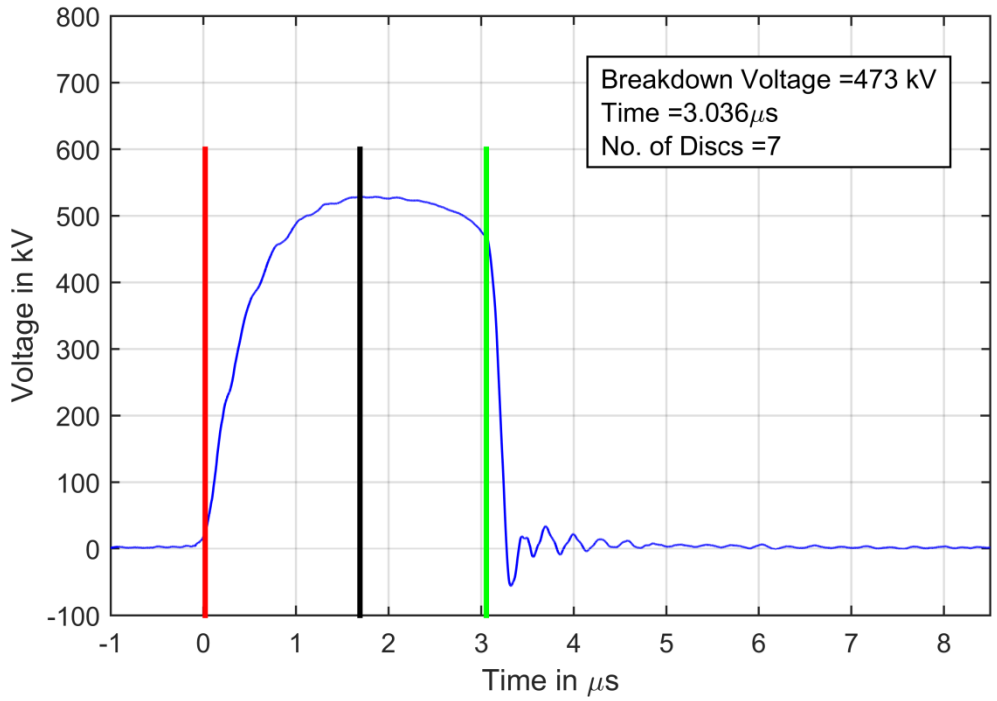
Breakdown Voltage =473 kV
Time =3.036μs
No. of Discs =7
Voltage in kV
Time in μs

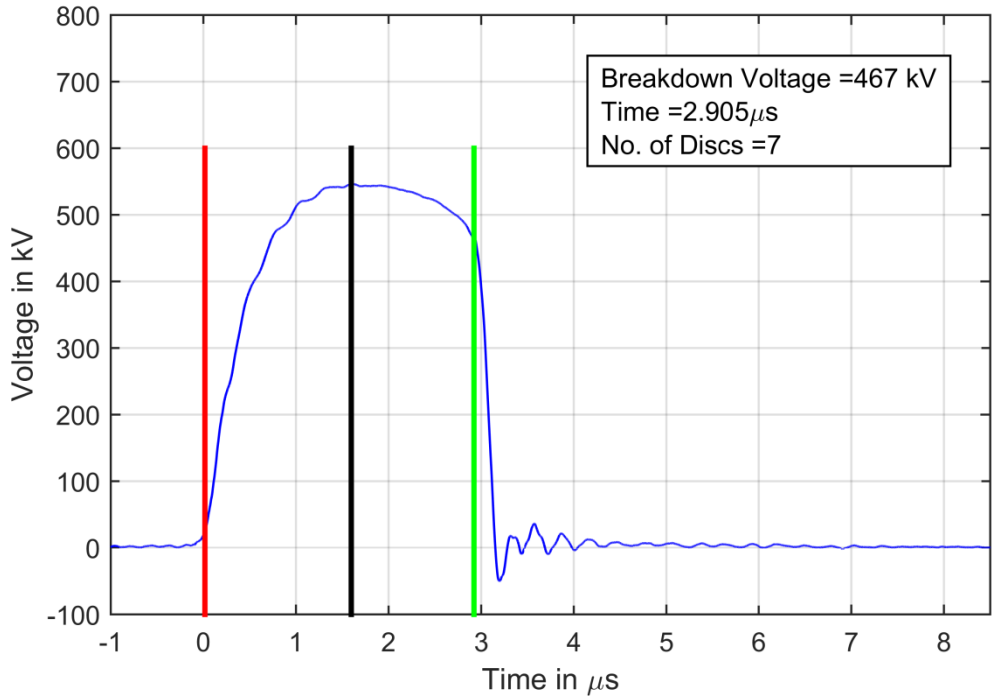
Breakdown Voltage =467 kV
Time =2.905μs
No. of Discs =7
Voltage in kV
Time in μs

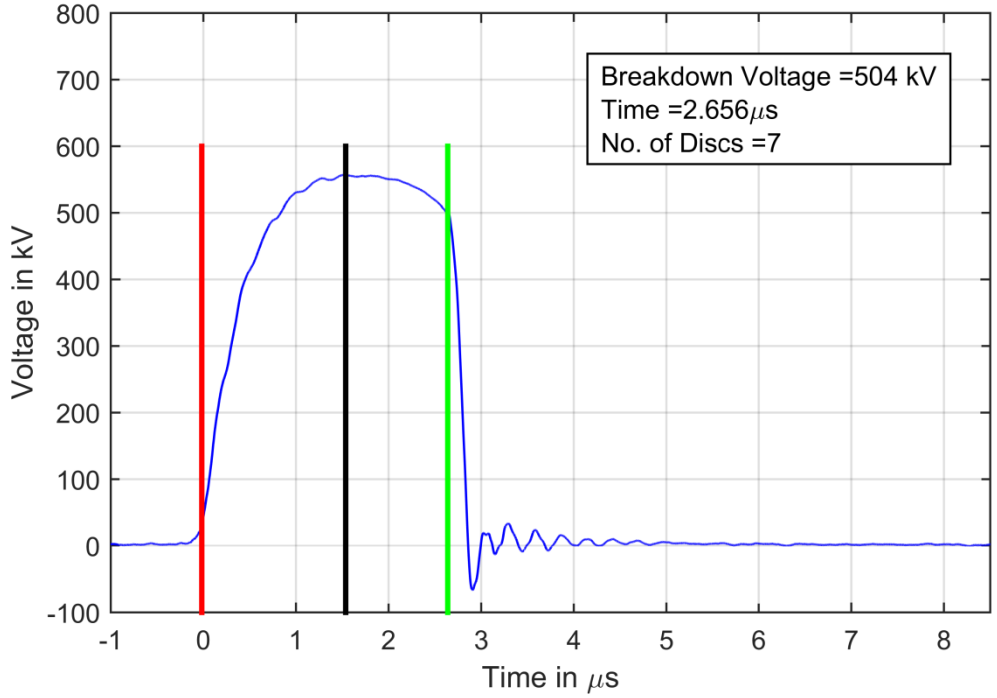
Breakdown Voltage =504 kV
Time =2.656μs
No. of Discs =7
Voltage in kV
Time in μs
800
700
600
500
400
300
200
100
0
-100
-1
0
1
2
3
4
5
6
7
8

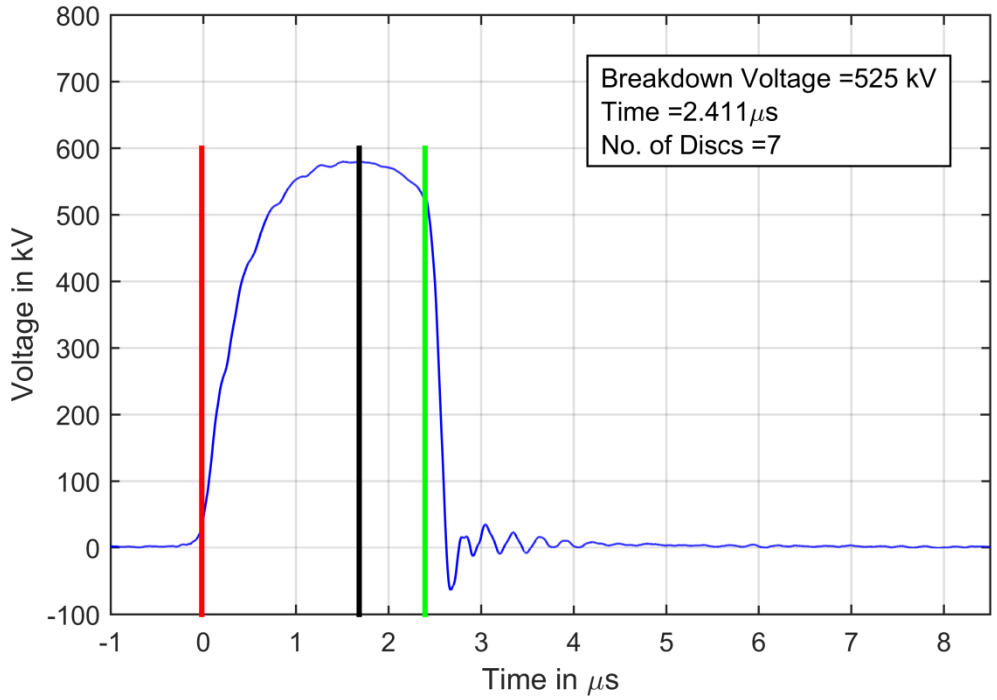
Breakdown Voltage =525 kV
Time =2.411μs
No. of Discs =7
Voltage in kV
Time in μs
800
700
600
500
400
300
200
100
0
-100
-1
0
1
2
3
4
5
6
7
8

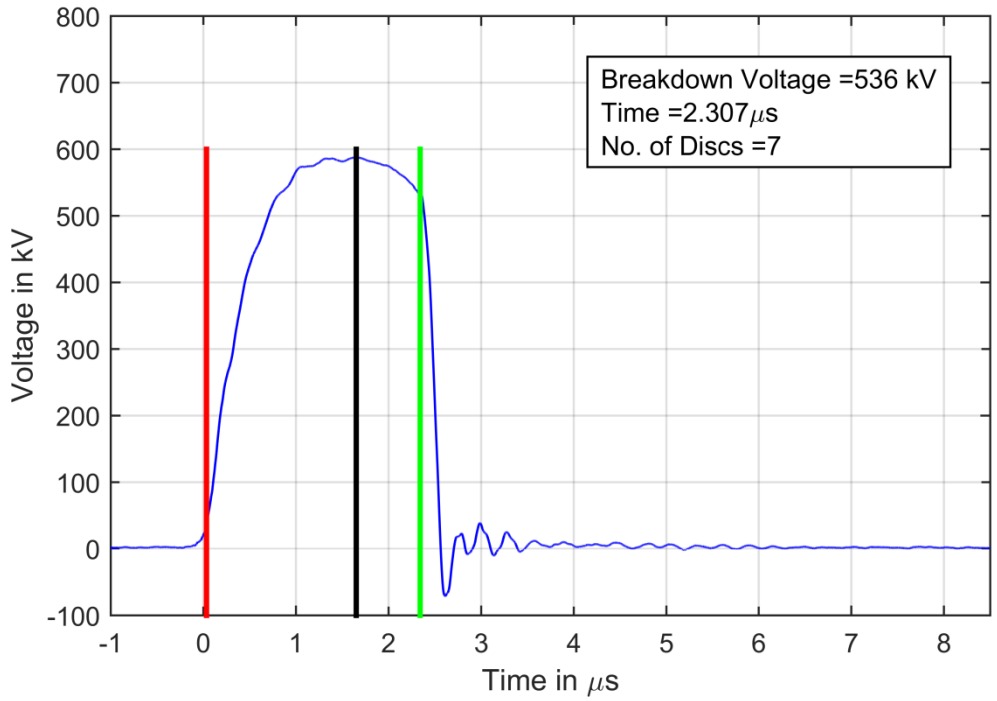
Breakdown Voltage =536 kV
Time =2.307μs
No. of Discs =7
Voltage in kV
Time in μs
800
700
600
500
400
300
200
100
0
-100
-1
0
1
2
3
4
5
6
7
8

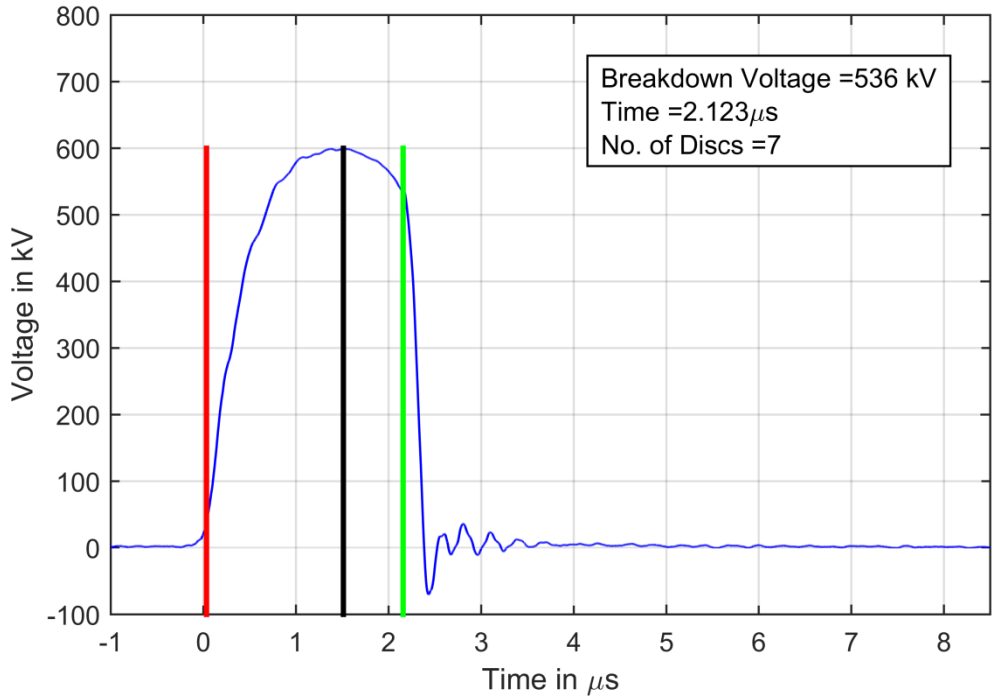
Breakdown Voltage =536 kV
Time =2.123μs
No. of Discs =7
Voltage in kV
Time in μs
800
700
600
500
400
300
200
100
0
-100
-1
0
1
2
3
4
5
6
7
8

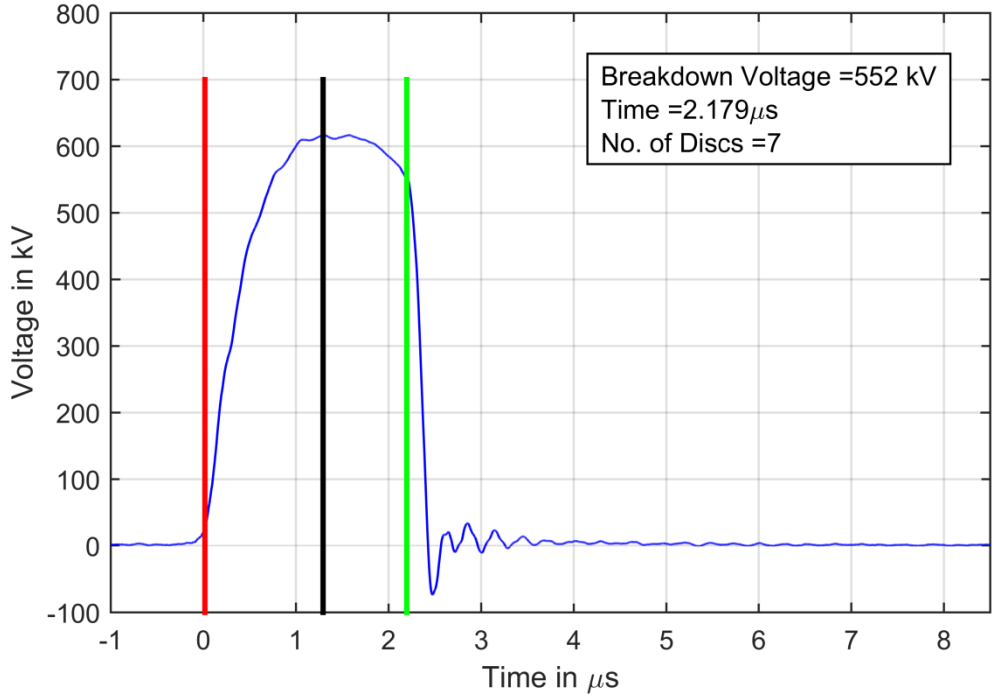
Breakdown Voltage =552 kV
Time =2.179μs
No. of Discs =7
Voltage in kV
Time in μs
800
700
600
500
400
300
200
100
0
-100
-1
0
1
2
3
4
5
6
7
8

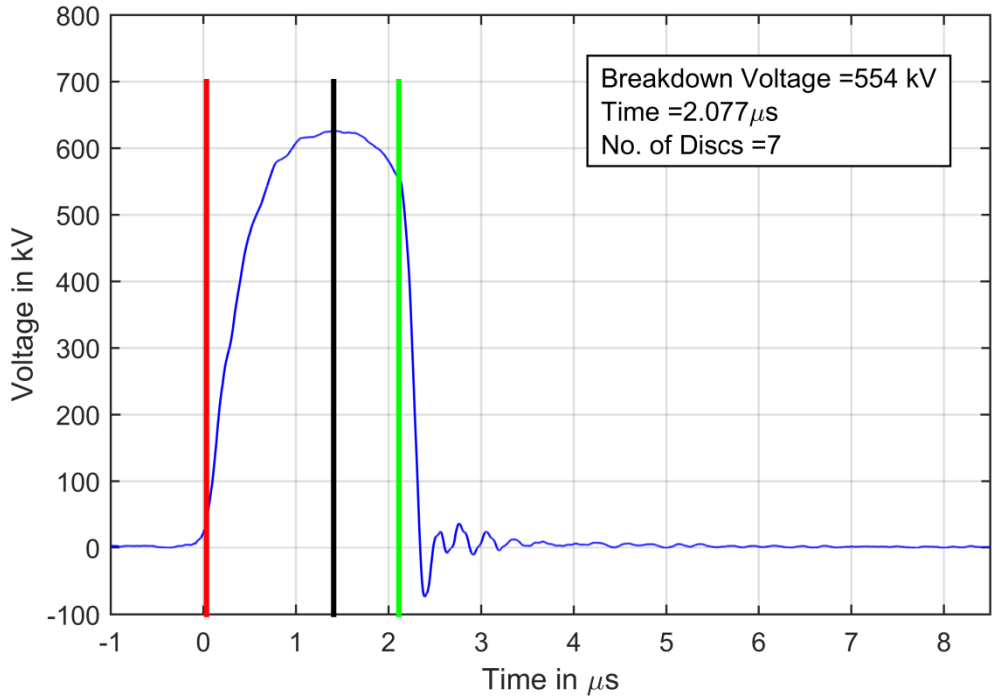
Breakdown Voltage =554 kV
Time =2.077μs
No. of Discs =7
Voltage in kV
Time in μs
800
700
600
500
400
300
200
100
0
-100
-1
0
1
2
3
4
5
6
7
8

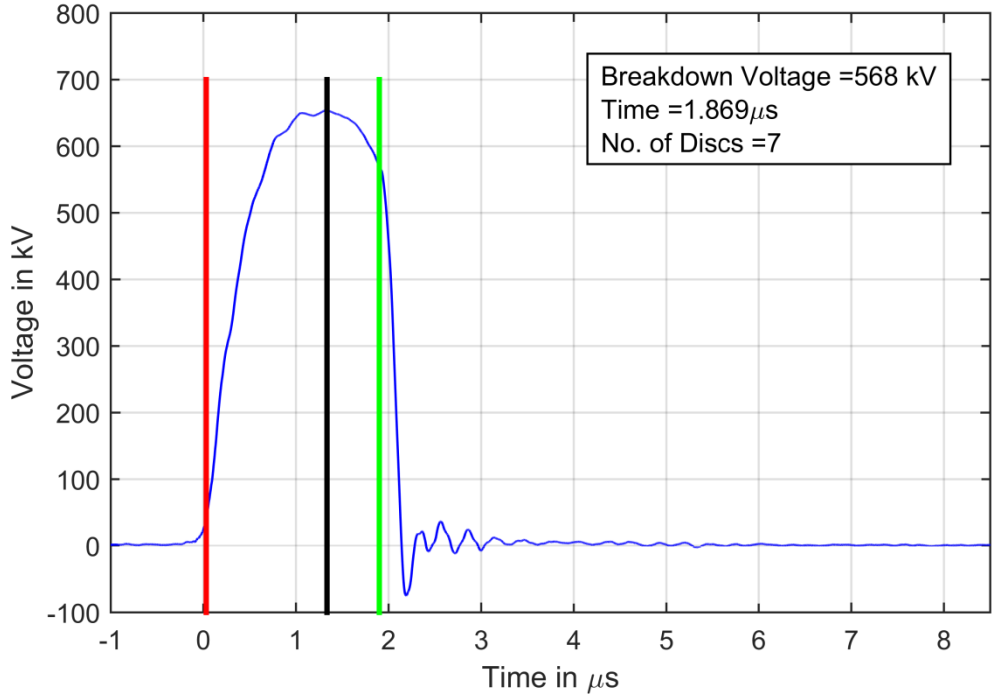
Breakdown Voltage =568 kV
Time =1.869μs
No. of Discs =7
Voltage in kV
Time in μs
800
700
600
500
400
300
200
100
0
-100
-1
0
1
2
3
4
5
6
7
8

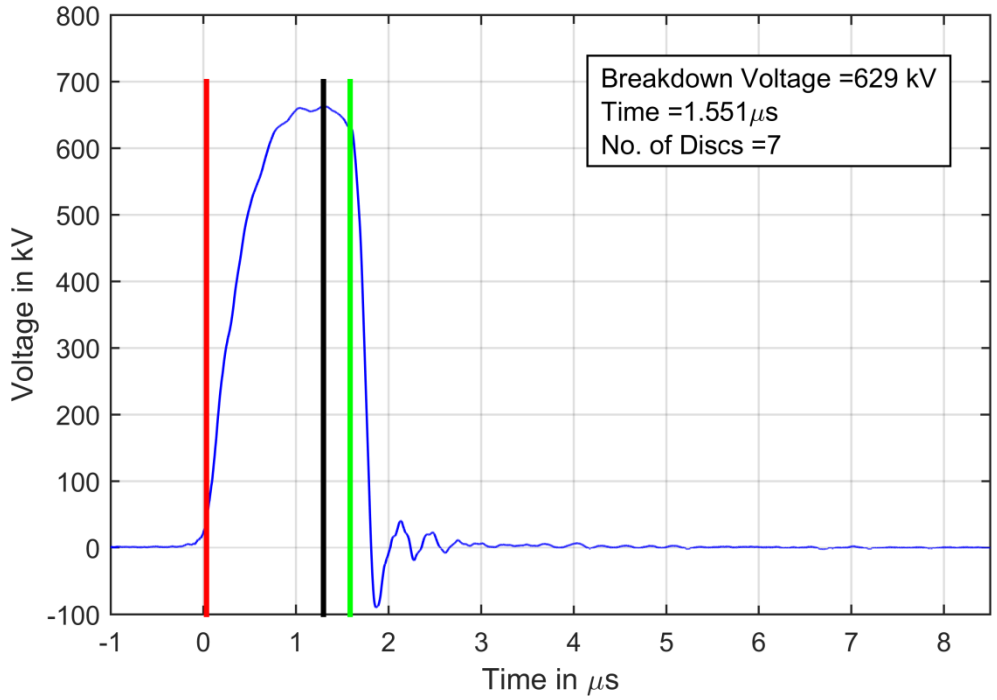
Breakdown Voltage =629 kV
Time =1.551μs
No. of Discs =7
Voltage in kV
Time in μs
800
700
600
500
400
300
200
100
0
-100
-1
0
1
2
3
4
5
6
7
8

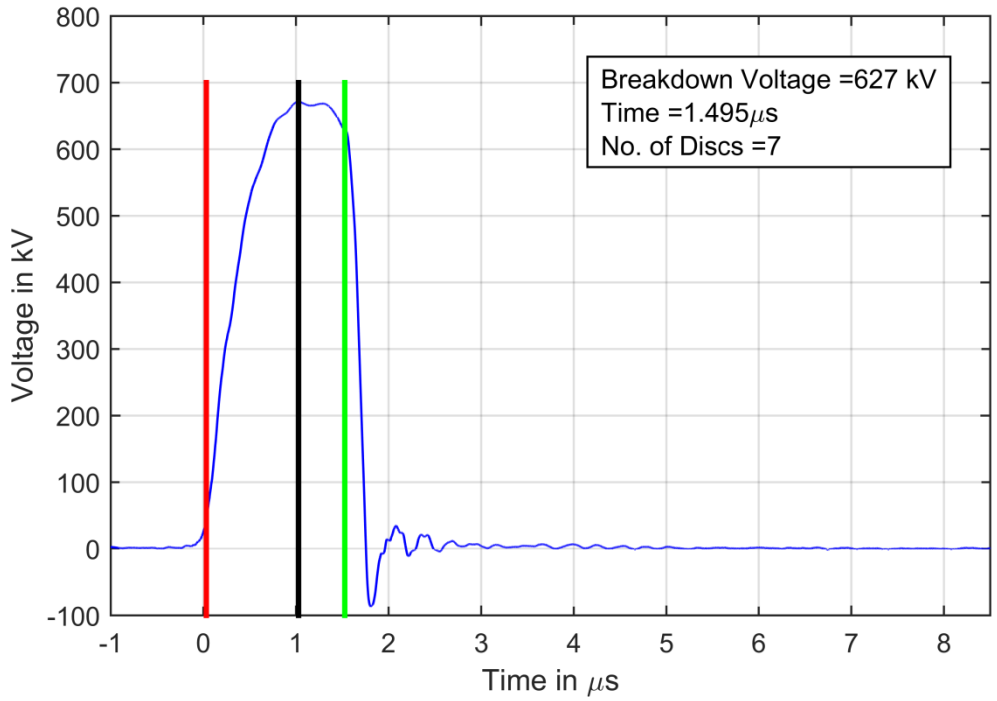
Breakdown Voltage =627 kV
Time =1.495μs
No. of Discs =7
Voltage in kV
Time in μs
800
700
600
500
400
300
200
100
0
-100
-1
0
1
2
3
4
5
6
7
8

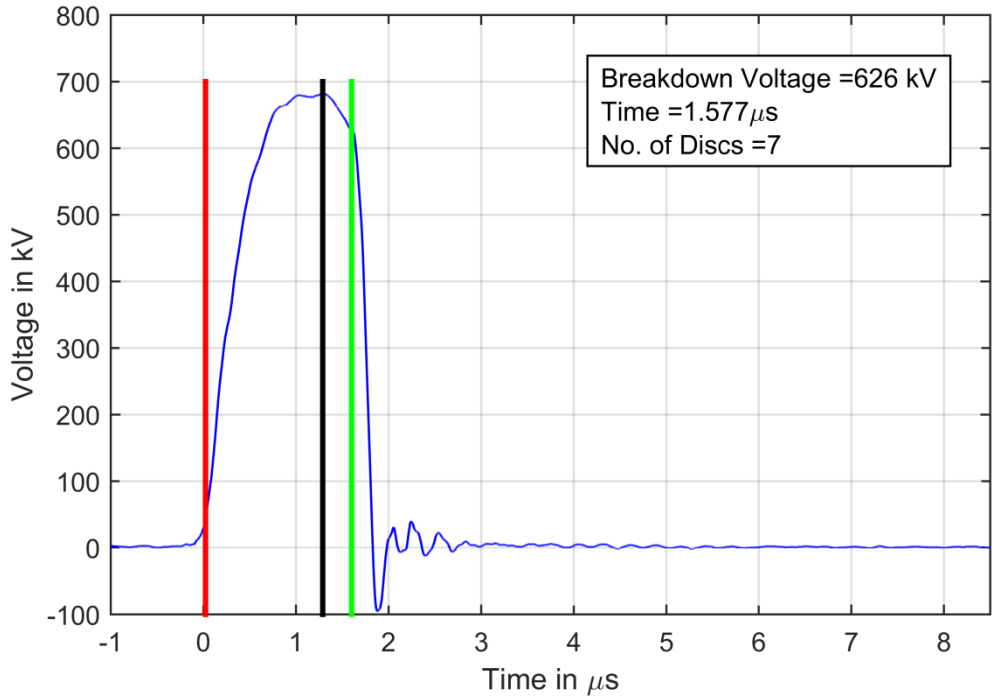
Breakdown Voltage =626 kV
Time =1.577μs
No. of Discs =7
Voltage in kV
Time in μs
800
700
600
500
400
300
200
100
0
-100
-1
0
1
2
3
4
5
6
7
8

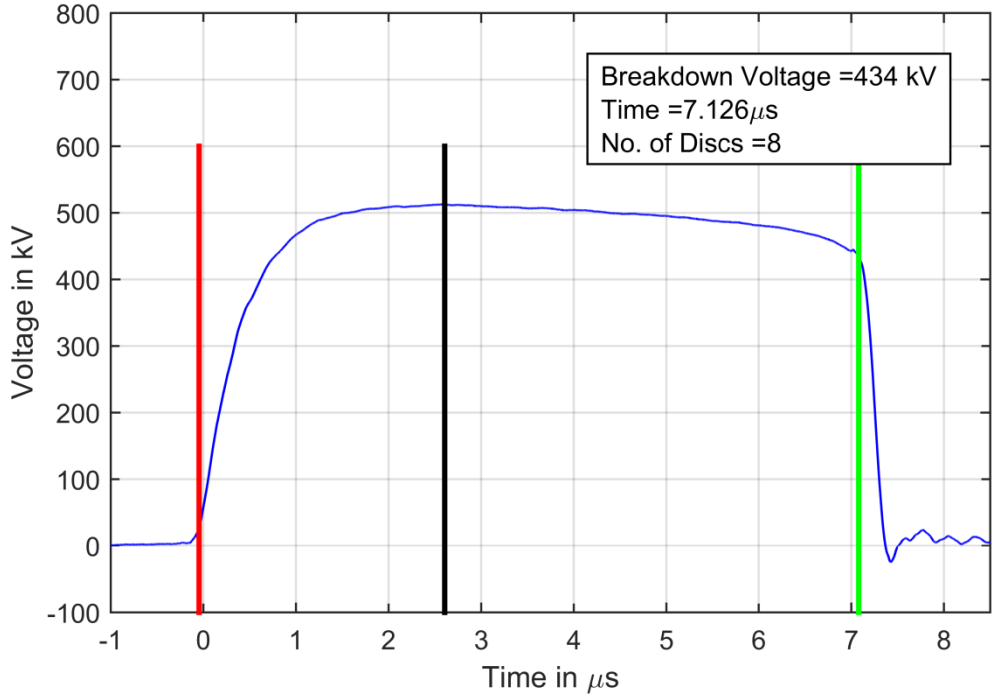
Breakdown Voltage =434 kV
Time =7.126μs
No. of Discs =8
Voltage in kV
Time in μs
800
700
600
500
400
300
200
100
0
-100
-1
0
1
2
3
4
5
6
7
8

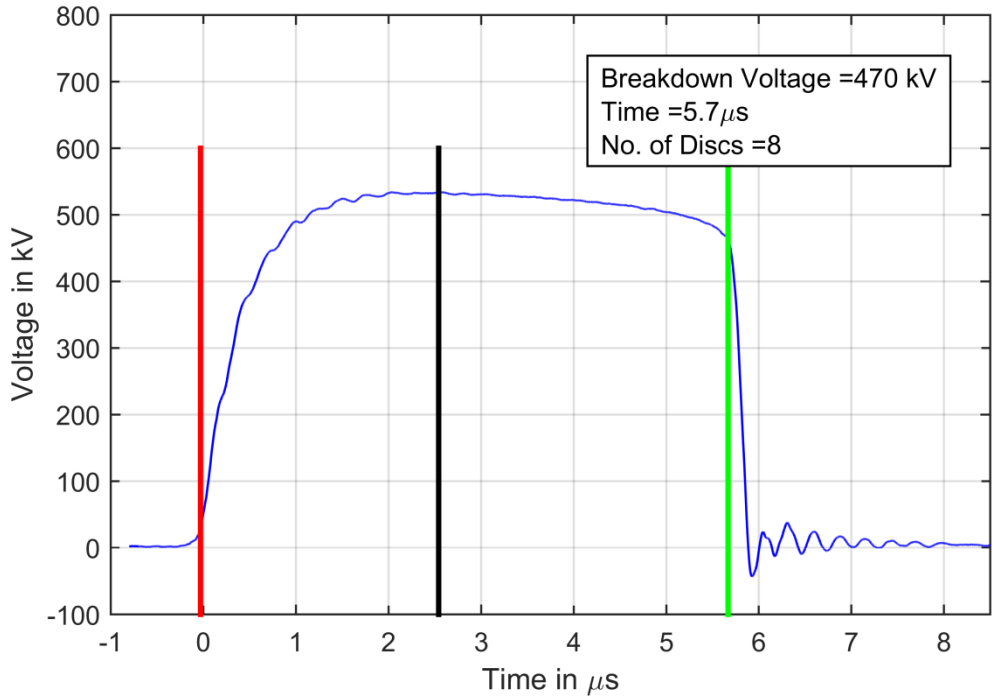
Breakdown Voltage =470 kV
Time =5.7μs
No. of Discs =8
Voltage in kV
Time in μs
800
700
600
500
400
300
200
100
0
-100
-1
0
1
2
3
4
5
6
7
8

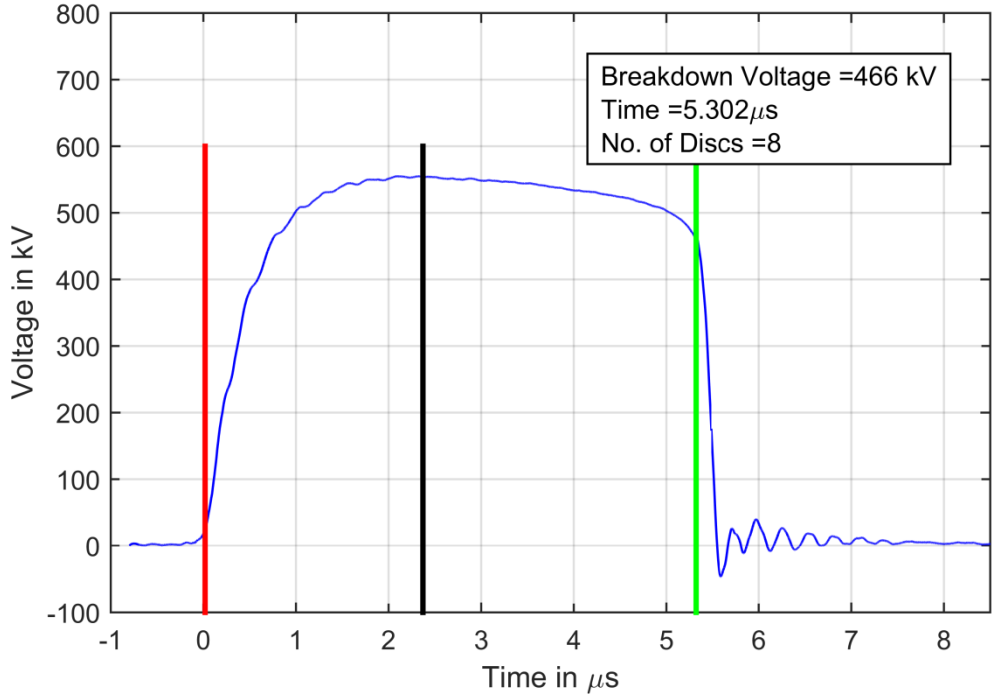
Breakdown Voltage =466 kV
Time =5.302μs
No. of Discs =8
Voltage in kV
Time in μs
800
700
600
500
400
300
200
100
0
-100
-1
0
1
2
3
4
5
6
7
8

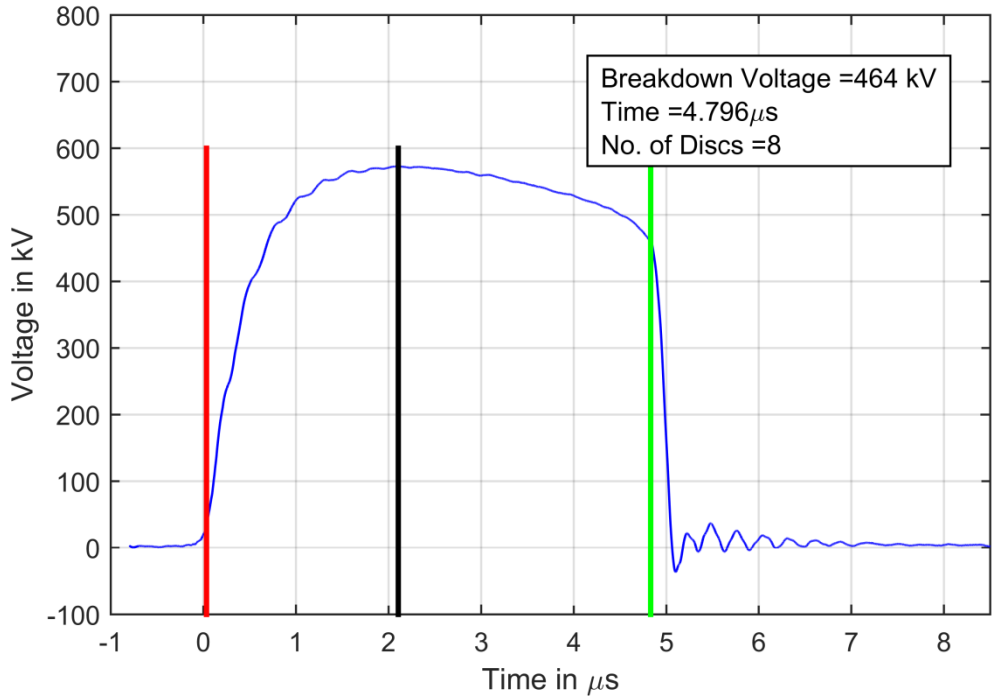
Breakdown Voltage =464 kV
Time =4.796μs
No. of Discs =8
Voltage in kV
Time in μs
800
700
600
500
400
300
200
100
0
-100
-1
0
1
2
3
4
5
6
7
8

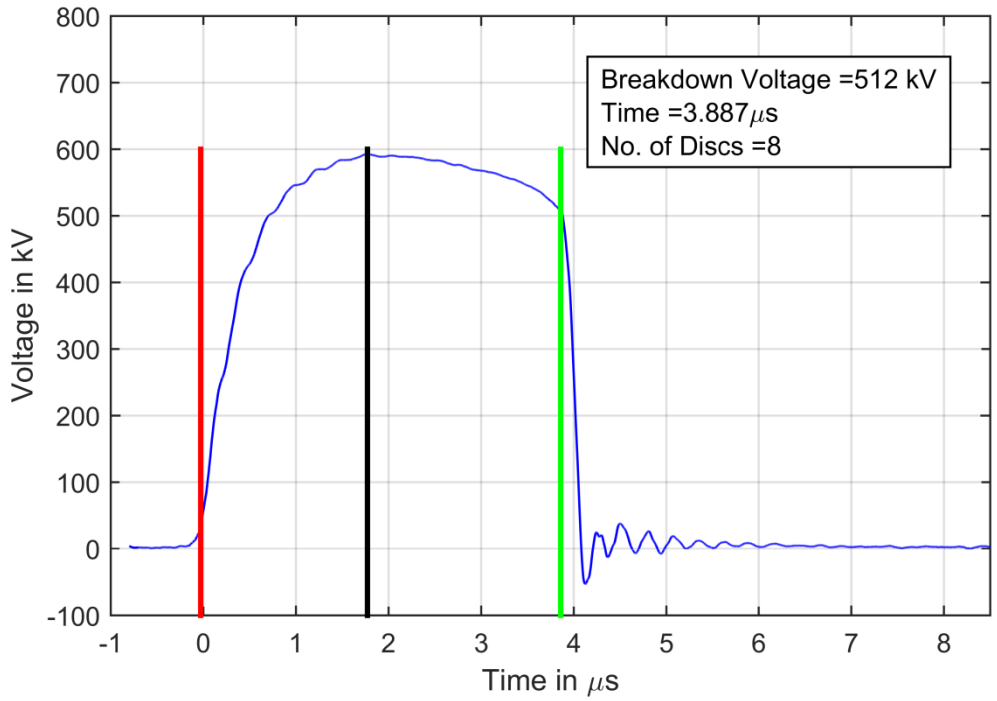
Breakdown Voltage =512 kV
Time =3.887μs
No. of Discs =8
Voltage in kV
Time in μs
800
700
600
500
400
300
200
100
0
-100
-1
0
1
2
3
4
5
6
7
8

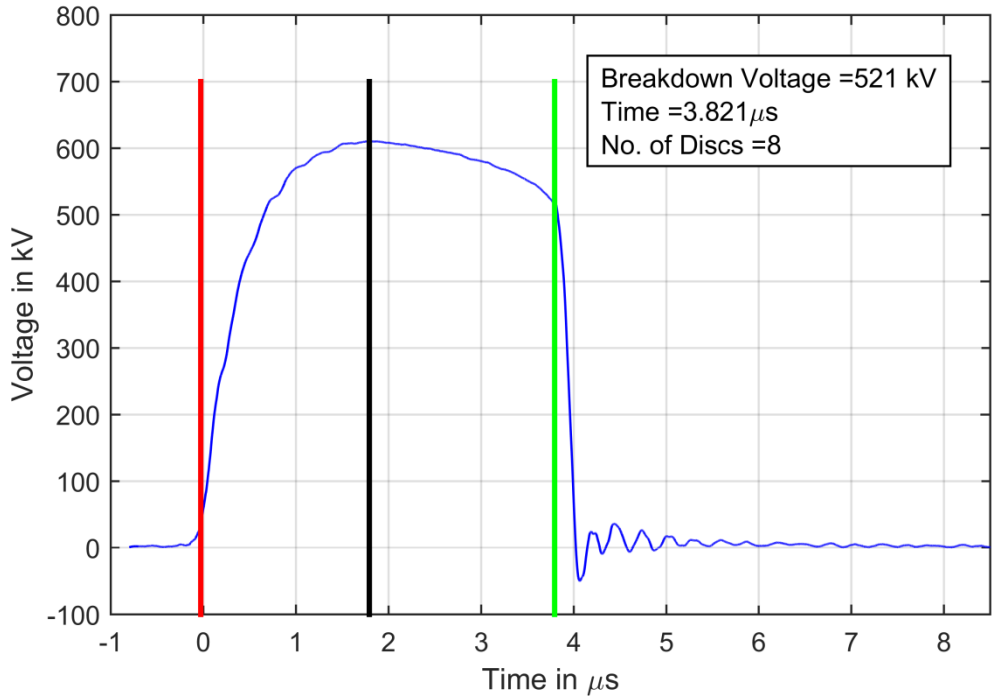
Breakdown Voltage =521 kV
Time =3.821μs
No. of Discs =8
Voltage in kV
Time in μs
800
700
600
500
400
300
200
100
0
-100
-1
0
1
2
3
4
5
6
7
8

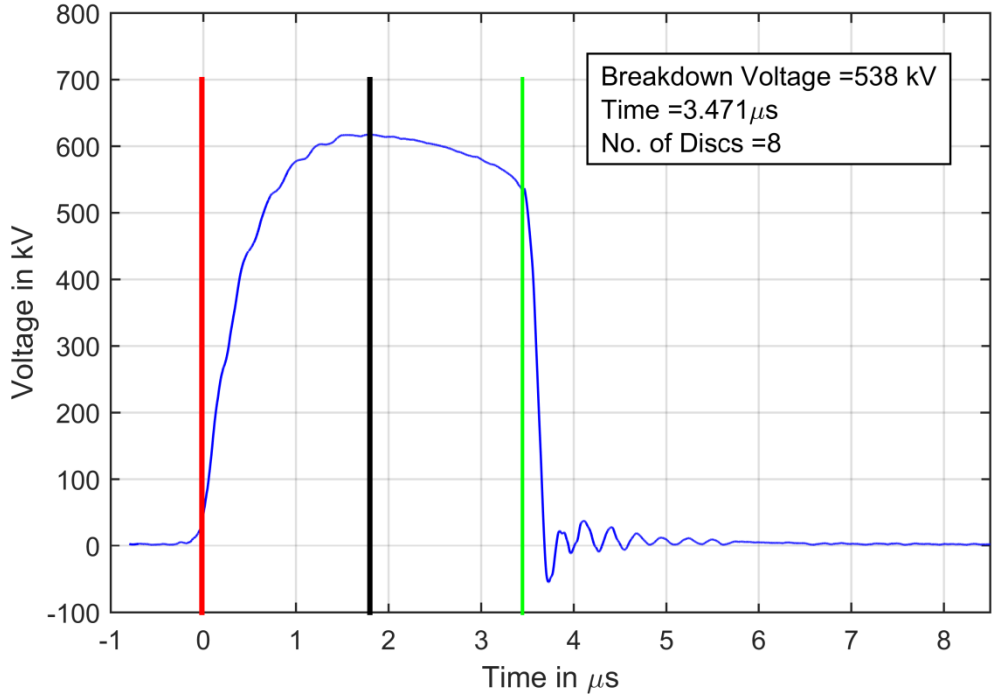
Breakdown Voltage =538 kV
Time =3.471μs
No. of Discs =8
Voltage in kV
Time in μs
800
700
600
500
400
300
200
100
0
-100
-1
0
1
2
3
4
5
6
7
8

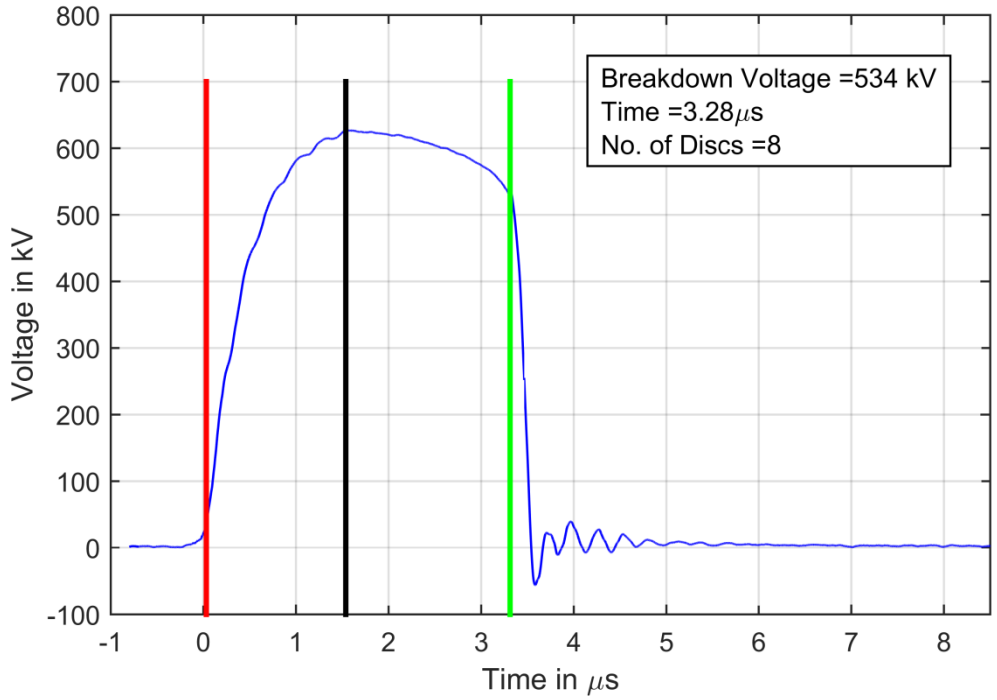
Breakdown Voltage =534 kV
Time =3.28μs
No. of Discs =8
Voltage in kV
Time in μs
800
700
600
500
400
300
200
100
0
-100
-1
0
1
2
3
4
5
6
7
8

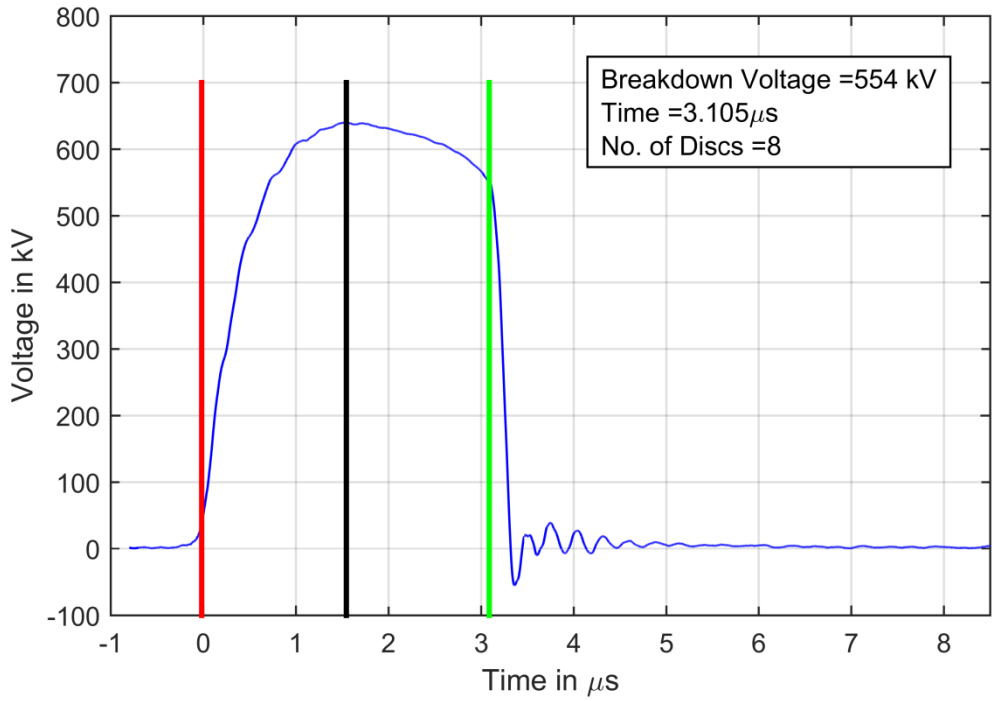
Breakdown Voltage =554 kV
Time =3.105μs
No. of Discs =8
Voltage in kV
Time in μs
800
700
600
500
400
300
200
100
0
-100
-1
0
1
2
3
4
5
6
7
8

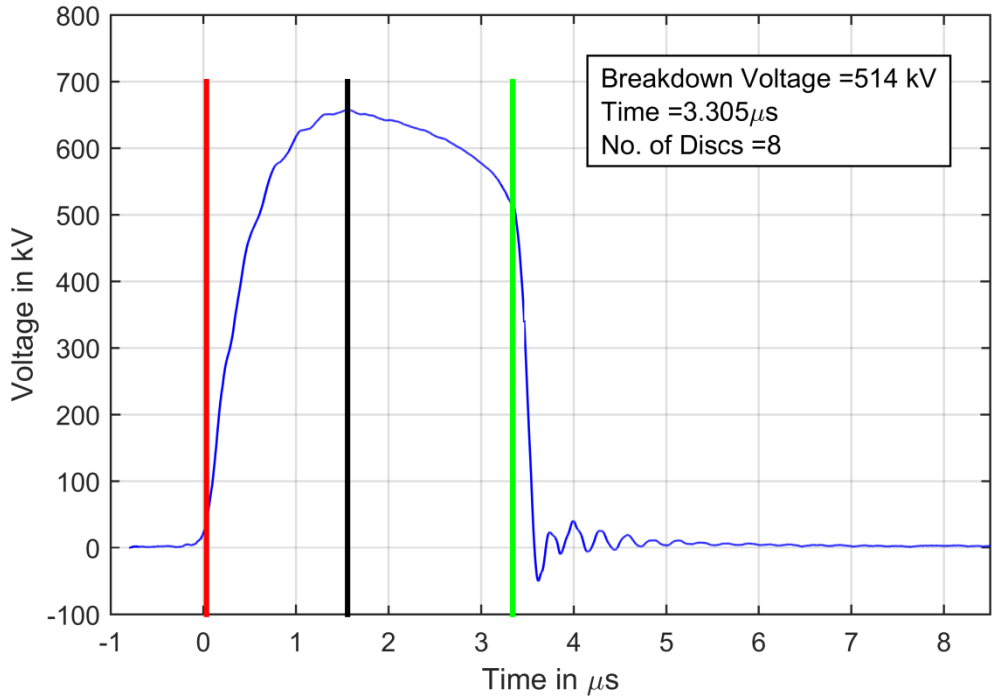
Breakdown Voltage =514 kV
Time =3.305μs
No. of Discs =8
Voltage in kV
Time in μs
800
700
600
500
400
300
200
100
0
-100
-1
0
1
2
3
4
5
6
7
8

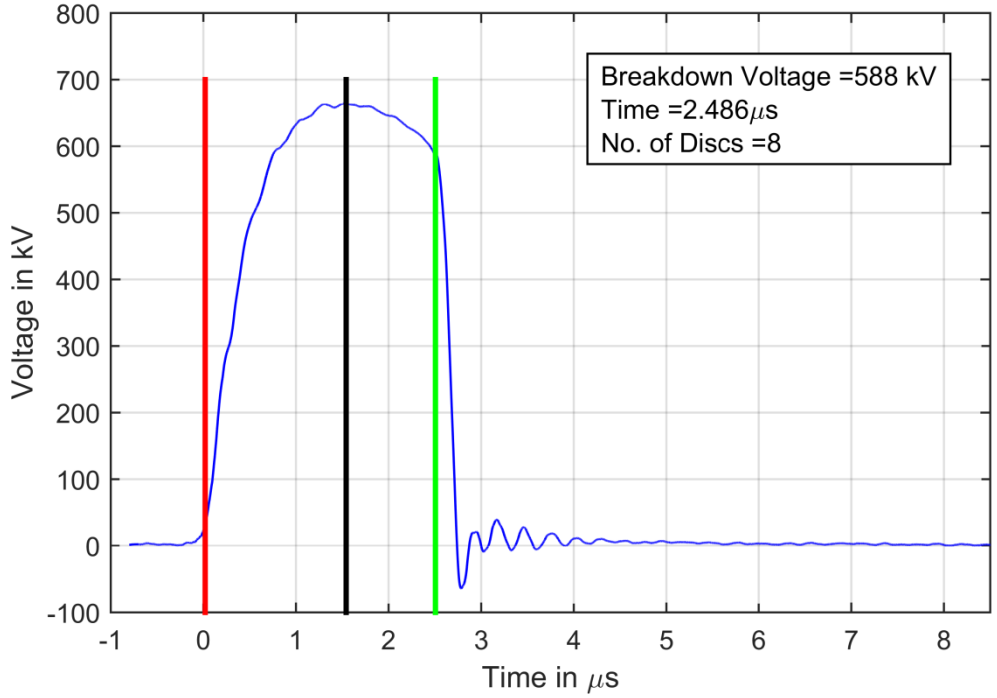
Breakdown Voltage =588 kV
Time =2.486μs
No. of Discs =8
Voltage in kV
Time in μs
800
700
600
500
400
300
200
100
0
-100
-1
0
1
2
3
4
5
6
7
8

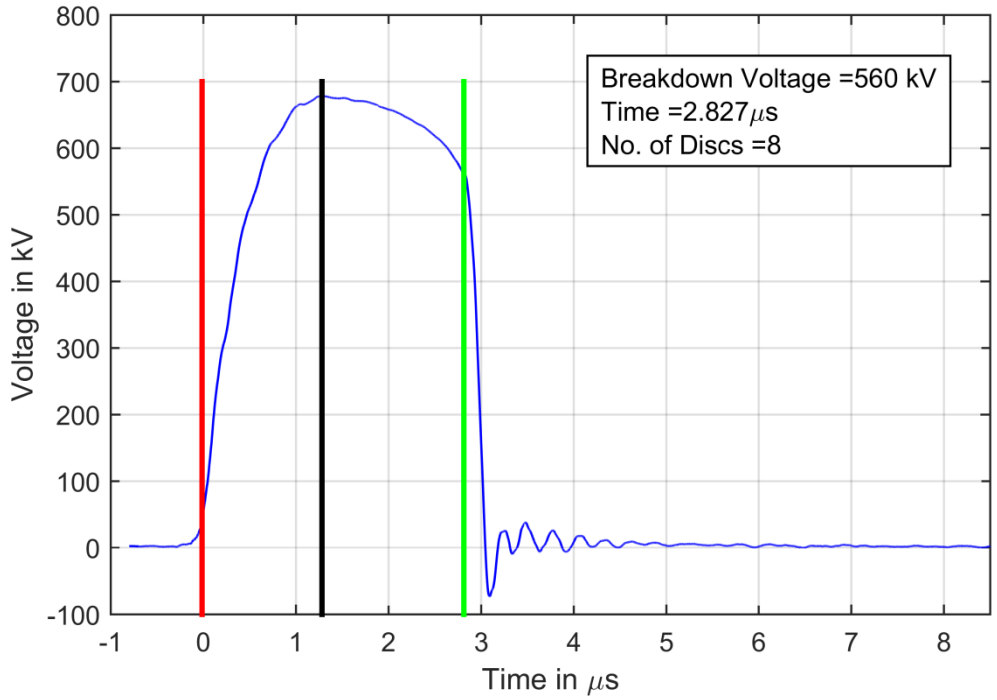
Breakdown Voltage =560 kV
Time =2.827μs
No. of Discs =8
Voltage in kV
Time in μs
800
700
600
500
400
300
200
100
0
-100
-1
0
1
2
3
4
5
6
7
8

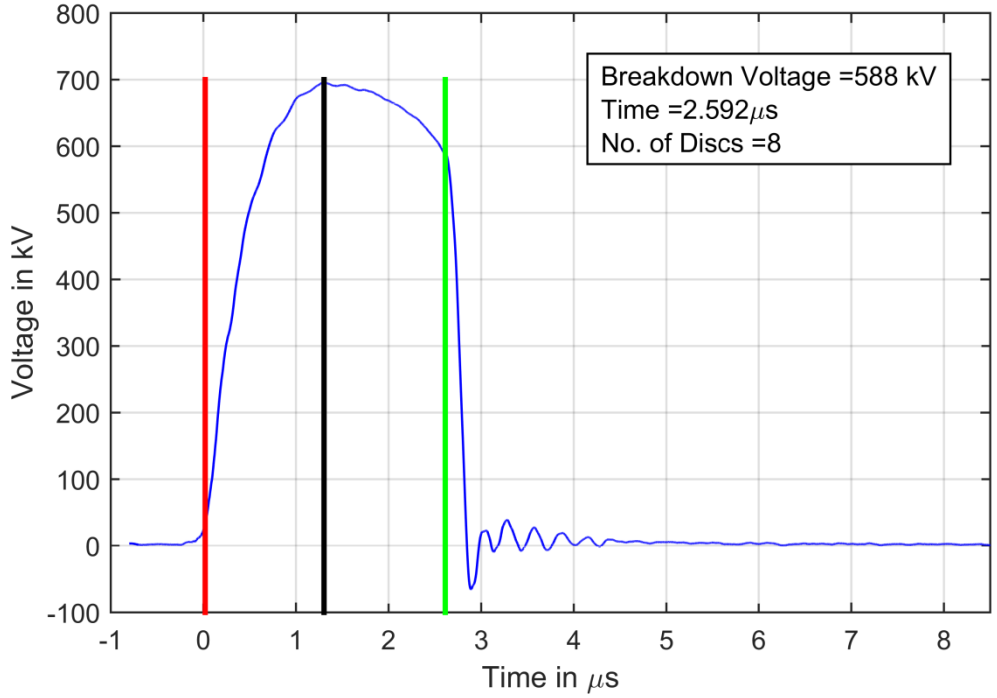
Breakdown Voltage =588 kV
Time =2.592μs
No. of Discs =8
Voltage in kV
Time in μs
800
700
600
500
400
300
200
100
0
-100
-1
0
1
2
3
4
5
6
7
8

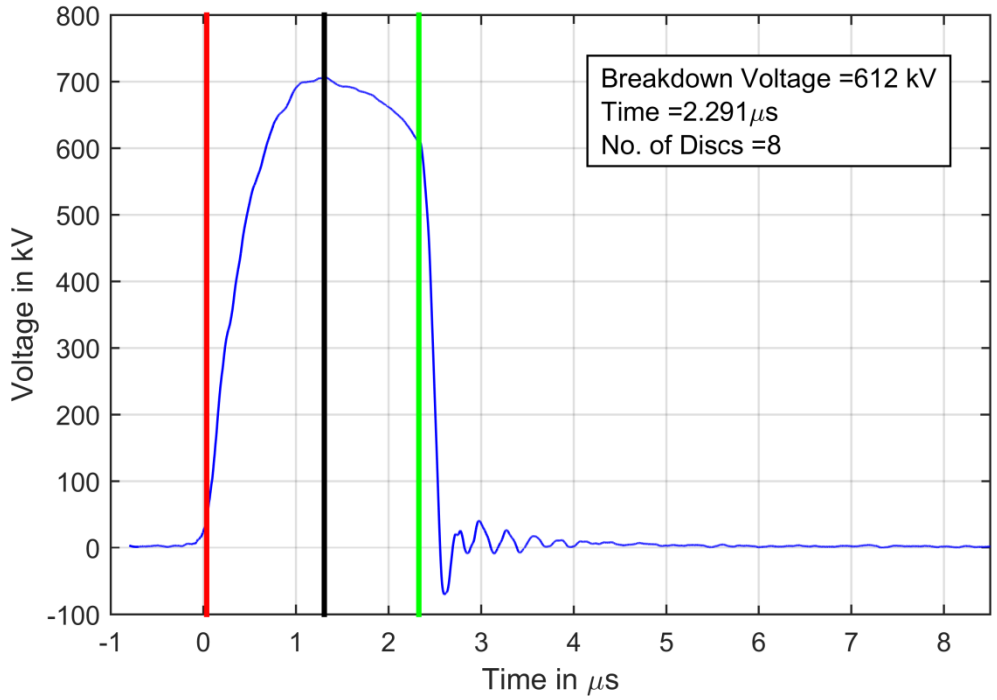
Breakdown Voltage =612 kV
Time =2.291μs
No. of Discs =8
Voltage in kV
Time in μs
800
700
600
500
400
300
200
100
0
-100
-1
0
1
2
3
4
5
6
7
8

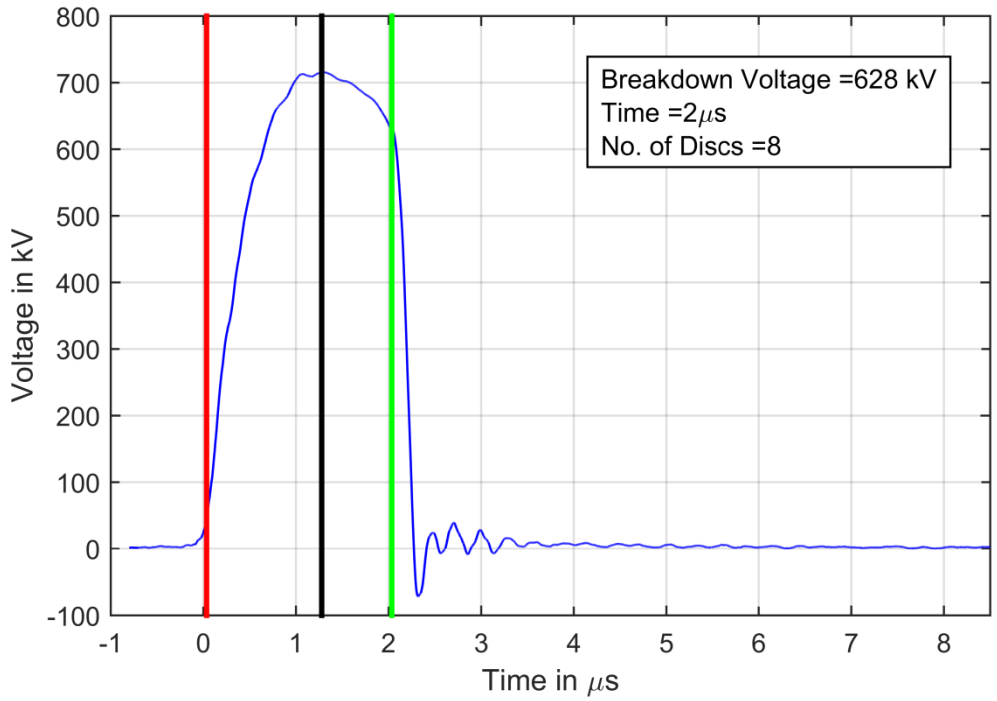
Breakdown Voltage =628 kV
Time =2μs
No. of Discs =8
Voltage in kV
Time in μs
800
700
600
500
400
300
200
100
0
-100
-1
0
1
2
3
4
5
6
7
8

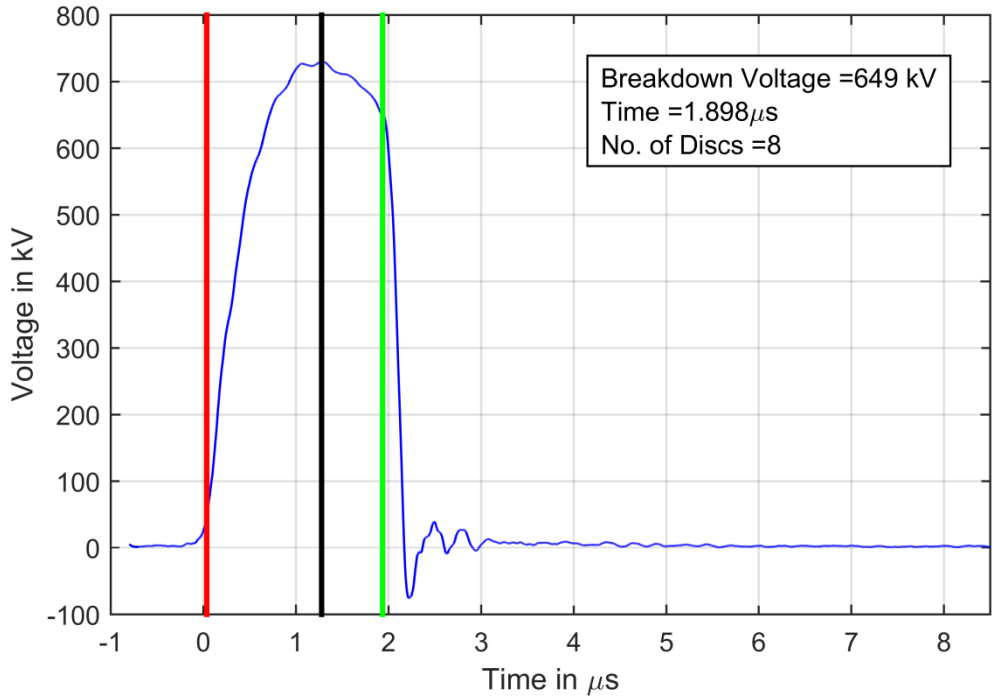
Breakdown Voltage =649 kV
Time =1.898μs
No. of Discs =8
Voltage in kV
Time in μs
800
700
600
500
400
300
200
100
0
-100
-1
0
1
2
3
4
5
6
7
8

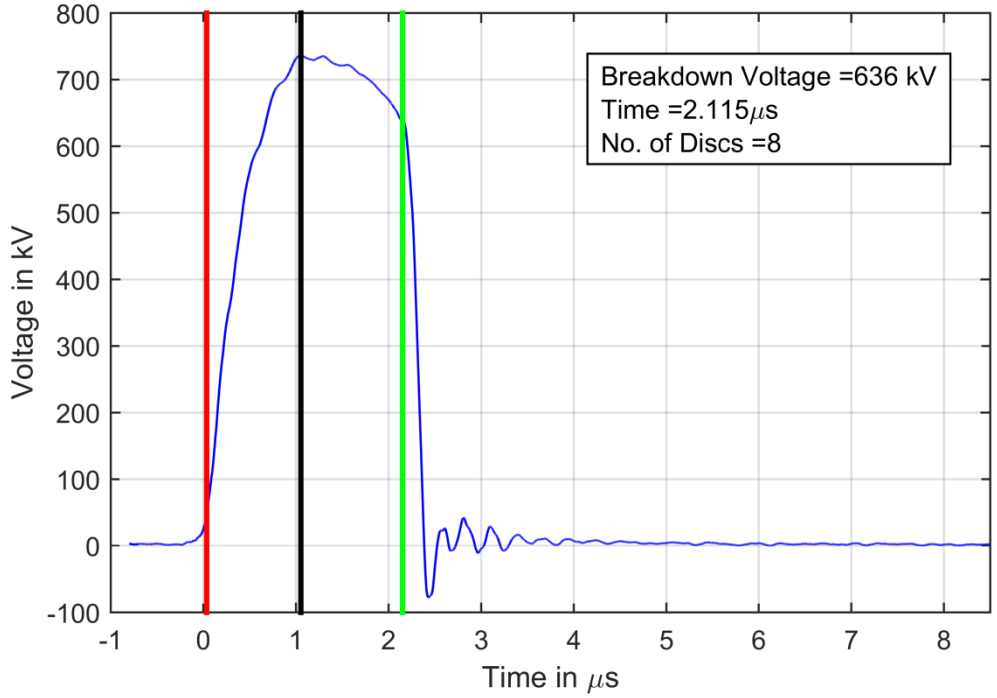
Breakdown Voltage =636 kV
Time =2.115μs
No. of Discs =8
Voltage in kV
Time in μs

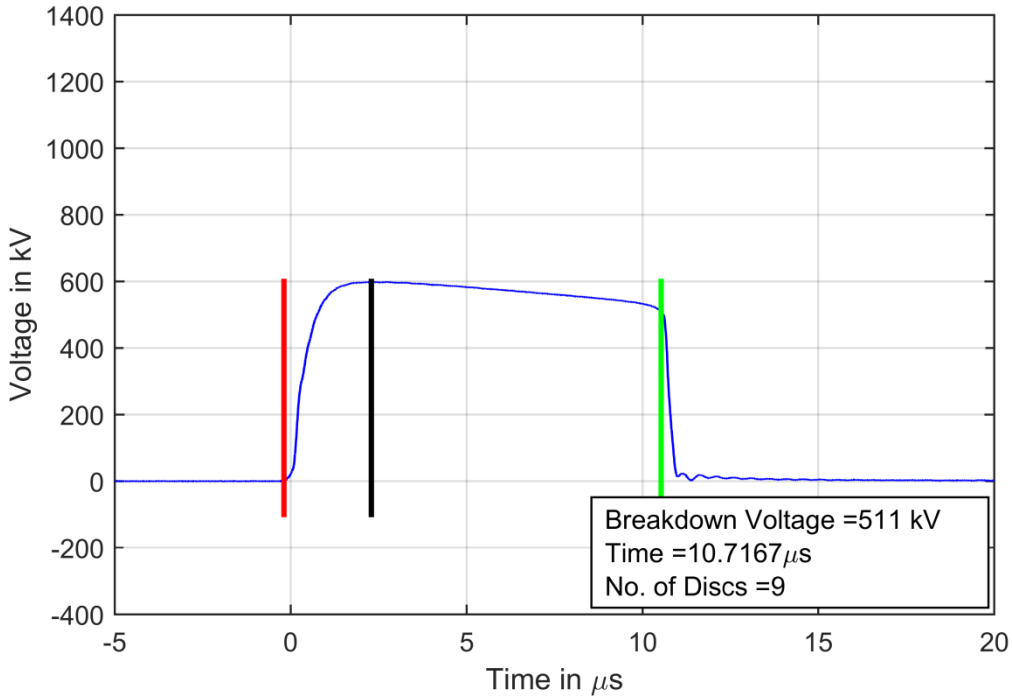
Breakdown Voltage =511 kV
Time =10.7167μs
No. of Discs =9
Voltage in kV
Time in μs

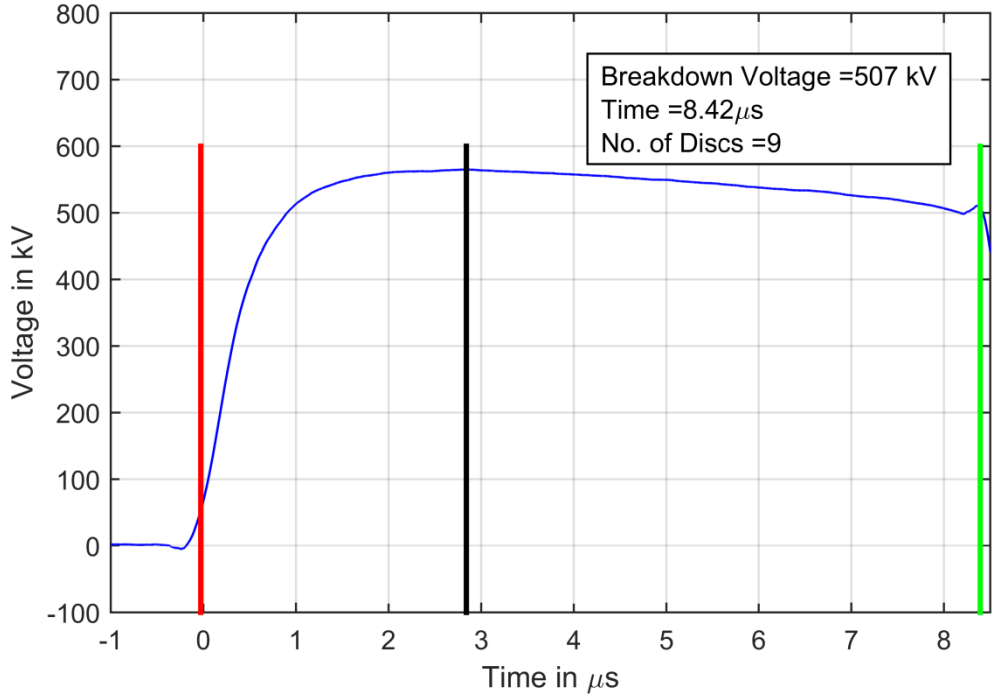
Breakdown Voltage =507 kV
Time =8.42μs
No. of Discs =9
Voltage in kV
Time in μs
800
700
600
500
400
300
200
100
0
-100
-1
0
1
2
3
4
5
6
7
8

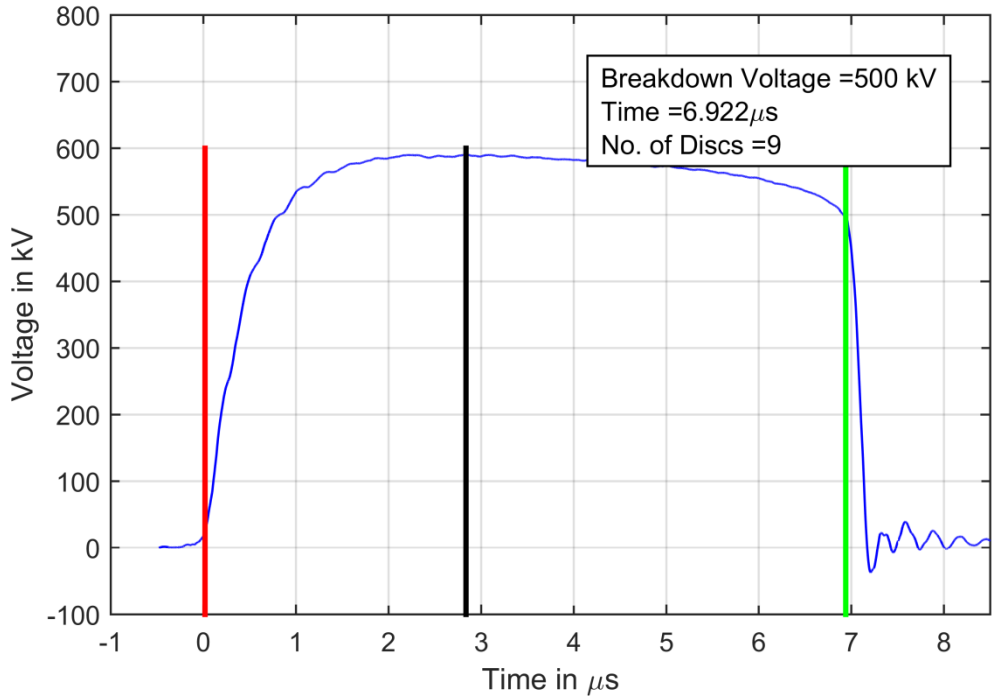
Breakdown Voltage =500 kV
Time =6.922μs
No. of Discs =9
Voltage in kV
Time in μs
800
700
600
500
400
300
200
100
0
-100
-1
0
1
2
3
4
5
6
7
8

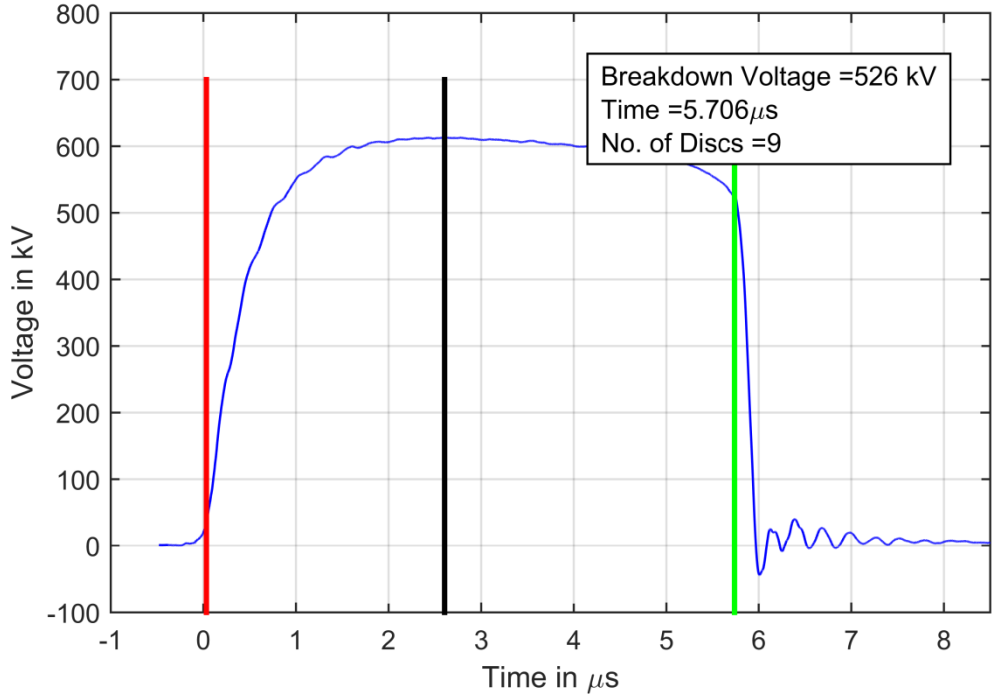
Breakdown Voltage =526 kV
Time =5.706μs
No. of Discs =9
Voltage in kV
Time in μs

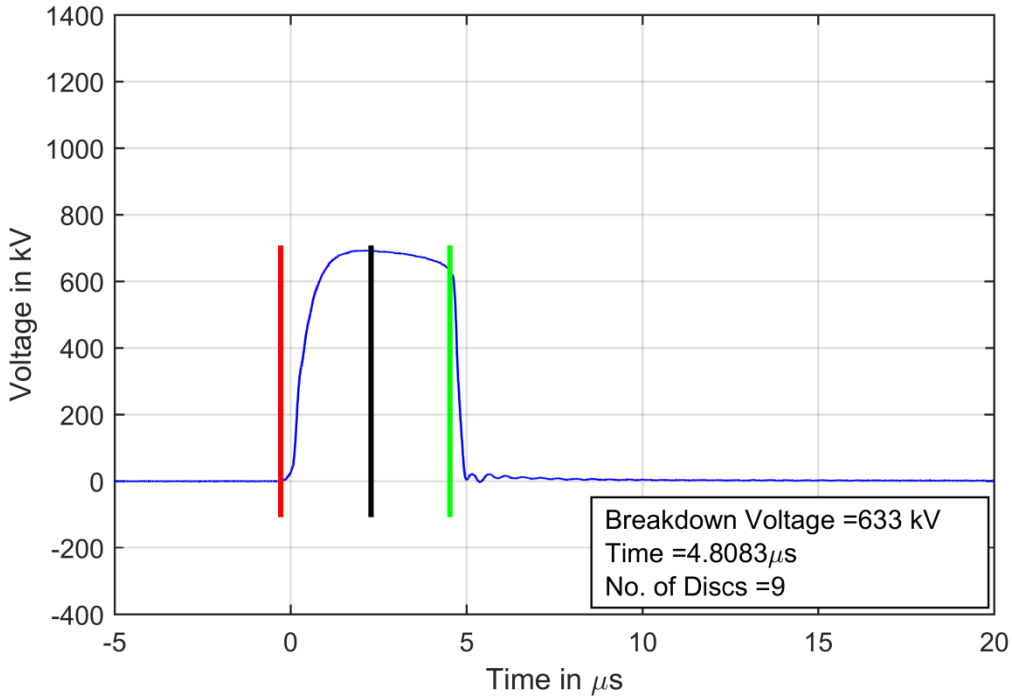
Breakdown Voltage =633 kV
Time =4.8083μs
No. of Discs =9
Voltage in kV
Time in μs

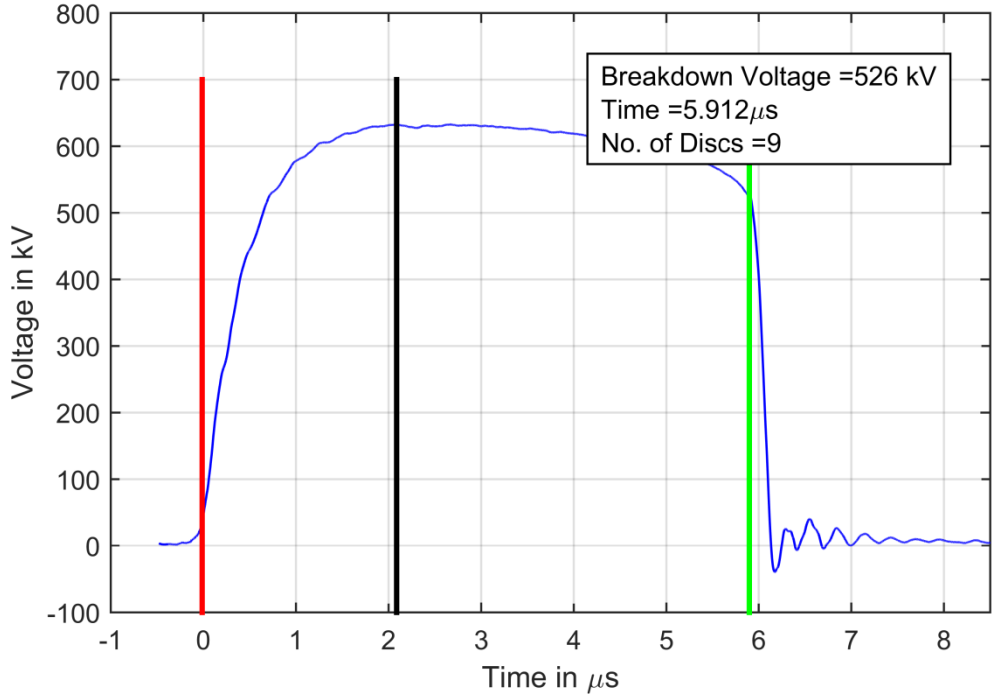
Breakdown Voltage =526 kV
Time =5.912μs
No. of Discs =9
Voltage in kV
Time in μs

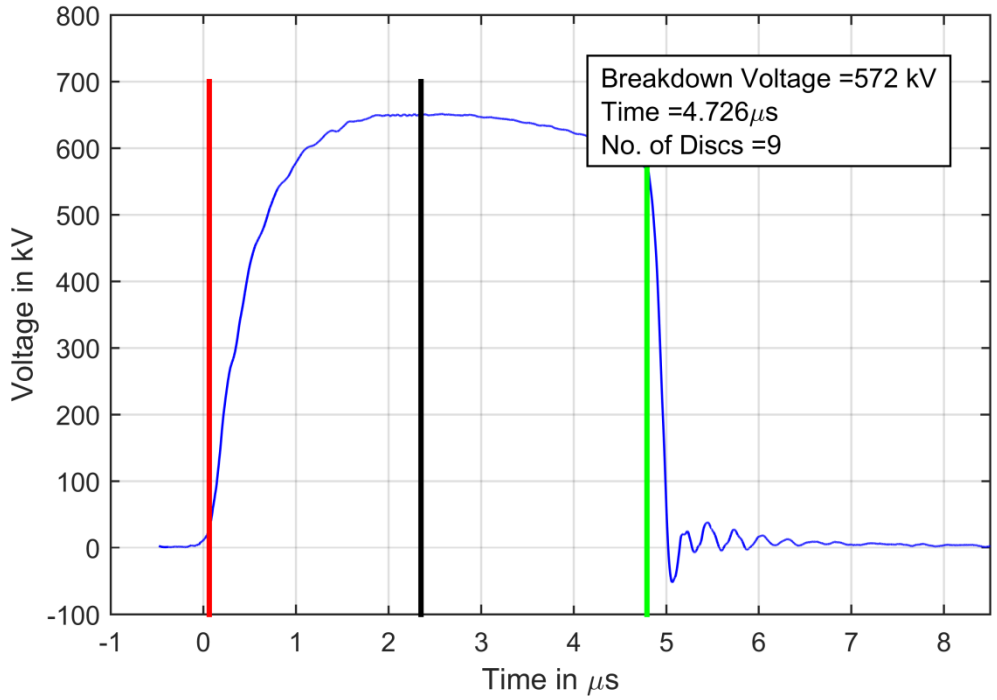
Breakdown Voltage =572 kV
Time =4.726μs
No. of Discs =9
Voltage in kV
Time in μs

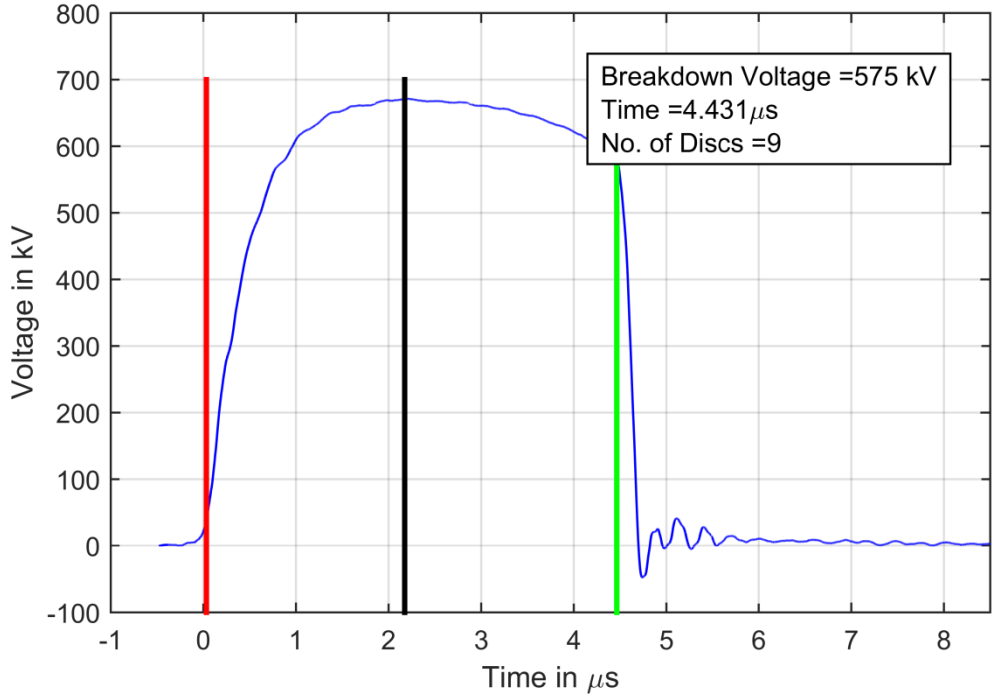
Breakdown Voltage =575 kV
Time =4.431μs
No. of Discs =9
Voltage in kV
Time in μs

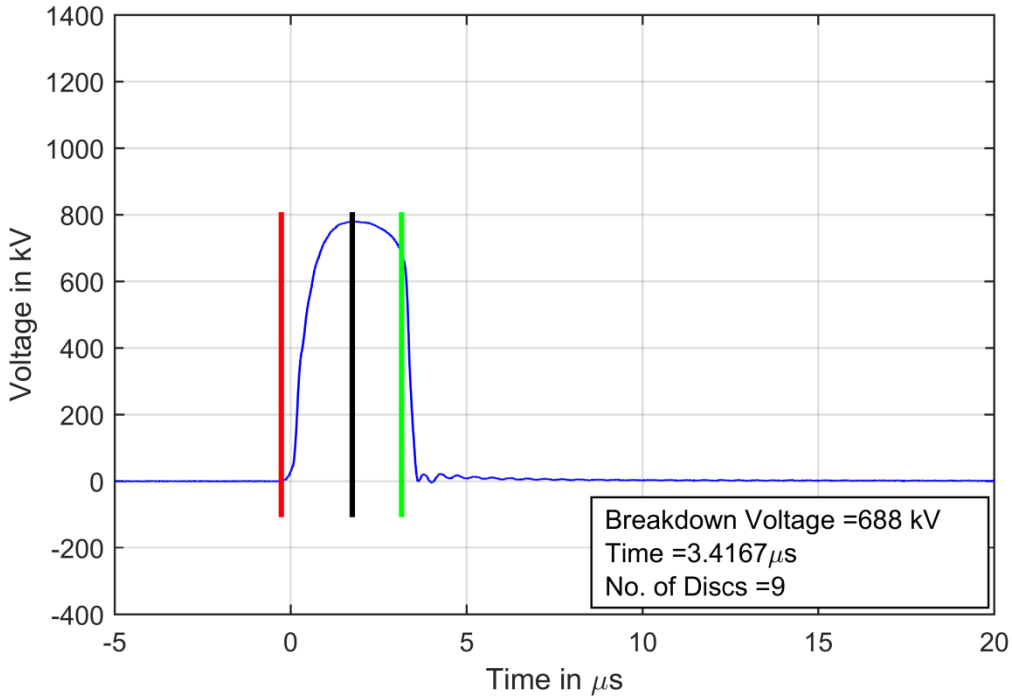
Breakdown Voltage =688 kV
Time =3.4167μs
No. of Discs =9
Voltage in kV
Time in μs

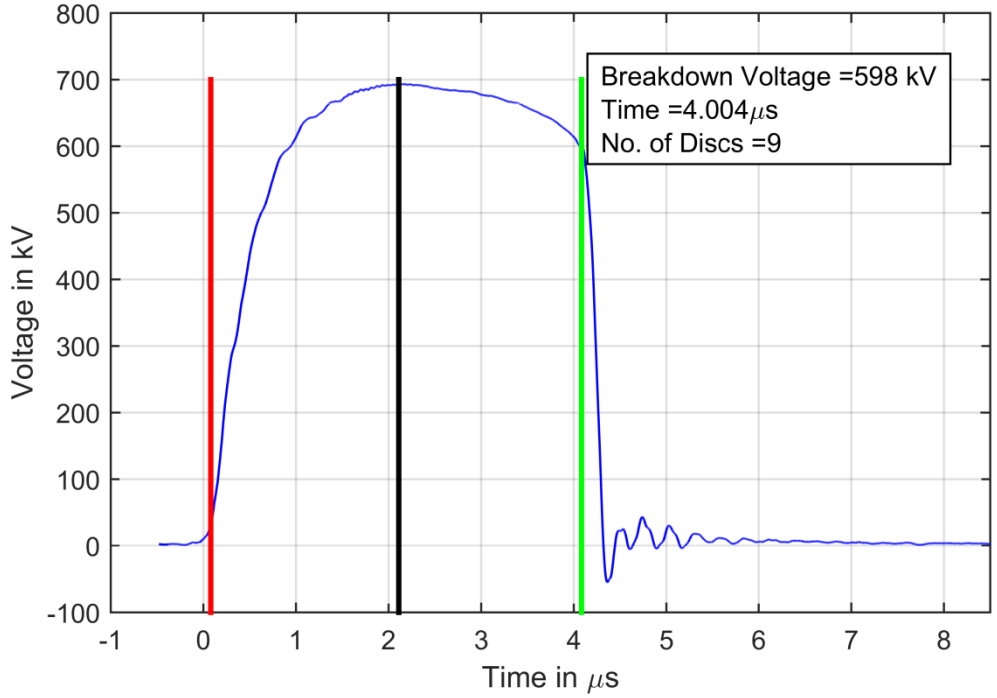
Breakdown Voltage =598 kV
Time =4.004μs
No. of Discs =9
Voltage in kV
Time in μs
800
700
600
500
400
300
200
100
0
-100
-1
0
1
2
3
4
5
6
7
8

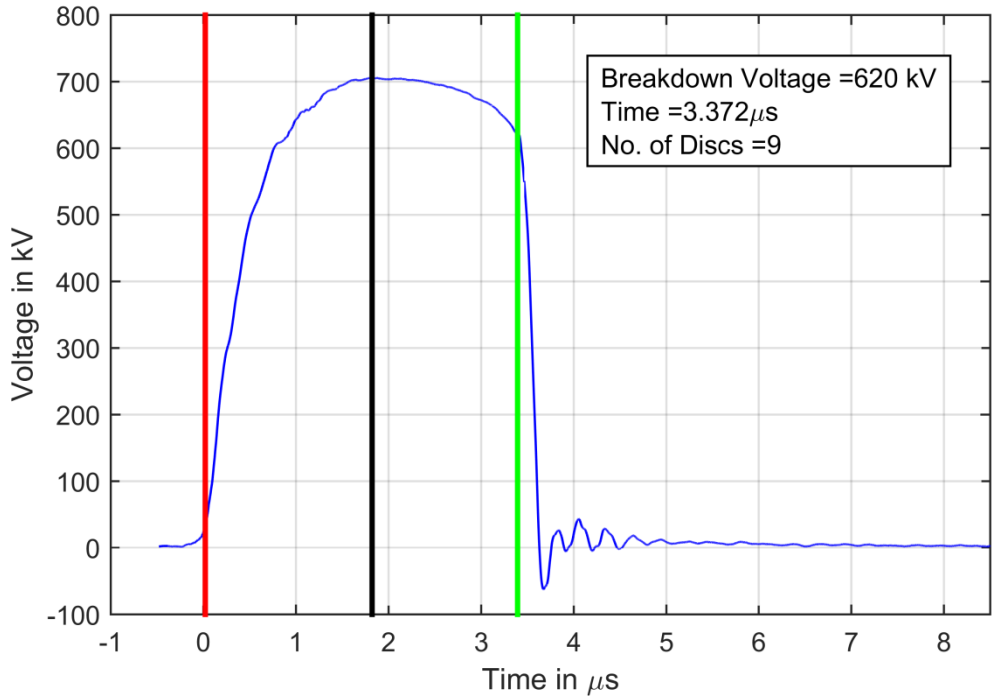
Breakdown Voltage =620 kV
Time =3.372μs
No. of Discs =9
Voltage in kV
Time in μs
800
700
600
500
400
300
200
100
0
-100
-1
0
1
2
3
4
5
6
7
8

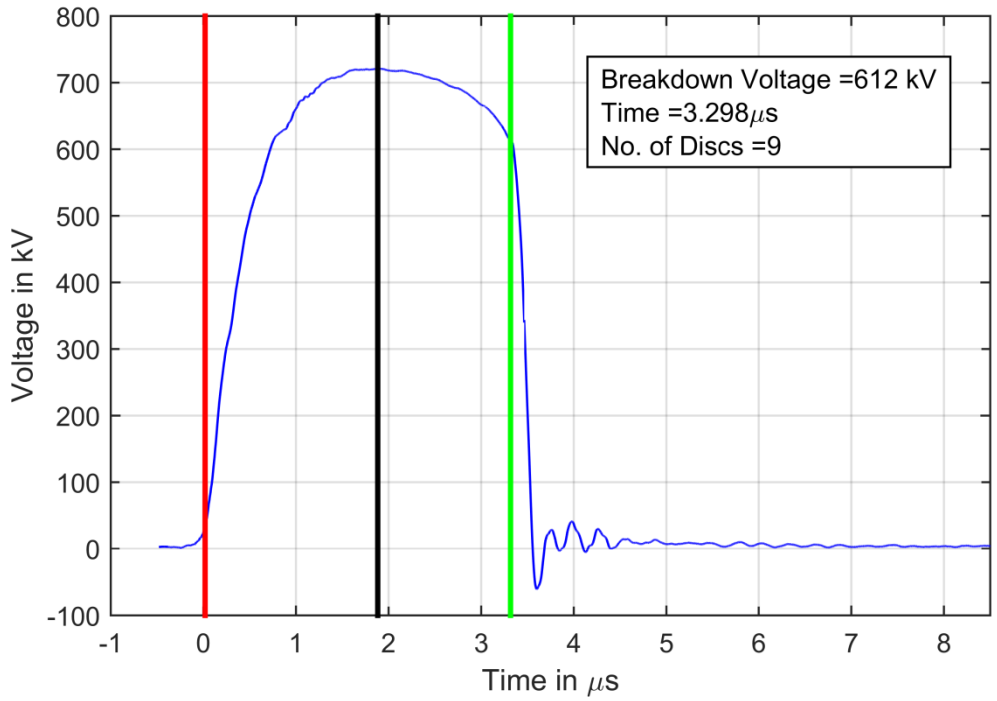
Breakdown Voltage =612 kV
Time =3.298μs
No. of Discs =9
Voltage in kV
Time in μs
800
700
600
500
400
300
200
100
0
-100
-1
0
1
2
3
4
5
6
7
8

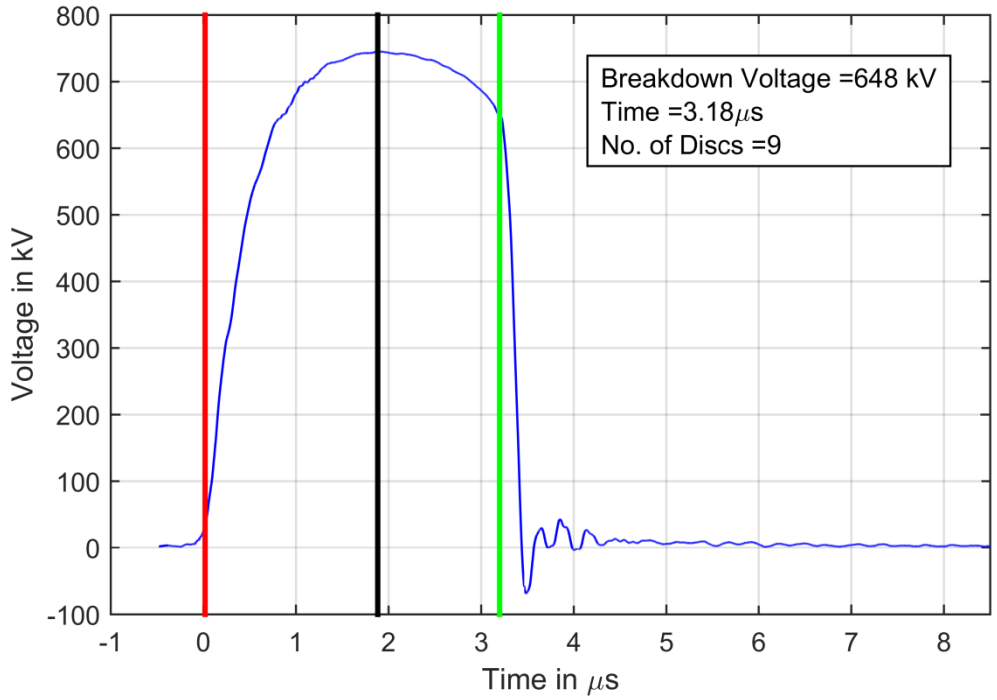
Breakdown Voltage =648 kV
Time =3.18μs
No. of Discs =9
Voltage in kV
Time in μs
800
700
600
500
400
300
200
100
0
-100
-1
0
1
2
3
4
5
6
7
8

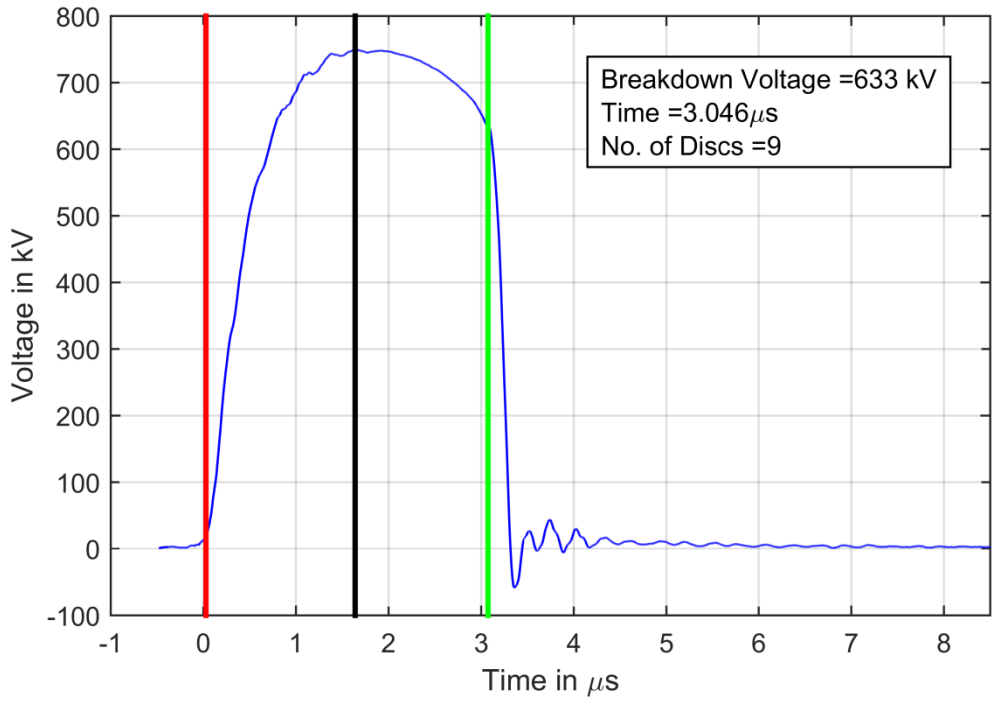
Breakdown Voltage =633 kV
Time =3.046μs
No. of Discs =9
Voltage in kV
Time in μs
800
700
600
500
400
300
200
100
0
-100
-1
0
1
2
3
4
5
6
7
8

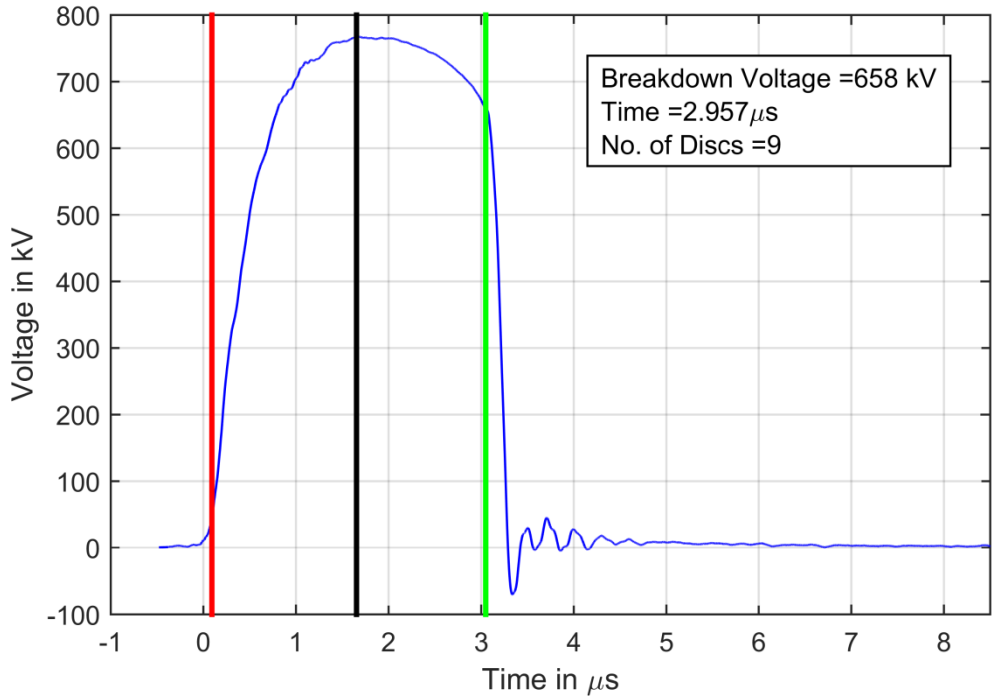
Breakdown Voltage =658 kV
Time =2.957μs
No. of Discs =9
Voltage in kV
Time in μs
800
700
600
500
400
300
200
100
0
-100
-1
0
1
2
3
4
5
6
7
8

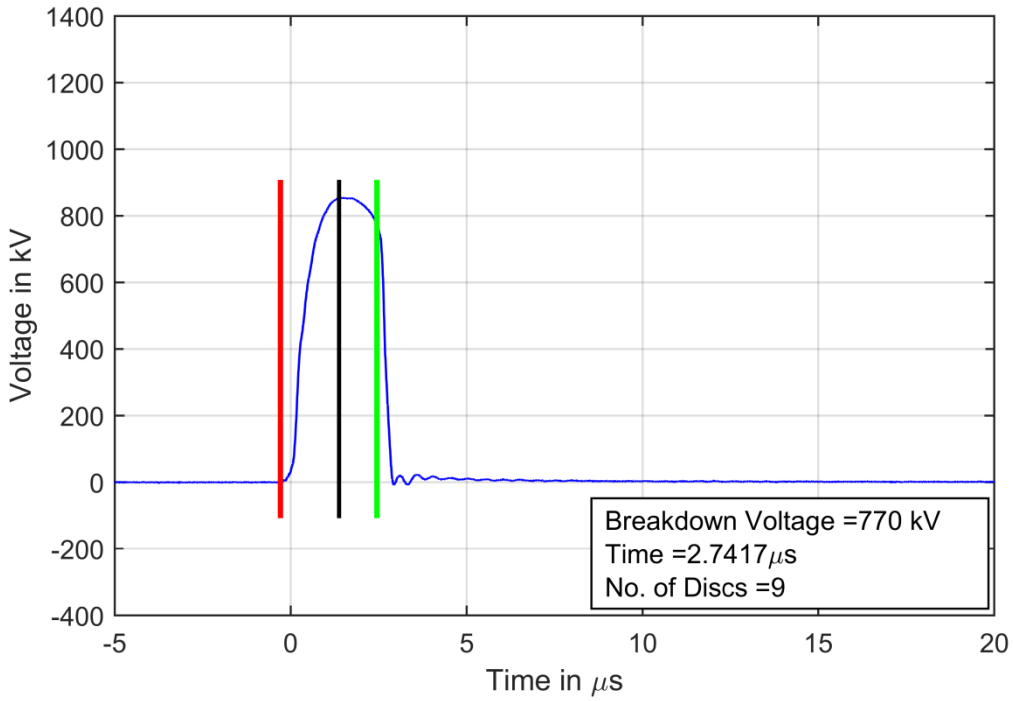
Voltage in kV
Time in μs
Breakdown Voltage =770 kV
Time =2.7417μs
No. of Discs =9

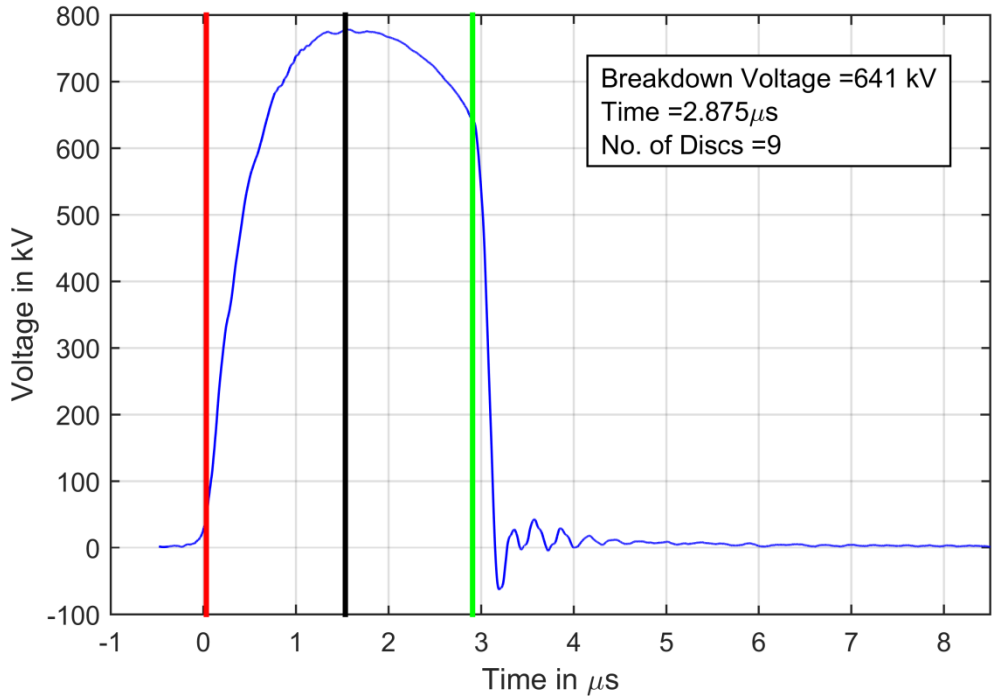
Voltage in kV
Time in μs
Breakdown Voltage =641 kV
Time =2.875μs
No. of Discs =9

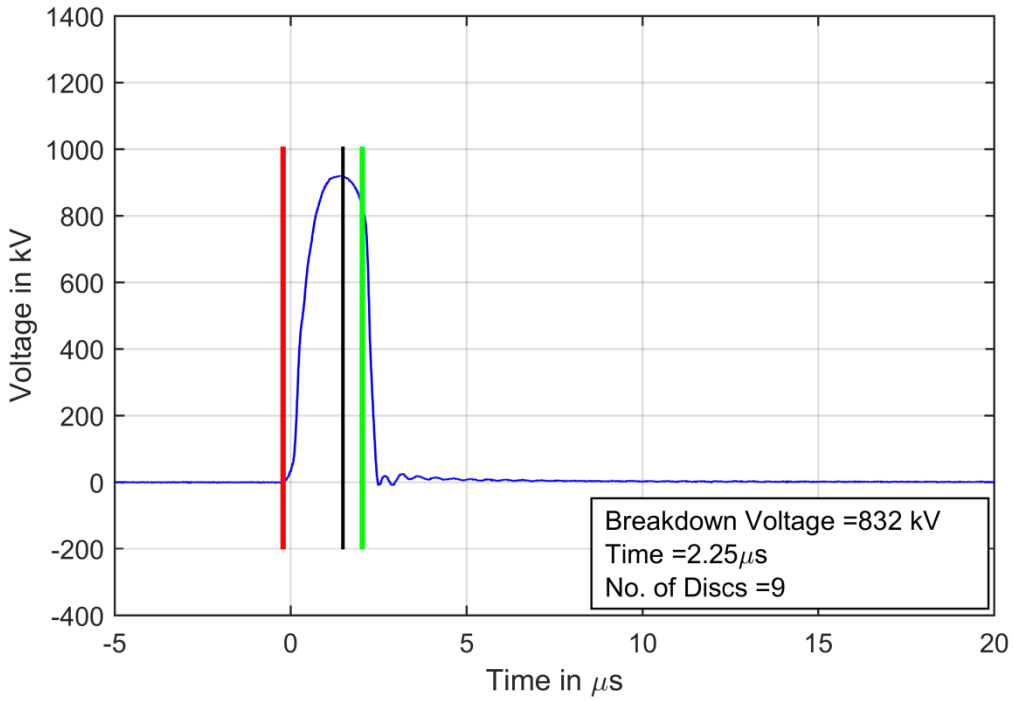
Voltage in kV
Time in μs
Breakdown Voltage =832 kV
Time =2.25μs
No. of Discs =9

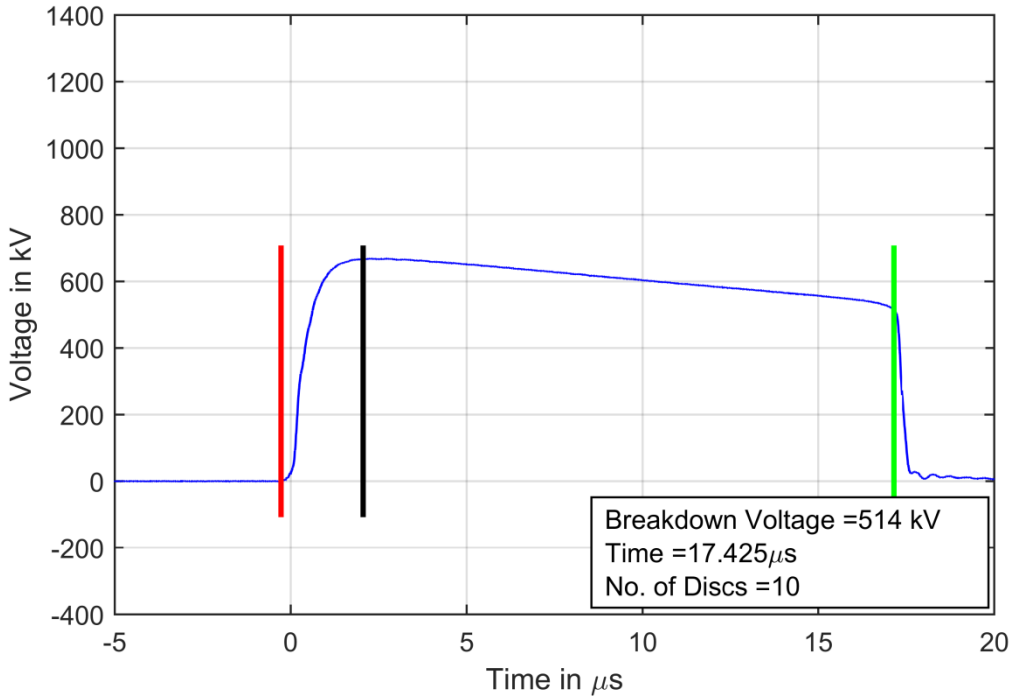
Voltage in kV
Time in μs
Breakdown Voltage =514 kV
Time =17.425μs
No. of Discs =10

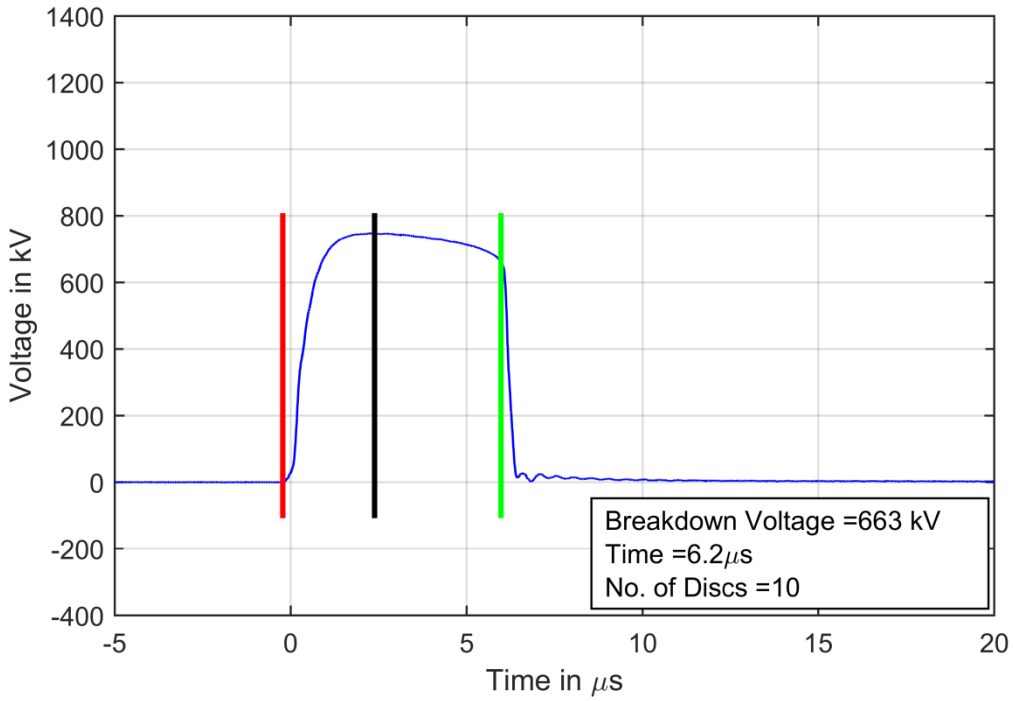
Voltage in kV
Time in μs
Breakdown Voltage =663 kV
Time =6.2μs
No. of Discs =10

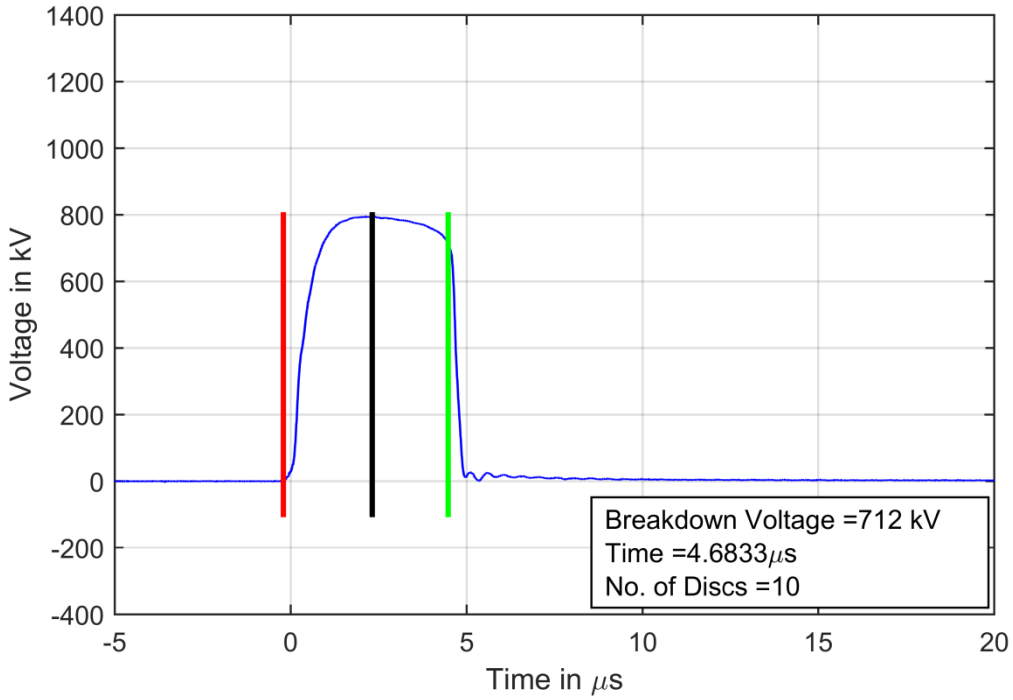
Voltage in kV
Time in μs
Breakdown Voltage =712 kV
Time =4.6833μs
No. of Discs =10

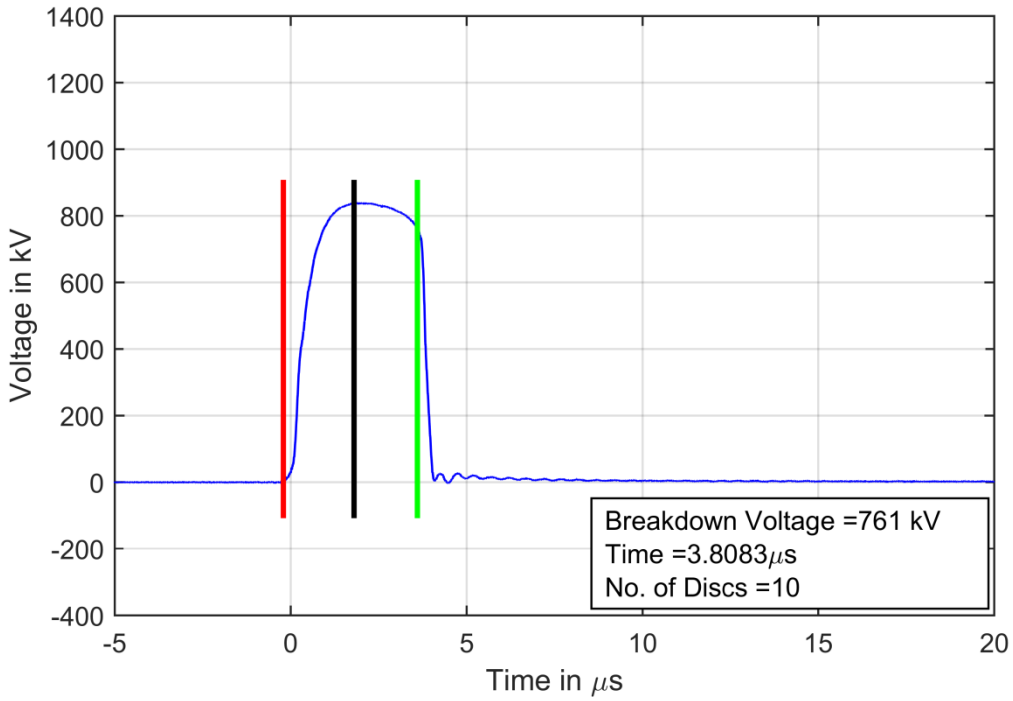
Voltage in kV
Time in μs
Breakdown Voltage =761 kV
Time =3.8083μs
No. of Discs =10

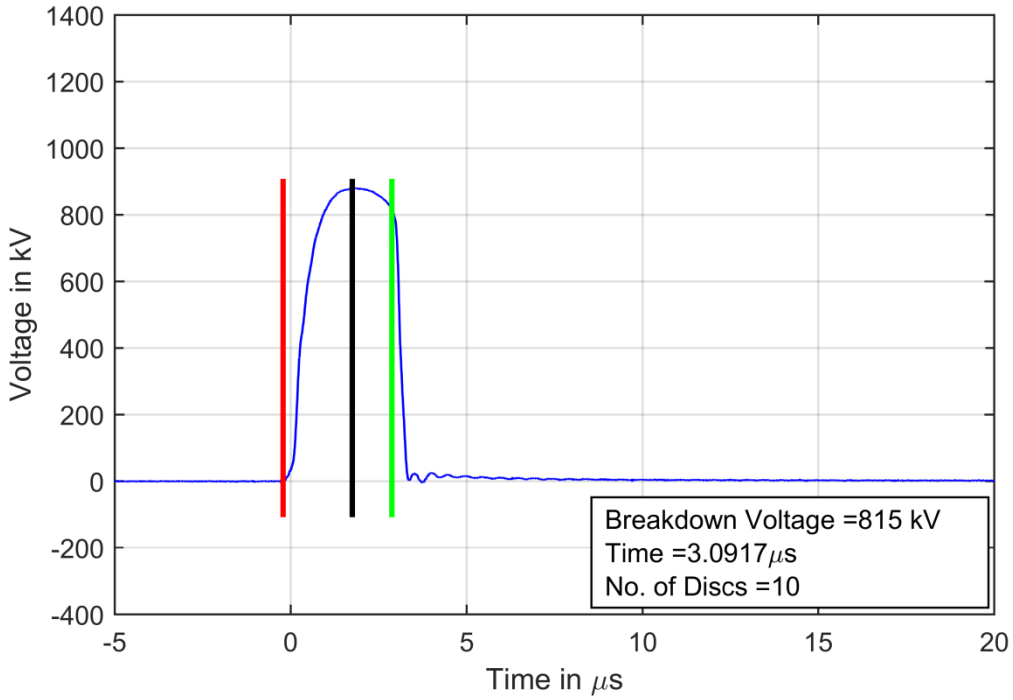
Voltage in kV
Time in μs
Breakdown Voltage =815 kV
Time =3.0917μs
No. of Discs =10

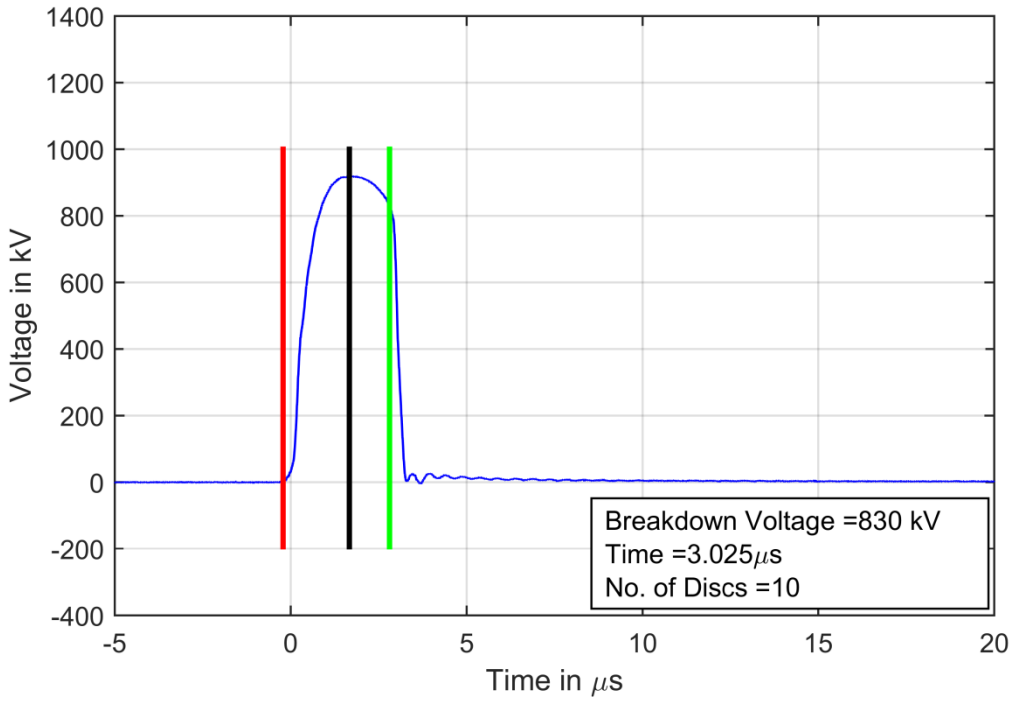
Voltage in kV
Time in μs
Breakdown Voltage =830 kV
Time =3.025μs
No. of Discs =10

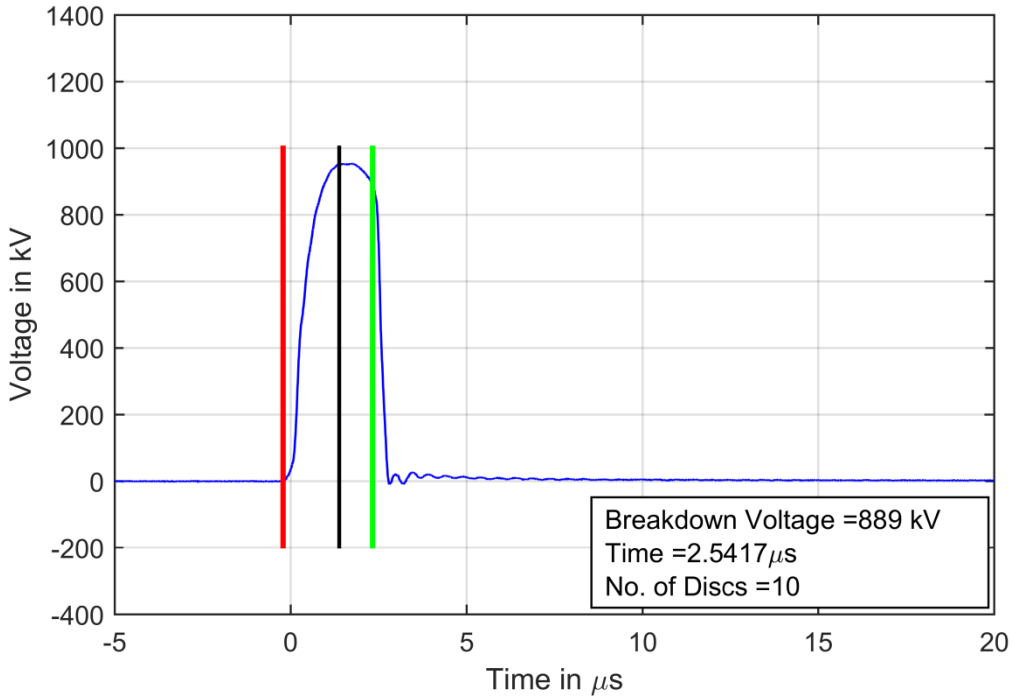
Voltage in kV
Time in μs
Breakdown Voltage =889 kV
Time =2.5417μs
No. of Discs =10

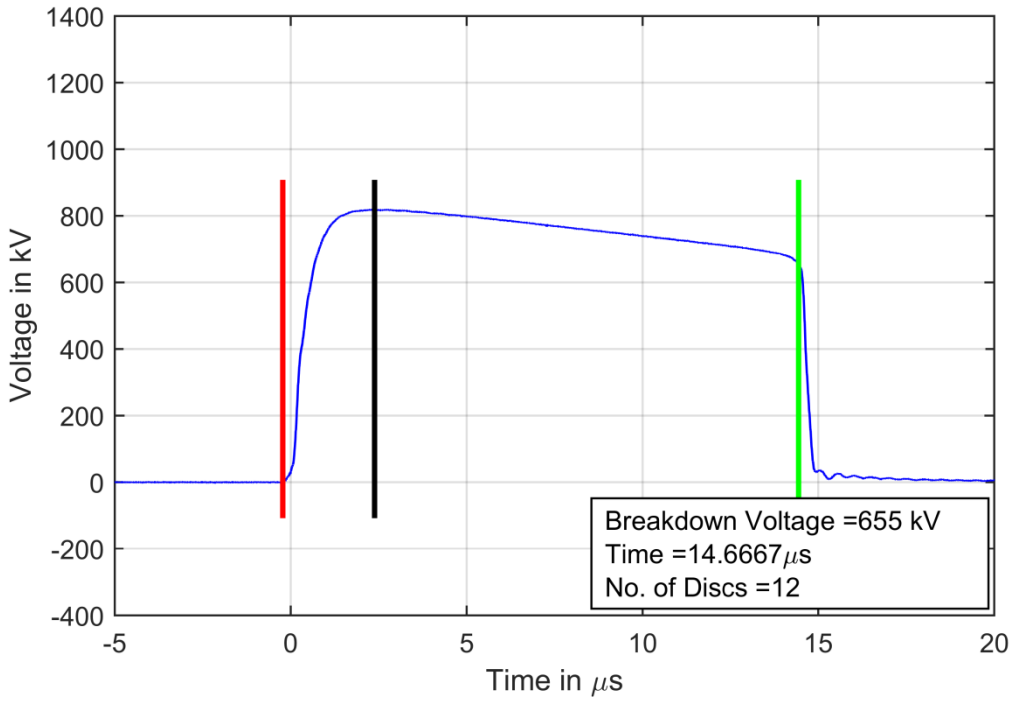
Voltage in kV
Time in μs
Breakdown Voltage =655 kV
Time =14.6667μs
No. of Discs =12

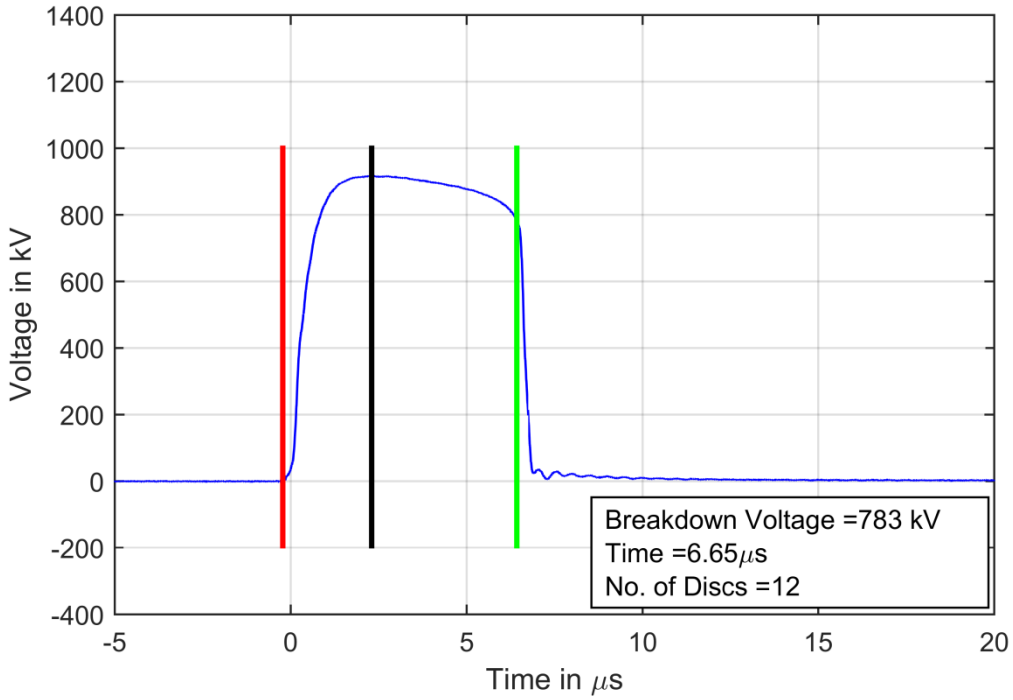
Voltage in kV
Time in μs
Breakdown Voltage =783 kV
Time =6.65μs
No. of Discs =12

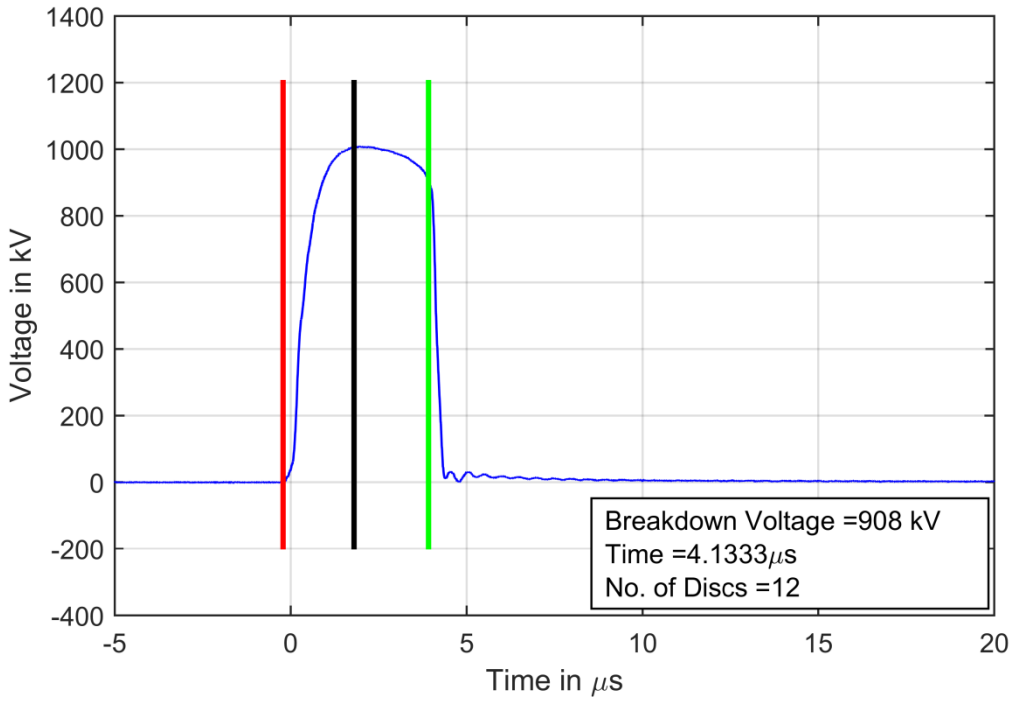
Voltage in kV
Time in μs
Breakdown Voltage =908 kV
Time =4.1333μs
No. of Discs =12

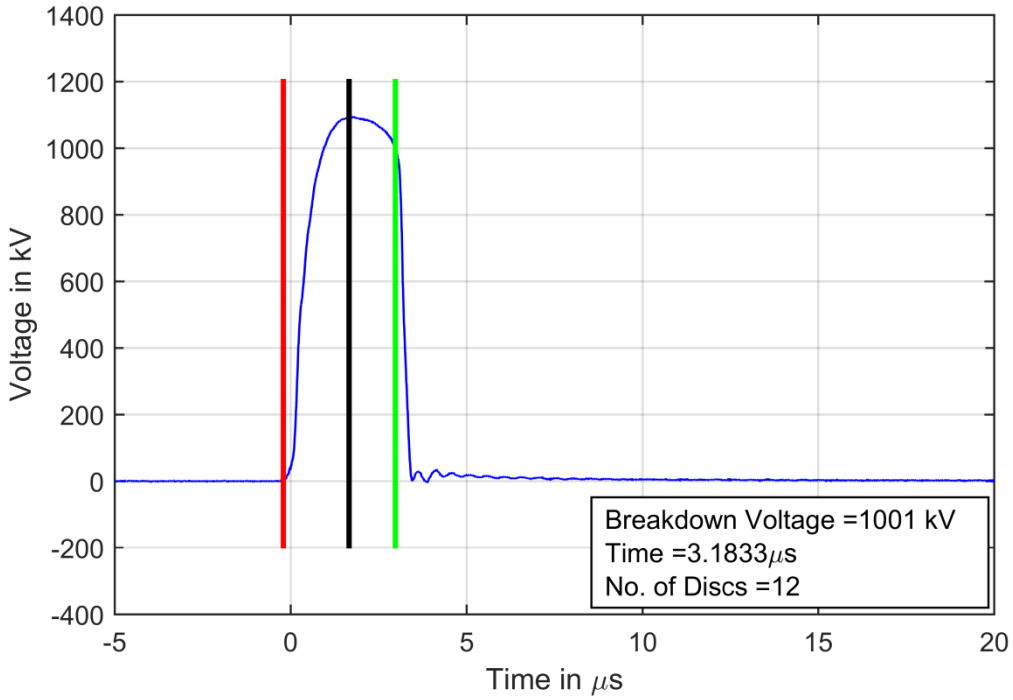
Voltage in kV
Time in μs
Breakdown Voltage =1001 kV
Time =3.1833μs
No. of Discs =12

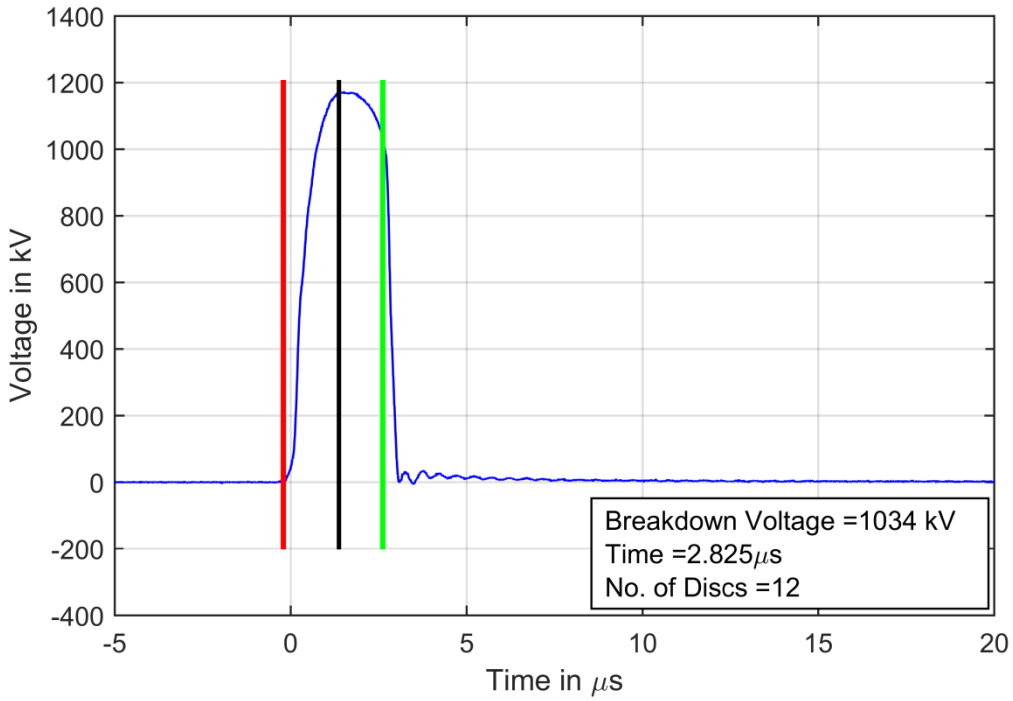
Voltage in kV
Time in μs
Breakdown Voltage =1034 kV
Time =2.825μs
No. of Discs =12

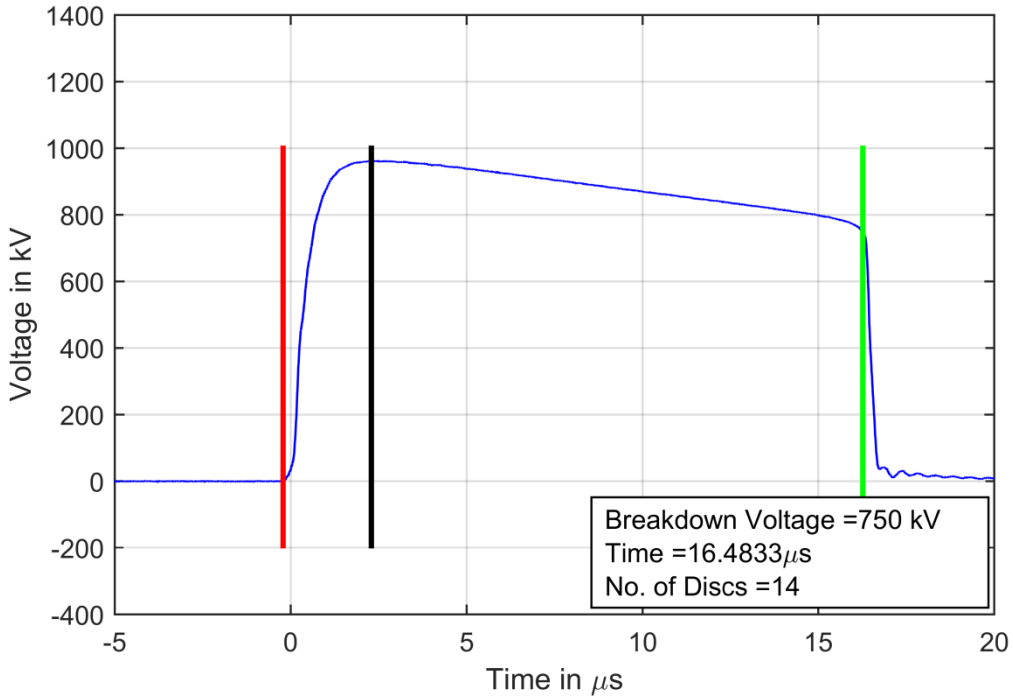
Voltage in kV
Time in μs
Breakdown Voltage =750 kV
Time =16.4833μs
No. of Discs =14

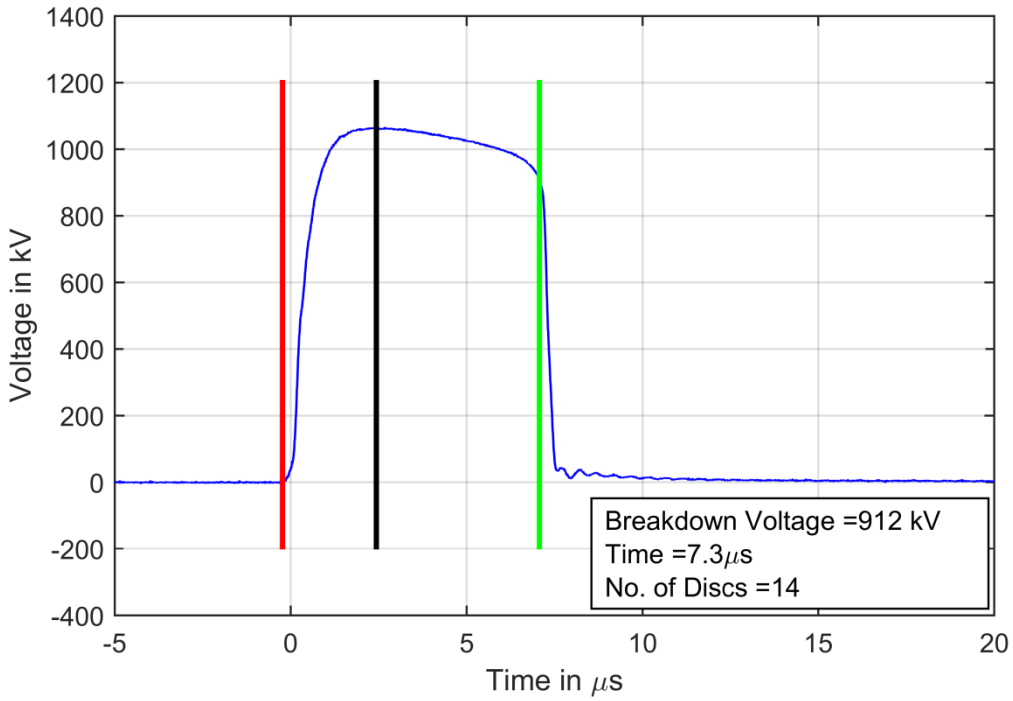
Voltage in kV
Time in μs
Breakdown Voltage =912 kV
Time =7.3μs
No. of Discs =14

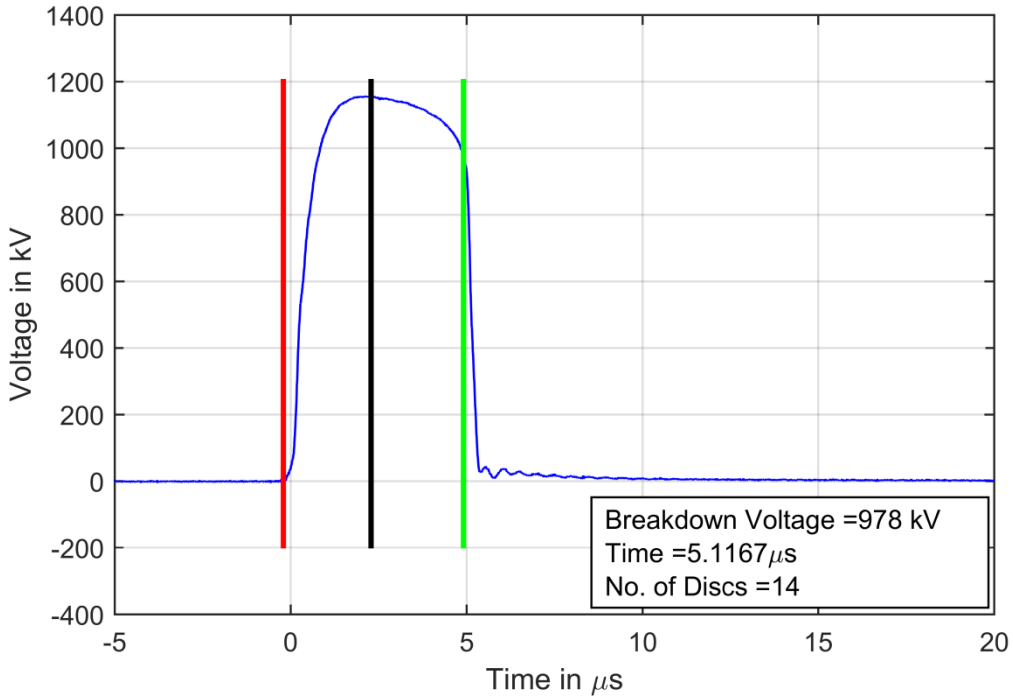
Voltage in kV
Time in μs
Breakdown Voltage =978 kV
Time =5.1167μs
No. of Discs =14

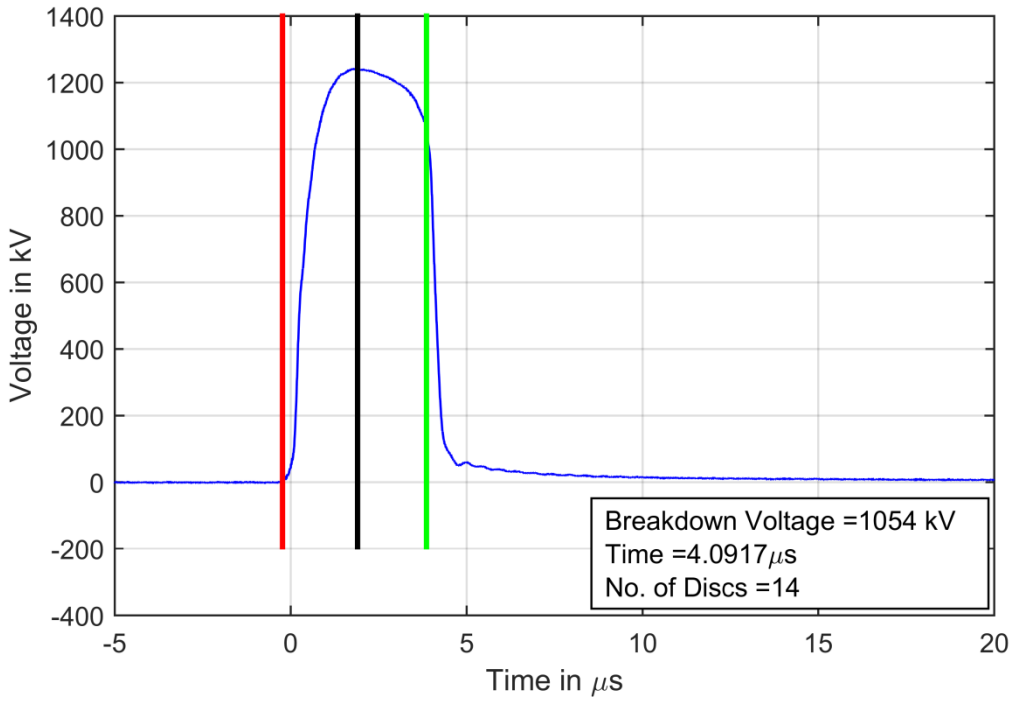
Voltage in kV
Time in μs
Breakdown Voltage =1054 kV
Time =4.0917μs
No. of Discs =14

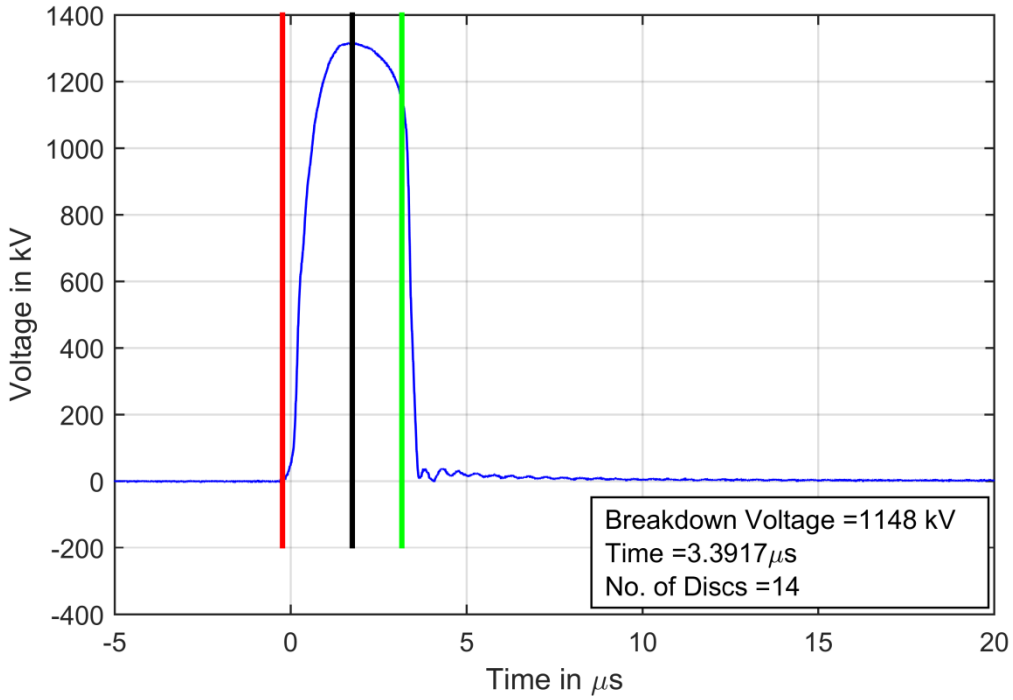
Voltage in kV
Time in μs
Breakdown Voltage =1148 kV
Time =3.3917μs
No. of Discs =14

C.5: RESULTS OF FLASHOVER TESTS FOR NEGATIVE POLARITY

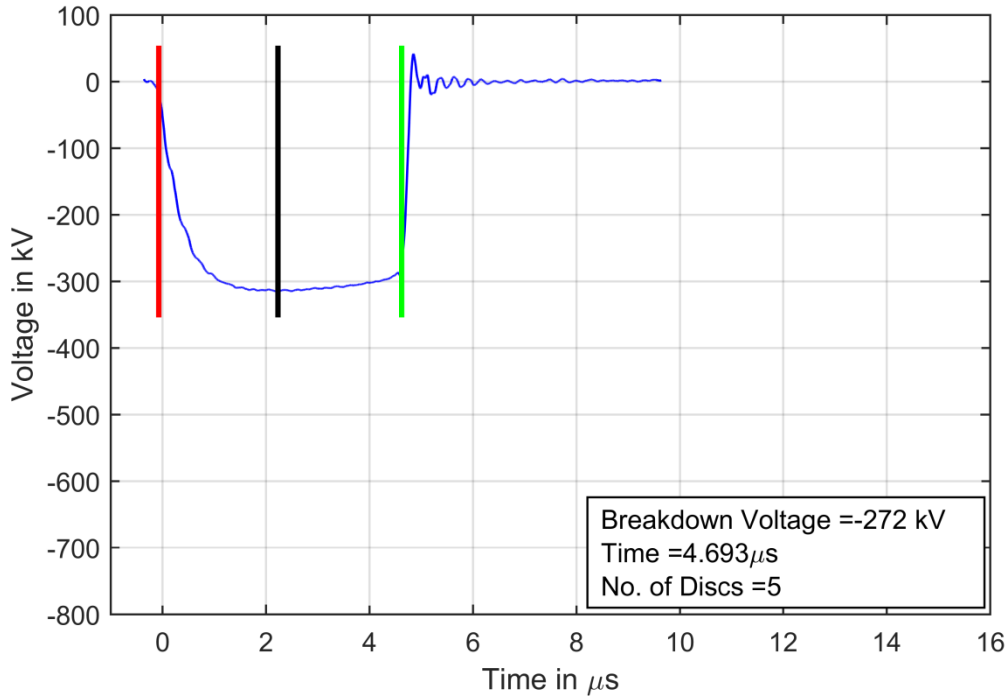

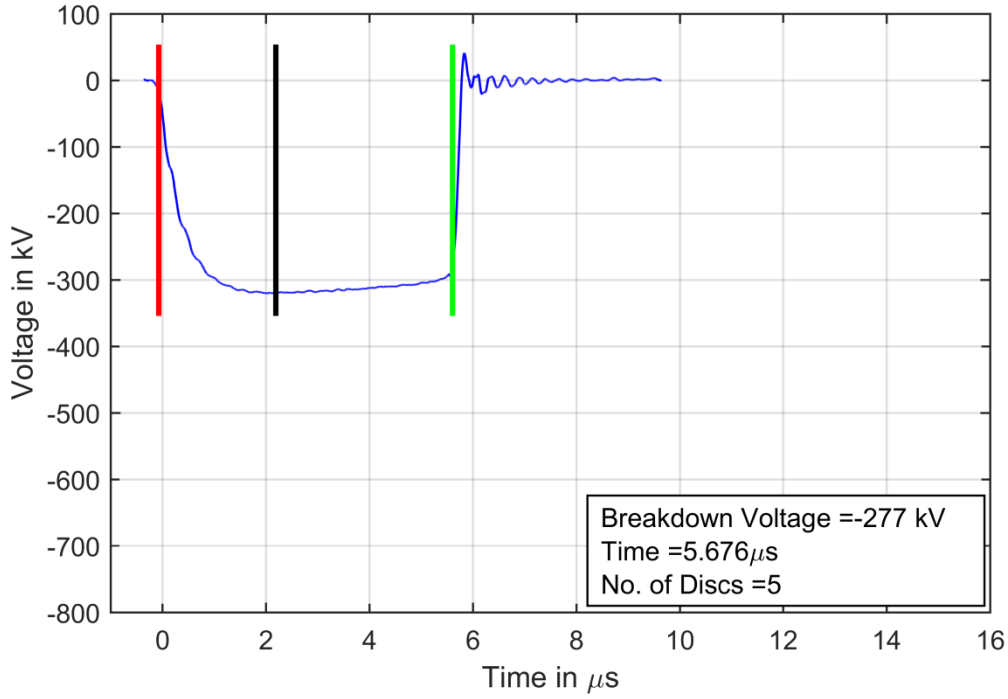

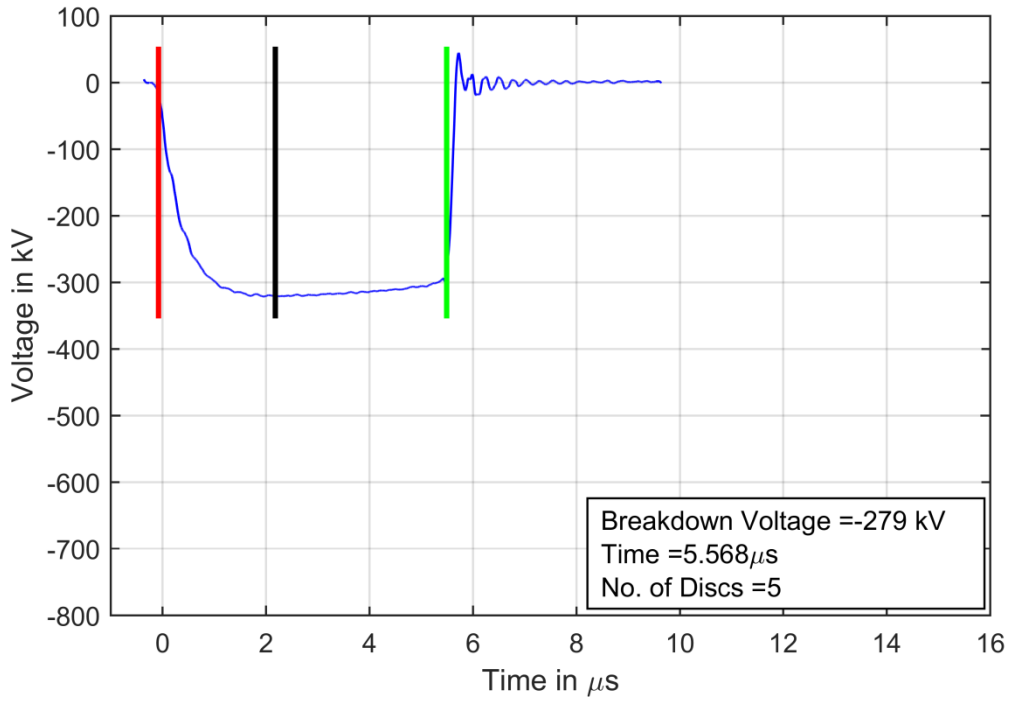
Voltage in kV
Time in μs
Breakdown Voltage =-279 kV
Time =5.568μs
No. of Discs =5

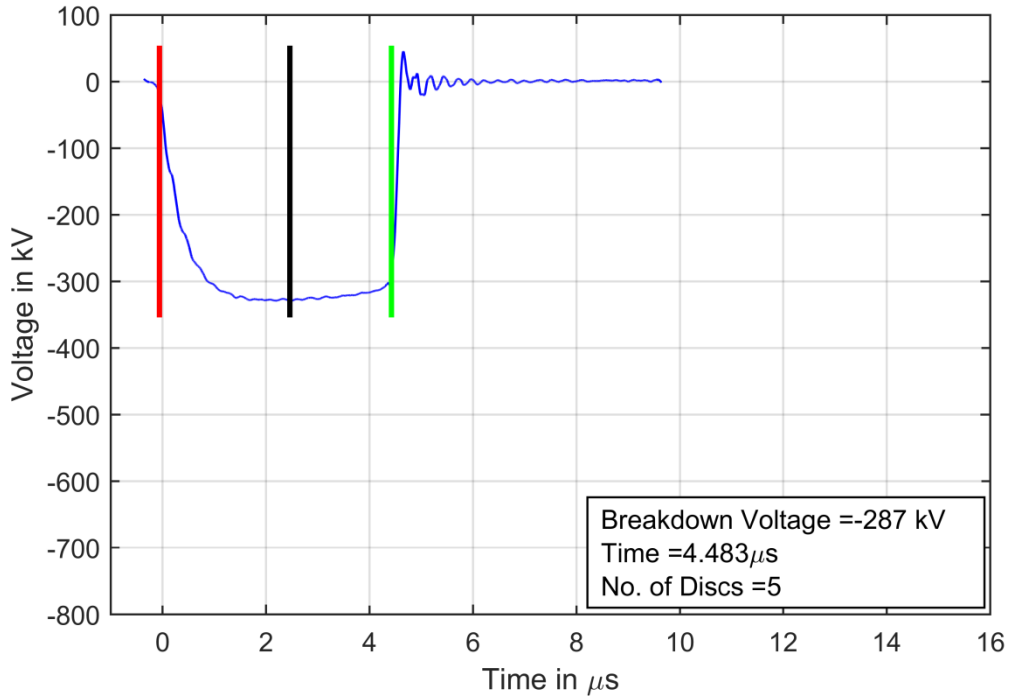
Voltage in kV
Time in μs
Breakdown Voltage =-287 kV
Time =4.483μs
No. of Discs =5

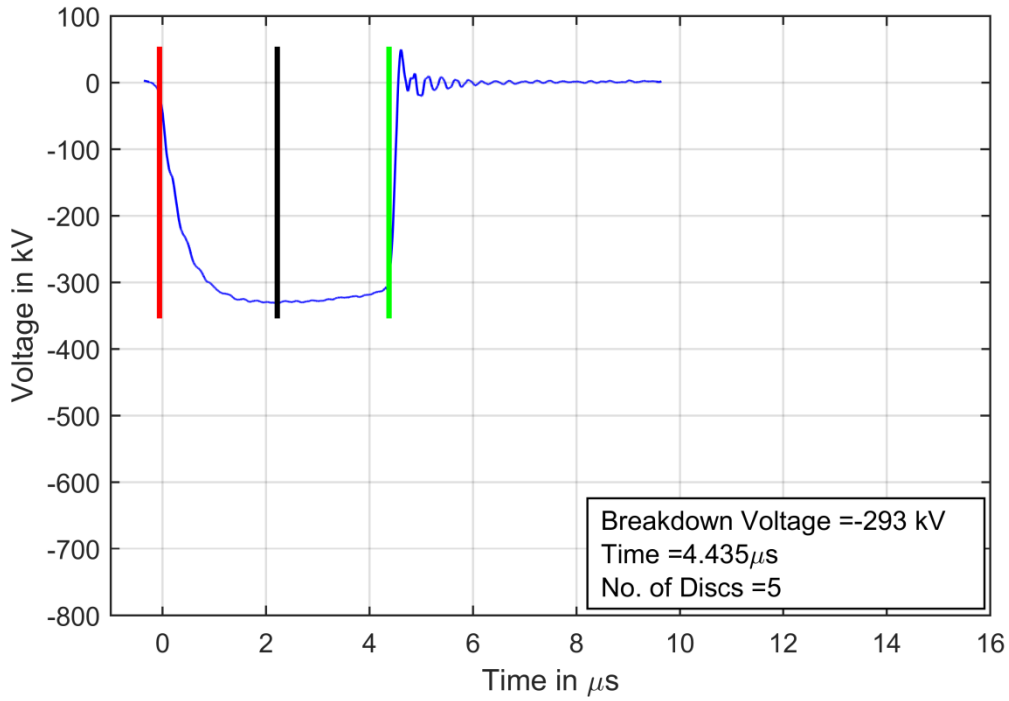
Voltage in kV
Time in μs
Breakdown Voltage =-293 kV
Time =4.435μs
No. of Discs =5

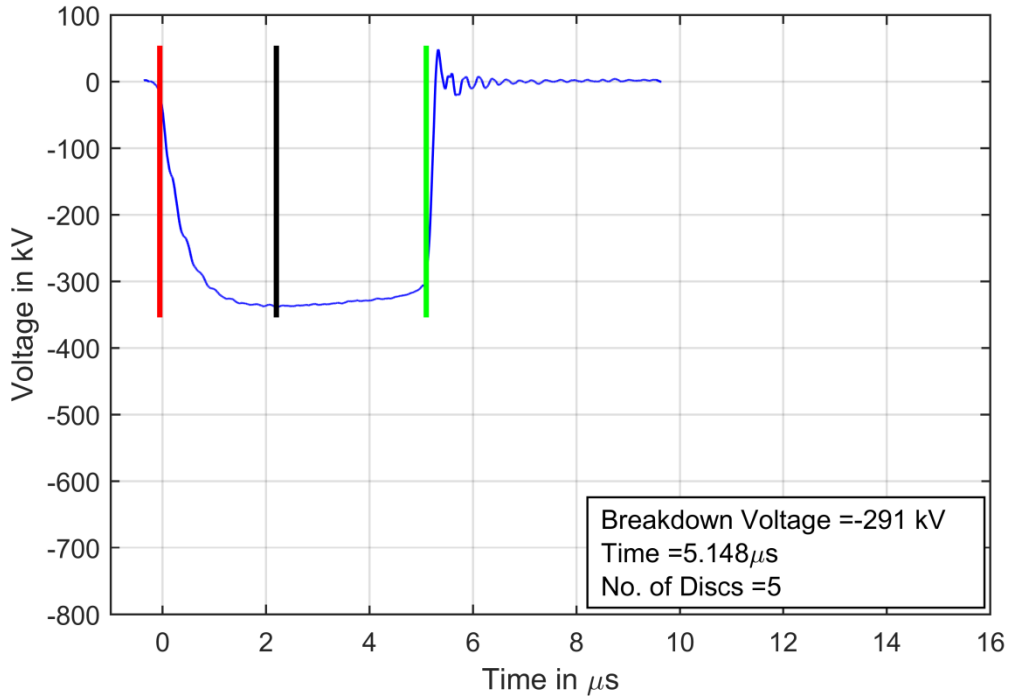
Voltage in kV
Time in μs
Breakdown Voltage =-291 kV
Time =5.148μs
No. of Discs =5

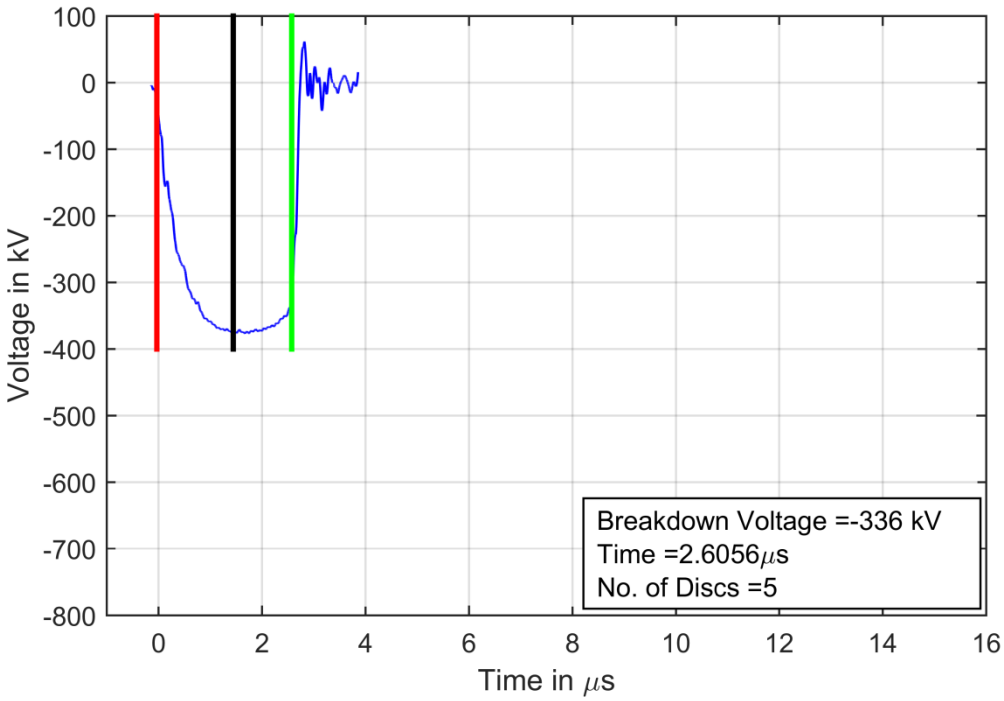
Voltage in kV
Time in μs
Breakdown Voltage =-336 kV
Time =2.6056μs
No. of Discs =5

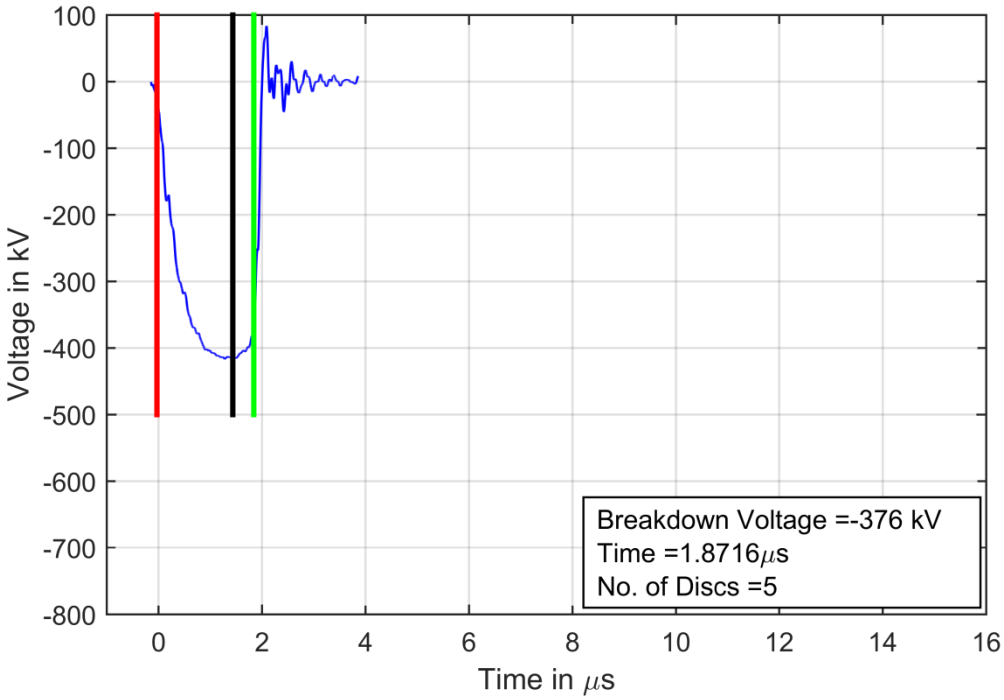
Voltage in kV
Time in μs
Breakdown Voltage =-376 kV
Time =1.8716μs
No. of Discs =5

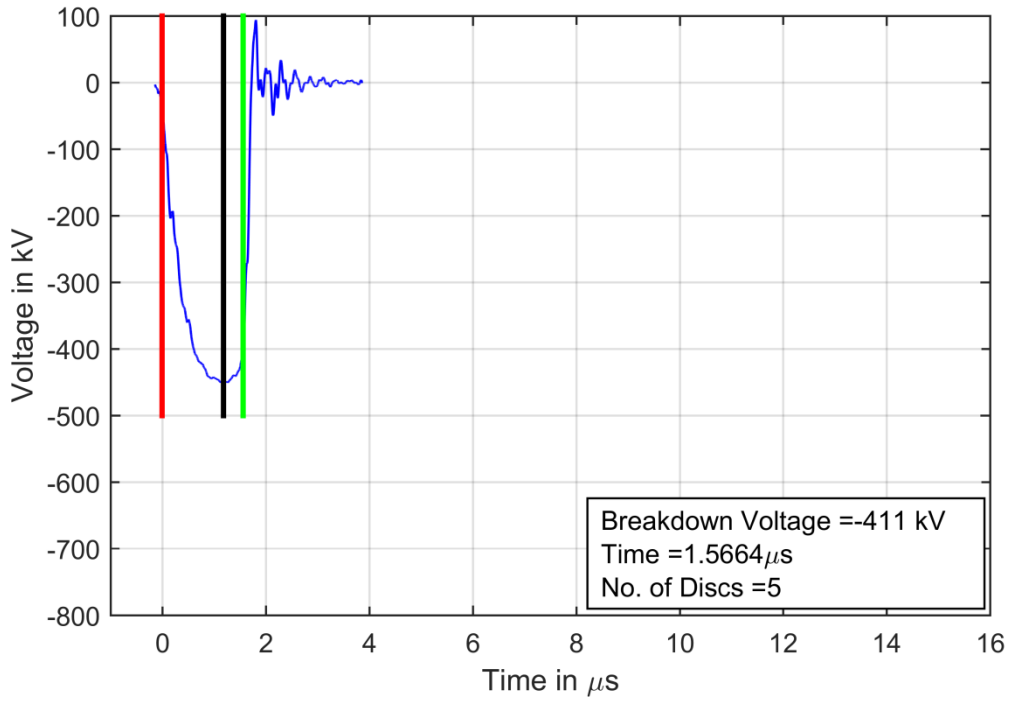
Voltage in kV
Time in μs
Breakdown Voltage =-411 kV
Time =1.5664μs
No. of Discs =5

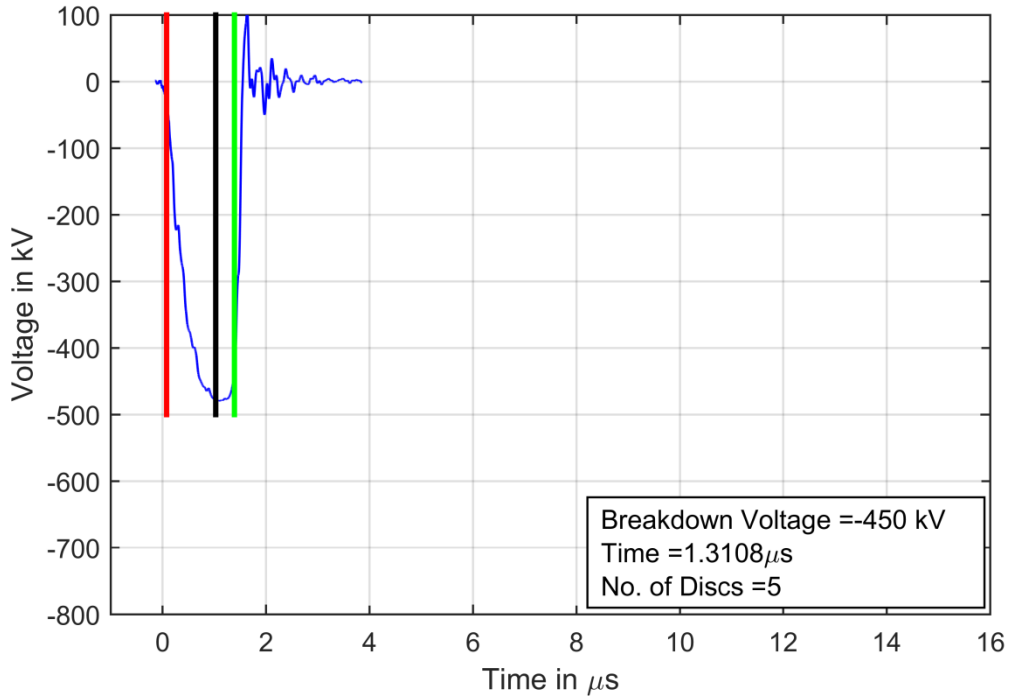
Voltage in kV
Time in μs
Breakdown Voltage =-450 kV
Time =1.3108μs
No. of Discs =5

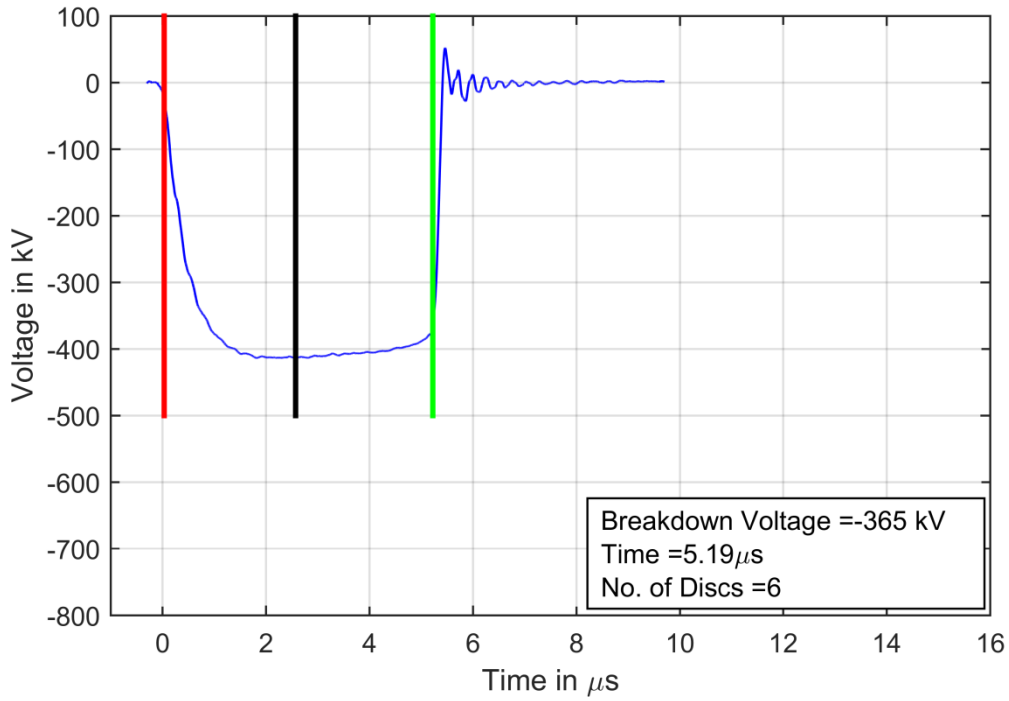
Voltage in kV
Time in μs
Breakdown Voltage =-365 kV
Time =5.19μs
No. of Discs =6

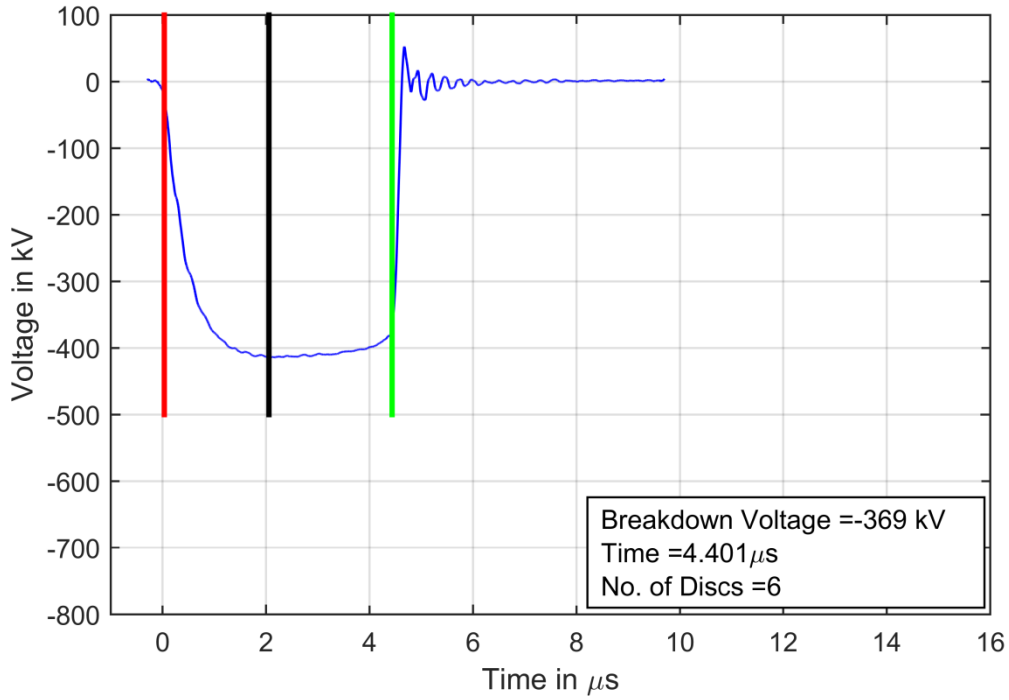
Voltage in kV
Time in μs
Breakdown Voltage =-369 kV
Time =4.401μs
No. of Discs =6

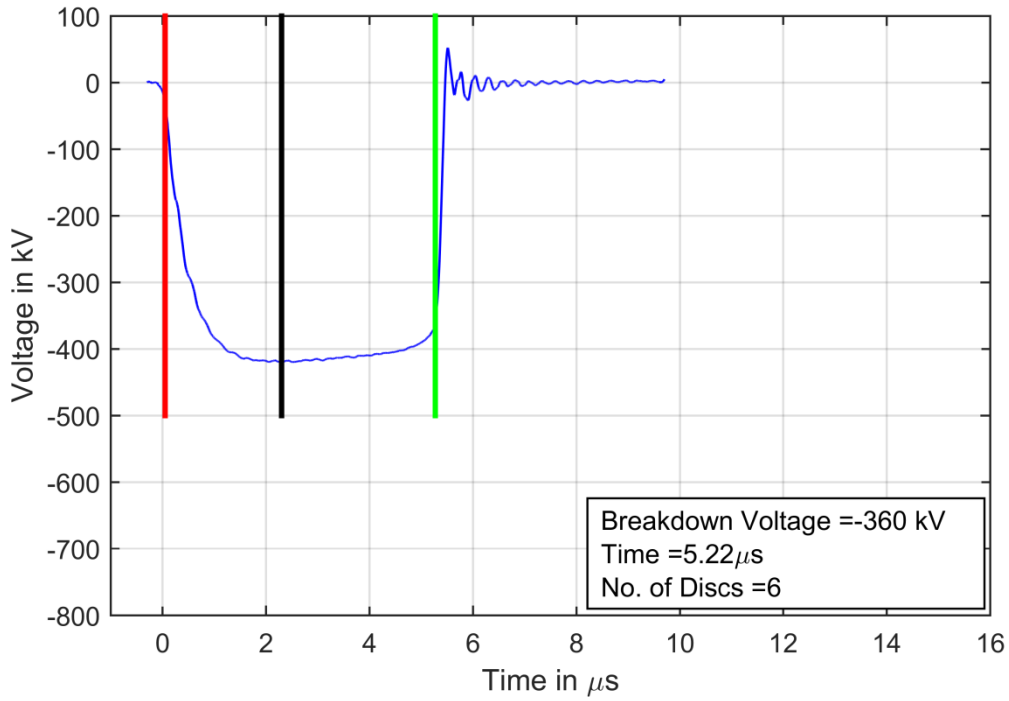
Voltage in kV
Time in μs
Breakdown Voltage =-360 kV
Time =5.22μs
No. of Discs =6

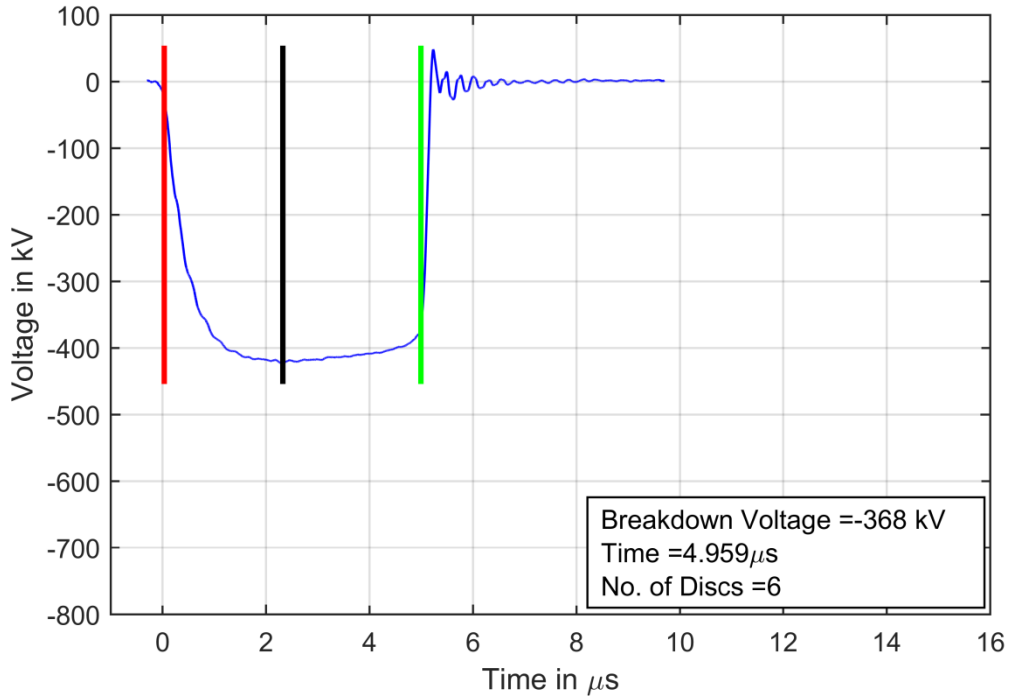
Voltage in kV
Time in μs
Breakdown Voltage =-368 kV
Time =4.959μs
No. of Discs =6

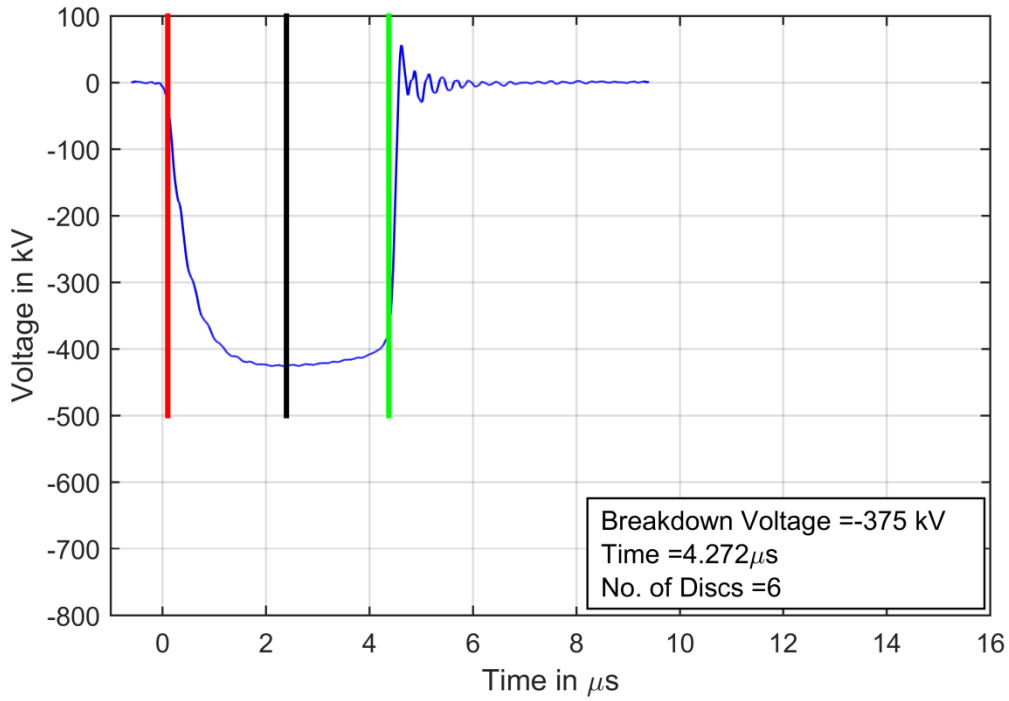
Voltage in kV
Time in μs
Breakdown Voltage =-375 kV
Time =4.272μs
No. of Discs =6

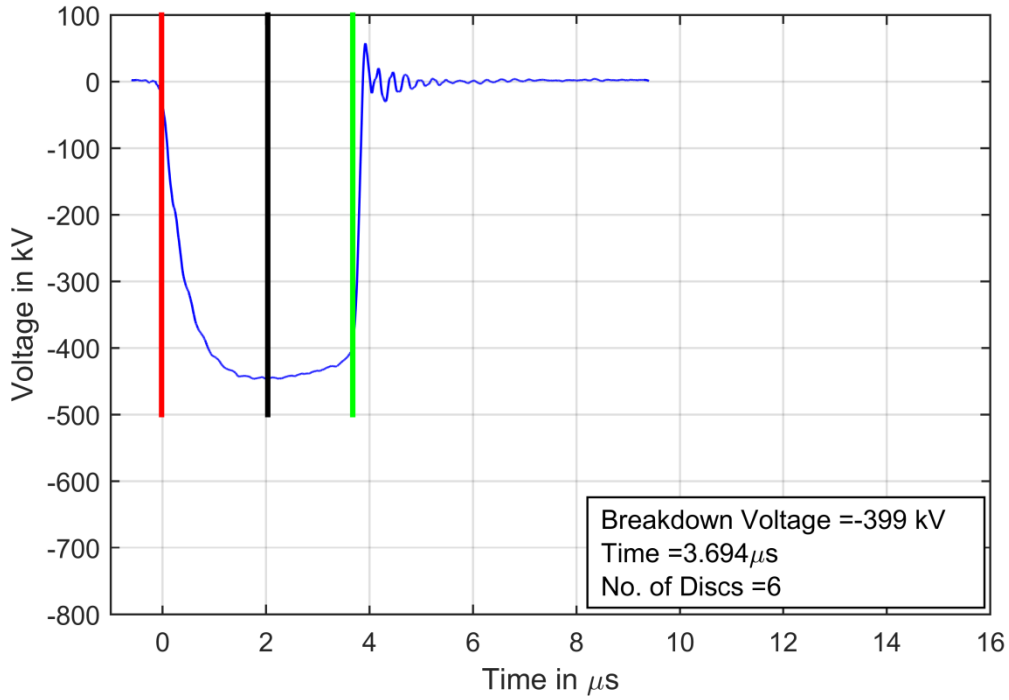
Voltage in kV
Time in μs
Breakdown Voltage =-399 kV
Time =3.694μs
No. of Discs =6

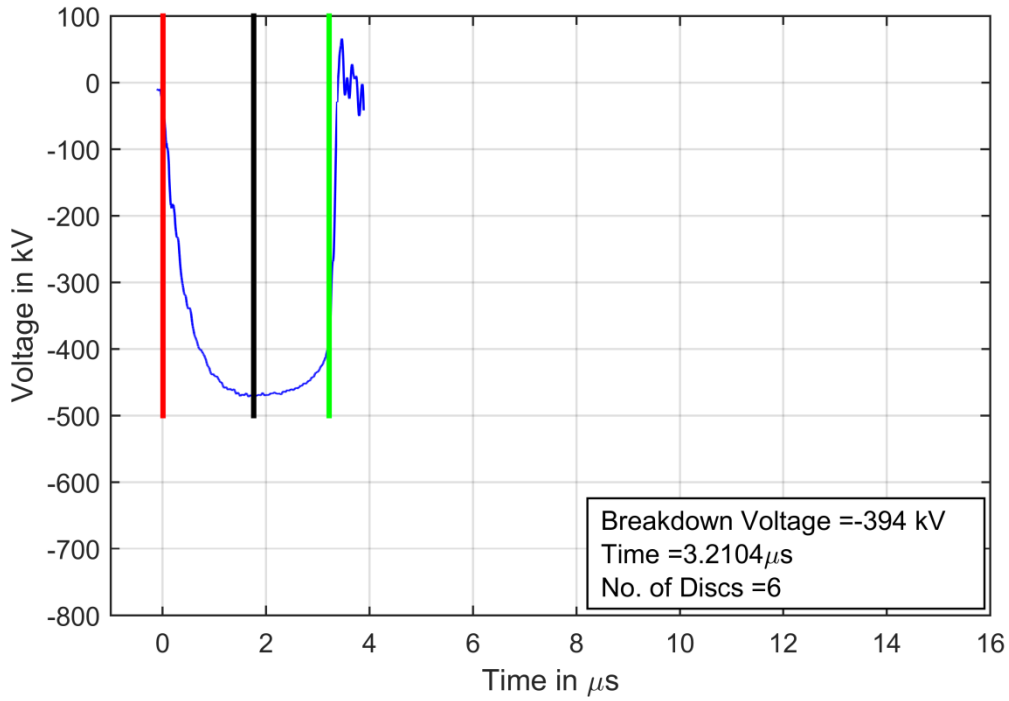
Voltage in kV
Time in μs
Breakdown Voltage =-394 kV
Time =3.2104μs
No. of Discs =6

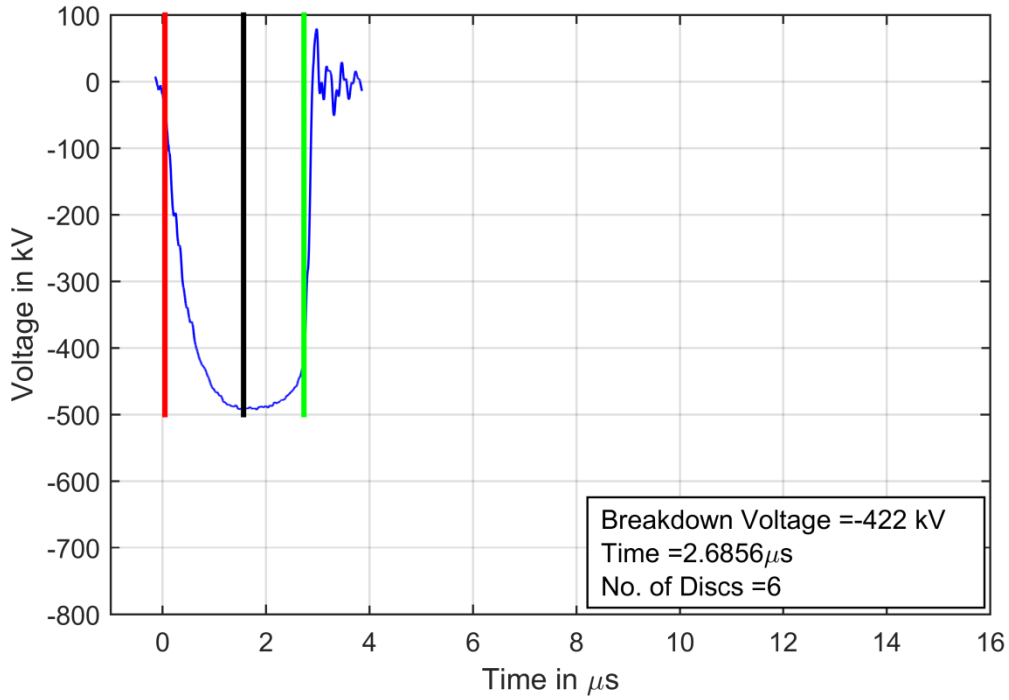
Voltage in kV
Time in μs
Breakdown Voltage =-422 kV
Time =2.6856μs
No. of Discs =6

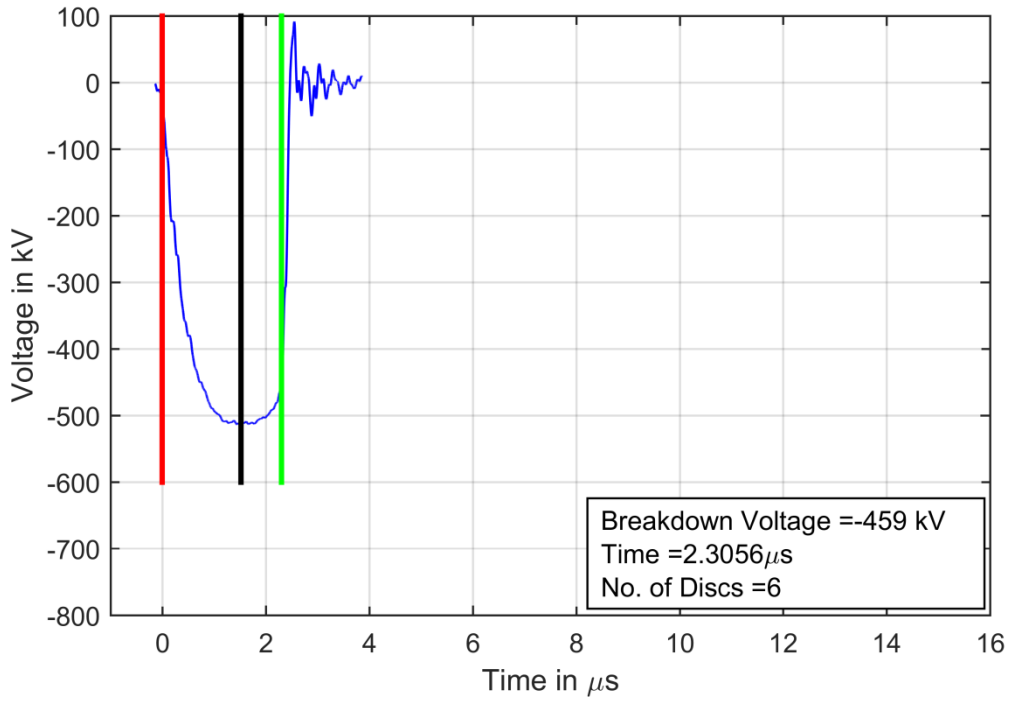
Voltage in kV
Time in μs
Breakdown Voltage =-459 kV
Time =2.3056μs
No. of Discs =6

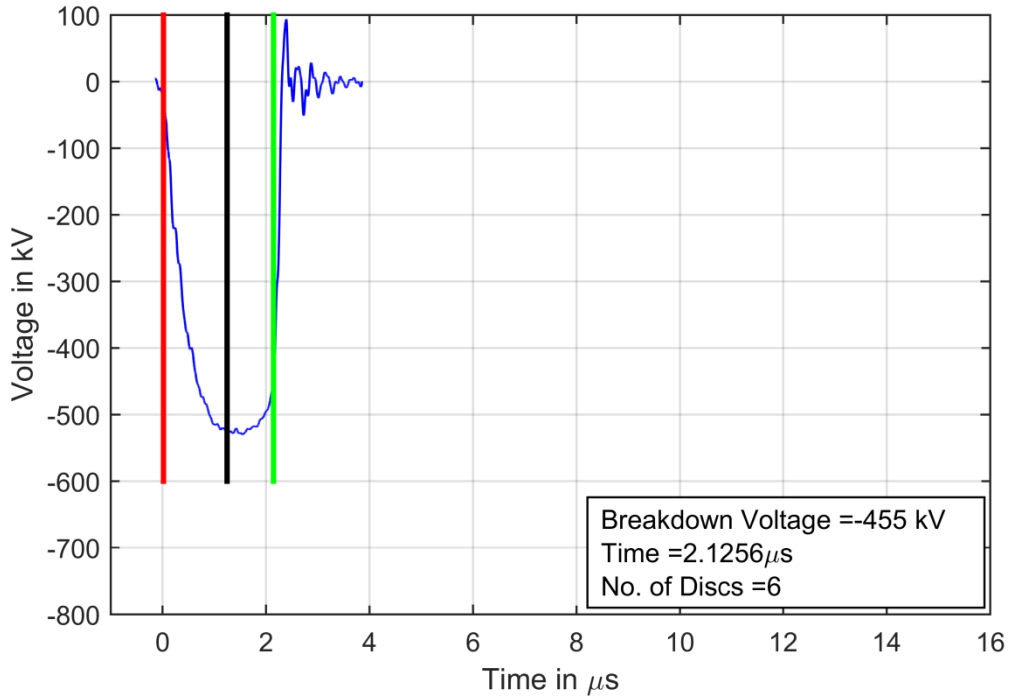
Voltage in kV
Time in μs
Breakdown Voltage =-455 kV
Time =2.1256μs
No. of Discs =6

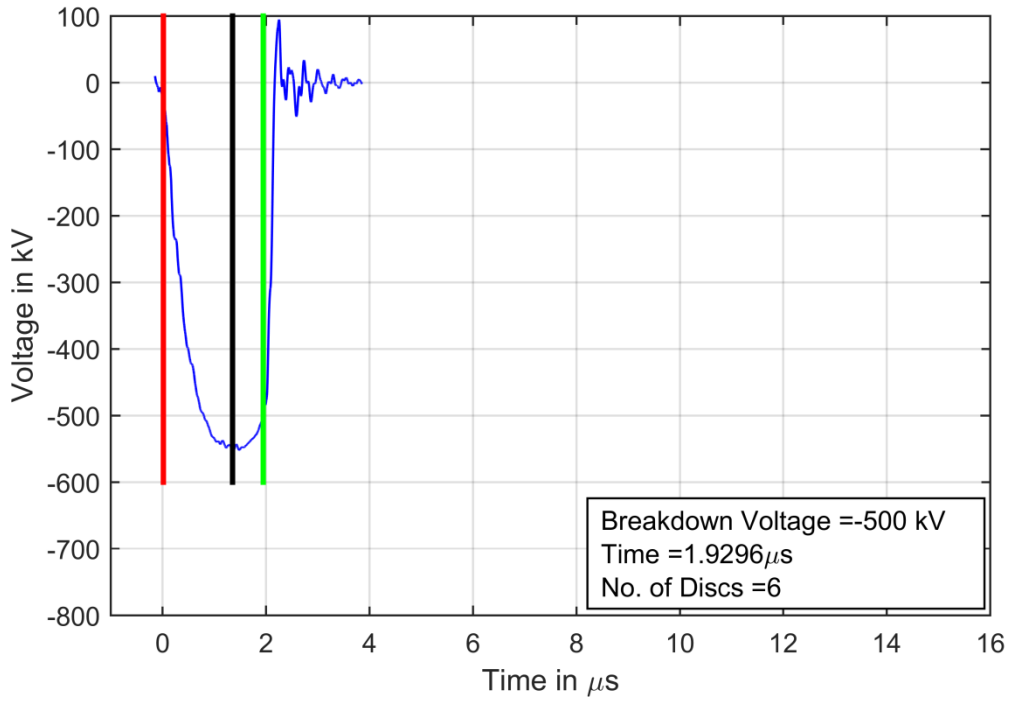
Voltage in kV
Time in μs
Breakdown Voltage =-500 kV
Time =1.9296μs
No. of Discs =6

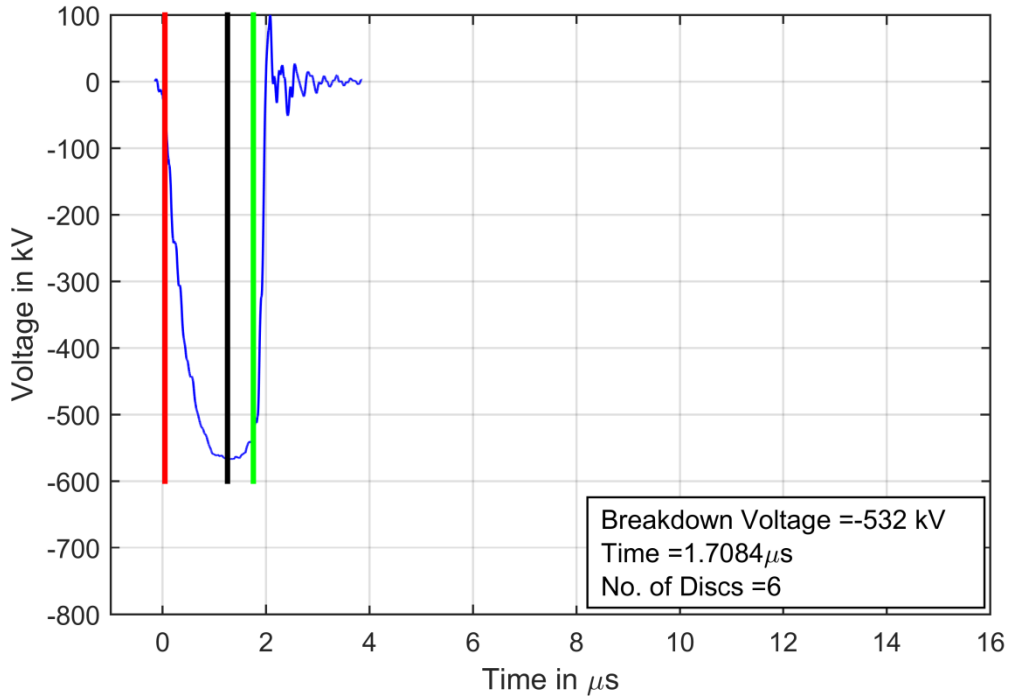
Voltage in kV
Time in μs
Breakdown Voltage =-532 kV
Time =1.7084μs
No. of Discs =6

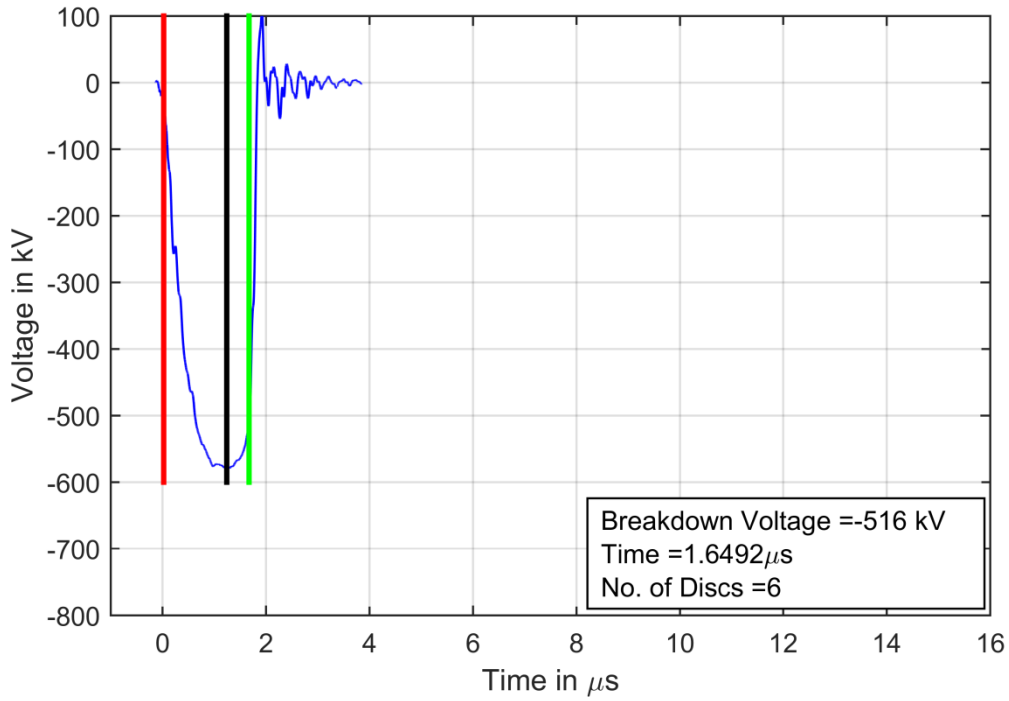
Voltage in kV
Time in μs
Breakdown Voltage =-516 kV
Time =1.6492μs
No. of Discs =6

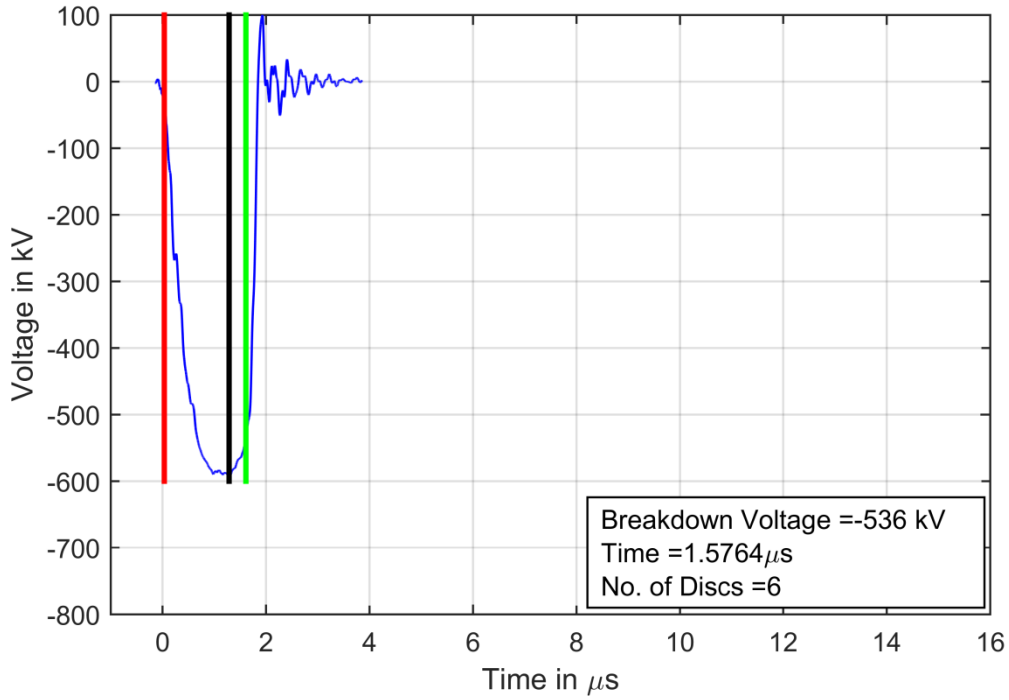
Voltage in kV
Time in μs
Breakdown Voltage =-536 kV
Time =1.5764μs
No. of Discs =6

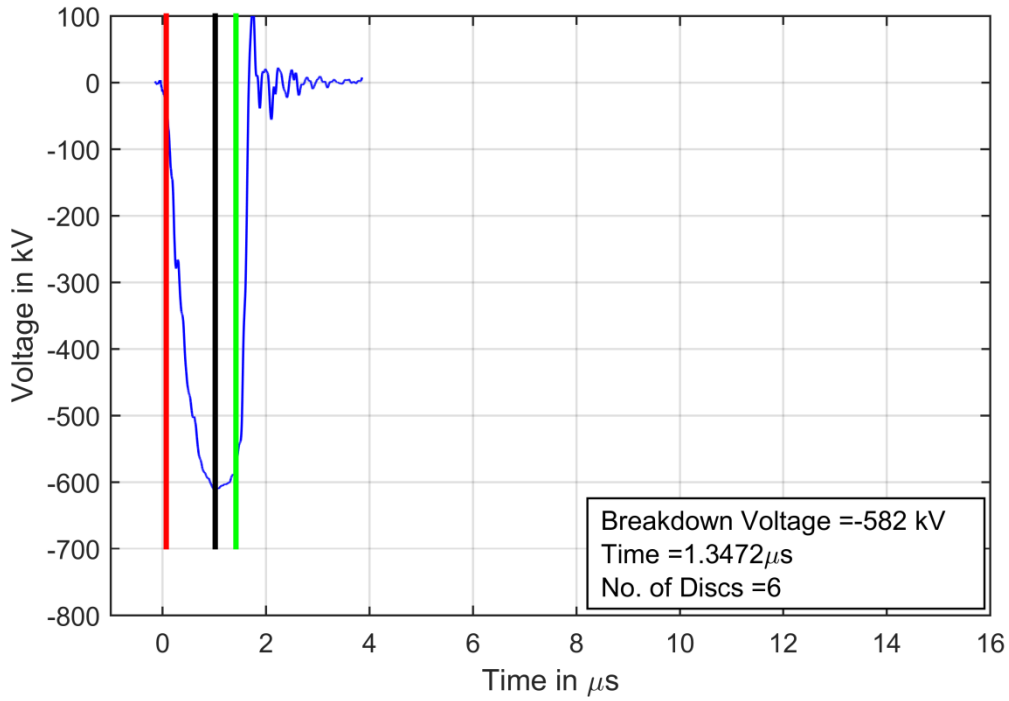
Voltage in kV
Time in μs
Breakdown Voltage =-582 kV
Time =1.3472μs
No. of Discs =6

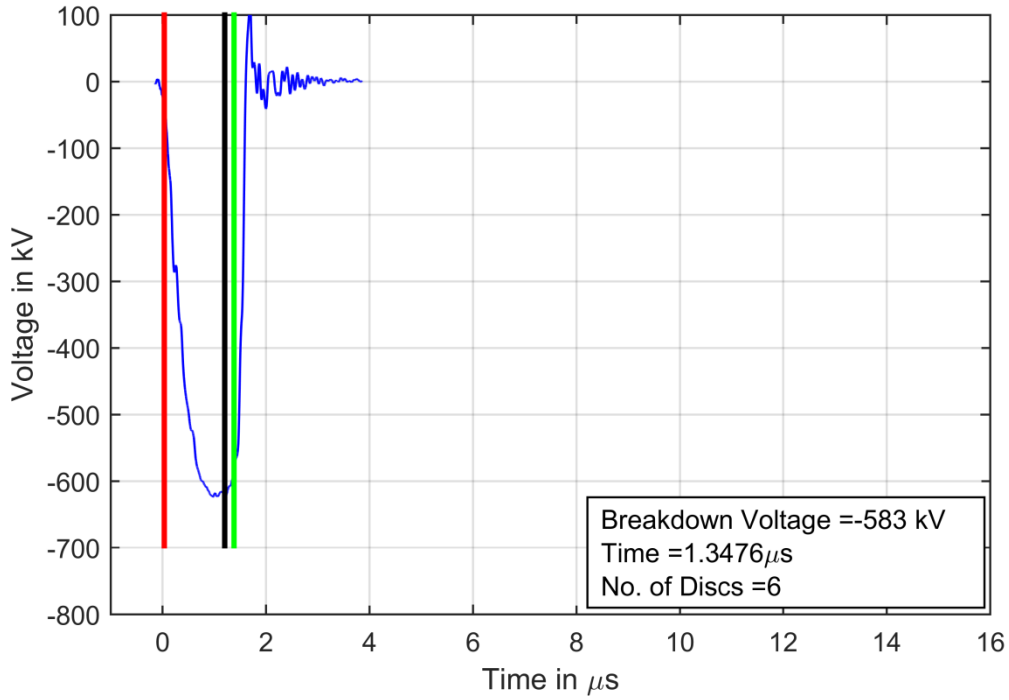
Voltage in kV
Time in μs
Breakdown Voltage =-583 kV
Time =1.3476μs
No. of Discs =6

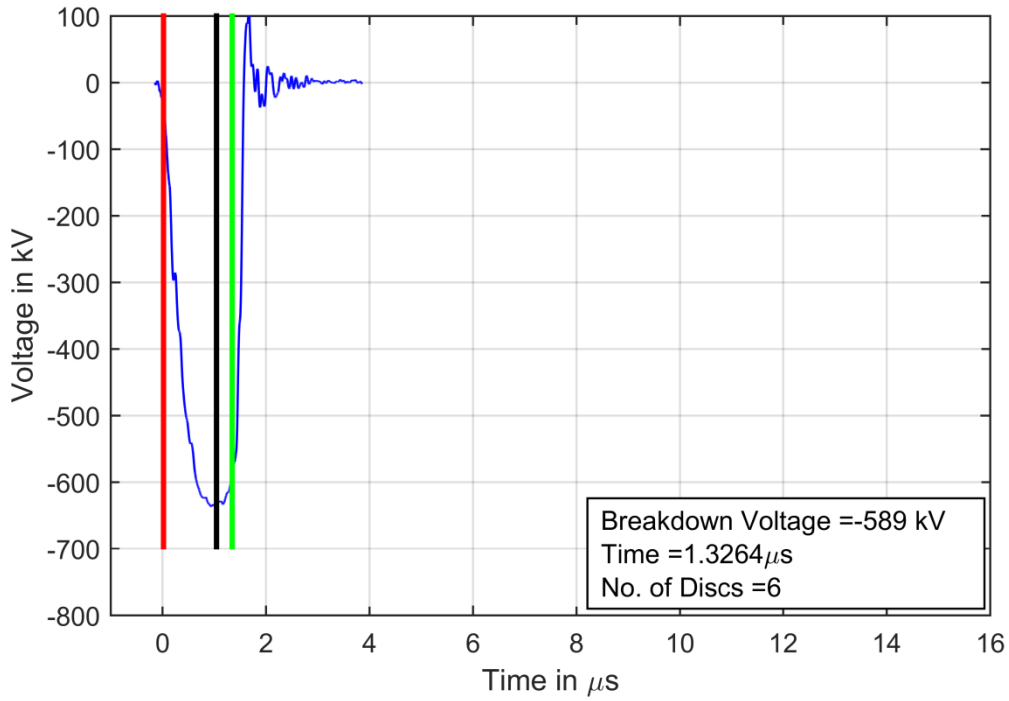
Voltage in kV
Time in μs
Breakdown Voltage =-589 kV
Time =1.3264μs
No. of Discs =6

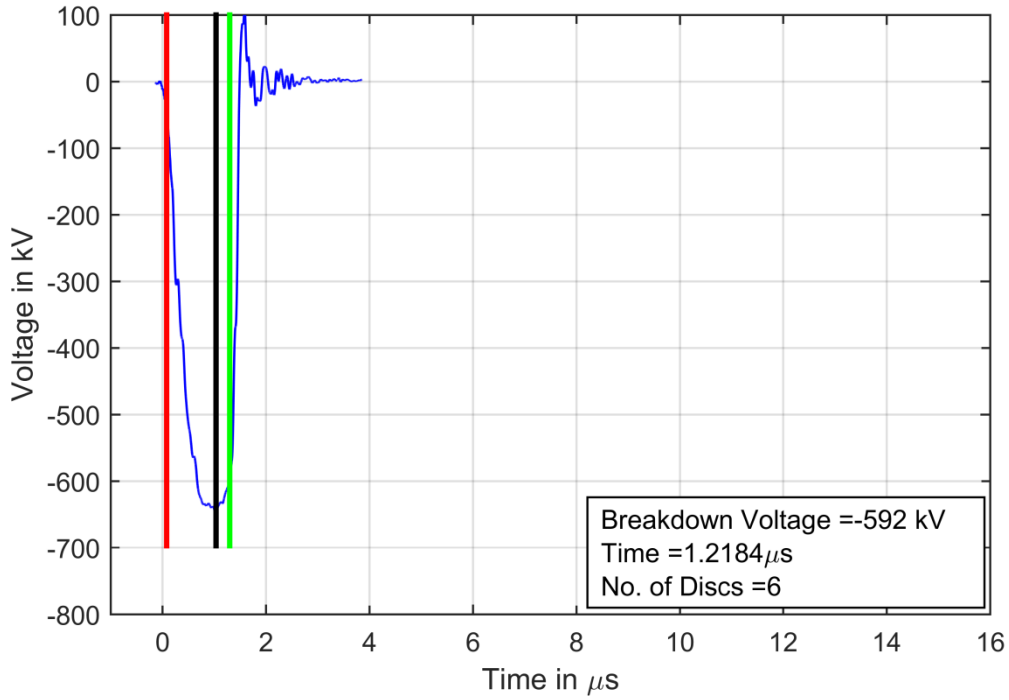
Voltage in kV
Time in μs
Breakdown Voltage =-592 kV
Time =1.2184μs
No. of Discs =6

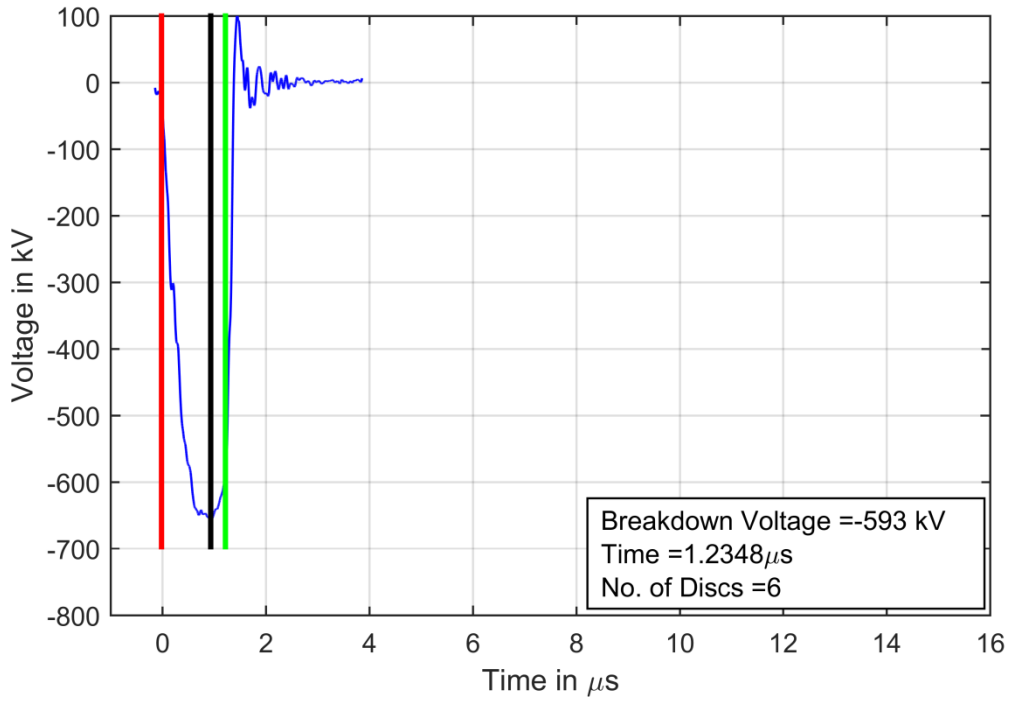
Voltage in kV
Time in μs
Breakdown Voltage =-593 kV
Time =1.2348μs
No. of Discs =6

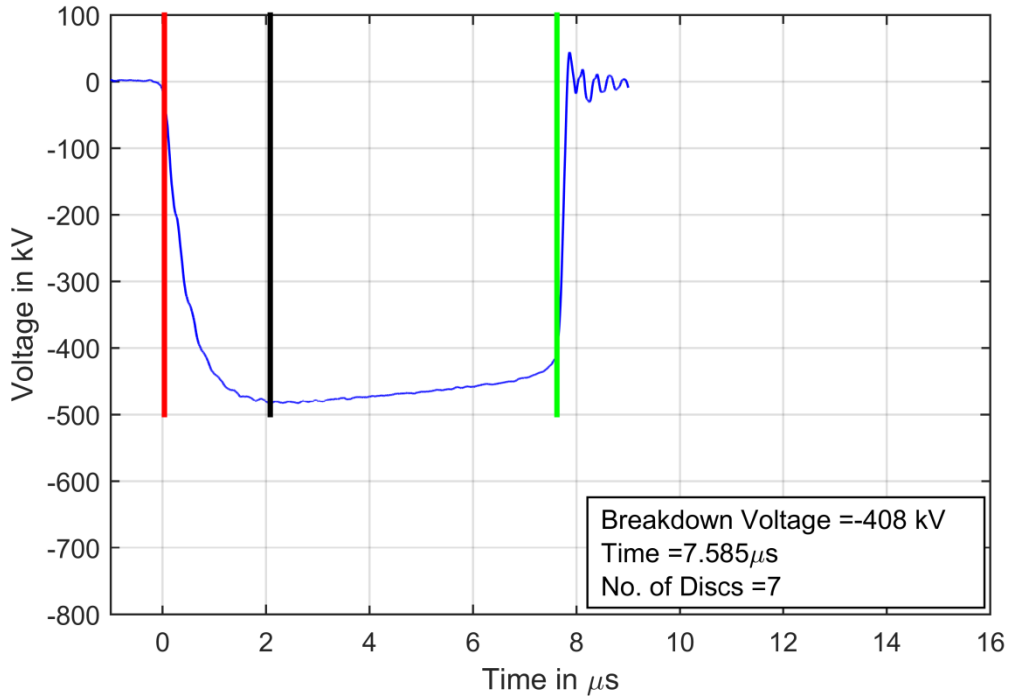
Voltage in kV
Time in μs
Breakdown Voltage =-408 kV
Time =7.585μs
No. of Discs =7

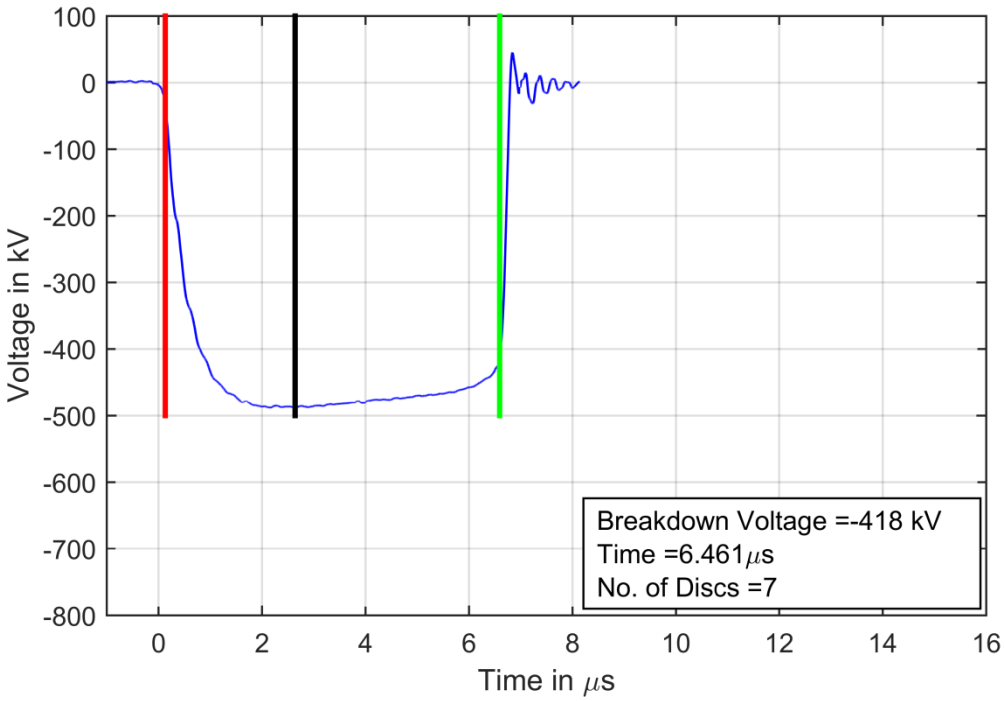
Voltage in kV
Time in μs
Breakdown Voltage =-418 kV
Time =6.461μs
No. of Discs =7

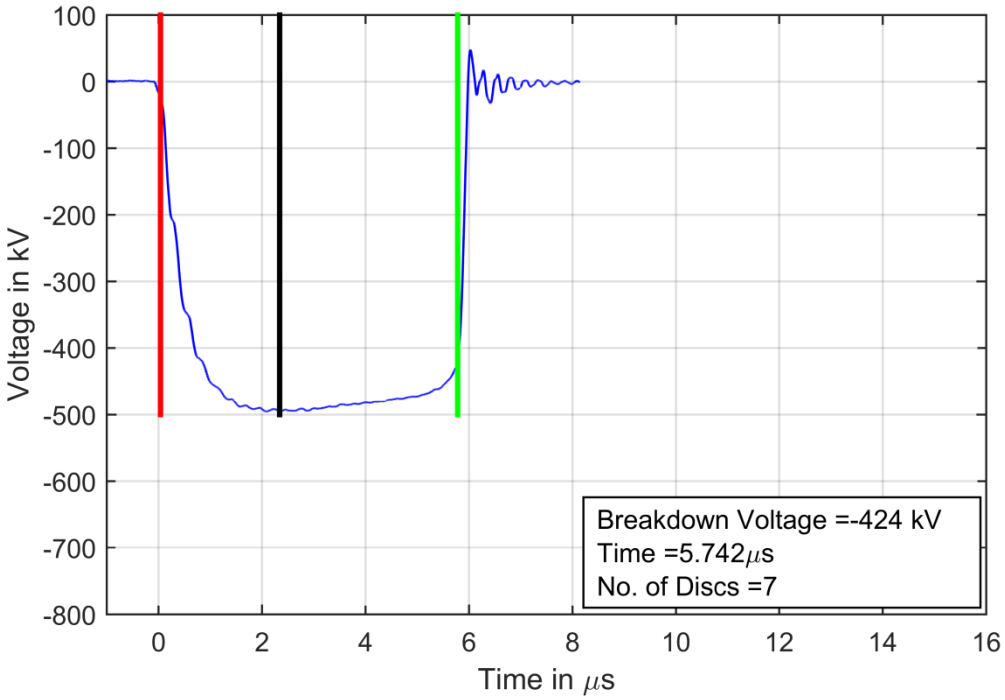
Voltage in kV
Time in μs
Breakdown Voltage =-424 kV
Time =5.742μs
No. of Discs =7

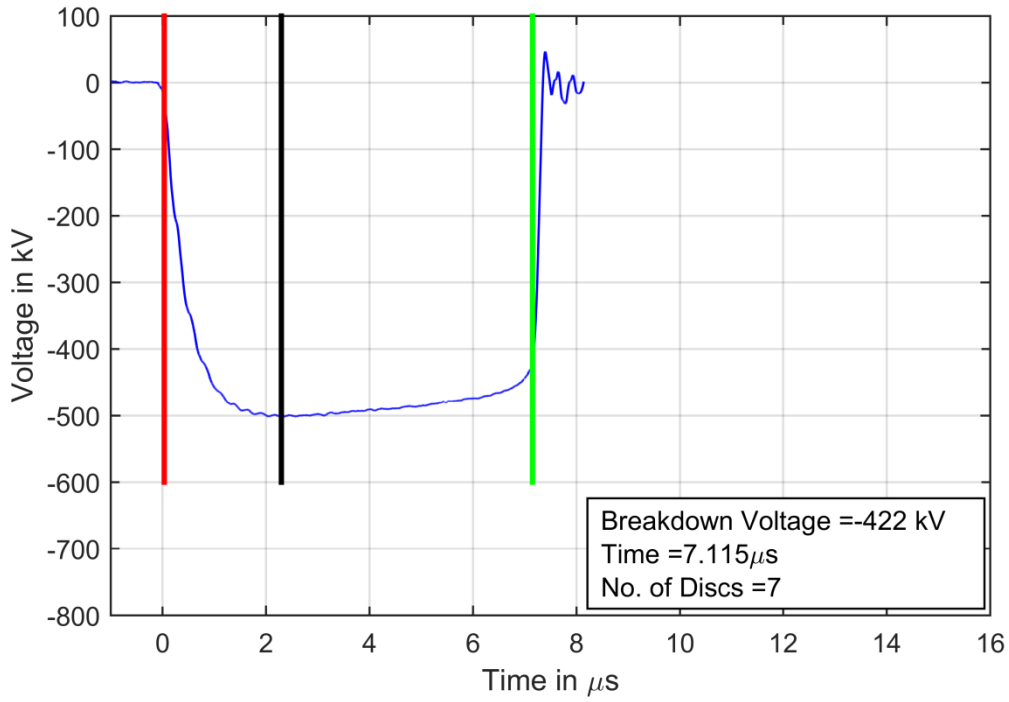
Voltage in kV
Time in μs
Breakdown Voltage =-422 kV
Time =7.115μs
No. of Discs =7

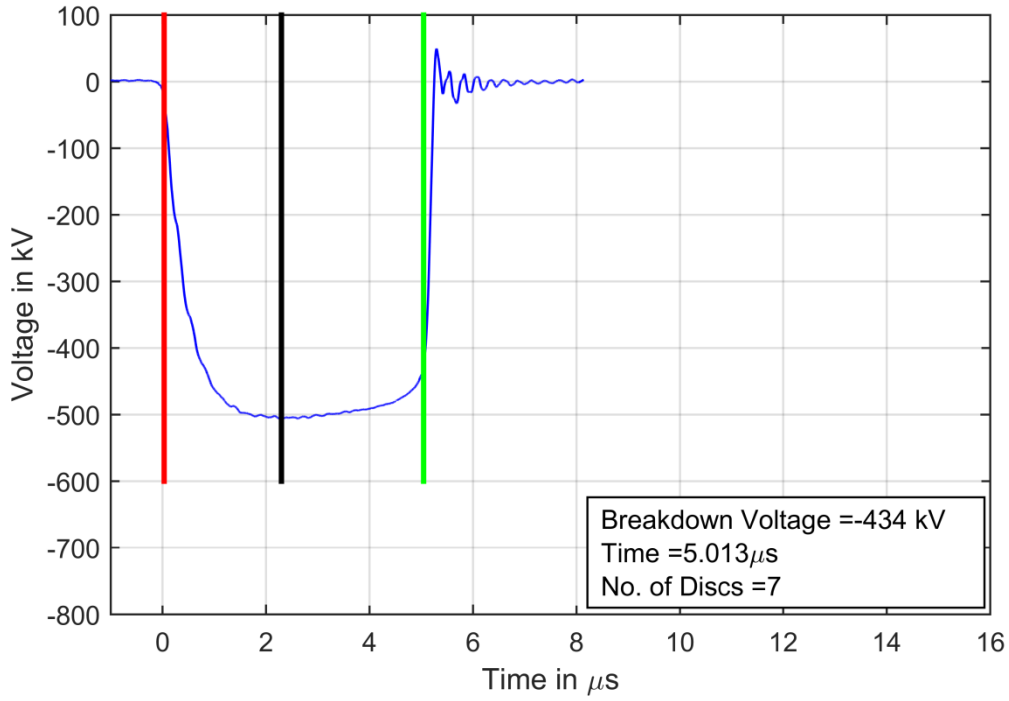
Voltage in kV
Time in μs
Breakdown Voltage =-434 kV
Time =5.013μs
No. of Discs =7

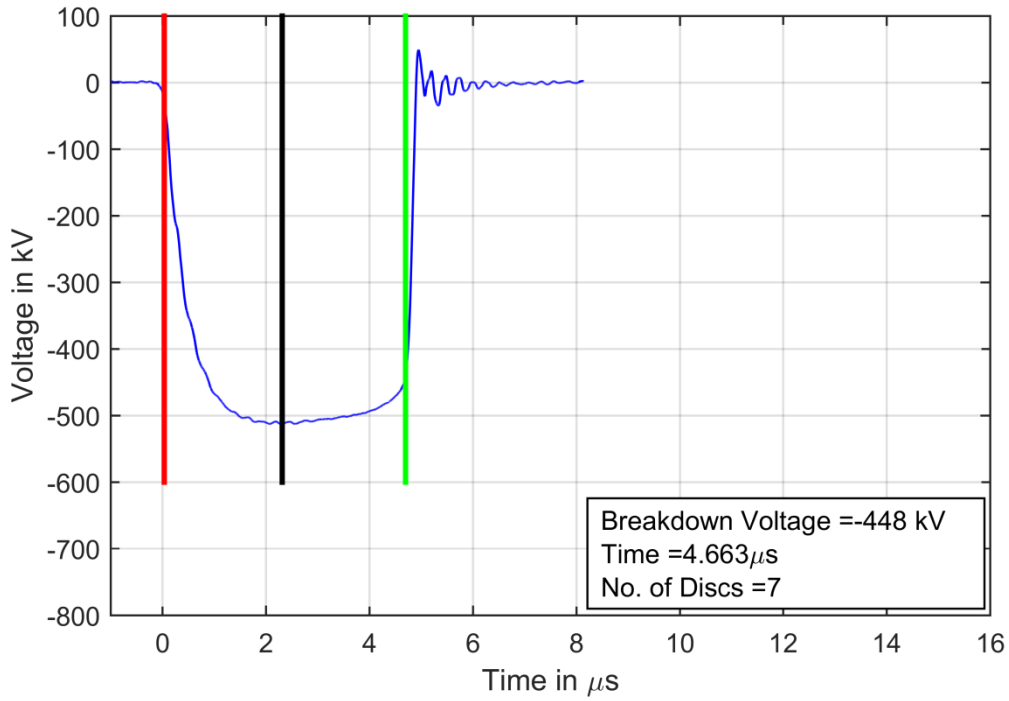
Voltage in kV
Time in μs
Breakdown Voltage =-448 kV
Time =4.663μs
No. of Discs =7

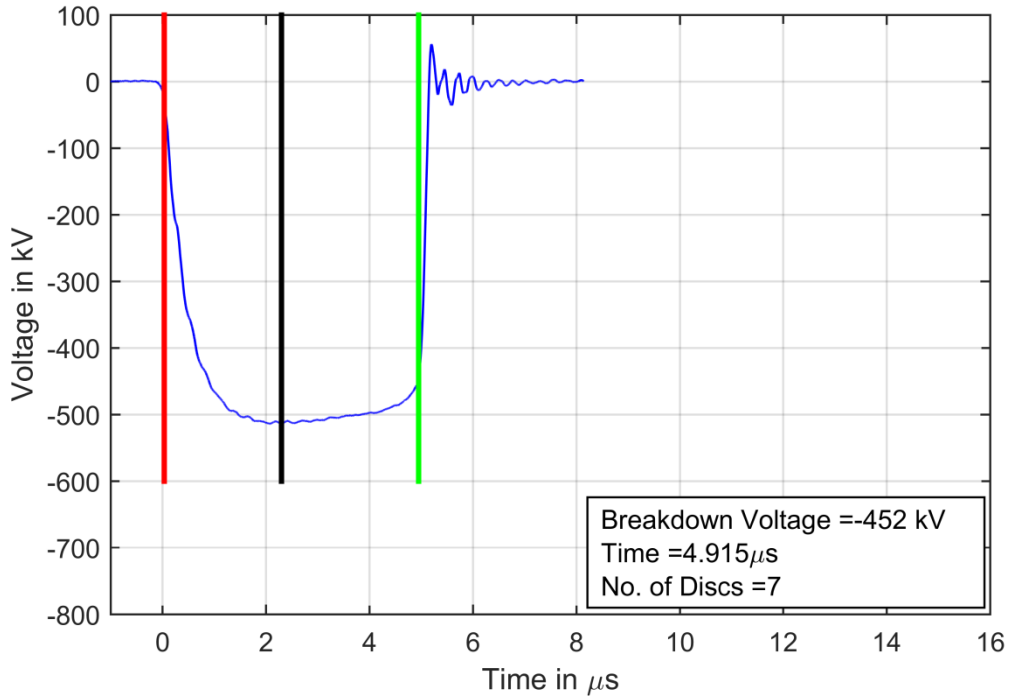
Voltage in kV
Time in μs
Breakdown Voltage =-452 kV
Time =4.915μs
No. of Discs =7

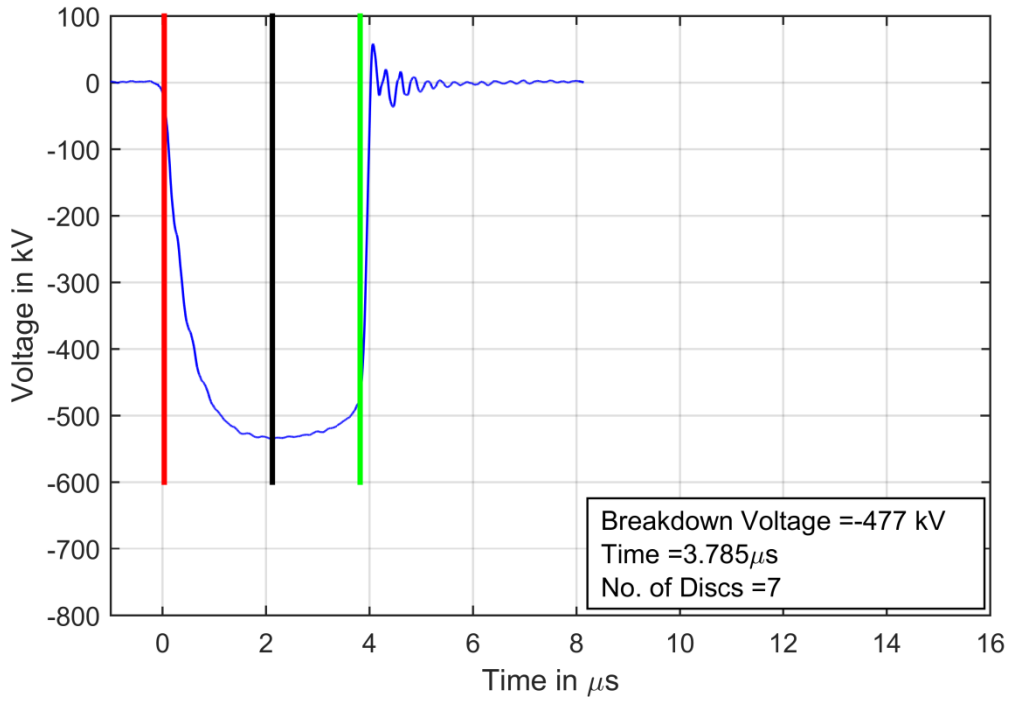
Voltage in kV
Time in μs
Breakdown Voltage =-477 kV
Time =3.785μs
No. of Discs =7

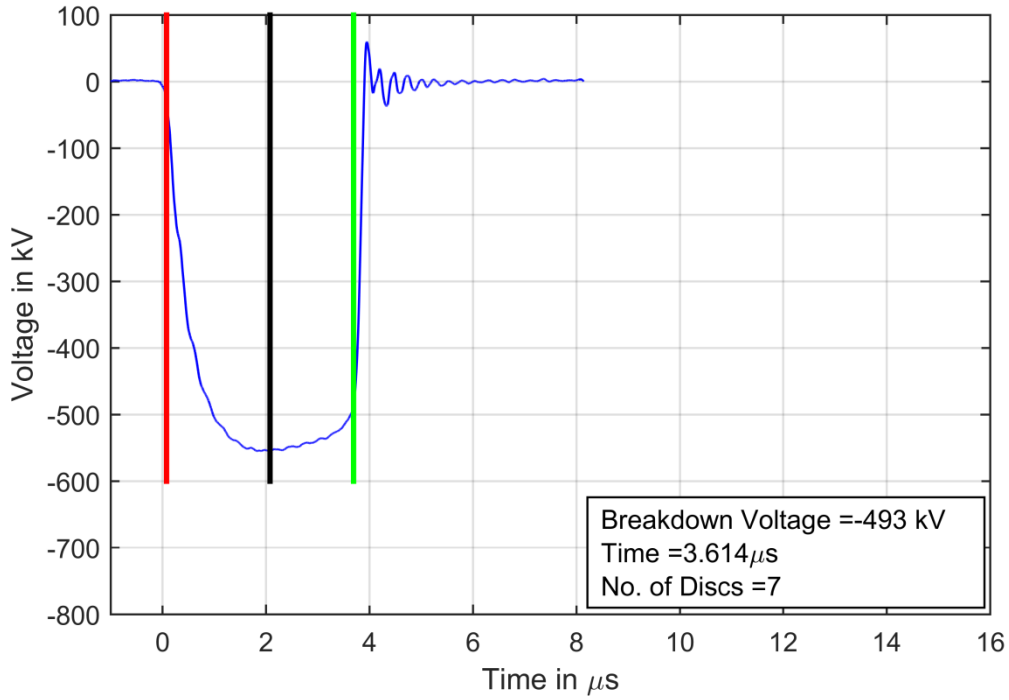
Voltage in kV
Time in μs
Breakdown Voltage =-493 kV
Time =3.614μs
No. of Discs =7

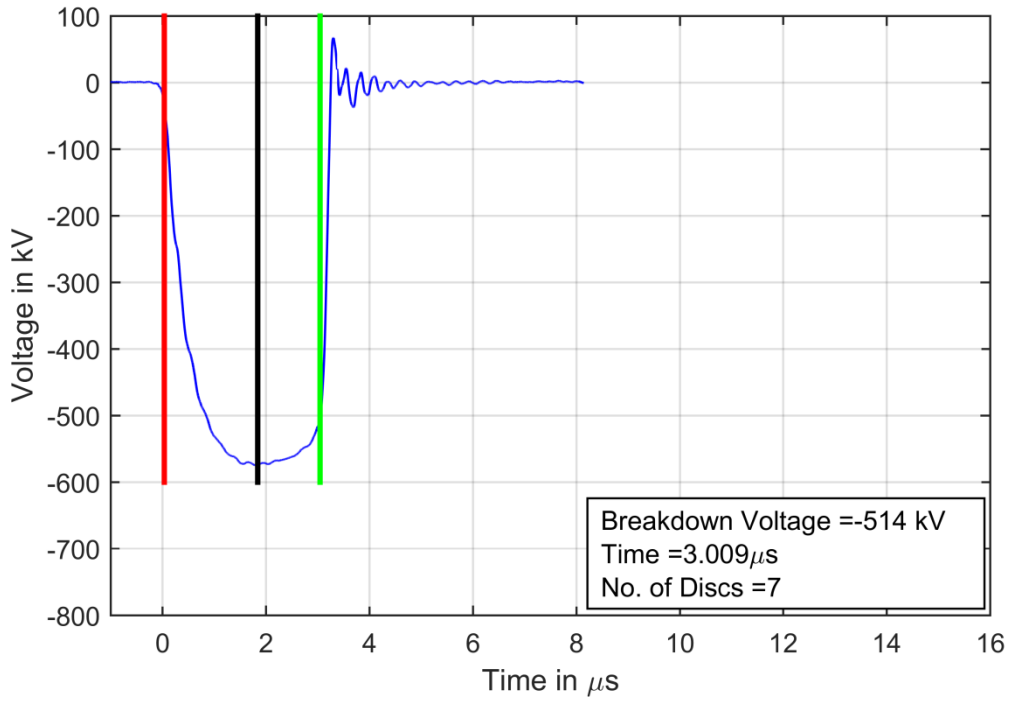
Voltage in kV
Time in μs
Breakdown Voltage =-514 kV
Time =3.009μs
No. of Discs =7

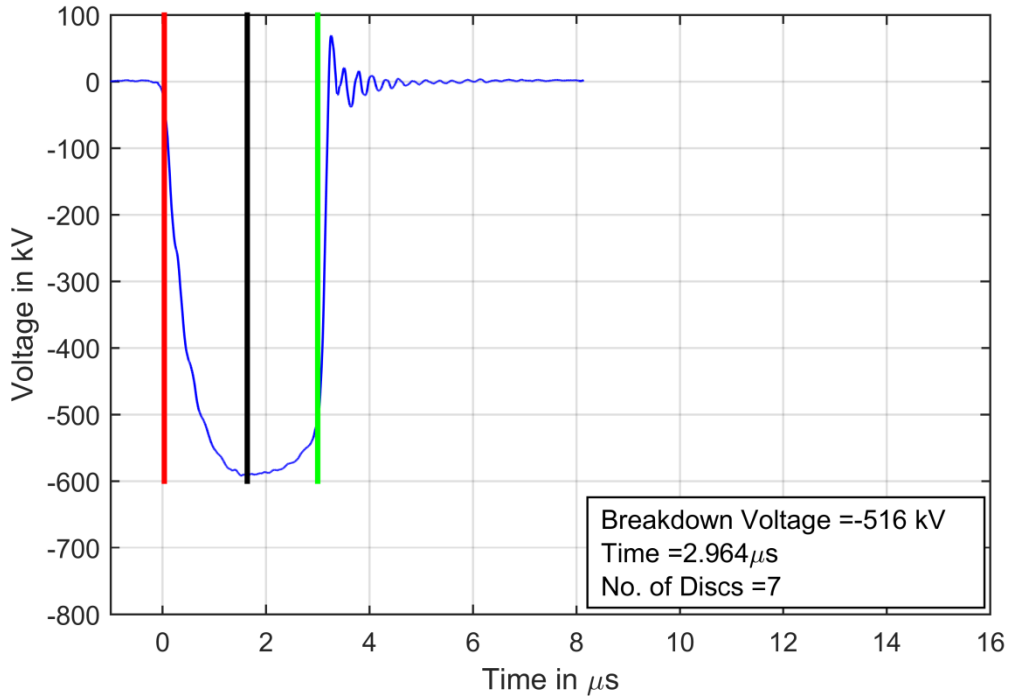
Voltage in kV
Time in μs
Breakdown Voltage =-516 kV
Time =2.964μs
No. of Discs =7

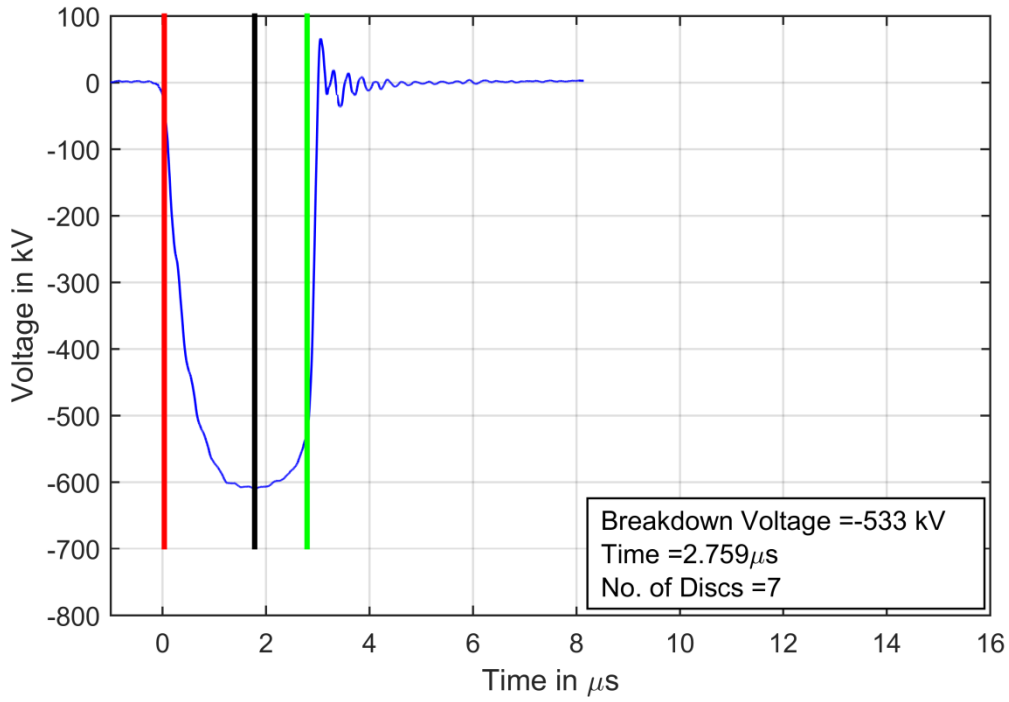
Voltage in kV
Time in μs
Breakdown Voltage =-533 kV
Time =2.759μs
No. of Discs =7

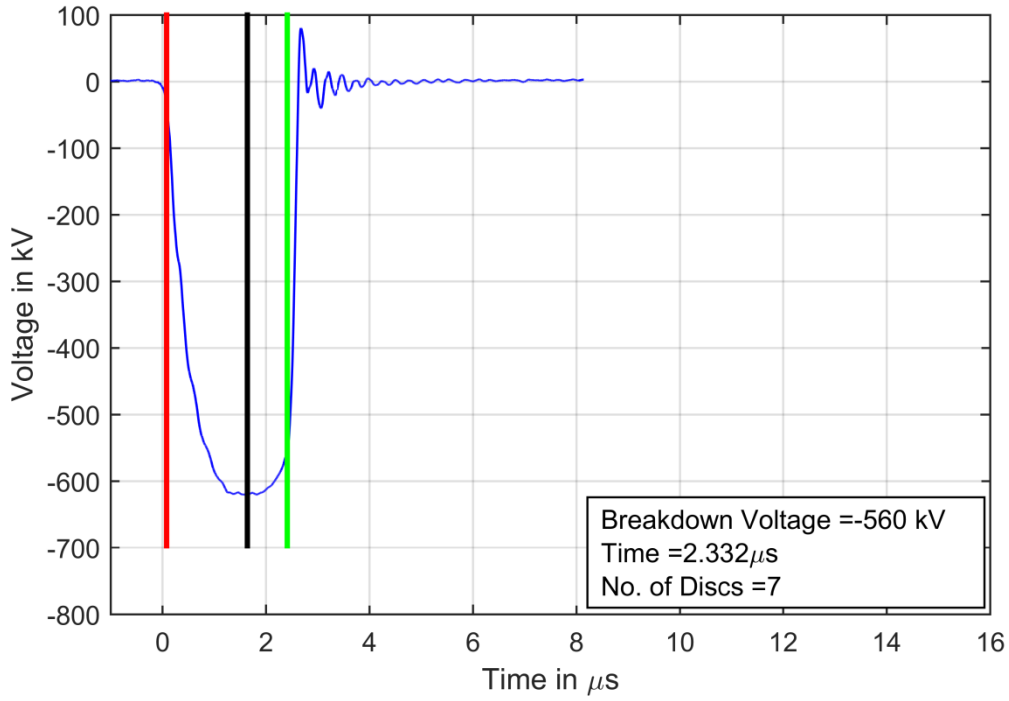
Voltage in kV
Time in μs
Breakdown Voltage =-560 kV
Time =2.332μs
No. of Discs =7

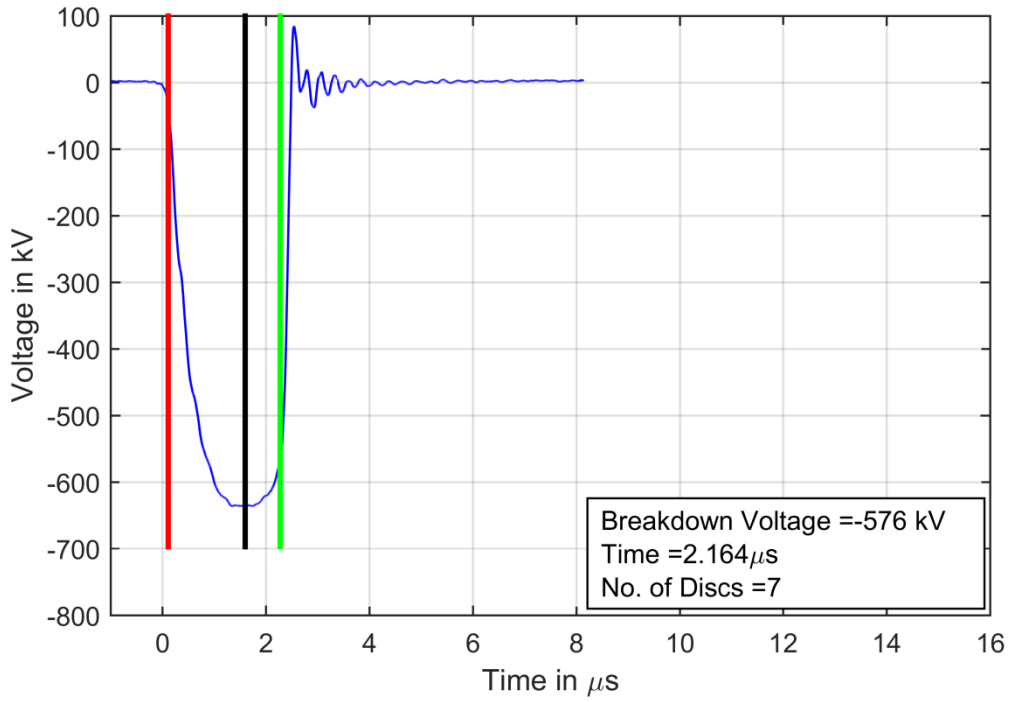
Voltage in kV
Time in μs
Breakdown Voltage =-576 kV
Time =2.164μs
No. of Discs =7

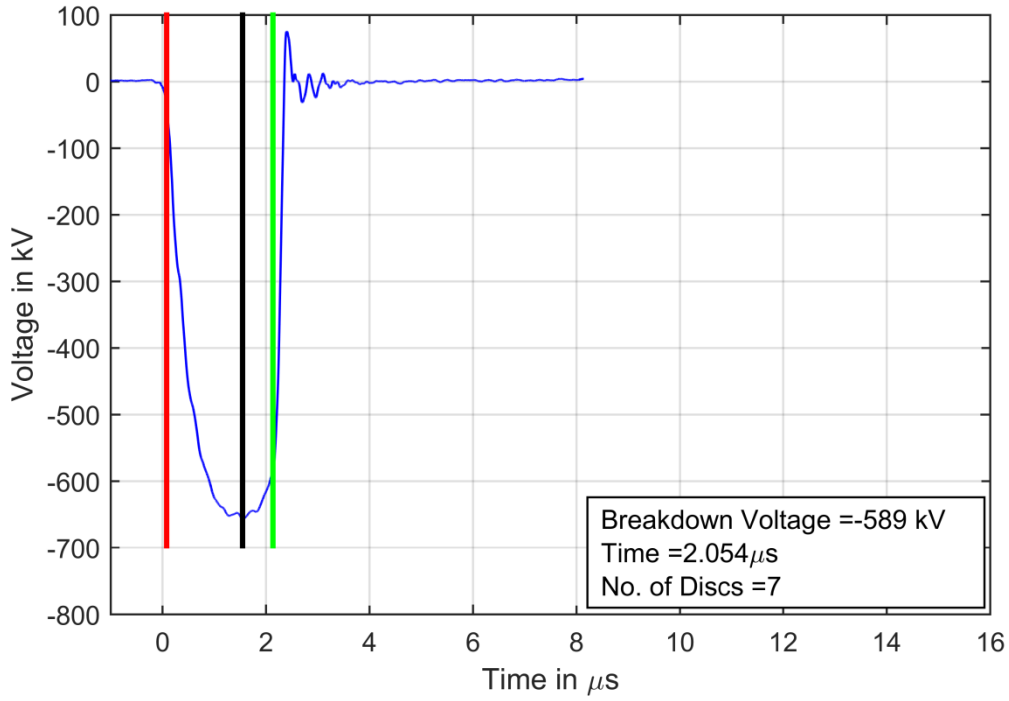
Voltage in kV
Time in μs
Breakdown Voltage =-589 kV
Time =2.054μs
No. of Discs =7

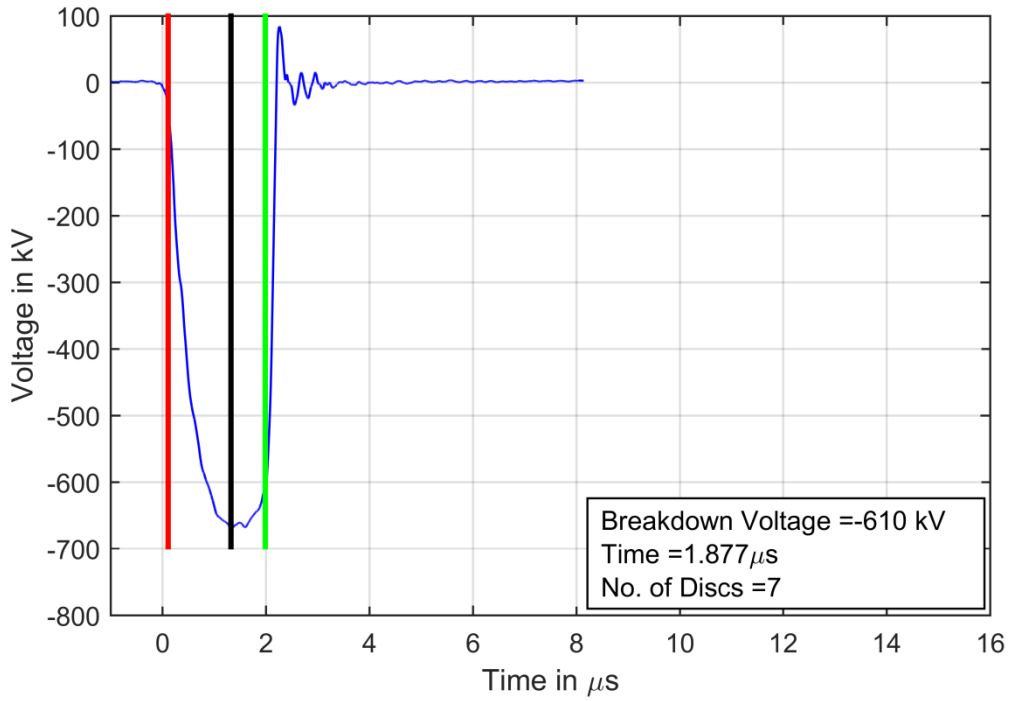
Voltage in kV
Time in μs
Breakdown Voltage =-610 kV
Time =1.877μs
No. of Discs =7

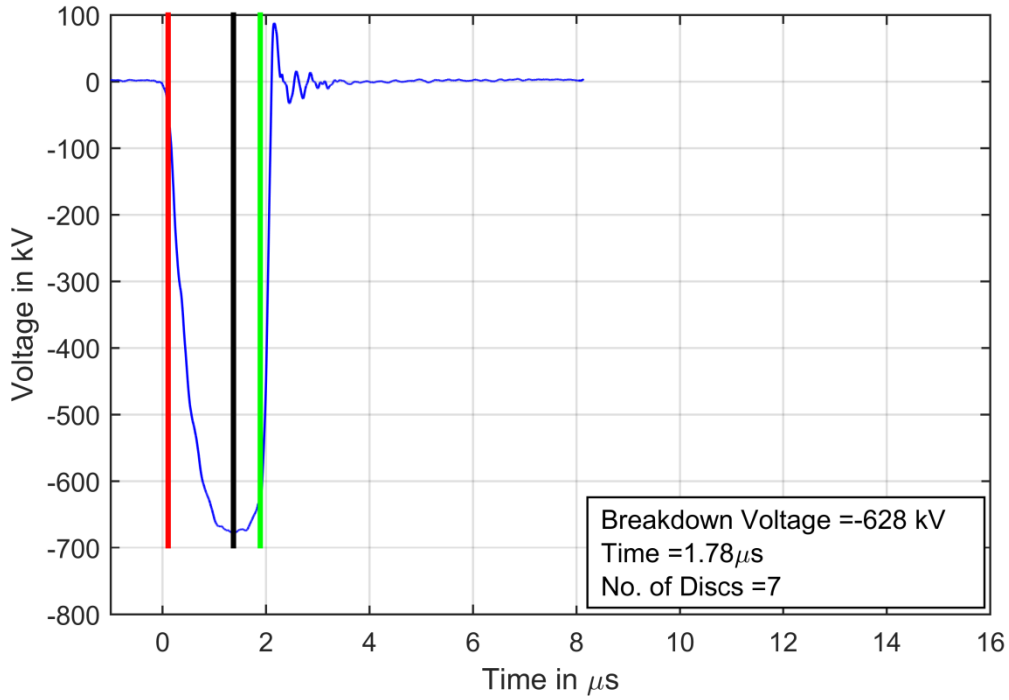
Voltage in kV
Time in μs
Breakdown Voltage =-628 kV
Time =1.78μs
No. of Discs =7

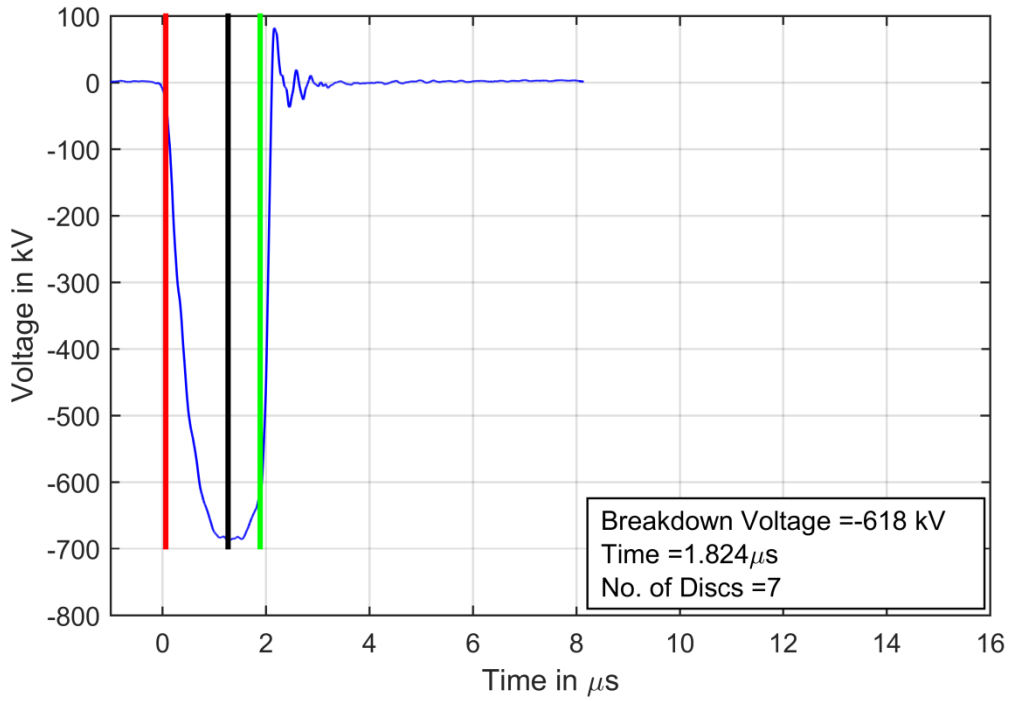
Voltage in kV
Time in μs
Breakdown Voltage =-618 kV
Time =1.824μs
No. of Discs =7

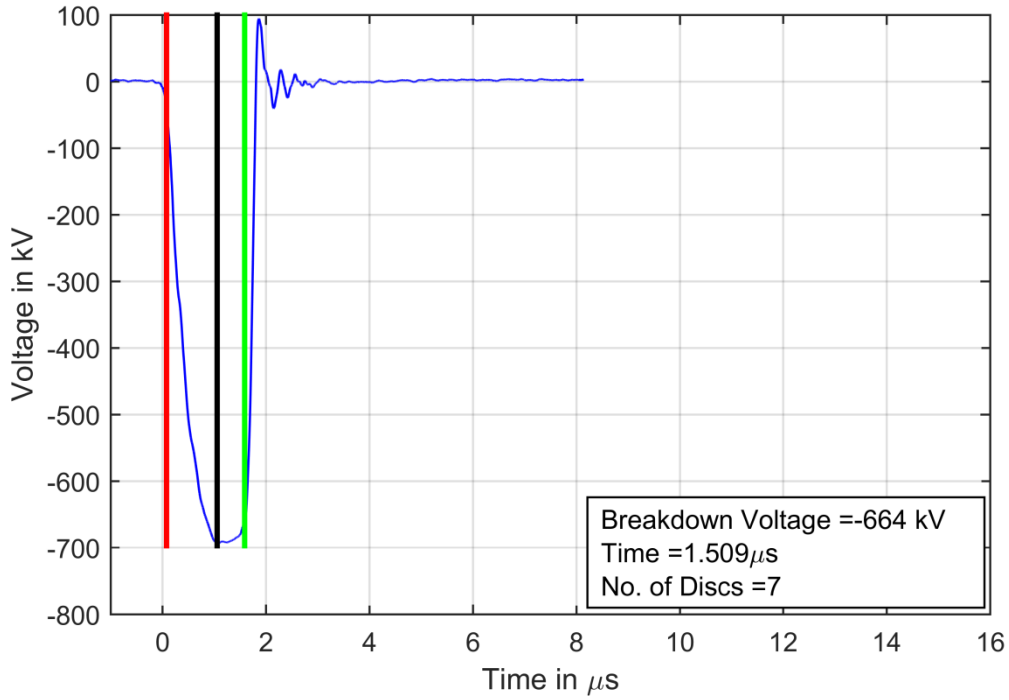
Voltage in kV
Time in μs
Breakdown Voltage =-664 kV
Time =1.509μs
No. of Discs =7

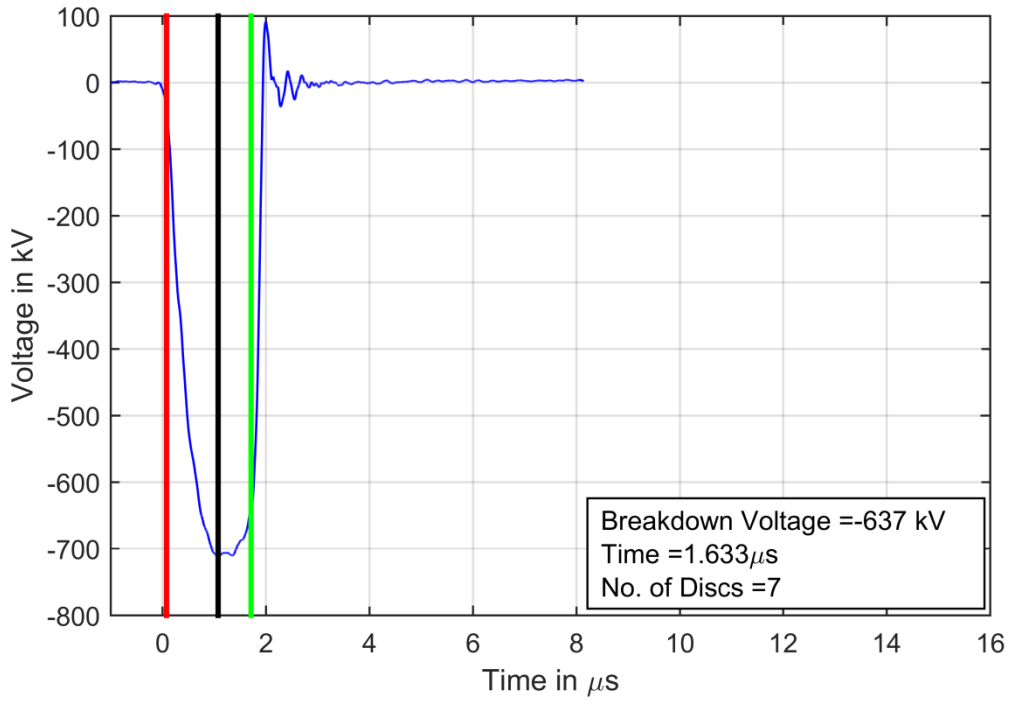
Voltage in kV
Time in μs
Breakdown Voltage =-637 kV
Time =1.633μs
No. of Discs =7

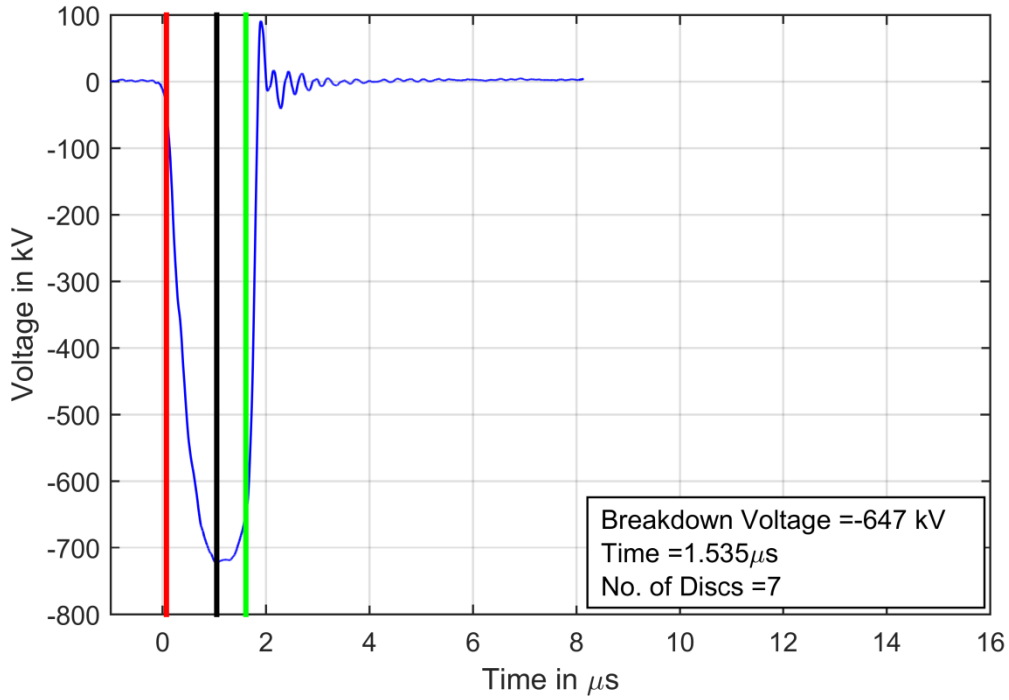
Voltage in kV
Time in μs
Breakdown Voltage =-647 kV
Time =1.535μs
No. of Discs =7

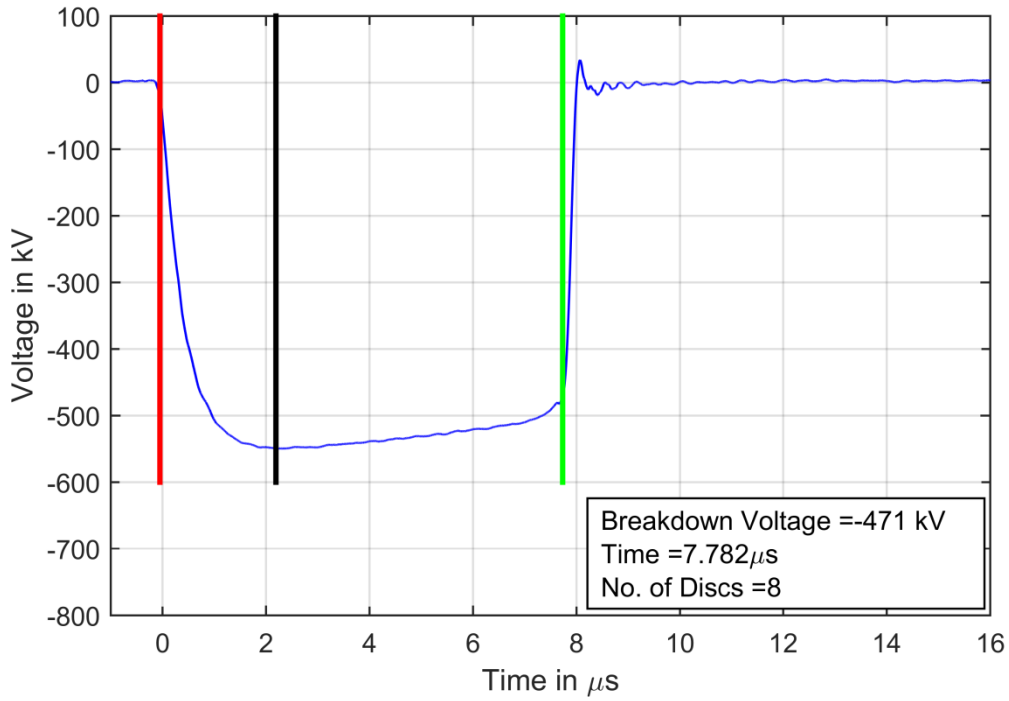
Voltage in kV
Time in μs
Breakdown Voltage =-471 kV
Time =7.782μs
No. of Discs =8

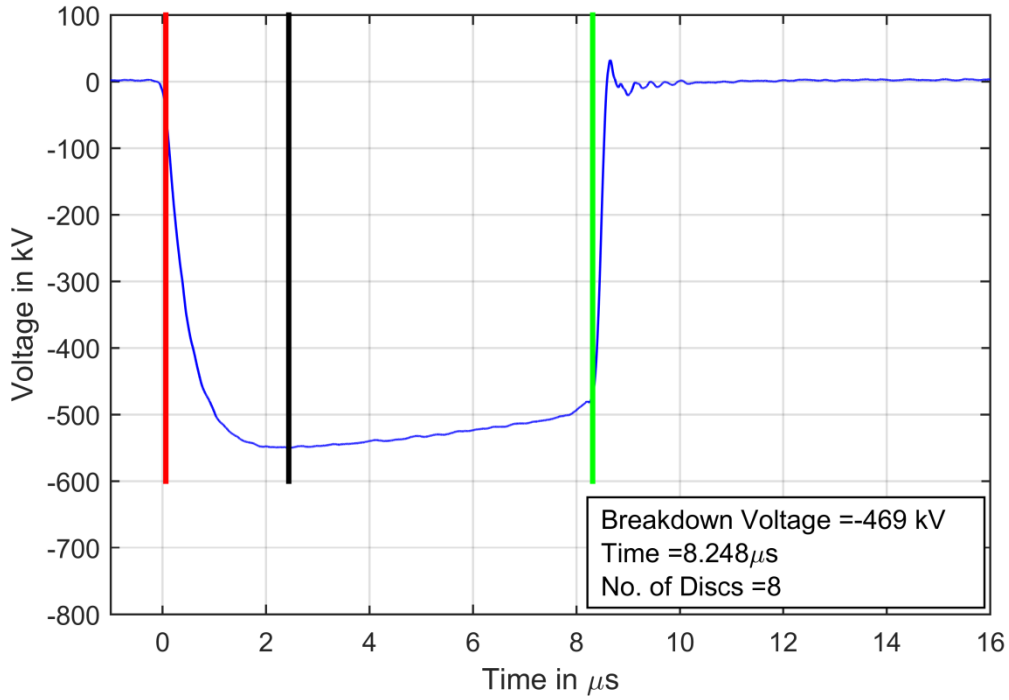
Voltage in kV
Time in μs
Breakdown Voltage =-469 kV
Time =8.248μs
No. of Discs =8

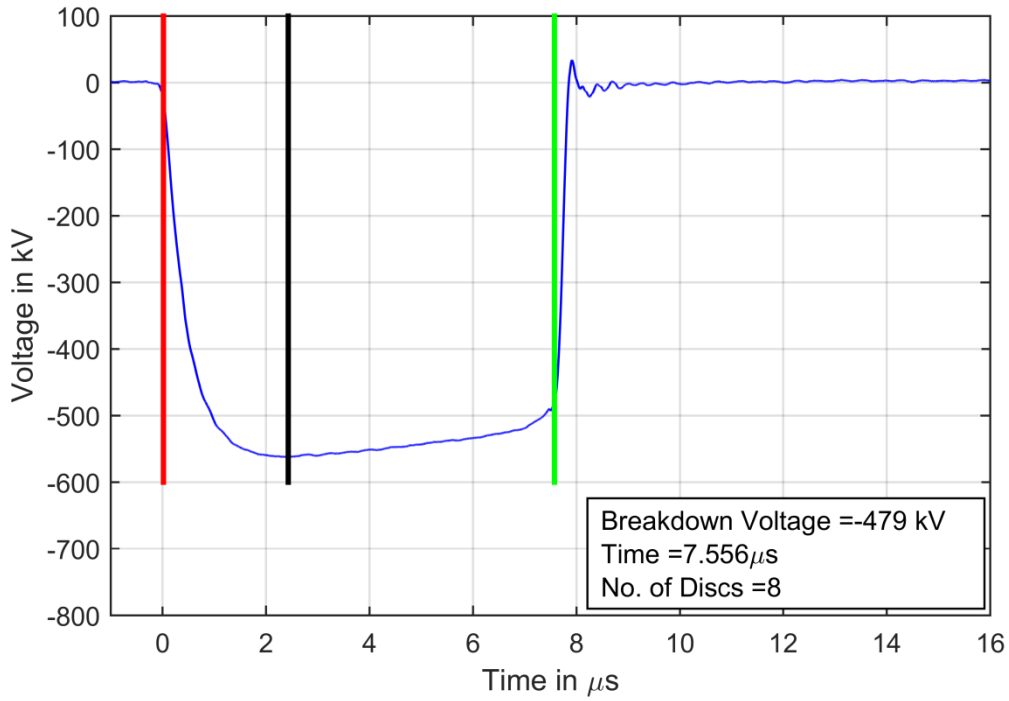
Voltage in kV
Time in μs
Breakdown Voltage =-479 kV
Time =7.556μs
No. of Discs =8

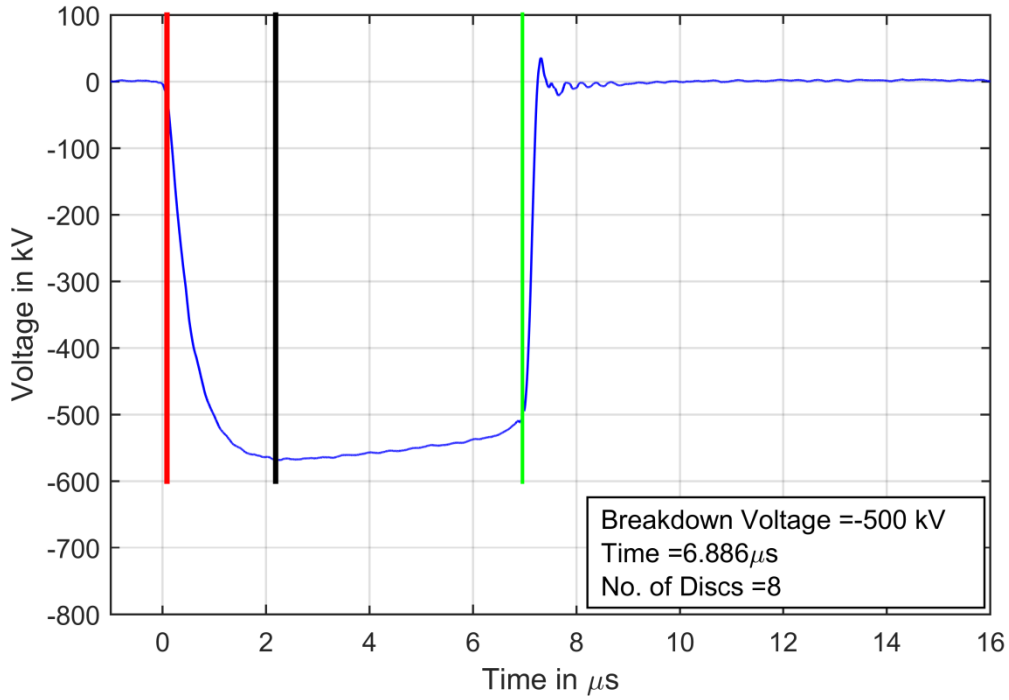
Voltage in kV
Time in μs
Breakdown Voltage =-500 kV
Time =6.886μs
No. of Discs =8

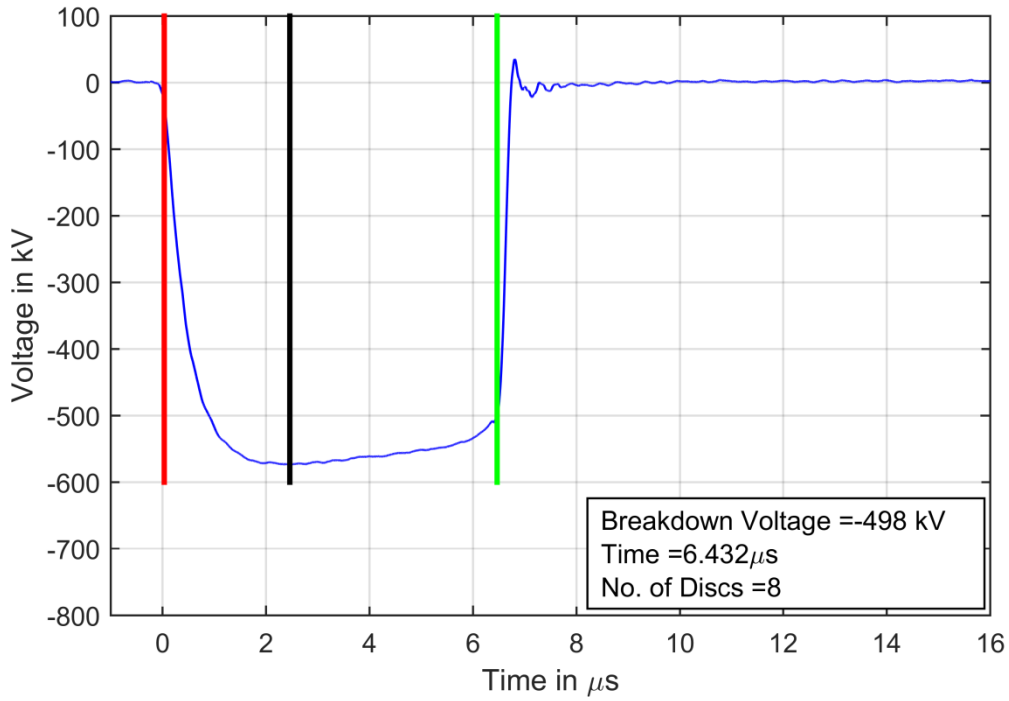
Voltage in kV
Time in μs
Breakdown Voltage =-498 kV
Time =6.432μs
No. of Discs =8

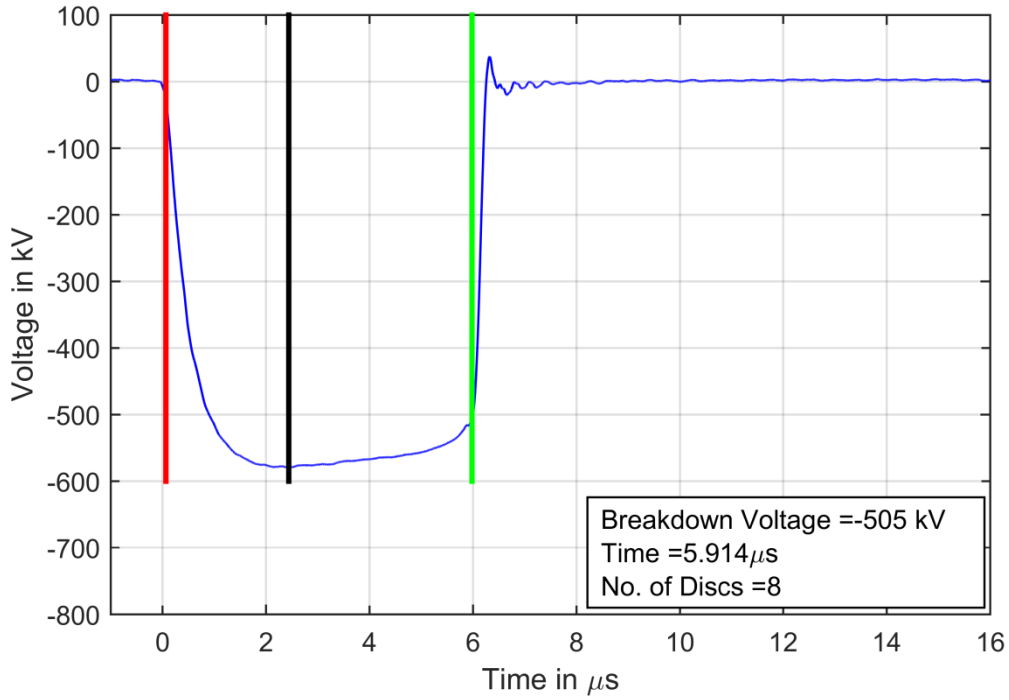
Voltage in kV
Time in μs
Breakdown Voltage =-505 kV
Time =5.914μs
No. of Discs =8

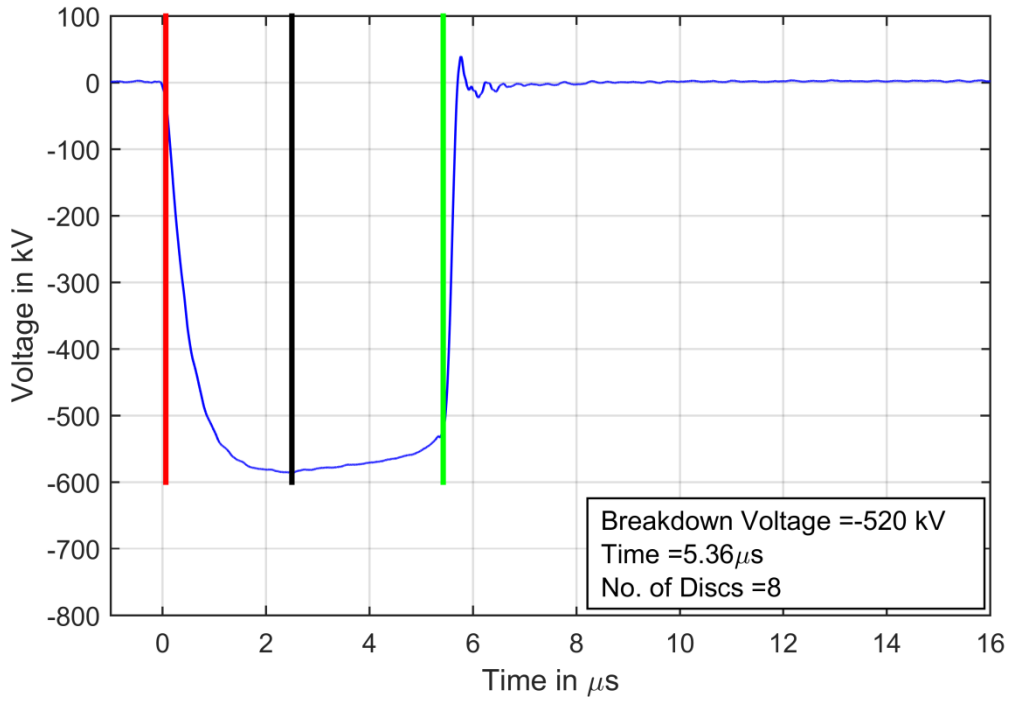
Voltage in kV
Time in μs
Breakdown Voltage =-520 kV
Time =5.36μs
No. of Discs =8

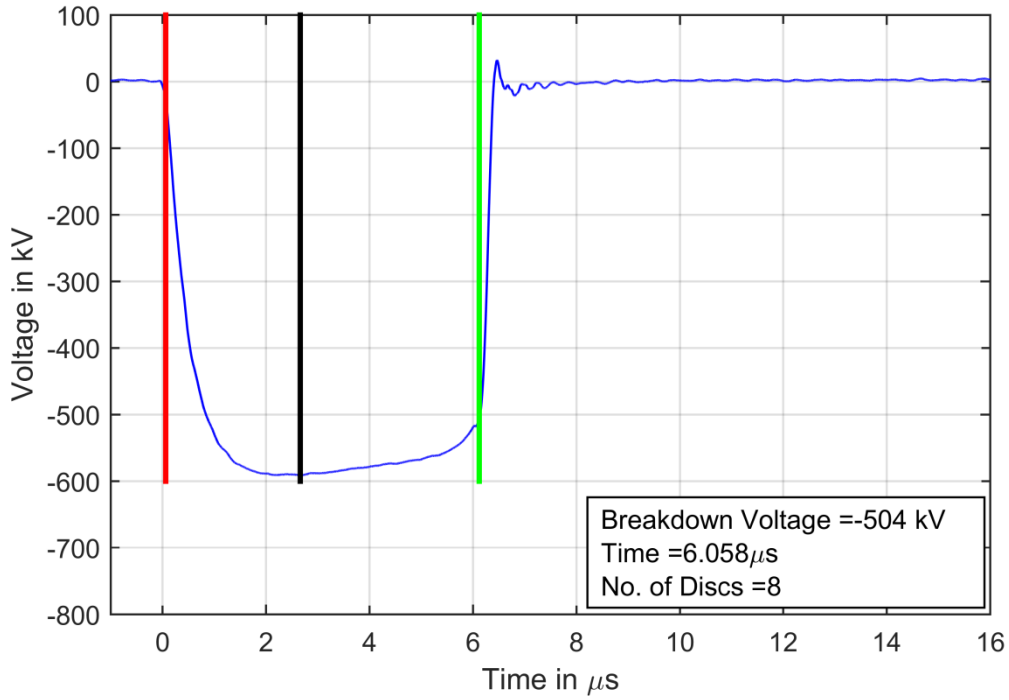
Voltage in kV
Time in μs
Breakdown Voltage =-504 kV
Time =6.058μs
No. of Discs =8

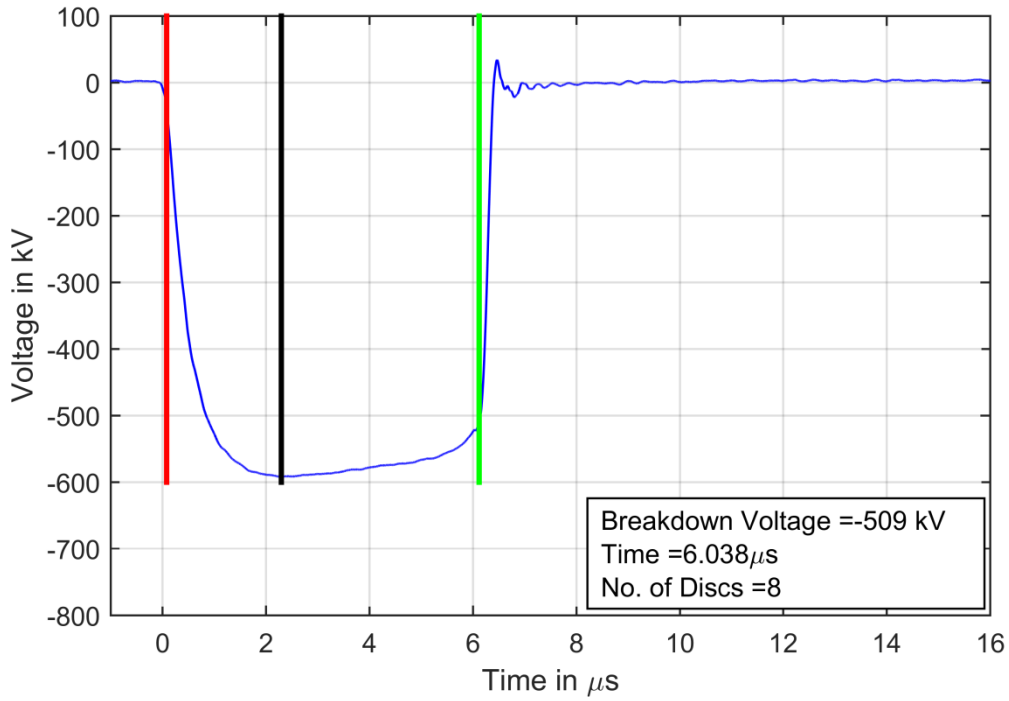
Voltage in kV
Time in μs
Breakdown Voltage =-509 kV
Time =6.038μs
No. of Discs =8

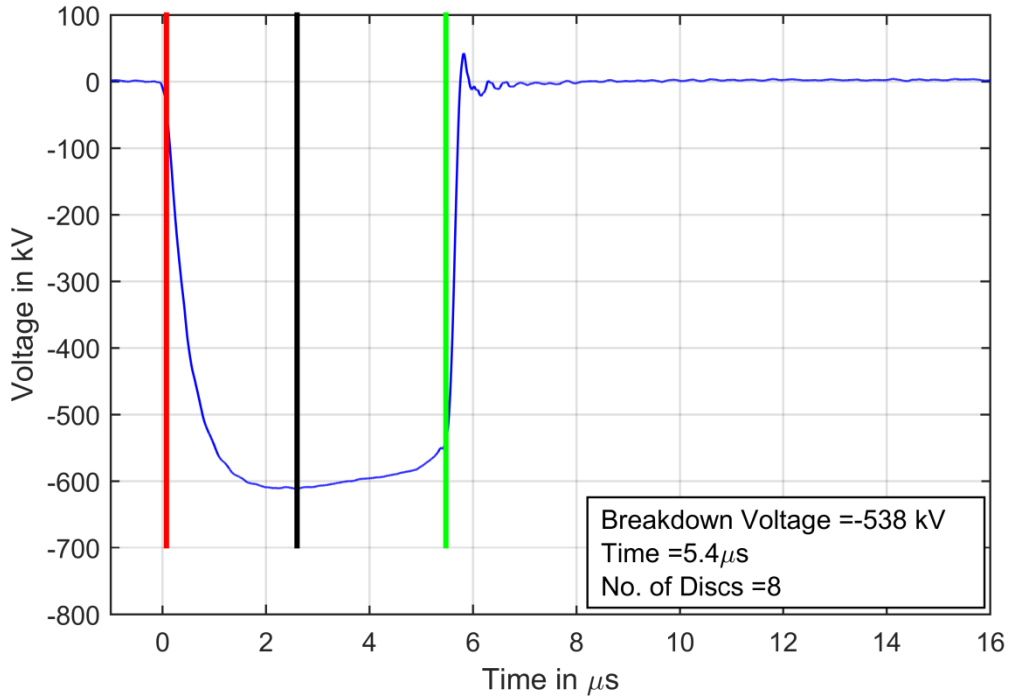
Voltage in kV
Time in μs
Breakdown Voltage =-538 kV
Time =5.4μs
No. of Discs =8

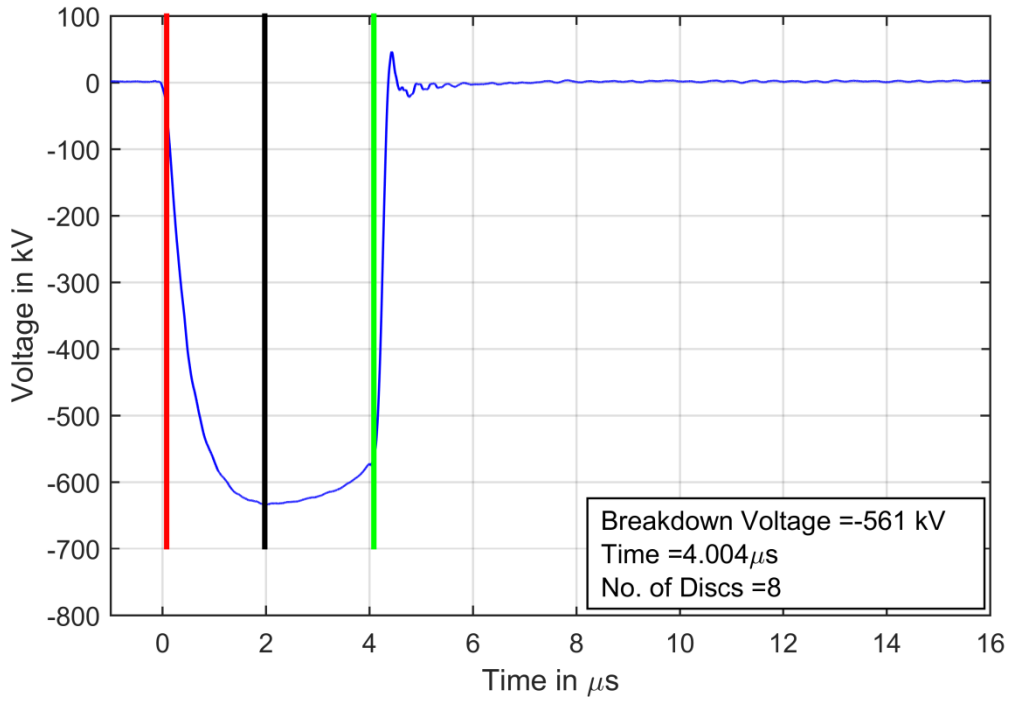
Voltage in kV
Time in μs
Breakdown Voltage =-561 kV
Time =4.004μs
No. of Discs =8

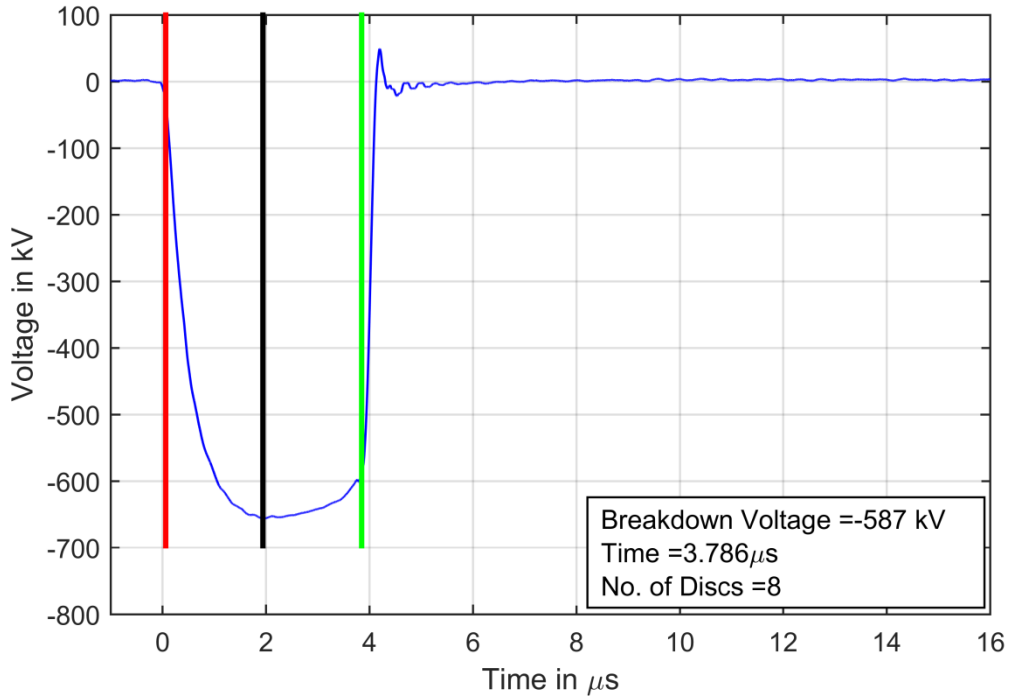
Voltage in kV
Time in μs
Breakdown Voltage =-587 kV
Time =3.786μs
No. of Discs =8

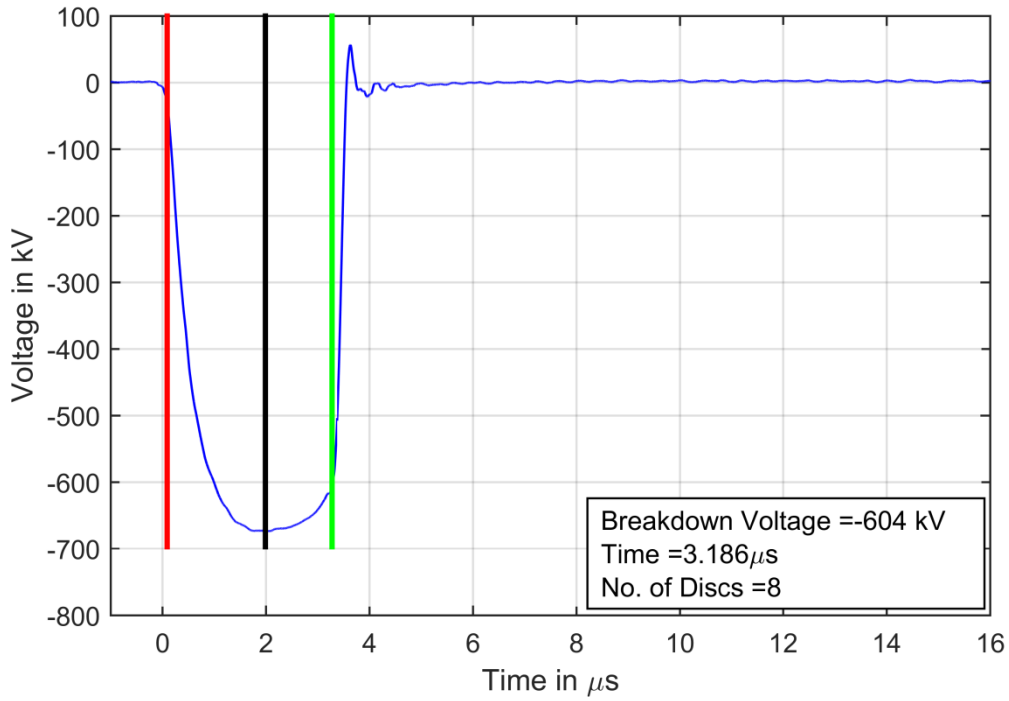
Voltage in kV
Time in μs
Breakdown Voltage =-604 kV
Time =3.186μs
No. of Discs =8

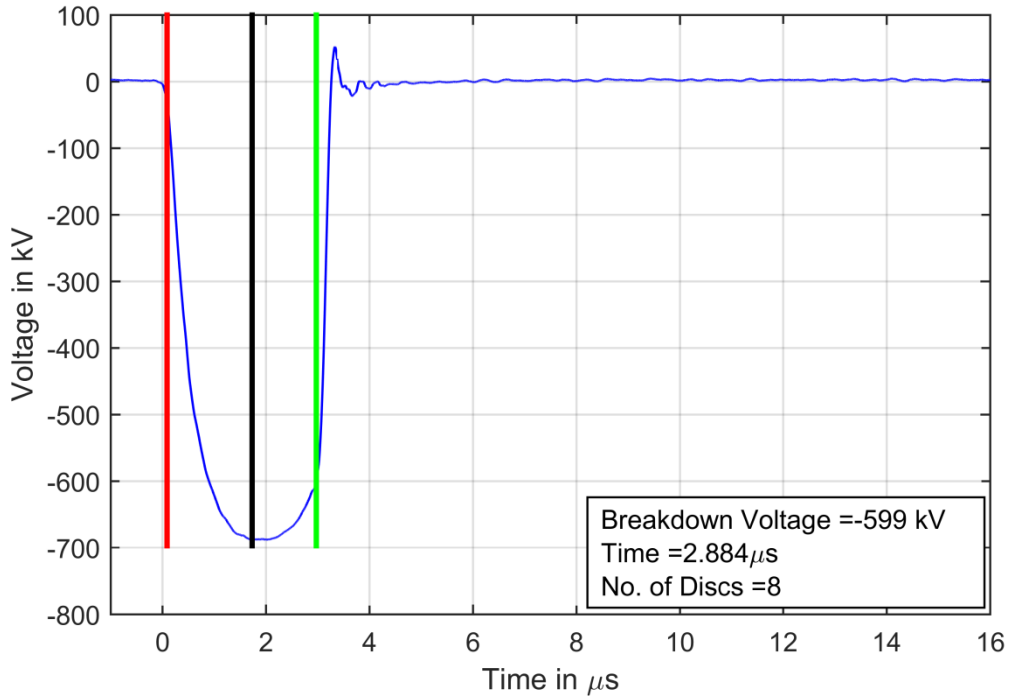
Voltage in kV
Time in μs
Breakdown Voltage =-599 kV
Time =2.884μs
No. of Discs =8

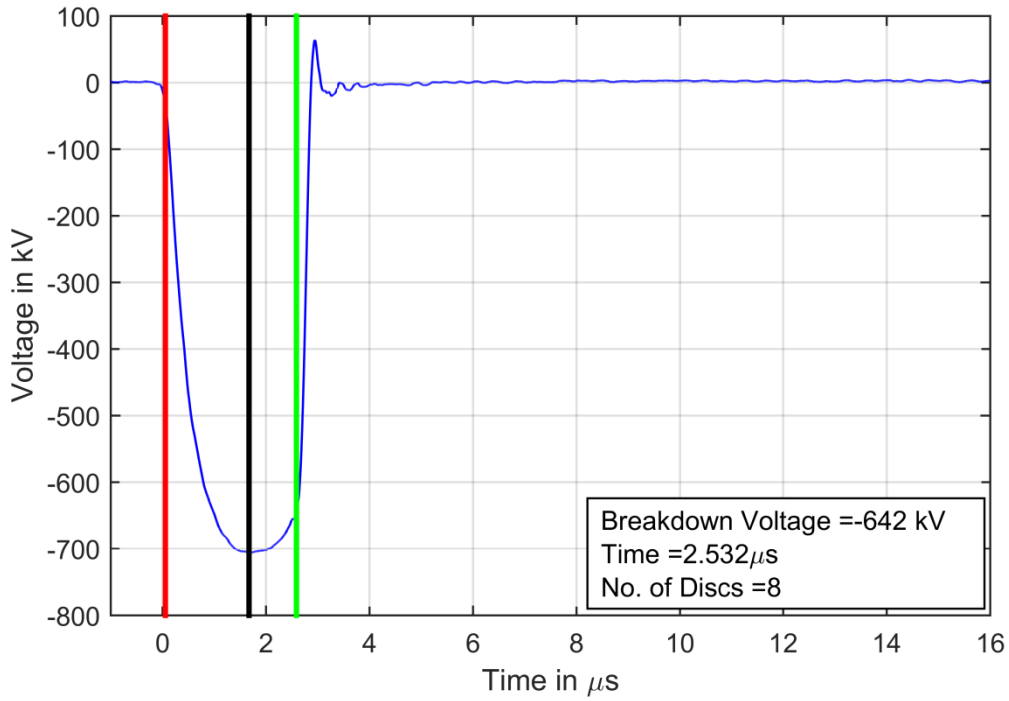
Voltage in kV
Time in μs
Breakdown Voltage =-642 kV
Time =2.532μs
No. of Discs =8

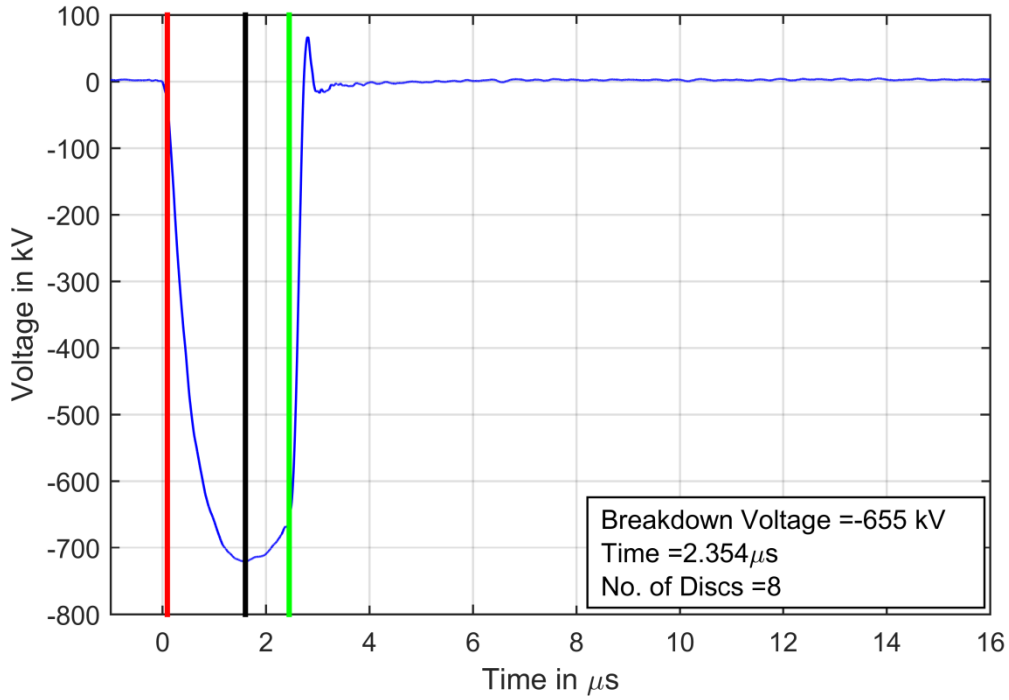
Voltage in kV
Time in μs
Breakdown Voltage =-655 kV
Time =2.354μs
No. of Discs =8

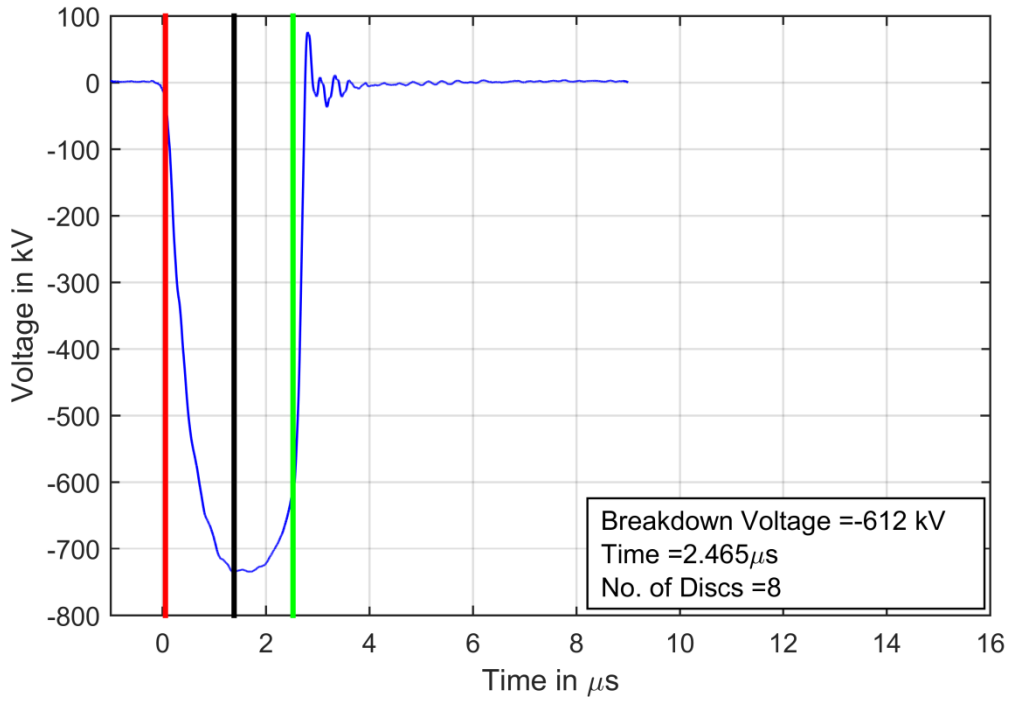
Voltage in kV
Time in μs
Breakdown Voltage =-612 kV
Time =2.465μs
No. of Discs =8

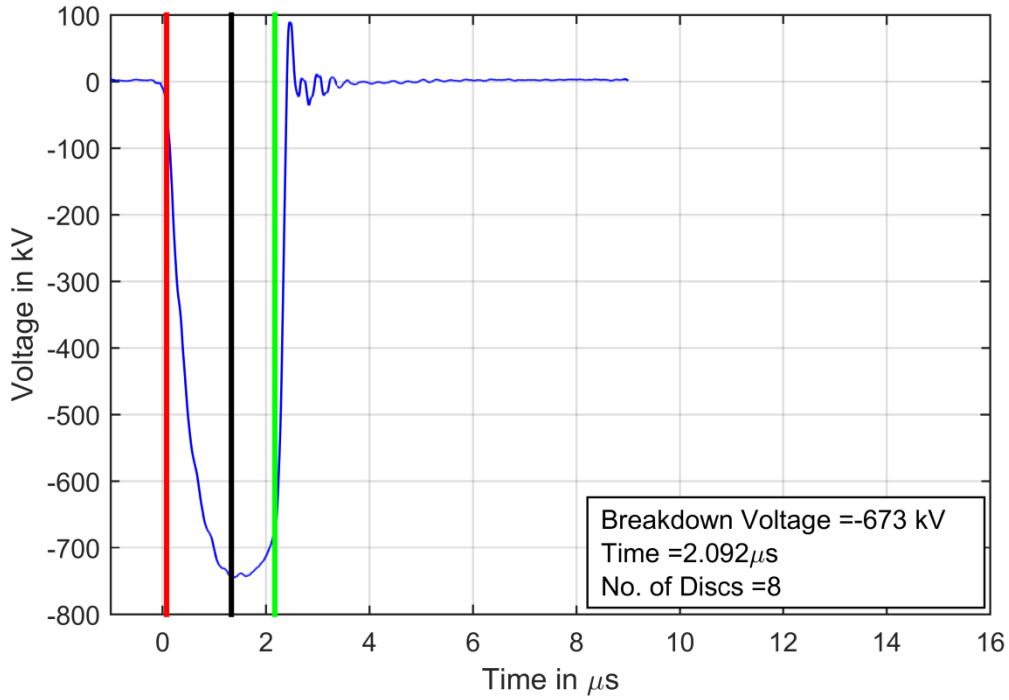
Voltage in kV
Time in μs
Breakdown Voltage =-673 kV
Time =2.092μs
No. of Discs =8

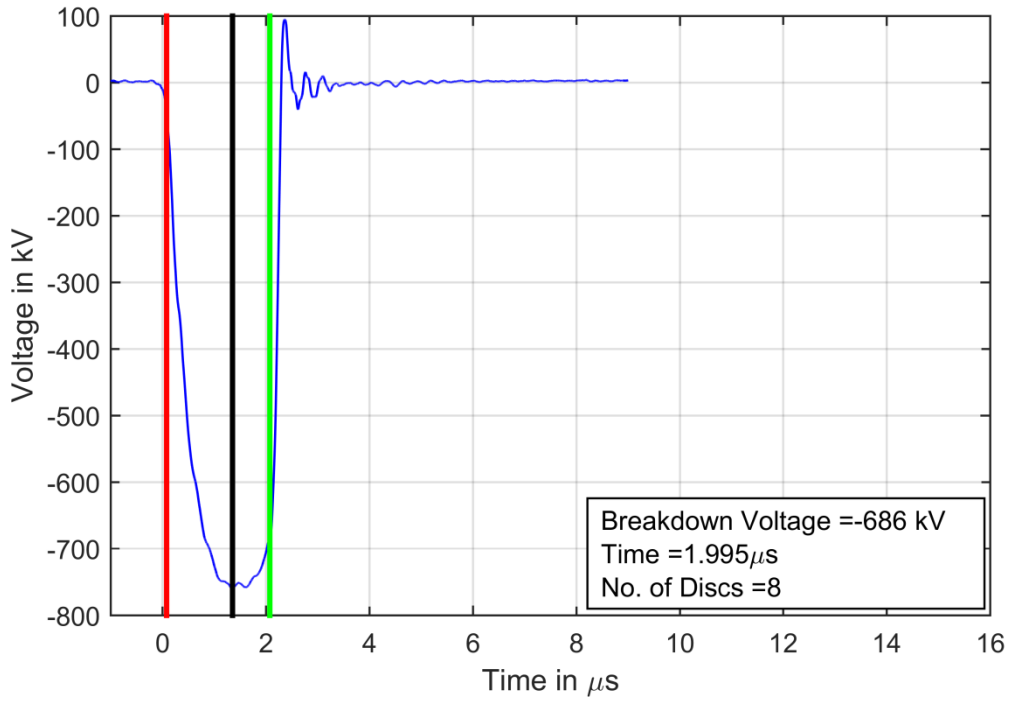
Voltage in kV
Time in μs
Breakdown Voltage =-686 kV
Time =1.995μs
No. of Discs =8

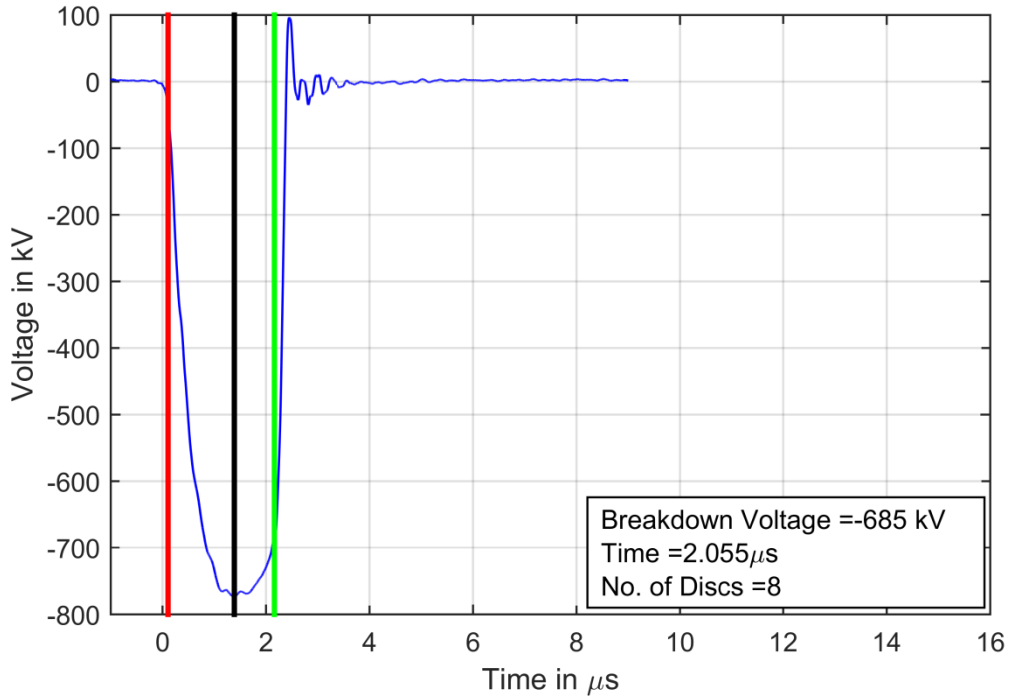
Voltage in kV
Time in μs
Breakdown Voltage =-685 kV
Time =2.055μs
No. of Discs =8

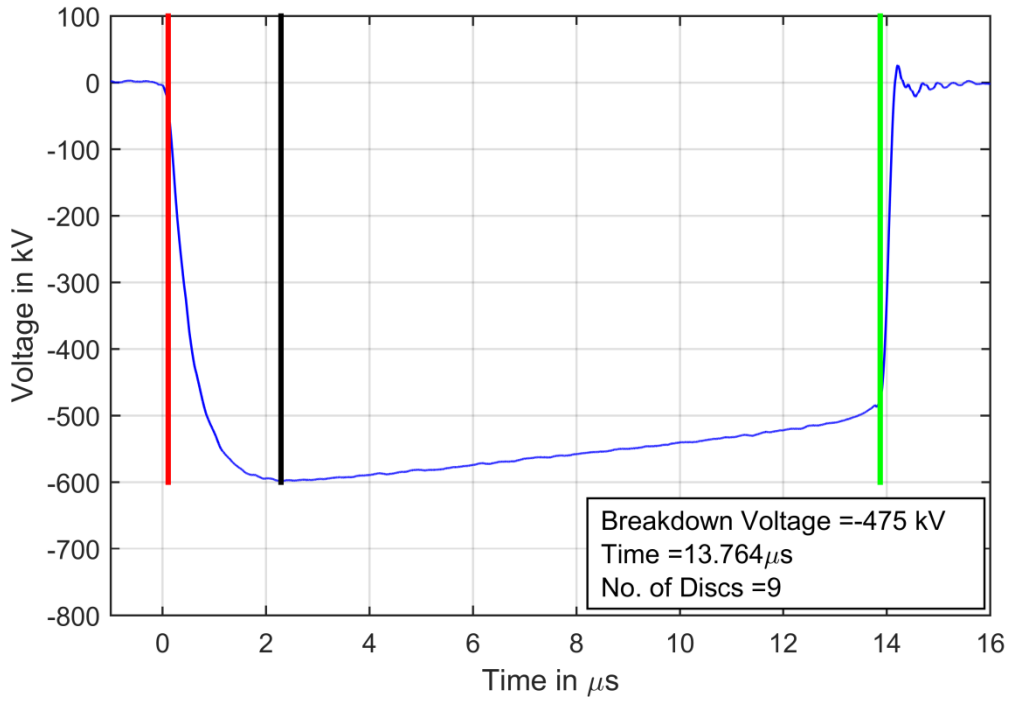
Voltage in kV
Time in μs
Breakdown Voltage =-475 kV
Time =13.764μs
No. of Discs =9

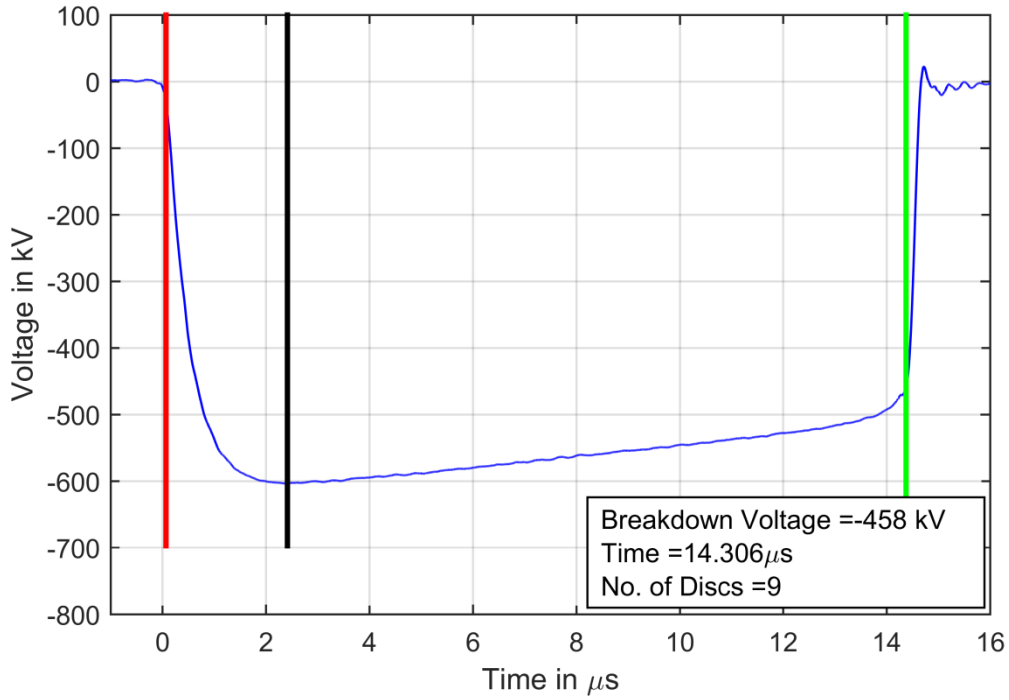
Voltage in kV
Time in μs
Breakdown Voltage =-458 kV
Time =14.306μs
No. of Discs =9

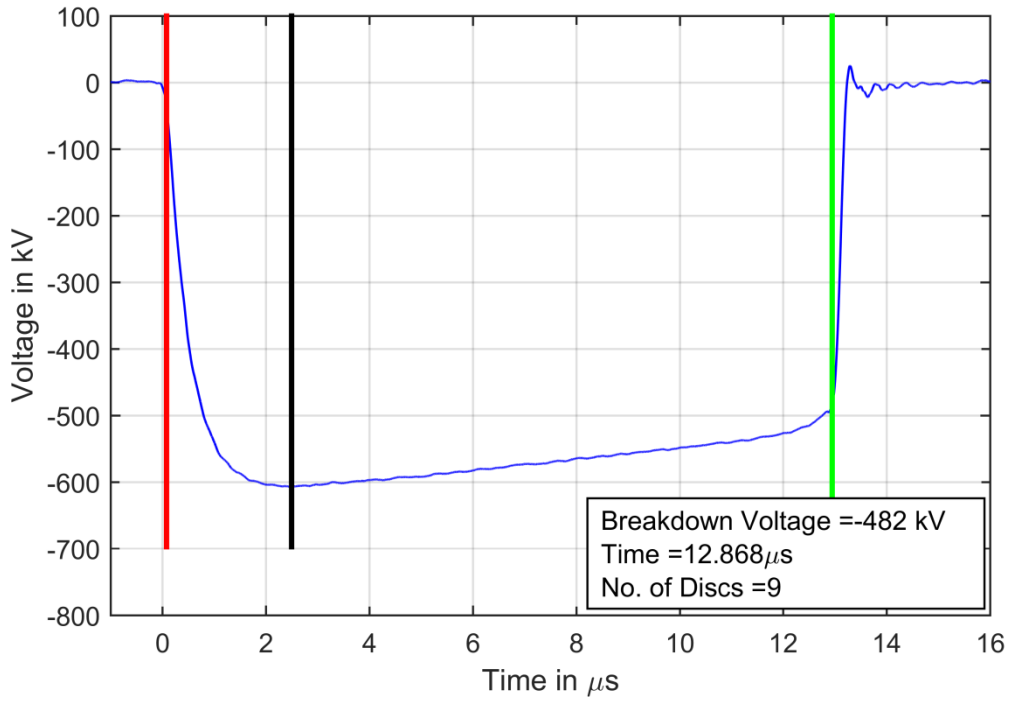
Voltage in kV
Time in μs
Breakdown Voltage =-482 kV
Time =12.868μs
No. of Discs =9

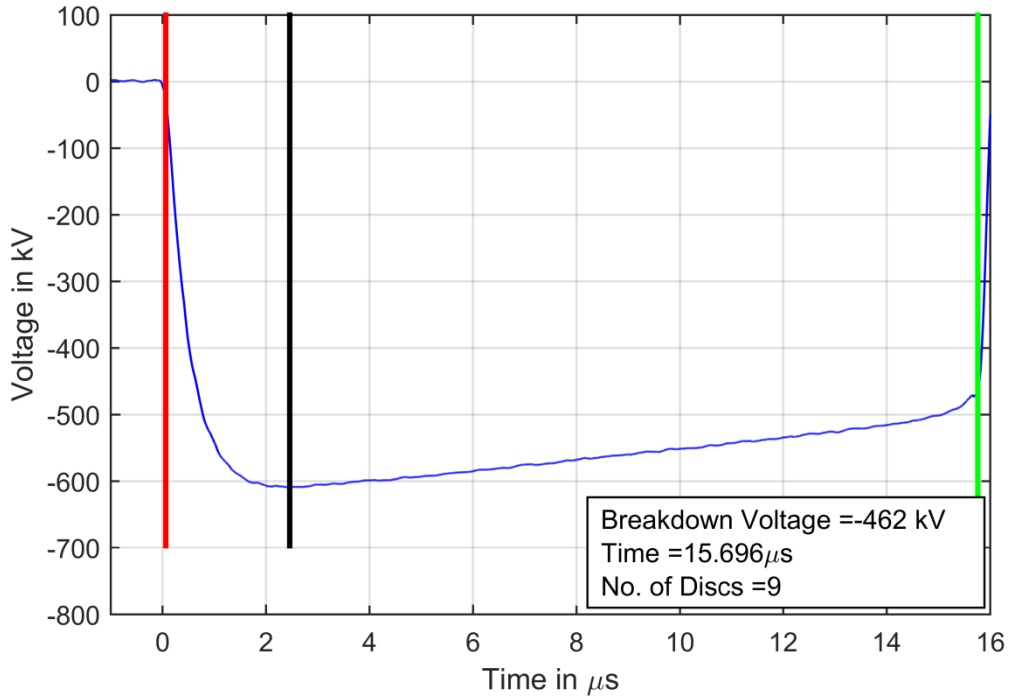
Voltage in kV
Time in μs
Breakdown Voltage =-462 kV
Time =15.696μs
No. of Discs =9

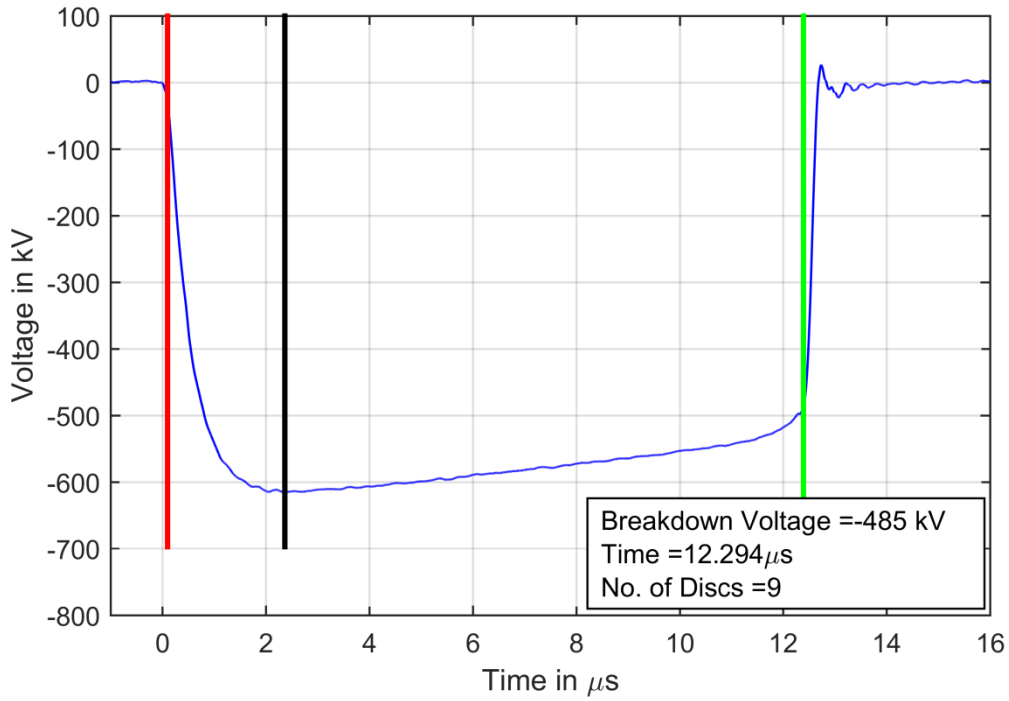
Voltage in kV
Time in μs
Breakdown Voltage =-485 kV
Time =12.294μs
No. of Discs =9

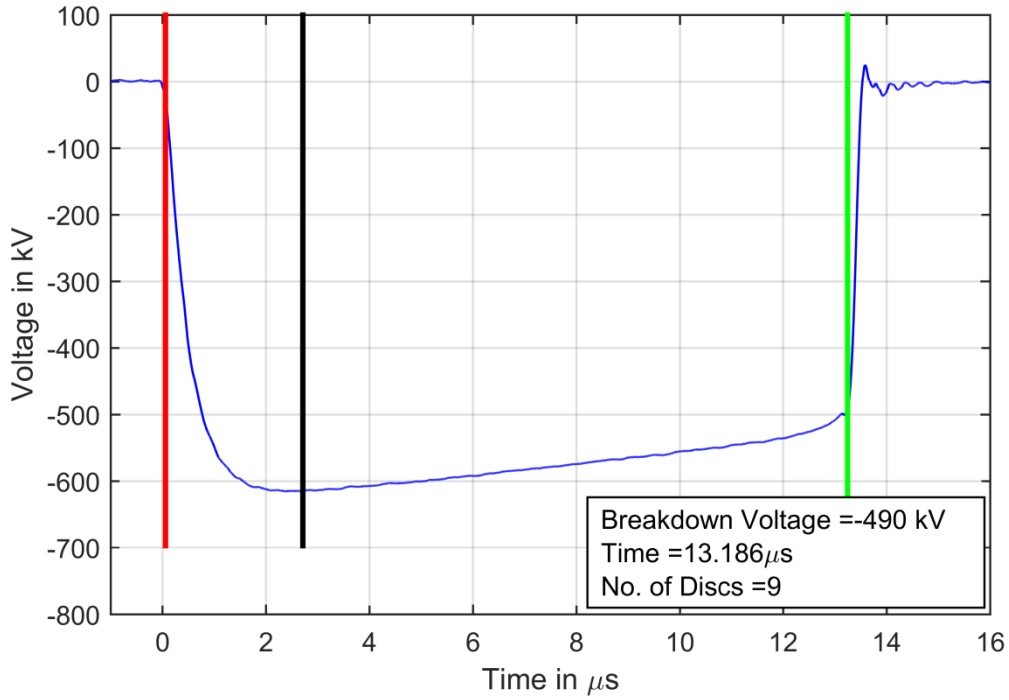
Voltage in kV
Time in μs
Breakdown Voltage =-490 kV
Time =13.186μs
No. of Discs =9

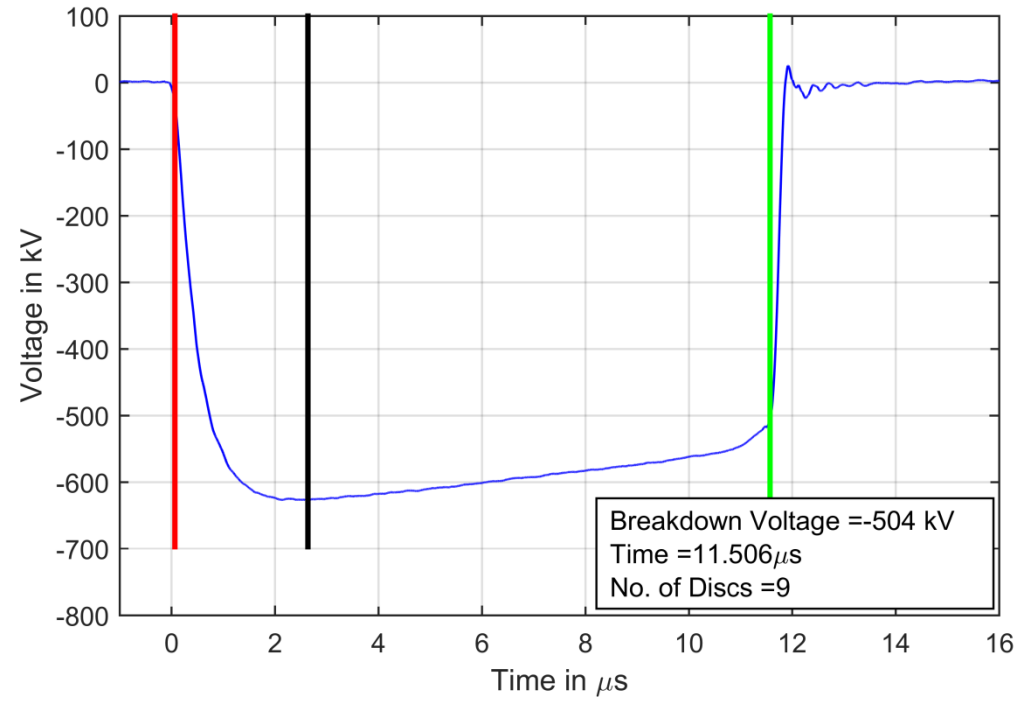
Voltage in kV
Time in μs
Breakdown Voltage =-504 kV
Time =11.506μs
No. of Discs =9

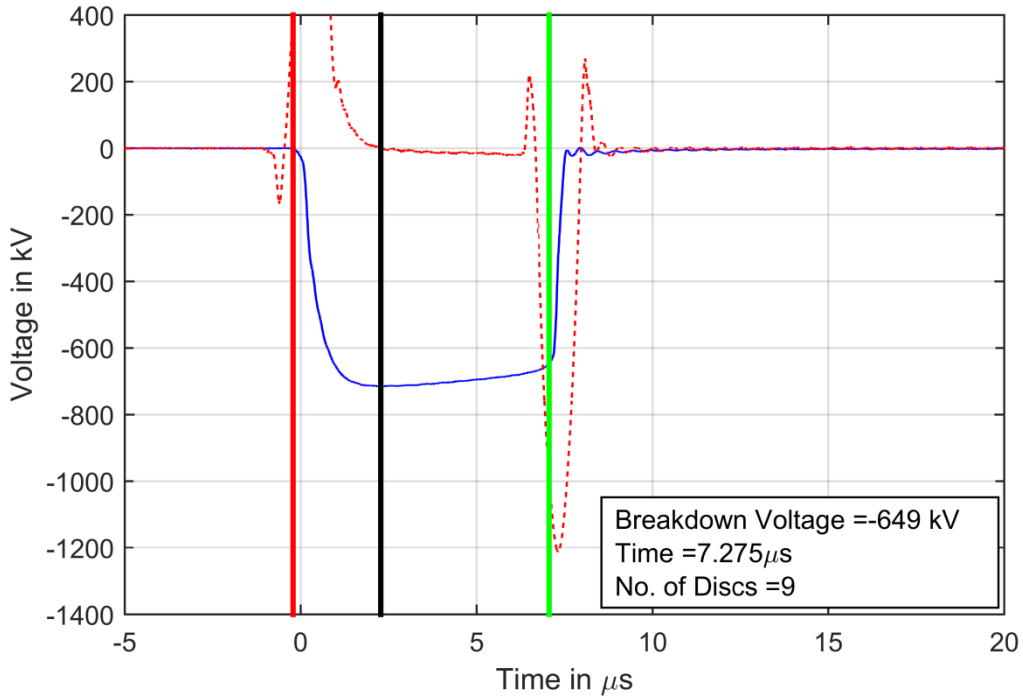
Voltage in kV
Time in μs
Breakdown Voltage =-649 kV
Time =7.275μs
No. of Discs =9

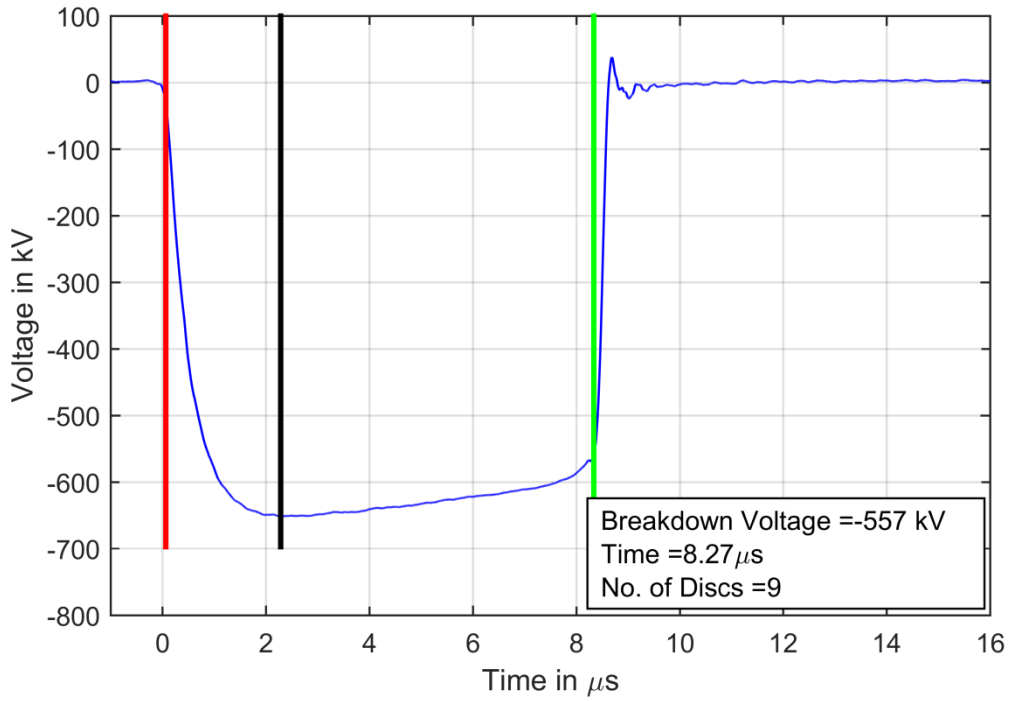
Voltage in kV
Time in μs
Breakdown Voltage =-557 kV
Time =8.27μs
No. of Discs =9

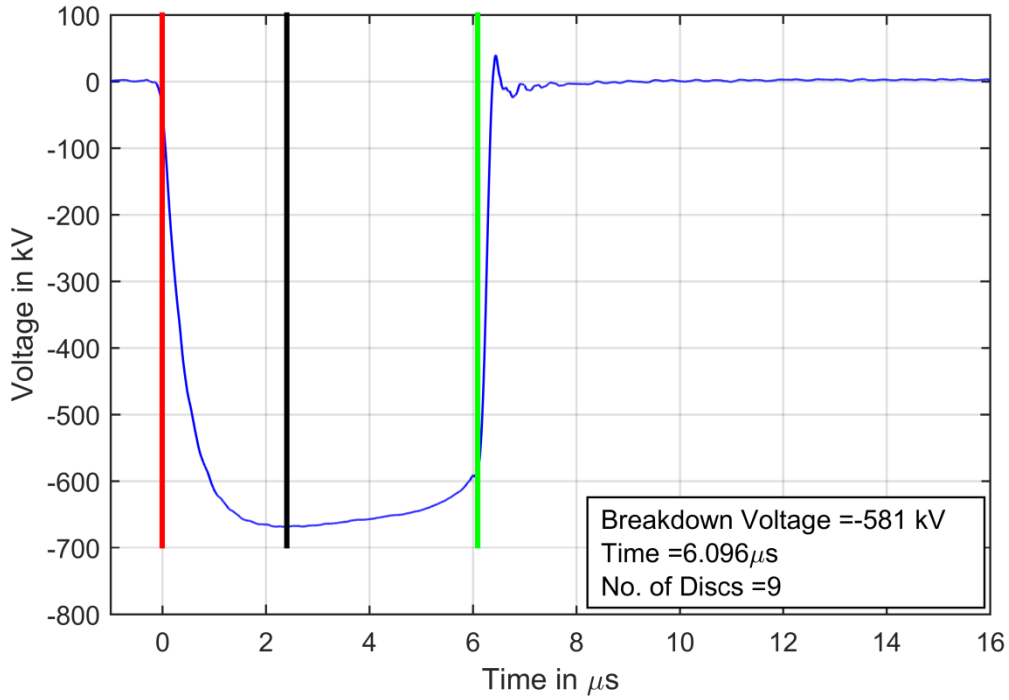
Voltage in kV
Time in μs
Breakdown Voltage =-581 kV
Time =6.096μs
No. of Discs =9

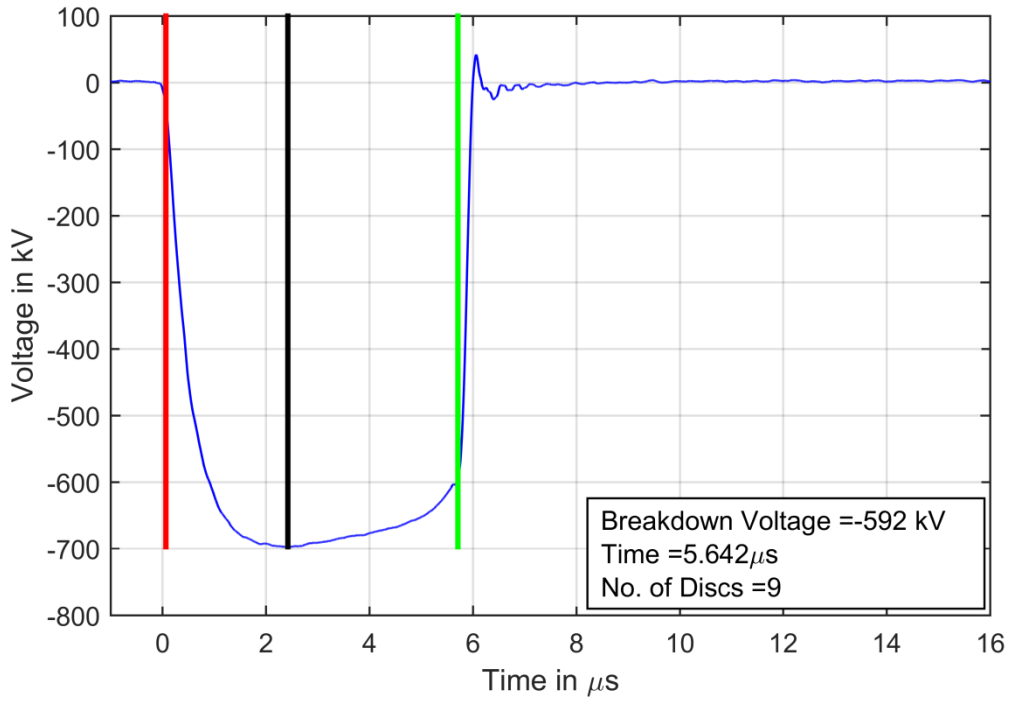
Voltage in kV
Time in μs
Breakdown Voltage =-592 kV
Time =5.642μs
No. of Discs =9

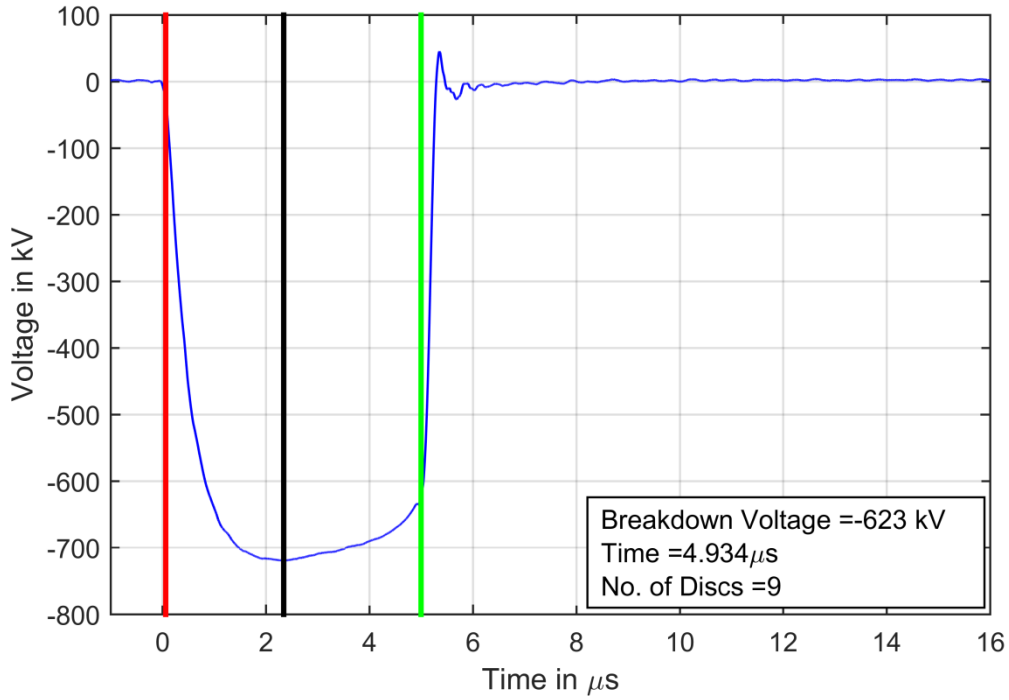
Voltage in kV
Time in μs
Breakdown Voltage =-623 kV
Time =4.934μs
No. of Discs =9

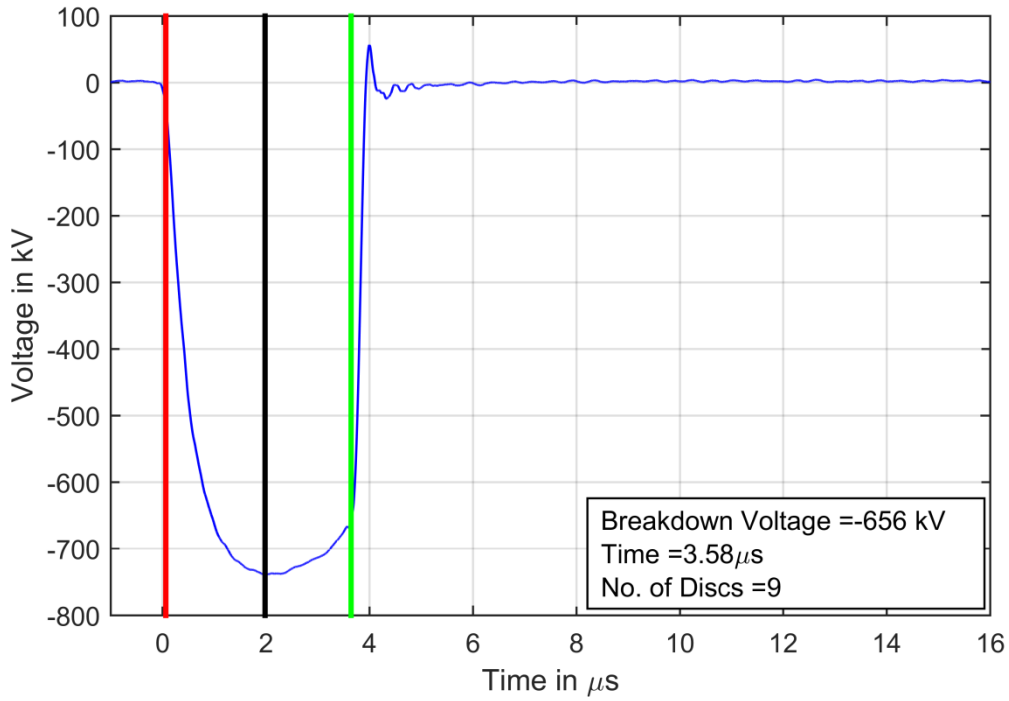
Voltage in kV
Time in μs
Breakdown Voltage =-656 kV
Time =3.58μs
No. of Discs =9

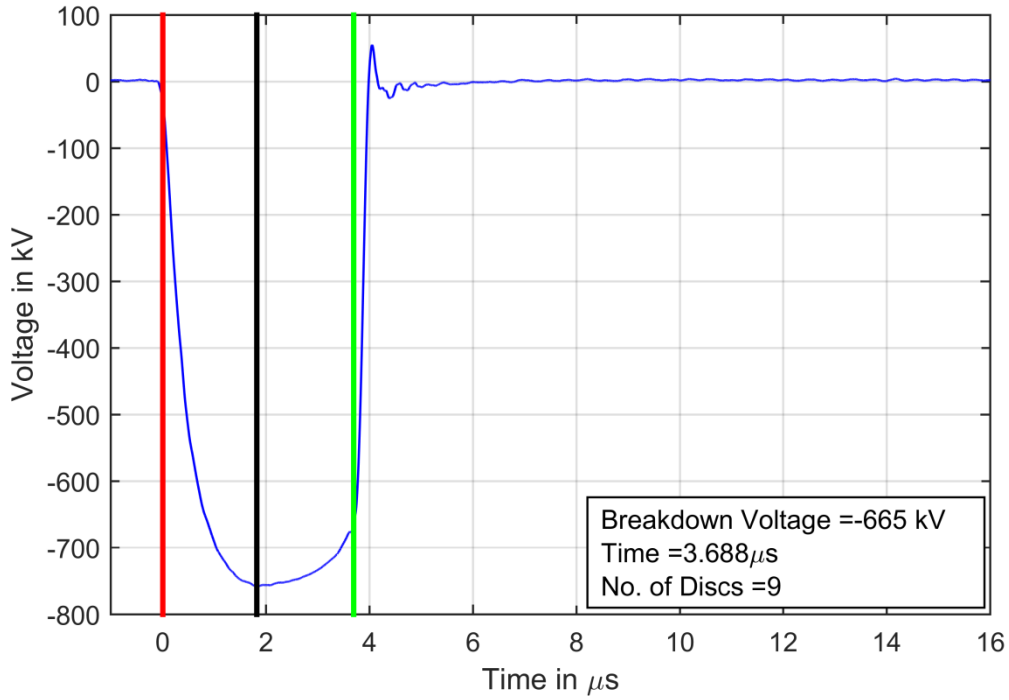
Voltage in kV
Time in μs
Breakdown Voltage =-665 kV
Time =3.688μs
No. of Discs =9

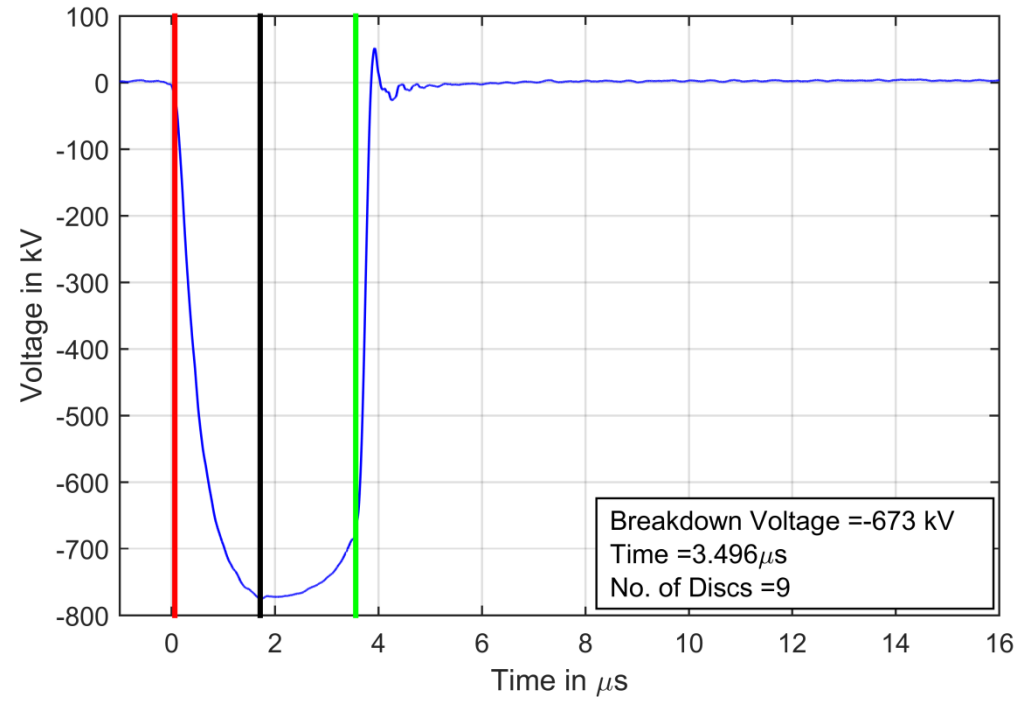
Voltage in kV
Time in μs
Breakdown Voltage =-673 kV
Time =3.496μs
No. of Discs =9

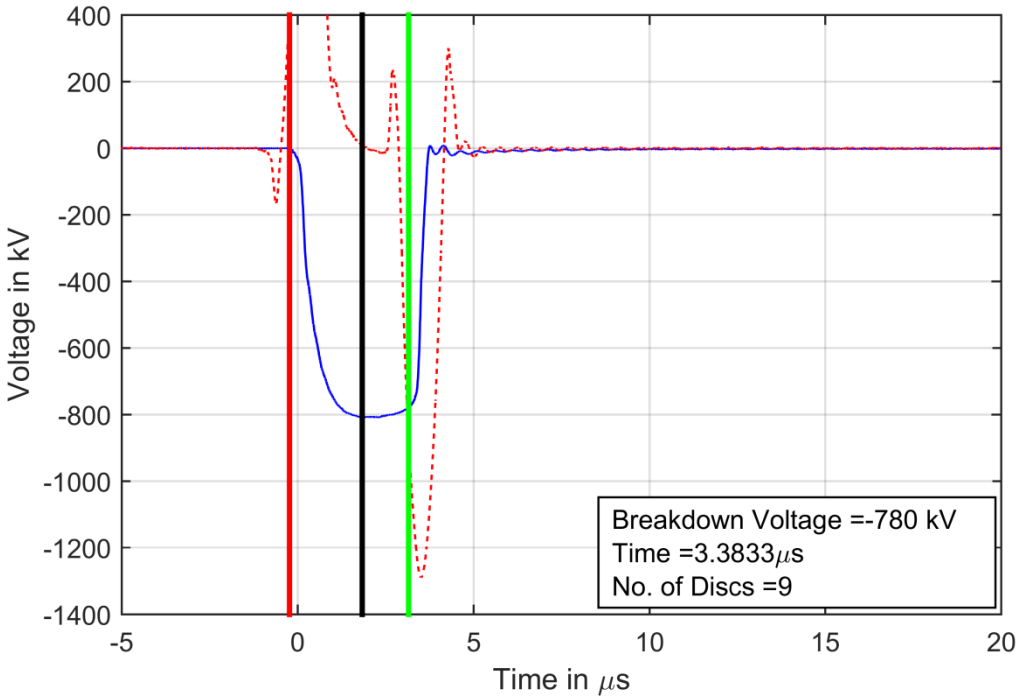
Voltage in kV
Time in μs
Breakdown Voltage =-780 kV
Time =3.3833μs
No. of Discs =9

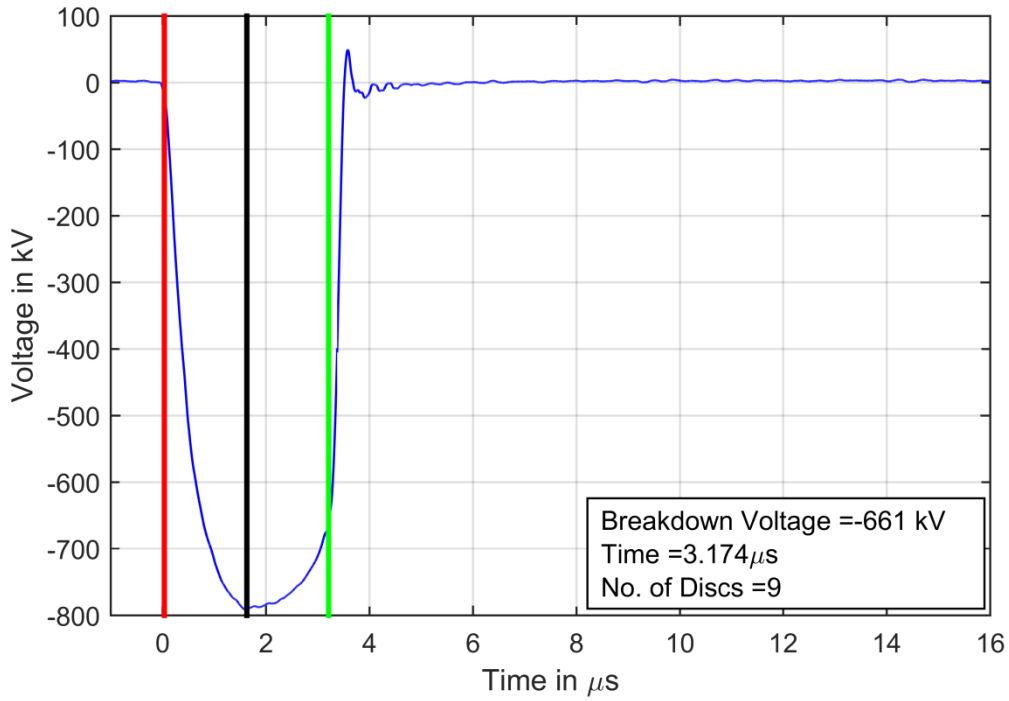
Voltage in kV
Time in μs
Breakdown Voltage =-661 kV
Time =3.174μs
No. of Discs =9

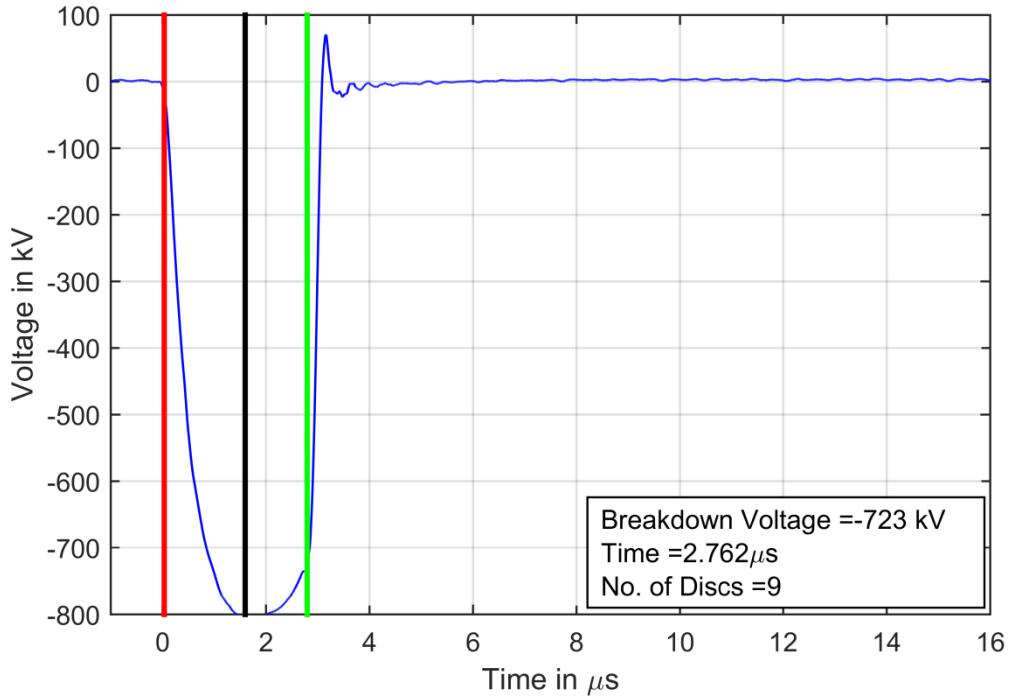
Voltage in kV
Time in μs
Breakdown Voltage =-723 kV
Time =2.762μs
No. of Discs =9

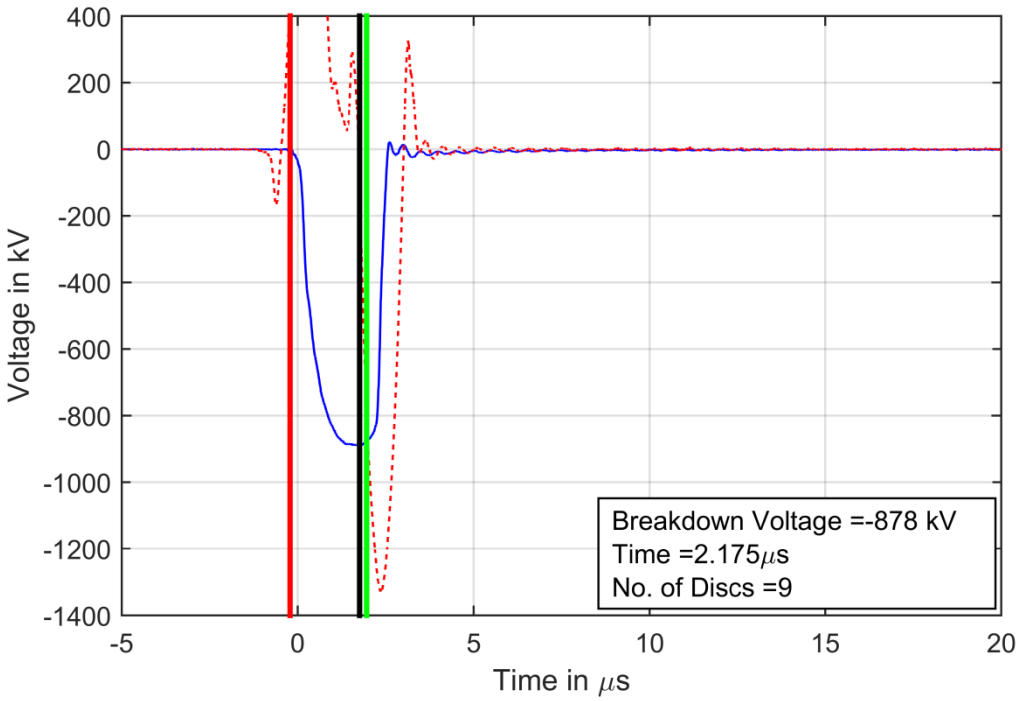
Voltage in kV
Time in μs
Breakdown Voltage =-878 kV
Time =2.175μs
No. of Discs =9

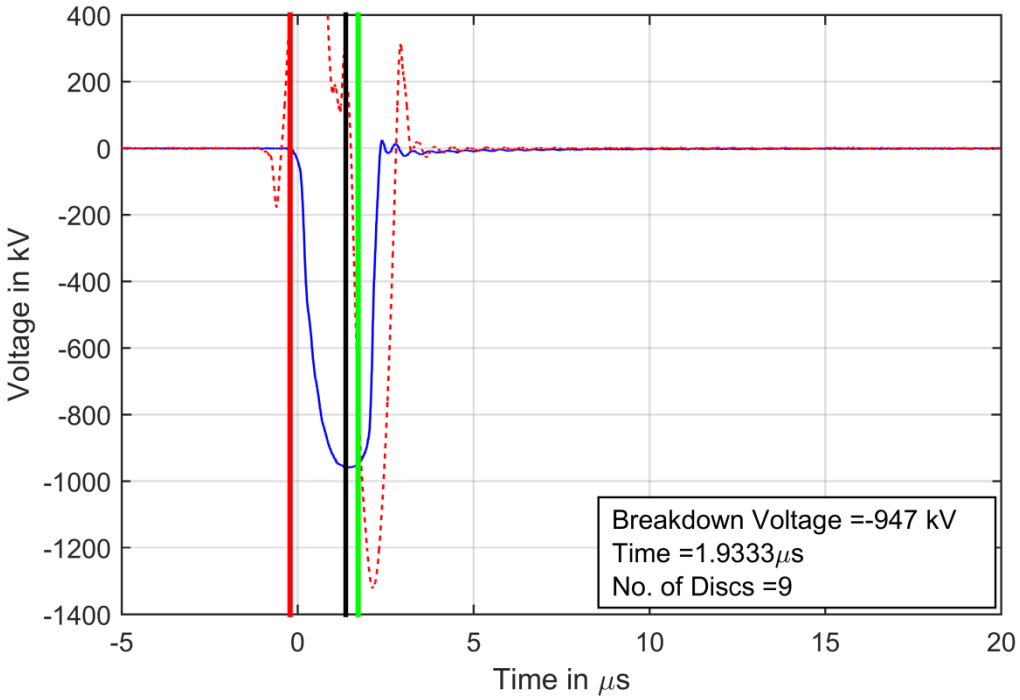
Voltage in kV
Time in μs
Breakdown Voltage =-947 kV
Time =1.9333μs
No. of Discs =9

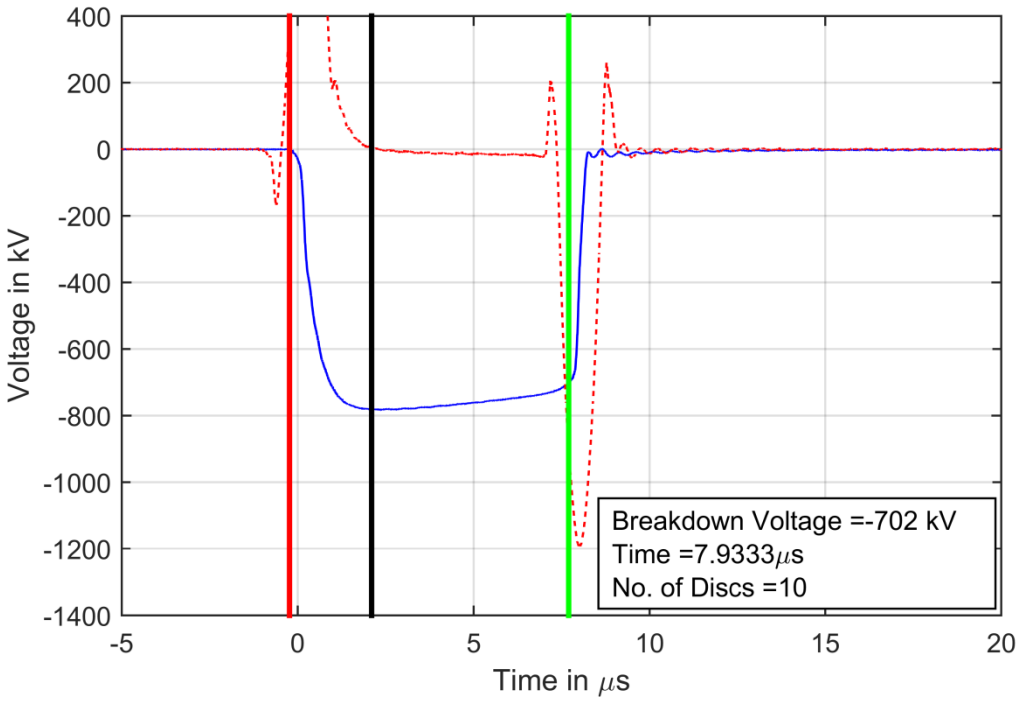
Voltage in kV
Time in μs
Breakdown Voltage =-702 kV
Time =7.9333μs
No. of Discs =10

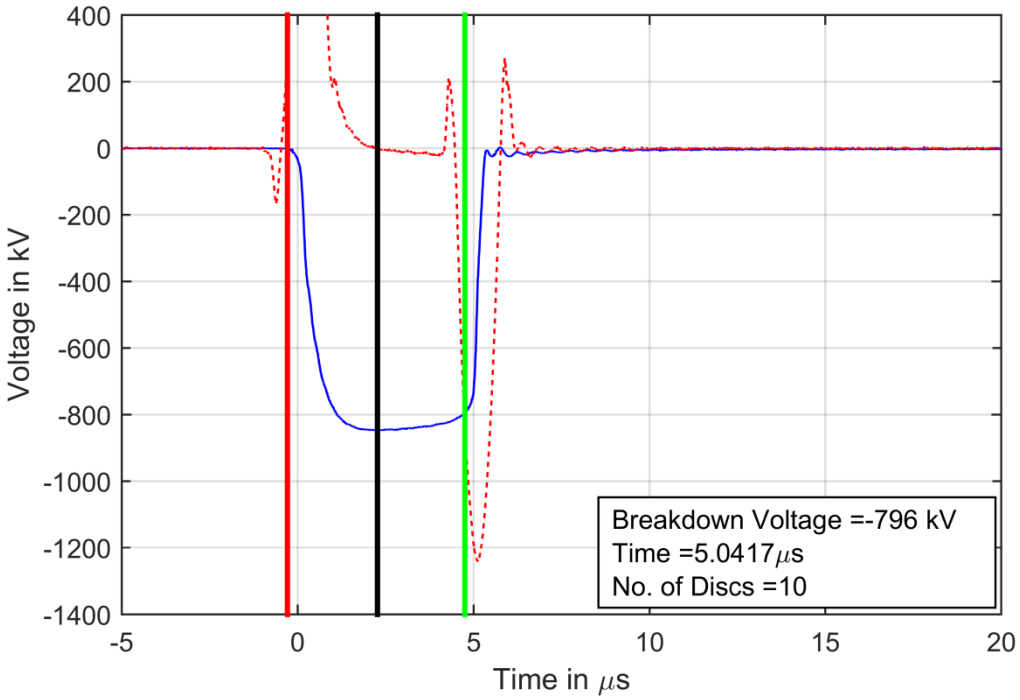
Voltage in kV
Time in μs
Breakdown Voltage =-796 kV
Time =5.0417μs
No. of Discs =10

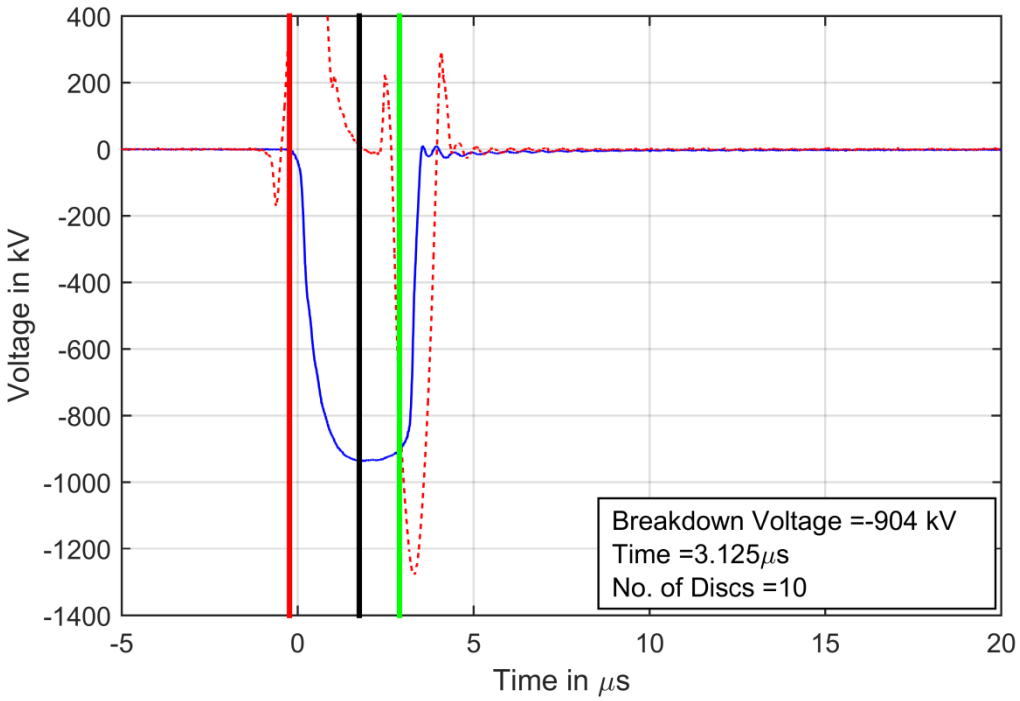
Voltage in kV
Time in μs
Breakdown Voltage =-904 kV
Time =3.125μs
No. of Discs =10

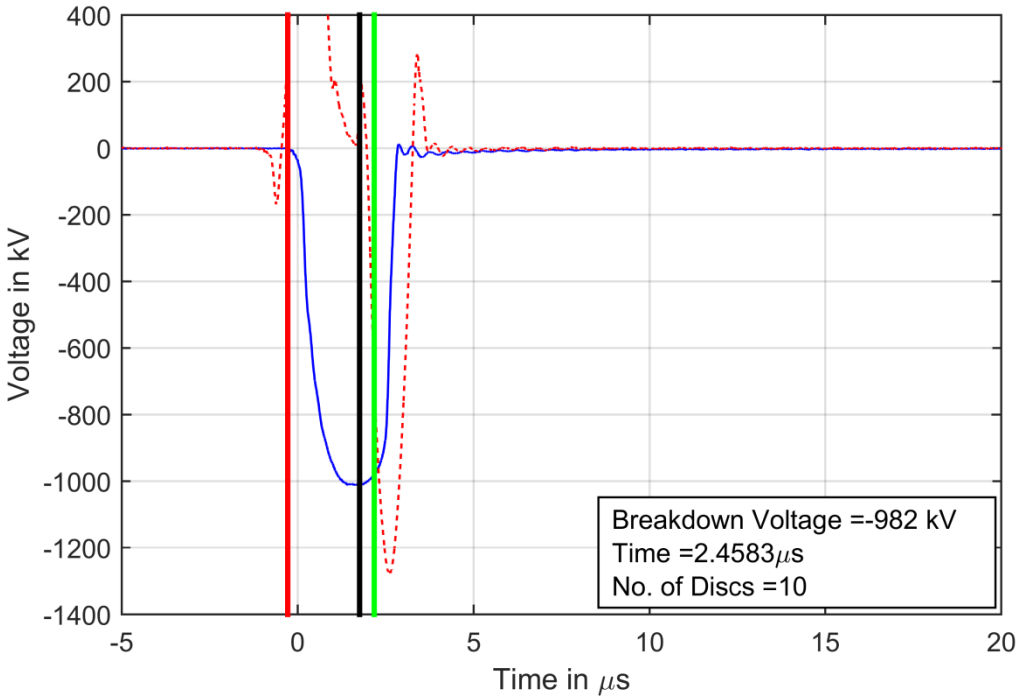
Voltage in kV
Time in μs
Breakdown Voltage =-982 kV
Time =2.4583μs
No. of Discs =10

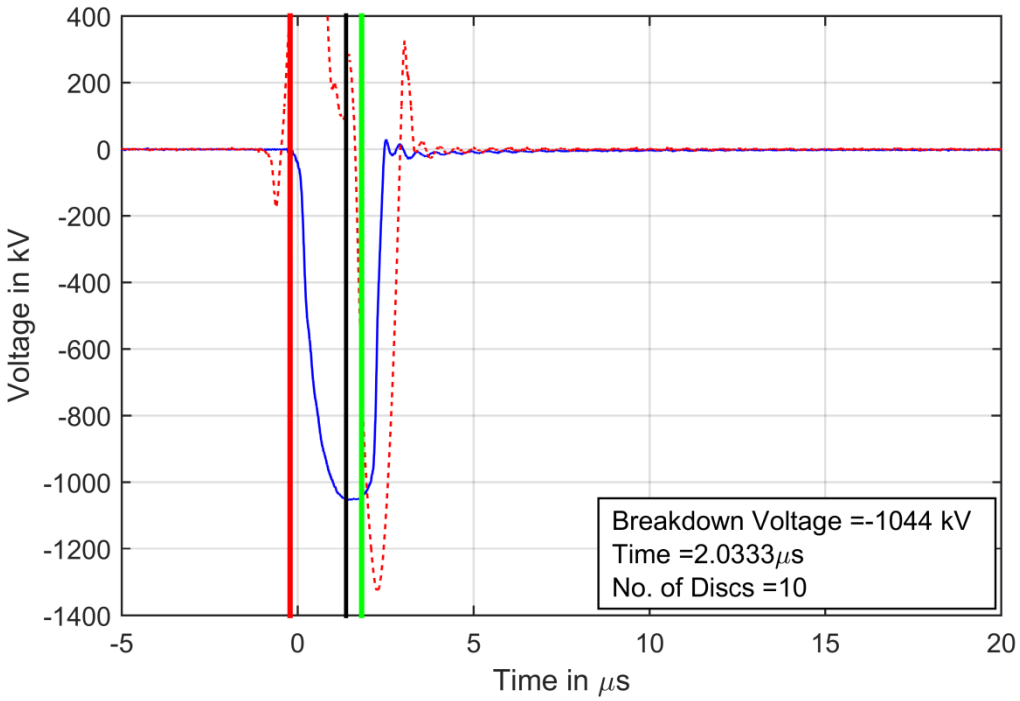
Voltage in kV
Time in μs
Breakdown Voltage =-1044 kV
Time =2.0333μs
No. of Discs =10

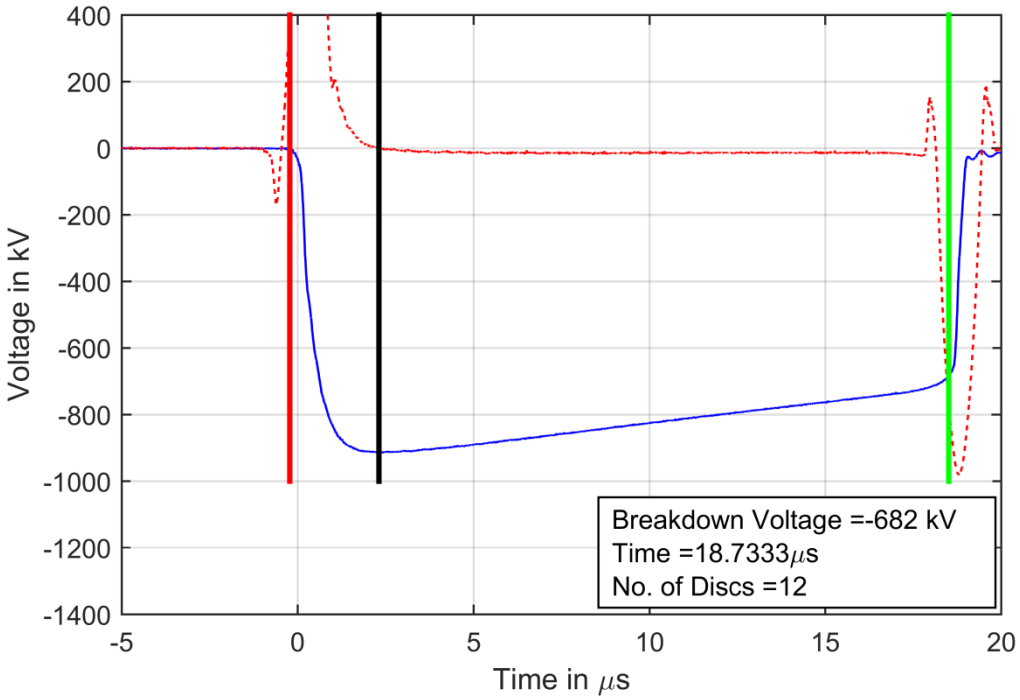
Voltage in kV
Time in μs
Breakdown Voltage =-682 kV
Time =18.7333μs
No. of Discs =12

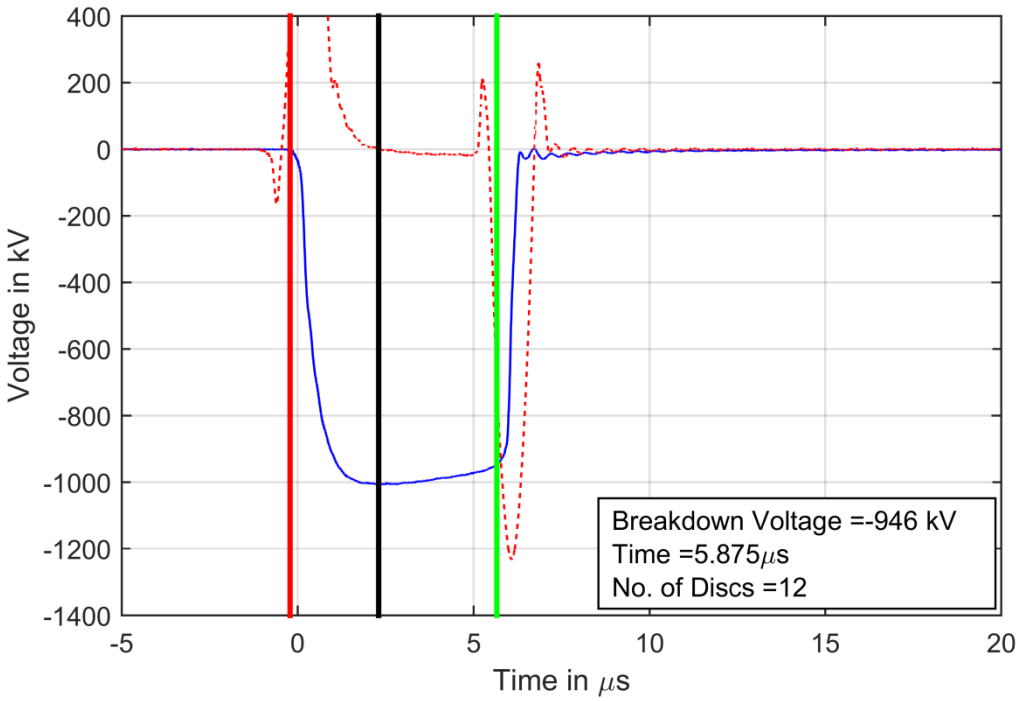
Voltage in kV
Time in μs
Breakdown Voltage =-946 kV
Time =5.875μs
No. of Discs =12

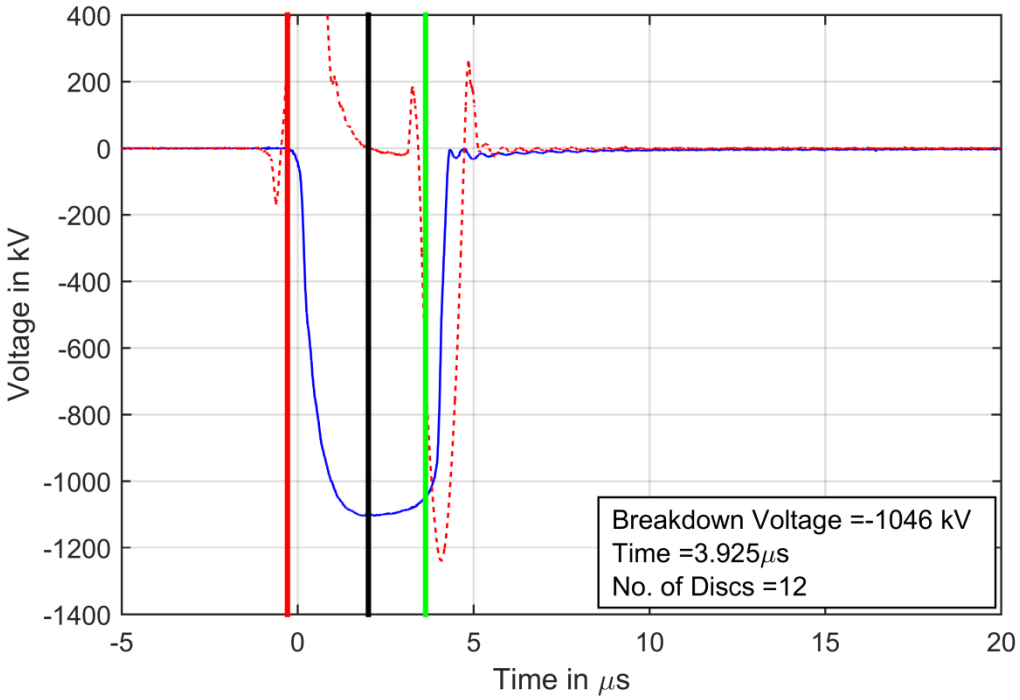
Voltage in kV
Time in μs
Breakdown Voltage =-1046 kV
Time =3.925μs
No. of Discs =12

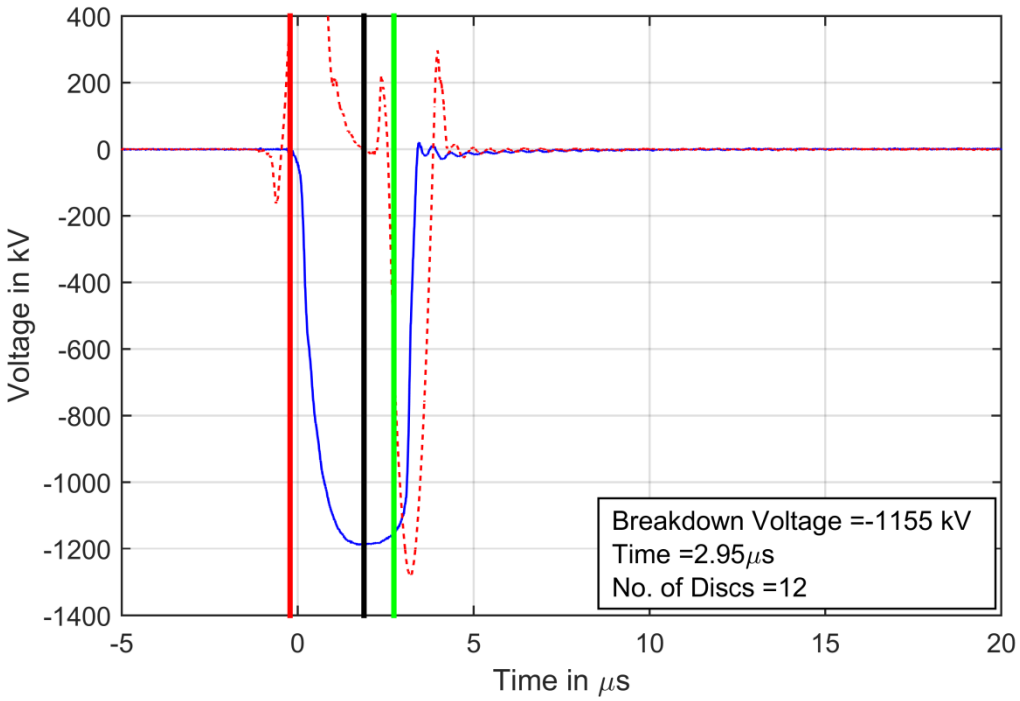
Voltage in kV
Time in μs
Breakdown Voltage =-1155 kV
Time =2.95μs
No. of Discs =12

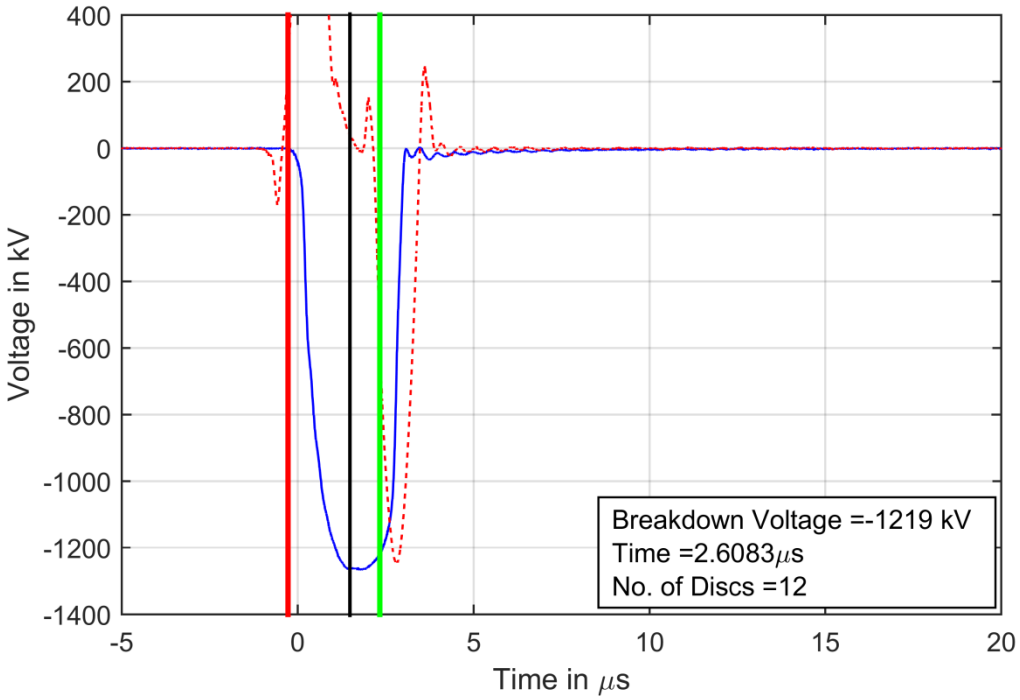
Voltage in kV
Time in μs
Breakdown Voltage =-1219 kV
Time =2.6083μs
No. of Discs =12

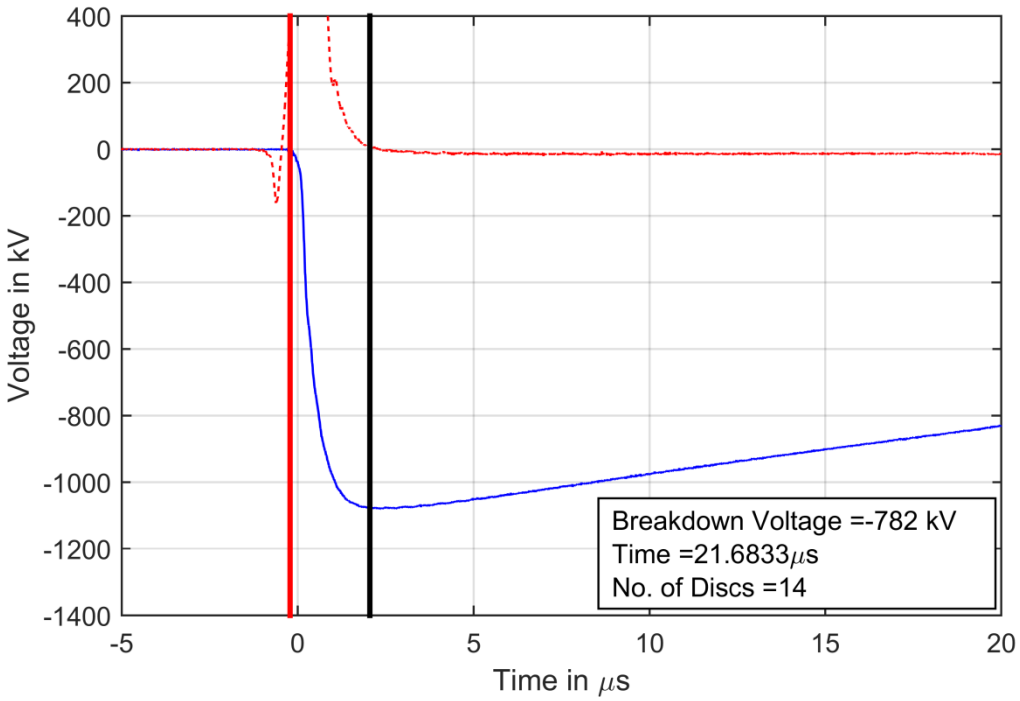
Voltage in kV
Time in μs
Breakdown Voltage =-782 kV
Time =21.6833μs
No. of Discs =14

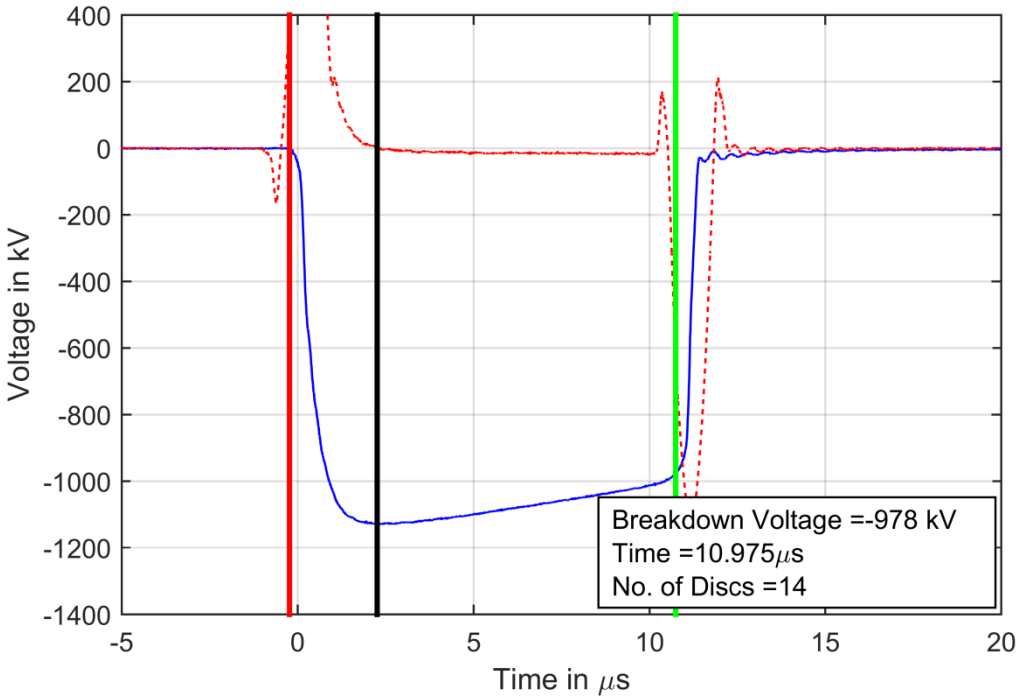
Voltage in kV
Time in μs
Breakdown Voltage =-978 kV
Time =10.975μs
No. of Discs =14

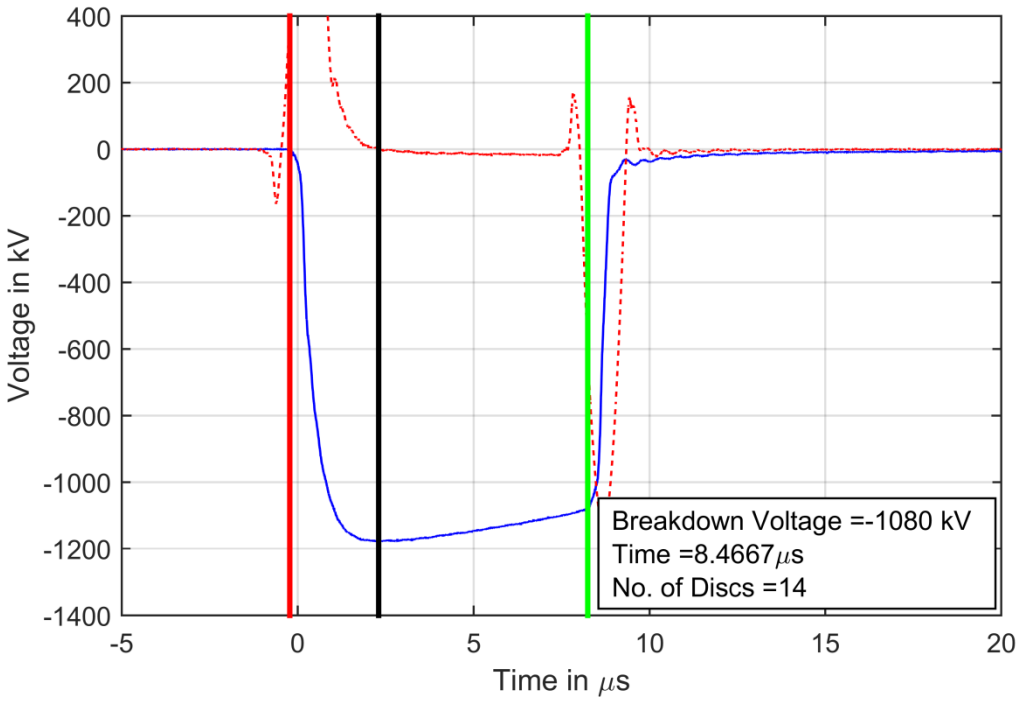
Voltage in kV
Time in μs
Breakdown Voltage =-1080 kV
Time =8.4667μs
No. of Discs =14

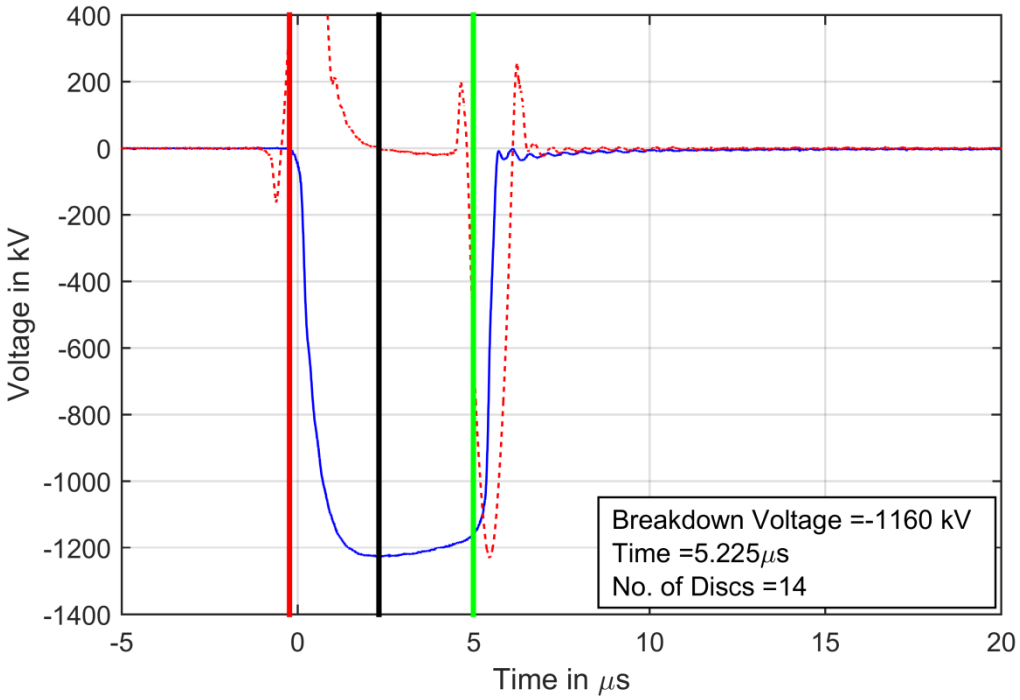
Voltage in kV
Time in μs
Breakdown Voltage =-1160 kV
Time =5.225μs
No. of Discs =14

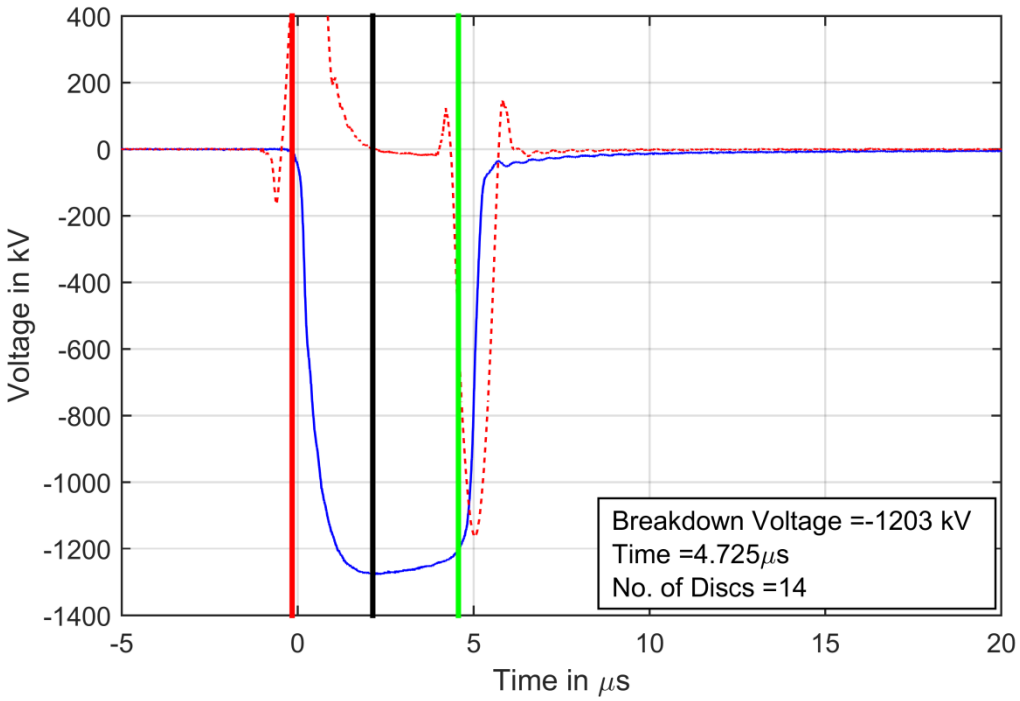
Voltage in kV
Time in μs
Breakdown Voltage =-1203 kV
Time =4.725μs
No. of Discs =14

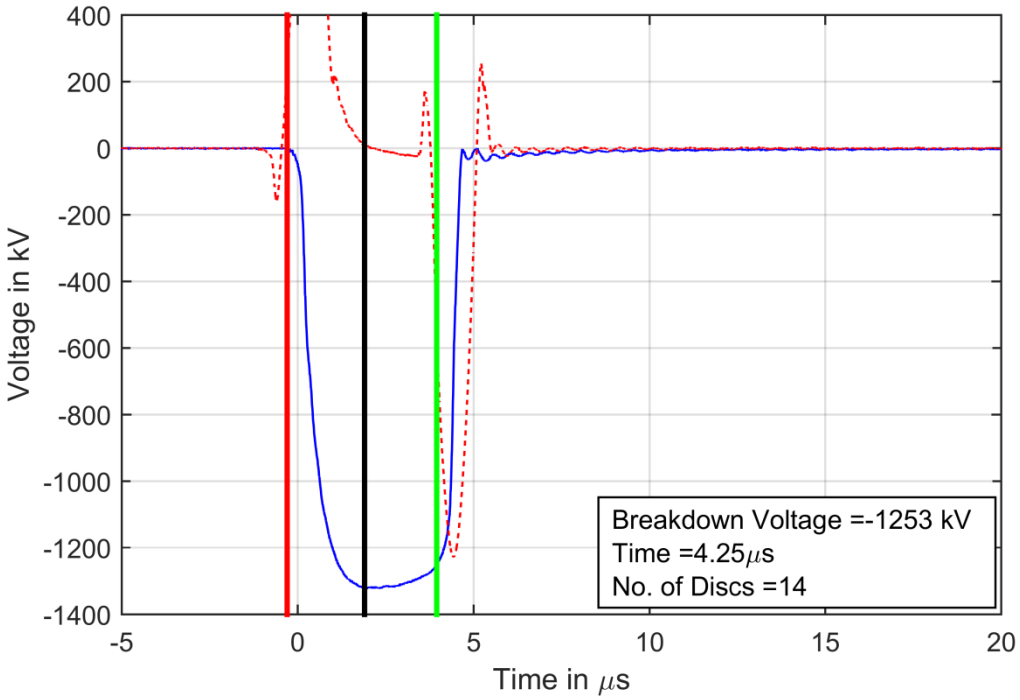
Voltage in kV
Time in μs
Breakdown Voltage =-1253 kV
Time =4.25μs
No. of Discs =14

APPENDIX D: TOWER EARTHING SYSTEMS

D.1: VERIFICATION OF NIXON'S IONISATION MODEL

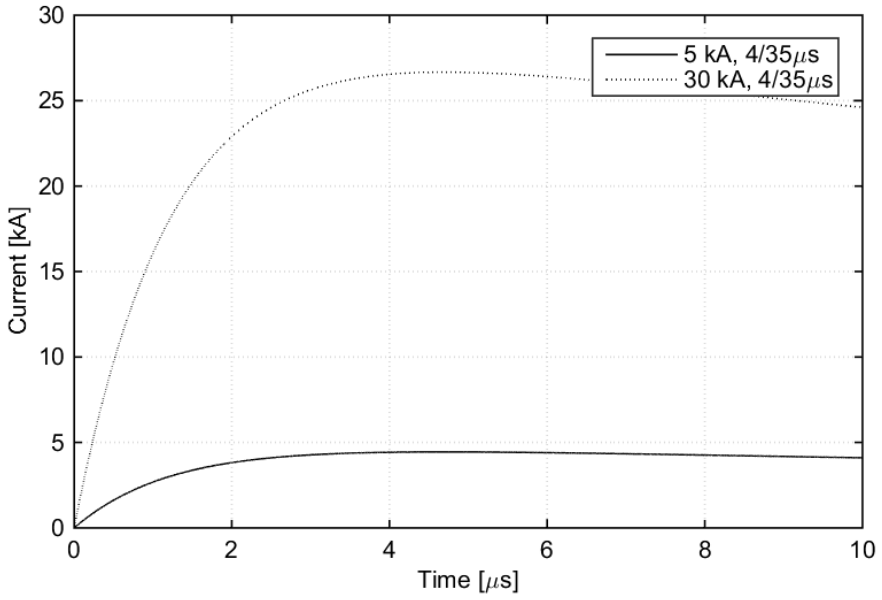

a) Current waveforms used in lab investigation in [288]**, implemented in PSCAD/EMTDC**

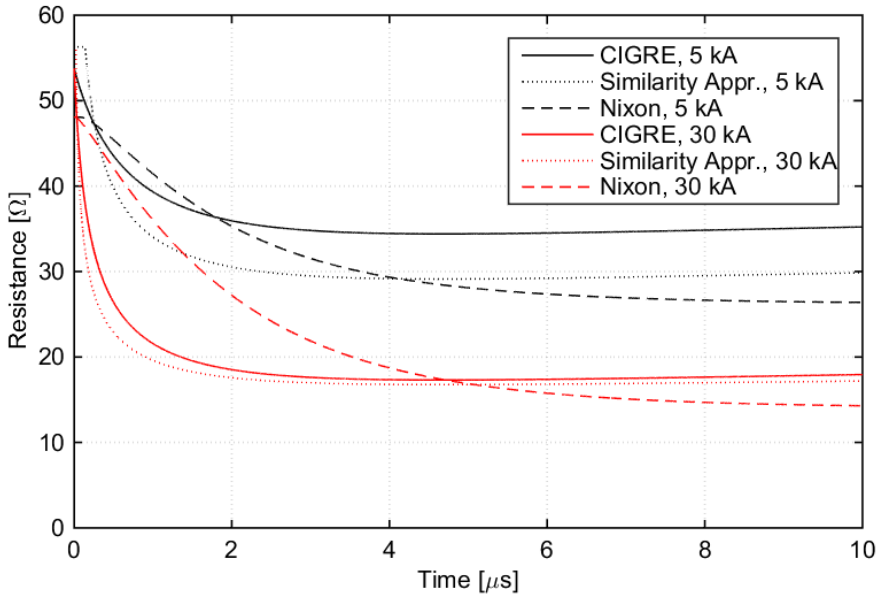

b) Simulation results from PSCAD/ETMDC of soil ionisation models according to Nixon [288] **and CIGRE** [24] **for a single rod**

Figure D-1: Simulation results of soil ionisation models according to Nixon [288]

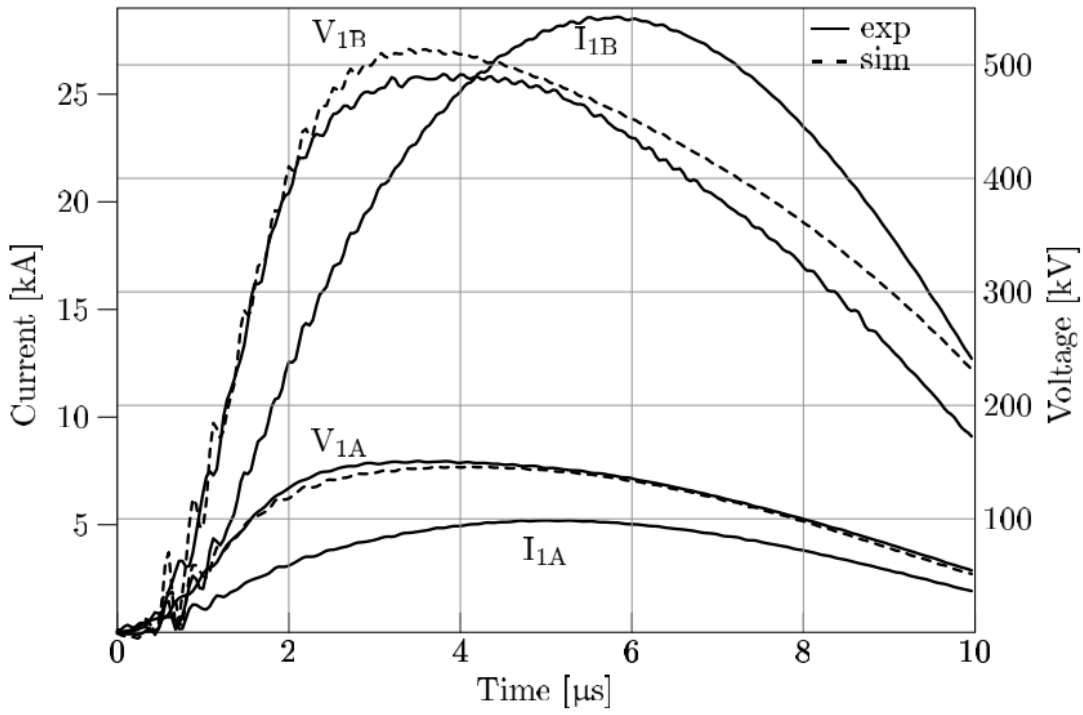

a) Current and voltage waveforms used in lab investigation from [288]

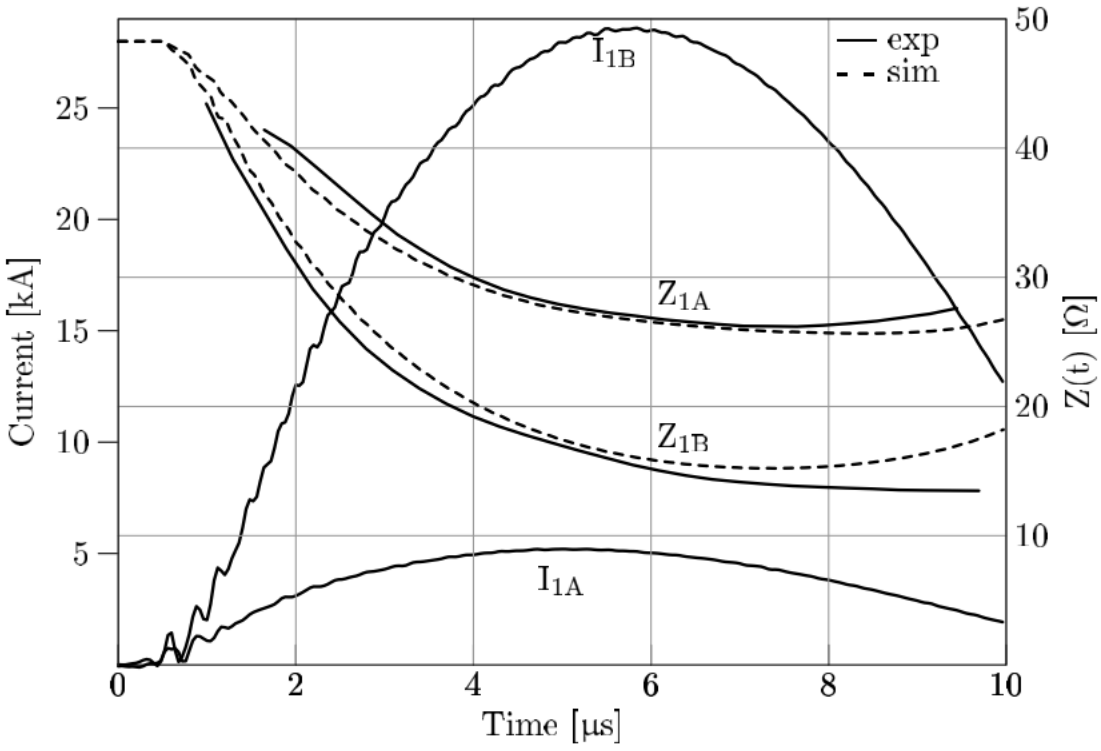

b) Current waveform and resistance from [288]

Figure D-2: Experimental and simulation results of soil ionisation models from [288]

D.2: VERIFICATION OF SEKIOKA'S FREQUENCY-DEPENDENT MODEL

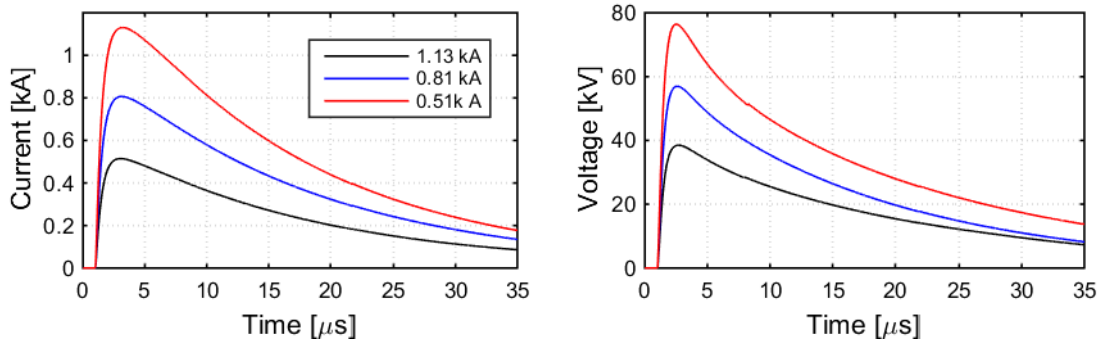

a) Current progression **b) Resulting voltages**

Figure D-3: Simulation results of frequency-dependent model according to Sekioka [213] **and Nixon ionization model** [288]**, lightning impulse to single rod in 160 Ωm soil**

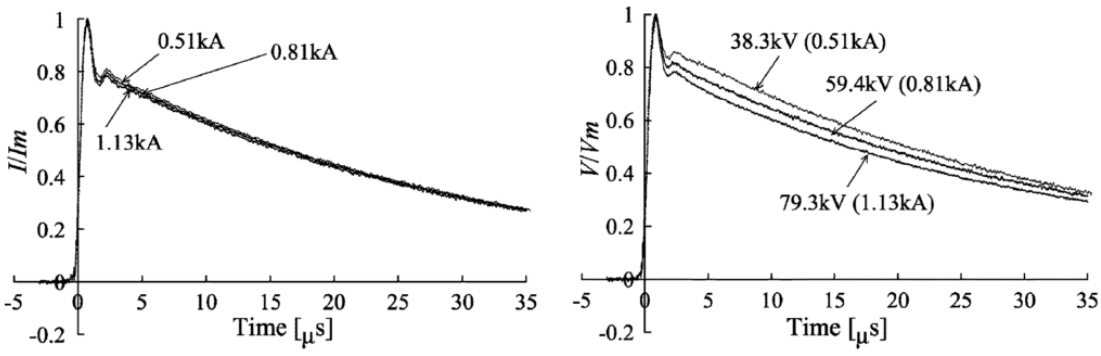

a) Current progression **b) Resulting voltages**

Figure D-4: Measured results of voltages and applied currents, lightning impulse to single rod in 160 Ωm soil, from [213]

D.3: DERIVATION OF THE FOUR RODS NIXON IONIZATION MODEL

$$A_1 = 2\pi rl \qquad A_2 = 2\pi r^2 \qquad r_0 < r \le d/2$$
$$A_1 = (2\pi - 4\theta)rl \qquad A_2 = 2\pi r^2 \cos\theta \qquad d/2 < r \le \sqrt{2}d/2$$
$$A_1 = \left(\frac{3}{2}\pi - 2\theta\right)rl \quad A_2 = 2\pi r^2 \cos\theta + r^2\theta(\sin\theta - \cos\theta) \qquad \frac{\sqrt{2}d}{2} < r \le \infty$$

$$J_{ion} = \frac{I}{4(A_1 + A_2)}$$

Case 1:

$$(A_1 + A_2) - \frac{I}{4J_{ion}} = 0$$

$$rl + r^2 - \frac{I}{8\pi J_{ion}} = 0$$

$$r = \frac{1}{2}\left(-l + \sqrt{l^2 + \frac{I}{2\pi J_{ion}}}\right)$$

Crossing to next radius @ $r = d/2$, determine I

$$rl + r^2 - \frac{I}{8\pi J_{ion}} = 0$$

$$\frac{d}{2}l + \left(\frac{d}{2}\right)^2 - \frac{I}{8\pi J_{ion}} = 0$$

$$2dl + d^2 - \frac{I}{2\pi J_{ion}} = 0$$

$$2\pi J_{ion}(d^2 + 2dl) = I$$

Case 2:

$$(2\pi - 4\theta)rl + 2\pi r^2 \cos\theta - \frac{I}{4J_{ion}} = 0$$

$$2\pi rl - 4rl\cos^{-1}\frac{d}{2r} + 2\pi r^2\cos\theta - \frac{I}{4J_{ion}} = 0$$

$$2\pi rl - 4rl\cos^{-1}\frac{d}{2r} + \pi rd - \frac{I}{4J_{ion}} = 0$$

Crossing to next radius @ $r = \sqrt{2}d/2$, determine I

$$\pi\sqrt{2}dl - \frac{\pi l\sqrt{2}d}{2} + \frac{\pi\sqrt{2}d^2}{2} = \frac{I}{4J_{ion}}$$

$$2\sqrt{2}dl - \sqrt{2}dl + \sqrt{2}d^2 = \frac{I}{2\pi J_{ion}}$$

$$2\sqrt{2}\pi J_{ion}(dl + d^2) = I$$

Determination of formulation for radius r for transition between Case 1 and 3:

$$m = \frac{2\sqrt{2}\pi J_{ion}(dl\ + d^2) - 2\pi J_{ion}(d^2 + 2dl)}{\frac{\sqrt{2}d}{2} - \frac{d}{2}}$$

$$m = \frac{4\pi J_{ion}\left(\sqrt{2}(dl\ + d^2) - (d^2 + 2dl)\right)}{\sqrt{2}d - d}$$

$$m = \frac{4\pi J_{ion}\left(\sqrt{2}l + \sqrt{2}d - d - 2l\right)}{\sqrt{2} - 1}$$

$$m = \frac{4\pi J_{ion}\left(l\left(\sqrt{2} - 2\right) + d\left(\sqrt{2} - 1\right)\right)}{\sqrt{2} - 1}$$

$$t = 2\pi J_{ion}(d^2 + 2dl) - \frac{4\pi J_{ion}\left(l\left(\sqrt{2} - 2\right) + d\left(\sqrt{2} - 1\right)\right)}{\sqrt{2} - 1}\frac{d}{2}$$

$$t = 2\pi J_{ion}d^2 + 2\pi J_{ion}2dl - \frac{2\pi J_{ion}d\left(l\left(\sqrt{2} - 2\right) + d\left(\sqrt{2} - 1\right)\right)}{\sqrt{2} - 1}$$

$$t = 2\pi J_{ion}d^2 + 2\pi J_{ion}2dl - 2\pi J_{ion}\frac{dl\left(\sqrt{2} - 2\right)}{\sqrt{2} - 1} - 2\pi J_{ion}d^2$$

$$t = 2\pi J_{ion}dl\left(2 - \frac{\left(\sqrt{2} - 2\right)}{\sqrt{2} - 1}\right)$$

Test at d/2:

$$f(r) = \frac{4\pi J_{ion}\left(l\left(\sqrt{2} - 2\right) + d\left(\sqrt{2} - 1\right)\right)}{\sqrt{2} - 1} \cdot \frac{d}{2} + 2\pi J_{ion}dl\left(2 - \frac{\left(\sqrt{2} - 2\right)}{\sqrt{2} - 1}\right)$$

$$f(r) = \frac{2\pi J_{ion}d\left(l\left(\sqrt{2} - 2\right) + d\left(\sqrt{2} - 1\right)\right)}{\sqrt{2} - 1} + 4\pi J_{ion}dl - 2\pi J_{ion}dl\frac{\left(\sqrt{2} - 2\right)}{\sqrt{2} - 1}$$

$$f(r) = 2\pi J_{ion}\frac{dl\left(\sqrt{2} - 2\right)}{\sqrt{2} - 1} + 2\pi J_{ion}d^2 + 4\pi J_{ion}dl - 2\pi J_{ion}dl\frac{\left(\sqrt{2} - 2\right)}{\sqrt{2} - 1}$$

$$I(r) = 2\pi J_{ion}d^2 + 4\pi J_{ion}dl$$

$$I(r) = 2\pi J_{ion}(d^2 + 2dl)$$

Quadratic Law:

$$I(r) = a(r - r_0)^2 + I_0$$

$$I(r) = a(r - d/2)^2 + 2\pi J_{ion}(d^2 + 2dl)$$

$$2\sqrt{2}\pi J_{ion}(dl\ + d^2) = a\left(\sqrt{2}d/2 - d/2\right)^2 + 2\pi J_{ion}(d^2 + 2dl)$$

$$a = \frac{2\sqrt{2}\pi J_{ion}(dl\ + d^2) - 2\pi J_{ion}(d^2 + 2dl)}{\left(\sqrt{2}d/2 - d/2\right)^2}$$

$$I(r) = a(r - r_0)^2 + I_0$$

$$\frac{I(r) - I_0}{a} = (r - r_0)^2$$

$$0 = r^2 - 2rr_0 + {r_0}^2 - \frac{I(r) - I_0}{a}$$

$$r = 0.5\left(2r_0 + \sqrt{4{r_0}^2 - 4\left({r_0}^2 - \frac{I(r) - I_0}{a}\right)}\right)$$

$$\sqrt{\frac{I(r) - I_0}{a}} + r_0 = r$$

Result for determination of radius r for Case 2:

$$I = \frac{4\pi J_{ion}\left(l\left(\sqrt{2} - 2\right) + d\left(\sqrt{2} - 1\right)\right)}{\sqrt{2} - 1}r + 2\pi J_{ion} dl\left(2 - \frac{\left(\sqrt{2} - 2\right)}{\sqrt{2} - 1}\right)$$

$$I\left(\sqrt{2} - 1\right) - 2\pi J_{ion} dl\left(2 - \frac{\left(\sqrt{2} - 2\right)}{\sqrt{2} - 1}\right)\left(\sqrt{2} - 1\right) = 4\pi J_{ion}\left(l\left(\sqrt{2} - 2\right) + d\left(\sqrt{2} - 1\right)\right)r$$

$$\frac{I\left(\sqrt{2} - 1\right) - 2\pi J_{ion} dl\left(2 - \frac{\left(\sqrt{2} - 2\right)}{\sqrt{2} - 1}\right)\left(\sqrt{2} - 1\right)}{4\pi J_{ion}\left(l\left(\sqrt{2} - 2\right) + d\left(\sqrt{2} - 1\right)\right)} = r$$

$$r = \frac{I\left(\sqrt{2} - 1\right) - 2\pi J_{ion} dl\left(2\left(\sqrt{2} - 1\right) - \left(\sqrt{2} - 2\right)\right)}{4\pi J_{ion}\left(l\left(\sqrt{2} - 2\right) + d\left(\sqrt{2} - 1\right)\right)}$$

$$r = \frac{I\left(\sqrt{2} - 1\right) - 2\pi J_{ion} dl\left(2\sqrt{2} - 2 - \sqrt{2} + 2\right)}{4\pi J_{ion}\left(l\left(\sqrt{2} - 2\right) + d\left(\sqrt{2} - 1\right)\right)}$$

$$r = \frac{\frac{I}{\pi J_{ion}}\left(\sqrt{2} - 1\right) - dl\sqrt{2}}{4\left(l\left(\sqrt{2} - 2\right) + d\left(\sqrt{2} - 1\right)\right)}$$

Case 3 @ $r = \sqrt{2}d/2$ to determine current:

$$\left(\frac{3}{2}\pi - 2\theta\right)rl + 2\pi r^2\cos\theta + r^2\theta(\sin\theta - \cos\theta) - \frac{I}{4J_{ion}} = 0$$

$$\left(\left(\frac{3}{2}\pi - 2\frac{\pi}{4}\right)\frac{\sqrt{2}d}{2}l + \pi\frac{\sqrt{2}d}{2}d\right) - \frac{I}{4J_{ion}} = 0$$

$$\left(\pi\frac{\sqrt{2}}{2}dl+\pi\frac{\sqrt{2}}{2}d^2\right)=\frac{I}{4J_{ion}}$$

$$2\sqrt{2}\pi J_{ion}(dl+d^2)=I$$

Case 3 @ $r=d$ to determine current:

$$4J_{ion}\left(\left(\frac{3}{2}\pi-2\frac{\pi}{3}\right)dl+\pi d^2+d^2\frac{\pi}{3}\left(\frac{\sqrt{3}}{2}-\frac{1}{2}\right)\right)=I$$

$$4\pi J_{ion}\left(\frac{5}{6}dl+d^2+d^2\frac{1}{3}\left(\frac{\sqrt{3}}{2}-\frac{1}{2}\right)\right)=I$$

$$m=\frac{4\pi J_{ion}\left(\frac{5}{6}dl+d^2+d^2\frac{1}{3}\left(\frac{\sqrt{3}}{2}-\frac{1}{2}\right)\right)-2\sqrt{2}\pi J_{ion}(dl+d^2)}{d-\frac{\sqrt{2}}{2}d}$$

$$m=\frac{4\pi J_{ion}\left(\frac{5}{6}l+d+d\frac{1}{3}\left(\frac{\sqrt{3}}{2}-\frac{1}{2}\right)\right)-2\sqrt{2}\pi J_{ion}(l+d)}{1-\frac{\sqrt{2}}{2}}$$

$$t=4\pi J_{ion}\left(\frac{5}{6}dl+d^2+d^2\frac{1}{3}\left(\frac{\sqrt{3}}{2}-\frac{1}{2}\right)\right)-\frac{4\pi J_{ion}\left(\frac{5}{6}l+d+d\frac{1}{3}\left(\frac{\sqrt{3}}{2}-\frac{1}{2}\right)\right)-2\sqrt{2}\pi J_{ion}(l+d)}{1-\frac{\sqrt{2}}{2}}d$$

$$t=4\pi J_{ion}\left(\frac{5}{6}dl+d^2+d^2\frac{1}{3}\left(\frac{\sqrt{3}}{2}-\frac{1}{2}\right)\right)-\frac{4\pi J_{ion}\left(\frac{5}{6}dl+d^2+d^2\frac{1}{3}\left(\frac{\sqrt{3}}{2}-\frac{1}{2}\right)\right)-2\sqrt{2}\pi J_{ion}d(l+d)}{1-\frac{\sqrt{2}}{2}}$$

$$r=\frac{I-t}{m}$$

D.4: VERIFICATION OF EARTH WIRE MODEL

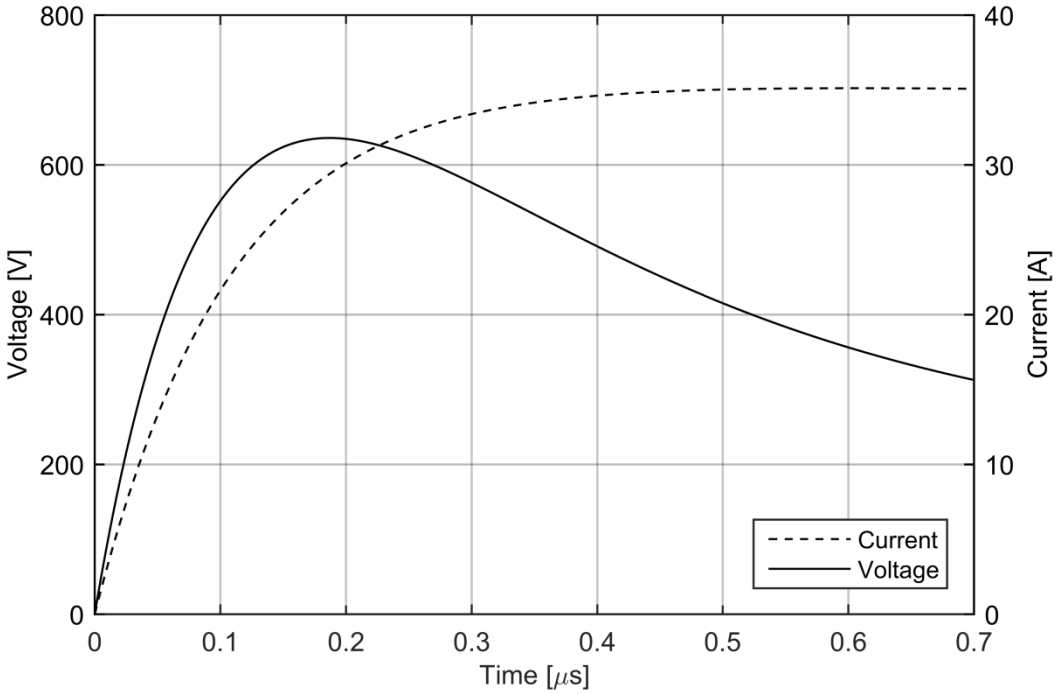

Figure D-5: PSCAD/EMTDC simulation of transient voltages to remote ground at the beginning point of 15 long horizontal wire

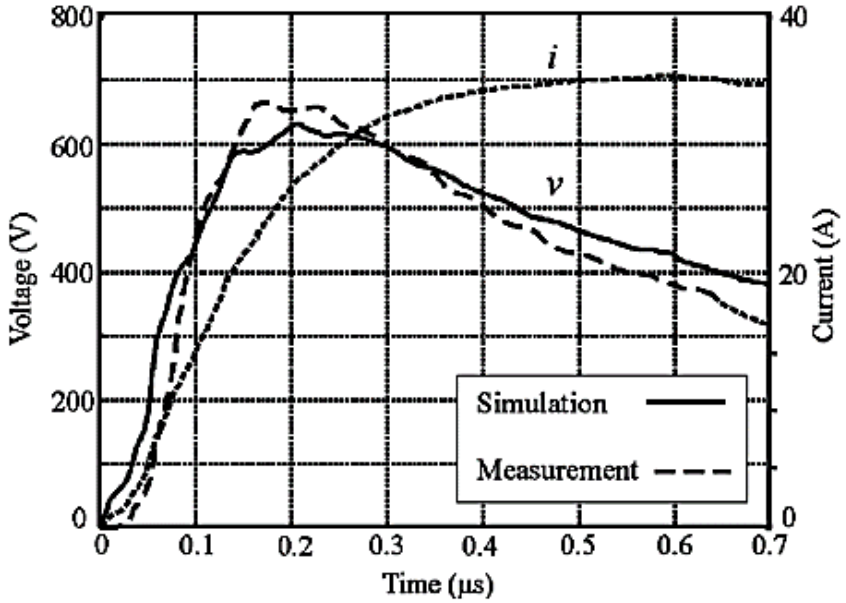

Figure D-6: Measurement and simulation of transient voltages to remote ground at the beginning point of 15 m long horizontal wire from [290]

D.5: VERIFICATION OF COUNTERPOISE MODEL

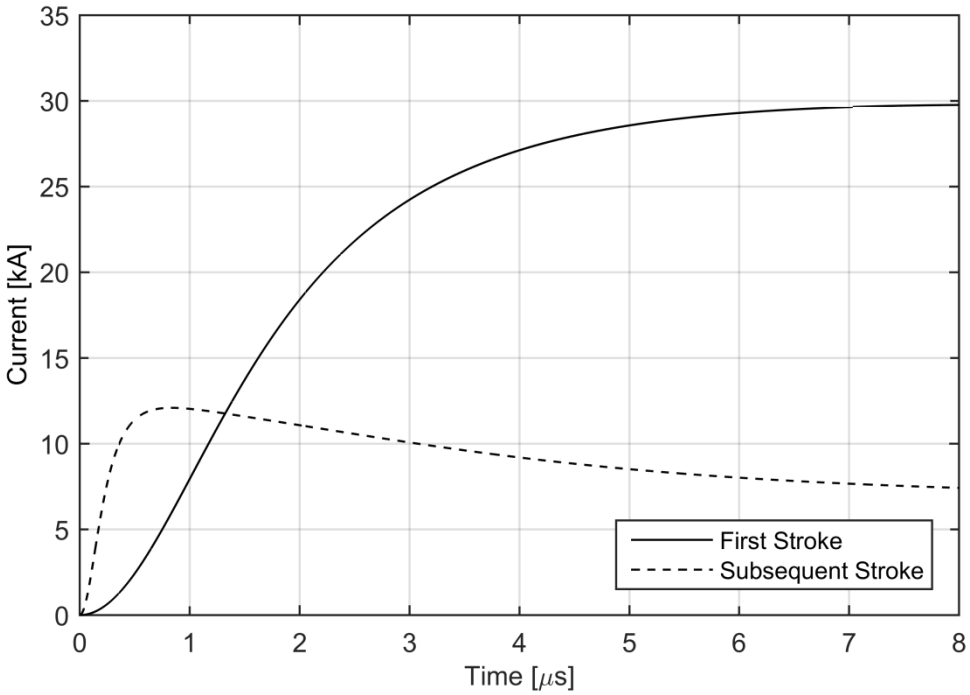

Figure D-7: Waveforms of injected current into counterpoise, PSCAD/EMTDC simulation

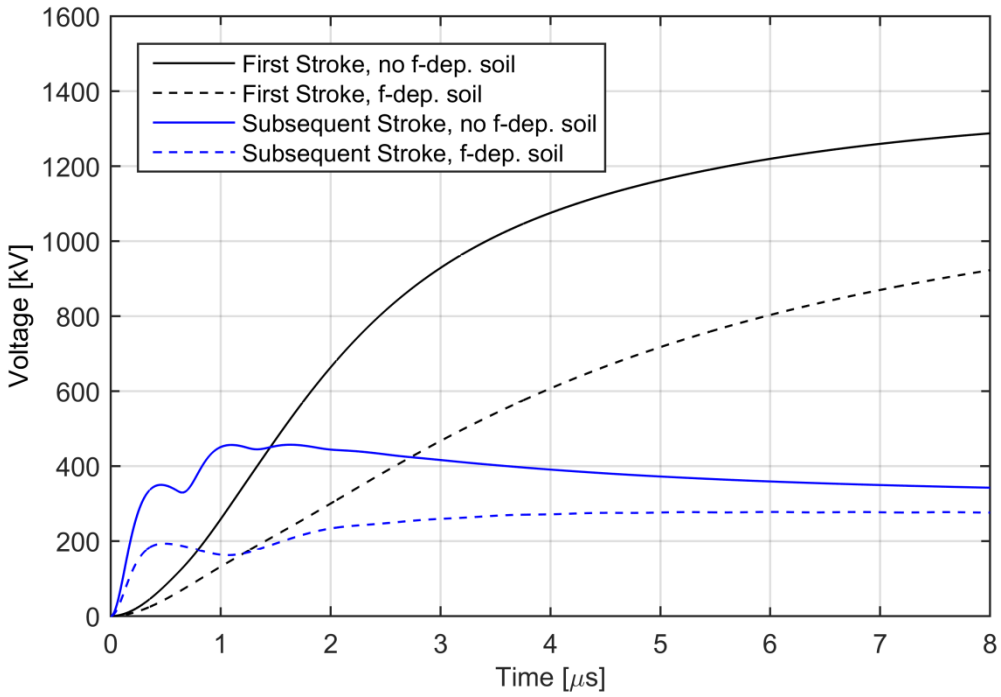

Figure D-8: Transient response of a typical transmission tower ground arrangement in a soil of 2400 Ωm, PSCAD/EMTDC simulation

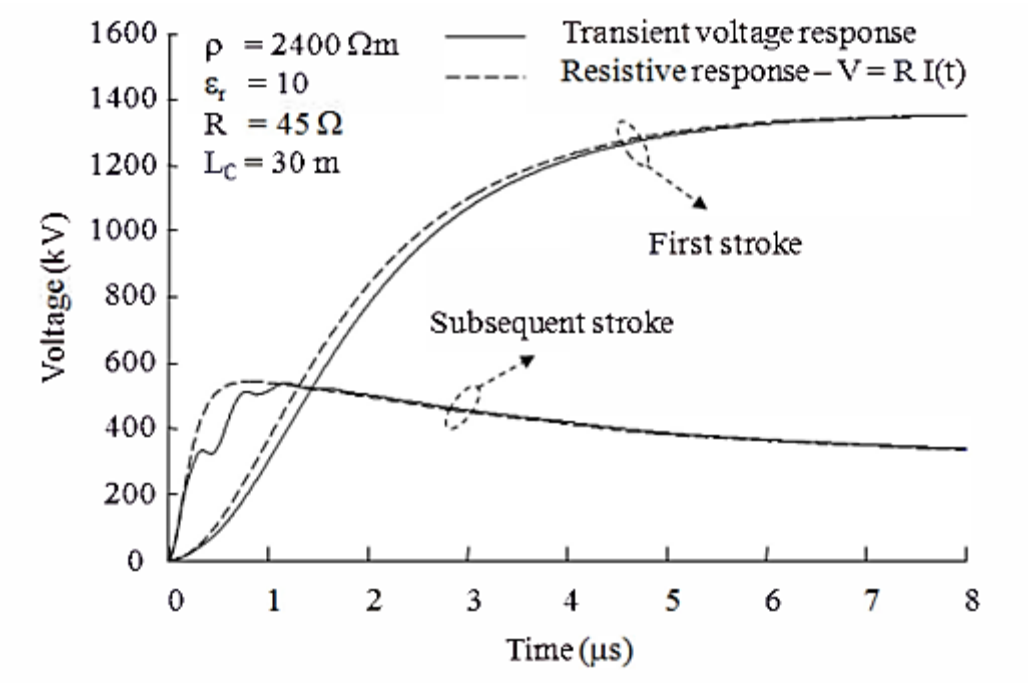

Figure D-9: **Transient and resistive response of a typical transmission tower ground arrangement in a soil of 2400 Ωm** [262]

APPENDIX E: VERIFICATION OF THE ARRESTER MODEL

APPENDIX F: DATA FOR SIMULATIONS

F.1: TOWER DATA

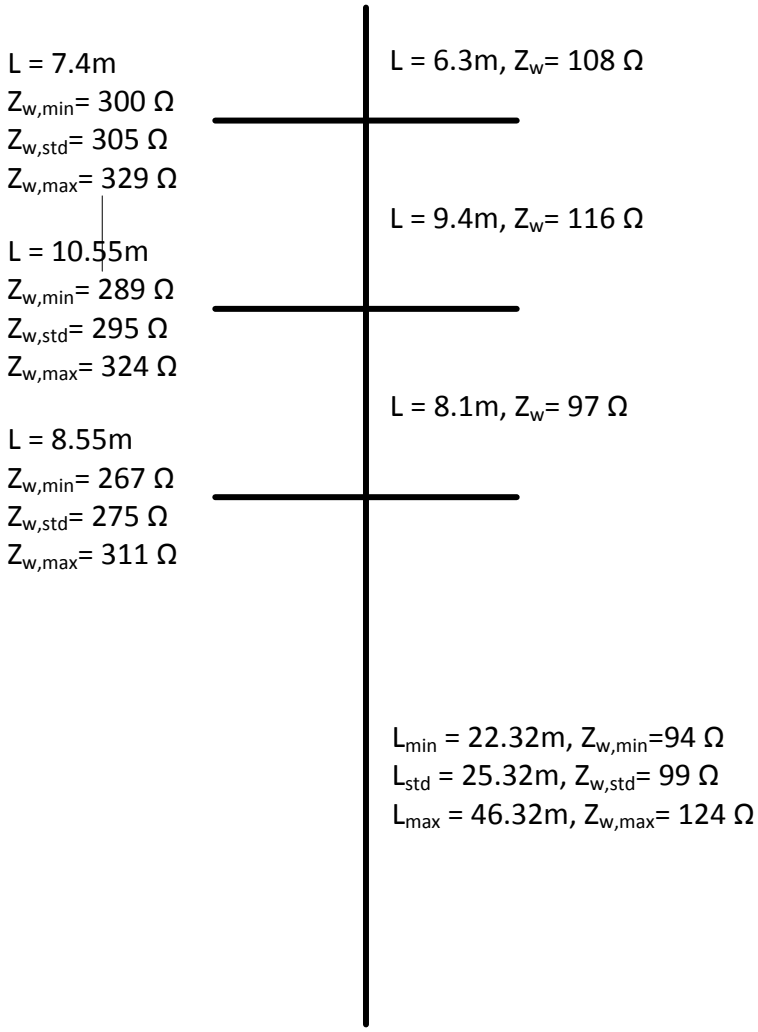

Figure F-1: 400 kV suspension tower dimensions

Figure F-2: 400 kV suspension tower line heights

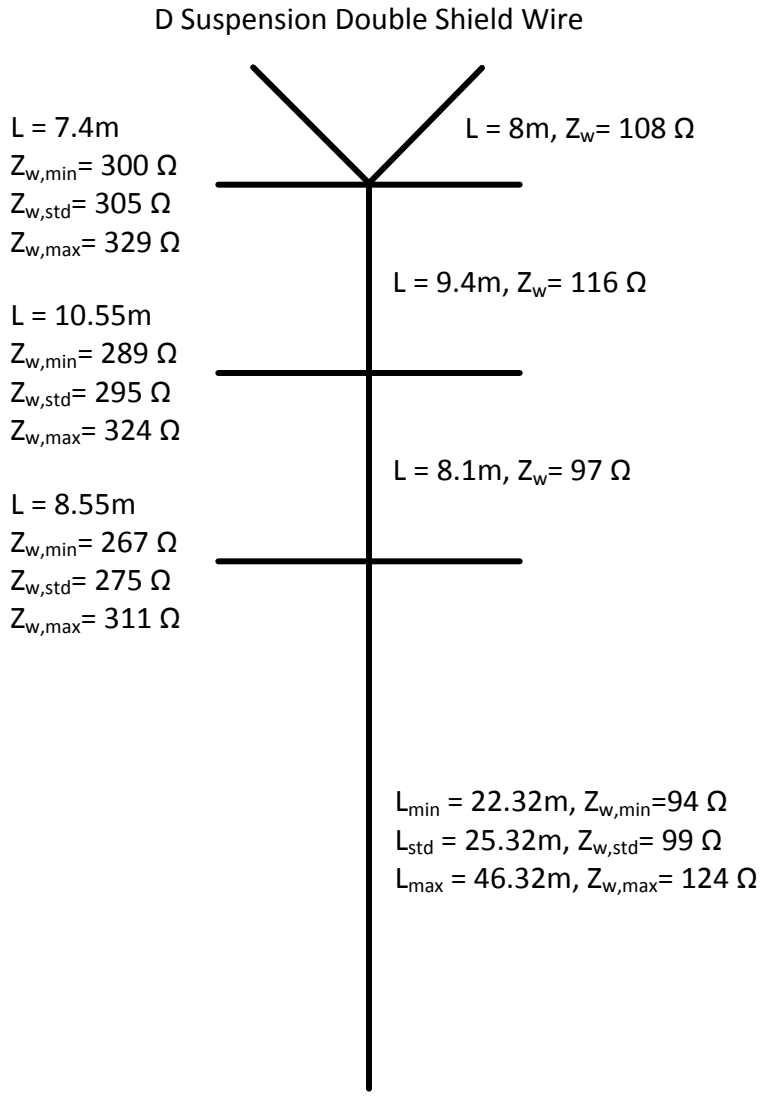

Figure F-3: 400 kV suspension double shield wire tower dimensions

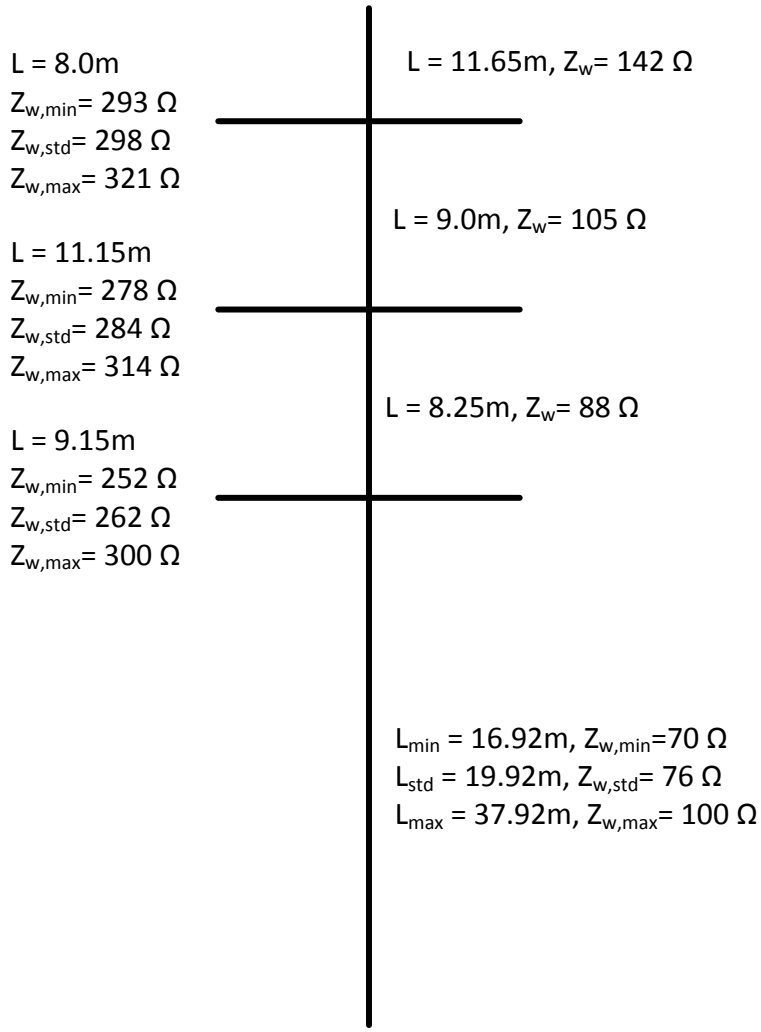

Figure F-4: 400 kV tension tower dimensions

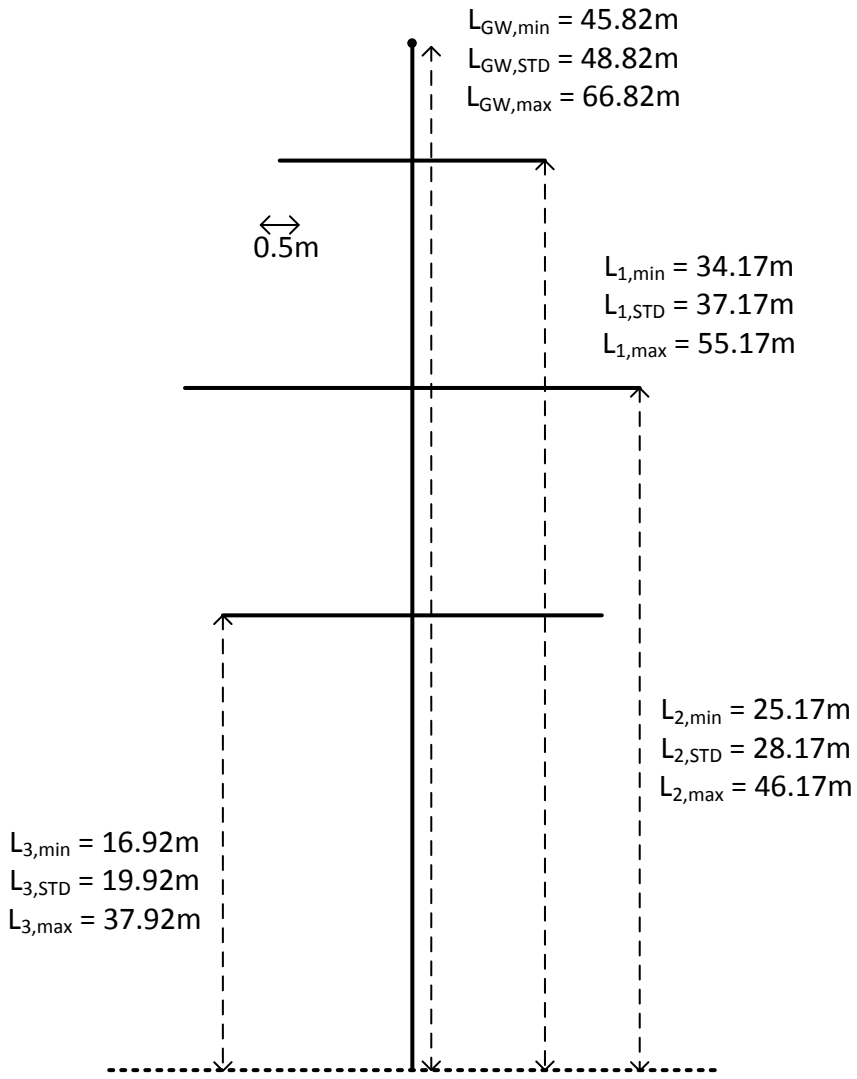

Figure F-5: 400 kV tension tower line heights

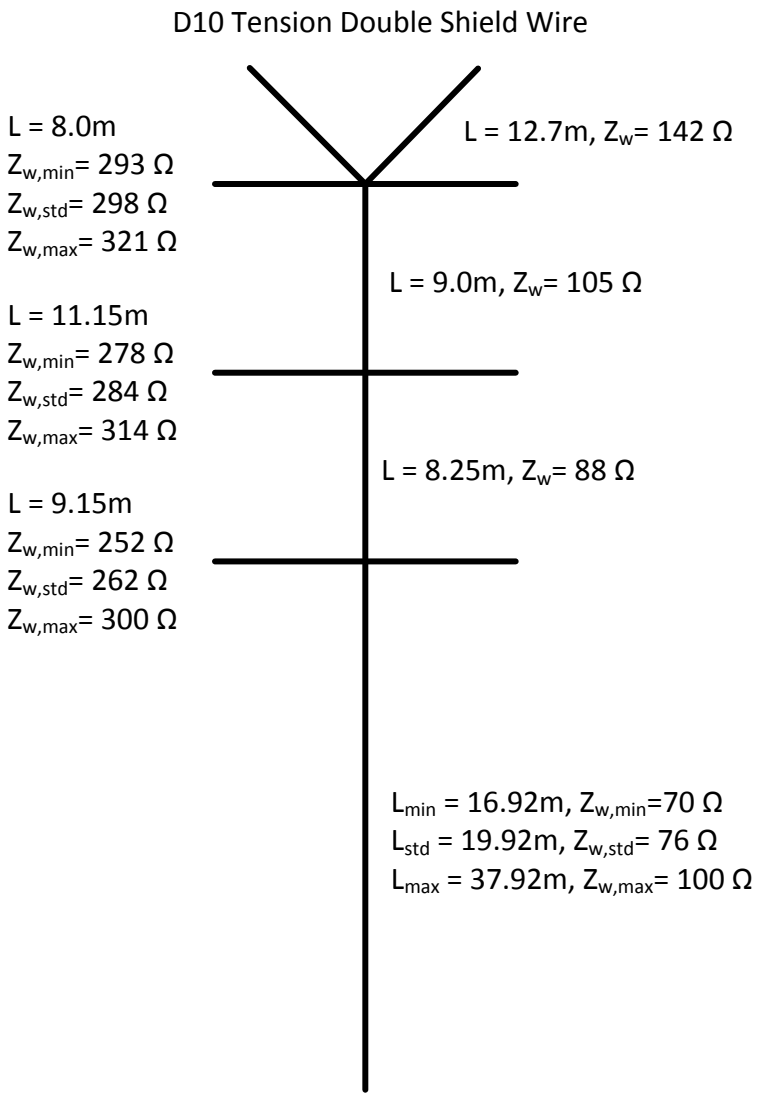

Figure F-6: 400 kV tension double shield wire tower dimensions

Sag calculation for ground wire according to **Error! Reference source not found.**:

$S = 200$ m / 350 m / 500 m assumed

$m = 1782\ kg/km$, from ground wire datasheet

$$w = m \cdot g\ \left[\frac{N}{m}\right] = \frac{1782}{1000}\frac{kg}{m} \cdot 9.81\frac{m}{s^2} = 17.48142\frac{N}{m}$$

$$H = 20\% \cdot H_{max} = 0.2 \cdot 300kN = 60kN$$

$$\text{sag} \approx \frac{w\left(\frac{S}{2}\right)^2}{2\,H} = \frac{w\,S^2}{8\,H} = 1.46 \text{ m} / 4.46 \text{ m} / 9.1 \text{ m}$$

Sag calculation for phase wire Q&Q according to **Error! Reference source not found.**:

$S = 200$ m / 350 m / 500 m assumed

$m = 2348\ kg/km$, from phase wire datasheet, 2 in a bundle

$$w = m \cdot g\ \left[\frac{N}{m}\right] = \frac{2 \cdot 2348}{1000}\frac{kg}{m} \cdot 9.81\frac{m}{s^2} = 46.06776\frac{N}{m}$$

$$H = 15\% \cdot H_{max} = 0.15 \cdot 300kN = 45kN$$

$$\text{sag} \approx \frac{w\left(\frac{S}{2}\right)^2}{2\,H} = \frac{w\,S^2}{8\,H} = 5.12\text{ m} / 15.65\text{ m} / 32\text{ m}$$

$$y = y_{GW} + r_{GW}\sin\varphi_{GW} = y_{LW} + r_{LW}\sin\varphi_{LW}$$

$$x = x_{GW} + r_{GW}\cos\varphi_{GW} = x_{LW} + r_{LW}\cos\varphi_{LW}$$

$$x_{GW} - x_{LW} + r_{GW}\cos\varphi_{GW} = r_{LW}\cos\varphi_{LW}$$

F.2: DEVELOPMENT OF AN IMPROVED EGM PROCEDURE

Calculation of leader attachment coordinates:

Current and attachment angle are given

$r = 8 \cdot \mathrm{I}^{0.65}$ from CIGRE, index g for ground, index sw for shield wire, index Lx for phase conductor

1. Determine coordinates of stroke point:

$$y_{SP} = r_g$$

$$x_{SP} = \frac{y_{SP}}{\tan\left(\frac{\pi}{2} - \Psi\right)}$$

2. Determine distance between (x_{SP}, y_{SP}) and $\left(x_{SW/LW}, y_{SW/LW}\right)$

$$\left|\overline{(x_{SP}, y_{SP})\left(x_{SW/LW}, y_{SW/LW}\right)}\right| = \sqrt{\left(x_{SP} - x_{SW/LW}\right)^2 + \left(y_{SP} - y_{SW/LW}\right)^2}$$

3. Determine distance between circles and stroke point

$$d_{SW/LW} = \left|\overline{(x_{SP}, y_{SP})\left(x_{SW/LW}, y_{SW/LW}\right)}\right| - r_{SW/LW}$$

4. Determine perpendicular lines of shield wire/line wire and line wire/line wire

$$x_{PL} = \frac{x_{SW/LW1} + x_{LW2}}{2}$$

$$y_{PL} = \frac{y_{SW/LW1} + y_{LW2}}{2}$$

$$m_{PL} = -\frac{x_{LW2} - x_{SW/LW1}}{y_{LW2} - y_{SW/LW1}}$$

$$t_{PL} = y_{PL} - m_{PL} \cdot x_{PL}$$

5. Determine shortest distance point between perpendicular line and stroke point

$$m_{PL} \cdot m_{SP} = -1 \xrightarrow{yields} m_{SP} = -\frac{1}{m_{PL}}$$

$$t_{SP} = y_{SP} - m_{SP} \cdot x_{SP}$$

$$x_{SP/PL} = \frac{t_{PL} - t_{SP}}{m_{SP} - m_{PL}}$$

$$y_{SP/PL} = m_{PL} \cdot x_{SP/PL} + t_{PL}$$

6. Determine whether point is above or below perpendicular line

$$y = m_{PL} \cdot x_{SP/PL} + t_{PL}$$

$$y \geq y_{SP/PL} \xrightarrow{yields} \left(x_{SP/PL}, y_{SP/PL}\right) \textit{ below or on perpendicular line}$$

$$y < y_{SP/PL} \xrightarrow{yields} \left(x_{SP/PL}, y_{SP/PL}\right) \textit{ above perpendicular line}$$

$d_{SP/PL} = y_{SP/PL} - y$

7. Conditions to determine which conductor or earth is hit

Ground hit: $d_{SW} > 0\ AND\ d_{LW1} > 0\ AND\ d_{LW2} > 0\ AND\ d_{LW3} > 0$

Shielding wire hit: $d_{SW} \leq 0\ AND\ d_{L1,\ SP/PL} > 0\ AND\ d_{L2,\ SP/PL} >$

$0\ AND\ d_{L3,\ SP/PL} > 0$

Line wire 1 hit:

$d_{LW1} \leq 0\ AND\ d_{L1,\ SP/PL} \leq 0\ AND\ d_{L2,\ SP/PL} > 0\ AND\ d_{L3,\ SP/PL} > 0$

Line wire 2 hit:

$d_{LW2} \leq 0\ AND\ d_{L1,\ SP/PL} \leq 0\ AND\ d_{L2,\ SP/PL} \leq 0\ AND\ d_{L3,\ SP/PL} > 0$

Line wire 3 hit:

$d_{LW3} \leq 0\ AND\ d_{L1,\ SP/PL} \leq 0\ AND\ d_{L2,\ SP/PL} \leq 0\ AND\ d_{L3,\ SP/PL} \leq 0$

APPENDIX G: SIMULATION RESULTS

G.1: CRITICAL CURRENT DETERMINATION METHOD

Table G-1: Critical Currents for base scenario with simple resistance, shield wire

Positive Stroke Polarity								
	Tower Height	MIN		STD		MAX		
Soil Resistivity	Span Length / Footing Resistance	200m	350m	200m	350m	200m	350m	500m
100Ωm	4.5Ω	1003	1003	1003	876	1003	921	1003
500Ωm	23Ω	444	339	446	276	458	277	296
1000Ωm	46Ω	299	222	300	197	306	191	193
2500Ωm	114Ω	181	126	182	145	189	130	111
5000Ωm	228Ω	119	82	120	81	125	85	73
10000Ωm	455Ω	77	53	77	54	81	56	48
Negative Stroke Polarity								
	Tower Height	MIN		STD		MAX		
Soil Resistivity	Span Length / Footing Resistance	200m	350m	200m	350m	200m	350m	500m
100Ωm	4.5Ω	613	657	563	650	670	631	748
500Ωm	23Ω	240	214	241	211	250	218	220
1000Ωm	46Ω	147	126	148	126	154	130	126
2500Ωm	114Ω	83	68	84	70	87	71	65
5000Ωm	228Ω	58	47	59	47	60	49	44
10000Ωm	455Ω	44	35	44	35	45	36	32
Negative Subsequent Stroke Polarity								
	Tower Height	MIN		STD		MAX		
Soil Resistivity	Span Length / Footing Resistance	200m	350m	200m	350m	200m	350m	500m
100Ωm	4.5Ω	470	466	460	455	418	414	583
500Ωm	23Ω	333	330	329	293	314	308	383
1000Ωm	46Ω	209	196	211	198	215	193	221
2500Ωm	114Ω	110	77	111	79	118	95	69
5000Ωm	228Ω	58	45	58	45	63	48	37
10000Ωm	455Ω	42	29	43	29	44	30	26

Table G-2: Critical Currents for base scenario with impedance, shield wire

Positive Stroke Polarity								
	Tower Height	MIN		STD		MAX		
Soil Resistivity	Span Length / Footing Resistance	200m	350m	200m	350m	200m	350m	500m
100Ωm	4.5Ω	1003	1003	1003	1003	1003	1003	1003
500Ωm	23Ω	1003	1003	1003	1003	1003	1003	1003
1000Ωm	46Ω	1003	1003	1003	1003	1003	1003	1003
2500Ωm	114Ω	706	495	1003	509	709	609	610
5000Ωm	228Ω	519	455	502	355	547	505	366
10000Ωm	455Ω	434	311	485	335	465	346	295
Negative Stroke Polarity								
	Tower Height	MIN		STD		MAX		
Soil Resistivity	Span Length / Footing Resistance	200m	350m	200m	350m	200m	350m	500m
100Ωm	4.5Ω	1003	1003	1003	896	1003	1003	1003
500Ωm	23Ω	623	709	837	705	600	574	1003
1000Ωm	46Ω	505	729	631	732	494	516	757
2500Ωm	114Ω	533	436	533	437	546	447	461
5000Ωm	228Ω	322	300	322	301	327	312	309
10000Ωm	455Ω	167	150	175	155	186	174	187
Negative Subsequent Stroke Polarity								
	Tower Height	MIN		STD		MAX		
Soil Resistivity	Span Length / Footing Resistance	200m	350m	200m	350m	200m	350m	500m
100Ωm	4.5Ω	504	483	474	474	430	427	606
500Ωm	23Ω	443	437	433	429	398	395	552
1000Ωm	46Ω	406	405	399	388	370	367	434
2500Ωm	114Ω	291	285	288	285	278	275	331
5000Ωm	228Ω	185	177	186	178	191	183	195
10000Ωm	455Ω	143	135	144	135	149	142	147

Table G-3: Critical Currents for base scenario with simple resistance, top phase wire

Positive Stroke Polarity								
	Tower Height	MIN		STD		MAX		
Soil Resistivity	Span Length / Footing Resistance	200m	350m	200m	350m	200m	350m	500m
100Ωm	4.5Ω	27	35	25	35	20	25	15
500Ωm	23Ω	22	28	21	26	18	22	14
1000Ωm	46Ω	21	26	21	25	18	22	14
2500Ωm	114Ω	21	25	20	24	18	21	14
5000Ωm	228Ω	20	24	20	25	18	21	14
10000Ωm	455Ω	20	24	20	25	18	20	14
Negative Stroke Polarity								
	Tower Height	MIN		STD		MAX		
Soil Resistivity	Span Length / Footing Resistance	200m	350m	200m	350m	200m	350m	500m
100Ωm	4.5Ω	9	10	12	14	14	9	8
500Ωm	23Ω	15	9	15	9	9	9	11
1000Ωm	46Ω	15	9	15	9	14	9	11
2500Ωm	114Ω	15	9	15	9	14	9	11
5000Ωm	228Ω	15	9	15	9	9	9	8
10000Ωm	455Ω	15	9	15	9	9	9	8
Negative Subsequent Stroke Polarity								
	Tower Height	MIN		STD		MAX		
Soil Resistivity	Span Length / Footing Resistance	200m	350m	200m	350m	200m	350m	500m
100Ωm	4.5Ω	9	9	11	8	10	8	9
500Ωm	23Ω	11	8	11	8	10	8	9
1000Ωm	46Ω	11	8	10	8	10	8	9
2500Ωm	114Ω	11	8	9	8	10	8	9
5000Ωm	228Ω	11	8	9	8	10	8	9
10000Ωm	455Ω	11	8	9	8	10	8	9

Table G-4: Critical Currents for base scenario with impedance, top phase wire

Positive Stroke Polarity								
	Tower Height	MIN		STD		MAX		
Soil Resistivity	Span Length / Footing Resistance	200m	350m	200m	350m	200m	350m	500m
100Ωm	4.5Ω	27	35	0	25	35	0	20
500Ωm	23Ω	22	28	0	21	27	0	18
1000Ωm	46Ω	21	26	0	21	25	0	19
2500Ωm	114Ω	21	25	0	20	24	0	18
5000Ωm	228Ω	20	24	0	20	24	0	18
10000Ωm	455Ω	20	25	0	20	25	0	18
Negative Stroke Polarity								
	Tower Height	MIN		STD		MAX		
Soil Resistivity	Span Length / Footing Resistance	200m	350m	200m	350m	200m	350m	500m
100Ωm	4.5Ω	15	10	0	15	9	0	9
500Ωm	23Ω	15	9	0	15	9	0	9
1000Ωm	46Ω	15	9	0	15	9	0	9
2500Ωm	114Ω	15	9	0	15	9	0	9
5000Ωm	228Ω	15	9	0	15	9	0	14
10000Ωm	455Ω	15	9	0	9	9	0	9
Negative Subsequent Stroke Polarity								
	Tower Height	MIN		STD		MAX		
Soil Resistivity	Span Length / Footing Resistance	200m	350m	200m	350m	200m	350m	500m
100Ωm	4.5Ω	9	9	0	11	8	0	10
500Ωm	23Ω	11	8	0	11	8	0	10
1000Ωm	46Ω	11	8	0	10	8	0	10
2500Ωm	114Ω	11	8	0	9	8	0	10
5000Ωm	228Ω	11	8	0	9	8	0	10
10000Ωm	455Ω	9	8	0	9	8	0	10

Table G-5: Flashover rates for base scenario with simple resistance and CIGRE distribution derived from critical current determination simulations

LFOR								
	Tower Height	MIN		STD		MAX		
Soil Resistivity	Span Length / Footing Resistance	200m	350m	200m	350m	200m	350m	500m
10000Ωm	455Ω	0.22432	0.3112	0.23369	0.31924	0.27697	0.35855	0.40252
5000Ωm	228Ω	0.13794	0.20634	0.14393	0.2162	0.19089	0.25239	0.29082
2500Ωm	114Ω	0.073905	0.11377	0.082532	0.11199	0.12829	0.16537	0.18741
1000Ωm	46Ω	0.038398	0.053658	0.047585	0.068765	0.09667	0.1185	0.12096
500Ωm	23Ω	0.025644	0.035335	0.035122	0.052221	0.086879	0.10079	0.101
100Ωm	4.5Ω	0.012652	0.011527	0.02129	0.022397	0.069145	0.073342	0.073787
SFFOR								
	Tower Height	MIN		STD		MAX		
Soil Resistivity	Span Length / Footing Resistance	200m	350m	200m	350m	200m	350m	500m
10000Ωm	455Ω	0.010964	0.013219	0.020332	0.022321	0.072421	0.07161	0.074199
5000Ωm	228Ω	0.010964	0.013219	0.020332	0.022321	0.072421	0.071209	0.074199
2500Ωm	114Ω	0.010693	0.013015	0.020332	0.022563	0.069956	0.071209	0.073507
1000Ωm	46Ω	0.010693	0.012826	0.020027	0.022321	0.069956	0.070812	0.073507
500Ωm	23Ω	0.010439	0.012494	0.020027	0.022095	0.072421	0.070812	0.073507
100Ωm	4.5Ω	0.012652	0.011527	0.02129	0.018249	0.069145	0.069654	0.073787
BFOR								
	Tower Height	MIN		STD		MAX		
Soil Resistivity	Span Length / Footing Resistance	200m	350m	200m	350m	200m	350m	500m
10000Ωm	455Ω	0.21335	0.29798	0.21335	0.29692	0.20455	0.28694	0.32832
5000Ωm	228Ω	0.12697	0.19313	0.1236	0.19388	0.11847	0.18118	0.21662
2500Ωm	114Ω	0.063213	0.10075	0.0622	0.089423	0.05833	0.094165	0.1139
1000Ωm	46Ω	0.027705	0.040832	0.027557	0.046444	0.026714	0.047684	0.047448
500Ωm	23Ω	0.015205	0.022842	0.015095	0.030126	0.014458	0.029976	0.027489
100Ωm	4.5Ω	0	0	0	0.004149	0	0.003688	0

Table G-6: Flashover rates for base scenario with simple resistance and LLS SCO distribution derived from critical current determination simulations

LFOR								
	Tower Height	MIN		STD		MAX		
Soil Resistivity	Span Length / Footing Resistance	200m	350m	200m	350m	200m	350m	500m
10000Ωm	455Ω	0.060912	0.10536	0.06486	0.10835	0.10236	0.12458	0.14394
5000Ωm	228Ω	0.040797	0.077132	0.044411	0.081726	0.083163	0.097764	0.11289
2500Ωm	114Ω	0.028293	0.058243	0.032477	0.058468	0.053284	0.080072	0.082295
1000Ωm	46Ω	0.020796	0.044252	0.024668	0.050839	0.046482	0.06953	0.066479
500Ωm	23Ω	0.017922	0.039107	0.022139	0.045599	0.062619	0.063934	0.060414
100Ωm	4.5Ω	0.036287	0.031751	0.029981	0.020798	0.041559	0.057786	0.06588
SFFOR								
	Tower Height	MIN		STD		MAX		
Soil Resistivity	Span Length / Footing Resistance	200m	350m	200m	350m	200m	350m	500m
10000Ωm	455Ω	0.017093	0.037	0.021041	0.041016	0.061225	0.060149	0.066441
5000Ωm	228Ω	0.017093	0.037	0.021041	0.041016	0.061225	0.059623	0.066441
2500Ωm	114Ω	0.016737	0.03674	0.021041	0.041322	0.042635	0.059623	0.05626
1000Ωm	46Ω	0.016737	0.036503	0.020641	0.041016	0.042635	0.059106	0.05626
500Ωm	23Ω	0.016407	0.036091	0.020641	0.040732	0.061225	0.059106	0.05626
100Ωm	4.5Ω	0.036287	0.031751	0.029981	0.020606	0.041559	0.057625	0.06588
BFOR								
	Tower Height	MIN		STD		MAX		
Soil Resistivity	Span Length / Footing Resistance	200m	350m	200m	350m	200m	350m	500m
10000Ωm	455Ω	0.043819	0.068363	0.043819	0.067336	0.041131	0.064436	0.077501
5000Ωm	228Ω	0.023704	0.040132	0.02337	0.04071	0.021938	0.038141	0.046449
2500Ωm	114Ω	0.011556	0.021503	0.011436	0.017146	0.010648	0.020449	0.026034
1000Ωm	46Ω	0.004059	0.007749	0.004027	0.009823	0.003847	0.010424	0.010218
500Ωm	23Ω	0.001516	0.003016	0.001498	0.004867	0.001394	0.004828	0.004154
100Ωm	4.5Ω	0	0	0	0.000192	0	0.000161	0

Table G-7: Flashover rates for base scenario with impedance and CIGRE distribution derived from critical current determination simulations

LFOR								
	Tower Height	MIN		STD		MAX		
Soil Resistivity	Span Length / Footing Resistance	200m	350m	200m	350m	200m	350m	500m
10000Ωm	455Ω	0.026971	0.039246	0.037016	0.045938	0.086631	0.09355	0.1012
5000Ωm	228Ω	0.022684	0.027824	0.03274	0.043914	0.080649	0.083491	0.093931
2500Ωm	114Ω	0.017297	0.025719	0.020332	0.03468	0.078969	0.080006	0.082278
1000Ωm	46Ω	0.010693	0.012826	0.020027	0.022321	0.072014	0.070812	0.073507
500Ωm	23Ω	0.010439	0.012494	0.020027	0.021884	0.072421	0.070812	0.073507
100Ωm	4.5Ω	0.009414	0.011527	0.018967	0.020679	0.07161	0.069654	0.073787
SFFOR								
	Tower Height	MIN		STD		MAX		
Soil Resistivity	Span Length / Footing Resistance	200m	350m	200m	350m	200m	350m	500m
10000Ωm	455Ω	0.010964	0.013015	0.023686	0.022321	0.072421	0.071209	0.073507
5000Ωm	228Ω	0.010964	0.013219	0.020332	0.022563	0.069956	0.071209	0.073507
2500Ωm	114Ω	0.010693	0.013015	0.020332	0.022563	0.072421	0.071209	0.073507
1000Ωm	46Ω	0.010693	0.012826	0.020027	0.022321	0.072014	0.070812	0.073507
500Ωm	23Ω	0.010439	0.012494	0.020027	0.021884	0.072421	0.070812	0.073507
100Ωm	4.5Ω	0.009414	0.011527	0.018967	0.020679	0.07161	0.069654	0.073787
BFOR								
	Tower Height	MIN		STD		MAX		
Soil Resistivity	Span Length / Footing Resistance	200m	350m	200m	350m	200m	350m	500m
10000Ωm	455Ω	0.016007	0.026231	0.013329	0.023617	0.014211	0.022341	0.027693
5000Ωm	228Ω	0.01172	0.014605	0.012407	0.021351	0.010693	0.012283	0.020424
2500Ωm	114Ω	0.006604	0.012704	0	0.012117	0.006548	0.008797	0.00877
1000Ωm	46Ω	0	0	0	0	0	0	0
500Ωm	23Ω	0	0	0	0	0	0	0
100Ωm	4.5Ω	0	0	0	0	0	0	0

Table G-8: Flashover rates for base scenario with impedance and LLS SCO distribution derived from critical current determination simulations

LFOR								
	Tower Height	MIN		STD		MAX		
Soil Resistivity	Span Length / Footing Resistance	200m	350m	200m	350m	200m	350m	500m
10000Ωm	455Ω	0.018704	0.040444	0.043971	0.04412	0.062563	0.062493	0.060446
5000Ωm	228Ω	0.018079	0.038419	0.022124	0.044016	0.043483	0.060688	0.058758
2500Ωm	114Ω	0.017129	0.037866	0.021041	0.042363	0.061612	0.060241	0.056875
1000Ωm	46Ω	0.016737	0.036503	0.020641	0.041016	0.060683	0.059106	0.05626
500Ωm	23Ω	0.016407	0.036091	0.020641	0.040469	0.061225	0.059106	0.05626
100Ωm	4.5Ω	0.015106	0.031751	0.019278	0.039024	0.060149	0.057625	0.06588
SFFOR								
	Tower Height	MIN		STD		MAX		
Soil Resistivity	Span Length / Footing Resistance	200m	350m	200m	350m	200m	350m	500m
10000Ωm	455Ω	0.017093	0.03674	0.042779	0.041016	0.061225	0.059623	0.05626
5000Ωm	228Ω	0.017093	0.037	0.021041	0.041322	0.042635	0.059623	0.05626
2500Ωm	114Ω	0.016737	0.03674	0.021041	0.041322	0.061225	0.059623	0.05626
1000Ωm	46Ω	0.016737	0.036503	0.020641	0.041016	0.060683	0.059106	0.05626
500Ωm	23Ω	0.016407	0.036091	0.020641	0.040469	0.061225	0.059106	0.05626
100Ωm	4.5Ω	0.015106	0.031751	0.019278	0.039024	0.060149	0.057625	0.06588
BFOR								
	Tower Height	MIN		STD		MAX		
Soil Resistivity	Span Length / Footing Resistance	200m	350m	200m	350m	200m	350m	500m
10000Ωm	455Ω	0.001611	0.003704	0.001192	0.003104	0.001338	0.00287	0.004186
5000Ωm	228Ω	0.000986	0.001419	0.001083	0.002695	0.000848	0.001065	0.002498
2500Ωm	114Ω	0.000392	0.001126	0	0.001042	0.000387	0.000618	0.000615
1000Ωm	46Ω	0	0	0	0	0	0	0
500Ωm	23Ω	0	0	0	0	0	0	0
100Ωm	4.5Ω	0	0	0	0	0	0	0

Table G-9: Critical Currents for mitigation scenario with simple resistance, shield wire

Positive Stroke Polarity										
	Tower Height	MIN			STD			MAX		
Soil Resistivity	Span Length / Footing Resistance	200m	350m	500m	200m	350m	500m	200m	350m	500m
100Ωm	4.5Ω	1003	1003	1003	1003	1003	1003	1003	1003	1003
500Ωm	23Ω	1003	695	571	695	501	413	719	545	454
1000Ωm	46Ω	637	469	395	467	326	272	572	418	354
2500Ωm	114Ω	394	292	240	268	183	157	442	317	266
5000Ωm	228Ω	275	212	175	174	121	104	366	260	216
10000Ωm	455Ω	201	164	134	115	84	71	316	224	185
Negative Stroke Polarity										
	Tower Height	MIN			STD			MAX		
Soil Resistivity	Span Length / Footing Resistance	200m	350m	500m	200m	350m	500m	200m	350m	500m
100Ωm	4.5Ω	1003	1003	1003	861	787	751	708	660	710
500Ωm	23Ω	409	363	352	306	265	247	486	448	473
1000Ωm	46Ω	265	229	216	196	163	150	274	370	306
2500Ωm	114Ω	164	138	128	116	93	83	344	310	313
5000Ωm	228Ω	123	104	96	83	67	59	206	292	293
10000Ωm	455Ω	99	85	80	64	52	46	188	282	283
Negative Subsequent Stroke Polarity										
	Tower Height	MIN			STD			MAX		
Soil Resistivity	Span Length / Footing Resistance	200m	350m	500m	200m	350m	500m	200m	350m	500m
100Ωm	4.5Ω	1003	1003	1003	518	514	514	407	403	563
500Ωm	23Ω	857	846	1003	396	388	387	385	361	384
1000Ωm	46Ω	539	527	288	262	247	246	348	290	276
2500Ωm	114Ω	336	319	321	154	136	131	334	241	262
5000Ωm	228Ω	261	217	246	100	68	58	330	303	198
10000Ωm	455Ω	208	205	165	70	51	39	327	324	325

Table G-10: Critical Currents for mitigation scenario with simple resistance, top phase wire

Positive Stroke Polarity										
	Tower Height	MIN			STD			MAX		
Soil Resistivity	Span Length / Footing Resistance	200m	350m	500m	200m	350m	500m	200m	350m	500m
100Ωm	4.5Ω	1003	1003	1003	1003	1003	1003	1003	1003	1003
500Ωm	23Ω	1003	695	571	695	501	413	719	545	454
1000Ωm	46Ω	637	469	395	467	326	272	572	418	354
2500Ωm	114Ω	394	292	240	268	183	157	442	317	266
5000Ωm	228Ω	275	212	175	174	121	104	366	260	216
10000Ωm	455Ω	201	164	134	115	84	71	316	224	185
Negative Stroke Polarity										
	Tower Height	MIN			STD			MAX		
Soil Resistivity	Span Length / Footing Resistance	200m	350m	500m	200m	350m	500m	200m	350m	500m
100Ωm	4.5Ω	1003	1003	1003	861	787	751	708	660	710
500Ωm	23Ω	409	363	352	306	265	247	486	448	473
1000Ωm	46Ω	265	229	216	196	163	150	274	370	306
2500Ωm	114Ω	164	138	128	116	93	83	344	310	313
5000Ωm	228Ω	123	104	96	83	67	59	206	292	293
10000Ωm	455Ω	99	85	80	64	52	46	188	282	283
Negative Subsequent Stroke Polarity										
	Tower Height	MIN			STD			MAX		
Soil Resistivity	Span Length / Footing Resistance	200m	350m	500m	200m	350m	500m	200m	350m	500m
100Ωm	4.5Ω	1003	1003	1003	518	514	514	407	403	563
500Ωm	23Ω	857	846	1003	396	388	387	385	361	384
1000Ωm	46Ω	539	527	288	262	247	246	348	290	276
2500Ωm	114Ω	336	319	321	154	136	131	334	241	262
5000Ωm	228Ω	261	217	246	100	68	58	330	303	198
10000Ωm	455Ω	208	205	165	70	51	39	327	324	325

Table G-11: Flashover rates for mitigation scenario with simple resistance and CIGRE distribution derived from critical current determination simulations

LFOR										
	Tower Height	MIN			STD			MAX		
Soil Resistivity	Span Length / Footing Resistance	200m	350m	500m	200m	350m	500m	200m	350m	500m
10000Ωm	455Ω	0.049878	0.066641	0.081668	0.12523	0.18929	0.23391	0.097671	0.10963	0.12145
5000Ωm	228Ω	0.032089	0.046003	0.057762	0.068779	0.1154	0.1475	0.092896	0.099815	0.11453
2500Ωm	114Ω	0.018588	0.028878	0.037249	0.032065	0.059517	0.076272	0.087721	0.095848	0.10559
1000Ωm	46Ω	0.008088	0.01392	0.018264	0.008862	0.021448	0.030116	0.082296	0.087129	0.094945
500Ωm	23Ω	0	0.006816	0.009902	0.00033	0.007421	0.013495	0.078785	0.081573	0.088308
100Ωm	4.5Ω	0	0	0	0	0	0	0.07161	0.069654	0.073787
SFFOR										
	Tower Height	MIN			STD			MAX		
Soil Resistivity	Span Length / Footing Resistance	200m	350m	500m	200m	350m	500m	200m	350m	500m
10000Ωm	455Ω	0	0	0	0	0	0	0.072421	0.070812	0.073507
5000Ωm	228Ω	0	0	0	0	0	0	0.072421	0.06737	0.074066
2500Ωm	114Ω	0	0	0	0	0	0	0.072421	0.070812	0.074066
1000Ωm	46Ω	0	0	0	0	0	0	0.072421	0.07042	0.073507
500Ωm	23Ω	0	0	0	0	0	0	0.072421	0.070812	0.073653
100Ωm	4.5Ω	0	0	0	0	0	0	0.07161	0.069654	0.073787
BFOR										
	Tower Height	MIN			STD			MAX		
Soil Resistivity	Span Length / Footing Resistance	200m	350m	500m	200m	350m	500m	200m	350m	500m
10000Ωm	455Ω	0.049996	0.066937	0.082056	0.13284	0.19645	0.2404	0.02525	0.038814	0.047944
5000Ωm	228Ω	0.032089	0.046093	0.057947	0.076387	0.12248	0.15404	0.020475	0.032445	0.040468
2500Ωm	114Ω	0.018588	0.028878	0.037249	0.039755	0.066671	0.082812	0.015301	0.025036	0.031529
1000Ωm	46Ω	0.008088	0.01392	0.018264	0.016552	0.028676	0.036657	0.009875	0.016709	0.021438
500Ωm	23Ω	0	0.006816	0.009902	0.00802	0.014649	0.020036	0.006364	0.010761	0.014655
100Ωm	4.5Ω	0	0	0	0	0	0	0	0	0

Table G-12: Flashover rates for mitigation scenario with simple resistance and LLS Scotland distribution derived from critical current determination simulations

LFOR										
	Tower Height	MIN			STD			MAX		
Soil Resistivity	Span Length / Footing Resistance	200m	350m	500m	200m	350m	500m	200m	350m	500m
10000Ωm	455Ω	0.00945	0.01382	0.01944	0.03123	0.05180	0.06323	0.06479	0.06671	0.06733
5000Ωm	228Ω	0.00491	0.00851	0.01228	0.01677	0.03379	0.04056	0.06372	0.04256	0.07164
2500Ωm	114Ω	0.00207	0.00429	0.00659	0.00817	0.02010	0.02439	0.06276	0.06265	0.06873
1000Ωm	46Ω	0.00054	0.00131	0.00206	0.00362	0.01061	0.01277	0.06197	0.06038	0.05897
500Ωm	23Ω	0.00000	0.00041	0.00075	0.00255	0.00799	0.00902	0.06160	0.05996	0.06432
100Ωm	4.5Ω	0.00000	0.00000	0.00000	0.00701	0.00654	0.00674	0.06015	0.05763	0.06588
SFFOR										
	Tower Height	MIN			STD			MAX		
Soil Resistivity	Span Length / Footing Resistance	200m	350m	500m	200m	350m	500m	200m	350m	500m
10000Ωm	455Ω	0.00000	0.00000	0.00000	0.00217	0.00681	0.00769	0.06123	0.05911	0.05626
5000Ωm	228Ω	0.00000	0.00000	0.00000	0.00217	0.00691	0.00686	0.06123	0.03701	0.06345
2500Ωm	114Ω	0.00000	0.00000	0.00000	0.00206	0.00681	0.00686	0.06123	0.05911	0.06345
1000Ωm	46Ω	0.00000	0.00000	0.00000	0.00206	0.00671	0.00686	0.06123	0.05860	0.05626
500Ωm	23Ω	0.00000	0.00000	0.00000	0.00206	0.00671	0.00686	0.06123	0.05911	0.06289
100Ωm	4.5Ω	0.00000	0.00000	0.00000	0.00701	0.00654	0.00674	0.06015	0.05763	0.06588
BFOR										
	Tower Height	MIN			STD			MAX		
Soil Resistivity	Span Length / Footing Resistance	200m	350m	500m	200m	350m	500m	200m	350m	500m
10000Ωm	455Ω	0.00945	0.01382	0.01944	0.02906	0.04499	0.05554	0.00357	0.00761	0.01107
5000Ωm	228Ω	0.00491	0.00851	0.01228	0.01460	0.02688	0.03370	0.00250	0.00555	0.00819
2500Ωm	114Ω	0.00207	0.00429	0.00659	0.00611	0.01329	0.01753	0.00153	0.00354	0.00528
1000Ωm	46Ω	0.00054	0.00131	0.00206	0.00156	0.00390	0.00591	0.00074	0.00178	0.00271
500Ωm	23Ω	0.00000	0.00041	0.00075	0.00048	0.00128	0.00216	0.00037	0.00086	0.00143
100Ωm	4.5Ω	0.00000	0.00000	0.00000	0.00000	0.00000	0.00000	0.00000	0.00000	0.00000

G.2: MONTE-CARLO METHOD

Table G-13: Flashover ratios for base scenario with footing resistance and CIGRE distribution derived from Monte-Carlo simulations

N/F SFFO								
	Tower Height	MIN		STD		MAX		
Soil Resistivity	Span Length / Footing Resistance	200m	350m	200m	350m	200m	350m	500m
10000Ωm	455Ω	26.7	27.3	30.8	27.2	55.7	54.6	55.3
5000Ωm	228Ω	23.9	24.4	30.5	29.8	55.5	54.4	55.5
2500Ωm	114Ω	26.8	24.8	30.5	27.4	55.3	54.6	55.9
1000Ωm	46Ω	26.9	25.2	25.141	27.5	55.5	54.9	55.7
500Ωm	23Ω	26.9	25	27.2	26.6	55.9	54.8	55.9
100Ωm	4.5Ω	26.3	26.544	29.9	24.8	55.9	54.4	55.4
N/F BFO								
	Tower Height	MIN		STD		MAX		
Soil Resistivity	Span Length / Footing Resistance	200m	350m	200m	350m	200m	350m	500m
10000Ωm	455Ω	21.7	30.9	21.6	30.8	18	22.5	24.1
5000Ωm	228Ω	3.9	8.4	8.7	19.9	7	17	19.7
2500Ωm	114Ω	3.3	2.7	3.3	9.9	2.7	5.1	6.7
1000Ωm	46Ω	0	0.3	0	0.7	0.3	0.6	1.3
500Ωm	23Ω	0	0	0	0.1	0	0.1	0.2
100Ωm	4.5Ω	0	0	0	0	0	0	0

Table G-14: Flashover ratios for base scenario with footing resistance and LLS SCO distribution derived from Monte-Carlo simulations

N/F SFFO								
	Tower Height	MIN		STD		MAX		
Soil Resistivity	Span Length / Footing Resistance	200m	350m	200m	350m	200m	350m	500m
10000Ωm	455Ω	31.7	30.6	39.337	33.1	58.797	57.7	59.9
5000Ωm	228Ω	29.358	30	35.7	38	55.3	57.6	58
2500Ωm	114Ω	31.75	27.9	35.7	37.9	55.5	57.3	60.2
1000Ωm	46Ω	30.446	28.3	29.9	36	55.355	58.5	60
500Ωm	23Ω	28.8	28.4	29.6	37.3	53.914	57.8	60
100Ωm	4.5Ω	27.965	28.778	35	35.3	57.238	57.4	60
N/F BFO								
	Tower Height	MIN		STD		MAX		
Soil Resistivity	Span Length / Footing Resistance	200m	350m	200m	350m	200m	350m	500m
10000Ωm	455Ω	5.2	11.3	3.1056	10.1	3.5635	6.6	7.5
5000Ωm	228Ω	2.3591	5.4	2	5.4	2.7	3.8	4.5
2500Ωm	114Ω	1.2746	1.6	0.7	1.6	0.3	1.3	2.2
1000Ωm	46Ω	0	0.9	0	0.3	0.11274	0.5	0
500Ωm	23Ω	0	0	0	0	0	0	0
100Ωm	4.5Ω	0	0	0	0	0	0	0

Table G-15: Flashover ratios for base scenario with footing impedance and CIGRE distribution derived from Monte-Carlo simulations

N/F SFFO								
	Tower Height	MIN		STD		MAX		
Soil Resistivity	Span Length / Footing Resistance	200m	350m	200m	350m	200m	350m	500m
10000Ωm	455Ω	27.2	26.4	0	27.6	26.5	0	56.8
5000Ωm	228Ω	26.8	26.4	0	27.6	26	0	56.8
2500Ωm	114Ω	26.8	26.1	0	27.6	26	0	56.6
1000Ωm	46Ω	26.8	26.1	0	27.6	26.3	0	56.7
500Ωm	23Ω	26.3	26.1	0	27	26.3	0	56.1
100Ωm	4.5Ω	26.3	26.1	0	27	26.3	0	55.3
N/F BFO								
	Tower Height	MIN		STD		MAX		
Soil Resistivity	Span Length / Footing Resistance	200m	350m	200m	350m	200m	350m	500m
10000Ωm	455Ω	0.1	0.1	0	0	0.1	0	0
5000Ωm	228Ω	0	0.1	0	0	0.1	0	0
2500Ωm	114Ω	0	0	0	0	0.1	0	0
1000Ωm	46Ω	0	0	0	0	0	0	0
500Ωm	23Ω	0	0	0	0	0	0	0
100Ωm	4.5Ω	0	0	0	0	0	0	0

Table G-16: Flashover rates for base scenario with footing resistance and CIGRE distribution derived from Monte-Carlo simulations

LFOR								
	Tower Height	MIN		STD		MAX		
Soil Resistivity	Span Length / Footing Resistance	200m	350m	200m	350m	200m	350m	500m
10000Ωm	455Ω	1.9996	2.7675	2.0378	2.4972	2.0436	2.4024	2.539
5000Ωm	228Ω	0.52548	0.90824	0.9858	1.8938	1.1452	1.9524	2.1814
2500Ωm	114Ω	0.50031	0.44655	0.54586	0.83211	0.79329	0.98407	1.1244
1000Ωm	46Ω	0.23158	0.25485	0.23056	0.29611	0.59921	0.61944	0.68285
500Ωm	23Ω	0.23158	0.22948	0.24985	0.24326	0.57739	0.57201	0.59625
100Ωm	4.5Ω	0.22739	0.23992	0.27166	0.22468	0.57739	0.5667	0.57462
SFFOR								
	Tower Height	MIN		STD		MAX		
Soil Resistivity	Span Length / Footing Resistance	200m	350m	200m	350m	200m	350m	500m
10000Ωm	455Ω	0.23049	0.24825	0.27682	0.24302	0.57607	0.56802	0.57423
5000Ωm	228Ω	0.20752	0.22341	0.27651	0.27137	0.57449	0.56643	0.57528
2500Ωm	114Ω	0.23126	0.22643	0.27682	0.23917	0.57317	0.56828	0.57819
1000Ωm	46Ω	0.23158	0.23039	0.23056	0.24488	0.57475	0.57053	0.57687
500Ωm	23Ω	0.23158	0.22948	0.24985	0.23006	0.57739	0.5696	0.57995
100Ωm	4.5Ω	0.22739	0.23992	0.27166	0.22468	0.57739	0.5667	0.57462
BFOR								
	Tower Height	MIN		STD		MAX		
Soil Resistivity	Span Length / Footing Resistance	200m	350m	200m	350m	200m	350m	500m
10000Ωm	455Ω	1.7692	2.5192	1.761	2.2542	1.4675	1.8344	1.9648
5000Ωm	228Ω	0.31796	0.68483	0.70929	1.6224	0.57069	1.386	1.6061
2500Ωm	114Ω	0.26904	0.22013	0.26904	0.59294	0.22013	0.41579	0.54624
1000Ωm	46Ω	0	0.024458	0	0.051232	0.024458	0.048917	0.10599
500Ωm	23Ω	0	0	0	0.013193	0	0.002412	0.016306
100Ωm	4.5Ω	0	0	0	0	0	0	0

Table G-17: Flashover rates for base scenario with footing resistance and LLS SCO distribution derived from Monte-Carlo simulations

LFOR								
	Tower Height	MIN		STD		MAX		
Soil Resistivity	Span Length / Footing Resistance	200m	350m	200m	350m	200m	350m	500m
10000Ωm	455Ω	0.62542	1.0463	0.4048	0.60898	0.64174	0.74872	0.79941
5000Ωm	228Ω	0.37669	0.59801	0.36004	0.59801	0.79329	0.65462	0.79024
2500Ωm	114Ω	0.30941	0.29491	0.30348	0.29491	0.59921	0.56851	0.62413
1000Ωm	46Ω	0.237	0.26534	0.24028	0.32165	0.57637	0.55201	0.55023
500Ωm	23Ω	0.23099	0.22908	0.26058	0.31472	0.56193	0.53074	0.55023
100Ωm	4.5Ω	0.23705	0.23632	0.27847	0.30008	0.51267	0.52779	0.54996
SFFOR								
	Tower Height	MIN		STD		MAX		
Soil Resistivity	Span Length / Footing Resistance	200m	350m	200m	350m	200m	350m	500m
10000Ωm	455Ω	0.26071	0.25371	0.31869	0.28046	0.52335	0.52944	0.55023
5000Ωm	228Ω	0.25194	0.29433	0.29538	0.29433	0.57317	0.52837	0.53252
2500Ωm	114Ω	0.26214	0.23556	0.28368	0.23556	0.57475	0.52532	0.55103
1000Ωm	46Ω	0.237	0.22925	0.24028	0.3079	0.5723	0.5354	0.55023
500Ωm	23Ω	0.23099	0.22908	0.26058	0.31472	0.56193	0.53074	0.55023
100Ωm	4.5Ω	0.23705	0.23632	0.27847	0.30008	0.51267	0.52779	0.54996
BFOR								
	Tower Height	MIN		STD		MAX		
Soil Resistivity	Span Length / Footing Resistance	200m	350m	200m	350m	200m	350m	500m
10000Ωm	455Ω	0.36471	0.79255	0.086112	0.32852	0.11839	0.21928	0.24918
5000Ωm	228Ω	0.12476	0.30368	0.064661	0.30368	0.22013	0.12625	0.25772
2500Ωm	114Ω	0.047277	0.059346	0.019801	0.059346	0.024458	0.043192	0.073094
1000Ωm	46Ω	0	0.036084	0	0.013747	0.004064	0.016612	0
500Ωm	23Ω	0	0	0	0	0	0	0
100Ωm	4.5Ω	0	0	0	0	0	0	0

Table G-18: Flashover rates for base scenario with footing impedance and CIGRE distribution derived from Monte-Carlo simulations

LFOR								
	Tower Height	MIN		STD		MAX		
Soil Resistivity	Span Length / Footing Resistance	200m	350m	200m	350m	200m	350m	500m
10000Ωm	455Ω	0.23624	0.23052	0.24822	0.23052	0.58386	0.58605	0.58605
5000Ωm	228Ω	0.23126	0.23052	0.24822	0.22599	0.58386	0.58386	0.58386
2500Ωm	114Ω	0.23126	0.22537	0.24885	0.22599	0.58281	0.58281	0.58281
1000Ωm	46Ω	0.23126	0.22537	0.24885	0.22685	0.5832	0.5832	0.5832
500Ωm	23Ω	0.22739	0.22537	0.244	0.22685	0.57924	0.57924	0.57924
100Ωm	4.5Ω	0.22739	0.22537	0.244	0.22685	0.57396	0.57396	0.57396
SFFOR								
	Tower Height	MIN		STD		MAX		
Soil Resistivity	Span Length / Footing Resistance	200m	350m	200m	350m	200m	350m	500m
10000Ωm	455Ω	0.23383	0.22825	0.24822	0.22825	0.58386	0.58122	0.58122
5000Ωm	228Ω	0.23126	0.22825	0.24822	0.22483	0.58386	0.58386	0.58386
2500Ωm	114Ω	0.23126	0.22537	0.24885	0.22483	0.58281	0.58281	0.58281
1000Ωm	46Ω	0.23126	0.22537	0.24885	0.22685	0.5832	0.5832	0.5832
500Ωm	23Ω	0.22739	0.22537	0.244	0.22685	0.57924	0.57924	0.57924
100Ωm	4.5Ω	0.22739	0.22537	0.244	0.22685	0.57396	0.57396	0.57396
BFOR								
	Tower Height	MIN		STD		MAX		
Soil Resistivity	Span Length / Footing Resistance	200m	350m	200m	350m	200m	350m	500m
10000Ωm	455Ω	0.002412	0.002271	0	0.002271	0	0.004825	0.004825
5000Ωm	228Ω	0	0.002271	0	0.00116	0	0	0
2500Ωm	114Ω	0	0	0	0.00116	0	0	0
1000Ωm	46Ω	0	0	0	0	0	0	0
500Ωm	23Ω	0	0	0	0	0	0	0
100Ωm	4.5Ω	0	0	0	0	0	0	0

Table G-19: Flashover ratios for mitigation scenario with simple resistance and CIGRE distribution derived from Monte-Carlo simulations

F/N SFFO													
	Tower Height	AR			Y			CP			UW		
Soil Resistivity	Span Length Footing Resistance	200m	350m	500m	200m	350m	500m	200m	350m	500m	200m	350m	500m
10000Ωm	455Ω	12.7	12.3	12.8	43.2	41.4	43.3	56.4	54.8	56.7	55.8	54.8	55.7
5000Ωm	228Ω	12.9	10.8	12.8	43.8	43.7	44.5	56.6	56.6	56.6	56.2	53.9	55.6
2500Ωm	114Ω	12.8	11.4	13.1	41.2	40.5	43.3	56.4	56.4	56.4	56.1	55.2	56
1000Ωm	46Ω	13.3	12.8	12.8	44.6	43.3	44.2	56.3	56.3	56.3	56.2	54.8	56
500Ωm	23Ω	13.2	13.2	12.8	43.2	45.8	43.4	56.5	56.5	56.5	56.3	54.6	56
100Ωm	4.5Ω	12.7	13.2	12.8	45.8	43.6	43.8	56.2	54.5	54.5	56.1	55	55.6
F/N BFO													
	Tower Height	AR			Y			CP			UW		
Soil Resistivity	Span Length Footing Resistance	200m	350m	500m	200m	350m	500m	200m	350m	500m	200m	350m	500m
10000Ωm	455Ω	2.3	3.6	4.9	7.3	17.4	20.7	0	0.2	0.3	4.4	5.2	13.2
5000Ωm	228Ω	1.1	1.7	2.6	2.4	6.9	9.3	0	0	0.3	2	1.8	5.5
2500Ωm	114Ω	0.2	0.3	1	0.9	2.8	2.7	0	0	0	0.5	0.5	2.4
1000Ωm	46Ω	0	0	0.1	0	0.3	0	0	0	0	0	0	0.4
500Ωm	23Ω	0	0	0	0	0	0	0	0	0	0	0	0
100Ωm	4.5Ω	0	0	0	0	0	0	0	0	0	0	0	0

Table G-20: Flashover rates for mitigation scenario with simple resistance and CIGRE distribution derived from Monte-Carlo simulations

LFOR													
	Tower Height	AR			Y			CP			UW		
Soil Resistivity	Span Length Footing Resistance	200m	350m	500m	200m	350m	500m	200m	350m	500m	200m	350m	500m
10000Ωm	455Ω	0.27397	0.37732	0.4866	0.92161	1.1595	1.6962	0.58096	0.58617	0.60792	0.93519	0.99004	1.653
5000Ωm	228Ω	0.17746	0.17866	0.29909	0.70583	0.99552	0.93084	0.58228	0.58228	0.607	0.74216	0.69499	1.0243
2500Ωm	114Ω	0.098356	0.091481	0.17062	0.44369	0.48126	0.48923	0.58096	0.58096	0.58096	0.61921	0.61077	0.77451
1000Ωm	46Ω	0.090416	0.087763	0.092736	0.40153	0.39707	0.4034	0.5803	0.5803	0.5803	0.57911	0.56711	0.61146
500Ωm	23Ω	0.089756	0.086158	0.087116	0.39551	0.40022	0.3824	0.57896	0.57896	0.57896	0.57977	0.56579	0.57885
100Ωm	4.5Ω	0.086456	0.086158	0.087116	0.39781	0.39128	0.38111	0.58394	0.56736	0.56736	0.57871	0.56869	0.57594
SFFOR													
	Tower Height	AR			Y			CP			UW		
Soil Resistivity	Span Length Footing Resistance	200m	350m	500m	200m	350m	500m	200m	350m	500m	200m	350m	500m
10000Ωm	455Ω	0.086456	0.083816	0.087116	0.38311	0.37134	0.38895	0.58096	0.56987	0.58347	0.57647	0.56609	0.57687
5000Ωm	228Ω	0.087776	0.074669	0.087116	0.3878	0.37497	0.39785	0.58228	0.58228	0.58254	0.57911	0.56325	0.57594
2500Ωm	114Ω	0.087116	0.079056	0.089096	0.3649	0.36426	0.38672	0.58096	0.58096	0.58096	0.57845	0.57001	0.57885
1000Ωm	46Ω	0.090416	0.087763	0.087116	0.40153	0.38408	0.4034	0.5803	0.5803	0.5803	0.57911	0.56711	0.57885
500Ωm	23Ω	0.089756	0.086158	0.087116	0.39551	0.40022	0.3824	0.57896	0.57896	0.57896	0.57977	0.56579	0.57885
100Ωm	4.5Ω	0.086456	0.086158	0.087116	0.39781	0.39128	0.38111	0.58394	0.56736	0.56736	0.57871	0.56869	0.57594

BFOR													
	Tower Height	AR			Y			CP			UW		
Soil Resistivity	Span Length Footing Resistance	200m	350m	500m	200m	350m	500m	200m	350m	500m	200m	350m	500m
10000Ωm	455Ω	0.18751	0.2935	0.39949	0.5385	0.78817	1.3072	0	0.016306	0.024458	0.35872	0.42394	1.0762
5000Ωm	228Ω	0.089681	0.10399	0.21197	0.31803	0.62055	0.533	0	0	0.024458	0.16306	0.13174	0.4484
2500Ωm	114Ω	0.01124	0.012425	0.081528	0.078783	0.117	0.10252	0	0	0	0.040764	0.040764	0.19567
1000Ωm	46Ω	0	0	0.00562	0	0.012994	0	0	0	0	0	0	0.032611
500Ωm	23Ω	0	0	0	0	0	0	0	0	0	0	0	0
100Ωm	4.5Ω	0	0	0	0	0	0	0	0	0	0	0	0